

UNIVERSITY OF
BIRMINGHAM

Characterisation and Mitigation of Radar Interference in Automotive Applications

Anum Ahmed Pirkani

The thesis submitted to the University of Birmingham

for the degree of

DOCTOR OF PHILOSOPHY

School of Electronic, Electrical and System Engineering
College of Engineering and Physical Sciences
The University of Birmingham
August 2023

UNIVERSITY OF
BIRMINGHAM

University of Birmingham Research Archive

e-theses repository

This unpublished thesis/dissertation is copyright of the author and/or third parties. The intellectual property rights of the author or third parties in respect of this work are as defined by The Copyright Designs and Patents Act 1988 or as modified by any successor legislation.

Any use made of information contained in this thesis/dissertation must be in accordance with that legislation and must be properly acknowledged. Further distribution or reproduction in any format is prohibited without the permission of the copyright holder.

This thesis is dedicated to
‘HOPE’

“We must accept finite disappointment, but never lose infinite hope.”
Martin Luther King, Jr.

‘Your work is going to fill a large part of your life, and the only way to be truly satisfied is to do what you believe is great work. And the only way to do great work is to love what you do. If you haven’t found it yet, keep looking. Don’t settle.’ Steve Jobs.

Abstract

Radar has emerged as an integral sensor for imaging and scene perception to achieve full situational awareness for vehicle automation. The increase in radar penetration rate and a limited spectrum availability for automotive uses have given rise to coexistence problems, where radars directly or indirectly interfere with each other. Interference causes a degradation in the radar performance, particularly an increased noise (interference) floor, making it difficult to detect, identify, and classify targets accurately, as well as perceive the vehicle's surroundings which is essential for trajectory estimation and path planning applications. This might lead to potential accidents especially in dense road conditions.

The work presented in this thesis investigates the mutual interference in 77 GHz millimetre-wave frequency modulated continuous wave radar to develop suitable mitigation strategies without a detrimental effect on the performance of the radar. A mathematical model is developed to systematically assess and quantify the performance of radars in an interference background. Various types of interference expected in automotive scenarios are first classified, such as fast-chirp, slow-chirp, synchronous, and asynchronous. The appearance and impact of interference are then evaluated at each stage of the victim radar's signal processing and analysed in the time, range, range-Doppler, and range-azimuth profiles.

The characteristics of interference in each profile are exploited to develop appropriate mitigation techniques along with their comparative performance analysis. For pre-detection mitigation, waveform randomisation and spectral windowing – inherently used in radar processing – are discussed to minimise the impact of interference. Techniques to detect interference and estimate the waveform parameters of the interfering radars are developed

using the radar data from real-road measurements, which are used for cognitive interference mitigation. In the spatial domain, adaptive digital beamforming is discussed to suppress interference for various radar configurations and penetration rates. In imaging techniques, Doppler beam sharpening is developed to significantly reduce the impact of interference with complete removal of interference from the radar's field of view in some cases.

A comprehensive statistical evaluation of interference and its comparison with the additive white Gaussian noise (AWGN) have demonstrated that most types of interference have statistics comparable to those of AWGN. Therefore, the currently existing detection techniques remain valid for target detection in an interference background.

Lastly, an experimentally verified holistic end-to-end system level radar simulator is developed to model, evaluate, and optimise radar performance in diverse scenarios with various traffic, roadside, and interference density conditions.

Keywords: 77 GHz, adaptive beamforming, adaptive digital beamforming, adaptive signal processing, automotive applications, automotive radar, automotive sensors, autonomous vehicles, beamforming, clutter modelling, cognitive interference mitigation, COSMOS, COSMOS dataset, DBS, digital beamforming, Doppler beam sharpening, environment modelling, extended target, FMCW radar, FMCW-MIMO radar, holistic simulator, INR, INR heatmap, interference correlation, interference distribution, interference mitigation, interference modelling, interference statistics, interference parameter estimation, interference suppression, I/Q channels, LCMV beamformer, low pass filter, millimetre wave communication, millimetre wave radar, MIMO-DBS, MIMO radar, mutual interference, NRMSE map, phased array, power detection, probability density function, probability of detection, radar data cube, radar detection, radar-environment interaction, radar interference, radar performance estimation, radar signal processing, radar simulator, randomisation, receiver detection curves, signal to interference ratio, signal to noise plus interference ratio, SINR, SIR, SNR, spatial filters, spatial suppression, statistical analysis, types of interference, windowing.

Declaration

I hereby declare that except where specific reference is made to the work of others, the contents of this dissertation are original and have not been submitted in whole or in part for consideration for any other degree or qualification in this, or any other university. This dissertation is my own work and contains nothing that is the outcome of work done in collaboration with others, except as specified in the text and acknowledgements.

Some part of this work has been reproduced from the author's publications along with necessary references where applicable.

This dissertation contains a maximum of 85961 words including appendices, bibliography, footnotes, tables, and equations, 161 figures, and 41 tables.

Anum Pirkani

August 2023

Acknowledgements

The doctorate journey has been a wonderful experience, full of challenges, sleepless nights, silent screams, and digging deep into the research material. The motivation behind all was an amazing support system.

First, I want to thank Prof. Mikhail Cherniakov for believing in me far beyond what I believed in myself. He provided me with an opportunity to work in the MISL group, which was a remarkable experience for me. His patient and thorough research style always inspired me and pushed me to do more. Most of the achievements in the presented work were only possible with his insightful comments and support. As a 'fresh' researcher, Prof. Cherniakov's supervision and exceptional teaching style inspired my research interest in automotive radars.

I also pay my utmost gratitude to Prof. Marina Gashinova, my mentor. With her motivation and guidance, this project materialised. Prof. Gashinova has always used her in-depth knowledge and experience to lead me towards developing the relevant soft and hard skills that will make me an independent researcher and professional down the line. I am extra thankful to her for teaching me the art of writing papers and how to think critically and introspectively. Beyond the appreciated mentoring and constructive advice, she always took the time to discuss my ambitions and career goals. Her guidance helped me grow personally and professionally, and made my doctorate journey full of learning opportunities, pushing me to think outside the box.

Due to the inspiring mentorship and guidance of Prof. Cherniakov and Prof. Gashinova, my fondness for radar systems developed much more than it was before the doctorate program. They helped me appreciate the beauty and sophistication of radars. A new emotion grew within me on how to do anything by loving it, intending to educate myself instead of doing it for the sake of completing it and getting good grades. I am additionally thankful to them for helping me polish the presented work in this dissertation.

Special thanks to Dr Norouzian for guiding me throughout the project, overseeing my regular progress, keeping a check on me when I got distracted, and helping me develop the patience required for research activities.

I am also grateful to Innovate UK for funding the project and to the project partners Jaguar Land Rover and HORIBA MIRA for their insightful comments throughout the work.

I want to pay my huge and humblest gratitude to Dr Graham Brooker and Dr Donya Jasteh for being my external examiners and for their insightful discussion during the viva and thorough feedback on the thesis. It was an honour to defend my research work in front of them.

Through my doctorate, I learned much from Dr Pooni, Dr Cassidy, Dr Daniel, and Dr Hoare. The field trials were extra-exciting yet full of challenges and learning grounds due to their expertise. They have always been extra patient, calm, and responsive to my plethora of questions directed their way. I'll always appreciate the tips and tricks given by Dr Hoare for thesis writing.

I would also pay my regards and gratitude to Muge, Dr Antoniou, Dr Jahangir, Dr Pooni, Elijah, Samina, and my family for regularly checking in on my thesis progress and giving motivation along the way.

Mr. Yates has been one of the biggest blessings at MISL for keeping me sane during Covid times, regular health checks, tips and tricks to survive and excel in a foreign country, and motivation during the thesis writing phase. My doctorate journey would not have been the same without him.

I have met amazing people and friends in MISL, Muge, Yang, Elijah, Ana, Shahrazad, Xiofei, Emidio, Dillon, Ali, Sam, and Ilaria. They have been highly cooperative and fun to work with. Many mornings turned bright after a fantastic smile and wave from Mandy. Special thanks to Muge and Elijah for listening to my long stories.

I am incredibly thankful to my RF and Microwave gurus, Prof. Peter Gardner, Sir Umar, and Sir Hassan, for providing me with an opportunity to study and work in this domain and for making me love my work.

When I came to the UK, I was introduced with a unique kind of nobility and kindness after meeting Prof. Gardner, that I had not experienced before. He has been a huge inspiration to me, and I wish down the line, I also inspire people the same way he inspired me.

I am grateful for the prayers and unconditional support of my parents, aunt, and siblings, who have always been there, day and night, keeping me calm and guiding me to be the best version of myself. My mother put in additional efforts trying to solve my formatting issues to making my MATLAB scripts work 'wirelessly,' being my head secretary, keeping a check on all the deadlines, bearing with my 'not-nice' behaviour, and calming me with her magical voice. My father steered me through life and helped me look past my mistakes. My aunt somehow made me believe in miracles when her 'impossible' prayers were actually successful. My brother Moiz has been an incredible support and a source of strength that allowed me to live wildly. From supplying delicious homemade food to setting special diet plans to stay healthy and fit, to being a motivator and a personal advisor, he made my time in the UK easy. I thoroughly enjoyed the tech/ non-tech discussions with Yasir, which gave me food for thought and helped me understand radars and life from a different and broader perspective. Ayesha, 'my anchor,' helped me understand and accept myself the way I am and led me toward the answers to my 'complicated' thoughts. The discussions with her always enlightened my brain. Samina was always there for me when she needed me more, gave me reality checks, motivated me, and made me smile when I didn't want to. To my family, thank you for your tremendous support through the challenges of work and life, for bearing my tantrums, and for never giving up on me. I love you all tremendously.

My friends have been amazing, who were with me throughout or not. My grandmother (Nano) was my first friend. I still miss my late night talks with her. If I could time travel, I would go back to the time when she was alive and spend more quality time with her. Special thanks to Zile Huma, Rabeea, Sadia, Aatqa, Amna, Amina, Sundus, Saba, Chaitali, Fatima, and more. Chaitali helped me settle in the UK and cooked amazing food to make me happy. She taught me basic skills such as using the Google Maps and buses in the UK. Zile Huma, my buddu, is a guardian angel to me and one of those people who taught me a lot about life. I know if I want honest and unbiased advice, she is one of the few people whom I can trust blindly.

My acknowledgements would not be complete without mentioning Dr Saad who has been a huge support to me and my family after my burn accident. He is the example I often give to people saying that doctors can actually be nice.

Finally, I want to pay my respect and gratitude to the people who have played a significant role during different phases of my life. My grandmother (Nano), Tooba, Ma'am Mushkbar, Zile Huma, Javaria, Dr Saad, a stranger at Khanpur Lake, Sir Umar, Prof. Gardner, Prof. Cherniakov, and Prof. Gashinova. Without them, I would not be where I am.

I want to thank all those people who have been kind to me and supported and motivated me through the challenges of life.

Studying at UoB has been by far the best experience of my life. It undoubtedly broadened the horizons of my mind. I am especially grateful to the faculty of the Electrical Engineering Department for providing a congenial environment to conduct research activities.

Last but not least, I hope Almighty Allah will give me the strength and resilience to do much more, beyond my wildest imagination, be a kind human being, and do something worthy and pure for the people and the universe.

Table of Contents

ABSTRACT ..... **IV**
ACKNOWLEDGEMENTS ..... **VII**
LIST OF FIGURES ..... **XVIII**
LIST OF TABLES ..... **XXX**
LIST OF PUBLICATIONS AND PRESENTATIONS ..... **XXXIII**
PROJECT DATASETS AT THE UNIVERSITY OF BIRMINGHAM REPOSITORY ..... **XXXVI**
NOMENCLATURE ..... **XXXVII**
LIST OF VARIABLES ..... **XLI**
CHAPTER 1. OVERVIEW **1**
1.1 Problem Statement 1
1.2 Challenges and Limitations 5
1.3 Objectives and Contributions 6
1.4 Automotive Radar and Environment Simulator 8
1.5 Glossary 9
1.6 Thesis Organisation 12
CHAPTER 2. TRENDS IN AUTOMOTIVE RADAR **14**
2.1 Brief History of Radar 16
2.2 Types of Radar 19
2.2.1 Bistatic vs Monostatic radar 20
2.2.2 Pulse and Continuous Wave Radar 21
2.3 Automotive Radars 21
2.3.1 Operational Spectrum 23
2.3.2 Modulation Schemes 25
I. FMCW 25
II. PMCW 26
2.3.3 MIMO Radar 28
I.Signal Orthogonality 29
II.Beamforming 30
2.3.4 Signal Processing 30
I.Transmit Chirp Signal 31
II.Radar Data Cube and Processing 32
III.Digital Beamforming in MIMO Radar 33
IV.Windowing 34
V.Target Detection 36

2.4 Automotive Radar Interference - Introduction 37
2.5 Literature Survey on Automotive Radar Interference 38
2.5.1 Industry-Led Projects 40
2.5.2 Radar Simulators 40
2.5.3 Interference Detection and Mitigation 41
I.Interference Detection and Parameter Estimation 41
II.Interference Mitigation 42
III.Interference Mitigation Based on Sense and Avoid 46
IV.Interference Mitigation Using Scalable Waveform Parameters 46
V.Interference Mitigation in the Spatial Domain 46
2.6 Interference Mitigation in the Temporal Domain 48
2.7 Summary 51
CHAPTER 3. AUTOMOTIVE RADAR INTERFERENCE 53
3.1 FMCW Radar Overview 54
3.2 Analytical Study of Interference 57
3.3 Effect of the Low Pass Filter on Interference Characteristics 61
3.3.1 Low Pass Filter Characteristics 64
3.3.2 Probability of Detection 67
3.3.3 Effect of Interference Mitigation 68
3.4 Interference Analysis in the Frequency Domain 69
3.4.1 Range Profile of Received Signal 69
3.4.2 Time-Frequency Analysis of Interference 71
3.4.3 Range-Doppler Profile of Received Signal 74
3.5 Interference Analysis in the Spatial Domain 75
3.6 Interference Classification 78
3.6.1 Types of Interference on the Basis of Sweep Time 79
3.6.2 Types of Interference on the Basis of Sweep Rate 81
I.Synchronous Interference 81
II.Semi Synchronous Interference 82
III.Asynchronous Interference 83
3.7 Interference Representation in Each Domain – Use Cases 84
3.8 Self Interference 85
3.9 Multiple Interference Sources 88
3.10 Summary 90

CHAPTER 4. POWER AND STATISTICAL ANALYSIS OF INTERFERENCE……93
4.1 State of the Art 94
4.2 Radar Model for Statistical Analysis 95
4.3 Power Budget Analysis of Interference 97
4.4 Statistical Characteristics of Interference 100
4.4.1 Types of Interference 101
4.4.2 Interference Correlation 102
4.4.3 Interference Power Along Processing Stages 103
4.4.4 Interference Statistical Distribution 105
4.4.5 Interference Mean and Standard Deviation 109
4.4.6 Case Studies 110
4.4.7 Effect of Coherent Processing Interval 113
4.5 Detection in an Interference Background 115
4.6 Summary 118
CHAPTER 5. MITIGATION OF RADAR INTERFERENCE……..... 120
5.1 Interference Detection 122
5.1.1 Power Detection 122
5.1.2 Radar in Listening Mode 125
5.1.3 Short Time Fourier Transform 126
5.2 Interference Parameter Estimation 127
5.2.1 Methodology 127
I.Measurement Setup 128
II.Interference Amplitude Characteristics 130
III.Interference Parameters 134
5.3 Cognitive Interference Avoidance/ Mitigation 139
5.3.1 Impact of Interference 139
5.3.2 Methodology 141
5.4 Windowing for Interference Mitigation 142
5.5 Randomisation for Interference Reduction 146
5.5.1 Randomisation Parameters 146
5.5.2 Effect of Randomisation on Interference Statistics 147
5.5.3 Performance Analysis 149
5.5.4 Detection Characteristics 152
5.6 Summary 153

CHAPTER 6. MITIGATION IN THE SPATIAL DOMAIN..... 155
6.1 Interference in the Spatial Domain..... 156
6.2 Mathematical Model 158
6.2.1 Echo Signal Reception 159
6.2.2 Interference Reception 159
6.3 Interference in Single Channel and Dual Channel Receivers 161
6.4 Interference in MIMO and Full Phased Array 162
6.5 Spatial Mitigation of Interference 166
6.5.1 Types of Mitigation Techniques 167
6.5.2 LCMV Beamformer 172
I. AoA of Targets 174
II. AoA of Interferers 175
III. Range-Azimuth after Adaptive Beamformer..... 176
6.6 Mitigation in Congested Environment 176
6.7 Spatial Mitigation in MIMO and FPA Radar..... 179
6.7.1 Dual (I/Q) Channel Receiver 179
6.7.2 Single (Real only) Channel Receiver..... 181
6.7.3 The PHSLL and SINR after Spatial Mitigation 183
6.8 Limitations of Spatial Domain Mitigation 186
6.9 Performance Comparison of Mitigation Techniques 187
6.10 Summary 188
CHAPTER 7. SINR ALONG THE RADAR PROCESSING STAGES..... 190
7.1 MIMO FMCW Processing..... 190
7.1.1 Block Diagram of Radar Processing Chain 191
7.2 SINR Improvement 192
7.2.1 Receiver Input 192
7.2.2 Receiver Output 194
7.3 Use-Cases for the SINR Assessment 196
7.3.1 Range Profile of Interference 199
7.3.2 Range-Doppler Representation of Interference 202
7.3.3 Spatial Domain Representation of Interference 204
I. Phased Array Configuration..... 205
II.MIMO Configuration..... 206
7.4 Performance Evaluation 210
7.5 Summary 210

CHAPTER 8. DOPPLER BEAM SHARPENING FOR INTERFERENCE MITIGATION..... 212
8.1 State of the Art 213
8.2 Phenomenology of Doppler Beam Sharpening 214
8.2.1 DBS for the Echo Signal 217
8.2.2 Block Level Representation of Signal Processing Chain 218
8.2.3 Resolution Enhancement 220
8.2.4 DBS Processing in an Interference Background 222
8.3 Interference Suppression with MIMO-DBS Beamforming 223
8.3.1 The Doppler Characteristics of Different Types of Interference 224
8.3.2 SINR Improvement after MIMO-DBS Processing 226
I.Periodic Interference 228
II.Aperiodic Interference 228
8.3.3 Effect of Platform Velocity 230
8.4 Performance Analysis 231
8.5 MIMO-DBS Beamforming - Validation 233
8.6 Summary 234
CHAPTER 9. CONCLUSIONS AND OUTLOOK..... 236
9.1 Conclusions 236
9.2 Outlook 239
9.2.1 Resolution Enhancement with DBS Beamforming 239
9.2.2 Digital Radars 240
9.2.3 Radar Communication 240
9.2.4 Cognitive Radar 240
9.2.5 Standardisation and Resource Allocation Mechanism 241
9.3 Radar Interference From Author's Perspective 241

REFERENCES..... 246

APPENDICES..... 289
APPENDIX 1. INDUSTRY-LED PROJECTS ON AUTOMOTIVE RADAR INTERFERENCE 289
APPENDIX 2. LITERATURE SURVEY ON RADAR SIMULATORS..... 292
APPENDIX 3. INTERFERENCE CLASSIFICATION..... 295
A3.1. Synchronous Interference 295
A3.2. Semi-Synchronous Interference 296
A3.3. Asynchronous Interference 298
I.Periodic Interference 299

II.Semi-Periodic Interference 300
III.Aperiodic Interference 301
APPENDIX 4. INTERFERENCE REPRESENTATION IN EACH DOMAIN – USE CASES..... 302
A4.1. Range Profiles 303
A4.2. Range-Doppler and Range-Azimuth Profiles 304
I.Synchronous Interference 305
II.Semi Synchronous Interference 306
III.Periodic Interference 307
IV.Semi Periodic Interference 309
V.Aperiodic Interference 310
APPENDIX 5. PERIODIC INTERFERENCE VALIDATION..... 313
APPENDIX 6. INTERFERENCE ANALYSIS IN SINGLE AND I/Q CHANNEL RECEIVER 315
APPENDIX 7. THE VALIDATION OF INTERFERENCE STATISTICS..... 318
APPENDIX 8. EFFECT OF RANDOMISATION ON THE ECHO SIGNAL..... 321
APPENDIX 9. THE EFFECT OF RANDOMISATION PARAMETERS..... 323
APPENDIX 10. INTERFERENCE APPEARANCE IN SPATIAL DOMAIN..... 325
APPENDIX 11. COSMOS DATASET COLLECTION AND METHODOLOGY..... 327
A11.1. Adaptive Cruise Control (ACC) Scenario 329
A11.2. Cross Traffic Alert (CTA) Scenario 329
APPENDIX 12. HOLISTIC RADAR SIMULATOR..... 330
A12.1. Overview of Holistic Simulator 331
A12.1.1 Block Level Representation 332
A12.1.2. Features of Simulator 336
A12.2. Sensor Dataset 337
A12.3. Environment Modelling – Propagation Channel Characterisation 338
A12.3.1. Road Definition and Topology 340
A12.3.2. Target and Clutter Modelling 341
I. Target Distribution 341
II. Clutter Distribution 345
A12.3.3. Multipath propagation from Reflective Infrastructure 347
A12.4. Radar Architecture and Modelling 351
A12.4.1. Analogue Signal Processing 351
I. Antenna Configuration 351
II. Signal Propagation 352
III. Link Budget Analysis 353

IV. Low Pass Filtering 353
A12.4.2. Radar Calibration 354
I. Amplitude Scaling 355
II. Azimuth Calibration 355
A12.4.3. Digital Signal Processing 357
A12.5. Interference Detection and Mitigation 358
A12.6. Validation and Data Analysis 358
APPENDIX 13. DIGITAL BEAMFORMING IN MIMO RADAR 364
APPENDIX 14. SPATIAL MITIGATION IN CONGESTED SCENARIO – VALIDATION 365
APPENDIX 15. LIMITATIONS OF SPATIAL DOMAIN MITIGATION 367

List of Figures

Figure 1.1: The levels of autonomous driving. 3

Figure 1.2: Methodology for analysing and mitigating radar interference. 7

Figure 2.1: Chronological flowchart of the automotive radar history. 17

Figure 2.2: Major types of radars. 20

Figure 2.3: Classification of radar: (a) bistatic configuration, (b) monostatic configuration. 20

Figure 2.4: Radar types and functionality to achieve advanced driver assistance system. 23

Figure 2.5: Automotive radar signal analysis: (a) FMCW with time domain, short-time Fourier transform, and spectrum, (b) PMCW with input code, time domain, and spectrum. 27

Figure 2.6: Beam pattern of MIMO and scanning radar with $N_{Tx} = 4$, $N_{Rx} = 16$ 29

Figure 2.7: Radar data cube: (a) typical signal processing chain, (b) illustration of the datacube. 32

Figure 2.8: Effect of spectral windowing on the frequency resolution and the side lobe level. 36

Figure 2.9: A typical on-road scenario demonstrating interference between radars. 38

Figure 2.10: Peak estimation for each interference pulse used in signal reconstruction. 49

Figure 2.11: Radar plots for assessing interference mitigation techniques: (a) time domain - no mitigation, (b) frequency domain - no mitigation, (c) time domain - interference zeroing, (d) frequency domain - interference zeroing, (e) time domain - interference chop-off, (d) frequency domain - interference chop-off, (g) time domain - signal reconstruction, (d) frequency domain - signal reconstruction. 50

Figure 3.1: Block diagram of FMCW radar system. 54

Figure 3.2: Simplified block-level diagram of an FMCW radar in an interference background. 57

Figure 3.3: FMCW radar chirp overlaps: (a) echo signal, (b) received interference. 62

Figure 3.4: Victim and interference chirps in the time-frequency representation and zoomed received signal. 63

Figure 3.5: Measurement setup to analyse the influence of LPF parameters on interference. . 64

Figure 3.6: Received signal in the time domain: a) the modelled VR1 with F_{LPF1} = 3.5 MHz, (b) the measured VR1 with F_{LPF1} = 3.5 MHz, (c) the modelled VR2 with F_{LPF2} = 10 MHz, (d) the measured VR2 with F_{LPF2} = 10 MHz. 65

Figure 3.7: Probability of detection for different LPF cut-off frequencies: (a) F_{LPF} = 3.5 MHz, (b) F_{LPF} = 10 MHz. 67

Figure 3.8: Interference spectrum for different sweep rates ratio $\left(K = K_{\text{int}} / K_v\right)$. 71

Figure 3.9: Generation of sub-regions for estimation of short-time Fourier transform. 72

Figure 3.10: Spectrogram of received interference: (a) the modelled VR1 with F_{LPF} = 3.5 MHz, (b) the measured VR1 with F_{LPF} = 3.5 MHz, (c) the modelled VR2 with F_{LPF} = 10 MHz, (d) the measured VR2 with F_{LPF} = 10 MHz. 73

Figure 3.11: MIMO FMCW radar's simplified signal processing chain. Tx and Rx represent the transmit and receive elements, respectively. 76

Figure 3.12: Radar data cubes for N_{Tx} = 3 and N_{Rx} = 4 element MIMO array: (a) data cube for received echo signal with 12 element virtual array, (b) data cube for interference with 4 element equivalent array according to N_{Rx}. Different colours represent signals received corresponding to different transmit elements of radar. 77

Figure 3.13: Received echo: (a) chirp representation, (b) time domain, (c) range profile. 79

Figure 3.14: Fast chirp interference: (a) chirp plot, (b) time domain, (c) range profile. 80

Figure 3.15: Slow chirp interference: (a) chirp plot, (b) time domain, (c) range profile. 81

Figure 3.16: Classification of radar interference based on the sweep rate difference. 81

Figure 3.17: Measurement setup to estimate the impact of interference. (a) Test setup for self-interference. (c) Test setup for mutual interference from front-looking radar. 86

Figure 3.18: Measured results for self-interference and front-looking interference. (a) Time domain profile in the absence of interference. (b) Time domain profile in the background of interference from front-looking interfering radar (mutual-interference case). (c) Time domain profile in the background of interference from corner-looking interfering radar (self-interference case). (d) Range profile. 87

Figure 3.19: Radar plots for multiple targets in the absence of interference: (a) PPI plot, (b) range-Doppler map, (c) range-azimuth map. 88

Figure 3.20: Radar plots at the background of interference from multiple interfering sources: (a) range-Doppler map, (b) range-azimuth map. 89

Figure 4.1: FMCW radar block level representation for interference statistical analysis. 95

Figure 4.2: Time domain representation of received signal: (a) signal with echo and interference pulses, (b) sinusoidal echo, (c) zoomed interference pulse. 96

Figure 4.3: Radar detector processing chain. y(j) represents the interference samples at the decision-making point 'D.' 97

Figure 4.4: Road scenario with target and interferer in the FoV of victim radar. 97

Figure 4.5: Received power from collocated target and interference as a function of range. .. 99

Figure 4.6: Chirp overlap plots of interference examples for the correlation analysis between interference pulses. 101

Figure 4.7: Average correlation 'ρ_{av}' for different types of interference. 102

Figure 4.8: Effect of integration on interference power: (a) normalised interference power level, (b) average correlation coefficient during the CPI. 104

Figure 4.9: NRMSE as a function of $BW_s = BW_v / BW_{\text{int}}$ and $T_s = T_{sv} / T_{\text{sint}}$: (a) NRMSE heatmap, (b) NRMSE contour plot of the critical cases. BW_V and BW_{int} represents the bandwidth of VR and IR, respectively and T_{sv} and T_{sint} represents the sweep time of VR and IR, respectively. 108

Figure 4.10: Normalised standard deviation $\left(\overline{\sigma_{\text{int}}}\right)$ as a function of T_{sv} / T_{sint} , BW_s=1. 110

Figure 4.11: NRMSE maps for the defined use cases: (a) NRMSE as a function of $T_s = T_{sv}/T_{\text{sint}}$ and $BW_s = 0.33$, (b) NRMSE as a function of $BW_s = BW_v/BW_{\text{int}}$ and $T_s = 1 \ldots 111$

Figure 4.12: PDF of close $(BW_s = 0.33,\ T_s = 0.73)$ and poor $(BW_s = 2,\ T_s = 1)$ approximation cases. 112

Figure 4.13: NRMSE value for difference coherent processing intervals. Insert shows the zoomed region for higher NRMSE values. 114

Figure 4.14: Effect of the CPI on interference distribution. 114

Figure 4.15: Probability of detection (P_d) vs. SIR for periodic $(T_s = 2, BW_s = 1)$ and aperiodic interference $(T_s = 2.2, BW_s = 1)$. 116

Figure 4.16: Detection curves for close $(T_s = 0.73, BW_s = 0.33)$ and poor $(T_s = 1, BW_s = 2)$ Gaussian case approximations. 117

Figure 4.17: Interference amplitude distributions at the radar detector under hypothesis H_{int} (red) and $H_{s,\text{int}}$ (blue). (a) Close case approximation $(T_s = 0.73,\ BW_s = 0.33)$, (b) Poor case approximation $(T_s = 1,\ BW_s = 2)$ 118

Figure 5.1: Pre-detection and post-detection interference mitigation techniques. 121

Figure 5.2: Interference detection: (a) reference, no interference in the time domain. (b) time-domain signal with interference, (c) envelope of the reference signal, (d) envelope of the signal with interference. 124

Figure 5.3: Interference detection using victim radar in the listening mode. 125

Figure 5.4: Interference detection using STFT: (a) weak interference pulse with power comparable to noise. (b) Short-time Fourier transform to separate interference from background noise. 127

Figure 5.5: Block-level representation of interference detection methodology. 128

Figure 5.6: Test setup: (a) forward and corner-looking radars, (b) side-looking radar. 129

Figure 5.7: Interference amplitude characteristics for fast chirp sequence in the test scene of Figure 5.6 (a) presented in: (a) time domain, (b) augmented range profiles. IF represents the interference frame. 131

Figure 5.8: Amplitude characteristics of interference after HPF: (a) time domain – Case 1, (b) augmented range profiles – Case 1, (c) time domain – Case 2, (d) augmented range profiles – Case 2, (e) time domain – Case 3, (f) augmented range profiles – Case 3. 132

Figure 5.9: Amplitude-based estimation of the number of interference sources. 133

Figure 5.10: Time domain representation of interference frame 'IF1.' (a) Extracted IF1, (b) subset of the VR MIMO sequence, (c) interference in the short time. 134

Figure 5.11: Time domain representation of interference frame 'IF2.' (a) Extracted IF 2, (b) subset of the VR MIMO sequence, (c) interference in the short time. 135

Figure 5.12: Time domain representation of interference frame 'IF3.' (a) Extracted IF 3, (b) subset of the VR MIMO sequence, (c) interference in the short time. 135

Figure 5.13: Time domain representation of interference frame 'IF4.' (a) Extracted IF 4, (b) subset of the VR MIMO sequence, (c) interference in the short time. 136

Figure 5.14: Steps used to estimate interference waveform parameters. 136

Figure 5.15: Interference pulse to pulse distance $\left(I_{PP}\right)$: (a) fast chirp, (b) slow chirp. 137

Figure 5.16: Interference to noise ratio (INR) heatmap to estimate interference impact. 140

Figure 5.17: Cognitive interference avoidance using idle time variation. The red highlighted region indicates victim and interference chirp overlap. 141

Figure 5.18: Time domain response for different interference temporal locations with different spectral windows. 143

Figure 5.19: Modelled radar plots after interference mitigation due to windowing applied before FFT across the fast-time: (a) no interference, (b) CW interference at 76.05 GHz, (c) CW interference at 76.15 GHz, (d) CW interference at 76.25 GHz. The blue plot in the time domain is the received signal after the window. 144

Figure 5.20: FMCW chirp sequence with scalable parameters for chirp randomisation. 147

Figure 5.21: NRMSE contour maps; (a) No randomisation, (b) Idle time randomisation. 148

Figure 5.22: Range-Doppler map of synchronous interference: (a) before randomisation, (b) after idle-time randomisation. 149

Figure 5.23: Effect of randomisation on different interference cases: (a) average correlation, (b) normalised interference level. 151

Figure 5.24: Validation of statistical and detection characteristics of periodic continuous wave (CW) interference: (a) distribution before randomisation, (b) probability of detection vs. SIR before randomisation, (c) distribution after randomisation, (d) probability of detection vs. SIR after randomisation. 152

Figure 6.1: Severity of radar interference: (a) typical roadside scenario, (b) modelled azimuth response without interference, (c) modelled azimuth response with interference from radars on the nearby vehicles. 157

Figure 6.2: The victim receiver's signal processing chain for interference mitigation in the spatial domain. 158

Figure 6.3: Range-azimuth plots for different receiver configurations: (a) single channel, (b) dual 'I/Q' channels. 162

Figure 6.4: An automotive scenario with a close spatial separation between the target and the interferer. 164

Figure 6.5: Modelled results for the example scenario in Figure 6.4: (a) range profile with and without interference, (b) range-azimuth plot for the MIMO array and FPA without interference, (c) range-azimuth plot for the MIMO array with interference, (d) range-azimuth plot for the full phased array with interference. 165

Figure 6.6: The methodology of adaptive digital beamforming. 166

Figure 6.7: Types of adaptive digital beamforming techniques assessed for the spatial domain mitigation of interference. 167

Figure 6.8: Examples of adaptive mitigation techniques: (a) least mean square, (b) constant modulus algorithm. 168

Figure 6.9: Spatial mitigation results for a well-separated target and interferer: (a) array response using adaptive weight, (b) range-azimuth plot before mitigation, (c) range-azimuth plot with LCMV-based adaptive weights. 170

Figure 6.10: Spatial mitigation for closely spaced target and interferer: (a) array response using adaptive weights, (b) range-azimuth plot with MSE-based adaptive weights, (c) range-azimuth plot with LCMV-based adaptive weights. 170

Figure 6.11: Adaptive weight estimation using LCMV beamformer. 174

Figure 6.12: Spatial mitigation using LCMV weights showing limited degrees for freedom to suppress all interferers. 177

Figure 6.13: Interference mitigation in the spatial domain for different numbers of interferers. (a) The PHSLL and SINR as a function of the number of interferers. The PHSLL and SINR values are in dB. (b) Array response after beamforming using adaptive weights for a different number of interferers. 178

Figure 6.14: Interference suppression using LCMV weights for I/Q channel receiver. The red highlighted region shows MIMO sidelobes greater than FPA sidelobes: (a) AoA for the MIMO array, (b) AoA for the full phase array, (c) range-azimuth plot after spatial suppression for the MIMO array, (d) range-azimuth plot after spatial suppression for the full phased array. 180

Figure 6.15: Interference suppression using LCMV spatial weights for a single channel victim receiver. Red highlighted region shows MIMO sidelobes greater than FPA sidelobes: (a) AoA for MIMO array, (b) AoA for full phased array (FPA), (c) range-azimuth plot after spatial suppression in MIMO array, (d) range-azimuth plot after spatial suppression in FPA. 182

Figure 6.16: (a) Peak to highest sidelobe level (PHSLL) as a function of spatial separation $(\Delta\theta)$ between the target and interferer. (b) SINR vs. spatial separation $(\Delta\theta)$ between target and interferer. Negative PHSLL indicates a sidelobe greater than the target peak. 184

Figure 6.17: Performance analysis of MIMO and full phased arrays. 185

Figure 7.1: Block diagram of a typical radar system with processing steps: (a) analogue front end, (b) digital signal processing. 192

Figure 7.2: Measurement setup for the SINR analysis in real road conditions. 196

Figure 7.3: Radar plots in the range domains for the defined use cases: (a) range profile of interference from radar 1, (b) range time of interference from radar 1, (c) range profile of interference from radar 2, (d) range time of interference from radar 2. 202

Figure 7.4: Range-Doppler plots for the SINR analysis: (a) radar 1, (b) radar 2. 204

Figure 7.5: Range cross-range for the SINR analysis: (a) interference from radar 1, (b) interference from radar 2. 209

Figure 7.6: The SINR and INR along the radar processing stages. 210

Figure 8.1: Degradation in target detection as a function of range from the radar. 215

Figure 8.2: Doppler beam sharpening illustration: (a) main beam, (b) sub-beam formation due to a moving victim radar, (c) The Doppler frequency of each sub-beam. 216

Figure 8.3: Block level representation of signal processing chain: (a) common for FMCW-based victim radar, (b) MIMO beamforming, (c) MIMO-DBS beamforming. 219

Figure 8.4: Enhancement in target resolution after applying MIMO-DBS beamforming. 221

Figure 8.5: Range-Doppler maps of each interference type for the analysis of DBS beamforming. 225

Figure 8.6: The heatmaps for interference to noise ratio (INR) analysis as a function of victim and interferer radars waveform parameters. (a) MIMO beamforming, (b) MIMO-DBS beamforming. 227

Figure 8.7: Range-cross range plot for periodic interference with $T_{sv}/T_{\text{sint}} = 5$, $B_{sv}/B_{\text{sint}} = 1$. (a) MIMO beamforming, (b) MIMO-DBS beamforming. 228

Figure 8.8: Range-cross range plot for aperiodic interference with $T_{\text{sv}}/T_{\text{sint}}$ = 2.1 and $B_{\text{sv}}/B_{\text{sint}}$ = 1 and a single channel receiver: (a) MIMO beamforming, (b) MIMO-DBS beamforming. 229

Figure 8.9: Interference to noise ratio (INR) as a function of the VR velocity. 230

Figure 8.10: Probability of detection as a function of the SINR. (a) MIMO beamforming and MIMO-DBS beamforming without interference zeroing. (b) MIMO beamforming and MIMO-DBS beamforming with interference zeroing. 232

Figure 8.11: Measured results for the comparison of MIMO and MIMO-DBS imagery: (a) measurement setup, (b) MIMO beamforming, (c) MIMO-DBS beamforming...234

Figure 9.1: Interference scenarios. (a) Vehicles facing each other. (b) The vehicle in black is about to overtake the vehicle in red. (c) Vehicles next to each other in different lanes. (d) Vehicles waiting at a junction. (e) Off-road source of interference. The black and red blocks represent the vehicles, and the corresponding beams show the orientation of each radar sensor. 243

Figure A3.1: Synchronous interference: (a) chirp plot, (b) time domain, (c) range profile. ..296

Figure A3.2: Semi-synchronous interference, Case 2(a): (a) chirp plot, (b) time domain, (c) range profile. 297

Figure A3.3: Semi-synchronous interference, Case 2 (b): (a) chirp plot, (b) time domain, (c) range profile. 298

Figure A3.4: Fast chirp periodic interference: (a) chirp plot, (b) time domain, (c) range profile. 299

Figure A3.5: Slow chirp periodic interference: (a) chirp plot, (b) time domain, (c) range profile. 300

Figure A3.6: Semi-periodic interference: (a) chirp plot, (b) time domain, (c) range profile. 301

Figure A4.1: Range profile of the types of interference stated in Table A4.1. 303

Figure A4.2: Radar plots in absence of interference: (a) range-Doppler, (b) range-azimuth. 304

Figure A4.3: Synchronous interference plots: (a) range-Doppler, (b) range-azimuth. 306

Figure A4.4: Semi-synchronous interference plots: (a) range-Doppler, (b) range-azimuth. .307

Figure A4.5: Radar plots of periodic interference: (a) range-Doppler of the single-channel receiver, (b) range-Doppler of the I/Q channels receiver, (c) range-azimuth of the single-channel receiver, (d) range-azimuth of the I/Q channels receiver. 308

Figure A4.6: Radar plots for semi-periodic interference: (a) range-Doppler for single channel receiver, (b) range-Doppler for I/Q channels receiver, (c) range-azimuth for single channel receiver, (d) range-azimuth for I/Q channels receiver. 309

Figure A4.7: Radar plots of aperiodic interference: (a) range-Doppler for fast chirp sequence, (b) range-Doppler for slow chirp sequence, (c) range-azimuth for single channel receiver, (b) range-azimuth for I/Q channels receiver. 311

Figure A5.1: Periodic interference example: a) measurement setup, (b) range-azimuth: model, c) range-azimuth: measured. 313

Figure A6.1: Receiver configurations in automotive radar chipsets: (a) single-channel receiver, (b) dual (in phase - quadrature) channels receiver. 315

Figure A6.2: The echo signal and interference in SoA automotive radar chipsets: (a) real-channel receiver, (b) dual (I/Q) channels receiver. 316

Figure A7.1: Measurement setup for the radar detector performance analysis: (a) aperiodic interference, (b) periodic interference. 318

Figure A7.2: Validation of aperiodic and periodic interference statistics: (a) probability density function - aperiodic, (b) probability density function - periodic. 319

Figure A7.3: Validation of interference detection curves: (a) probability of detection vs. SIR – aperiodic, (b) probability of detection vs. SIR – periodic. 320

Figure A8.1: Range-Doppler coupling in the received echo due to start frequency randomisation: (a) model, (b) measured. 322

Figure A9.1: Effect of randomisation value on different randomisation techniques. 323

Figure A10.1: Measurement setup in an anechoic chamber for periodic and aperiodic interference analysis in the spatial domain. 325

Figure A10.2: Periodic and aperiodic interference in the range-azimuth domain: (a) periodic CW interference – modelled, (b) periodic CW interference – measured, (c) aperiodic FMCW interference – modelled, (d) aperiodic FMCW interference – measured. 326

Figure A11.1: Test vehicle with measurement sensor suite for ‘COSMOS’ dataset collection. 327

Figure A11.2: Adaptive cruise control scenario for the collection of COSMOS dataset. 329

Figure A11.3: Cross traffic alert scenario for the collection of COSMOS dataset. 329

Figure A12.1: Interaction between sensors and road actors in an automotive scenario. 330

Figure A12.2: Modular description of the developed simulator. 332

Figure A12.3: Block-level representation of the holistic radar simulator. 333

Figure A12.4: Radar configuration interface of the simulator: (a) scene modelling, (b) measured data analysis. 335

Figure A12.5: An example of post-processed results obtained from the radar simulator. The plots on top show results after a short time Fourier transform (STFT), and the plots on the bottom show azimuth response after beamforming. The plots on the left are before interference mitigation, and those on the right are after interference mitigation (interference zeroing in this case). 337

Figure A12.6: Range response from the corner reflector and propagation model curves. The blue line indicates the theoretical 2-ray propagation curve, the red line represents the free-space propagation curve, and the black lines show the response from the corner reflector at various distances. 339

Figure A12.7: Road schematics from the simulator: (a) road definition tool, (b) straight lane, (c) junction, (d) roundabout, (e) exit lane. 340

Figure A12.8: Integrated RCS from sedan vehicle as a function of aspect angles 342

Figure A12.9: Modelled and measured results of the extended target at 9.4 m from the vehicle with ego radar. (a) Test setup, (b) modelled range-Doppler, (c) measured range-Doppler, (d) modelled range cross-range, (e) measured range cross-range. 343

Figure A12.10: Modelled and measured results of the extended target at 1.1 m from the vehicle with ego radar. (a) Test setup, (b) modelled range-Doppler, (c) measured range-Doppler, (d) modelled range cross-range, (e) measured range cross-range. 344

Figure A12.11: Clutter response: (a) test Scene, (b) model, (c) measurement. 346

Figure A12.12: Appearance of false targets due to multipath: (a) single bounce – configuration A, (b) single bounce – configuration B, (b) double bounce. 347

Figure A12.13: Test setup for a reflective scenario: (a) scene corresponding to modelled results, (b) the full extent of facades. 348

Figure A12.14: Modelled and measured results showing the appearance of false targets: (a) range-Doppler, (b) range cross-range: MIMO beamforming, (c) range cross-range: MIMO-DBS beamforming. 350

Figure A12.15: Element patterns of the radars used during measurements. 352

Figure A12.16: Received signal after filtering in the presence of interference from TI radar: (a) model, (b) measurement. 354

Figure A12.17: Azimuth calibration effect on interference: (a) Radarlog (64 MIMO channels), (b) Radarbook (32 MIMO channels). 356

Figure A12.18: Stages of digital signal processing incorporated in the simulator. 357

Figure A12.19: Interference detection and mitigation interface. 358

Figure A12.20: Snapshots of measured scenarios with different positions of the target vehicle. 359

Figure A12.21: Modelled and measured results corresponding to case 1 from Figure A12.20. (a) Range-Doppler, (b) range cross-range. 359

Figure A12.22: Modelled and measured results corresponding to case 2 from Figure A12.20. (a) Range-Doppler, (b) range cross-range. 361

Figure A12.23: Modelled and measured results corresponding to case 3 from Figure A12.20. (a) Range-Doppler, (b) range cross-range. Inserts show the zoomed region with the target. 363

Figure A13.1. Block diagram of the digital beamformer. 364

Figure A14.1: Outdoor measurement scenario with multiple targets and interferers. 365

Figure A14.2: Modelled and measured array response after spatial mitigation. 366

List of Tables

Table 1.1: Latest death toll due to road traffic accidents (2019). 2

Table 2.1: Chronological history of the radar. 18

Table 2.2: Typical automotive radar parameters in the 77 GHz band. 22

Table 2.3: Applications of various types of automotive radars. 23

Table 2.4: Characteristics of the spectral windows used in the presented work. 35

Table 2.5. State-of-the-art interference mitigation techniques. 42

Table 2.6: Literature survey on the spatial mitigation techniques. 47

Table 2.7. Performance analysis of the time domain mitigation techniques. 51

Table 3.1. The ratio of T_{INT}/T_{sv} for different cut-off frequencies and filter order. 66

Table 3.2. The appearance of various types of interference in frequency and spatial domains. 85

Table 3.3. Radar parameters for the analysis and comparison of self and mutual interference. 86

Table 3.4. Target and interferer position, SNR, and SINR values to analyse the impact of multiple interference sources. 90

Table 4.1. Interference parameters to analyse the correlation between interference pulses. . 101

Table 4.2. SIR for periodic and aperiodic interference. 105

Table 4.3. Types of interference demonstrating a deviation from $\overline{\sigma_{\text{int}}} = 1$. 110

Table 4.4. Conditions for interference deviation from Gaussian behaviour for defined cases. 111

Table 4.5. Examples of the close case and poor case Gaussian approximations. 112

Table 4.6. Statistical characteristics of various radar interference. 119

Table 5.1. Estimated interference parameters from various interfering sources. 138

Table 5.2. Mean interference power and interference to noise ratio (INR). IF represents interference frames, identified in Figure 5.8. 139

Table 5.3. The SINR after range compression and the SINR improvement due to the applied spectral window. 145

Table 5.4. Performance comparison of randomisation techniques, $\overline{NRMSE}$ value is in dB. .. 150

Table 6.1: Side lobe level (SLL) for well-separated and closely spaced target and interferer. 171

Table 6.2: Performance comparison of time domain and spatial domain mitigation 187

Table 7.1: Sensor parameters for the SINR analysis. 197

Table 7.2: Probability of occurrence of interference $\left(PR_{\text{int}}\right)$. 199

Table 7.3: Time shift and sampling interval for long and short-range radar. 205

Table 7.4: The estimated SINR and INR after victim radar processing stages. 211

Table 8.1: Performance comparison of MIMO beamforming, time domain interference zeroing, and MIMO-DBS beamforming 231

Table A2.1: ADAS simulators to model environment 292

Table A3.1: Example interference parameters classified based on the sweep rate difference. 295

Table A4.1. Types of interference and waveform parameters for the analysis in frequency and spatial domains. 302

Table A7.1. Radar configuration parameters for the validation of interference statistics. 319

Table A7.2. SIR required for $P_d = 0.9$ $\left(P_{FA} = 10^{-4}\right)$ – Periodic and aperiodic interference. . 320

Table A10.1: Radar parameters for periodic and aperiodic interference analysis and validation in the spatial domain. 325

Table A11.1: Radar parameters for the 'COSMOS dataset.' 328

Table A12.1: Input and outputs of the holistic simulator. 334

Table A12.2: One-way range, velocity, and the azimuth of false targets from multipath. 348

Table A12.3: Target distribution for case 2 from Figure A12.20. 362

Table A12.4: Target distribution for case 3 from Figure A12.20. 362

Table A14.1: Targets/ interferer positions and radars parameters for multiple targets and interferers scenario. 366

List of Publications and Presentations

Conference Papers

1. A. Pirkani, F. Norouzian, E. Hoare, M. Gashinova and M. Cherniakov, "Statistical Analysis of Automotive Radar Interference," *2020 IEEE Radar Conference (RadarConf20)*, 2020, pp. 1-6, doi: 10.1109/RadarConf2043947.2020.9266653.
2. F. Norouzian, A. Pirkani, E. Hoare, M. Cherniakov and M. Gashinova, "A Graphical Heatmap Tool to Analyse the Effects of Interference in Automotive Radar," 2020 IEEE Radar Conference (RadarConf20), 2020, pp. 1-6, doi: 10.1109/RadarConf2043947.2020.9266353.
3. F. Norouzian, A. Pirkani, E. Hoare, M. Cherniakov and M. Gashinova, "Automotive Radar Waveform Parameters Randomisation for Interference Level Reduction," *2020 IEEE Radar Conference (RadarConf20)*, 2020, pp. 1-5, doi: 10.1109/RadarConf2043947.2020.9266375.
4. A. Pirkani, F. Norouzian, E. Hoare, M. Cherniakov and M. Gashinova, "Analysis of Automotive Radar Interference in Spatial Domain," 2021 21st International Radar Symposium (IRS), 2021, pp. 1-8, doi: 10.23919/IRS51887.2021.9466171.
5. F. Norouzian, A. A. Pirkani, E. G. Hoare, M. Cherniakov and M. Gashinova, "Characterization of the Effect of Low Pass Filter Response on the Interference in FMCW Automotive Radar," 2021 21st International Radar Symposium (IRS), 2021, pp. 1-6, doi: 10.23919/IRS51887.2021.9466189.
6. A. Pirkani, F. Norouzian, E. Hoare, M. Cherniakov and M. Gashinova, "Automotive Interference Suppression in MIMO and Phased Array Radar," 2021 18th European Radar Conference (EuRAD), 2022, pp. 413-416, doi: 10.23919/EuRAD50154.2022.9784453.
7. A. Pirkani, S. Cassidy, F. Norouzian, M. Gashinova and M. Cherniakov, "Doppler Beam Sharpening for Enhanced MIMO Imagery in the Presence of Automotive Interference," 2021 18th European Radar Conference (EuRAD), 2022, pp. 417-420, doi: 10.23919/EuRAD50154.2022.9784499.
8. A. Pirkani, F. Norouzian, M. Cherniakov and M. Gashinova, "Automotive Radar Parameter Estimation for Cognitive Interference Mitigation," 2022 19th European Radar Conference (EuRAD), 2022, pp. 161-164, doi: 10.23919/EuRAD54643.2022.9925005.

9. A. Pirkani et al., "SINR Improvement Across the Automotive Radar Signal Processing Chain," 2022 19th European Radar Conference (EuRAD), 2022, pp. 5-8, doi: 10.23919/EuRAD54643.2022.9924759.
10. S. L. Cassidy, S. Pooni, A. Pirkani, E. G. Hoare, M. Cherniakov and M. S. Gashinova, "Doppler Beam Sharpening for High-Resolution Imaging in Dynamic Automotive Scenes," 2022 19th European Radar Conference (EuRAD), 2022, pp. 325-328, doi: 10.23919/EuRAD54643.2022.9924919.
11. A. Pirkani, S. Cassidy, S. Pooni, M. Cherniakov, M. Gashinova, "Modelling and experimental validation of radar - environment interaction in automotive scenarios," International Conference on Radar Systems (RADAR 2022), Edinburgh, UK, 2022, pp. 395-400.
12. Y. Xiao et al., "Automotive radar image segmentation with frame fusion," International Conference on Radar Systems (RADAR 2022), Hybrid Conference, Edinburgh, UK, 2022, pp. 243-247.

Journal Papers

1. Pirkani, A., et al.: Automotive interference statistics and their effect on radar detector. IET Radar Sonar Navig. 16(1), 9– 21 (2022).
2. Norouzian, F., et al.: Phenomenology of automotive radar interference. IET Radar Sonar Navig. 15(9), 1045– 1060 (2021).
3. A. Pirkani, F. Norouzian, S. Pooni, M. Cherniakov, M. Gashinova, "Characterisation and Mitigation of Automotive Radar Interference in Spatial Domain," submitted to IET Journal of Engineering, 2023.
4. A. Pirkani, S. Cassidy, F. Norouzian, M. Cherniakov, M. Gashinova, "Doppler Beam Sharpening for Augmenting Radar Performance in Interference Background," to be submitted to IET Radar Sonar Navig., 2023.
5. F. Norouzian, A. Pirkani, E. Hoare, M. Cherniakov, M. Gashinova, "Generalized Approach to Interference Power Analysis for FMCW Automotive Radars," submitted to IET Radar Sonar Navig., 2023.

Conference Presentations

1. IET Radar Conference, Edinburgh, UK, Oct. 2022: Oral presentation on “Automotive Radar Image Segmentation with Frame Fusion.”
2. IET Radar Conference, Edinburgh, UK, Oct. 2022: Oral Presentation on “Systematic Modelling and Analysis of Automotive Radar Characterised by Real Road Measurements.”
3. 19th European Radar Conference (EuRAD), Milan, Italy, Sept. 2022: Oral presentation on "SINR Improvement Across the Automotive Radar Signal Processing Chain."
4. 19th European Radar Conference (EuRAD), Milan, Italy, Sept. 2022: Oral presentation on "Automotive Radar Parameter Estimation for Cognitive Interference Mitigation."
5. 18th European Radar Conference (EuRAD 2021), London, UK, Feb. 2022: Oral presentation on "Automotive Interference Suppression in MIMO and Phased Array Radar."
6. 18th European Radar Conference (EuRAD 2021), London, UK, Feb. 2022: Oral presentation on "Doppler Beam Sharpening for Enhanced MIMO Imagery in the Presence of Automotive Interference."
7. International Radar Symposium (IRS) Jun. 2021, Ulm, Germany: Oral presentation on "Analysis of Automotive Radar Interference in Spatial Domain."
8. IEEE Radar conference, Sept 2020, Florence, Italy: Oral presentation on "Statistical Analysis of Automotive Radar Interference."

Poster Presentations

1. The Electro Magnetic Systems Interest Group (EMSIG) 2022, London, UK. Sept 2022: Poster presentation on ‘Doppler Beam Sharpening for Interference Suppression.’
2. The Electro Magnetic Systems Interest Group (EMSIG) 2022, London, UK. Sept 2022: Poster presentation on ‘Automotive Radar Parameter Estimation for Cognitive Interference Mitigation.’

Project Datasets at the University of Birmingham Repository[1]

1. Pirkani et al., 'COSMOS dataset for co-existence/ interference analysis and simultaneous scene representation by automotive radar and video with GPS/IMU ground truth,' the University of Birmingham, Jan. 19, 2022. doi: 10.25500/edata.bham.00000777.
2. Pirkani et al., 'COSMOS dataset for co-existence/ interference analysis and simultaneous scene representation by automotive radar and video with GPS/IMU ground truth - Sub-Dataset B,' the University of Birmingham, Jan. 30, 2022. doi: 10.25500/edata.bham.00000785.
3. Pirkani et al., 'COSMOS dataset for co-existence/ interference analysis and simultaneous scene representation by automotive radar and video with GPS/IMU ground truth - Sub-Dataset C,' the University of Birmingham, Jan. 30, 2022. doi: 10.25500/edata.bham.00000786.
4. Pirkani et al., 'COSMOS dataset for co-existence/ interference analysis and simultaneous scene representation by automotive radar and video with GPS/IMU ground truth - Sub-Dataset D,' the University of Birmingham, Jan. 30, 2022. doi: https://doi.org/10.25500/edata.bham.00000788.
5. Pirkani et al., 'COSMOS dataset for co-existence/ interference analysis and simultaneous scene representation by automotive radar and video with GPS/IMU ground truth - Sub-Dataset E,' the University of Birmingham, Jan. 30, 2022. doi: 10.25500/edata.bham.00000788.
6. Pirkani and M. Gashinova, 'COSMOS "Adaptive Cruise Control (ACC) dataset" for co-existence/ interference analysis and simultaneous scene representation by automotive radar and video,' the University of Birmingham, Mar. 01, 2022. doi: 10.25500/edata.bham.00000800.
7. Pirkani and M. Gashinova, 'COSMOS "Cross Traffic Alert (CTA) dataset" for co-existence/ interference analysis and simultaneous scene representation by automotive radar and video,' the University of Birmingham, Mar. 01, 2022. doi: 10.25500/edata.bham.00000801.

[1] Dataset description is presented in Appendix 11.

Nomenclature

3D	3 dimensional
AAF	Anti-aliasing filter
ACC	Adaptive cruise control
ADAS	Advanced driver assistance systems
ADBF	Adaptive digital beamforming
ADC	Analogue to digital converter
AEB	Autonomous emergency braking
AFE	Analogue front end
AoA	Angle of arrival
ATD	Automatic target detection
AVs	Autonomous vehicles
AWGN	Additive white Gaussian noise
BPM	Binary phase modulation
BPSK	Binary phase shift keying
BSD	Blind spot detection
BW	Bandwidth
CA-CFAR	Cell averaging CFAR
CAV	Connected autonomous vehicles
CDM	Code division multiplexing
CFAR	Constant false alarm rate
CLT	Central Limit Theorem
CMA	Constant modulus algorithm
CMOS	Complementary metal oxide semiconductor
COSMOS	CO-existence Simulation MOdelling of radars for Self-driving
COTS	Commercial off-the-shelf
CPI	Coherent processing interval
CR	Corner reflector
CUT	Cell under test
CW	Continuous wave

CWS	Collision warning system
DBF	Digital beamforming
DBS	Doppler Beam Sharpening
DCM	Digital code modulation
DDM	Doppler division multiplexing
DoF	Degrees of freedom
DSP	Digital signal processing
EIRP	Effective isotropic radiated power
EM	Electromagnetic
(F/RCTA)	Front/ Rear Cross Traffic Alert
FDM	Frequency division multiplexing
FFT	Fast Fourier transform
FM	Frequency modulated
FMCW	Frequency modulated continuous wave
FoV	Field of view
FPA	Full phased array
FSK	Frequency shift keying
GPS	Global positioning system
HPF	High pass filter
HR	Host radar
I/Q	In-phase/quadrature
IF	Interference frame
IMU	Inertial measurement unit
INR	Interference to noise ratio
IR	Interferer radar
ISM	Industrial, scientific, and medical
ITU	International Telecommunication Union
JLR	Jaguar Land Rover
L4	Level 4 autonomy
L5	Level 5 autonomy
LCA	Lane change assist

LCMV	Linearly constrained minimum variance
LFM	Linear frequency modulation
Lidar	Light detection and ranging
LMS	Least mean square
LNA	Low noise amplifier
LO	Local oscillator
LoS	Line of sight
LPF	Low pass filter
LRR	Long range radar
MIMO	Multiple input multiple output
MISL	Microwave integrated systems laboratory
mmWave	Millimetre wave
MRR	Medium range radar
MSE	Mean square error
MTI	Moving target indicator
MVDR	Minimum variance distortion-less response
NHSTA	National Highway Traffic Safety Administration
NLMS	Normalised least mean square
NLoS	Non-line of sight
NRMSE	Normalised root mean square error
OFDM	Orthogonal frequency division multiplexing
PC-FMCW	Phase coded – frequency modulated continuous wave
PDF	Probability density function
PEC	Perfect electric conductor
PHSLL	Peak to highest side lobe level
PMCW	Phase modulated continuous wave
PPI	Plan position indicator
PRF	Pulse repetition frequency
PRI	Pulse repetition interval
PSD	Power spectral density
PSK	Phase shift keying

PHSLL	Peak to highest side lobe level
Radar	Radio detection and ranging
RadCom	Radar communication
RCS	Radar cross section
RF	Radio frequency
RMS	Root mean square
ROC	Receiver operating characteristic
RPR	Radar penetration rate
RTM	Ray tracing models
SAR	Synthetic aperture radar
SIMO	Single input, multiple output
SINR	Signal to interference plus noise ratio
SIR	Signal to interference ratio
SLL	Side lobe level
SNR	Signal to noise ratio
SoA	State of the art
SRR	Short range radar
STFT	Short time Fourier transform
SV	Steering vector
TDM	Time division multiplexing
TFD	Time frequency domain
TI	Texas Instruments
UoB	University of Birmingham
VCO	Voltage controlled oscillator
VGA	Variable gain amplifier
VR	Victim radar
WHO	World health organization
WSS	Wide sense stationary

List of Variables

T_{sv}	Sweep time of the victim radar
ΔCR	Cross range resolution
R	Slant range of an object from the radar
$\boldsymbol{c}$	Speed of light/ signal propagation
τ_D	Two-way propagation delay between radar and target
f_D	Doppler frequency shift
v_{vr}	Velocity of victim radar
φ_{IF-t}	Phase of down-converted echo signal
t	Fast-time
t_s	Slow-time
τ_v	Propagation delay of echo signal
K_v	Sweep rate of victim radar waveform
F_{cv}	Carrier frequency of victim radar
f_{IF-T}	Intermediate frequency of echo signal
F_s	Sampling frequency
N_{SB}	Number of sub-beams
f_{d-BW}	Doppler bandwidth
φ_{IF-i}	Phase of down-converted interference
$\Delta K = K_v - K_{\text{int}}$	Difference between the VR and IR waveform sweep rates
K_{int}	Sweep rate of interfering radar waveform
K_v	Sweep rate of victim radar waveform
τ_{int}	Propagation delay of interfering signal
$\Delta F = F_{cv} - F_{\text{cint}}$	Difference between the VR and IR carrier frequencies
F_{cint}	Carrier frequency of interfering radar
f_{IF-i}	Intermediate frequency of interference

$f_{D-i}(t_s)$	Doppler shift of interference across the slow-time
$f_{D-t}(t_s)$	Doppler shift of echo signal across the slow-time
N_{CPI}	Number of radar chirps coherently integrated
v_r	Radial velocity
f	Frequency
N_{Tx}	Number of transmit elements
N_{Rx}	Number of receive elements
F_{LPF}	Cut off frequency of low pass filter
Δv	Velocity resolution
$v_{\max}$	Maximum unambiguous velocity
P_{FA}	Probability of false alarm
T_{sint}	Sweep time of interfering radar
B_{sint}	Sweep bandwidth of interfering radar
R_T	Distance between the VR and target
T_{INT}	Interference duration
R_I	Distance between interferer radar and victim radar
N_{INT}	Number of interfered samples
P_d	Probability of detection
PDF_{bf}	Best fit Gaussian distribution
PDF_{int}	Interference distribution
$BW_s = BW_v / BW_{\text{int}}$	Ratio of victim and interferer radar bandwidth
$T_s = T_{sv} / T_{\text{sint}}$	Ratio of victim and interferer radar sweep times
PRI_{VR}	Pulse repetition interval of victim radar

Chapter 1. OVERVIEW

The next-generation vehicles are being developed with the potential of improved road safety, passenger comfort, and economic and environmental benefits. The automotive industry, including car manufacturers and tier-1 and tier-2 suppliers, is keen on developing advanced driver assistance systems (ADAS) which ultimately will facilitate the development of fully autonomous self-driving vehicles [1]. Traditional automotive companies, such as Ford, BMW, and new players, such as Tesla, and Google, have an ongoing race to progress towards 'level 4' (deep driver assistance) and 'level 5' (fully autonomous) vehicle autonomy. The companies that will first present fully connected and autonomous vehicles (CAV) to the mass market will gain a significant competitive edge in the industry [2].

1.1 Problem Statement

Road traffic accidents are the main reason for death among all age groups and the leading cause of death among 5–29 year olds. Vulnerable road users, such as motorcyclists, cyclists, and pedestrians, account for the majority of these fatalities. The leading causes behind these accidents are untrained drivers, heavy traffic, using mobile phones while driving, and using intoxicants. The resulting injuries result in a substantial financial loss for the victims, their families, and the economy [3].

The World Health Organization (WHO) estimates that traffic accidents globally result in about 1.3 million fatalities per annum. As many as 50 million are wounded yearly, costing an average of 3% of the country's gross domestic product (2021) [4], with one death due to a road accident every 24 seconds [5]. The statistics predicted by WHO suggest a rise of about 65% in accidents over the upcoming years without improvements made in vehicles and driving

conditions. Road traffic accidents, the ninth leading cause of mortality worldwide, will move up to the fifth spot by 2030 [6]. Table 1.1 shows the latest death toll according to WHO due to road traffic accidents in various regions worldwide (2019) [7].

Table 1.1: Latest death toll due to road traffic accidents (2019).

Location	Value
Global	1,282,150 [1,008,400 - 1,554,236]
Eastern Mediterranean	126,958 [103,682 - 152,610]
Americas	154,780 [128,107 - 184,289]
Africa	297,087 [238,813 - 356,057]
South-East Asia	317,069 [235,964 - 385,698]
Western Pacific	317,393 [246,835 - 389,964]
Europe	68,863 [55,000 - 85,619]

Considering the global impact of road traffic accidents, a modern approach is required to deal with the problem.

With the research into autonomous vehicles (AVs) and their implementation worldwide, the number of roadside accidents can be reduced drastically, with an estimated 94% reduction in traffic-related deaths [8]. The Society of Automotive Engineers has defined 5 levels for vehicle automation ranging from level 0 (fully manual) to level 5 (fully autonomous) [9]. The description of these levels and required specifications have been summarised in Figure 1.1 [10], [11]. With these autonomous functions, a human driver's control of driving tasks will be removed. Instead, it will rely on the system's ability to perceive and understand the vehicle's surroundings through a complex sensor system to provide capabilities like traffic monitoring, navigation, vehicle tracking, path planning, and surveillance.

The adoption of sensor-based technology in the automobile industry is growing in response to the growing concern about passenger and vehicle safety [12]. The sensors are at the core of autonomy that, together with artificial intelligence (AI), will not only take the place of

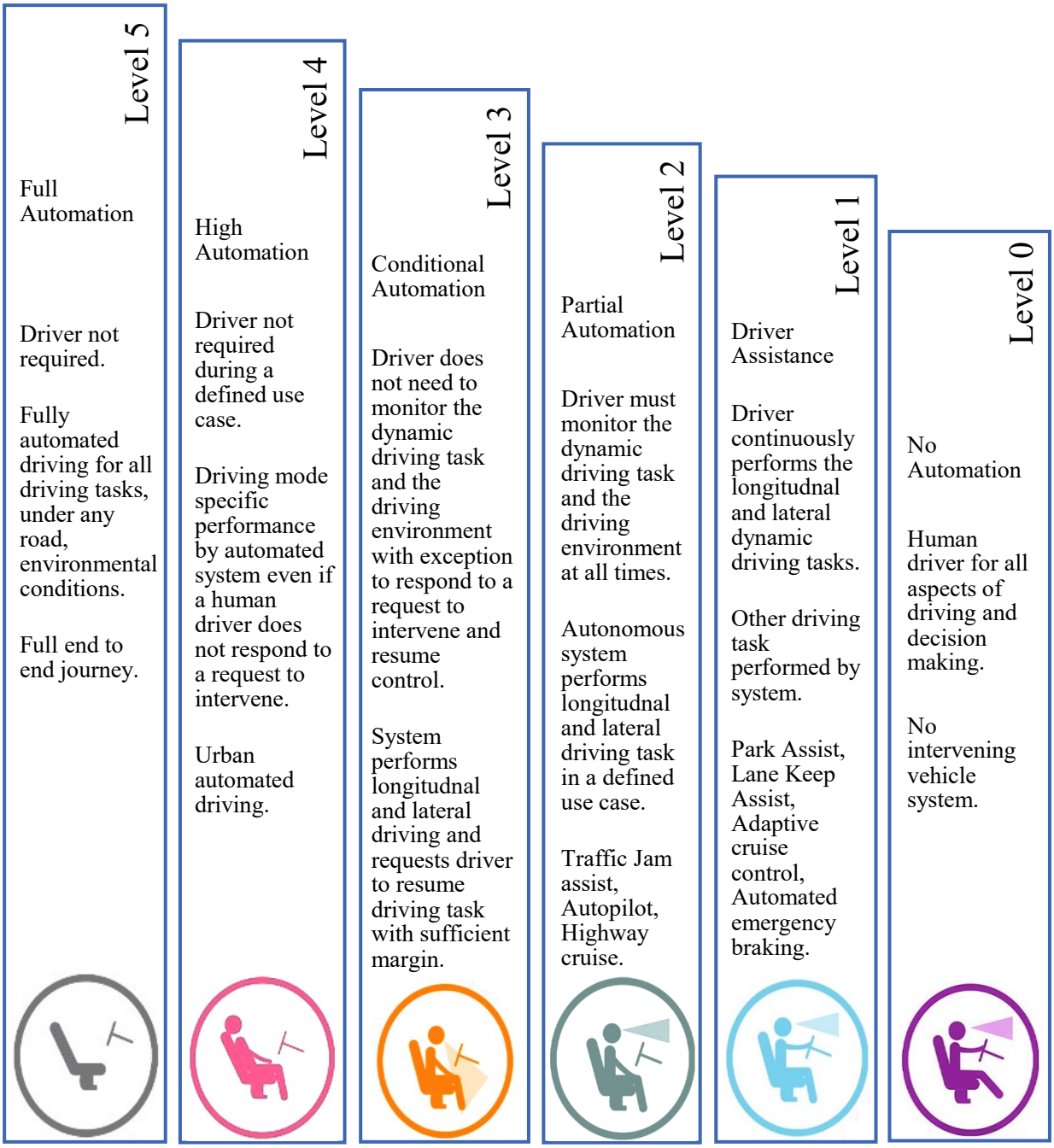


Figure 1.1: The levels of autonomous driving.

a human's capacity to 'see the road' but, in most circumstances, are expected to outperform it. Sensor's data-processing algorithms are crucial for environment perception, enabling the autonomous function control system to adapt to prevailing conditions. As a result, there is a growing need for ADAS systems with built-in sensor capabilities. For environment sensing and perception, a variety of sensors are utilised, including radio detection and ranging (radar),

ultrasound, cameras, and light detection and ranging (lidar) [13]. Most of these sensors transmit a signal and process the reflections from various objects to understand and image the scene.

As CAV shall operate 24/7 in all weather and lighting conditions, radar is the most reliable sensor since it uses electromagnetic (EM) waves to sense the environment [14]–[16] which are considerably less impacted by the environment such as adverse weather or time of the day [17]. The radar is also capable of estimating the target's distance, radial speed, and spatial position with near-instantaneous precision and a high resolution [18]. Additionally, compared to the other sensors, it has a substantially extended detection range [13], [19]. At the same time, automotive radar costs are dropping substantially due to the advancements in RF CMOS technology, the development of multiple-input, multiple-output (MIMO) radars, and improved imaging techniques at 76-77 GHz and 77-81 GHz bands [20]. This is accompanied by notable developments in radar capabilities for accurate imaging, target classification, and path planning [21]–[26]. Therefore, radar is a key sensing modality for ADAS and complements lidar and cameras quite well [27], [28]. According to the current vision, each CAV will be equipped with at least a dozen radars overlooking 360-degree vehicle surrounding and seeing from a meter to hundreds of meters ahead and around to achieve autonomy [16], [29].

As a result of the numerous applications of radar sensors in the automotive industry, it is an active research area [19], [30], [31]. Some of the first applications were adaptive cruise control (ACC), blind-spot detection (BSD), and collision-warning systems (CWS). Recently, other applications have been implemented such as automatic emergency braking (AEB), lane-change assist (LCA), and vulnerable user detection. Radar-enabled driver assistance systems will provide comprehensive information about the vehicle's surroundings and assist drivers in anticipating potential hazards. However, the robustness of sensors to detect and evaluate dangerous road situations is one of the critical barriers to CAV development.

1.2 Challenges and Limitations

The widespread use of automotive radars to map the environment is a crucial step towards vehicle autonomy, with a projected market radar penetration rate (RPR) of 58% by 2035 [32]. As the vehicles with radar sensors will share the same road space, the performance evaluation of these radars in a coexistence scenario is essential for reliable on-road autonomy.

A radar continuously transmits a signal, which is reflected by the surrounding cars and other objects, such as foliage and crash barriers near the road. These reflections are detected and processed by the radar to sense its surroundings. However, the immediate future challenge comes from the co-existence of a large number of active radars in a diverse traffic environment. When this technology is used by several vehicles on the road, it becomes challenging for a radar to distinguish between its desired signal and the signal reflected or transmitted from the radars installed on other vehicles. Therefore, introducing a large number of radars to precisely image the environment also presents a new problem called *'Automotive Radar Interference'* [33], [34].

"In complex traffic, where hundreds of radars may operate in a coexistence scenario, the uncoordinated radar parameters will lead to mutual interference between them. Each radar will act as a jammer to its neighbours."

The forecast 5 – 18 billion-dollar automotive industry is facing a major issue of radar interference making it a current research area [35], [36]. The interference leads to a malfunction of sensors and makes the detection of targets, especially the ones with a small radar cross section (RCS), such as a pedestrian, cyclist, or even a farther-located vehicle, ambiguous. This impacts safety, traffic flow, and driving convenience, especially in high-traffic areas. Therefore, even though radar is the most reliable sensor for operation in all weather conditions, its reliability could be reduced in an interference background. Furthermore, due to the limited spectrum currently available for automotive radars [37], the increased RPR will increase the likelihood

that radars may encounter interference, resulting in greater received interference strengths. The issue is further compounded due to the lack of waveform standardization in automotive sensors.

Automated driving systems have to make real-time decisions that are often safety critical. Therefore, interference that hinders radar performance and affects its detection capability must be mitigated to make roads safer in the automated driving era.

1.3 Objectives and Contributions

Understanding and resolving the problem of mutual interference in automotive radar is the research topic in the presented work. This research intends to assess the entire interference chain, from fundamental concepts of waveform interaction in radar sensors through the impact of interference on the signal processing and finally effective mitigation techniques to improve radar's detection performance. The approach undertaken has been presented in Figure 1.2.

The mitigation techniques discussed in the presented research have been classified into temporal, spatial, and imaging-based, and also the fusion of mitigation techniques to optimise the radar performance. The following key contributions have been made through this work.

- A thorough review and assessment of the state-of-the-art (SoA) interference analysis and mitigation methods.
- Characterisation and analysis of radar interference by developing a mathematical model that quantifies the system-level performance of frequency-modulated continuous wave (FMCW) radar in an interference background.
- Qualitative and quantitative estimation of the interference power as a function of radar hardware and software characteristics and the waveform parameters.
- The effects of various interference scenarios on the signal to interference plus noise ratio (SINR).

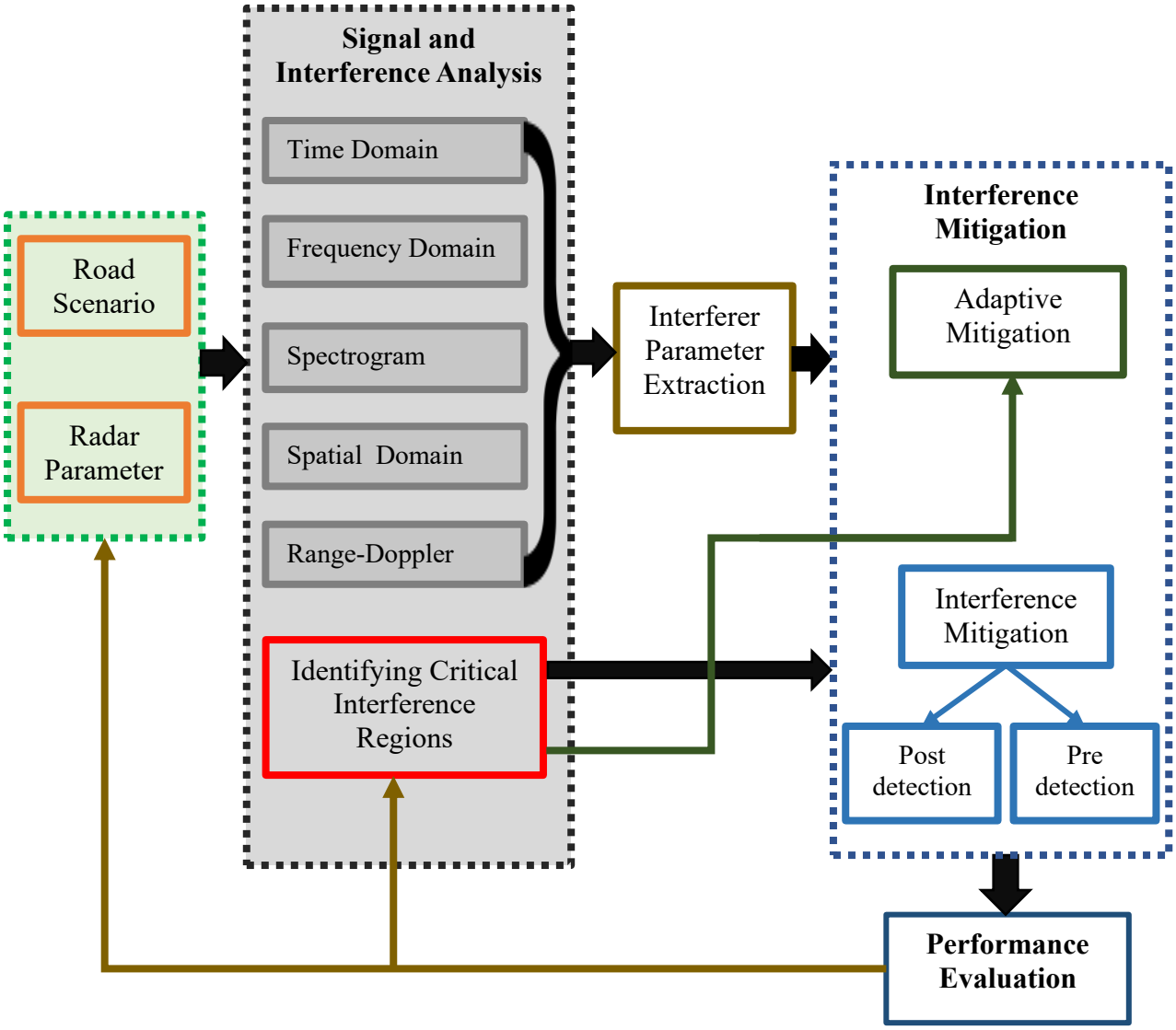


Figure 1.2: Methodology for analysing and mitigating radar interference.

- A systematic SINR analysis at each stage of the radar processing chain.
- Statistical characterisation of interference and its effect on the radar's detector performance.
- Development and comparative analysis of interference mitigation techniques.
- Evaluation of the interference mitigation techniques after their implementation in the radar chipsets.
- Interference mitigation to suppress interference and at the same time enhance target detectability by using Doppler beam sharpening (DBS).

- Validation of the developed analytical model and mitigation techniques.
- Assessment and the impact of radar interference potential in an actual road scene with commercial off-the-shelf (COTS) radar sensors already available in the market.
- Development of a comprehensive and realistic tool, '*Automotive radar holistic simulator*,' to understand radar-environment interactions and characterise and mitigate interference.
- Recommendations and guidelines to mitigate radar interference.

The project has been funded by Innovate UK and undertaken at the University of Birmingham (UoB) at the Microwave Integrated System Laboratory (MISL) in collaboration with industrial partners Jaguar Land Rover (Industrial lead) and HORIBA MIRA.

1.4 Automotive Radar and Environment Simulator

In an automotive scenario, endless situations are possible, such as different hardware characteristics, waveform modulations and parameters, antenna radiation patterns, mode of signal transmission, beamforming techniques, the geometry of scenarios, and the number of simultaneously operating radars. These factors must be considered while analysing the performance of radars in a coexistent scenario. However, a comprehensive understanding of the radar-environment interaction is logistically impractical using real-world conditions. An experimentally verified software tool would facilitate the analysis of complex scenarios and aid in identifying the critical situations and configurations that affect the radar performance. Therefore, the techniques to mitigate these effects can be implemented before testing in the real world. For this, a systematic analysis of potential factors influencing radar performance is needed to develop and validate a radar sensor model.

As part of the presented work, an experimentally verified holistic simulation tool based on the specifications of SoA automotive radars has been developed and detailed in Appendix 12. Radar-environment interactions have been demonstrated for extended targets, clutter, and

transmissions from nearby sensors – radar interference. Furthermore, various aspects of sensor configuration and signal processing according to the radar hardware and software capabilities have been investigated. The tool is a test environment for modelling and performance analysis of radars and will act as a guide toward developing robust radar sensors. Furthermore, it will provide the ability to bring real-world conditions into the software and facilitate the performance analysis of sensors currently expected to be used for ADAS [38]–[40].

Compared to similar tools [41], [42], the developed simulator provides a comparative analysis of various interference mitigation techniques in terms of the SINR improvement, target detectability, and possible ambiguity in the target parameter estimation due to interference. Moreover, due to the integration of various types of targets, interferers, road types, and hardware-specific functionality, the effects of these parameters and configurations can be estimated.

1.5 Glossary

Various terminologies used in the presented work have been described below:

- Victim radar (VR) – Radar installed on the host vehicle that receives interference from surrounding radars.
- Host radar (HR) – Radar installed on the test vehicle that is taking radar measurements in the absence of interference. It is also called the ego-radar.
- Interferer radar (IR) – Radar that transmits an interference signal. In most cases, the interference received at the VR is expected to be transmitted by an IR, unless stated otherwise.
- Target – Any objects (cars, pedestrians, infrastructure, etc.) in the field of view (FoV) of the radar that the radar should detect.

- Echo signal – The signal reflected from targets and received by the radar. This is the desired signal for the host/ victim radar.
- Interference floor – Due to possibly higher received interference power, an increase in the receiver noise floor is observed, referred to as the interference floor.
- Fast-chirp interference sequence – Type of interference for which the sweep time of IR is less than the sweep time of the VR.
- Slow-chirp interference sequence – Type of interference for which the sweep time of IR is larger than the sweep time of the VR.
- Pulse repetition interval (PRI) – The time after which each new pulse/ chirp signal is transmitted by the radar.
- Fast-time – Time during each PRI.
- Slow-time – Time across multiple PRIs.
- Radar data cube – Radar data is arranged as a 3-dimensional (3D) matrix with fast-time samples, slow-time samples, and the number of array channels along each dimension, respectively.
- Range compression – Performed to estimate the range of the targets. In this work, this has been done by applying a fast Fourier transform (FFT) across the fast-time samples.
- Doppler Compression – Performed to extract the relative speed of the targets. In this work, it has been done by applying an FFT across the slow-time samples.
- Spatial compression – Performed across multiple array elements of the radar to estimate the spatial position of targets. In the presented work, due to the availability of radar chipsets for the measurements, the spatial resolution across elevation was not provided. Therefore, spatial compression provides information on the azimuth position of the targets only, considering elevation = 0^o.

- Frequency domain – Analysis and results after range compression, and combined range and Doppler compressions.
- Spatial domain – Analysis and results obtained after spatial compression.
- Range profile – Obtained after range compression. It indicates the target's range as a function of its received power that is represented in dBm in the presented work, unless stated otherwise.
- Range-Doppler – Analysis and results obtained after range and Doppler compressions, plotted as relative speed as a function of range to the targets.
- Range-azimuth – Analysis and results obtained after range, Doppler, and spatial compressions, plotted either as a polar map representing the azimuth angle as a function of the slant range to the target or as a Cartesian map representing the range and cross-range of the target[2,3].
- CPI – Coherent processing interval over which the Doppler compression is performed.
- PPI – Plan position indicator plot representing the range and cross-range of the target.
- Frequency bins – Discrete frequency component after range compression. Each frequency bin resolution is $F_s/NFFT$, where F_s is the sampling frequency and $NFFT$ represents the number of FFT points. Nth frequency bin can be expressed as: $nF_s/NFFT$.
- Range bins – Frequency bins are often converted to range bins to interpret the range to the target better. Range bin is estimated as $cf/2K_v$ in a dual (in-phase/quadrature) channel

[2] The range-azimuth map have been plotted showing the range and azimuth values for the maximum Doppler bin.

[3] In some instances (mentioned in the text), range-azimuth map has been generated after only range and spatial compressions.

receiver and $cf/4K_v$ in a real channel receiver, where c is the speed of signal propagation, f represents the frequency bin, and K_v is the waveform's sweep rate.

- Doppler bins: Discrete frequency bins after Doppler compression. The resolution of each bin is represented as: $1/CPI$.
- Doppler frame – Formed with chirps received during a coherent processing interval (CPI). The Doppler compression has been applied across the Doppler frame.
- Azimuth frame – Equivalent to $N_{Tx}N_{Rx}$ elements in MIMO mode or N_{Rx} in a phased array configuration, N_{Tx} and N_{Rx} are the number of transmit and receive elements, respectively. Spatial compression has been applied across the azimuth frame.
- Time series representation – Augmented range profiles representing time as a function of range to the target.
- Single channel receiver – Radar receiver based on a real-only channel.
- Dual channel receiver – Radar receiver based on in-phase and quadrature (I/Q) channels.
- NRMSE – Normalised root mean square error used to compare the interference and additive white Gaussian noise (AWGN) statistics.
- Mutual Interference – The type of interference between the radars installed on different vehicles.
- Self interference – The type of interference between the radars installed on the same vehicle.

1.6 Thesis Organisation

The presented work addresses the simulation, development, implementation, and experimental testing of radars in the presence of interference.

Chapter 2 reviews the theoretical background, including the fundamentals of radar, modulation schemes used in the contemporary radars, basic signal processing stages in SoA automotive radar chipsets, as well as recent advances in interference analysis and mitigation techniques.

Chapter 3 focuses on the analytical analysis of radar interference, discussing various types of interference expected in typical automotive scenarios, and interference hotspots where a high level of interference is expected depending upon its orientation with respect to the VR and the VR and IR parameters. The appearance of interference across various signal processing stages of the VR, alongside the effect of each stage on interference, is also discussed.

Chapter 4 characterises the statistical properties of interference, its comparison to the statistical characteristics of AWGN, and the effect of interference on the radar detector.

Chapter 5 presents various techniques for interference detection, interfering radar waveform parameter extraction, and interference mitigation, followed by the effect of different mitigation techniques on radar performance.

Chapter 6 details the mitigation of interference in the spatial domain for different array configurations and types of radars. A comparative analysis of the spatial domain mitigation with the temporal domain mitigation for various RPRs is also presented.

Chapter 7 examines the SINR along the radar processing stages using real-road radar data gathered for different orientations of the radar sensors.

Chapter 8 discusses the application of DBS – a resolution enhancement technique – to mitigate radar interference. The effectiveness of DBS is evaluated compared to other mitigation techniques.

Chapter 9 presents the research outcomes of the conducted research on radar interference alongside the project outlook.

Chapter 2. TRENDS IN AUTOMOTIVE RADAR

Radar is an acronym for 'Radio detection and ranging' and can operate in harsh conditions such as dark, fog, bad weather, bad light, and extreme temperatures. Moreover, it can reliably function at long, medium, and short ranges for navigation, target detection, tracking, search and surveillance, and high-resolution imaging and mapping of the surroundings. Over the last few decades, radar applications in the automotive and industrial space have captured significant interest from researchers worldwide.

A radar sensor illuminates the environment by transmitting EM waves and processing the received 'reflected' radio waves (echo signals). In the presence of objects within the radar's operational range and FoV, some of the energy that the radar radiates is intercepted and reflected by these objects in different directions. The radar receiver then receives a fraction of the reflected energy. After signal amplification and processing [43], radar detects and measures the characteristics of objects, such as their range, relative speed, and spatial location (azimuth and elevation).

The target range 'R_T' is determined by estimating the round-trip time of the signal from the radar's transmitter back to its receiver and given as follows:

$$R_T = \frac{c\tau_D}{2} \tag{2-1}$$

where, τ_D is the signal's two-way propagation delay from the radar's transmitter to the target and back to the radar receiver, and *c* is the speed of light. The relative speed between the radar and the target is estimated from the Doppler frequency shift (f_D) across multiple radar pulses and calculated as follows:

$$f_D = -\frac{2v_r}{\lambda} \tag{2-2}$$

where, v_r is the radial velocity in the direction of the target, and λ is the wavelength of the transmitted signal. For an approaching target, due to its decreasing range, $v_r = \frac{dR_T}{dt} < 0$. This gives, $f_d > 0$. In contrast, for a receding target, the range increases with time with $\frac{dR_T}{dt} > 0$ consequently, $f_d < 0$. The target's angular position is estimated from the signal's phase shift across multiple antenna elements. The target type can be identified by estimating the micro-Doppler from the target, where the target's motion modulates the received signal [44], and using the target signature in the classification algorithms [45], [46].

In the ground imaging scenario, after the required signal processing, the radar accomplishes three essential functions [47]:

1. Target detection: The presence of a target in the background of noise and interference(s).
2. Target tracking: Alongside target detection, their respective distances, radial speeds, and spatial locations with respect to the radar are estimated with high accuracy. These are then used to predict the target trajectory and possibly identify passable and impassable regions for the host vehicle.
3. Imaging: The radar forms a map of a region in the environment showing the respective positions of targets in common occupancy grid maps or the world coordinates [48], [49]. The imaging maps include the following:
   - Clutter map showing the static environment.
   - Tracks of the moving targets.

   These maps assist in monitoring the details of the vehicle's surroundings and deciding the vehicle's trajectory accordingly.

2.1 Brief History of Radar

The phenomenology of radar goes back to the 1800s when Heinrich Hertz demonstrated the radio wave reflection by metallic objects at 455 MHz [50]. Nicola Tesla, in 1900 suggested that the reflection of EM waves could be used to detect metallic objects. The first patent on radar was acquired in 1904 by Christian Hulsmeyer, who called this 'Telemobiloskop – A remote object viewing device' for obstacle detection and ship navigation. Hulsmeyer developed a prototype device to locate nearby ships in thick fog that were otherwise invisible to the human eye. Albert Taylor and Leo C. Young filed a patent in 1922 for a ship detection system using radio waves [35].

However, the late nineteenth and early twentieth centuries saw the emergence of technologies that eventually led to the development of contemporary radar systems. At that time, radar applications were primarily focused on military [51], ionosphere sounding [52], and commercial use. Modern radar system was rapidly developed during World War II for its use in air defence, such as the long-range air surveillance and the short-range low-altitude target identification. In 1939, the US Navy created the acronym, 'RADAR.' The invention of the cavity magnetron by British physicists John Randall and Harry Boot marked a significant advancement in the use of radar. Cavity magnetron shortened the radio wave pulse, increased the available transmit power, and allowed for the compact radar systems [53].

In the post-war period, improvements were made in developing continuous wave (CW) and pulsed radar systems for military and civilian applications. Notable civilian applications of radar were the weather radar and the air-traffic control radar for air traffic safety in airports. The radar gun was later developed during the 1950s and 1960s and was used by police officers to ensure the speed limits of vehicles.

Since the 1970s, digital technology has undergone incredible development, making the signal processing requirements for contemporary radar achievable [54]. Significant advances were made in the airborne pulse-Doppler radar, which enhanced its ability to detect aircraft amid dense ground clutter. Over the next decade, technology further evolved, and radars could distinguish between different types of targets. As the computer technology advanced, more information about the characteristics of targets and the radar surroundings became possible, therefore, paving the way towards modern imaging radars.

During the 1970s, radar applications in the automotive sector also emerged. At that time, radars were used to provide parking assistance, lane change assist and lane departure warning [55], and collision warnings to the driver [33], [56]. In the coming years, a rising interest in self-driving cars for safe and reliable driving acted as a main driving force toward the advancement of the automotive industry. Instead of supporting the driver, modern automotive radars can accurately sense and perceive the environment to provide reliable information to the vehicle's control systems for efficient path planning. The chronological flow diagram highlighting the development of automotive radar is demonstrated in Figure 2.1.

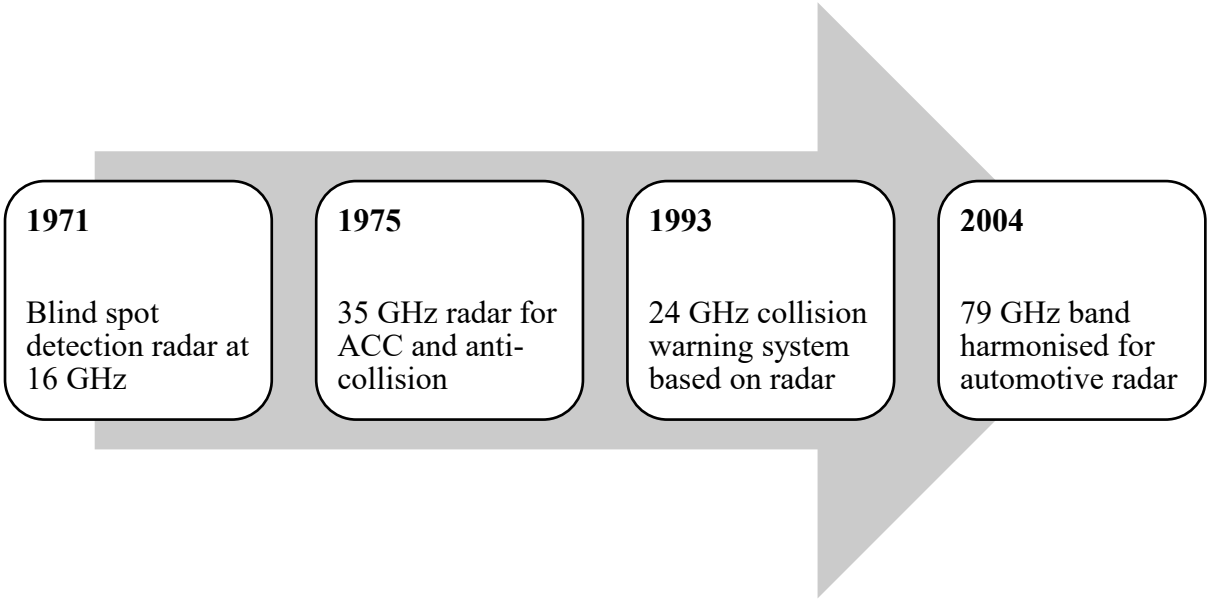


Figure 2.1: Chronological flowchart of the automotive radar history.

The evolution of automotive radar has been thoroughly discussed in [57]. A prototype radar for automotive applications operating at 35 GHz was tested in the early 1970s [29], [57]. However, due to its large size and high cost, it was not widely integrated into the vehicles. Luxury cars since the late 1990s included some form of driver assistance functionality [58]–[60]. Due to radar's ability to look through optically opaque environments, Mercedes-Benz S-class introduced radar in its vehicle as a key component for environment perception [33] in 1999.

Since then, radar has undergone advancements in terms of its size and signal-processing algorithms. ACC systems based on millimetre wave (mmWave) radar have been under development for several decades [61]–[63]. Compact automotive radars can be developed with highly integrated and inexpensive mmWave circuit implementation in silicon. This would decrease the impact of the deployed sensor on a vehicle's aerodynamics and appearance.

The chronological history of radar is summarised in Table 2.1.

Table 2.1: Chronological history of the radar.

Pre-World War II Era (1800s-1930s)	
1887	Heinrich Hertz demonstrated the existence of radio waves.
1904	Christian Hülsmeyer patented the Telemobiloskop, an early form of radar.
1922	Albert Taylor and Leo C. Young filed a patent for a ship detection system using radio waves.
World War II Era (1930s-1940s)	
1935	Robert Watson-Watt and his team in the UK developed the first practical radar system for aircraft detection.
1939	Sir Robert Watson-Watt presented his research on the radar to the British government, leading to the establishment of a chain of radar stations along the UK coastline.
1939	The acronym 'RADAR' was proposed by the US Navy.

1941	Rapid development and deployment of radar technology by the US.
1943	The cavity magnetron, a key component of modern radar systems, was developed in the UK.
1944	The first airborne radar system was used, providing vital navigational assistance.
Post-World War II Era (1950s-1970s)	
1950s	Development of radar technology continued, with advancements in areas such as pulse compression, frequency agility, and phased array antennas.
1957	The Soviet Union launched the world's first artificial satellite, Sputnik, sparking the Space Age and leading to advancements in radar systems for space surveillance.
1960s	The introduction of digital signal processing revolutionized radar technology, enabling improved target detection and tracking capabilities.
1970s	Radar systems became increasingly sophisticated, incorporating computerized controls, advanced signal processing techniques, and higher frequencies for improved performance.
Modern Era (1980s-Present)	
1980s	The development of radar technology expanded into areas such as weather radar, synthetic aperture radar, and radar altimetry.
1990s	Global Positioning System integrated with radar systems, allowing for more precise position determination and navigation.
2000s	Introduction of phased array radar systems, multi-function radar systems, and advancements in radar imaging.
2010s	Research and development on improving radar capabilities for autonomous vehicles, collision avoidance systems, and adaptive radar systems.
Present	Radar technology continues to advance, with ongoing research in areas like cognitive radar, mmWave radar, and radar-based remote sensing applications.

2.2 Types of Radar

Broadly, radar can be classified into two types, as indicated in Figure 2.2. These types have been briefly discussed in this section.

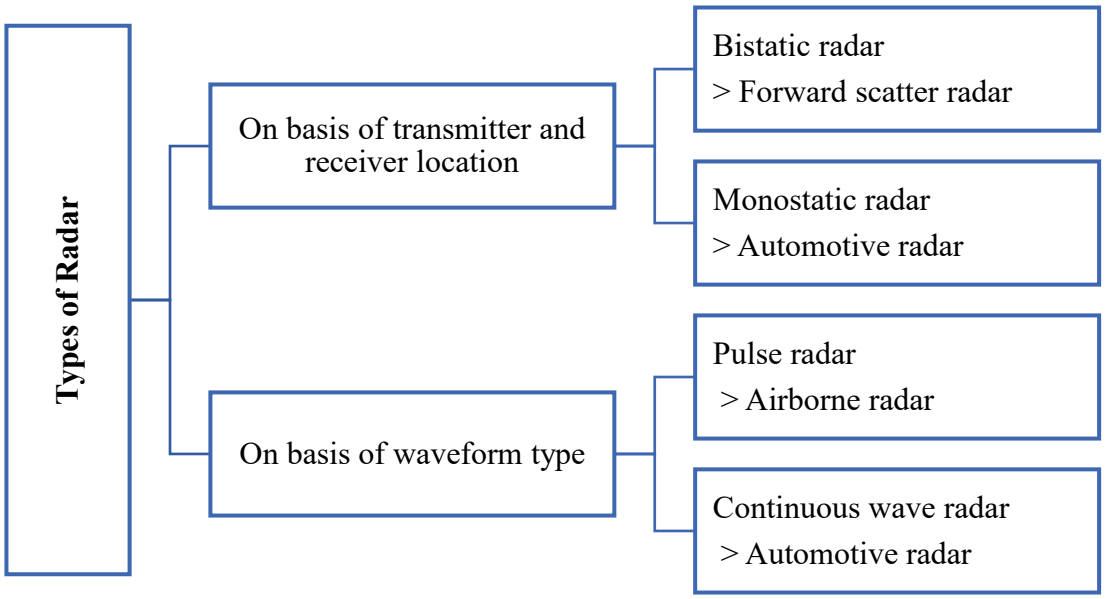


Figure 2.2: Major types of radars.

2.2.1 Bistatic vs Monostatic radar

In a bistatic radar, the transmitter and receiver are at separate locations if observed from the target's perspective. Therefore, they can operate simultaneously. In comparison, a monostatic radar has a collocated transmitter and receiver. Therefore, the radar can transmit or receive at a specific instant of time [64]. The bistatic and monostatic radar configurations have been illustrated in Figure 2.3.

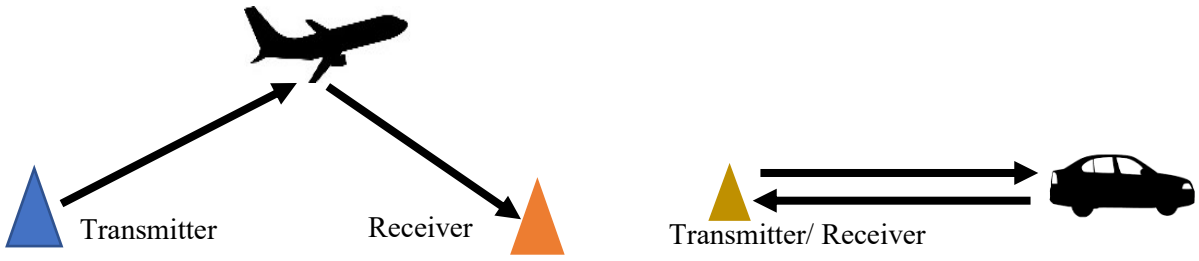


Figure 2.3: Classification of radar: (a) bistatic configuration, (b) monostatic configuration.

Automotive radars that are a subject of discussion in the presented work are monostatic.

2.2.2 Pulse and Continuous Wave Radar

Pulse radars transmit a short-duration pulse and then switch to the listening mode. During this time, they receive and process the echo signal before the new transmission. These radars are commonly used for longer ranges. A typical example of pulse radar is airborne radar [65].

CW radars operate continuously and therefore can have a lower average power than the pulse radars while still providing the same average transmit power. Therefore, they are more suitable for comparatively short and medium-range applications. The CW radars are further divided into the following:

1. Unmodulated CW radars: These radars transmit a CW signal of a specific frequency and are typically used to measure the speed of the targets. An example is the radar gun used to monitor the vehicles' speed [66].
2. Modulated CW radars: In these radars, the CW wave is modulated with either frequency modulation, termed as FMCW radars, or phase modulation, termed as phase modulated continuous wave (PMCW) radars. These radars are used to estimate the targets' range and relative speed.

2.3 Automotive Radars

Automotive radar has transformed the safety and efficiency of modern vehicles, enabling vehicles to sense and perceive their surroundings with precision. These radars employ the principles of radio waves and advanced signal processing to detect objects and measure their distance, relative velocity, and spatial position. By providing accurate sensing and perception of the environment, automotive radar plays a crucial role in vehicle autonomy.

International Telecommunication Union (ITU) [67] has classified automotive radars as the long-range radar (LRR) mainly used for ACC, the medium-range radar (MRR) for broader FoV applications, and the short-range radar (SRR) to detect objects closer to the vehicle.

Depending upon the application, precise situational awareness could be achieved by using either multiple radars mounted next to each other, in different orientations, or by one multi-modal sensor incorporating sensor fusion [68]. Highly automated and autonomously operating vehicles require up to 12 radar sensors to guarantee reliable 360° coverage [69]. To achieve this, four SRRs can be deployed at the four corners of the vehicle, two MRRs deployed at both the front and rear side, two MRRs deployed at the sides, and two LRR sensors deployed at the front [70]. However, as the number of radars operating in the same band increases [18], the chances of overlapping bandwidth also increase, resulting in interference between them. This has been discussed in detail in the subsequent chapters. The typical radar parameters used in automotive radars [64] are mentioned in Table 2.2.

Table 2.2: Typical automotive radar parameters in the 77 GHz band.

Parameter	SRR	MRR	LRR
Frequency band (GHz)	77-81	77-81	76-77
Operational range (m)	0.15-30	1-100	10-250
Installation location	Corner/ Side	Front/Rear/Side	Front/ Rear
Azimuth field of view (Degree)	$\pm 80^{o}$	$\pm 40^{o}$	$\pm 15^{o}$
Elevation field of view (Degree)	$\pm 10^{o}$	$\pm 5^{o}$	$\pm 5^{o}$
Maximum power (EIRP)	55 dBm	-9 dBm/MHz	-9 dBm/MHz

Each type of radar has different capabilities and applications [61], [71], [72], which are summarised in Table 2.3. The LRRs are typically used for applications with a narrower FoV in the azimuth and a higher transmitted power. However, the higher power results in a more significant impact of interference from these radars. MRRs have a medium coverage range and a broader FoV compared to the LRR and are generally used for features such as cross-traffic alerts. SRR has the widest FoV and shortest-range coverage.

Table 2.3: Applications of various types of automotive radars.

Type of Radar	Short Range Radar	Medium Range Radar	Long Range Radar
Applications	• Emergency braking • Pre-Crash sensing • Obstacle Detection • Pedestrian Detection • Side impact • Parking assistance • Blind spot detection (BSD)	• Pedestrian/ Object detection • Collision avoidance • Autonomous Emergency Braking (AEB) • Front/ Rear Cross Traffic Alert (F/RCTA) • Lane change assist (LCA) • Blind Spot Detection • Stop & Go	• Adaptive Cruise Control • Automated highway driving • Large RCS target detection • Curve speed control

Figure 2.4 presents the pictorial representation of different types of radars and their functionality to achieve ADAS [73], [74].

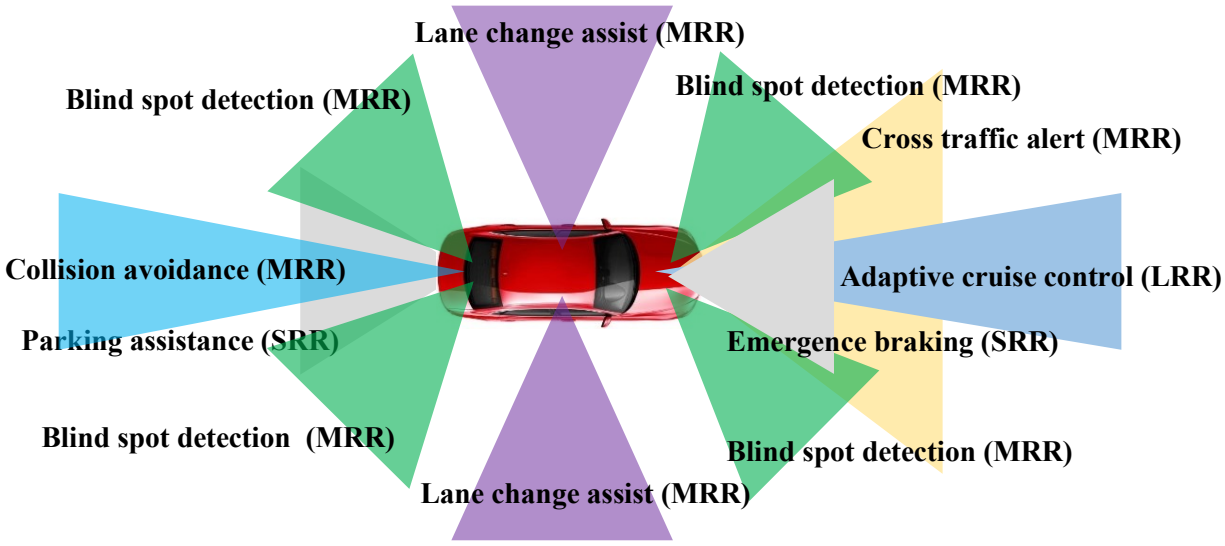


Figure 2.4: Radar types and functionality to achieve advanced driver assistance system.

2.3.1 Operational Spectrum

There have been developments of automotive radar systems in 24 GHz and 77 GHz bands [75]–[78]. The 24 GHz band includes the following two sub-bands [71]:

1. Narrowband: An industrial, scientific, and medical (ISM) band from 24.05 to 24.25 GHz.
2. Ultra-wideband: From 21.65 to 26.65 GHz.

However, due to the following factors, the 24 GHz band is unattractive for modern automotive radar systems.

- Lack of wider bandwidth and industry requirement for high resolution to improve imagery.
- High hardware cost and large size of the radar.

The latest and upcoming radar technologies operate in a 76 – 81 GHz band, which enables accurate detection of targets due to shorter wavelengths. Moreover, due to the availability of wider bandwidth, a higher range resolution is provided. The 77 GHz band (76 GHz to 77 GHz) is preferred for ACC applications, whereas the 79 GHz band (77 – 81 GHz) is a suitable choice for environment sensing for short/ medium range radars with an enhanced resolution [71], [79], [80]. In this band, radar's form factor is compact, and antenna size is small, resulting in a larger number of antenna elements that can be incorporated in the same size array as compared to the 24 GHz band. This results in higher angular and cross-range resolutions [29]. As the velocity resolution is inversely proportional to the frequency for a specific observation time, the 77 GHz band also provides a better velocity resolution. Therefore, imaging and target detection capability improve at the higher band.

Various market solutions taking advantage of the 77 GHz band have been proposed for autonomous radar applications [29], [81], [82]. Some of the examples include 77 GHz automotive radars from NXP Semiconductors [83]–[85], Infineon [86], [87], Texas Instruments (TI) [38], [88], [89], INRAS [90], [91].

Research into the terahertz band is advancing to enhance the resolution whilst maintaining a small form factor [92], [93]. Current automotive radar sensors, however, operate primarily in the 77 GHz band and will continue to do so in the future because the ITU has defined this section of the spectrum for future automotive radar sensors [94].

2.3.2 Modulation Schemes

For applications such as ACC, automotive radar systems should be operational at longer ranges, while achieving a fine range resolution to distinguish closely spaced targets. High peak power is required for a longer range whereas a narrow pulse (hence high bandwidth) is needed for a high-range resolution. However, there is a regulation limit on the peak power for automotive radars, which is approximately 10 dBm [95]. This makes it challenging to achieve the desired unambiguous range of ~ 300 m for ACC. Therefore, automotive radars use pulse compression techniques where the transmitted pulse is modulated with a signal of a specific bandwidth, and the received echo is compressed by down-converting it.

Various modulation schemes have been discussed in the literature [96]–[98], which typically include FMCW [99], PMCW [100], phase coded – frequency modulated continuous wave (PC-FMCW) [101], combined frequency shift keying (FSK), and linear frequency modulation (LFM) [102]. FMCW and PMCW modulations, the current competing technologies in automotive radars, have been summarised below.

I. FMCW

In FMCW modulation, a signal is swept for bandwidth B_{sv} during the duration T_{sv}. The transmitted FMCW signal with linearly increasing and decreasing frequency is expressed as

$$S_{FMCW}(t) = A_o \exp\left(j2\pi\left(f_{cv}t \pm 0.5K_v t^2\right)\right) \tag{2-3}$$

where, A_o is the amplitude of the signal, $K_v = B_{sv}/T_{sv}$ is the sweep rate, f_{cv} is the carrier frequency, and *t* represents the fast-time expressed as $t = 0 : t_s : T_{sv} - t_s$, where t_s is the sampling interval. At any instant '*t*,' the instantaneous frequency of the transmitted signal $\left(f^{'}(t)\right)$ is expressed as:

$$f^{'}(t) = \frac{1}{2\pi}\frac{d\left(2\pi\left(f_{cv}t + 0.5K_v t^2\right)\right)}{dt} \tag{2-4}$$

After solving,

$$f^{'}(t) = f_{cv} + K_v t \tag{2-5}$$

The spectrum of an FMCW signal is then obtained using the following:

$$S(W) = \frac{1}{2\pi} \int_{-\infty}^{\infty} S_{FMCW}(t) \exp(-jwt)\, dt \tag{2-6}$$

The spectrum appears like a pedestal [103] with peaks at the input signal frequencies. The time domain plot of the FMCW signal, its short time Fourier transform (STFT), and spectrum have been given in Figure 2.5 (a) for T_{sv} = 1 µs, B_{sv} = 50 MHz, and f_{cv} = 50 MHz.

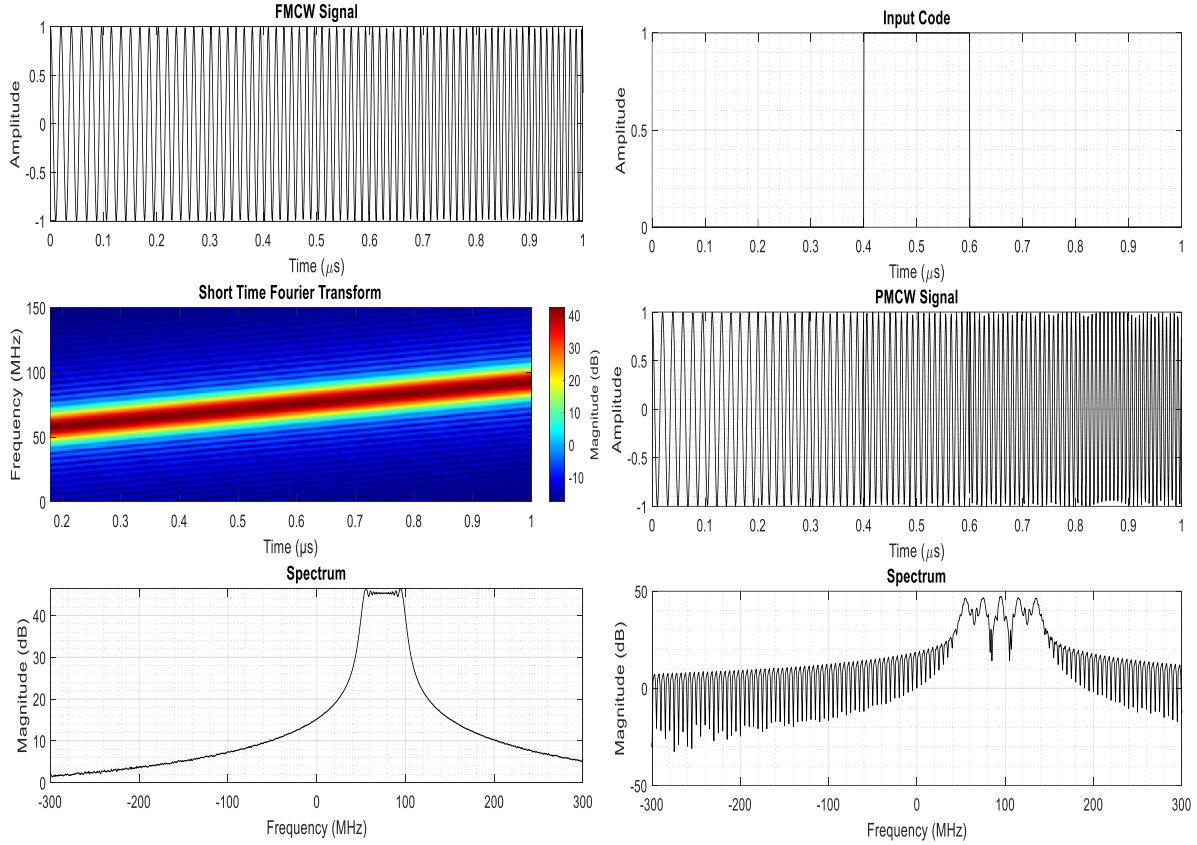
II. PMCW

The concept of PMCW radar has been presented in [104], [105] as an alternative to the FMCW radar. In digital PMCW modulation, the LFM signal with a sweep duration of '*T*' is divided into *N* bits, where the bit duration (T_b) is expressed as $T_b = T/N$. Each bit duration is then modulated according to the input code with a length equal to *N*.

To ensure signal orthogonality across the transmit elements of radar (critical for MIMO radar), the input code is embedded into the LFM signal using phase shift keying (PSK). In the discussed example, binary – PSK (BPSK) has been used, and the phase shifts between 0^o and 180^o, depending upon the bit sequence. The input code, time domain plot of the PMCW signal, and its spectrum have been demonstrated in Figure 2.5 (b). The spectrum contains side lobes due to a phase reversal from bit 0 to bit 1 or vice versa. Moreover, a peak at the carrier frequency (50 MHz in this case) is observed, followed by peaks at regular intervals.

To satisfy the requirement of high-range resolution and unambiguous range and velocity, the bit duration must be short, and the code length must be large [105], [106].

The research on the suitability of PMCW is being investigated as a replacement to FMCW for improved parameter estimation and target detectability, especially in the background of interference from other radars [104], [107].



(a) (b)

Figure 2.5: Automotive radar signal analysis: (a) FMCW with time domain, short-time Fourier transform, and spectrum, (b) PMCW with input code, time domain, and spectrum.

FMCW is the widely used modulation scheme in SoA automotive radars [33], [61], [108] due to its advantages such as [58], [109]–[112]:

- Low transmit power.
- A simple homodyne processing chain.
- Ability to measure objects at relatively short ranges.
- Ability to measure the target range and its relative speed simultaneously.

- Low-frequency signal processing makes the implementation of processing circuits and real-time imagery achievable.
- Effective utilisation of the spectrum with lower frequency sidelobes.

Therefore, the FMCW modulated signal shall be considered in the presented work.

2.3.3 MIMO Radar

The key requirement for modern radar sensors is to provide high resolution for precise detection and scene reconstruction. This relies on the signal bandwidth, the signal integration time, and the antenna's geometry [113]. An urban environment is inherently congested with targets, having different speeds and RCSs. The range-Doppler separation of targets is inadequate in this scenario. Therefore, advanced sensing with an image-like resolution, where the targets are resolved in azimuth and elevation, is also required to perceive the surroundings accurately. The azimuth and elevation resolutions for Level 4 and Level 5 (L4/L5) autonomous driving should ideally be less than 1º [30], [114], [115]. For a higher angular resolution, a larger antenna aperture is required [116]. However, this would increase the radar size, making its integration into the vehicle difficult.

Early automotive radars used mechanically scanned antennas or several fixed antennas for one-dimensional (azimuth) angle-detection capability [19], [61]. The concept of MIMO radar was proposed to improve the angular resolution of radar while keeping a small form factor and low system cost [117]. MIMO radars became an alternative to the conventional scanning radars that had a narrow transmit beam and performed sequential scanning by transmitting the phase-shifted version of the same signal. In contrast, a MIMO radar transmits multiple independent signals from each transmit element, with a broader beam that covers a large FoV [118]–[120]. Due to the waveform diversity provided by these independent transmit beams, resolution can be enhanced with more 'degrees of freedom (DoFs)' but with fewer sensor

elements and without the use of phase shifters. This also allows for simultaneous illumination of the targets within the broad FoV of each transmit element. Moreover, a MIMO array may operate at a shorter distance, which is physically impossible with a traditional phased array, making it suitable for automotive applications.

The received signals corresponding to each transmit element can be distinguished at the receiver due to the orthogonality between transmitted waveforms. Therefore, a large aperture array of $N_{Tx} \cdot N_{Rx}$ elements with virtual antenna positions is created compared to that created by the physical transmit and receive antennas $\left(N_{Tx} + N_{Rx}\right)$ where, N_{Tx} and N_{Rx} represent the number of transmit and receive elements in the array, respectively. The equivalent virtual array of a large number of elements provides higher resolution than the two-way beam of scanning radars with the same number of physical elements, as shown in Figure 2.6 for $N_{Tx} = 4$ and $N_{Rx} = 16$.

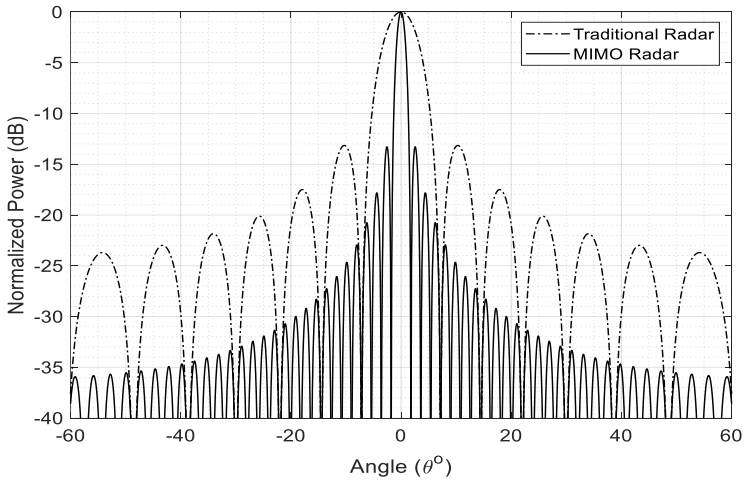


Figure 2.6: Beam pattern of MIMO and scanning radar with $N_{Tx} = 4$, $N_{Rx} = 16$.

I. Signal Orthogonality

Various techniques can be utilised to achieve orthogonality between transmitted signals in MIMO radar. One of these is the time-division multiplexing (TDM). Under TDM-MIMO, a series of FMCW chirps are transmitted sequentially from each transmitter. At a specific instant

in time, only one transmitter is active. Therefore, it is trivial to associate the received signals with their originating transmitter. Other methodologies include frequency division multiplexing (FDM) [121], Doppler division multiplexing (DDM) [122], and code-division multiplexing [123], [124]. However, they are outside the scope of this work. MIMO radars have been used in the presented work, and orthogonality is achieved using TDM [125]–[128].

II. Beamforming

Digital beamforming (DBF) at the receiver gives precise spatial positions of the targets within the area illuminated by a wide transmit beam [118], [129], [130]. Therefore, MIMO radars provide a cost-effective solution for a larger antenna aperture with enhanced spatial resolution [37], [131], [132]. These characteristics make it attractive for applications such as precise 2D angle-detection capability across azimuth and elevation, parking aids, collision detection, cruise control especially at shorter ranges, pedestrian and object detection and parameter estimation, high-resolution target identification, localisation, classification, and profile reconstruction.

2.3.4 Signal Processing

Automotive radars require a baseband processing system to provide the required computing power for real-time functionality. The desired lower power used in these systems [99] leads to the feasibility of digital-intensive architecture that is relatively fast. A variety of signal processing algorithms for different radar types, road scenarios, and traffic density have been developed [113], [133]–[137] to estimate the following:

- Target features, such as a micro-Doppler spectrum of the moving objects [138]–[140].
- Range–Doppler [141]–[143] and range-azimuth profiles [144] of the surrounding environment.

The algorithms are traditionally based on the following:

1. Range compression, Doppler compression, and spatial compression to extract the range, relative speed, and azimuth information[4].
2. STFT for the time-frequency decomposition [145].
3. Filtering to reduce the sampling requirements at the receiver.
4. Windowing to suppress the sidelobes [146].
5. Beamforming to estimate the direction of the received signal [116].
6. Target detection to detect the presence of the target in the background of noise/ clutter.

For MIMO radars, due to the relative motion of the targets and platform, additional phase shift compensation is also required to achieve the maximum beamforming performance [147].

Techniques based on artificial intelligence and deep neural networks [148]–[153] have also been used for target recognition and classification. Different aspects of signal processing are discussed below.

I. Transmit Chirp Signal

Each transmit signal chirp comprises three parts: active time, also called the sweep time $\left(T_{sv}\right)$, a fly-back time, and an idle time between multiple chirps defined to allow enough reset time to the analogue to digital converters (ADCs). The collective time is termed a pulse repetition interval (PRI)[5], after which each new chirp is transmitted by the radar. The duty cycle is defined as $DC_v = T_{sv} / PRI$.

A sequence of chirps is transmitted within a coherent processing interval (CPI). The corresponding received chirps at each receive channel of the radar are stored as a 2-D matrix

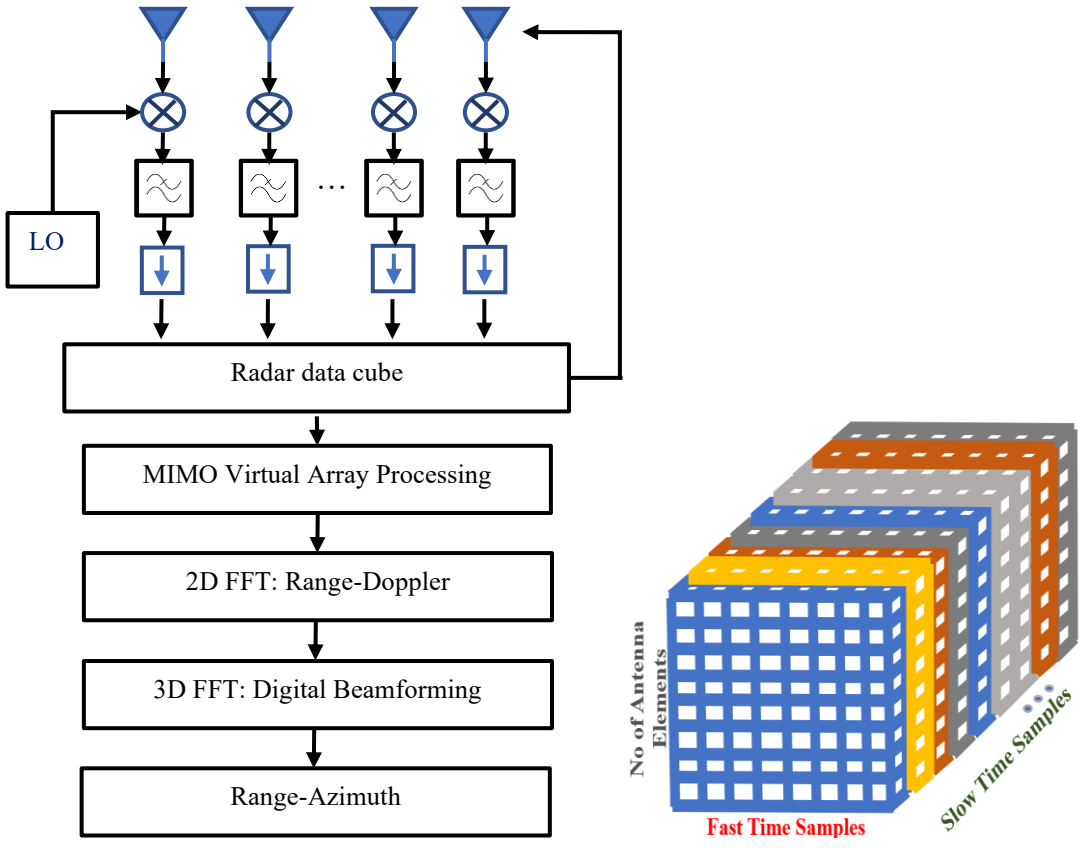
[4] In this work, range compression, Doppler compression, and spatial compression have been performed by applying an FFT along each dimension of the radar data cube.

[5] Due to the nature of waveform in FMCW radars, some researchers use the term chirp repetition interval instead of PRI.

with the size $N \times M$, where N is the number of samples in each chirp (fast-time samples) and M is the number of chirps transmitted within a CPI (slow-time samples).

II. Radar Data Cube and Processing

A typical signal processing chain is demonstrated in Figure 2.7 (a). The signal generated by the local oscillator (LO) is used in the transmit chain and also at the receiver to down-convert the received signal at a homodyne mixer. The output signal at the mixer is low pass filtered to limit its frequency to the maximum expected intermediate (beat) frequency in the radar. The low pass filter (LPF) also functions as an anti-aliasing filter (AAF) for digital signal processing (DSP). The received signal across multiple receive channels is stored as a 3D matrix typically called the 'radar data cube,' as illustrated in Figure 2.7 (b).



(a) (b)

Figure 2.7: Radar data cube: (a) typical signal processing chain, (b) illustration of the datacube.

The first dimension of the radar data cube corresponds to returns across the fast-time – the time during one chirp defined by PRI. The second dimension corresponds to the returns across the slow-time – the time across multiple radar chirps updated after every PRI. The third dimension corresponds to the returns across multiple channels of the radar. It can be equal to the receive array size in the case of a full phased array (FPA) or the number of virtual channels in the case of MIMO radars. This is followed by the digital signal processing on the radar data cube to estimate the target's range, Doppler, and spatial information.

Range compression (an FFT across the fast-time) converts the time domain signal into the frequency domain. Doppler compression (an FFT across the slow-time) allows energy accumulation over the CPI and estimates the relative speed between the radar and the targets. The resulting velocity resolution (Δv) and maximum unambiguously resolvable velocity $(v_{\max})$ are defined as:

$$\Delta v = \frac{\lambda}{2N_{CPI}PRI} \tag{2-7}$$

$$v_{\max} = \pm\frac{\lambda}{4T_{MIMO}} \tag{2-8}$$

where, $T_{MIMO} = N_{Tx}PRI$ and N_{CPI} is the number of chirps within a CPI. Beamforming (spatial compression[6]) is performed for a 2D representation of the scene as range and azimuth/ cross–range. At this stage, the targets are separated into bins by range, azimuth angle, and radial speed.

III. Digital Beamforming in MIMO Radar

Beamforming adapts an antenna array's radiation pattern toward a specific direction to maximise the response from that direction. This is achieved by altering the signal's phase and

[6] Conditionally an FFT across the array elements of the radar and discussed in the following sub-section.

amplitude across different antennas, thereby creating constructive or destructive superpositions of the signal.

With the modern MIMO radars, the beamforming process can be implemented in the digital space compared to traditional arrays, where beamforming happens in the physical space. Therefore, the whole region of interest can be illuminated with a single transmission and DBF at the receiver narrows the beam towards the direction of the target. The received signal at each virtual element of MIMO radar is expressed as follows:

$$S_n = \exp\left(j\frac{2\pi}{\lambda}(n-1)d\sin\theta \right) \tag{2-9}$$

where, $n = 1:N_{Tx}N_{Rx}$, and θ represents the angle of arrival (AoA). If the spacing between antenna elements $'d'$ is $\lambda/2$, the DBF algorithm can be reformulated and applied by FFT across signals obtained by multiple antenna elements, efficiently computed in real-time with current DSPs [154].

DBF has advantages over analogue beamforming approaches in terms of power usage, flexibility, and precision [155]. Moreover, digital systems have programmable interfaces adding versatility to the system and providing the capability of adaptive nulling, using super-resolution algorithms [156], [157], array self-calibration, and power and time management of the radar [158]. Adaptive digital beamforming (ADBF) can also improve radar performance by suppressing any interference, as discussed in Chapter 6.

IV. Windowing

The beat frequency signal in FMCW radars is a sinusoidal signal with a sinc-shaped spectrum [159]. Therefore, sidelobes approximately 13 dB lower than the main lobe are observed and the waveform from each target results in multiple signals at different FFT grids.

To reduce this spectral leakage, an optimal window is applied to the sampled signal before each FFT [146]. This is, however, done at the cost of a reduction in the frequency resolution.

The window's main lobe is centred at each frequency content of the signal. Therefore, when the main lobe width of the window's spectrum increases, the frequency resolution and the ability to resolve closely spaced targets are reduced [146], [160], [161]. Whereas, as the main lobe of the spectrum narrows, the resolution improves, but the signal energy spreads into sidelobes, worsening the spectral leakage. Hence, a trade-off is required between the main lobe width and sidelobe suppression.

Table 2.4 lists the characteristics of various windows [162] that have been used in the later chapters of the presented work. As windows are multiplied with the signal, they introduce a distortion effect which reduces the overall signal amplitude [146]. Therefore, the resulting signal is often scaled by the coherent gain of the window. Compared to the sidelobe level obtained without windowing,

Table 2.4: Characteristics of the spectral windows used in the presented work.

Window	3-dB main lobe width (bins)	SLL (dB)	Sidelobe roll-off rate (dB/decade)	Scaling factor
Rectangular	0.88	-13	20	1
Hann	1.44	-32	60	0.5
Blackman-Harris	1.62	-71	20	0.42

The Hann window has a reasonable resolution and a lower sidelobe level (SLL) than a rectangular window; therefore, it has been used before the Doppler and spatial compressions, whereas the Blackman Harris window has a good sidelobe reduction and has been used before range compression in the presented work, unless stated otherwise. The effect of applying the aforementioned windows on a sinusoidal signal of frequency 50 Hz is shown in Figure 2.8.

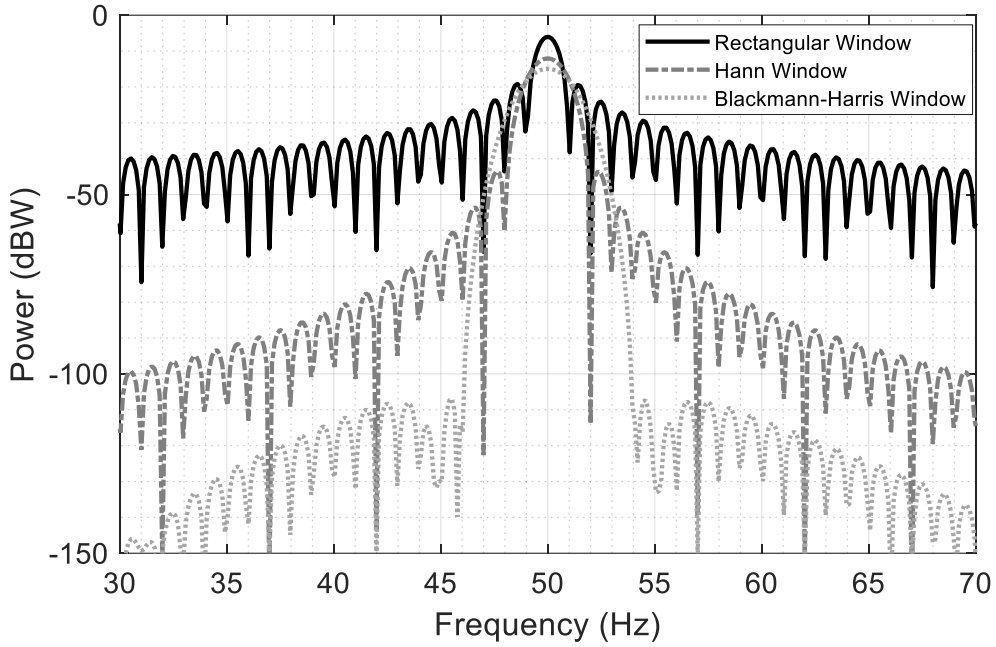


Figure 2.8: Effect of spectral windowing on the frequency resolution and the side lobe level.

V. Target Detection

The input signal to the receiver is composed of the radar echo signal, AWGN, and received interference. AWGN is spatially incoherent and uncorrelated with the echo signal. Similarly, interference in most cases is also incoherent (as discussed in detail in Chapter 4) and uncorrelated with the signal.

Automatic target detection is based on the estimate of the signal to interference plus noise ratio (SINR) at the decision-making point of the receiver (typically after the 3D-FFT). In modern radar systems, a constant false alarm rate (CFAR) algorithm with an adaptive threshold is often used for target detection on the local background noise/interference power [163]. If the background against which targets are to be detected is relatively stable with time and has a Gaussian distribution, such as AWGN, a fixed threshold can be chosen to achieve the required probability of a false alarm $\left(P_{FA}\right)$. However, in realistic automotive scenarios, an adaptive threshold is more suited for target detection due to the presence of clutter and varying interference statistics.

In the presented work, cell-averaging CFAR (CA-CFAR) has been used for target detection. The threshold has been estimated by calculating the average power level within the cells around a cell-under-test (CUT), given as:

$$T = \frac{\alpha}{N} \sum_{i=1}^{N} x_i \tag{2-10}$$

where, N is the number of adjacent training cells, x_i is the estimated power of each cell, and α is a scaling factor. A target is detected when the power level in CUT is greater than the average power of adjacent cells.

2.4 Automotive Radar Interference - Introduction

With a large number of operational radars from different sensor manufacturers and Tier 1 suppliers, co-existence problems arise. This is especially significant in dense traffic conditions, where hundreds of radars may operate simultaneously and lead to mutual interference between them. Radar interference is a significantly complex issue and a major obstacle to the attainment of full automation and widescale deployment of radars.

Interference occurs when two or more radar signals access the same portion of the frequency spectrum, 76-81 GHz, for contemporary automotive radars [37]. To achieve a broad FoV with 360^o sensing around the vehicle and to obtain high range, speed, and azimuth resolutions, industry trends have demonstrated the use of higher bandwidth and higher active duty cycles with multiple sensors per vehicle [164]. However, this leads to a higher probability of victim and interfering signals overlapping in temporal, frequency, and spatial domains [165]. Furthermore, in the absence of regulatory limitations and resource allocation mechanisms, there is no coordination between radars to share resources, making interference more likely.

An example of a typical road scene is demonstrated in Figure 2.9, where the VR will receive interfering signals from the radars installed on the nearby vehicles.

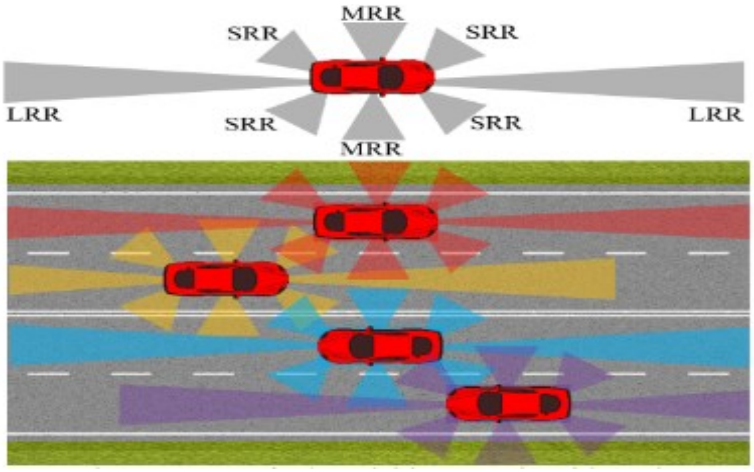


Figure 2.9: A typical on-road scenario demonstrating interference between radars.

Vehicles moving in opposite directions, in the same direction, and through crossings can cause interference.

2.5 Literature Survey on Automotive Radar Interference

Due to the requirement for robust and reliable radars, there is a growing activity aimed at understanding and addressing the problem of interference between them.

Mutual interference was initially assessed by Hischke in 1995 using simulations in various traffic densities [166]. Although it was concluded that targets closer to the radar were detected in the presence of interference, Hischke indicated the importance of developing 'interference-free' radars for target identification. Through real-time measurements, Oprisan [167] suggested that interference is not a significant problem in the co-existence of 2 radars. However, if the power of an interfering signal is higher (interference located closer to the VR), it can degrade the VR's performance.

The impact of interference is expected to increase as soon as the number of coexisting radars increases. Moreover, the VR might receive interference with different parameters and power/ orientation. Based on the analytical estimation, Brooker [168] and Goppelt [169] highlighted the degradation in radar performance due to interference. A reduction in sensitivity

in ultra-wideband automotive radars has been reported in [170]. The saturation of the VR receiver's front-end components due to high-power interference has been discussed in [171].

The probability of interference by considering the spatial, temporal, and frequency overlaps has been discussed in [168], where the interference magnitude is estimated with a conclusion that the probability of interference is significantly high in a coexistence scenario. Moreover, it has been indicated that interference characteristics depend mostly on the temporal and frequency characteristics of the interfering waveforms [78], [168]. For the overlapping chirps[7] of interfering radars, an increase in the noise floor is observed with potentially missed targets [78], [168], [169], [172]. In contrast, ghost targets appear in the processed radar data for parallel chirps – commonly known as synchronous interference[8] [169]. However, this occurs with a rare possibility [78].

Interference by considering various modulation schemes of interfering radars has also been investigated, such as interference between FMCW and pulsed radars [78], [168], [169], FMCW and FMCW radars [168], [169], [173], PMCW and PMCW radars, FMCW and PMCW radars [18], [107]. In each case, an increased interference floor at the VR has been reported. Moreover, interference patterns in the FMCW-based VR due to different interfering waveforms have also been discussed in [174], demonstrating a unique interference pattern for each waveform type. However, the interaction of all these waveforms results in an increased interference floor level. A study of interference between FMCW and random pulse sequences has been studied in [18], indicating a similar impact to the FMCW – FMCW interference scenario.

[7] The type of interference where the chirps of VR and IR cross each other. This has been explained in section 3.6.

[8] Discussed in section 3.6.2.I.

The impact of interference not only depends on the radar's waveform parameters but also on the road geometry and traffic density. The first model of interference stochastic behaviour based on the spatial randomness of the interferer's position has been presented in [165]. The work in [166] provides a statistical study on the interference power levels for various road geometry and traffic conditions. Both works highlight an increase in interference probability as the number of interferers rises. Consequently, a higher interference power is expected.

There is limited literature on the analysis of interference within the signal processing stages of the VR. Moreover, the analysis is limited to the front-end of radar, such as interference power estimates across the VR front-end [175], [176], the influence of traffic flow on the received interference power at the radar antenna [177], and the saturation of front-end due to high interference power [171]. However, the effect of a wide range of FMCW waveform parameters on the interference power and radar functionality is also not adequately presented in the literature. It is a subject of discussion in the presented research.

2.5.1 Industry-Led Projects

There are a few industry-led projects that have undertaken advanced research in the area of characterisation and mitigation of interference. The details of all major projects have been given in Appendix 1.

2.5.2 Radar Simulators

Within the frame of research projects, the automotive industry has supported the development of system simulators [178]. They are instrumental in investigating the interaction between radars as the number of radars on the street can be increased arbitrarily in simulations. Therefore meaningful results can be derived [41], [179]. Existing radar simulators have been summarised in Appendix 2.

2.5.3 Interference Detection and Mitigation

It is crucial to develop interference detection and mitigation techniques for dynamic road scenes that can be applied in real-time with minimal impact on echo signal detection. The techniques proposed in the literature are primarily based on the following:

- Using complex transmit waveforms with different modulation schemes [180]–[187]. The aim is to avoid or minimise the probability of the VR and IR signals overlapping.
- Utilising advanced signal processing at the receiver side, such as interference detection and removal in the time domain [173], [188], [189], estimating the impact of interference in the frequency domain [190], and digital beamforming [191]–[193]. The aim is to mitigate interference and improve target detectability in the background of interference and noise.

A subset of the techniques discussed in the literature has been summarised in this sub-section.

I. Interference Detection and Parameter Estimation

An adaptive threshold-based interference detection methodology using high amplitude interference pulses in the time domain received signal has been proposed in [194]. The technique is based on the assumption that interference power is much stronger than echo signal power. Therefore, it is not suitable in the presence of strong echo returns or with a larger number of interfered samples.

As discussed in Appendix 6, in an in-phase quadrature (I/Q) channel receiver, the image frequency band only contains contributions from noise or interference. In contrast, the real part of the frequency band also contains target returns. Using this distinction, interference detection is proposed in [195].

Interference detection using image processing after STFT has been proposed in [173], where the interference pattern is identified using a maximally stable extremal regions algorithm.

A few studies have also been proposed to estimate the modulation characteristics of the interference signal [196], [197] using frequency-domain information. The interference signals in the frequency domain are split into sub-regions and used as training sets. However, due to the huge dataset input to the classifier, the complexity of learning is comparatively high. A computationally fast interference identification and classification method based on its modulation has also been proposed in [198], where interference features are extracted from the time domain signal using a support vector machine for training and validation.

II. Interference Mitigation

A survey of SoA interference mitigation techniques is presented in Table 2.5.

Table 2.5. State-of-the-art interference mitigation techniques.

Ref.	Mitigation Technique	Limitations
	Pre-Detection	
[181], [199]–[204]	Scalable waveform parameters are used. The chirp sweep frequency and time are reconfigured for every cycle. • Noise-like frequency response for interference • Removes the ghost target.	• An increase in the noise floor is observed. • There are possibilities of the existence of another interferer in the reconfigured waveform parameters. • It is difficult to implement in dense automotive scenarios with increasing radar penetration rates and a requirement for wider bandwidth.
[205], [206]	Non-overlapping TDM waveforms are proposed. • Reduces interference probability.	• Difficult to maintain in the dense automotive scenario.
[207]–[209]	Different antenna polarization for each radar is proposed.	• Increased complexity of the antenna design. • Only two options (horizontal/ vertical) are available. • Cannot be implemented without regulations and international coordination.
[210]–[212]	Coding Technique	• High modulation and demodulation efforts are required and increased hardware cost.

	Post detection	
[168]	Interference Zeroing • Adaptive threshold based on the interference power in each victim chirp.	• Higher sidelobes are observed that might mask weaker targets. • The threshold estimation is ambiguous in the presence of strong target reflections. • Due to a large dynamic range of radars, threshold estimation is difficult in real-world scenarios. • Performance degradation is expected if the number of interfered samples increases or with multiple interference pulses within the VR chirp. • The part of the echo signal is also removed. • Phase discontinuities are introduced, resulting in target-response broadening thus, reducing the resolution. • Challenging as the number of interferers increases. • Not practical for narrowband interference or when the sweep rate of the VR and IR waveforms is similar.
[195]	Interference estimation using real and image frequency bands	• An additional I/Q mixer is required. • Increased system cost.
[173]	Windowing on interfered data Removing distorted samples from time domain signals.	• Precise detection of interfered samples is required. • Ringing artefacts due to the phase discontinuities. • Increased sidelobes are observed.
[190]	Cancelling interference in real frequency band based on correlated interference in image band.	• Close-range interference is not mitigated. • An additional I-Q mixer is required. • Increased system cost.
[189], [213]	Interference nulling using localised windowing.	• Small improvement and computational complexity. • A small part of the echo signal is also removed. • Higher sidelobes due to phase discontinuities.

[173], [214], [215]	Inverse windowing on detected interference regions.	• Requires smoothing between the signal and interference. • Signal-to-noise ratio (SNR) loss.
[154], [191]–[193], [216], [217]	Adaptive beamforming to reduce power from the direction of the interferer.	• A large array size is needed for effective mitigation. • Implementation is challenging in a congested environment. • The angle of arrival of the interferer should be known. • Reduces the return power from a collocated target. • High computational complexity.
[181], [218]–[220]	Frequency Hopping	• The probability of another interferer existing at the shifted frequency may be high in dense scenarios.
[149], [221]–[224]	Deep learning methods	• Computational complexity. • Generally requires a large volume of the training dataset acquired in various situations.
[163], [225], [226]	CFAR-based interference mitigation	• Might mask weaker targets if the threshold is increased to suppress interference effects.
[170]	Interference clipping	• Ringing artefacts due to the discontinuity in the frequency band. • Increases sidelobes. • Threshold estimation is challenging if multiple interference pulses are present or there is a short-range target with a strong echo signal.
[145], [227]	Signal reconstruction	• Threshold estimation is challenging if multiple interference pulses are present or there is a short-range target with a strong echo signal. • Increased sidelobes if phase discontinuities are introduced between the reconstructed part of the signal.

[228]	Interference reconstruction and cancellation • Characteristics of the interfering signal are estimated and then subtracted from the overall signal.	• High interference power is required for accurate reconstruction. • High calculation effort is required. • The effectiveness of this technique depends on the number of interfered samples. • Does not work if an interfering signal with different parameters overlaps in time or if the sweep rate difference between the VR and IR waveforms is small.

Despite the mentioned research on interference mitigation, there is still a requirement to develop robust mitigation techniques that restore the SINR loss after mitigation. For example, to avoid ringing artefacts caused by introduced phase discontinuities after interference removal, a localised window [173] can be used to smooth echo signal samples next to interfered samples. Alternatively, signal interpolation [229] might be used for precise reconstruction. However, these methods rely on the accurate detection of interference location and duration. This becomes particularly challenging with smaller interference amplitude, multiple interference pulses within the VR chirp, or a stronger echo signal. Moreover, computational load is added to the radar processor. The techniques based on interference avoidance reduce the available bandwidth and FoV for radar operation.

The limitations of reviewed mitigation techniques have been investigated and analysed in this work. Moreover, based on a comparative analysis of different mitigation techniques, scenarios have been identified where the developed mitigation techniques can be implemented without the VRs' performance degradation. This will lay a foundation to investigate the prospects of combining different mitigation techniques and developing an effective technique, practical in automotive scenarios, as discussed in Chapters 5-8.

III. Interference Mitigation Based on Sense and Avoid

Mitigation based on the estimation of interference parameters (amplitude and phase) and its removal from the received signal has been discussed in [172], [188]. However, the method is computationally complex and requires significant interference amplitude with a large number of interfered samples. Interference parameter estimation based on a spectrogram has been presented in [230]. However, the accuracy of results degrades for wider bandwidth and longer sweep time interference. The practical implementation of these techniques on real-time measured data has not been evaluated.

IV. Interference Mitigation Using Scalable Waveform Parameters

Techniques based on scalable waveform parameters have also been proposed in the literature to improve signal detectability in the background of interference and to reduce the impact of interference. They include frequency ramp modulation with time [231], quasi-orthogonal waveforms [232], fast chirps sweep time with alternate chirp directions [201], and randomising the VRs' slope [199], [202], [233], idle time [207], start frequency [234], start time [234]–[236]. However, a qualitative and quantitative analysis of introduced randomness and its effect on the radar detector and interference statistics is missing in the literature. This will be addressed in Chapter 4.

V. Interference Mitigation in the Spatial Domain

Mitigation in the spatial domain is also not a new radar technology. Adaptive beamforming for null steering is one of the efficient methods to suppress interference and improve the SINR. The SoA mitigation techniques exploiting spatial information of interfering signals are summarised in Table 2.6.

Table 2.6: Literature survey on the spatial mitigation techniques.

No.	Methodology	Limitations
[191], [192]	• Interference is detected in the time and frequency domain. • Beamformed weights associated with the receive array are calculated based on the signal AoA. • The receive antenna pattern is modified with a notch towards the direction of interference.	• The AoA of the interference signal is required. • Only applicable to IQ mixer.
[216]	• Beamforming weights are adaptively estimated. • 20-23 dB improvement in the SINR is observed.	• Computationally complex.
[217]	• Interference is detected across all the array elements. • Null is placed in the direction of interference using digital beamforming.	• AoA of interference is required. • Simulation-based. • Requires a large number of interference samples.
[193]	• LMS (least mean square) algorithm is used to compute weights followed by adaptive beamforming.	• The collocated target is also suppressed. • Efficient in I/Q receivers.
[154]	• AoA of interference is determined from the interfered samples. • The adaptive beam steering vector is computed with a null towards the interference direction. • An autoregressive filter is additionally used to improve the angular resolution.	• Methods to compute weights and null are not explained. • Computationally complex.
[237]	• Adaptive side lobe suppression.	• Efficient for a large number of array elements (30 in the paper). • Effective for sidelobe interference.
[164]	• Interference detected in the time domain. • Blind adaptive beamforming using mean square error estimation is used to minimise interference impact.	• The reference signal and the interference signal are required. • Applicable to CW interference. • The collocated target also disappears. • High interference power is required for better suppression.

Other techniques where interference is first detected and then removed from the received signal at the VR have also been discussed. However, they either result in loss of echo signal samples, for example, when interfered samples are replaced with zeros, require complex hardware such as an I/Q channel receiver, or create a blind FoV with higher sidelobes such as after adaptive beamforming [238]. Therefore, novel techniques that perform reasonably well in all road conditions are required. This has been a focus of the presented work.

2.6 Interference Mitigation in the Temporal Domain

Before developing advanced mitigation approaches, assessing basic mitigation techniques is essential. Three techniques have been discussed in this section based on interference zeroing, interference chop-off, and signal reconstruction.

1. Interference Zeroing: Interfered samples are first detected in the time domain using the methodology proposed in section 5.1.1. The interfered samples are then replaced with zeros. However, some high-frequency interference samples with an amplitude below the threshold remain. These might affect the higher frequency band of the VR. Moreover, this method has the disadvantage of losing a part of the signal due to interference zeroing which leaves a blank region in the radar data.
2. Interference chop-off: Any samples of the received signal with an amplitude greater than the estimated threshold are clipped and made equal to the threshold level. Clipping does not entirely remove the interfered samples. The interfered signal still contains frequency components that spread across the frequency spectrum to increase the interference floor. However, the mean interference floor is reduced compared to the results before clipping.
3. Signal reconstruction: The interfered samples are detected in the time domain and replaced with the clean ‘interference-free’ signal from the same VR chirp. In this work, the introduced phase discontinuities due to reconstruction have been reduced using the following steps:

i. The peak closest to the first interfered sample of each interference pulse is identified. This is done using an iterative process, summarised in Figure 2.10. The amplitude difference between two adjacent signal samples is then compared. When the product of two consecutive amplitude differences is less than 0, the sample under consideration is a peak. Otherwise, the sample value is iterated to the next value.

ii. A clean signal of length equal to the estimated interfered samples is copied from the peak point, and the mirror version of this signal is placed next to the identified peak.

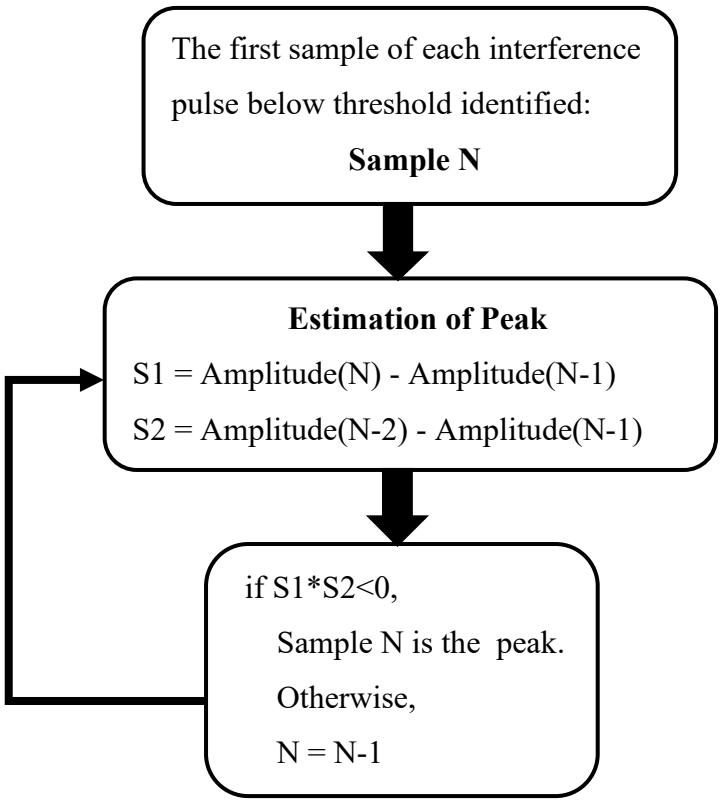


Figure 2.10: Peak estimation for each interference pulse used in signal reconstruction.

The results with and without applying mitigation for techniques discussed above have been shown in Figure 2.11. The VR with 100 µs sweep time, 0.5 GHz bandwidth and IR with 33 µs sweep time, 0.5 GHz bandwidth have been used. The starting frequency of both the VR and IR waveforms is 76 GHz. Three targets, with RCS 10 dBsm, have been positioned at 15 m, 50 m, and 100 m. The target at 50 m is also the source of interference.

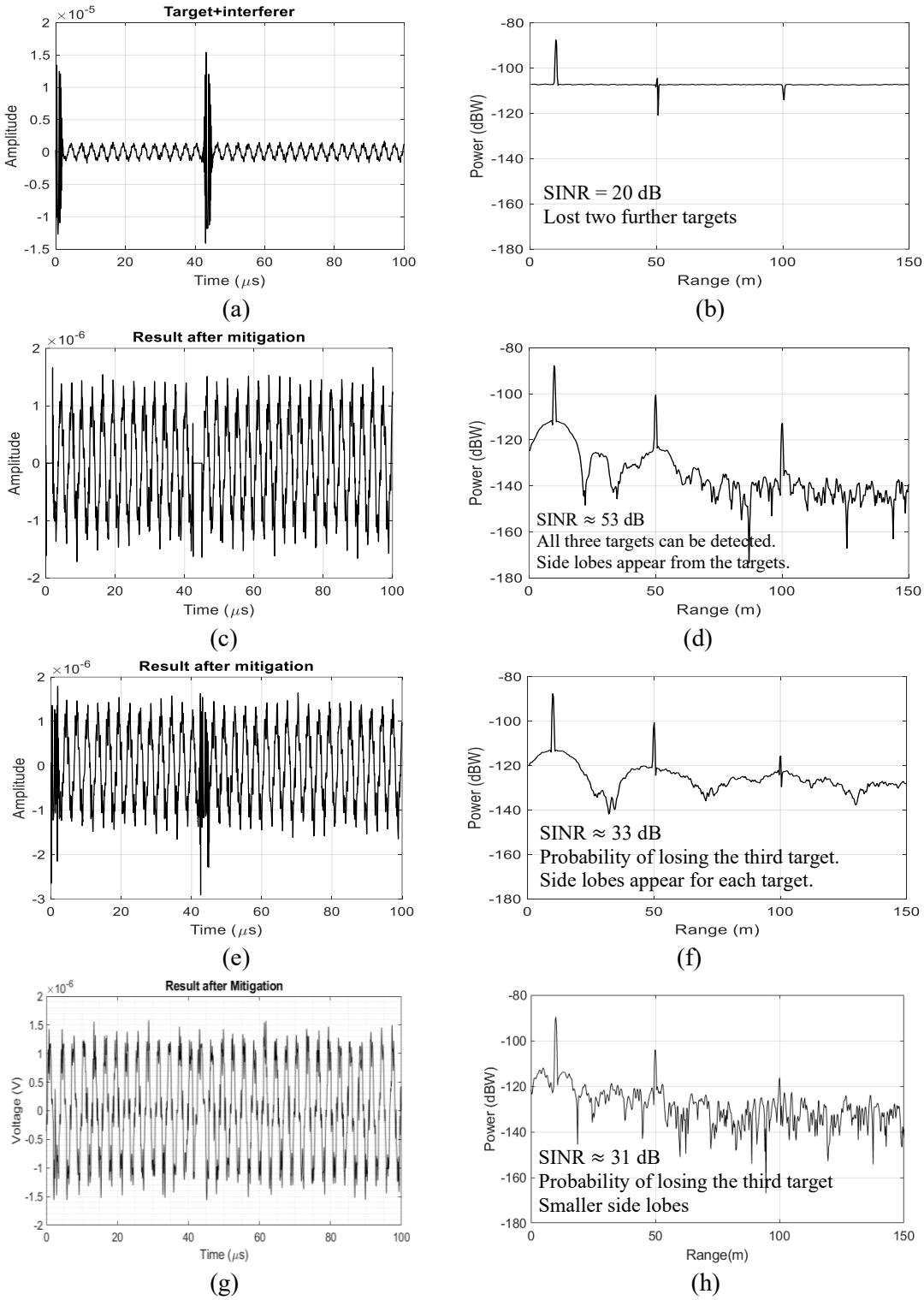


Figure 2.11: Radar plots for assessing interference mitigation techniques: (a) time domain - no mitigation, (b) frequency domain - no mitigation, (c) time domain - interference zeroing, (d) frequency domain - interference zeroing, (e) time domain - interference chop-off, (d) frequency domain - interference chop-off, (g) time domain - signal reconstruction, (d) frequency domain - signal reconstruction.

After removing the interfered samples, discontinuities have been introduced in the baseband signal which causes high sidelobes in the frequency domain. The best improvement, in the discussed examples, is observed after interference zeroing, where all three targets have been detected with a reasonable SINR. As the interfered samples below the threshold remain in the received signal after applying chop-off based mitigation, sidelobes are much higher in this case. The observations after applying mitigation are summarised in Table 2.7.

Table 2.7. Performance analysis of the time domain mitigation techniques.

Techniques	SINR improvement	Drawbacks
Zeroing	33 dB	Wider return from targets with range sidelobes
Chop-off	13 dB	Large side lobes from the targets with high chances of not detecting the third target
Reconstruction[9]	11 dB	Smaller side lobes level

The techniques discussed above are based on exploiting the temporal domain. However, interference mitigation in the temporal domain becomes particularly challenging when the number of interfered samples increases. Furthermore, due to the introduced phase discontinuities, higher sidelobes are observed which might affect the detectability of closely spaced targets.

2.7 Summary

This chapter presented an overview of radar systems with a specific focus on automotive radars. The operational spectrum, modulation schemes, and array configurations used in the radars for environment sensing have been analysed. The suitability of these factors for

[9] It is to be noted that signal reconstruction is expected to have an improved side lobe level. However, with the applied algorithm, the absolute signal amplitude is reduced, and the noise floor is increased causing a reduction in SINR.

contemporary radar systems which are moving towards image-like resolution is also assessed. The signal processing techniques used in SoA automotive radars are discussed alongside the methods to enhance the radar resolution in all the domains (frequency, Doppler, and spatial) while maintaining a small form factor to make integration of radar sensors possible in modern vehicles.

An extensive review of SoA automotive radar interference analysis and mitigation is presented along with the shortcomings of the proposed techniques. In the literature, interference mitigation techniques exploiting various time, frequency, and spatial domains are proposed. However, some of these techniques are computationally complex and often become ineffective in congested automotive scenarios. Moreover, interference mitigation can often result in a detrimental effect on radar performance, as discussed in subsequent chapters.

Additionally, it has been observed that most of the proposed mitigation techniques are for a single target situation. In the case of multiple targets, the scenarios with well-separated targets and interferers have been considered. However, in real traffic environments, vehicles are often congested, and scenarios with well-separated targets and interferers are rare. These circumstances will further be investigated in Chapter 6 where the impact and the mitigation of interference has been discussed as a function of the spatial separation between targets and interferers.

Chapter 3. AUTOMOTIVE RADAR INTERFERENCE

Mutual interference between radars can affect the performance of the VR, such as saturating the receiver front-end due to high interference power, blinding the receiver due to an increase in the interference floor [18], [78], [169], degrading dynamic range and sensitivity, missing the targets, specifically the ones with a relatively small RCS, or generating ghost (false) targets [169], [207]. Therefore, it is essential to understand the impact of mutual interference and devise practical schemes to mitigate these impacts. A systematic analysis of how interference manifests along the processing stages of the VR is essential to: a) assess the impact of each processing stage on interference and, if necessary, optimise that stage, and b) develop efficient avoidance and mitigation techniques.

This chapter explains interference mathematically and its expected types in an automotive scenario. The impact and appearance of interference have been analysed in the time, time-frequency, frequency, and spatial domains. The main contributions are as follows:

- Analysing interference phenomenology and its mathematical representation.
- Investigating the effect of the LPF on the appearance of interference and the VR's detection performance.
- Developing an analytical framework for interference classification and its power estimation for various radar parameters.
- Evaluating the impact of interference in the time, time-frequency, frequency, and spatial domains through experimentally verified models.
- Analysing the effect of interference received from multiple interference sources on the VR's signal processing chain and detection performance.

3.1 FMCW Radar Overview

The basic signal processing chain used in the presented work to analyse the performance of FMCW radar in the background of FMCW interference has been shown in Figure 3.1.

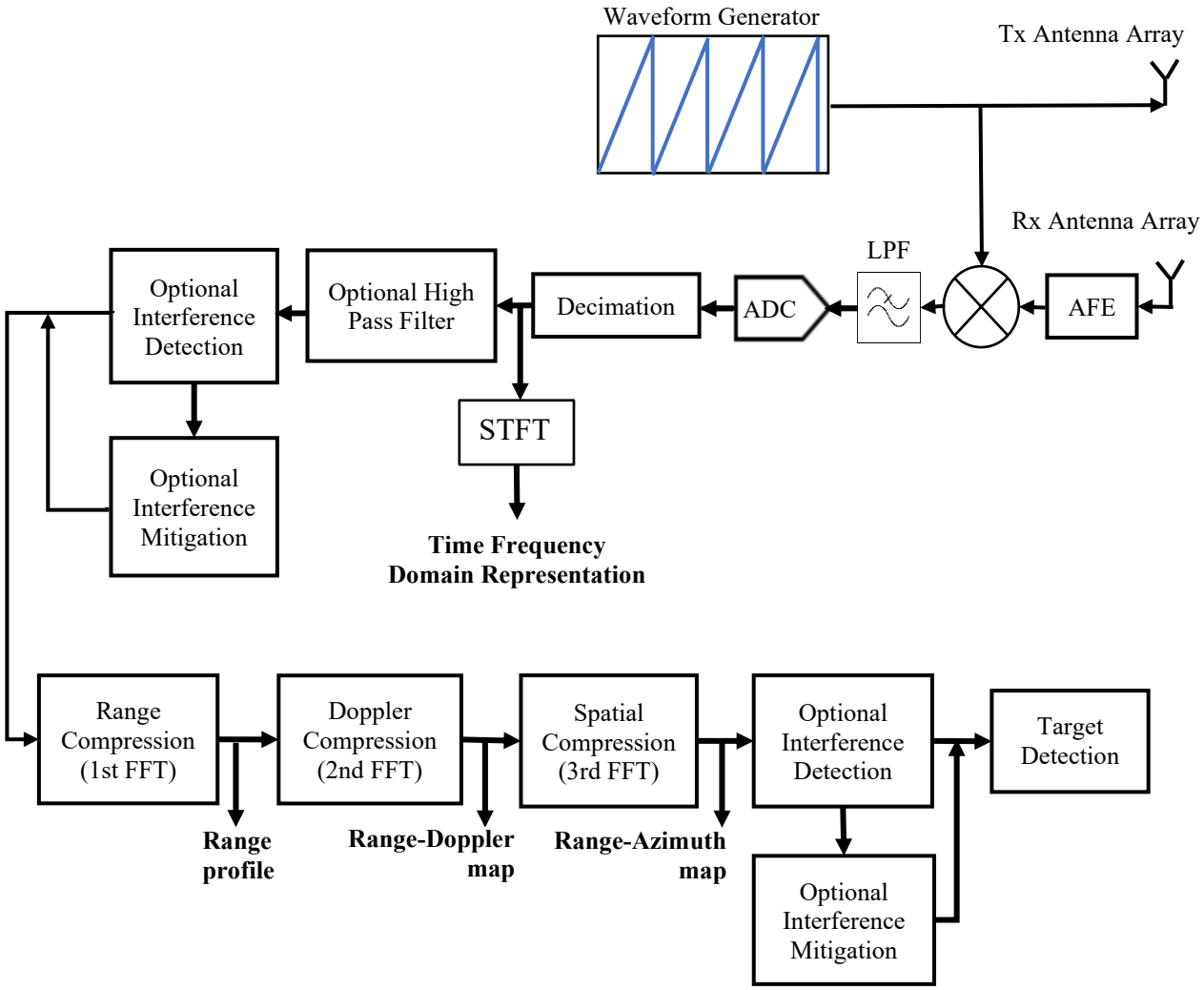


Figure 3.1: Block diagram of FMCW radar system[10,11].

The oscillator in the radar transmitter generates an FMCW chirp signal. Multiple chirps are transmitted by the radar during a CPI, as a Doppler frame, to provide resolution along speed.

[10] Depending upon the radar configuration and environmental conditions, interference detection and mitigation can be performed after each signal processing stage.

[11] Spatial compression is a conditional 3rd FFT when the spacing between array elements is half the wavelength.

The CPI for typical automotive radars is ~10 ms [239]. The signal is transmitted and received by multiple collocated transmit and receive elements, respectively to provide a resolution across the spatial direction [116]. In a coexistence scenario, interference signals from nearby radars might also be received by the VR.

At the receiver, the echo signal is first processed at the analogue front end (AFE). The signal bandwidth in automotive radars is high, typically in the order of a few GHz, which would require a high data rate ADC to sample the signal. Therefore, the signal is first down-converted to a lower intermediate frequency 'beat signal' at the mixer using the LO signal from the transmitter. The LPF is then applied to limit the maximum processing frequency (range) and suppress harmonic frequencies generated at the mixer. Depending upon the bandwidth of the LPF, interference duration and the energy that goes to subsequent processing stages are also limited, as will be discussed later in this chapter. The filtered signal is then sampled and digitised at the ADC. The digitised signal is often decimated by an integer value to reduce the sampling frequency [240]. It is to be noted that each receiver element will have a dedicated AFE and down-conversion module. The detailed study of AFE and its contributions to the received signal has been presented in Chapter 7.

After analogue signal processing, digital signal processing (DSP) has been performed on the radar data cube [99] by applying the following:

1. A short-time Fourier transform (STFT) to the time domain signal to analyse the signal and interference in the time-frequency domain (TFD).
2. Range compression across the fast-time to estimate the range of targets.
3. Doppler compression across the slow-time to estimate the relative speed of the targets by comparing the phase differences across chirps in the Doppler frame [141], [241]. This also results in signal integration to improve the SINR.

For interference analysis in the frequency domain, range-Doppler maps have been generated after the range and Doppler compressions.

4. Beamforming across multiple array elements to a) resolve the targets along the azimuth direction, and b) provide spatial information of the targets from the signal's phase shift across different array elements (section 3.5).

   Range-azimuth maps have been generated after the range, Doppler, and spatial compressions for interference analysis in the spatial domain, unless stated otherwise[12,13]. This has been elaborated later in Figure 3.11 for MIMO radars.

The range, Doppler, and spatial compressions have been performed by applying an FFT along each dimension of the radar data cube. As the FFT is a linear process, the order of applying FFT across each dimension of the radar data cube can be changed. The above sequence has been used in this work.

In the FMCW radars, the waveforms are transmitted continuously. Therefore, the direct leakage signal from the radar's transmitter is also present at its receiver. This high power signal might saturate the amplifiers in the AFE [242] or cause high amplitude peaks at the initial few range bins, thus, reducing the radar's dynamic range. Therefore, a high pass filter (HPF) has been additionally applied to suppress the leakage signal.

In this chapter, interference characteristics across analogue and digital signal processing stages have been presented. In the presence of interference, it is optionally detected and mitigated after each processing stage. Finally, automatic target detection (ATD) detects targets in the background of noise and interference. These will be discussed in the subsequent chapters.

[12] It is to be noted that in the presented work, due to the availability of radar chipsets for the measurements, the spatial resolution across elevation was not provided. Therefore, spatial compression provides information of the azimuth position of the targets only, considering elevation = 0^o.

[13] The range azimuth maps have been plotted for the maximum Doppler bin.

3.2 Analytical Study of Interference

A simplified processing chain discussed in this chapter has been shown in Figure 3.2. As demonstrated, alongside the echo signal, the VR also receives signals from radars installed on nearby vehicles. This results in interference if the interfering waveform is within the LPF band of the VR.

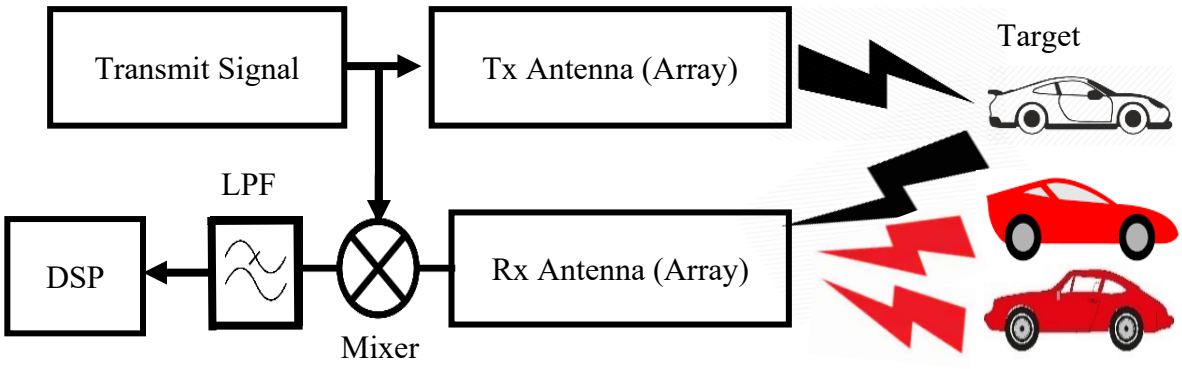


Figure 3.2: Simplified block-level diagram of an FMCW radar in an interference background.

The chirp signal transmitted by the VR linearly sweeps between frequencies F_{cv} and $F_{cv}+B_{sv}$ during the sweep time T_{sv}, where, F_{cv} is the carrier frequency of the VR and B_{sv} is the bandwidth of the VR. The transmit frequency is expressed as follows [243]:

$$f_T(t) = F_{cv} + \frac{B_{sv}}{T_{sv}}t; \qquad -\frac{T_{sv}}{2} \le t \le \frac{T_{sv}}{2} \tag{3-1}$$

where, $B_{sv}/T_{sv} = K_v$ is the chirp slope, and t is the fast-time within a chirp duration. The phase $\varphi_T(t)$ of the transmitted chirp may be represented as:

$$\varphi_T(t) = 2\pi\int_0^t f_T(t)dt = 2\pi\left(F_{cv}t + \frac{1}{2}K_v t^2\right)\Big|_0^t \tag{3-2}$$

After substituting the limits of the integral,

$$\varphi_T(t) = 2\pi\left(F_{cv}t + \frac{1}{2}K_v t^2 \right) + \varphi_{T_o} \tag{3-3}$$

At $t = 0$, the phase $\varphi_T(t) = 0$. Therefore, $\varphi_{T_o} = 0$. The chirp signal can be represented as [244]:

$$s_{Tx}(t) = A_o \exp\left(j2\pi\left(F_{cv}t \pm \frac{1}{2}K_v t^2 \right) \right) \tag{3-4}$$

where, $A_o = \sqrt{2P_t}$ is the effective transmit power of the VR normalised to a 1 ohm resistor.

The transmit signal from interferer radar (IR) with chirp duration T_{sint}, bandwidth B_{sint}, and centre frequency F_{cint}, is expressed as follows:

$$s_{Tx_{\text{int}}}(t) = A_{oi} \exp\left(j2\pi\left(F_{\text{cint}}t \pm \frac{1}{2}K_{\text{int}}t^2 \right) \right) \tag{3-5}$$

where, $A_{oi} = \sqrt{2P_i}$ is the effective transmit power of IR normalised to a 1 ohm resistor, and $K_{\text{int}} = B_{\text{sint}}/T_{\text{sint}}$ is the slope of the interfering waveform.

The received signal is attenuated and time-shifted compared to the transmit signal and generally expressed as:

$$s_{Rx}(t) = A_o \cdot s_{Tx}(t - \tau) \tag{3-6}$$

where, τ represents the propagation delay. Using (3-4) and (3-5), the echo signal from the target $s_{Rx_t}(t)$ and received interference $s_{Rx_i}(t)$ at the VR are expressed as follows:

$$s_{Rx_t}(t) = A_t \cdot \exp\left(j2\pi\left(F_{cv}(t - \tau_D) + \frac{1}{2}K_v(t - \tau_D)^2 \right) \right) \tag{3-7}$$

$$s_{Rx_i}(t) = A_i \cdot \exp\left(j2\pi\left(F_{\text{cint}}(t - \tau_{\text{int}}) + \frac{1}{2}K_{\text{int}}(t - \tau_{\text{int}})^2 \right) \right) \tag{3-8}$$

$A_t = \sqrt{2P_{Rx}}$ and $A_i = \sqrt{2P_{Rx_i}}$ are the attenuation factors for the target and interference, respectively. These are calculated from the propagation path loss model and discussed in section 4.3. The received echo signal has a round trip propagation delay τ_D, and interference has a propagation delay τ_{int}, that depends on the distance R_T and R_I between the target and the VR, and the interference source and the VR, respectively.

In the presence of multiple targets (N_T) and interferers (N_I), the received echo signal and interference can be expressed as follows:

$$\begin{aligned} s_{Rx_t}(t) &= \sum_{n=1}^{N_T} A_t(n) \cdot s_{Tx}(n)\left(t - \tau_D(n)\right) \\ s_{Rx_{\text{int}}}(t) &= \sum_{n=1}^{N_I} A_i(n) \cdot s_{Tx_{\text{int}}}(n)\left(t - \tau_{\text{int}}(n)\right) \end{aligned} \tag{3-9}$$

where, $A_t(n)$ and $A_i(n)$ represents the attenuation factors due to path loss of echo signals and interference, respectively, $\tau_D(n)$ and $\tau_{\text{int}}(n)$ represents the propagation delay of echo signals and interference signals, respectively. The received signal is the sum of signals from targets and interferers, and is expressed as follows:

$$s_{Rx}(t) = s_{Rx_t}(t) + s_{Rx_{\text{int}}}(t) \tag{3-10}$$

The received signal is down-converted by mixing it with the LO signal generated at the transmitter to generate an intermediate frequency signal s_{IF}. This can be expressed as follows:

$$s_{IF}(t) = s_{Tx}(t) \cdot s_{Rx}(t)^* \tag{3-11}$$

$$s_{IF}(t) = s_{Tx}(t) \cdot \left(s_{Rx_t}(t) + s_{Rx_{\text{int}}}(t)\right)^* \tag{3-12}$$

$$s_{IF}(t) = s_{Tx}(t) \cdot s_{Rx_t}(t)^* + s_{Tx}(t) \cdot s_{Rx_{\text{int}}}(t)^* \tag{3-13}$$

The down-converted frequency is typically in the range of kHz to a few MHz for automotive radars [13]. In the presence of an echo signal only,

$$s_{Rx}(t) = s_{Rx_t}(t) \tag{3-14}$$

The corresponding down-converted signal is expressed as:

$$\begin{aligned} s_{IF-t}(t) &= s_{Tx}(t) \cdot s_{Rx_t}(t)^* \\ s_{IF-t}(t) &= A_t \cdot \exp\left(j2\pi \left(F_{cv} t + \frac{1}{2} K_v t^2 - F_{cv}(t - \tau_D) - \frac{1}{2} K_v (t - \tau_D)^2 \right) \right) \end{aligned} \tag{3-15}$$

After simplification,

$$s_{IF-t}(t) = A_t \cdot \exp\left(j2\pi \left(F_{cv}\tau_D + K_v t\tau_D - \frac{1}{2} K_v {\tau_D}^2 \right) \right) \tag{3-16}$$

The last term can be neglected because $\tau_D / T_{sv} \ll 1$. $F_{cv}\tau_D$ represents the number of cycles of F_{cv} during the round-trip propagation time, $K_v t\tau_D$ is a linearly increasing term that represents the echo signal's intermediate (beat) frequency.

The intermediate frequency is generally estimated as follows [245]:

$$f_{IF} = \frac{1}{2\pi} \frac{d}{dt}\left(\varphi(t)\right) \tag{3-17}$$

Using (3-17), the beat frequency of the echo signal $\left(f_{IF-T}\right)$ can be expressed as:

$$f_{IF-T} = \frac{1}{2\pi} \frac{d}{dt}\left(2\pi \left(F_{cv}\tau_D + K_v t\tau_D - \frac{1}{2} K_v {\tau_D}^2 \right) \right) = K_v \tau_D \tag{3-18}$$

From (3-18), the beat frequency of the echo signal is a constant frequency term. The delay τ_D is estimated as:

$$\tau_D = \frac{2\left(R_T + vt\right)}{c} \tag{3-19}$$

where, *v* is the target's speed, and factor 2 is included due to the two-way propagation delay of the echo signal.

In the background of interference, the second term of (3-13) is estimated as:

$$s_{IF-i}(t) = s_{Tx}(t) \cdot s_{Rx_i}(t)^*$$
$$s_{IF-i}(t) = A_i \exp\left(j2\pi \left(\left(F_{cv} - F_{\text{cint}}\right)t + \frac{1}{2}\left(K_v - K_{\text{int}}\right)t^2 + F_{\text{cint}}\tau_{\text{int}} + K_{\text{int}}t\tau_{\text{int}} - \frac{1}{2}K_{\text{int}}\tau_{\text{int}}^2 \right)\right) \quad (3\text{-}20)$$

The beat frequency component due to the received interference is expressed as:

$$f_{IF-I} = \frac{1}{2\pi}\frac{d}{dt}\left(2\pi \left(\left(F_{cv} - F_{\text{cint}}\right)t + \frac{1}{2}\left(K_v - K_{\text{int}}\right)t^2 + F_{\text{cint}}\tau_{\text{int}} + K_{\text{int}}t\tau_{\text{int}} - \frac{1}{2}K_{\text{int}}\tau_{\text{int}}{}^2 \right)\right) \quad (3\text{-}21)$$

After solving (3-21),

$$f_{IF-I} = \left(F_{cv} - F_{\text{cint}}\right) + \left(K_v - K_{\text{int}}\right)t + K_{\text{int}}\tau_{\text{int}} \quad (3\text{-}22)$$

where, the propagation delay is expressed as:

$$\tau_{\text{int}} = \frac{R_{\text{I}} + v_{\text{int}}t}{c} \quad (3\text{-}23)$$

v_{int} is the speed of IR and R_I is the distance between the IR and the VR.

The down-converted signal is then low-pass filtered and discussed in the following section.

3.3 Effect of the Low Pass Filter on Interference Characteristics

One of the main blocks in the FMCW radar receiver is the LPF which has the following functionality:

1. Limiting the receiver bandwidth to the cut-off frequency of the LPF $\left(F_{LPF}\right)$.
2. Limiting the maximum detection range – unambiguous range $\left(R_{\max}\right)$.
3. Suppressing the harmonics generated after the mixer.
4. Limiting the interference duration.
5. Setting the minimum required sampling frequency to avoid aliasing (the Nyquist frequency).

For a dual channel receiver, $R_{\max}$ after the LPF is defined as [246]:

$$R_{\max} = \frac{cF_{LPF}}{2K_v} \tag{3-24}$$

$R_{\max}$ for a single channel receiver is half that shown in (3-24), discussed in Appendix 6. For example, for typical radar parameters with T_{sv} = 102.4 µs, B_{sv} = 500 MHz, F_{LPF} = 10 MHz [91], $R_{\max}$ = 307.2 m.

To investigate the impact of the LPF on the interference characteristics, the victim and interfering radars' chirp overlap plots have been illustrated in Figure 3.3.

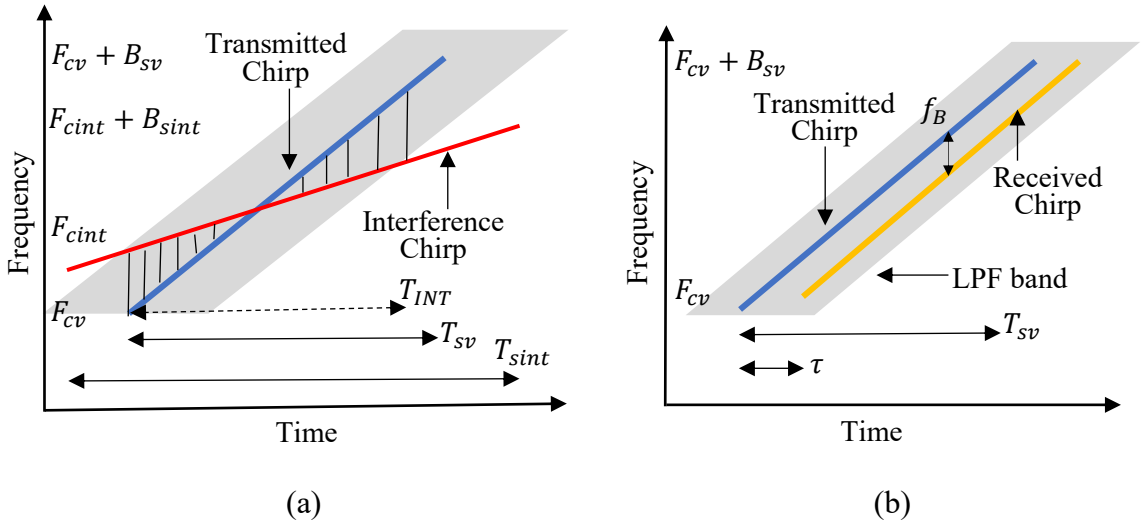


Figure 3.3: FMCW radar chirp overlaps: (a) echo signal, (b) received interference.

Interference appears in the VR's baseband signal as long as the interfering signal is within the receiver bandwidth, that after the LPF is defined by F_{LPF}. The equation (3-22) indicates that the spread of interference is defined by the time-dependent term: $\left(\left|K_v - K_{\text{int}}\right|\right)t$. As illustrated in Figure 3.3, after the LPF, interference duration (T_{INT}) is limited by the upper and lower bounds of the LPF i.e., $-F_{LPF}$ and F_{LPF}. Based on these observations, interference duration can be estimated as follows:

$$-F_{LPF} \le \left(K_v - K_{\text{int}}\right)t \le F_{LPF} \tag{3-25}$$

$$T_{INT} = \frac{2F_{LPF}}{|K_v - K_{\text{int}}|} \tag{3-26}$$

The smaller the difference between the VR and IR waveform slopes, the longer is the interference duration. For SoA automotive radars, the LPF bandwidth is typically in the range of 3 – 15 MHz [195], [247]. Therefore, due to $F_{LPF} \ll B_{\text{sint}}$, interference has a short duration in the time domain with a 'pulse-like' appearance. This has been illustrated in Figure 3.4, where interference appears like a double-sided LFM pulse with high amplitude due to one-way propagation loss [168]. In contrast, the target manifests as a 'monotonic' sinusoidal signal.

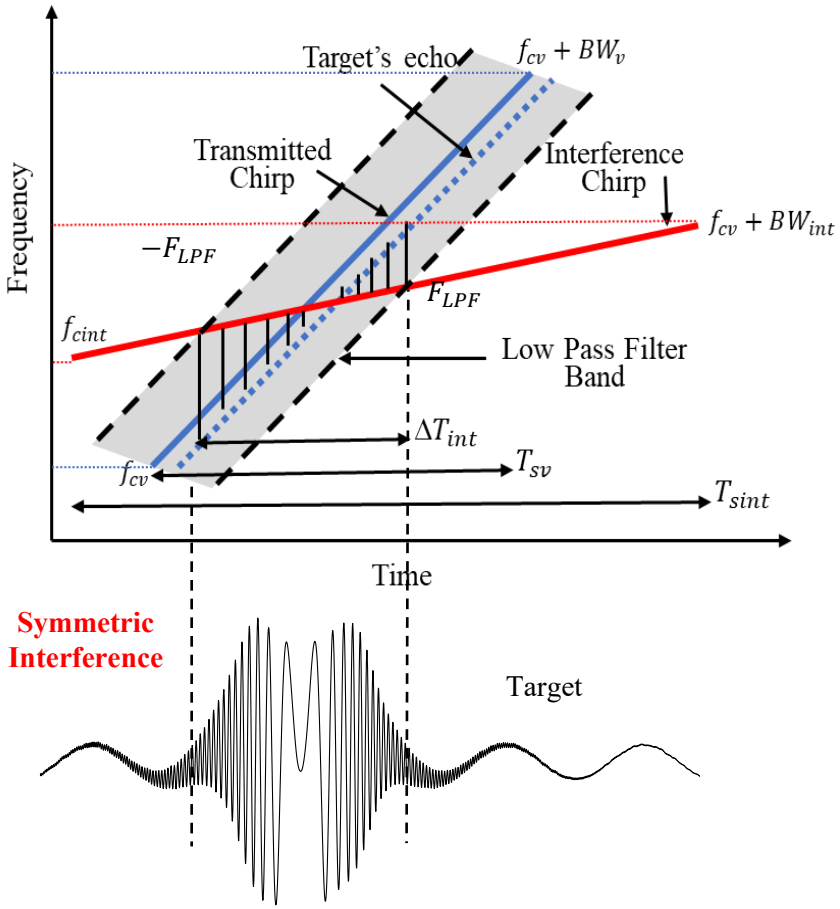


Figure 3.4: Victim and interference chirps in the time-frequency representation and zoomed received signal.

Additionally, the LPF characteristics such as the filter order, and roll-off also affect T_{INT}. These are not included in (3-26), and are discussed next.

3.3.1 Low Pass Filter Characteristics

The influence of the LPF on received interference has been studied from three aspects:

1. Interference duration,
2. The appearance of interference, and
3. Effect of the LPF parameters on the radar's detector performance.

To analyse these, the two representative FMCW VRs with different LPF characteristics have been used for measurements[14] in the background of 76.2 GHz CW interference:

- The INRAS Radarbook [40] as VR1 with F_{LPF1} = 3.5 MHz.
- The NXP Dolphin [39] as VR2 with F_{LPF2} = 10 MHz.

Similar waveform parameters have been used for the VRs: F_{cv} = 76 GHz, B_{sv} = 500 MHz, and T_{sv} = 102.4 µs, with the LPF orders 3 and 6. For calibration, a trihedral corner reflector (CR) with a 14 dBsm RCS was placed at 5 m from the VRs. The measurement setup is shown in Figure 3.5.

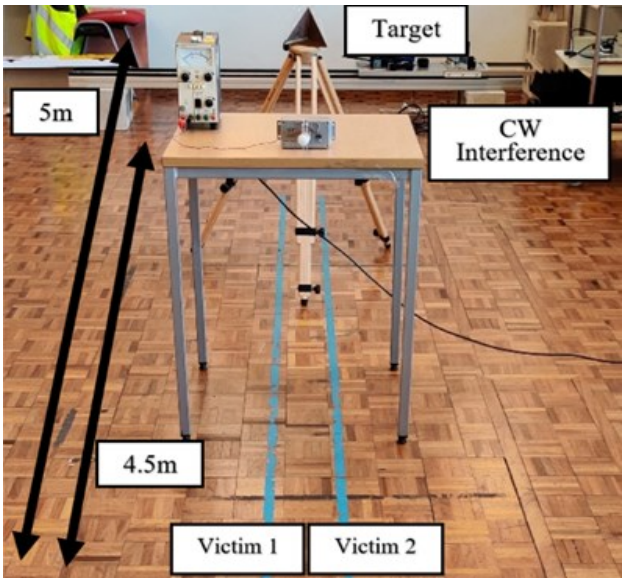


Figure 3.5: Measurement setup to analyse the influence of LPF parameters on interference.

[14] In reality, the radar chipsets can have a broad range of LPF characteristics. However, due to the availability of the mentioned radar chipsets, this section has been focused in determining their effect on interference.

A reasonable agreement has been observed between the modelled and measured results after the LPF stage, shown in Figure 3.6.

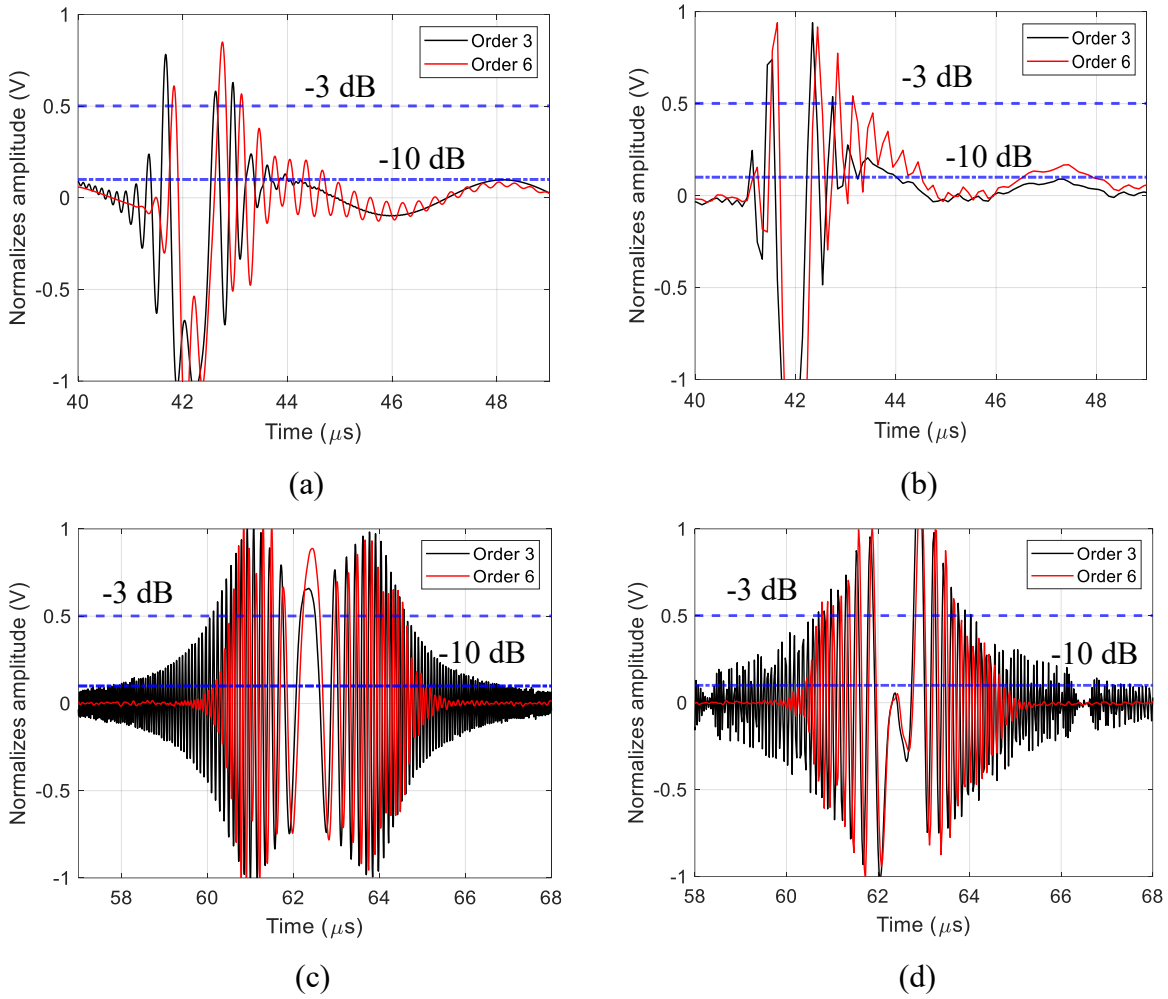


Figure 3.6: Received signal in the time domain: a) the modelled VR1 with F_{LPF1} = 3.5 MHz, (b) the measured VR1 with F_{LPF1} = 3.5 MHz, (c) the modelled VR2 with F_{LPF2} = 10 MHz, (d) the measured VR2 with F_{LPF2} = 10 MHz.

Theoretical T_{INT} for F_{LPF1} and F_{LPF2} calculated using (3-26) are 1.4 µs and 4.1 µs, respectively. To estimate T_{INT} from the modelled and measured results, the -3 dB and -10 dB threshold levels have been defined. T_{INT} at the higher '-3 dB' threshold are 1.5 µs and 4.5 µs for F_{LPF1} and F_{LPF2}, respectively, and the results are comparable for the two filter orders. This

indicates a linear relationship between the interference duration and the LPF cut-off frequency, which is expected, as interference appears as two-sided LFM waveforms.

Assessing the relationship between interference duration and LPF order is a complex task. As shown in Figure 3.6, at the '-3 dB' threshold level, the filter order does not fundamentally change T_{INT}. However, T_{INT} changes significantly at the lower '-10 dB' threshold level for different filter orders. T_{INT} increases when the filter order for F_{LPF1} is increased but decreases for F_{LPF2} with a high order LPF.

For performance evaluation, the percentage ratio of interference duration versus the VR's sweep time $\left(T_{INT}/T_{sv}\right)$ has been estimated for the used cut-off frequencies, filter orders, and threshold levels, and summarised in Table 3.1. A higher percentage indicates a larger number of fast-time samples affected by interference with a dominant effect observed at the -10 dB threshold level.

Table 3.1. The ratio of T_{INT}/T_{sv} for different cut-off frequencies and filter order.

	-3 dB threshold		**-10 dB threshold**	
	F_{LPF}		F_{LPF}	
Filter order	3.5 MHz	10 MHz	3.5 MHz	10 MHz
3	1.4 %	4.4 %	2.6 %	9 %
6	1.3 %	3.9 %	4.4 %	4.7 %

As indicated in Table 3.1, after applying the LPF, T_{INT} depends not only upon the F_{LPF} but also on the LPF order. A higher filter order with lower F_{LPF} results in an apparent ringing due to a sharper roll-off of the LPF. Consequently, additional fast-time samples are affected by interference thus, increasing T_{INT}. Ringing due to a higher filter order is also observed for F_{LPF2} (10 MHz) but with a much smaller amplitude as compared to F_{LPF1}. This might affect the probability of detection at the VR's detector stage, analysed in the following sub-section.

3.3.2 Probability of Detection

The probability of detection (P_d) in the presence of interference is essential to evaluate its impact on radar detector performance. As will be discussed in Chapter 4, the statistics of interference are not always Gaussian, which is the well-known distribution of AWGN [103]. Therefore, we cannot entirely rely on interference power to evaluate P_d. In this section, by direct modelling, P_d has been estimated in an interference background for various LPF parameters. The radar detector and methodology to generate the P_d curves have been discussed in detail in Chapter 4.

The P_d curves as a function of signal to interference ratio (SIR) for the two VRs' with F_{LPF} values of 3.5 MHz and 10 MHz in the presence of CW interferer have been shown in Figure 3.7 (a) and (b), respectively with 10^{-4} probability of false alarm (P_{fa-i}). The results have been assessed for different filter orders (3, 6, and 10). For reference, the P_d curve for AWGN has also been plotted with a solid line. Any deviation from P_d in the background of AWGN can affect the detection and tracking performance of the radar.

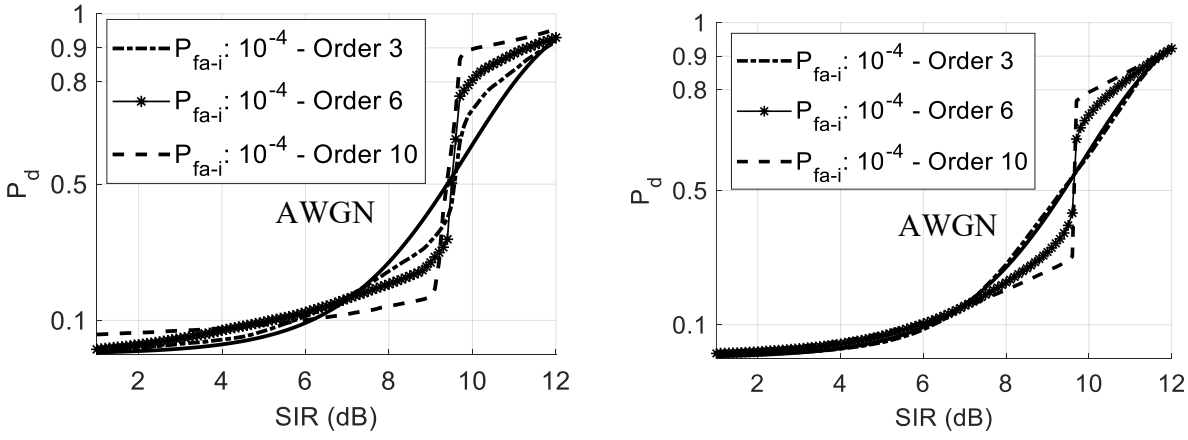


Figure 3.7: Probability of detection for different LPF cut-off frequencies: (a) F_{LPF} = 3.5 MHz, (b) F_{LPF} = 10 MHz.

By examining the results in Figure 3.7, it can be seen that the P_d curve for the VR with a higher F_{LPF} (10 MHz) follows the reference AWGN line very closely (Figure 3.7 (b)). In contrast, the result for the same filter order (order 3), but a lower F_{LPF} (3.5 MHz), shows a more significant deviation from the reference line (Figure 3.7 (a)). Therefore, for a higher F_{LPF} and lower filter order, the detection curve in the background of interference is much closer to that of AWGN. Interference, in this case, has a less detrimental effect on the detector's performance. A larger deviation from the detection curve of AWGN is observed as the filter order increases, especially for a lower F_{LPF}. This can be explained by the steepness of the filters' roll-off and the ringing effect, which is more significant at higher filter orders.

The results also highlight a trade-off between reduction in T_{INT} and its effect on the radar's probability of detection. This critical observation should be considered while designing robust radar sensors, with extra consideration to the radar chipset's filter design, particularly when they might receive interference.

After the LPF, the analogue signal is digitised by the ADC and then processed at the digital signal processor, which has been discussed in the subsequent sections.

3.3.3 Effect of Interference Mitigation

After the ADC, the number of VR samples that are affected by interference is given as:

$$N_{INT} = T_{INT} F_s \tag{3-27}$$

where, N_{INT} is the number of fast-time samples being interfered with, and F_s is the sampling frequency. The smaller the number of interfered samples, the better is the performance of mitigation technique, specifically the ones applied in time domain. An example is interference zeroing, where interfered samples are replaced with zeros as shown in Figure 2.11 [215].

As discussed in (3-26), one way to decrease T_{INT} is to modify the sweep rate of the VR signal to have a larger difference between the VR and IR waveforms. This, however, requires a knowledge of the interference chirp rate, which is often difficult to estimate [188]. Another way to decrease T_{INT} is by reducing F_{LPF} however, as discussed, it can often cause ringing effects. Therefore, a trade-off is often needed when developing the radar chipsets.

3.4 Interference Analysis in the Frequency Domain

During digital signal processing, the time domain signal is first converted into the frequency domain to enable the signal's frequency content estimation. In a typical scene, returns are expected from multiple targets. Due to a linear superposition of the corresponding beat frequencies, they have been separated in the digital domain by compressing the signal along each dimension of the radar data cube (section 2.3.4.II).

Interference, however, appears differently than the echo signal as discussed in the preceding section. Therefore, it has a distinct effect in the frequency domain which has been analysed in this section. Due to time-limited interference pulse, it spread through the range, and the range-Doppler profiles of the received signal which has been assessed in this section.

3.4.1 Range Profile of Received Signal

After range compression, the time-limited interference pulses, being frequency modulated, spread over multiple frequency bins. Due to possibly higher interference power than the echo signal, an increase in the VR's noise floor is expected, referred to as the 'interference floor.' The number of interfered resolution cells and the interference power level in each cell depends upon the waveform characteristics of the VR and IR, which have been estimated in this section.

The echo signal from each target, being a monochromatic waveform, is concentrated over a single frequency bin or a limited number of frequency bins depending upon the FFT

resolution. Interference, on the other hand, is a wideband signal that spreads across multiple frequency bins. The constant frequency term in (3-22) depends on the term $F_{cv} - F_{\text{cint}} + K_{\text{int}}\tau_{\text{int}}$, and the interference spectrum is centred around this. Additionally, f_{IF-I} also contains a time-dependent term $(K_v - K_{\text{int}})t$ due to which interference spreads in the frequency domain. Therefore, the number of frequency (range) bins corrupted by interference times the frequency resolution $(1/T_{sv})$ should be equal to $|K_v - K_{\text{int}}|T_{sv}$. The number of interfered bins (N_{INT}) in the range profile can be estimated as:

$$N_{INT} = |K_v - K_{\text{int}}|T_{sv}^2 \tag{3-28}$$

As discussed earlier, the LPF limits the interference duration, which would also limit the maximum number of interfered bins in the frequency domain, given as:

$$\begin{aligned} N_{INT} &= |K_v - K_{\text{int}}|T_{sv}^2 && |K_v - K_{\text{int}}|T_{sv}^2 < T_{sv}F_{LPF} \\ N_{INT} &= T_{sv} \cdot F_{LPF} && |K_v - K_{\text{int}}|T_{sv}^2 \geq T_{sv}F_{LPF} \end{aligned} \tag{3-29}$$

The mean interference power (P_{INT}) can then be estimated from N_{INT} using:

$$P_{INT} = \frac{V_{INT}^2}{\sqrt{N_{INT}}} \tag{3-30}$$

where, V_{INT} represents the interference power level at the VR receiver input.

To categorise the amount of interference spread based on the waveform parameters, a factor ΔK has been defined, where:

$$\Delta K = |K_v - K_{\text{int}}| = K_v \left|1 - \frac{K_{\text{int}}}{K_v}\right| \tag{3-31}$$

Depending on the value of ΔK, the interference spectrum may or may not be uniform. Equation (3-31) indicates that when the ratio of the victim and interference waveform sweep rates $K = K_{\text{int}}/K_v$ is close to 1, ΔK is a small value. This results in a reduced, non-uniform spread

of interference in the frequency domain, which is the well-known spectrum of the two-sided LFM signal [248]. However, the mean interference floor will be higher, as indicated in (3-30). As the value of K deviates from 1, interference components spread across a larger number of frequency bins, thus becoming more uniform. However, the mean interference floor will be reduced in this case resulting in improved SINR. This has been demonstrated in Figure 3.8 for the example cases with different values of K, along with an AWGN floor for comparison. The power is normalised to the interference power at the input of the victim receivers' mixer stage. As expected, interference spread increases with a reduction in the K value. However, in all the discussed cases, the interference floor is still much higher than the AWGN floor, indicating the requirement for appropriate interference mitigation.

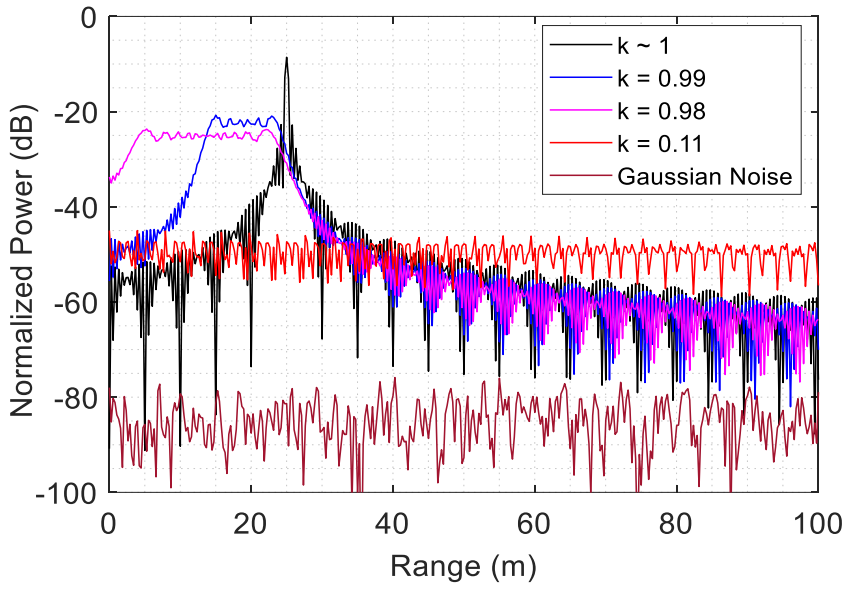


Figure 3.8: Interference spectrum for different sweep rates ratio $\left(K = K_{\text{int}}/K_{v}\right)$.

If the range to the interferer is sufficiently long, such that the received power of interference is reduced below the AWGN floor, then no mitigation is required.

3.4.2 Time-Frequency Analysis of Interference

Accurately detecting interference is crucial for its mitigation. In the time domain, the echo signal is sinusoidal-like, whereas interference is time-limited with high amplitude. In the

frequency domain, an echo signal is focused on a single or a limited number of frequency bins, whereas interference spreads across a larger number of frequency bins. This characteristic has been utilised to separate the echo signal and interference in the time-frequency domain (TFD). Based on this, interference can be detected, and its waveform parameters can be estimated, which is crucial for interference avoidance/ mitigation, as discussed in 5.1.3.

In this work, the received signal has been represented in the TFD by generating a spectrogram after applying STFT [170], [249]. A STFT can be used to estimate the change in the frequency of the received signal over a period of time. This time is equal to the sweep time of radar in the discussed case. Firstly, the received signal is divided into sub-regions, each having overlapping samples from the previous sub-region, to minimise discontinuities. An example has been illustrated in Figure 3.9 for an FMCW waveform with a duration of 5 µs. Each sub-region has a duration of 1 µs in this case.

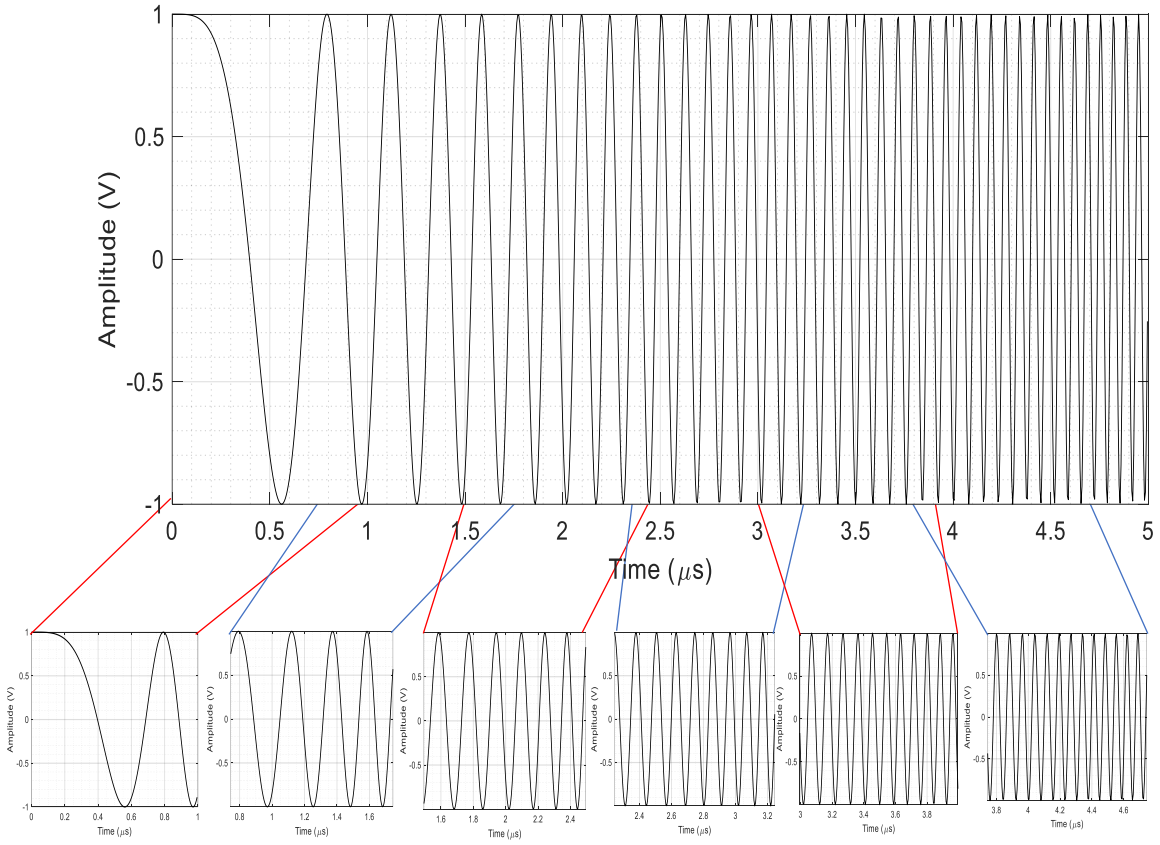


Figure 3.9: Generation of sub-regions for estimation of short-time Fourier transform.

Next, a sliding temporal window is applied across each sub-region. This is followed by the Fourier transform of each sub-region, given as:

$$X(f)=\left[X_1(f),X_2(f),...,X_n(f)\right] \tag{3-32}$$

where, n is the number of sub-regions. Finally, $\left|X(f)\right|^2$ has been used to estimate the STFT of each chirp. The echo signal from the target appears as a horizontal line with a distinct frequency in the spectrogram. Interference pulses have a chirp-like appearance with an increasing and decreasing frequency and appear as a 'V-shaped' spectrum at a distinct time. This time represents the instantaneous time of occurrence of interference.

The modelled and measured spectrograms for two scenarios in Figure 3.6 – the VR1 with F_{LPF} = 3.5 MHz and the VR2 with F_{LPF} = 10 MHz have been shown in Figure 3.10.

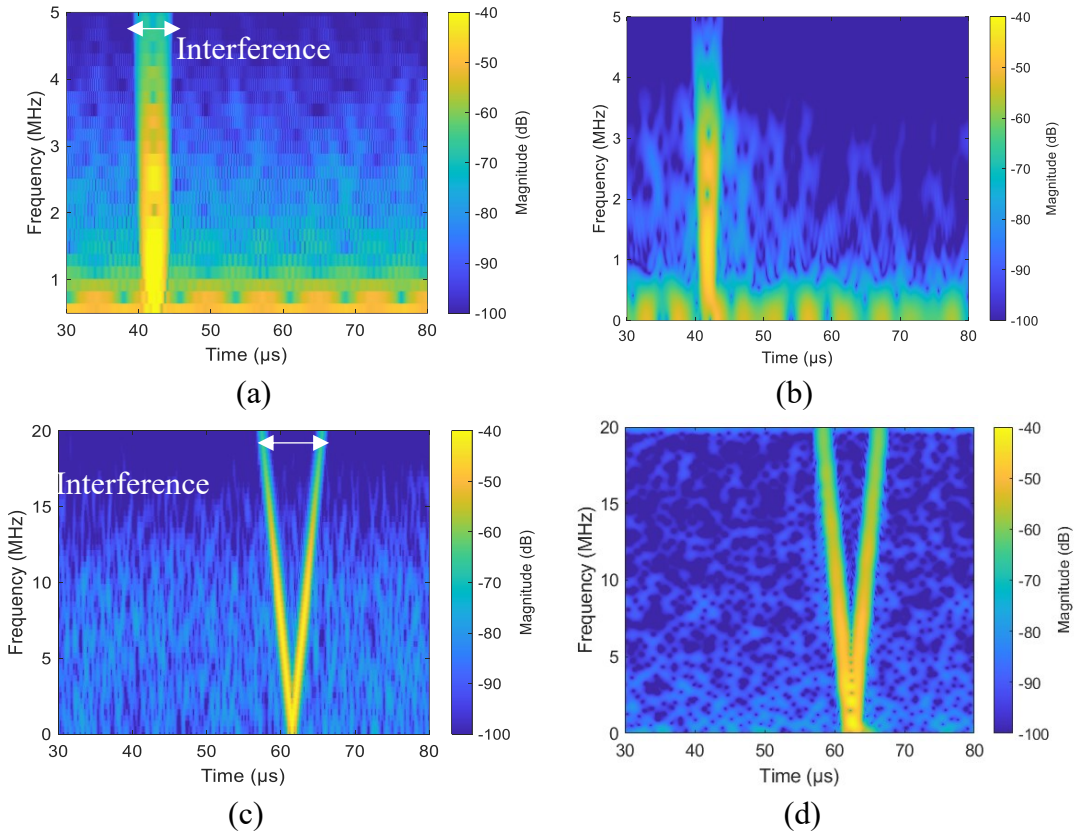


Figure 3.10: Spectrogram of received interference: (a) the modelled VR1 with F_{LPF} = 3.5 MHz, (b) the measured VR1 with F_{LPF} = 3.5 MHz, (c) the modelled VR2 with F_{LPF} = 10 MHz, (d) the measured VR2 with F_{LPF} = 10 MHz.

Due to a smaller F_{LPF} of the VR1, the received interference shows a sharp and narrow 'V-shaped' spectrogram with smaller T_{INT} (Figure 3.10 (a) and (b)) compared with interference received by the VR 2 (Figure 3.10 (c) and (d)). Therefore, TFD can be used to detect the presence of interference.

To get detailed information about interference and its parameters, a wide-band LPF will be more useful as it will increase the duration of the interference. However, the cut-off frequency of wide-band LPF should be less than half the sampling frequency at the ADC. This is discussed in [230], the LPF has been applied in two stages, one for traditional signal processing and another with a wide-band LPF to estimate interference waveform parameters.

3.4.3 Range-Doppler Profile of Received Signal

Understanding how interference manifests in the range-Doppler domain is essential to estimate the effect of interference spread on target parameter estimation. The frequency domain representation of interference at the output of the 2D-FFT has been summarised in this section using range-Doppler radar maps.

The intermediate frequency of interference from (3-22) can be modified to estimate the phase of the down-converted interference $\left(\varphi_{IF-i}\right)$ across the fast-time 't' and the slow-time 't_s'. It is expressed as:

$$\varphi_{IF-i}\left(t,t_s\right)=\Delta K t^2+2K_{\text{int}}t\tau_{\text{int}}\left(t_s\right)+2\Delta F t-K_{\text{int}}\tau_{\text{int}}^2\left(t_s\right)+2F_{\text{cint}}\tau_{\text{int}} \tag{3-33}$$

where, $\Delta F=F_{cv}-F_{\text{cint}}$. The intermediate frequency is estimated by the differentiation of phase, given as:

$$f_{IF-i}=\frac{1}{2\pi}\left(\frac{d\varphi_{IF-i}}{dt}\right) \tag{3-34}$$

After simplification,

$$f_{IF-i}\left(t,t_s\right)=\Delta Kt+\Delta F+K_{\text{int}}\tau_{\text{int}}\left(t_s\right) \tag{3-35}$$

Due to the time dependence of f_{IF-i}, a corresponding phase shift $\phi_{\text{int}}\left(t_s\right)$ is incorporated across the slow-time 't_s'. Therefore, with a one-way propagation delay of the received interference, the phase difference between the interference and the signal transmitted from the VR $\left(\varphi_i(t_s)\right)$ becomes:

$$\varphi_i(t_s)=-R_i(t_s)\frac{2\pi}{\lambda}+\phi_{\text{int}}(t_s) \tag{3-36}$$

After differentiating and solving (3-36), the Doppler shift of interference across the slow-time $f_{D-i}\left(t_s\right)$ can be expressed as follows:

$$f_{D-i}(t_s)=\frac{v_{vr}}{\lambda}\cos(\theta_{SB-t_s})+\frac{d\phi_{\text{int}}(t_s)}{dt_s} \tag{3-37}$$

Due to the time-dependent second term in (3-37), a distinct interference behaviour is observed across the slow-time which depends upon the waveform parameters of the interfering radars (see (3-35)). Based on this, the example cases for various types of interference have been discussed in detail in section 3.6.

After extracting the range and Doppler information, the signal has been analysed in the spatial domain, as discussed next.

3.5 Interference Analysis in the Spatial Domain

It is crucial to characterise interference in the spatial domain, particularly in terms of its angular resolution, as this determines the FoV of the VR that is impacted by interference. Any potential targets in this region might be partially or fully masked.

Currently, the majority of the SoA automotive radar chipsets are MIMO based [39], [40], [91], [250], [251], which provide an enhanced angular resolution in a small form factor. Under

MIMO beamforming, the radar scene is illuminated by multiple transmit antenna elements. A small proportion of the transmitted signal is reflected towards the radar by targets in the scene and is received by individual receive antenna elements. By associating the signals transmitted from each transmitter with those received by each receiver, a virtual receive array is synthesised from a smaller total number of transmitters and receivers than would be required by a conventional array. The synthesised virtual array is equivalent to a single transmit element that illuminates the whole FoV, and a receive array of $N_{Tx}N_{Rx}$ elements. This maintains a reasonably low complexity of the physical antenna elements. Moreover, as the targets are illuminated during the entire radar transmission duration, the integration time and Doppler resolution are potentially enhanced.

A simplified signal processing block diagram for MIMO FMCW radar with $N_{Tx} = 4$ and $N_{Rx} = 16$ based on the INRAS Radarlog configuration has been shown in Figure 3.11, and used to generate radar plots in section 3.6. The signal processing is based on a 2D FFT for range-Doppler, followed by beamforming achieved with a third FFT.

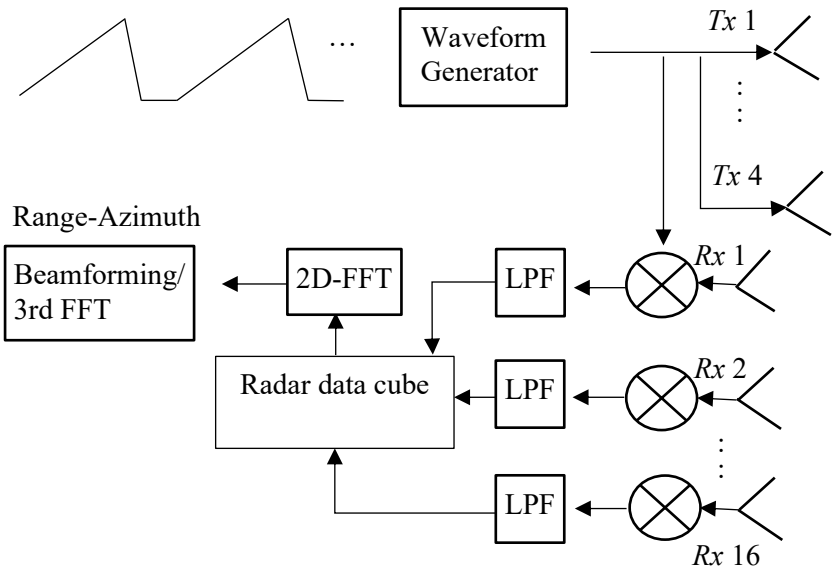


Figure 3.11: MIMO FMCW radar's simplified signal processing chain. Tx and Rx represent the transmit and receive elements, respectively.

Each receiving element of the array (*Rx*) receives the signal with a phase difference $kd\sin\theta$ between the signals across consecutive array elements, where $k = 2\pi/\lambda$, d is the spacing between the antenna elements and θ is the AoA. As the receiving element of the VR receives signals corresponding to the transmit elements (*Tx*) of the same radar, the target's spatial location is based on the resolution provided by the virtual aperture of the radar. In contrast to this, the VR receives an interference signal transmitted by multiple transmit elements of the interfering source. Therefore, the received interference at the VR cannot be associated with the transmit elements of the VR. Consequently, after beamforming, the beam towards interference may or may not follow the virtual aperture.

To understand this, radar data cubes for received echo and interference have been illustrated in Figure 3.12 (a) and (b), respectively.

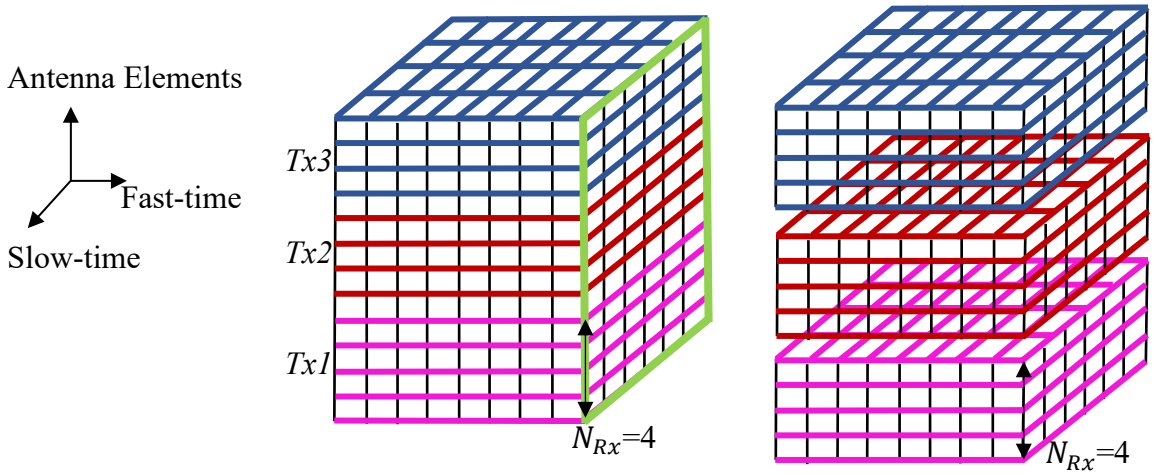


Figure 3.12: Radar data cubes for N_{Tx} = 3 and N_{Rx} = 4 element MIMO array: (a) data cube for received echo signal with 12 element virtual array, (b) data cube for interference with 4 element equivalent array according to N_{Rx}. Different colours represent signals received corresponding to different transmit elements of radar.

For ease of illustration, an array of N_{Tx} = 3 and N_{Rx} = 4 have been used. For the echo signal, a virtual array of 12 elements is formed due to the phase coherency of the received signal across

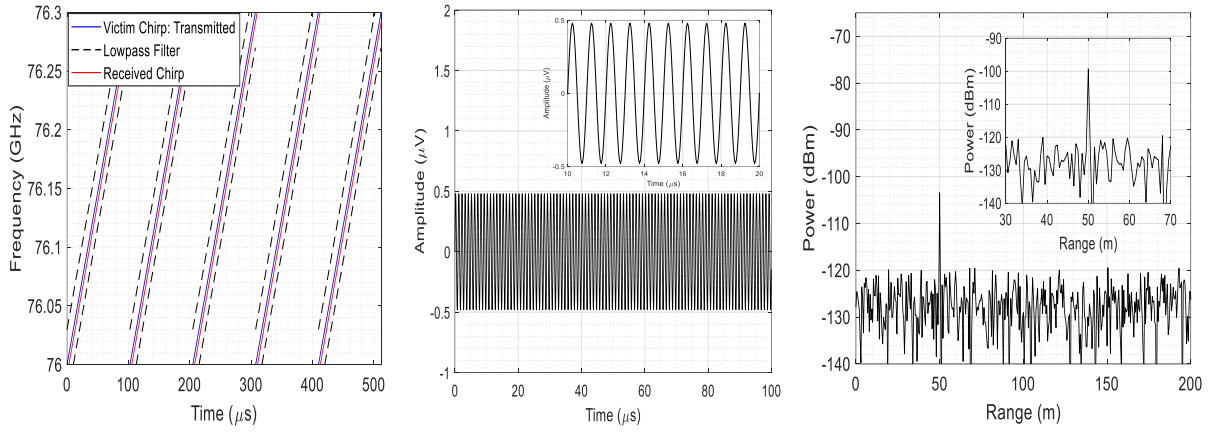
all virtual elements (green square in Figure 3.12 (a)) with a phase difference $kd\sin\theta$ between the consecutive virtual elements. In contrast, due to a different source of the interference signal, it is coherent with a phase difference $kd\sin\theta$ across the receive elements of the VR only. Therefore, beam resolution follows the real aperture of $N_{Rx} = 4$ in this case.

However, if the IR has waveform parameters that make it coherent across all the virtual elements of the VR, similar to an echo signal, a beam towards the interference will have a resolution determined by the virtual aperture. The criterion of virtual array formation for interference essentially depends upon the waveform characteristics of the interfering radars, which have been discussed in section 3.7.

3.6 Interference Classification

It has been shown in section 3.4 that interference spreads in the frequency domain. The number of interfered frequency bins and the interference power in each bin depends upon the waveform parameters of the VR and IR. Based on these parameters, interference has been classified, such that each type manifests itself differently at the VR. However, for all the types, target detectability is affected, which has been characterised by the SINR value.

For comparison, radar plots without interference have been shown in Figure 3.13 for the echo signal only. The modelled results are generated for a target (car) with 10 dBsm RCS positioned 50 m from the VR with T_{sv} = 102.4 µs, B_{sv} = 0.3 GHz, and F_{cv} = 76 GHz. The same VR parameters have been used throughout this section. Interference parameters are changed to generate different types of interference. The hardware configuration of the VR is based on the INRAS Radarlog chipset with a 14 dB noise figure [91].



(a) (b) (c)

Figure 3.13: Received echo: (a) chirp representation, (b) time domain, (c) range profile.

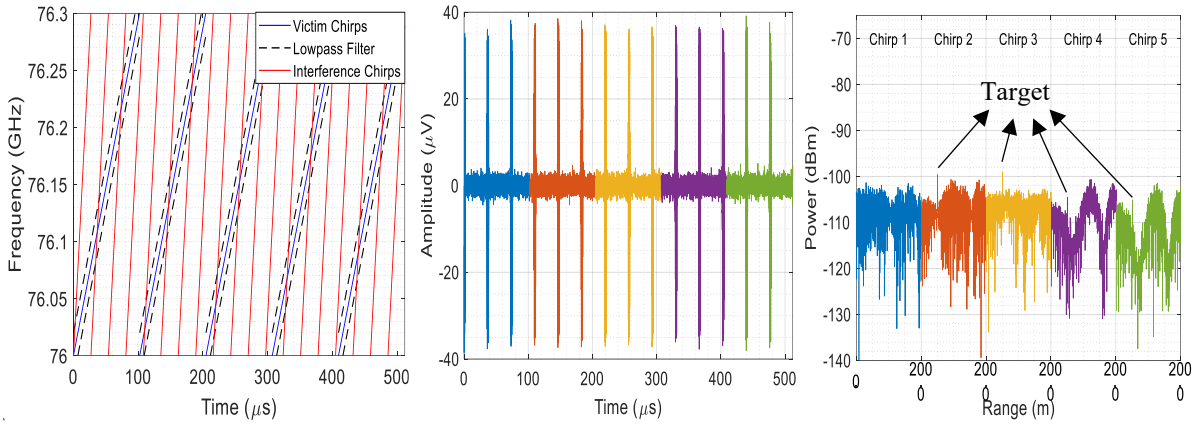
It is to be noted that, for illustration, the thermal noise has not been included in the time domain plot in Figure 3.13 (b). However, it has been considered in the signal processing chain and in the range profile (Figure 3.13 (c)). In the absence of interference, the target at 50 m is detectable with a reasonable signal to noise ratio (SNR) of 20 dB.

3.6.1 Types of Interference on the Basis of Sweep Time

Based on the sweep time of the victim and interfering chirps, interference has been classified into two types:

1. Fast chirp sequence with $T_{\text{sint}} \leq 0.5T_{sv}$

The chirp overlap, time domain, and frequency domain (range profile) representation of the fast chirp interference sequence with $T_{\text{sint}} = 27\mu\text{s}$ and the slow chirp interference sequence with $T_{\text{sint}} = 423\mu\text{s}$ have been presented in Figure 3.14 and Figure 3.15, respectively for the interference $B_{\text{sint}} = 0.3$ GHz and $F_{\text{cint}} = 76$ GHz. The results are shown for the five consecutive VR chirps. The received signal is composed of an echo signal and interference from a collocated target at 50 m. For visualisation, only interference chirps have been shown in the chirp overlap plot and ranges from 0 to 200 m have been plotted.



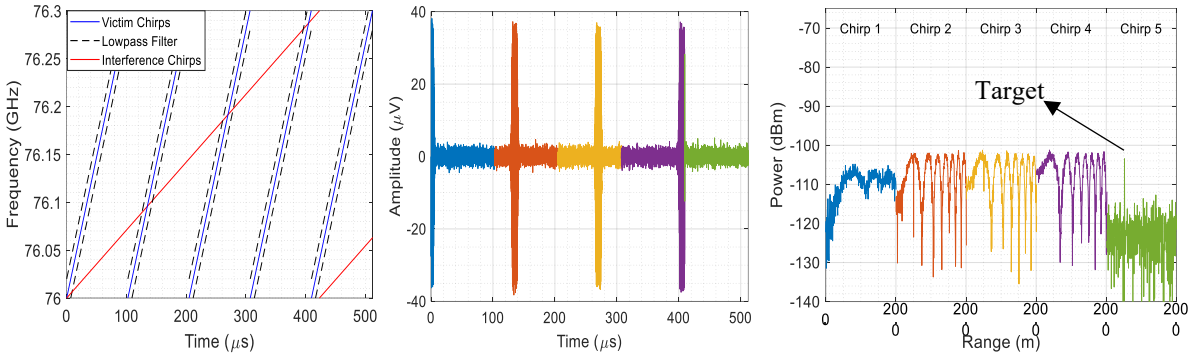
(a) (b) (c)

Figure 3.14: Fast chirp interference: (a) chirp plot, (b) time domain, (c) range profile.

For the fast chirp sequence, compared to the results without interference in Figure 3.13 with 20 dB SNR, the SINR has significantly reduced with a 3 dB mean SINR across the 5 VR chirps. The 3 out of 5 VR chirps have a target peak fully masked by the interference floor, which might affect target detectability and is discussed in the later chapters. Moreover, interference pulses are uncorrelated due to the appearance of multiple pulses within each VR chirp and a different instantaneous time of occurrence of each pulse. This results in a uniform interference floor across all the range bins.

2. Slow chirp sequence with $T_{\text{sint}} > T_{sv}$

In a slow chirp sequence, each VR chirp has a maximum of one interference pulse. If a full double-sided interference pulse appears, e.g., the second, third, and fourth victim chirps in Figure 3.15, well-defined periodic peaks and nulls – the scalloping pattern [144] – are observed in the interference floor. This is due to phase periodicity between the samples of the interference pulse. The SINR is strongly attenuated if the target appears in the nulls of the interference scalloping pattern. If a single-sided interference chirp appears, e.g., the first VR chirp in Figure 3.15, peaks and nulls are observed, but they are not well-defined. In the discussed example, the target is fully masked by the interference floor for the initial four VR chirps, whereas the fifth VR chirp does not interfere. Consequently, the SNR = SINR = 20 dB across this chirp.



(a) (b) (c)

Figure 3.15: Slow chirp interference: (a) chirp plot, (b) time domain, (c) range profile.

3.6.2 Types of Interference on the Basis of Sweep Rate

The types of interference classified based on the VR and IR sweep rates have been mentioned in Figure 3.16. Detailed analysis of each interference type has been presented in Appendix 3, while a summary is included in this section.

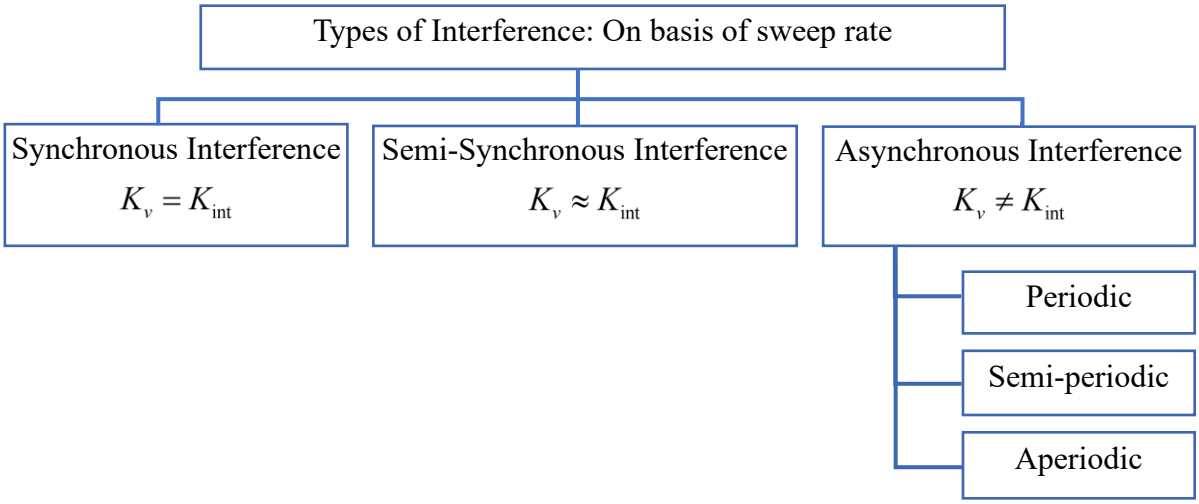


Figure 3.16: Classification of radar interference based on the sweep rate difference.

I. Synchronous Interference

When two radars with identical waveform parameters interfere such that $K_v = K_{\text{int}}$, and $F_{cv} - \frac{F_{LPF}}{2} \leq F_{ci} \leq F_{cv} + \frac{F_{LPF}}{2}$, the interference signal chirp is completely synchronised with the VR chirp. If the entire interferer chirp is within the LPF band of the VR, similar to the echo signal, after signal processing, a well-defined ghost target appears with similar characteristics

to the echo signal. The down-converted synchronous interference contribution to the beat signal in (3-22) is monotonic and expressed as:

$$f_{IF-Synchronous} = K_{\text{int}}\tau_{\text{int}} \tag{3-38}$$

Synchronous interference can also occur if the VR's signal is received through multipath reflections such as in tunnels, highways with guard rails, car parks, etc. Consequently, ghost targets appear at arbitrary distances and directions that depend upon the position of reflecting surface i.e., the propagation delay between the transmitted and received (multipath) signal.

II. Semi Synchronous Interference

The sweep rates of the VR and IR for semi-synchronous interference are similar but not identical $\left(K_v \approx K_{\text{int}}\right)$. Analogous to synchronous interference, semi-synchronous interference is present within the entire duration of the victim's chirp. However, the time-dependent term in (3-22) is non-zero, resulting in interference spread across multiple frequency (range) bins. Two types of semi-synchronous interference have been observed based on the IR parameters.

- When the VR and IR have similar sweep times but a slight bandwidth difference, a chirp-like interference pattern is observed in the down-converted signal. In this case, interference spreads across a fraction of the range bins with a higher power, forming a pedestal-like interference floor.
- For a similar bandwidth of the VR and IR waveforms but a slight difference in sweep time, there is an absence of complete coherence between the VR and IR chirps. Therefore, interference appears like a ghost target but with a broad peak centred around the frequency $K_{\text{int}}\tau_{\text{int}}$ rather than a sharp peak observed for the echo signals.

Synchronous and semi-synchronous interference are unlikely to occur in real-world settings because they need perfect synchronisation between the VR and IR waveforms. Nevertheless, they cannot be entirely excluded, especially in highway scenarios, where many radars may

operate simultaneously and often for extended periods of time. Therefore, even events with low probabilities could occur, and simulation models must take this into account.

III. Asynchronous Interference

In a typical automotive scenario, radars from various manufacturers, different waveform parameters, and configurations will be present. Interference between them gives rise to asynchronous interference, a more common type of radar interference. It occurs when the waveforms of two interfering radars have different sweep rates such that $K_v \neq K_{\text{int}}$. In this case, the interference signal lies within the LPF band of the VR at a few locations. Consequently, unlike synchronous and semi-synchronous interference that are focused across limited frequency (range) bins, asynchronous interference is time-limited (Figure 3.14 and Figure 3.15). and spreads over a large number of frequency bins with a uniform interference pattern.

Asynchronous interference has been classified into periodic, semi-periodic, and aperiodic interference. For understanding, the instantaneous times of interference occurrence within each VR chirp have been defined as a vector, given as follows:

$$t_{\text{int}} = \left[t_1, t_2, ..., t_M\right] \tag{3-39}$$

where, *M* represents the total of interference pulses within each VR chirp.

1. **Periodic Interference:** It occurs when the t_{int} vector across all the VR chirps is similar. Therefore, the interference pattern is the same across each VR chirp.
2. **Semi-Periodic Interference:** t_{int} vector for the initial few victim chirps within each CPI is different, but then it repeats for the remainder of the chirps so that $mT_{\text{sint}} = nT_{sv}$ for an integer m ≥ 2.
3. **Aperiodic Interference:** The interference sequence is random for all the VR chirps during a CPI. Therefore, the vector t_{int} is unique for each chirp.

Synchronous and semi-synchronous interference are also called narrowband interference, as they affect a small portion of the frequency spectrum. Asynchronous interference is called broadband interference, as it affects a larger portion of the VR's frequency band. The use cases for each interference type in different domains have been discussed next.

3.7 Interference Representation in Each Domain – Use Cases

A thorough analysis of interference along the signal processing stages is essential to develop effective mitigation techniques. This aids to:

1. Analyse signals in different domains, enabling a range of possible interference detection and mitigation algorithms.
2. Analyse the impact of each processing stage on interference to allow for stage optimisation.
3. Provide a comparative performance analysis of mitigation techniques in different domains.
4. Determine the optimal domain for robust interference detection, parameter estimation, and avoidance/ mitigation strategies for various road scenes.

The detailed analysis of each interference type in the range profile, range-Doppler profile, and range-azimuth profile has been presented in Appendix 4. A summary is included in Table 3.2 for the waveform parameters in Table A4.1.

For different types of interference, periodicity between interference pulses causes a non-uniform spread of interference along the Doppler axis. Interference is focused across a few Doppler bins in this case. Aperiodic interference spreads uniformly across the Doppler axis with a lower mean interference power. In terms of the interference spatial characteristics, MIMO radar provides maximal virtual array resolution for both target and periodic interference cases. Aperiodicity between interference pulses causes broader resolution defined by the receive aperture of the radar.

Table 3.2. The appearance of various types of interference in frequency and spatial domains.

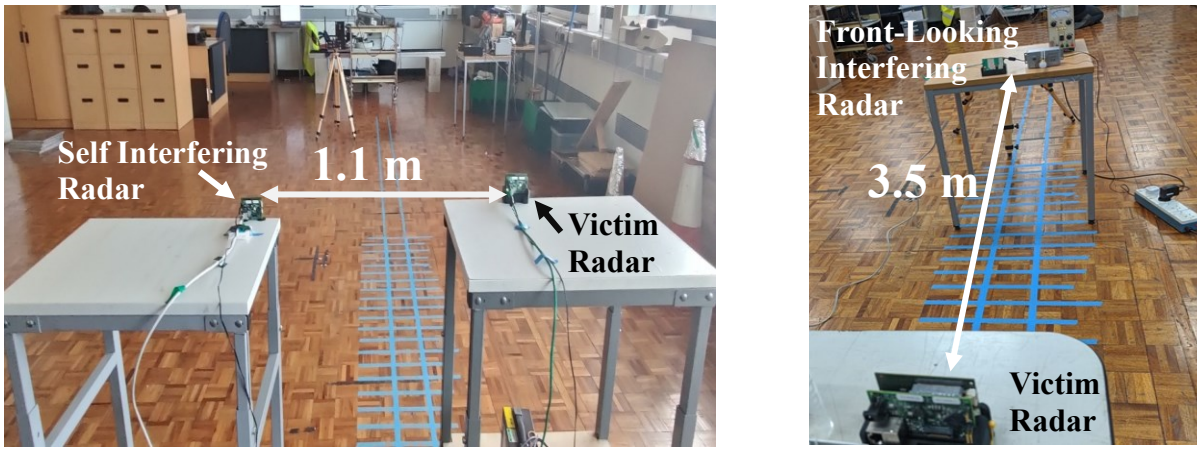
Interference		Frequency Domain		Spatial Domain
		Range Compression	**Doppler Compression**	**Azimuth Compression**
Synchronous Figure A4.3		A ghost target at an arbitrary distance.	A ghost target at an arbitrary distance/ Doppler.	Virtual Aperture
Semi-synchronous Figure A4.4		Pedestal-like spectrum with high power.	Short interference energy spread across range bins and focused across Doppler.	Virtual Aperture
Periodic Figure A4.5	Fast Chirp	Uniform interference floor, random peaks/nulls.	Two distinctive lines with random peaks and nulls – Single channel Rx.	Virtual Aperture
	Slow Chirp	Scalloping pattern with bows and nulls.	Two distinctive lines with scalloping pattern – Single channel Rx.	Virtual aperture
Semi-periodic Figure A4.6		Scalloping pattern with bows and nulls.	Interference energy across multiple Doppler bins.	Real aperture
Aperiodic Figure A4.7	Fast Chirp	Uniform interference spread.	Diagonal ridges that get random when the number of interference pulses in each VR chirp increases.	Real aperture
	Slow Chirp	Scalloping pattern with bows and nulls.	Diagonal ridges	Real aperture

The waveform parameters in automotive radars are much wider than the range discussed in this study. The main point is to illustrate the high variation of interference effect expected as radar waveform parameters of the VR and IR change.

3.8 Self Interference

As discussed each vehicle will have multiple radars installed on it for 360-degree imagery. Therefore, there is also a possibility of self-interference, where radars installed in the same platform (vehicle) interference with each other. To evaluate this, measurements were

conducted in a controlled laboratory environment using SoA NXP TEF810X radar chipsets as the VR and IR. The IR was placed at different orientations with respect to the VR to depict the scenario of self-interference and mutual interference (interference between the radars installed on different platforms). The test setup for self-interference is shown in Figure 3.17 with the corner-looking orientation of the IR wrt. the VR $\left(30^{o}\right)$ and 1.1 m separation, which is half the width of a typical luxury vehicle [252]. The test setup for mutual interference case is shown in Figure 3.18 (b) where the IR was placed in the front (boresight) of the VR at a 3.5 m distance.



(a) (b)

Figure 3.17: Measurement setup to estimate the impact of interference. (a) Test setup for self-interference. (c) Test setup for mutual interference from front-looking radar.

The corresponding radar parameters have been given in Table 3.3.

Table 3.3. Radar parameters for the analysis and comparison of self and mutual interference.

Parameter	**Value**
Victim Radar Sweep Time	204.8 µs
Victim Radar Bandwidth	0.5 GHz
Interference Radar Sweep Time	25.6 µs
Interference Radar Bandwidth	1 GHz

The measured results for the two cases have been presented in Figure 3.18. As expected, due to the orientation of the VR and front-looking IR, interference with a higher amplitude is

observed in the time domain profile, consequently a higher interference to noise ratio (INR) after range compression (15 dB in the discussed case), shown in Figure 3.18 (c). Interference is also received from the corner-looking radar (self-interference case), however, with a significantly smaller amplitude (Figure 3.18 ©). Consequently, the INR, in this case, is comparable to the thermal noise floor of the VR after range compression.

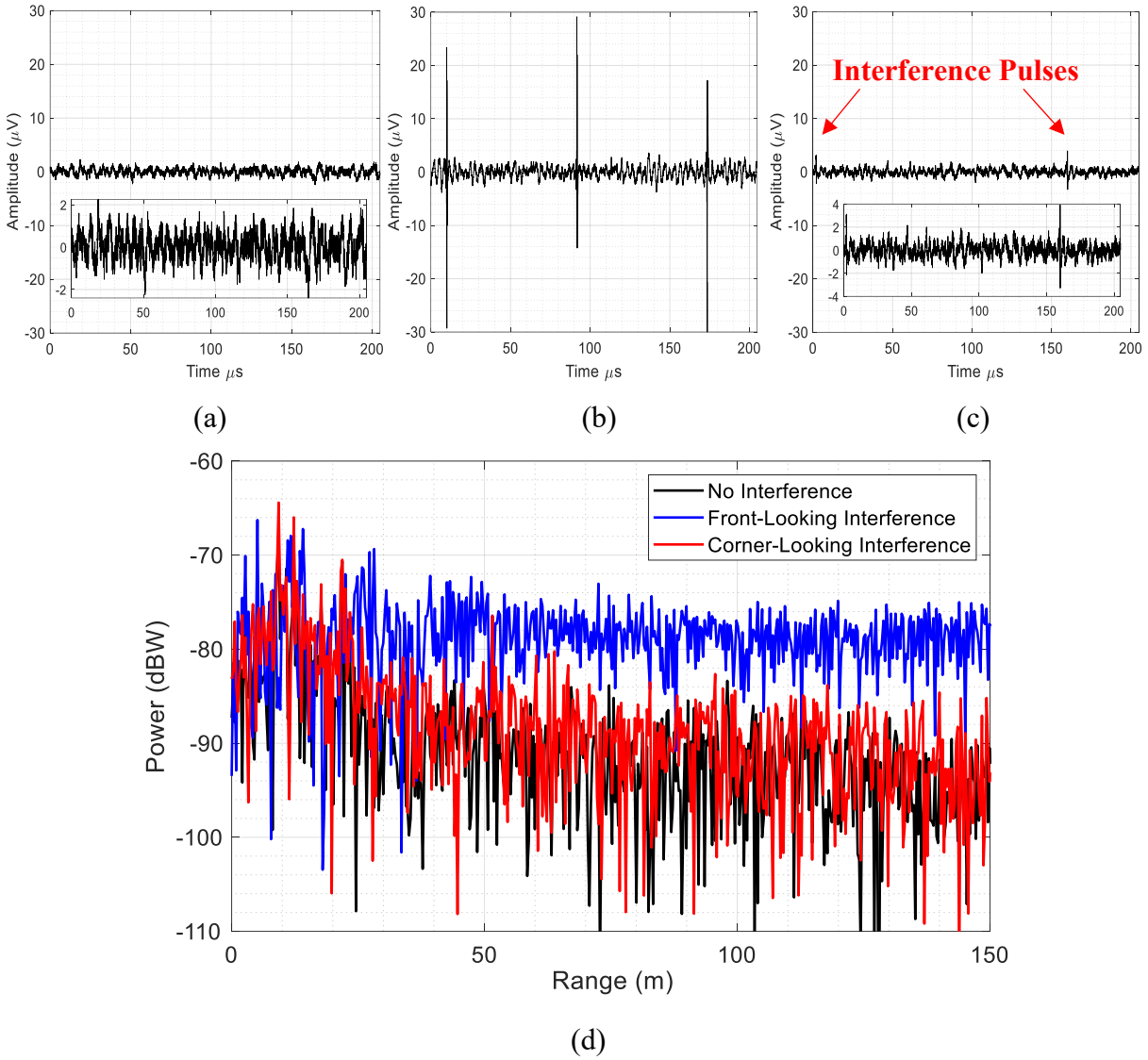


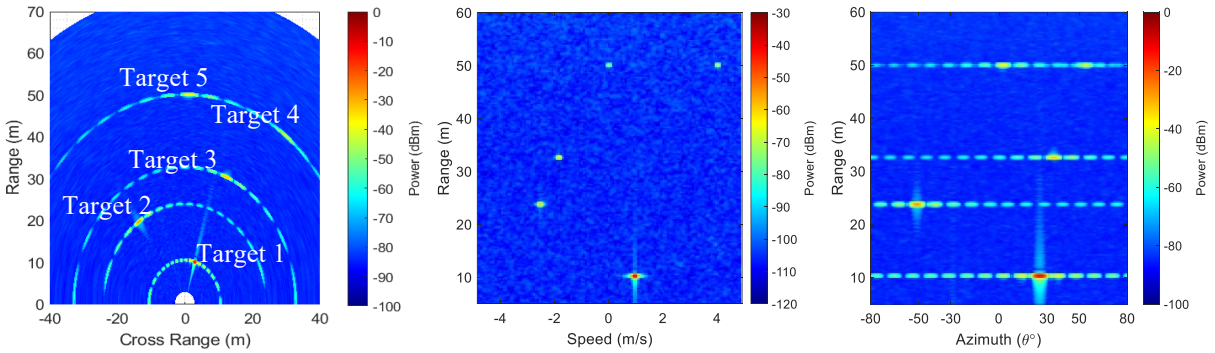
Figure 3.18: Measured results for self-interference and front-looking interference. (a) Time domain profile in the absence of interference. (b) Time domain profile in the background of interference from front-looking interfering radar (mutual-interference case). (c) Time domain profile in the background of interference from corner-looking interfering radar (self-interference case). (d) Range profile.

Therefore, it can be concluded that although the radars installed on the same vehicle will interfere with each other (if they are operating in the same band), however with a much smaller amplitude. With a smart frequency allocation mechanism on the radars installed on the same platform, their probability of interfering can be significantly reduced [187], [253]. The impact of radar orientation on the SINR has been discussed in detail in Chapter 7.

3.9 Multiple Interference Sources

The results presented earlier correspond to interference received from a single source. However, in a typical road scene, there is a high probability of receiving interference from multiple radars at a time.

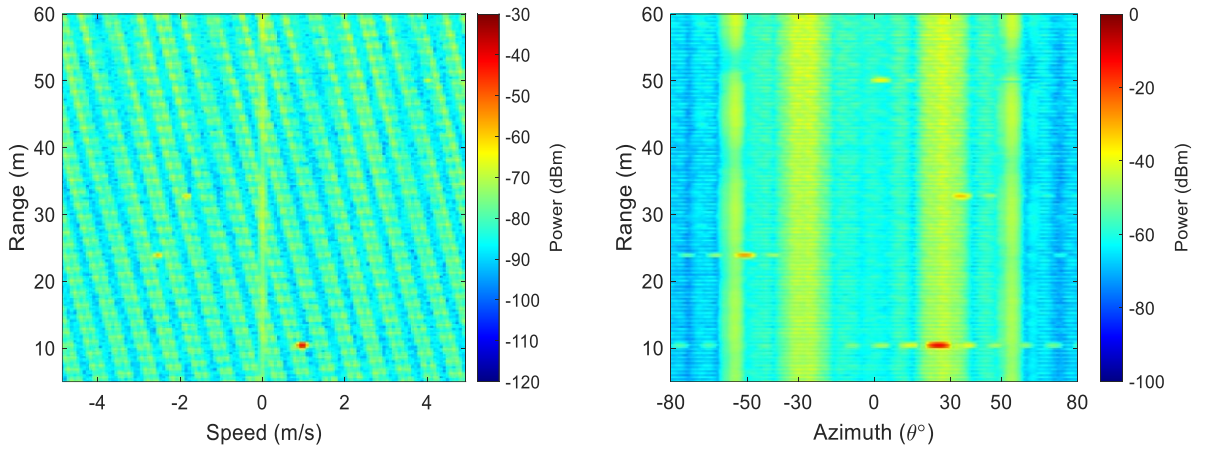
The modelled example of a scenario where multiple interferers are transmitting in the FoV of the VR has been shown in Figure 3.19. Five target vehicles, each with a 10 dBsm RCS, drive in the FoV of the VR. The radar installed on each vehicle also transmits an interfering signal toward the VR. The position and speed of the targets are given in Table 3.4. For reference, plan position indicator (PPI), range-Doppler, and range-azimuth plots after signal processing at the host vehicle radar have been shown in Figure 3.19 (a), (b) and (c), respectively. SNR of all the targets has been stated in Table 3.4. All the targets are detected with a reasonable SNR.



(a) (b) (c)

Figure 3.19: Radar plots for multiple targets in the absence of interference: (a) PPI plot, (b) range-Doppler map, (c) range-azimuth map.

The same scenario with active interference from the radars on each vehicle has been shown as range-Doppler and range-azimuth maps for a single channel receiver (Appendix 6) in Figure 3.20 (a) and (b), respectively.



(a) (b)

Figure 3.20: Radar plots at the background of interference from multiple interfering sources: (a) range-Doppler map, (b) range-azimuth map.

IRs can have a wide range of waveform parameters; however, for modelling, the set of waveform parameters for each IR have been stated in Table 3.4. The extracted SINR values of the targets at the background of interference have also been mentioned in Table 3.4. Table 3.4 shows a significant degradation in the SINR values in the background of interference from multiple sources, which affects target detectability. Furthermore, due to signal reception from multiple interfering radars, their signals are uncorrelated. Therefore, the interference pattern in the frequency domain is closer to aperiodic interference with diagonal ridges in the range-Doppler plot. Moreover, after beamforming, a larger FoV of the VR would be affected by interference, especially in the single (real) channel receiver.

Interference appearance along the radar processing stages is a complex phenomenon, with a unique interrelationship between the radar parameters, road scenarios, and effect on target detectability. This indicates the importance of developing an appropriate simulator to study interference effects and has been discussed in Appendix 12.

Table 3.4. Target and interferer position, SNR, and SINR values to analyse the impact of multiple interference sources.

	Target 1/ Interferer 1	**Target 2/ Interferer 2**	**Target 3/ Interferer 3**	**Target 4/ Interferer 4**	**Target 5/ Interferer 5**
Position (Range, Angle, Speed)	10 m, 24^o, 1 m/s	24 m, -50.1^o, -2.5 m/s	32 m, 34^o, -2 m/s	50.1 m, 0^o, 4 m/s	50.4 m, 54^o, 0 m/s
Interferer parameters (Sweep time, bandwidth, start frequency)	10 µs, 0.5 GHz, 76 GHz	10.3 µs, 0.5 GHz, 76 GHz	423 µs, 0.5 GHz, 76 GHz	150 µs, 0.5 GHz, 76 GHz	CW, 76.2 GHz
			SNR/ SINR		
No Interference (SNR)	74 dB	59 dB	56 dB	41 dB	43 dB
Multiple Interference: Range-Doppler (SINR)	30 dB	23 dB	20 dB	Masked by interference floor	Masked by interference floor
Multiple Interference: Range-Azimuth (SINR)	32 dB	17 dB	14 dB	Masked by interference floor	2 dB

3.10 Summary

Due to an increase in the radar penetration rate, the mutual interference between radars is expected in a coexistence environment. The likelihood that the signals from these radars may overlap in the time and frequency domains is high due to: a) the use of a higher duty cycle to achieve a longer unambiguous range, and b) the increase in bandwidth to achieve a high range resolution. Furthermore, a close spatial separation between the vehicles, as expected in

automotive conditions, also increases the likelihood of spatial domain overlap of the interfering signals.

The analytical understanding of radar interference has been established in this chapter. Firstly, interference has been mathematically represented, followed by a systematic analysis of interference power and its impact on target detectability. It has been shown that for the specific radar configuration, due to one-way propagation of received interference, interference power in many cases could be much higher than the echo signal power. Consequently, an increase in noise floor is observed which causes degradation of the VR's performance and reduces the SINR.

Additionally, the effect of the LPF has been assessed by evaluating interference duration for various filters used in the SoA radar chipsets. A lower cut-off frequency and higher filter order reduce interference duration. However, this results in a steeper roll-off of the LPF with a ringing effect, causing a larger deviation from the probability of detection in the background of AWGN.

At the output of the LPF, the interference pulse has a double-sided chirp-like modulation that spreads over multiple frequency bins. The number of interfered resolution cells and the interference power in each cell depends upon the waveform parameters of the VR and IR. A scalloping pattern with well-defined arches and nulls is observed for a slower interference chirp sequence. In contrast, random peaks and nulls with a uniform pattern appear for the fast chirp interference sequences.

In a typical automotive scenario, the majority of the interference is asynchronous and aperiodic. However, as interference fundamentally appears as a stochastic process, all kinds of interference have been investigated in this work. Nevertheless, as a wide range of waveform parameters can be used by automotive radars, it has been shown that the interaction of these waveforms with the VR is always unique. Based on this, interference has been classified into

synchronous and semi-synchronous interference cases with a comparatively low probability of occurrence and asynchronous interference that can be expected in a typical road scene.

Different interference manifests itself distinctly in the range-Doppler and range-azimuth domains. In the range-Doppler domain, the energy from interferers can either cluster in specific Doppler bins with a higher power or spread across a large number of Doppler bins with comparatively lower power when the interfering signal exhibits a slight asynchrony. A detailed discussion of the effect of interference Doppler frequency on the processing stages of the VR has been presented in Chapter 8. After beamforming, periodic interference pulses have a finer angular resolution due to the synthesised virtual array of the VR. In contrast, aperiodic pulses have a broader angular resolution according to the receive array of the VR. This has been analysed in detail in Chapter 6. The interference effect on the VR detector primarily depends upon the interference statistics discussed in the following chapter.

Chapter 4. POWER AND STATISTICAL ANALYSIS OF INTERFERENCE

Most COTS automotive radars have been designed and optimised under the assumption of signal reception in the background of AWGN, which is always present in the receiver. However, as shown in Chapter 3, interference is expected to have much higher power than AWGN. Therefore, the radar's noise floor will be defined by interference – interference floor.

To understand the impact of interference on radar detectors' performance and target detectability, one of the foremost requirements is the characterisation of interference power, the statistics of interference, and their similarity to that of AWGN. Interference pulses are LFM sinusoidal waveforms at the output of the LPF. As they are independent of the echo signal received at the VR, they appear as random stochastic processes [254]. Therefore, based on IR waveform parameters, interference statistics might change, which has been analysed in this chapter by determining the following:

- Interference power across the radar processing stages.
- Correlation between the interference pulses.
- Interference distribution.
- Probability of detection in an interference background.

If these characteristics are similar to those of AWGN, then classical well-established detection techniques [255] remain optimal. In the opposing case, a loss in detection performance is expected, and traditional techniques (matched filtering) will not be optimal anymore. For these two scenarios, interference parameters have been identified and analysed in this chapter. The performance evaluation has been carried out by Monte Carlo simulations, and the results are presented as receiver operating characteristic (ROC) curves.

An initial input to this analysis comes from the fact that during signal integration, interference normalisation can be expected if the Central Limit Theorem (CLT) [256] requirements are satisfied i.e.,

1. The interference pulses have a similar statistical distribution to each other,
2. Interference pulses are independent, and
3. The number of interference pulses averaged is large enough.

These conditions have been assessed for various waveform parameters.

The main contributions of this chapter are as follows:

- Interference power budget analysis and its comparison to the power of the echo signal.
- Qualitative and quantitative comparison of the level of degradation due to interference along the signal processing stages of the VR.
- Statistical analysis of radar interference by determining:
  i. The correlation between interference pulses received at the VR.
  ii. The probability density function (PDF) of the interference.
- Investigating interference statistics and their similarity with AWGN for various waveform parameters.
- Identifying the critical waveform parameters that cause a deviation of interference statistics from Gaussian noise statistics.
- Analysing the effect of interference on radar detection performance.

4.1 State of the Art

Limited literature is available on interference statistics in automotive scenarios, with generally broad conclusions. The work in [166] and [177] provides statistical modelling of interference power for different road geometry and traffic conditions. Stochastic behaviour of the interference based on the interferers' position has been modelled in [165], concluding that

interfering radars generate random noise-like interference. Authors in [181], [199], [232], [257], [258] have predicted the behaviour of frequency-modulated (FM) interference as a random process that raises the noise floor. An argument discussed in [168] states that in a practical road scenario, the cross-correlation between interference pulses from the same interfering source is small, resulting in a random behaviour similar to noise. However, a generalised conclusion in [174] states that interference from other radars cannot be considered random noise. Furthermore, it is discussed in [259] that interference from other radars cannot be considered white noise and that different types of interfering waveforms lead to a different shaping of the frequency domain data. However, a detailed analysis and the conditions under which interference can be considered noise have not been mentioned.

The observed discrepancies and a lack of statistical analysis of radar interference is the motivation behind this chapter. The primary goal is to understand if target detectability and tracking are possible in the background of interference using well-defined ROC curves for signal detection against AWGN [255], [260], [261].

4.2 Radar Model for Statistical Analysis

A simplified block-level representation used for the statistical analysis of interference is shown in Figure 4.1. Signal processing has been detailed in section 3.1, and a summary is included in the subsequent paragraphs.

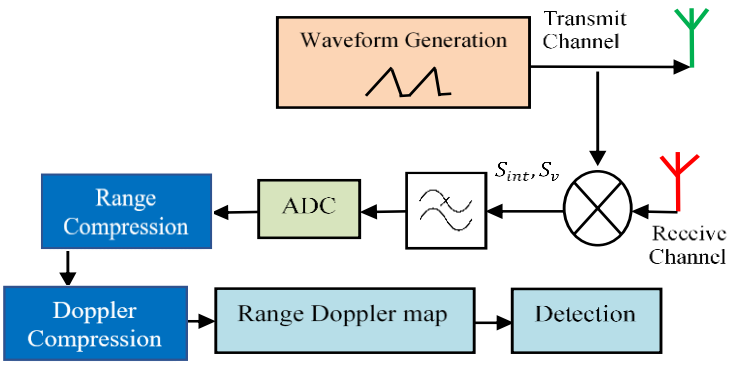


Figure 4.1: FMCW radar block level representation for interference statistical analysis.

The received signal contains target echo(s) and interference signals from the nearby radars. The mixer down-converts the received signal, the LPF limits R_{max} and interference duration, and the ADC converts the analogue signal to a digital one. The modelled time domain representation of a single victim chirp at the output of the ADC with three occurrences of interference pulses has been shown in Figure 4.2 (a). The received echo signal appears as a continuous sinusoidal waveform (Figure 4.2 (b)). In contrast, each interfering pulse appears as a two-sided LFM waveform, shown in Figure 4.2 (c).

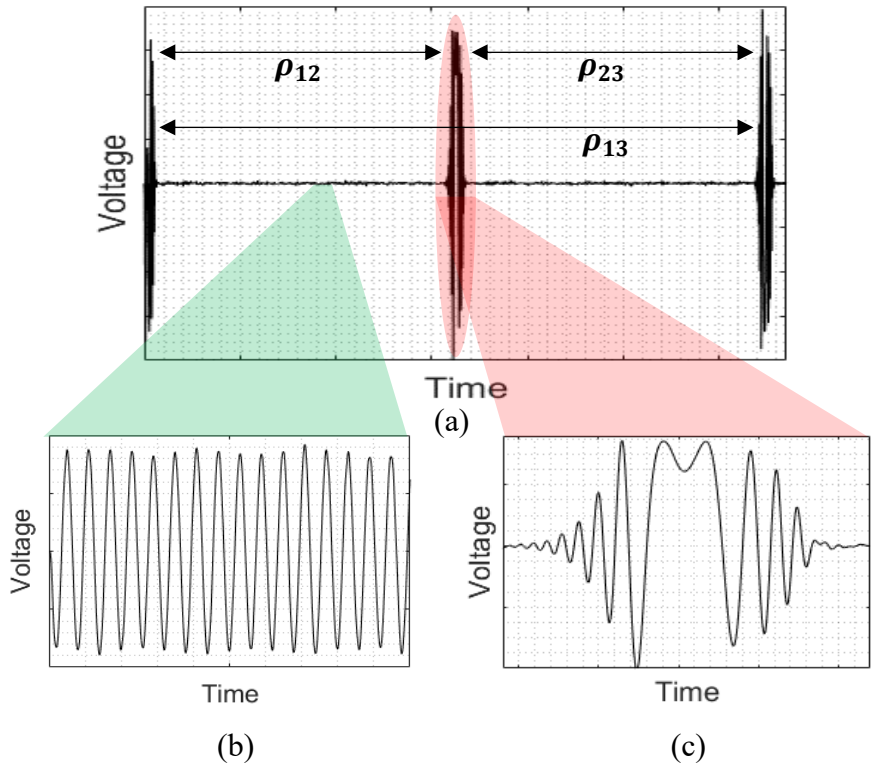


Figure 4.2: Time domain representation of received signal: (a) signal with echo and interference pulses, (b) sinusoidal echo, (c) zoomed interference pulse.

As discussed in Chapter 3, the amount of interference spread in the frequency domain depends upon the VR and IR's waveform parameters. For similar waveform parameters, interference spread is non-uniform across limited frequency bins. In contrast, the interference spreads uniformly when the waveform parameters differ (Figure 3.8). The interference spectrum can be expected to be much wider than the range and Doppler resolution cells in both

cases. At the output of the Doppler compression, echo and interference are further averaged over a CPI.

The next step in the processing chain is target detection against background noise and interference. In this chapter, the energy detection method [261], summarised in Figure 4.3, has been used to evaluate the detector's performance where *y(j)* represents interference samples at the decision-making point '*D.*' A detailed analysis has been presented in section 4.5.

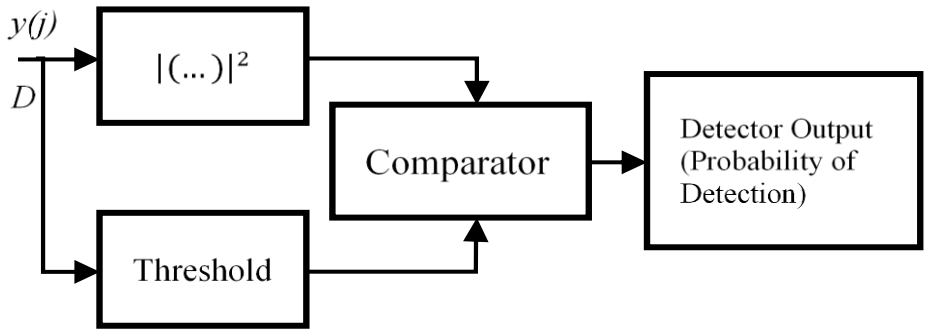


Figure 4.3: Radar detector processing chain. y(j) represents the interference samples at the decision-making point 'D.'

4.3 Power Budget Analysis of Interference

Along with interference statistics, a precise estimate of its power and power variation along the signal processing stages is also essential to analyse the interference impact at the detector. To evaluate this, a roadside scenario in Figure 4.4 with one target and interferer in the VR's FoV has been analysed considering a free-space propagation model. However, the presented analysis is equally valid for other propagation models.

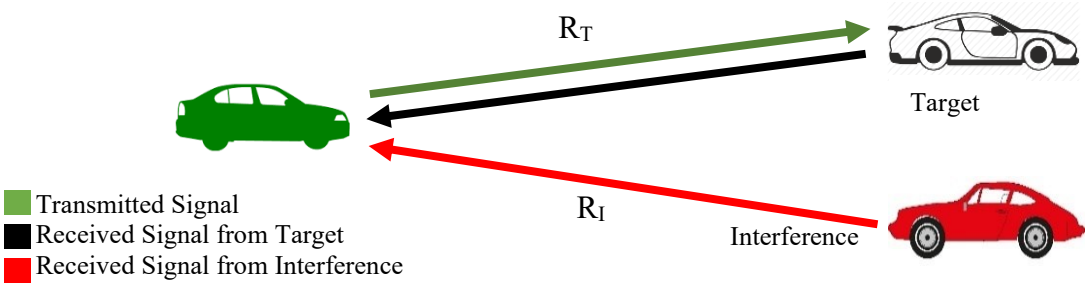


Figure 4.4: Road scenario with target and interferer in the FoV of victim radar.

The radar transmitter transmits a signal of power P_T (typically 10 mW in SoA automotive radars [168]) through the transmit antenna with gain G_T. The echo signal power received by radar with receive antenna gain G_r can be expressed as follows:

$$P_{RT} = \frac{P_T G_T}{4\pi R_T^{\,2}} \cdot \frac{\sigma_T A_e}{4\pi R_T^{\,2}} = \frac{P_T G_T G_R \lambda^2 \sigma_T}{(4\pi)^3 R_T^{\,4}} \tag{4-1}$$

where, P_{RT} is the received power from a target, $\frac{P_T G_T}{4\pi R_T^{\,2}}$ represents the incident power on a target, σ_T is the RCS of a target, $\frac{\sigma_T A_e}{4\pi R_T^{\,2}}$ represents reflected power from the target, and A_e is the effective antenna aperture estimated as $\frac{G_R \lambda^2}{4\pi}$.

For one-way interference propagation, received interference power can be expressed as:

$$P_{RI} = \frac{P_{TI} G_{TI}}{4\pi R_I^{\,2}} \cdot A_e = \frac{P_{TI} G_{TI} G_R \lambda_I^{\,2}}{(4\pi R_I)^2} \tag{4-2}$$

where, P_{RI} represents received interference power, P_{TI} and G_{TI} represents the interferer transmit power and transmit antenna gain, respectively, and λ_i is the interfering signal's wavelength. Assuming that the transmit power, transmit and receive gains, and wavelength of the VR and IR are similar, the following expressions have been obtained:

$$P_{RT} = \frac{P_T G^2 \lambda^2 \sigma_T}{(4\pi)^3 R_T^{\,4}} \tag{4-3}$$

$$P_{RI} = \frac{P_T G^2 \lambda^2}{(4\pi R_I)^2} \tag{4-4}$$

The echo signal attenuates by the fourth power of range (two-way propagation), while the interference signal attenuates with the square of range (one-way propagation). Consequently, interference power from other radars will likely exceed the echo signal power. This can often saturate amplifiers at the VR receiver and in some instances mask targets, especially weak echoes from targets with small RCS or the ones at a longer range. Moreover, received

interference power can be significant for interferers having a higher radiated power, such as the LRR or the traffic control radar.

An example of the received power from the scene with collocated target and interferer at 50 m with P_T = 10 dBm, G = 14 dBi, σ = 5 dBsm, and F_{cv} = 76.5 GHz has been given in Figure 4.5. The VR and IR have similar transmit power and antenna gains. It can be seen from Figure 4.5 that the interference power is approximately 41 dB stronger than the echo power.

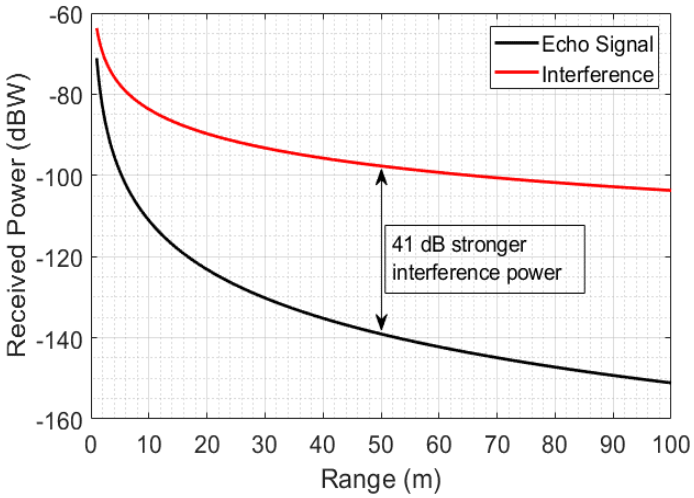


Figure 4.5: Received power from collocated target and interference as a function of range.

Although the LPF limits interference duration, the remaining interference power is still greater than the system noise floor in most cases. After the LPF, only a fraction of the received interference is processed by the VR. The mean interference power after the LPF can be expressed as [262]:

$$P_{RI} = \frac{P_T G_T G_R \lambda^2}{(4\pi R_I)^2} \cdot \psi \tag{4-5}$$

where, ψ is the fraction of the interfering power in the VR chirp after the LPF. Its value ranges from 0 to 1, where 1 means all the interference power remains after the LPF, and 0 means there is no interference after the LPF.

In this work, the SINR and interference to noise ratio (INR) have been used as metrics to estimate the interference impact and the VR's susceptibility to interference. For similar output

power and antenna gains of the VR and IR, the SINR at the input of the receiver has been estimated as follows:

$$SINR = \frac{P_{RT}}{P_{RI}} = \frac{\sigma R_I^{\,2}}{4\pi R_T^{\,4}} \tag{4-6}$$

In the frequency domain, interference spreads across multiple frequency bins. Its impact and statistical features after each signal processing stage have been discussed next.

4.4 Statistical Characteristics of Interference

This section focuses on the study of statistical characteristics of interference and its comparison with that of white Gaussian noise at the decision-making point '*D*' in Figure 4.3.

Firstly, different types of FMCW interference (section 3.6) received by the VR have been characterised in terms of the correlation between interference pulses. This has been done by estimating the correlation coefficient $'\rho_{ab}'$, where *a* and *b* represent the interference pulse number. An example is shown in Figure 4.2 (a) where ρ_{12} represents the correlation between interference pulse with $a = 1$ and $b = 2$, and so on. Next, a comparison of the interference probability density function $\left(PDF_{\text{int}}\right)$ and a corresponding best fit Gaussian distribution $\left(PDF_{bf}\right)$ has been performed to identify waveform parameters with statistical characteristics similar to random noise and the critical parameters that show a deviation from it.

It has been assumed that the VR receives interference from a single interferer with $F_{cv} = F_{\text{cint}}$ and the duty cycles of both the VR and IR are 100%. This results in the maximum overlap between the two radars and corresponds to a worst-case interference scenario – where interference power will be maximum at the input of the detector. The results will change with a change in the waveform parameters, discussed in section 4.4.4.

4.4.1 Types of Interference

Statistical characteristics depend upon the type of interference, previously classified as synchronous, semi-synchronous, and asynchronous. Asynchronous interference has been further divided into periodic, semi-periodic, and aperiodic interference. Examples of each type have been shown in Table 4.1, where $T_s = T_{sv}/T_{\text{sint}}$ and $BW_s = BW_v/BW_{INT}$. These parameters are used in this section to estimate the correlation coefficient between interference pulses.

Table 4.1. Interference parameters to analyse the correlation between interference pulses.

Interference Type	**Example Parameters**
Synchronous	$T_s = 1, BW_s = 1$
Semi-synchronous	$T_s = 1, BW_s = 0.99$
Periodic	$T_s = 2, BW_s = 1$
Semi-periodic	$T_s = 0.8, BW_s = 1$
Aperiodic	$T_s = 0.21, BW_s = 1$

For illustration purpose, the VR and IR signals chirp overlap plot has been shown in Figure 4.6 for $N_{CPI} = 10$, where N_{CPI} is the number of the VR chirps within a CPI.

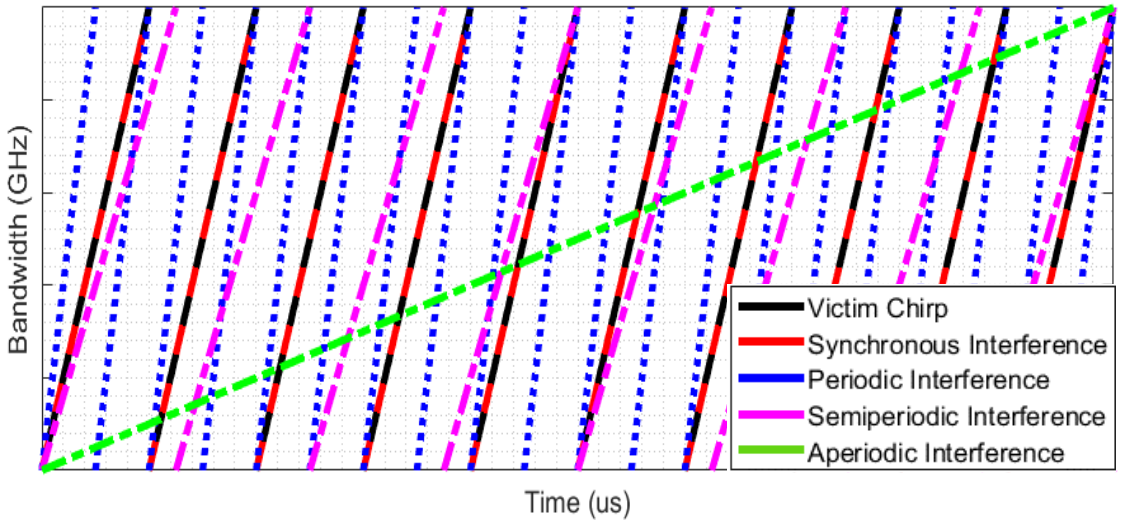


Figure 4.6: Chirp overlap plots of interference examples for the correlation analysis between interference pulses.

4.4.2 Interference Correlation

To estimate the correlation between interference pulses, a correlation coefficient matrix has been generated using the Pearson correlation coefficient [263]. The matrix shows the correlation between each interference pair within a CPI.

$$\text{Correlation Matrix} = \begin{bmatrix} \rho_{11} \cdots \rho_{1N} \\ \vdots \\ \rho_{M1} \cdots \rho_{MN} \end{bmatrix} \tag{4-7}$$

where, $-1 \le \rho_{MN} \le 1$ represent the correlation coefficient between interference pulses '*M*' and '*N,*' and its value depends on the interference parameters. An average Pearson correlation coefficient $\rho_{av} = \rho_s / N_{CPI}$ has then been estimated, where ρ_s is the sum of correlation coefficients across the interference pulses across the VR chirps during a CPI. The values of ρ_{av} for different types of interference with parameters in Table 4.1 are shown in Figure 4.7.

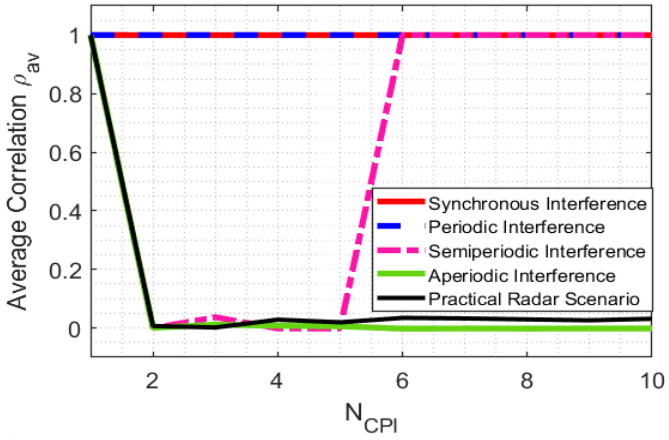


Figure 4.7: Average correlation 'ρ_{av}' for different types of interference.

The results show $\rho_{av} \sim 1$ for synchronous and periodic interference throughout the whole integration time (CPI) due to their periodicity across the VR chirps. A rapid decrease in correlation value has been observed for a semi-periodic interference at the start of the CPI, where the interference pulses are aperiodic. Later, as the interference sequence becomes periodic, the average correlation increases and stays closer to 1 during the remainder of the CPI.

In the semi-periodic interference example, the interference sequence becomes periodic after the 5 VR chirps. Therefore, semi-periodic interference is partially coherent. The average correlation value for aperiodic interference stays close to 0. In some instances, $\rho_{av} < 0$. This indicates a negative correlation between the interference pulses. The measured value of average correlation between interference pulses for an example of aperiodic interference with $T_s = 0.21$ is also shown in Figure 4.7 which validates an average correlation close to 0 for the aperiodic interference. As expected, the highest correlation has been observed due to the periodicity of interference pulses. In contrast, the absence of periodicity reduces ρ_{av} with a value close to 0, similar to that expected for random noise.

In a practical automotive scenario, due to the parameters such as radar's LO phase noise, its frequency stability, ADC starting time jitter, fly-back, idle time between chirps and frames [264], and transmit frequency offset [265], the phase between synchronous, periodic or semi-periodic interference pulses changes, which reduces the correlation value. Though periodicity between the VR and IR signals may be rare they cannot be entirely excluded. For example, several vehicles may surround the VR for a relatively long time, particularly in a motorway scenario. Therefore, such relatively low-probability events may occur and must be considered in simulation models.

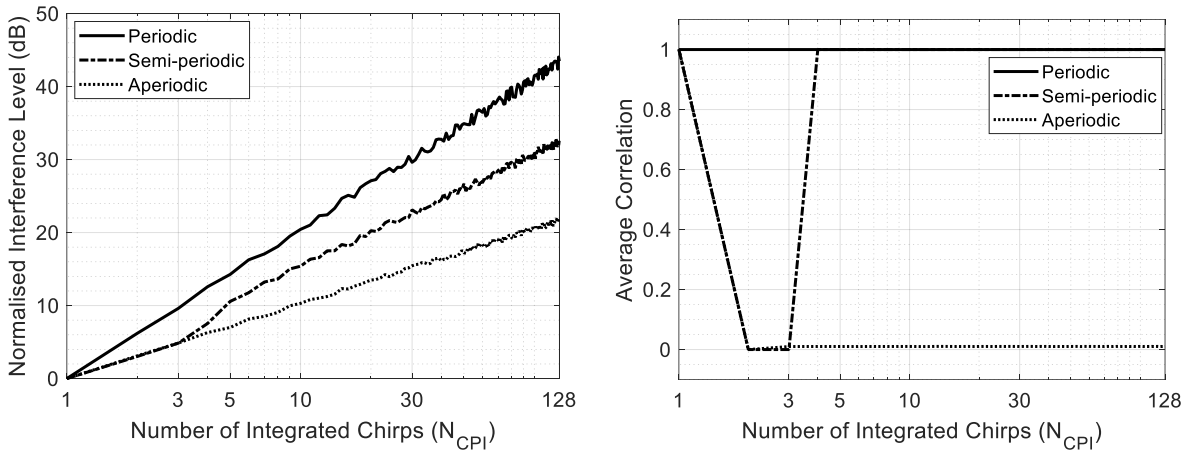
4.4.3 Interference Power Along Processing Stages

The multiple VR chirps are integrated over the CPI to improve the SINR. If the echo signal remains coherent across these chirps, its power increases by N_{CPI}^2 times. In contrast, the thermal noise power increases by N_{CPI} times as noise is uncorrelated across the chirps.

The impact of interference on radar detector depends on the SINR value during a CPI. This has been estimated using two metrics:

1. Interference correlation during CPI,
2. Interference power level after integration.

The modelled results are presented in Figure 4.8 with the waveform parameters in Table A4.1.



(a) (b)

Figure 4.8: Effect of integration on interference power: (a) normalised interference power level, (b) average correlation coefficient during the CPI.

In Figure 4.8 (a), the interference power level as a function of the number of integrated chirps, normalised to interference power at the first VR chirp, is shown for asynchronous interference.

- The highest power increase is observed for periodic interference, where interference pulses are correlated across the VR chirps during the CPI. The interference level increases by $20\log(N_{CPI})$ after integration.
- Aperiodic interference has uncorrelated pulses across the VR chirps within the CPI. Therefore, non-coherent gain is expected with the interference power level increasing by $10\log(N_{CPI})$.
- Semi-periodic interference is partially coherent. Interference power also increases by $10\log(N_{CPI})$ for aperiodic interference pulses (non-coherent gain at the start of CPI) and by $20\log(N_{CPI})$ where the interference sequence repeats periodically.

- Synchronous and semi-synchronous interference are similar to the periodic interference where interference pulses are correlated with the coherent integration gain $20\log\left(N_{CPI}\right)$.

Incoherent interference might affect the detection probability of low RCS targets (pedestrians, cyclists) over a significant proportion of the range and Doppler bins. On the other hand, coherent interference being concentrated across the limited range and Doppler bins (Appendix 4), with a higher power, might even mask high RCS targets (such as vehicles). The signal to interference ratio (SIR) for the periodic and aperiodic interference examples is summarised in Table 4.2. *A* represents signal power and σ_{int}^2 represents the interference power.

Table 4.2. SIR for periodic and aperiodic interference.

Description	**Periodic Interference**	**Aperiodic Interference**
Process	Deterministic	Random
Interference power after integration	$N_{CPI}^2\sigma_{\text{int}}^2$	$N_{CPI}\sigma_{\text{int}}^2$
SIR	$\frac{A^2}{N_{CPI}^2\sigma_{\text{int}}^2}$	$\frac{A^2}{N_{CPI}\sigma_{\text{int}}^2}$
SIR gain (dB)	0	$10\log\left(N_{CPI}\right)$

In a dynamic scenario, the interference power level at the VR will vary depending upon the relative position of the VR and IR, the orientation of interfering radars, their aspect-dependent gains, and the waveform parameters of the radars. This has been discussed in Chapter 7, along with the interference power and the SINR evaluation across the VR processing stages.

4.4.4 Interference Statistical Distribution

Interference pulses are LFM sinusoidal waveforms (Figure 4.2), and independent of the VR echo signal. Therefore, after being sampled at the VR, interference appears as a random process [254] with the following two distributions:

1. Sinusoidal distribution due to high correlation and periodicity between interference pulses.
2. Gaussian distribution for uncorrelated interference pulses across the VR chirps.

The Gaussian distribution is the well-known distribution of AWGN. Therefore, its similarity to the interference distribution $\left(PDF_{\text{int}}\right)$ has been used as a metric to assess the PDF_{int}. For comparison, a normalised root mean square error (NRMSE) [266] has been determined between the PDF_{int} and a corresponding Gaussian best fit $\left(PDF_{bf}\right)$, estimated as follows:

$$NRMSE = \frac{\left|\sqrt{\frac{\sum_{n=1}^{N}\left(PDF_{\text{int}}(\text{n}) - PDF_{\text{bf}}(\text{n})\right)^2}{N}}\right|}{\frac{\sum_{n=1}^{N} PDF_{\text{int}}(n)}{N}} \tag{4-8}$$

where, N is the total number of samples over which the PDF_{int} has been estimated. To classify the PDF_{int} into Gaussian or sinusoidal distributions, a threshold of $NRMSE = 0.3$ (-5 dB) has been used, which is determined by averaging the NRMSE values of the following cases:

1. Cases with lower interference power (due to a lower number of the VR and IR signals overlap) but having a deviation from Gaussian.
2. Cases with a higher NRMSE value and a power greater than $10\log\left(N_{CPI}\right)$ after integration. The cases with high interference power (due to a specific relationship between the VR and IR parameters [230]) but with a distribution matching well with a Gaussian have not been considered.

Based on the NRMSE threshold, two cases have been defined:

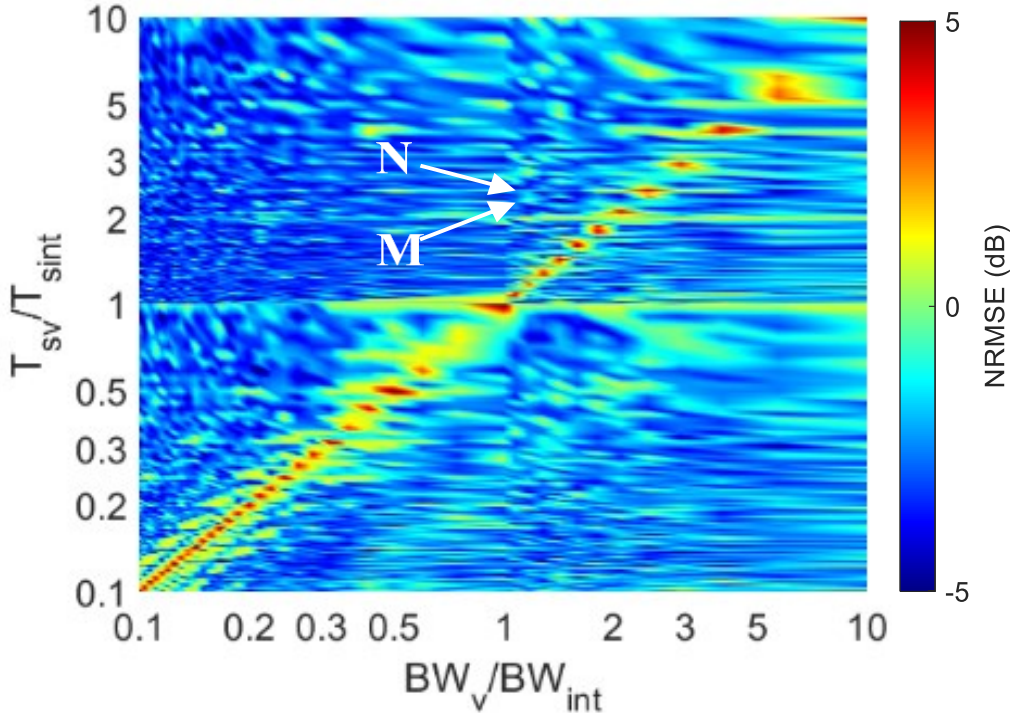
1. Non-critical cases: The PDF_{int} of these cases with $NRMSE \leq 0.3$ (- 5 dB) have a reasonable Gaussian approximation $\left(PDF_{bf}\right)$.

2. Critical cases: PDF_{int} with NRMSE > 0.3 shows a deviation from Gaussian approximation $\left(PDF_{bf}\right)$. For these cases, PDF_{int} may or may not be approximated by a sinusoidal distribution which has been discussed in the subsequence paragraphs.

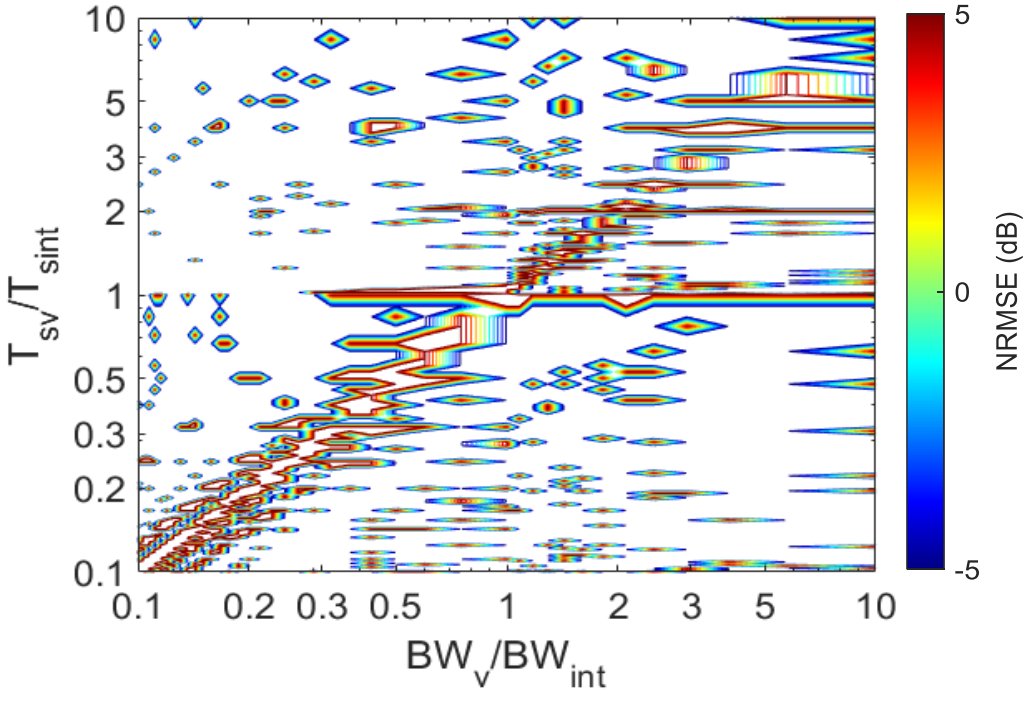
The NRMSE heatmap plot as a function of BW_s and T_s for $F_{\text{cint}} = F_{cv}$, T_{sv} = 100 µs, and BW_v = 0.3 GHz has been shown in Figure 4.9 (a), with a CPI = 1 ms. Interference parameters have been varied to generate the NRMSE heatmap. For better visualization, the NRMSE contour map for the critical region (NRMSE > 0.3) has been presented in Figure 4.9 (b). The results are plotted in the logarithmic scale.

The critical cases in Figure 4.9 (b) with NRMSE > -5 dB primarily arise for the reasons stated below. Their example cases are discussed later in this section.

1. Synchronous interference: Highest NRMSE value, which appears along the diagonal of Figure 4.9. A sinusoidal PDF can approximate this interference distribution due to its deterministic and periodic behaviour across the VR chirps.
2. Semi-synchronous interference: NRMSE in the critical region and a sinusoidal-like distribution (the diagonal region in Figure 4.9) as the interference is within the VR receiver bandwidth for its entire sweep time and appears across all the VR chirps during the CPI.
3. Periodic/ semi-periodic interference: Periodicity between interference pulses causes a deviation from a random process, resulting in a high NRMSE value. When $BW_s > 1$, due to the increased spectral width of the interference, the PDF_{int} can be approximated by a sinusoidal distribution. In contrast, when $BW_s \leq 1$, the PDF_{int} falls between sinusoidal and Gaussian distributions. However, the NRMSE value for both cases is greater than the threshold.



(a)



(b)

Figure 4.9: NRMSE as a function of $BW_s = BW_v/BW_{\text{int}}$ and $T_s = T_{sv}/T_{\text{sint}}$: (a) NRMSE heatmap, (b) NRMSE contour plot of the critical cases. BW_V and BW_{int} represents the bandwidth of VR and IR, respectively and T_{sv} and T_{sint} represents the sweep time of VR and IR, respectively.

4. Reduced overlaps between victim and interference signals during the CPI: When only 30% or fewer VR chirps within the CPI have an interference pulse appearance, the conditions of CLT have been violated. Interference integration does not approximate to a random process. This results in a high NRMSE value (> -5 dB).
5. $T_s \gg 1$ and $BW_s \gg 1$: Small BW_{int} and T_{sint} results in the following:
   - Less than 30% of the VR and IR chirps overlap during a CPI, and
   - Interference appearance at a similar instantaneous frequency across each VR chirp.

   Therefore, regions with high NRMSE have been observed.

For the latter 2 cases, the PDF_{int} falls between sinusoidal and Gaussian distributions, as discussed later.

For all the other waveform parameters, the NRMSE's value is in the non-critical region (NRMSE < -5 dB). Therefore, a close match between interference and AWGN statistics is expected at the detector's input. For this interference, the pre-existing radar detection characteristics for target detection hold valid.

4.4.5 Interference Mean and Standard Deviation

Along with interference distribution, its mean (μ_{int}) and standard deviation (σ_{int}) are also essential to evaluate statistics.

As discussed, the majority of interference pulses at the output of the LPF are double-sided symmetric (with respect to the mid-point of each interference pulse) LFM waveforms (Figure 4.2 (c)). This results in $\mu_{\text{int}} \approx 0$.

The normalised standard deviation $\overline{\sigma_{\text{int}}} = \sigma_{\text{int}} / A_{\text{int}}$ has been evaluated at the input of the detector and compared with that of thermal noise. $\overline{\sigma_{\text{int}}}$ as a function of T_s for $BW_s = 1$ and $F_{\text{cint}} = F_{cv}$ = 78 GHz is given in Figure 4.10. For most cases, $\overline{\sigma_{\text{int}}} \approx 1$, showing a similarity

between interference and AWGN standard deviations. However, certain cases labelled as: A (semi-periodic interference), B (synchronous interference), and C (periodic interference) show a deviation from $\overline{\sigma_{\text{int}}}$ = 1. For these cases, their distributions are in the critical region, with maximum value for synchronous interference.

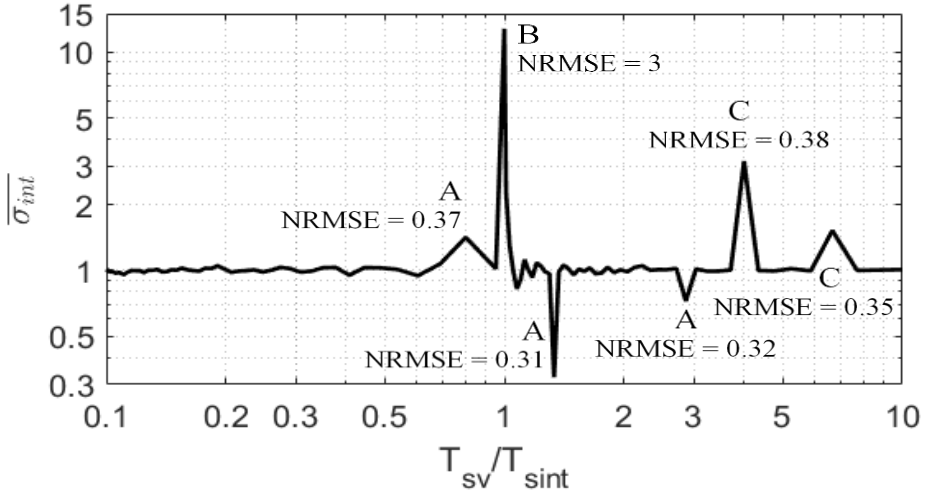


Figure 4.10: Normalised standard deviation $\left(\overline{\sigma_{\text{int}}}\right)$ as a function of T_{sv}/T_{sint} , BW_s=1.

The example cases with their parameters and NRMSE values have been stated in Table 4.3.

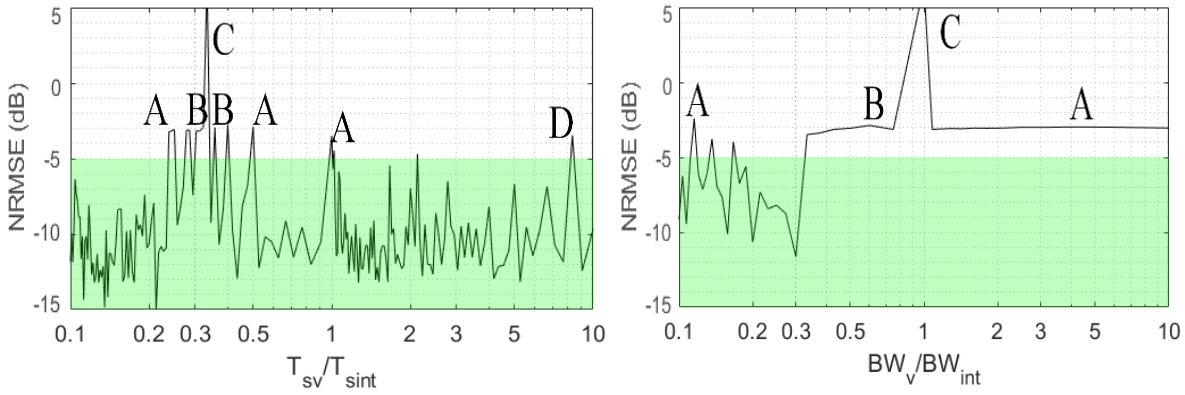
Table 4.3. Types of interference demonstrating a deviation from $\overline{\sigma_{\text{int}}}$ = 1.

Cases	Type of Interference	T_s	NRMSE
A	Semi periodic Interference	$T_s = 0.8$	0.37
		$T_s = 1.33$	0.31
		$T_s = 2.86$	0.32
B	Synchronous Interference	$T_s = 1$	3
C	Periodic Interference	$T_s = 6.67$	0.33
		$T_s = 4$	0.5

4.4.6 Case Studies

For the analysis of interference distributions, T_s and BW_s cuts have been obtained from Figure 4.9 (a), and shown in Figure 4.11. The NRMSE as a function of T_s for $BW_s = 0.33$ has

been presented in Figure 4.11 (a) whereas the NRMSE as a function of BW_s for $T_s = 1$, which is a typical example of periodic interference, has been presented in Figure 4.11 (b). The green highlighted region shows non-critical cases.



(a) (b)

Figure 4.11: NRMSE maps for the defined use cases: (a) NRMSE as a function of $T_s = T_{sv}/T_{\text{sint}}$ *and* $BW_s = 0.33$, *(b) NRMSE as a function of* $BW_s = BW_v/BW_{\text{int}}$ *and* $T_s = 1$.

The description of points A-D and conditions where deviation from Gaussian distribution is significant have been given in Table 4.4.

Table 4.4. Conditions for interference deviation from Gaussian behaviour for defined cases.

Label	Description	Figure 4.11 (a) $BW_s = 0.33$		Figure 4.11 (b) $T_s = 1$	
		Example case	$\overline{\sigma_{\text{int}}}$	Example case	$\overline{\sigma_{\text{int}}}$
A	Periodic interference	$T_s = 1$	< 1	$BW_s = 2$	≈ 1
B	Lesser interference and victim chirp overlaps – CLT conditions violated	$T_s = 0.4$	≈ 1		
C	Synchronous interference	$T_s = 0.33$	>1	$BW_s = 1$	> 1
D	Semi-periodic interference	$T_s = 8.33$	≈ 1		

Next, two example cases with parameters in Table 4.5 have been assessed, corresponding to a close case and poor case Gaussian approximation.

Table 4.5. Examples of the close case and poor case Gaussian approximations.

Case	Description	Parameters	NRMSE
1	Close Approximation (Aperiodic Interference)	$BW_s = 0.33$, $T_s = 0.73$	0.05
2	Poor Approximation (Periodic Interference)	$BW_s = 2$, $T_s = 1$	0.5

The PDF of the cases in Table 4.5, along with best fit Gaussian and sinusoidal distributions, have been shown in Figure 4.12. As expected, the distribution of the close case matches well with a Gaussian. However, the distribution for the poor case is closer to a sinusoidal distribution in this case.

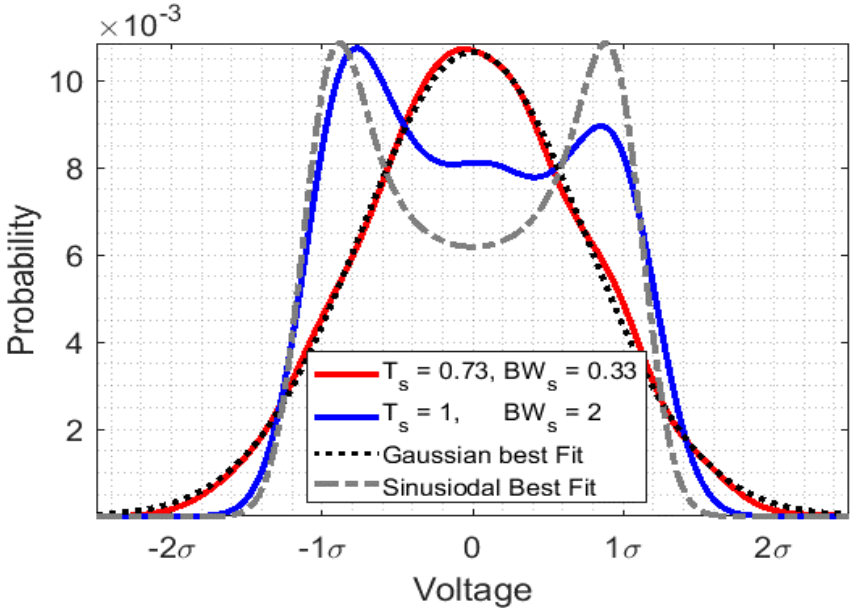


Figure 4.12: PDF of close $(BW_s = 0.33,\ T_s = 0.73)$ *and poor* $(BW_s = 2,\ T_s = 1)$ *approximation cases.*

The following observations have been made from the results in Figure 4.12:

1. Interference pulses are independent with a Gaussian distribution when they appear randomly in the victim chirps. Integration improves SIR and interference power increase by $N_{CPI}\sigma_{\text{int}}{}^2$.

2. Due to a high correlation and periodicity between interference pulses, a sinusoidal distribution has been observed and σ_{int}^2 increases in a similar manner to a deterministic process with $N_{CPI}^2\sigma_{\text{int}}^2$ power increase.
3. For specific waveform parameters such as semi-periodic interference, the distribution falls between sinusoidal and Gaussian distributions. Interference pulses are independent for the few VR chirps; however, the interference sequence becomes deterministic for the remaining chirps. The interference power is between $N_{CPI}\sigma_{\text{int}}^2$ and $N_{CPI}^2\sigma_{\text{int}}^2$.

In the background of interference from multiple sources, there is a low correlation between interference signals. Therefore, a low NRMSE value with a close to Gaussian distribution is observed at the input of the detector. The effect of the CPI on interference normalisation at the input of the VR detector has been analysed in the subsequent section.

4.4.7 Effect of Coherent Processing Interval

Signal normalisation at the input of the detector is more pronounced for a longer CPI as it reduces the periodicity between interference pulses. NRMSE values as a function of $T_{\text{sint}}/T_{\text{sv}}$ for $BW_s = 1$ with a CPI = 1 ms and 10 ms have been shown in Figure 4.13.

As the CPI increases, a lower NRMSE value has been observed. For both CPIs, the highest NRMSE occurs when $T_{\text{sint}}/T_{\text{sv}}$ = 1 (synchronous interference). NRMSE, for this case, does not significantly change with a change in the CPI as interference remains synchronised with the VR chirps throughout the CPI. When the value of $T_{\text{sint}}/T_{\text{sv}}$ is close to 1, there are fewer overlaps between the VR and IR waveform chirps. These regions are marked as ‘A’ in Figure 4.13. For these cases, a Gaussian approximation is more pronounced with a longer CPI as the number of interference pulses to be averaged increases, and the CLT conditions are well-met.

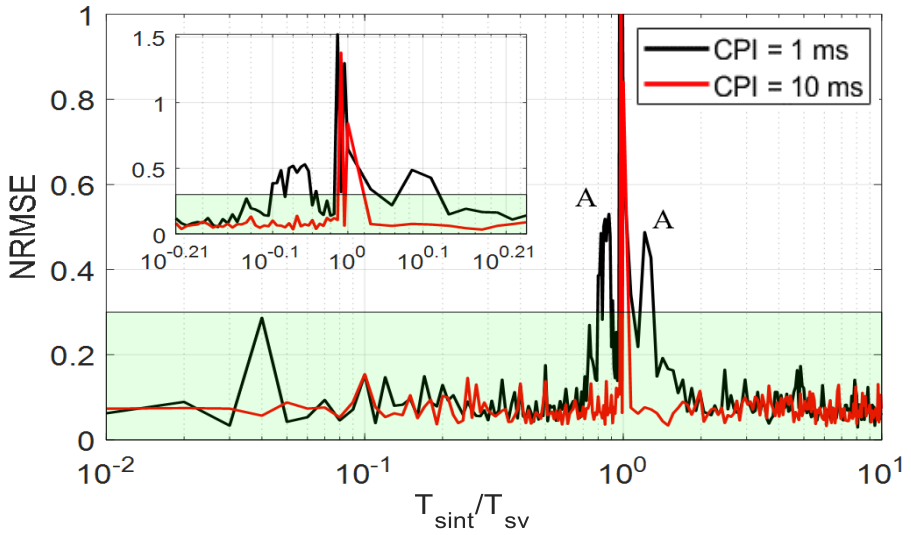


Figure 4.13: NRMSE value for difference coherent processing intervals. Insert shows the zoomed region for higher NRMSE values.

An example case to illustrate the effect of CPI of interference normalisation has been shown in Figure 4.14 for T_s = 1.23 and BW_s = 10. Blue histograms represent the Gaussian best fit for each case, and the interference distribution is shown in red.

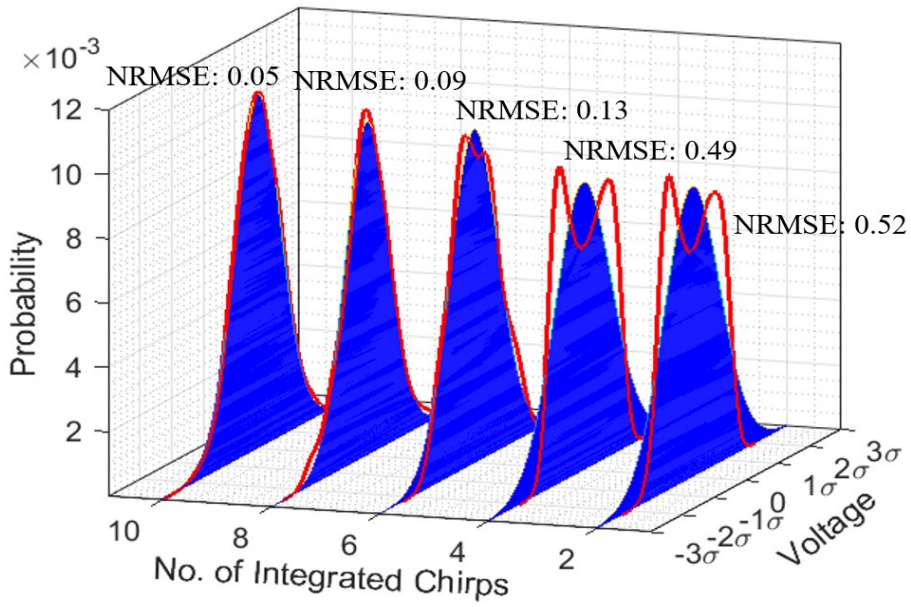


Figure 4.14: Effect of the CPI on interference distribution.

As the number of integrated VR chirps increases, the NRMSE value reduces, and after integrating 6 VR chirps in the considered example, a NRMSE < 0.3 has been achieved.

4.5 Detection in an Interference Background

Lastly, the detector's performance has been analysed for the identified cases by estimating the probability of detection (P_d) and illustrated using the ROC curves for the identified cases. These curves are typically based on the assumption of an underlying Gaussian PDF for the background thermal noise. Any deviation from AWGN detection curves indicates a requirement for non-linear matched filtering and an appropriate detection technique [267].

The signal detection process in a background of interference has been modelled as a hypothesis testing problem, given as:

$$S(t) = \begin{cases} S_{int}(t) & H_{\text{int}} \\ S_v(t) + S_{\text{int}}(t) & H_{s,\text{int}} \end{cases} \tag{4-9}$$

where, $S(t)$ is the received signal, $S_v(t)$ and $S_{\text{int}}(t)$ are the received echo and interference, respectively. The hypothesis H_{int} represents the case when the received signal has only interference, and $H_{s,\text{int}}$ represents the case when the received signal has an echo signal plus interference. The interference power P_{int} at the detector input has been used to estimate the detection threshold V_T [268]. A probability of false alarm (P_{FA}) 10^{-4} has been used.

$$V_T = \sqrt{-P_{\text{int}} \log(P_{FA})} \tag{4-10}$$

Using the estimated V_T, P_d has been estimated in the background of interference. The results are then compared with a theoretical P_d for a non-fluctuating target in the background Gaussian noise, computed using [25]:

$$P_d = \frac{1}{2} erfc\left(erfc^{-1}\left(2P_{FA} - \sqrt{SIR}\right)\right) \tag{4-11}$$

As discussed earlier, a slight change in interference parameters results in entirely different statistics and, consequently, different effects on the detector performance. To assess this,

detection curves for two points, M (periodic interference, $T_s = 2, BW_s = 1$) and N (aperiodic interference, $T_s = 2.2, BW_s = 1$) identified from Figure 4.9 (a), have been shown in Figure 4.15. SIR has been determined at the input of the detector. For periodic interference, the SIR required to achieve the same P_d as the aperiodic interference is $\sim 10\log(N_{CPI})$ times greater.

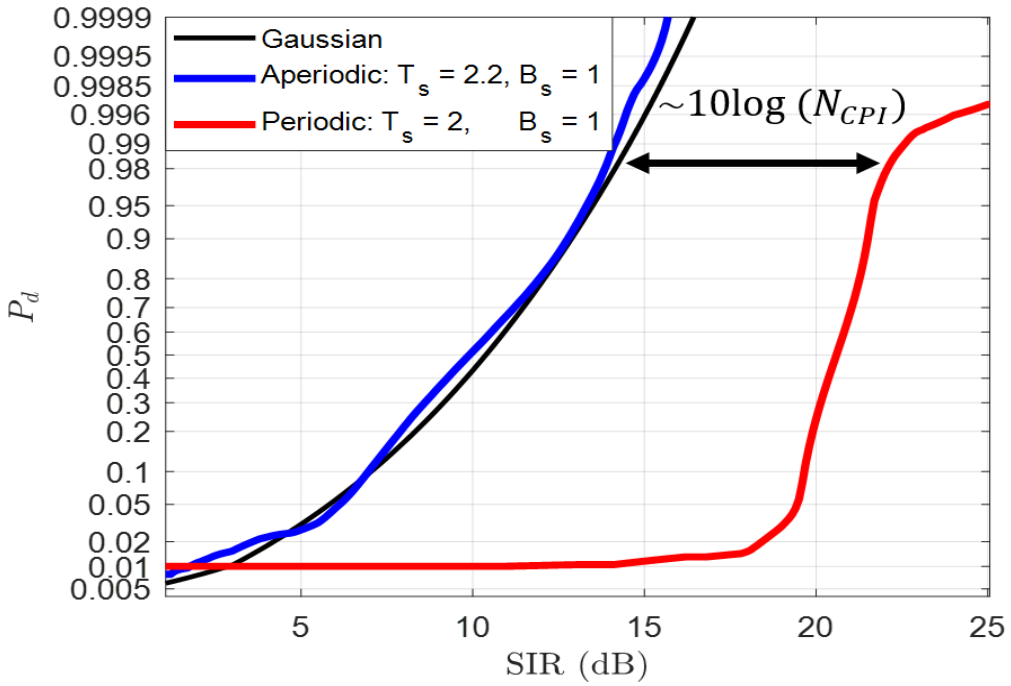


Figure 4.15: Probability of detection (P_d) *vs. SIR for periodic* $(T_s = 2, BW_s = 1)$ *and aperiodic interference* $(T_s = 2.2, BW_s = 1)$.

The detection curve of AWGN has a close correspondence to the aperiodic interference curve. However, it deviates significantly from the periodic interference curve. For better visualisation and comparison between the detection curves for various types of interference, the detection curves of periodic interference cases appearing after Figure 4.15 have been scaled by $10\log(N_{CPI})$.

ROC curves for the cases in Table 4.5, close case $(T_s = 0.73, BW_s = 0.33)$, and poor case $(T_s = 1, BW_s = 2)$ Gaussian approximations have been given in Figure 4.16, along with the ROC

curve for AWGN. The detection process has been based on Monte Carlo analysis with 10^6 trials, after which the results converge with a statistical accuracy of 10%[15].

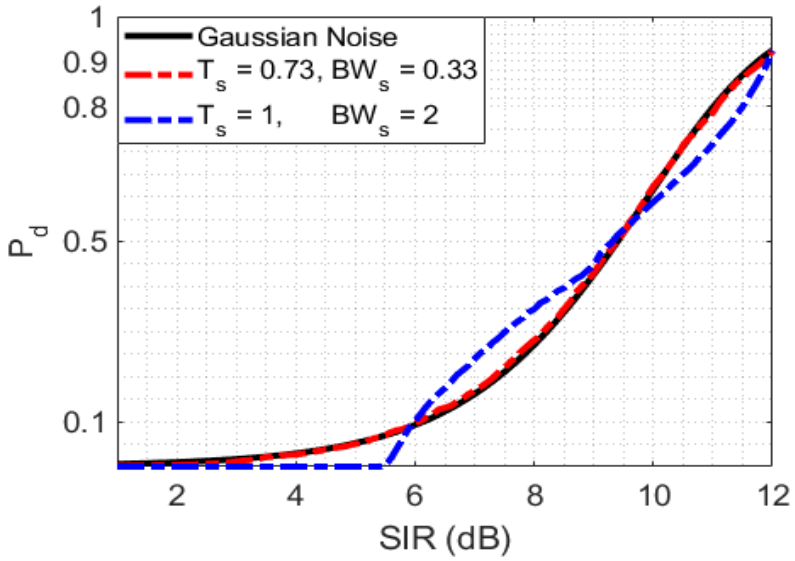


Figure 4.16: Detection curves for close $(T_s = 0.73, BW_s = 0.33)$ *and poor* $(T_s = 1, BW_s = 2)$ *Gaussian case approximations.*

The detection curves for a close case Gaussian approximation coincide well with the AWGN curve but indicate poor performance in the sinusoidal distribution case.

The distributions of two examples from Figure 4.16 have been analysed at 7 dB SIR and are shown in Figure 4.17 with the best-fit Rayleigh and Rician distributions for comparison. For a close approximation case in Figure 4.17 (a), under the hypothesis H_{int}, interference amplitude $R_s = \sqrt{\left|y(j)^2\right|}$ follows a Rayleigh distribution [269], where $y(j)$ represents interference samples at the decision-making point. Whereas, under the hypothesis $H_{s,\text{int}}$, R_s follows a Rician distribution and $y(j)$ represents samples of the echo signal plus interference at the decision-making point.

[15] For a 10^{-4} probability of false alarm (1 false alarm in 10^4 measurements), at least two order more measurements (10^6) are required for reliable results. Therefore, 100 independent measurements will give $\frac{1}{\sqrt{100}} = 10\%$ statistical accuracy.

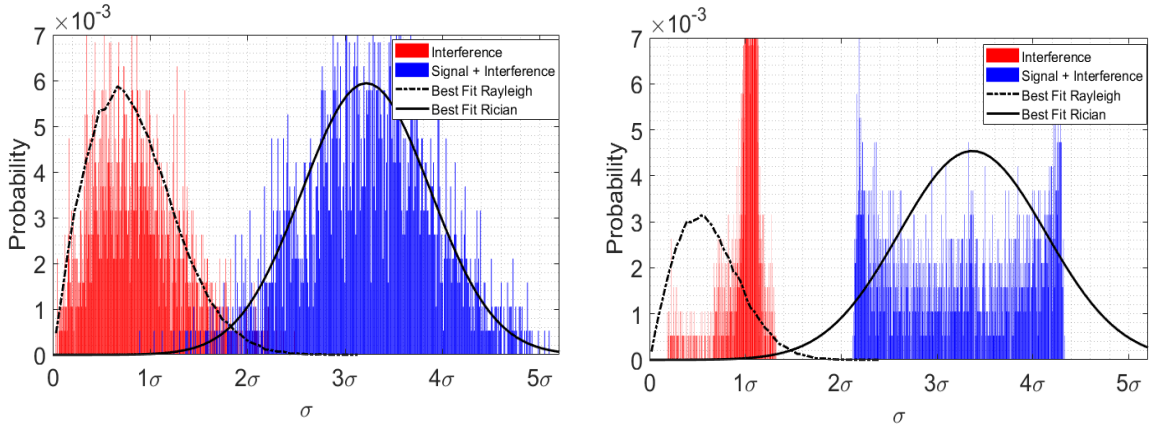


Figure 4.17: Interference amplitude distributions at the radar detector under hypothesis H_{int} *(red) and* $H_{s,\text{int}}$ *(blue). (a) Close case approximation* $\left(T_s = 0.73,\ BW_s = 0.33\right)$*, (b) Poor case approximation* $\left(T_s = 1,\ BW_s = 2\right)$.

A deviation from the Rayleigh and Rician distribution has been observed for the poor approximation case, shown in Figure 4.17 (b). The experimental validation of the discussed examples has been presented in Appendix 7.

4.6 Summary

The statistical characteristics and radar detection performance in the background of various types of interference have been analysed in this chapter. This has been done by estimating interference power, the correlation between interference pulses, and the statistical distribution of interference at the detector's input. NRMSE heatmaps have been developed to facilitate the analysis of a wide range of VR and IR waveform parameters. For the majority of the waveform parameters, it is identified that:

- There is a low correlation between the interference pulses received at the VR, and
- Interference follows the statistical characteristics similar to AWGN at the output of the coherent integrator. Therefore, an increased interference floor according to $10\log\left(N_{CPI}\right)$ is expected. For these cases, the well-established detection techniques for AWGN hold valid for target detection in the background of interference.

Nevertheless, for some waveform parameters, a high correlation has been observed between interference pulses. The interference statistical distribution essentially deviates from AWGN statistics for these cases, with distribution closer to sinusoidal, consequently, a degradation in detector performance occurs. Therefore, non-linear matched filtering along with the appropriate detection techniques might be required. For these cases, interference power increases between $10\log(N_{CPI})$ with a maximum value of $20\log(N_{CPI})$ at the output of the integrator.

The statistical characteristics of various types of interference have been summarised in Table 4.6.

Table 4.6. Statistical characteristics of various radar interference.

Interference	**Condition**		**Correlation**	**Distribution**	**Interference Power**
Synchronous	$T_{\text{sint}} = T_{sv}, B_{\text{sint}} = B_{sv}$		~1	Sinusoidal-like	$N_{CPI}^2\sigma_{\text{int}}^2$
Periodic	$mT_{\text{sint}} = T_{sv}$, m = 2,3, … $T_{\text{sint}} < T_{sv}$	$T_{\text{sint}} > 0.5T_{sv}$	~1	Between Gaussian and sinusoidal	$N_{CPI}^2\sigma_{\text{int}}^2$
		$T_{\text{sint}} \le 0.5T_{sv}$	~1	Gaussian-like	$N_{CPI}^2\sigma_{\text{int}}^2$
Semi-periodic	$mT_{\text{sint}} = nT_{sv}$ m = 2,3, …, n = 2,3, …	$T_{\text{sint}} > 0.5T_{sv}$	~0 to ~1	Sinusoidal if $T_{\text{sint}} \approx T_{sv}$	$N_{CPI}\sigma_{\text{int}}^2 < P_{INT} < N_{CPI}^2\sigma_{\text{int}}^2$
		$T_{\text{sint}} \gg 0.5T_{sv}$	~0	Gaussian-like	$N_{CPI}\sigma_{\text{int}}^2 < P_{INT} < N_{CPI}^2\sigma_{\text{int}}^2$
Aperiodic	$mT_{\text{sint}} \neq nT_{sv}$, For any integer m and n		~0	Gaussian-like	$N_{CPI}\sigma_{\text{int}}^2$

The interference statistics and its power along the processing stages are crucial for interference detection and mitigation. An optimal strategy for interference mitigation based on waveform randomisation using scalable waveform parameters has been discussed in the following chapter for the critical cases.

Chapter 5. MITIGATION OF RADAR INTERFERENCE

Automotive radars have been developed by various manufacturers with different waveform parameters and hardware configurations. Therefore, the interaction of their waveforms is always unique, as discussed in Chapter 3 and Chapter 4. For the interoperability of radars with reliable performance, especially in dynamic road conditions where the relative position of the radars changes rapidly, it is essential to devise interference detection and mitigation strategies that can be implemented in real time without a detrimental effect on the echo signal detection.

The most intuitive way to avoid interference is using a different frequency band for each radar. However, this is difficult to apply considering the wide bandwidth of radar signal and the limited spectrum availability (76 GHz – 81 GHz). Therefore, effective countermeasures must be introduced to minimise interference, especially in high traffic densities (e.g., large cities). Although the LPF limits the interference duration and hence its average power, the remaining interference power is often higher than the noise floor (section 4.4.3). Consequently, targets with low RCS, such as pedestrians or cyclists, are most vulnerable to mutual interference because even a slight increase in noise floor may affect their detection.

Interference mitigation is, however, a significant challenge for automotive manufacturers and Tier 1 suppliers. Several interference countermeasures have been proposed in the recent years (section 2.5.3). However, due to their limitations, there is still a requirement to develop a robust mitigation strategy that shows an acceptable performance in all driving scenarios. As a result, exploring interference mitigation in each domain is essential. This will enable the

identification of a suitable domain/ radar configuration where interference can be efficiently detected and mitigated without any detrimental effect on the radar performance. Furthermore, this will enable the possibility of combining various mitigation techniques to achieve the desired performance.

Interference mitigation techniques have been broadly classified into pre-detection and post-detection. The former uses various methodologies at the radar transmitter, whereas the latter are implemented at the receiver side once interference has been detected. These techniques are summarised in Figure 5.1 and discussed in Chapter 5 - Chapter 8.

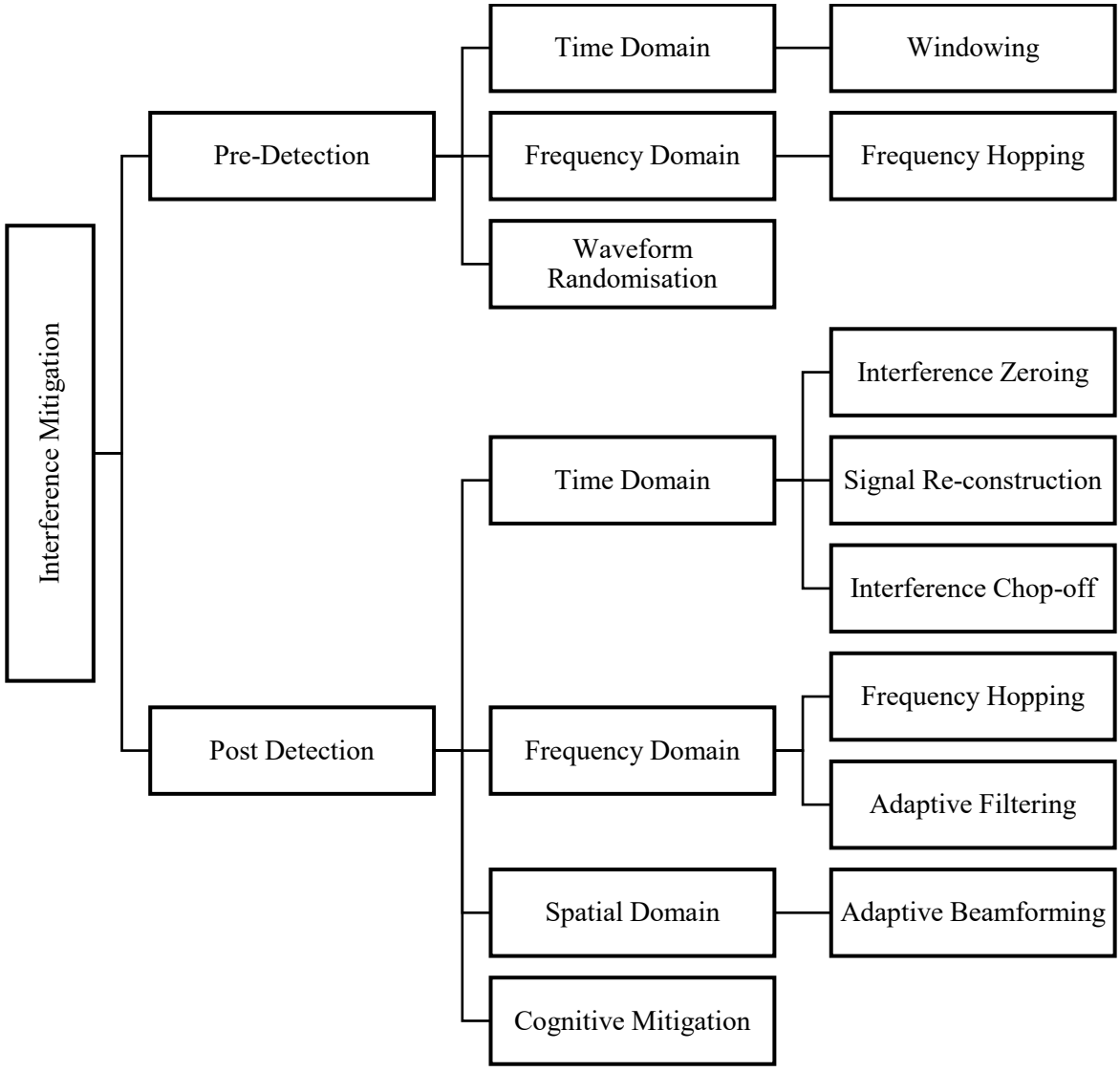


Figure 5.1: Pre-detection and post-detection interference mitigation techniques.

The main contributions of this chapter are as follows:

- Investigating pre-detection and post-detection mitigation strategies and their suitability for SoA automotive radars and different road scenarios.
- Methodology of detecting interference and extracting its waveform parameters.
- Analysing interference mitigation techniques in the time domain.
- Characterising the effect of windowing on the interference level.
- Implementing waveform randomisation using scalable waveform parameters to improve radar performance in an interference background.
- Developing a methodology to cognitively adapt the VR's waveform parameters to mitigate interference.

5.1 Interference Detection

Accurately detecting interference is a crucial step for its effective mitigation. Interference detection is often suited to the time domain, as interference appears as time-limited pulses within the VR chirp (section 3.3). Whereas after subsequent processing stages, interference spreads across multiple frequency bins, discussed in section 3.4. This makes its detection difficult, especially in the case of high SINR, where the interference floor is comparable to the thermal noise floor.

Three techniques based on time-domain interference detection have been proposed in this section.

5.1.1 Power Detection

When the echo signal power is comparable to or larger than the interference power in the time domain, interference detection becomes difficult with the traditional power detection methodology. This sub-section presents an interference detection methodology based on adaptive thresholding which is effective in detecting even low-power interference.

The received signal (after down-conversion and low pass filtering) has first been high pass filtered. The HPF removes strong reflections from the nearby clutter and also the echo signals at closer ranges, which might make threshold-based detection of weaker interference ambiguous. As interference is a wide-band LFM pulse, most interfered samples are retained after the HPF.

After the HPF, interference detection is carried out using an envelope detector across each VR chirp. The threshold Th_{INT} to estimate interfered samples has been estimated in three stages:

1. Firstly, a trailing moving mean filter [270], given as follows, has been applied to the received signal to estimate the received signal's envelope.

$$A(x) = \left| \frac{1}{N_s} \sum_{i=1}^{N_s} x(i) + x(i-1) + \ldots + x(i-N_s) \right| \tag{5-1}$$

   where, *x* represents the fast-time samples and N_s represents the number of trailing samples before each fast-time sample under consideration.

2. The mean amplitude has then been estimated as follows:

$$A = \frac{1}{N} \sum_{x=1}^{N} A(x) \tag{5-2}$$

   where, *N* is the total number of fast-time samples.

3. Lastly, the threshold to detect interference is estimated using the following:

$$Th_{INT} = \alpha A \tag{5-3}$$

   where, α is a scaling factor. When the amplitude of the received signal's envelope exceeds Th_{INT}, it indicates the presence of interference.

The interference detection results have been demonstrated in Figure 5.2 for the VR with T_{sv} = 204.8 µs, B_{sv} = 1 GHz, and IR with T_{sint} = 250 µs, and B_{sint} = 0.95 GHz. The HPF with a cut-off frequency of 488 kHz has been applied, equivalent to a 15 m cut-off range in this case.

This attenuates the echo signal power in the demonstrated results. The threshold value has been estimated for $\alpha = 1.2$ and $N_s = 150$ samples. Figure 5.2 (a) and (b) show the high pass filtered time domain reference signal (in the absence of interference) and the signal with interference, respectively. The estimated envelope and threshold for the two cases have been demonstrated in Figure 5.2 (c) and (d), respectively. The interfered samples are precisely detected using the proposed methodology.

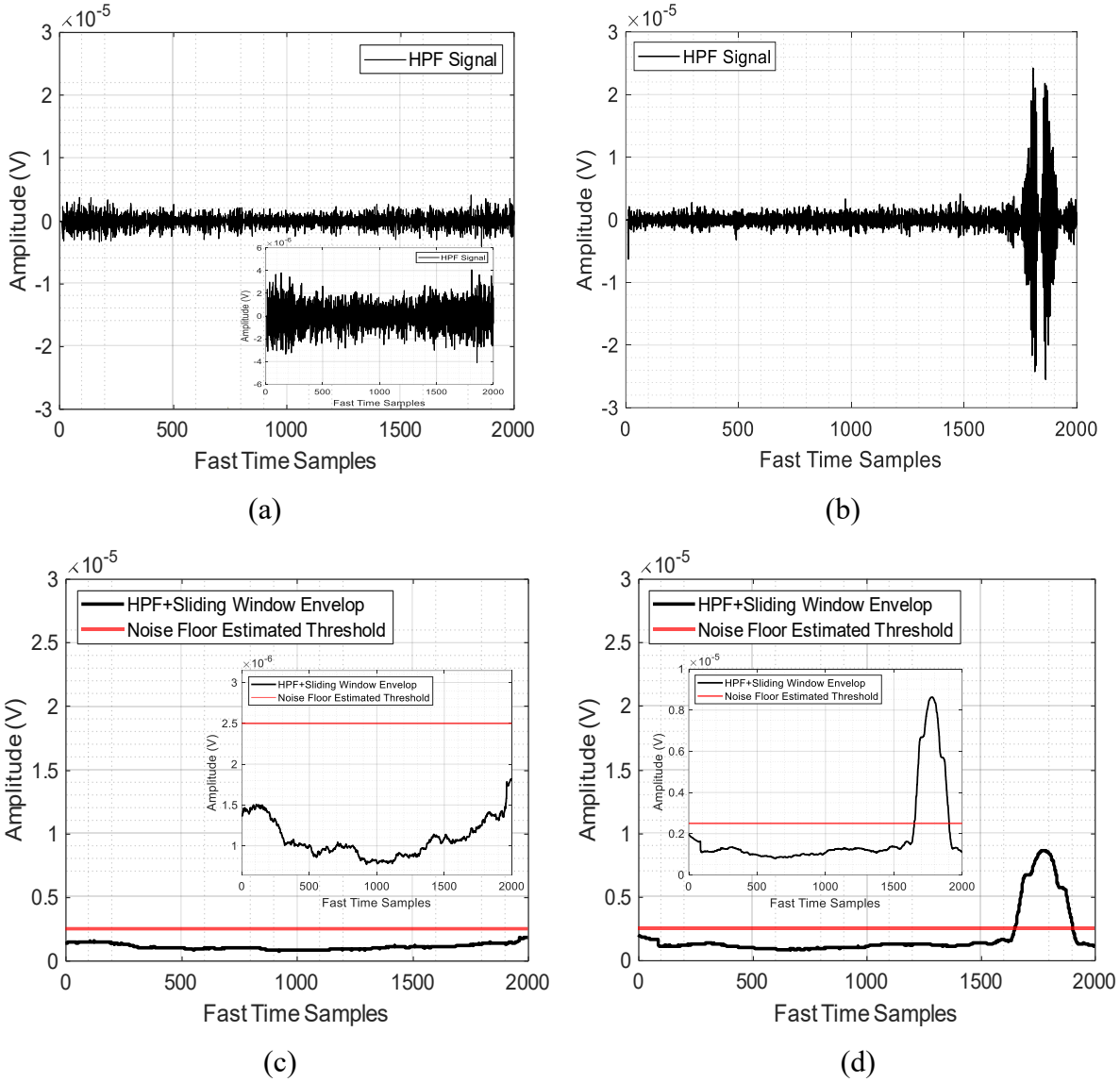


Figure 5.2: Interference detection: (a) reference, no interference in the time domain. (b) time-domain signal with interference, (c) envelope of the reference signal, (d) envelope of the signal with interference.

The proposed methodology is suitable as it removes strong echo returns before performing interference detection. Thereby making the detection of weaker interference pulses unambiguous. This methodology has been later used to detect interference for its parameter estimation, as discussed in section 5.2.

5.1.2 Radar in Listening Mode

In the second technique, a 'sense and avoid' approach has been proposed to detect and avoid interference. This methodology has been used in Chapter 6 to detect the presence of interference in the spatial domain.

The VR transmitters are switched off for a frame duration while receivers are kept active[16]. This turns the radar into a listening mode. In the absence of transmissions from the nearby radar sensors (interference signals), ADC data in the time domain shows only the thermal noise floor. However, any high-amplitude signal received at the VR corresponds to the presence of interference during this duration. Therefore, this period can conditionally be called the radar training period and is used to estimate the parameters/ temporal location of the received interfering signals. This has been illustrated in Figure 5.3.

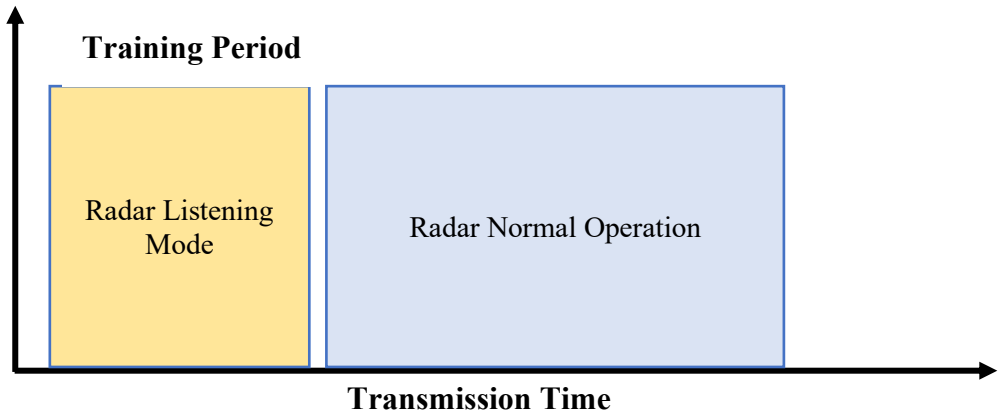


Figure 5.3: Interference detection using victim radar in the listening mode.

[16] As this is a homodyne process [271], the chirp signal is still generated in the transmitter section and used to down-convert the received signal even though the signal is not radiated.

This technique is additionally instrumental in adapting the VR parameters based on the estimated interference parameters during the radar training period.

5.1.3 Short Time Fourier Transform

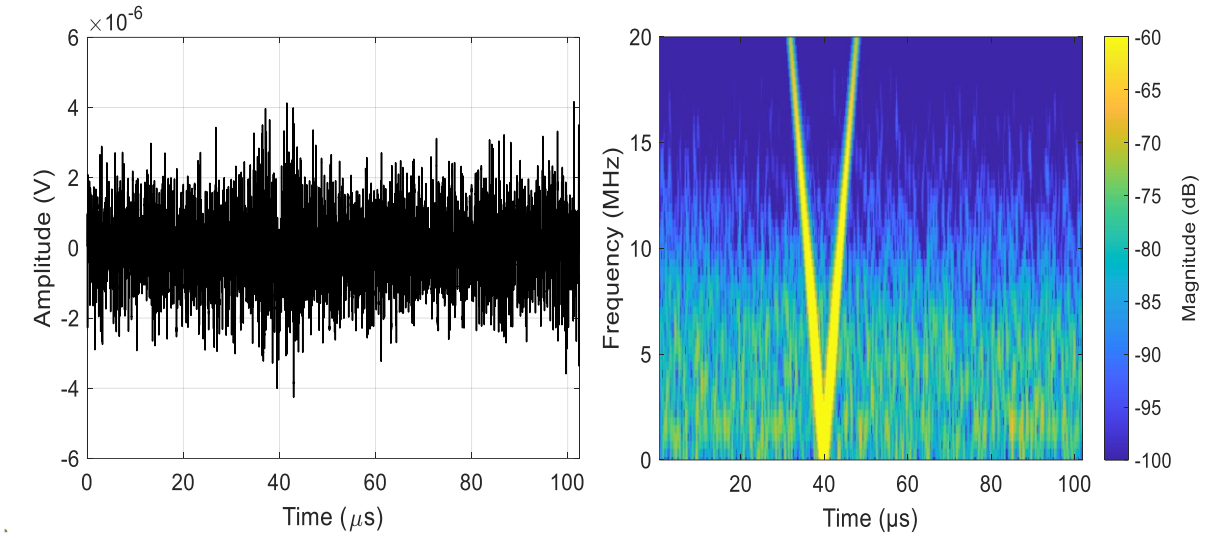
The spectrogram generated after applying a STFT is another effective technique to detect and estimate interference parameters [230]. In the time-frequency domain (TFD), a horizontal line along a specific frequency bin corresponds to the echo signal. In contrast, each interference pulse appears 'V-shaped' with oblique lines and spread along the frequency spectrum, as discussed in section 3.4.2.

Based on the STFT,

- The exact location of interference in time can be estimated, and
- Weak interference can be detected and separated from the thermal noise floor and the strong echo returns.

An example has been demonstrated in Figure 5.4. Figure 5.4 (a) shows the received signal at the VR with a weak interference pulse centred at 40 μs. The interference power is comparable to the thermal noise power at the VR receiver. Based on the traditional power detection method, interference cannot be accurately separated from the thermal noise floor or the echo signal. This would make interference detection ambiguous. However, using the characteristic of interference in the TFD, interference has been identified and separated from the noise, as shown in Figure 5.4 (b).

It is essential to detect the weak interference and adapt the VR accordingly because often this can be a case when the source of interference is located at a larger distance (hence lower power) and the VR can adapt well before the interferer will come close to it, resulting in stronger interference power.



(a) (b)

Figure 5.4: Interference detection using STFT: (a) weak interference pulse with power comparable to noise. (b) Short-time Fourier transform to separate interference from background noise.

5.2 Interference Parameter Estimation

In this section, a post-detection, 'sense and avoid' approach has been developed to estimate the waveform parameters of an unknown interferer based on its amplitude and spectral characteristics. The parameters have been estimated using the radar data from real-road measurements. Once the parameters are estimated, the VR transmitter can use them to cognitively adapt its waveform parameters, such as idle time, start frequency, bandwidth, or sweep time to avoid interference, as discussed in the subsequent section.

The proposed methodology is equally accurate for weak amplitude, fast-chirp (interference sweep time is less than the VR sweep time), or slow-chirp (interference sweep time is larger than the VR sweep time) interference sequences.

5.2.1 Methodology

The methodology to estimate interference parameters has been summarised in Figure 5.5.

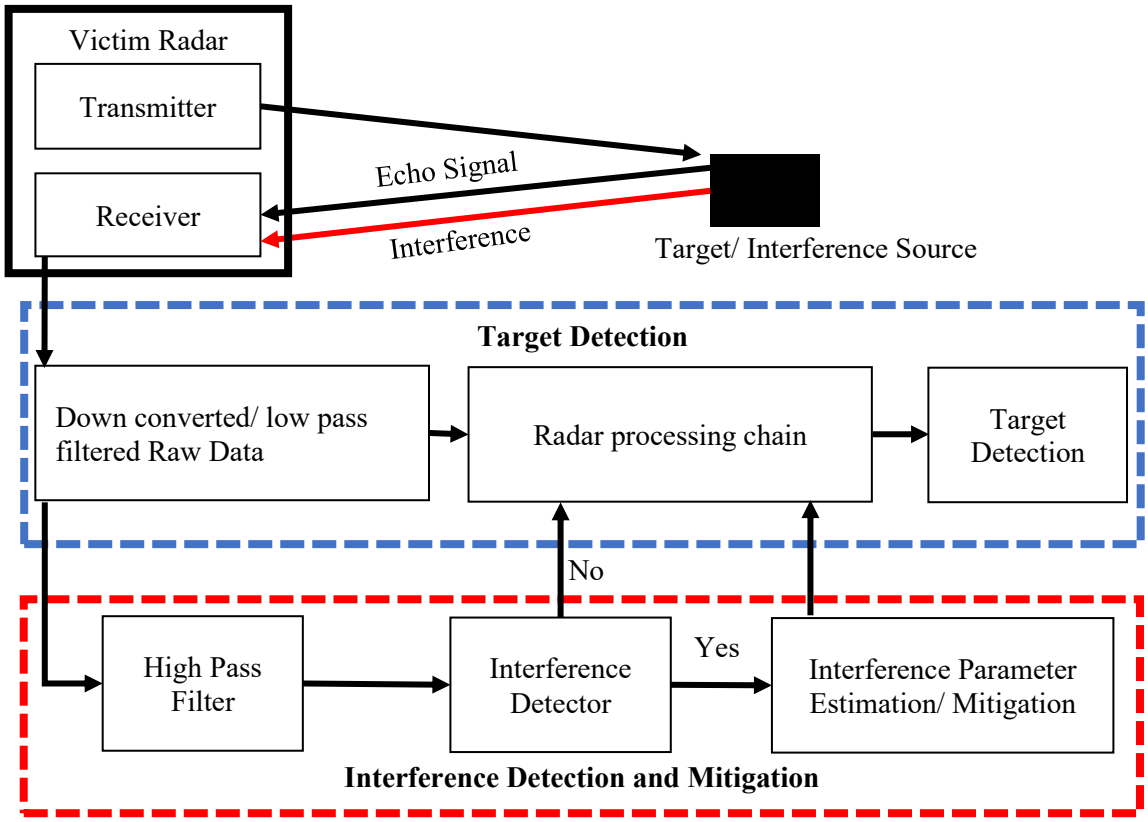


Figure 5.5: Block-level representation of interference detection methodology.

Various stages of interference parameter estimation have been described as follows:

1. The received signal is organised as the time series representation generated from the augmented range profiles of the VR chirps during the radar frame duration.
2. The amplitude and spectral characteristics of the interference are then assessed.
3. Based on this, interference is detected using the power detection method in section 5.1.1.

If interference is detected, its parameters are estimated next and used to adapt the waveform parameters of the VR to avoid or suppress the impact of interference. Otherwise, traditional signal processing is performed for target detection using the received down-converted raw data.

I. Measurement Setup

The example cases from real-time measured data have been presented in this sub-section. In the measurement, 'unknown interference of opportunity' sequences of fast and slow chirps from commercial automotive radars installed on one of the vehicles sharing the road with the

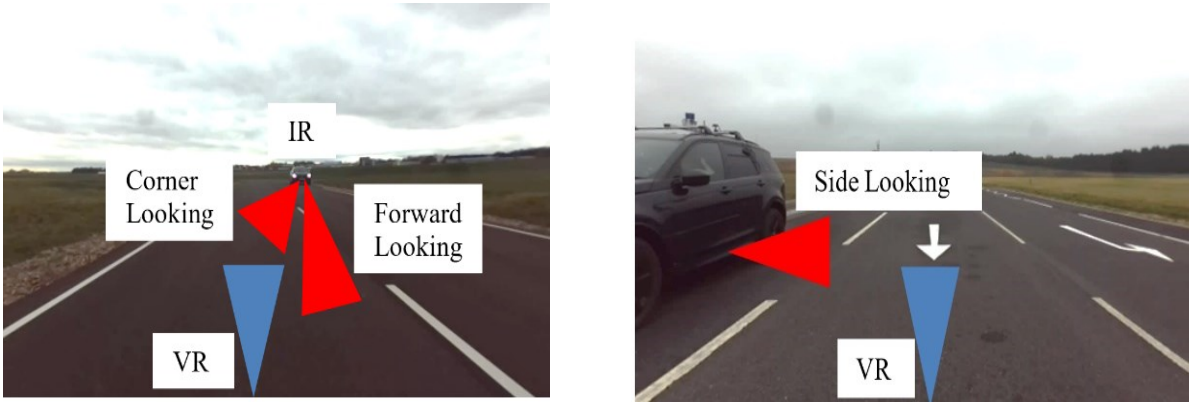
host vehicle (carrying the measurement sensor suite) have been detected and analysed. For convenience, based on the following,

- Scene assessment during measurements,
- Received interference amplitude, and
- Estimated interference parameters (as shown later),

the terms 'forward-looking,' 'corner-looking,' and 'side-looking' have been used for the interfering radars. The direction of interference estimation has been discussed in Chapter 6.

In the measurement sensor suite, the VR was a forward-looking INRAS Radarlog RDL-77G-TX4RX16-D02 with 4 transmit and 16 receive elements [91], operating in TDM - MIMO mode. F_{cv} = 76 GHz, B_{sv} = 1 GHz, T_{sv} = 204.8 µs, and PRI_{VR} = 230 µs. Each VR frame of 128 ms has been generated with 512 chirps, transmitted sequentially from 4 transmit elements of Radarlog.

The test setup has been shown in Figure 5.6 (a) for presumably forward-looking and corner-looking interference. This is a close representation of a scenario that can be expected in a real road scene.



(a) (b)

Figure 5.6: Test setup: (a) forward and corner-looking radars, (b) side-looking radar.

In this setup, the vehicle with the VR drove towards the interfering vehicle. In the discussed radar frame, the IR has been positioned at 14 m from the VR in the adjacent lane (3.6 m lane

width). The test scene for presumably side-looking interference has been shown in Figure 5.6 (b). The interfering vehicle in the adjacent lane of the static VR drove past it at 2.8 m/s. The detailed data collection methodology has been discussed in Appendix 11.

For forward-looking interference, two sets of parameters have been used, whereas one set has been used for side-looking interference, mentioned as follows:

1. Case 1: Fast chirp interference sequence – forward-looking and side-looking interference,
2. Case 2: Slow chirp interference sequence – forward-looking interference,
3. Case 3: Fast chirp interference sequence – side-looking interference.

In Case 1, interference from two different sources has been received at the discussed radar frame, shown later in this section, whereas interference from a single source has been received for Cases 2 and 3.

In the scenario of two vehicles facing each other, as shown in Figure 5.6 (a), the VR will receive interference from both forward and corner-looking radars. The corresponding radar frame has been shown in Figure 5.7. In contrast, in the test setup of Figure 5.6 (b), as the vehicles pass each other, interference is to be predominantly received from the side-looking radar due to the sensor orientations. The corresponding radar frame has been shown in Figure 5.8 (c).

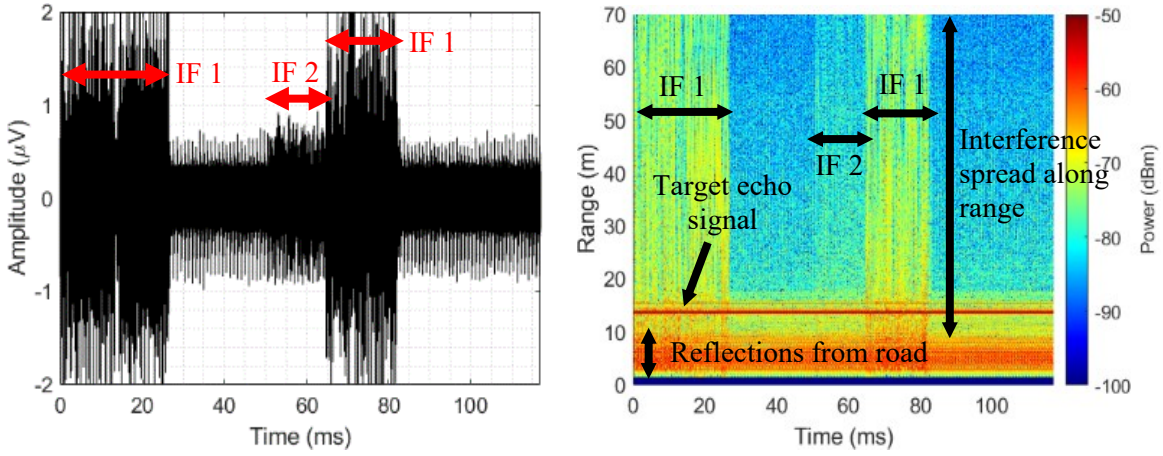
The presented work in this section has been focused on the methodology to estimate interference parameters using the context-based information. Firstly, amplitude characteristics of interference have been assessed, as discussed in the subsequence paragraphs.

II. Interference Amplitude Characteristics

Interference amplitude characteristics have been estimated in two representations, as discussed below.

- Time domain profile of received victim chirps for the duration 'T' corresponding to each VR frame of 128 ms in this case. This has been shown in Figure 5.7 (a), and
- Augmented range profiles, generated after an FFT across the fast-time, within the same time 'T' for a single receive element. This is shown in Figure 5.7 (b).

The results in Figure 5.7 are for the test scene in Figure 5.6 (a), where the VR will receive interference from both forward and corner-looking radars.



(a) (b)

Figure 5.7: Interference amplitude characteristics for fast chirp sequence in the test scene of Figure 5.6 (a) presented in: (a) time domain, (b) augmented range profiles. IF represents the interference frame.

Based on the amplitude characteristics, interference frames (IFs) corresponding to each source of interference have been identified. Because amplitude and, as shown later, waveform parameters of interference within frame duration 0 – 27 ms are similar to that from 64 – 83 ms, they are assumed to be coming from the same source of interference, 'IF1' in Figure 5.7. Based on the amplitude difference, 'IF2' is received from presumably corner-looking radar. The amplitude of 'IF2' is significantly lower than 'IF1' and also the echo signal. This might reduce the accuracy of interference detection, which later affects its parameter estimation. Therefore, a HPF with a cut-off frequency of 488 kHz, corresponding to a 15 m range, has been applied to suppress the strong echo return from the vehicle at 14 m. The corresponding filtered results

have been shown in Figure 5.8 (a) and (b) for interference Case 1, and Figure 5.8 (c) and (d) for interference Case 2 for the scene in Figure 5.6 (a). Figure 5.8 (e) and (f) show similar results for Case 3, corresponding to the scene in Figure 5.6 (b).

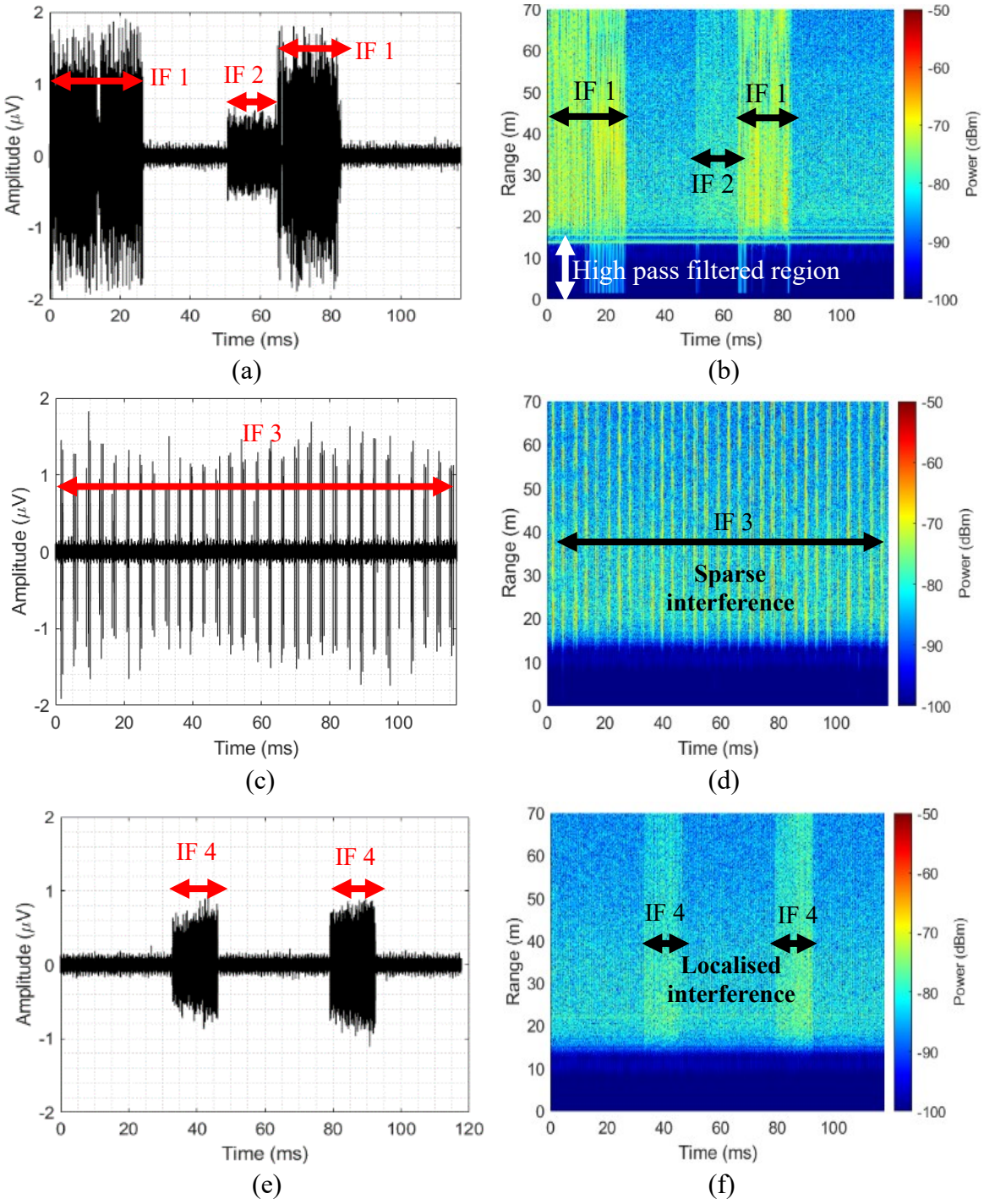


Figure 5.8: Amplitude characteristics of interference after HPF: (a) time domain – Case 1, (b) augmented range profiles – Case 1, (c) time domain – Case 2, (d) augmented range profiles – Case 2, (e) time domain – Case 3, (f) augmented range profiles – Case 3.

The time domain and augmented range profiles of the slow chirp interference sequence in Figure 5.8 (c) and (d) show a sparse interference appearance across the entire VR frame. For other cases (fast-chirp), interference is localised within a subset of chirps in the VR frame.

a) Interference Detector

After organising the received data as the time series representation, interference detection has been performed using an envelope detector across each victim chirp, as discussed in section 5.1.1. If interference is detected, the next step is to estimate its impact and the interfering signal's waveform parameters.

b) Number of Interfering Sources

From the envelope of interference, adaptive thresholding based on maximum and minimum interference amplitude has been used to categorise the interference pulses according to their amplitude. The amplitude difference is then used to identify the number of interfering sources in the FoV of the VR. This has been demonstrated in Figure 5.9 for the road scene in Figure 5.6 (a), case 1 (fast chirp interference sequence).

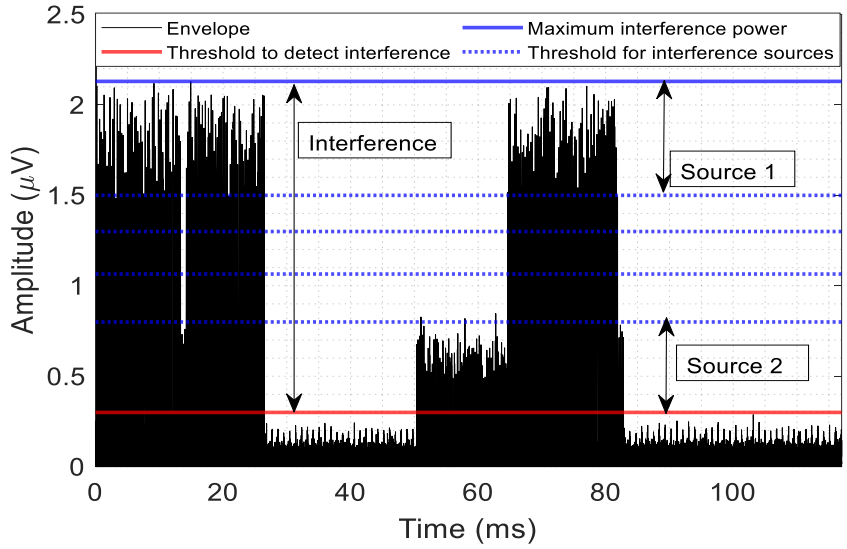


Figure 5.9: Amplitude-based estimation of the number of interference sources.

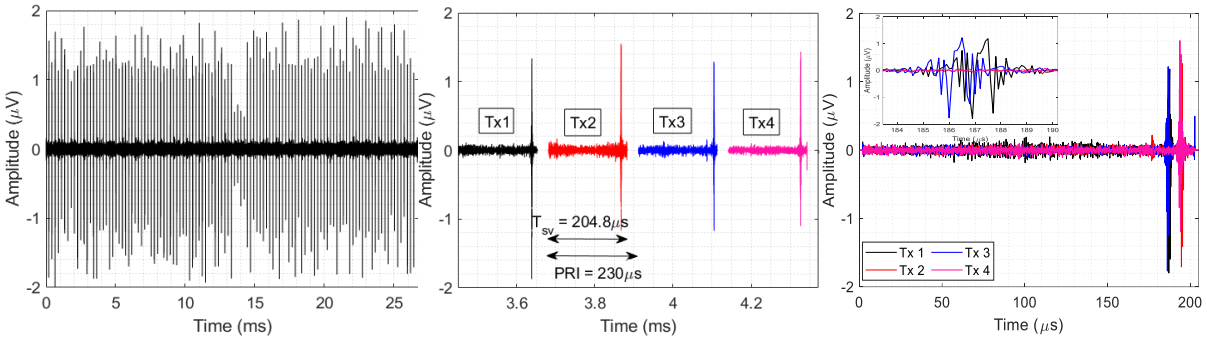
An assumption has been made here that the interference pulses from the same source will have comparable amplitude.

Due to a different propagation delay from different interfering sources and flexibility in the choice of waveform parameters of the radar signals [265], there is a high chance that signals from multiple sources of interference interfere with a different set of victim chirps, i.e., are separated in the time series. However, considering the receiver linearity, even if some victim chirps have interference pulses from multiple sources with an amplitude difference, the number of interference sources can be estimated.

III. Interference Parameters

After identifying the number of interference sources, the waveform parameters of interference including sweep time, bandwidth, start frequency, and PRI, have been estimated by analysing each identified IF separately.

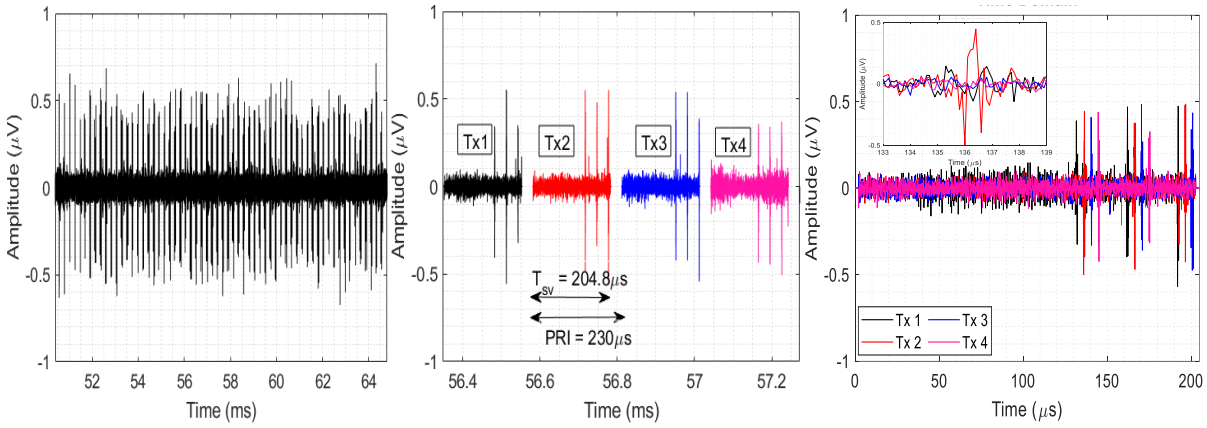
The extracted IFs from the VR frame for each case discussed above have been shown in Figure 5.10 (a) – Figure 5.13 (a). From each IF, the VR MIMO frame of 4 victim chirps corresponding to each transmit channel of the Radarlog has been extracted and shown in Figure 5.10 (b) – Figure 5.13 (b). A MIMO frame has been used to estimate parameters because it corresponds to 4 consecutive transmissions of the VR (TDM-MIMO mode). Therefore, it is a better representation of the time progression. Figure 5.10 (c) – Figure 5.13 (c) show each sweep time slot of Radarlog (204.8 µs) with overlapping received victim chirps corresponding to 4 transmit channels (Txs). All results have been shown for a single receive element of Radarlog.



(a) (b) (c)

Figure 5.10: Time domain representation of interference frame 'IF1.' (a) Extracted IF1, (b) subset of the VR MIMO sequence, (c) interference in the short time.

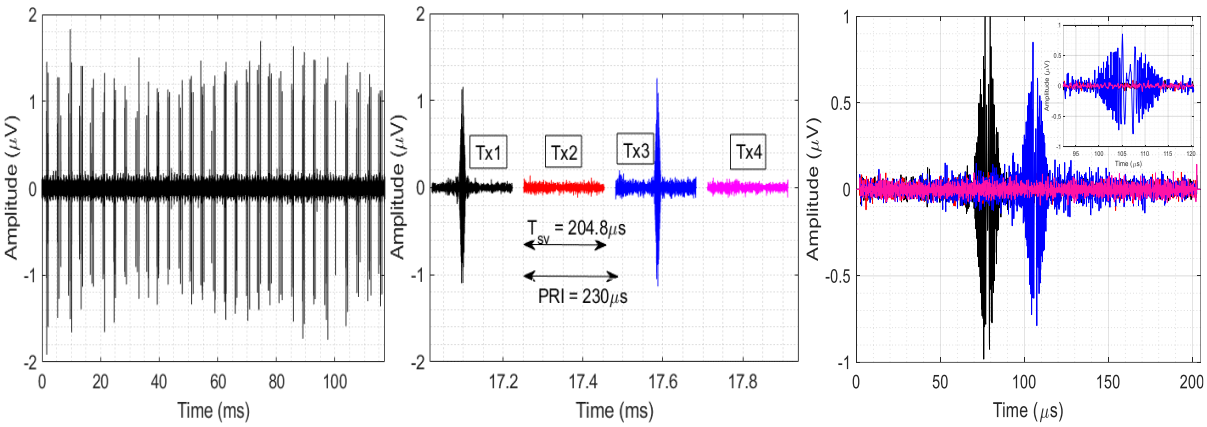
For IF1, as observed from Figure 5.10 (c), interference pulses in the received chirp corresponding to Tx1 and Tx3 overlap in time, and Tx2 and Tx4 overlap in time.



(a) (b) (c)

Figure 5.11: Time domain representation of interference frame 'IF2.' (a) Extracted IF 2, (b) subset of the VR MIMO sequence, (c) interference in the short time.

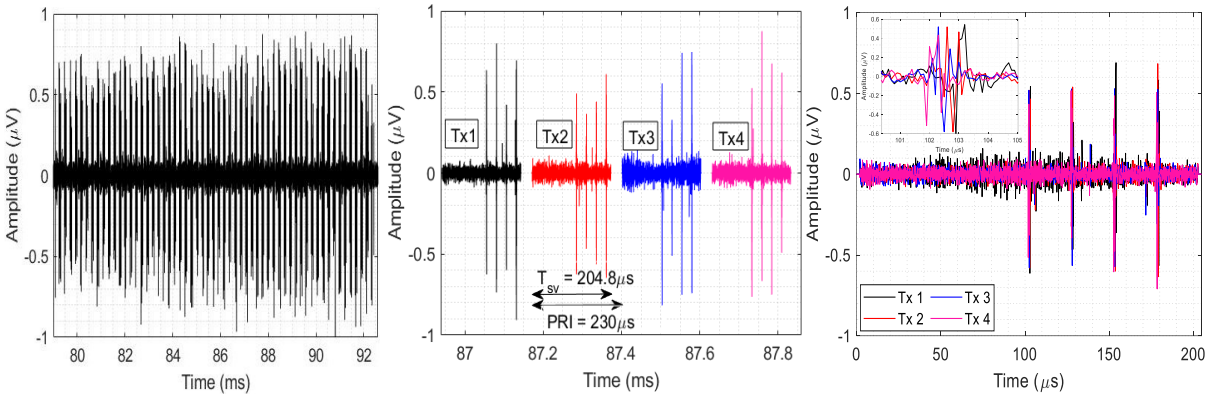
For IF2, all the interference pulses in the MIMO frame are separated in time, as observed in Figure 5.11 (b) and (c).



(a) (b) (c)

Figure 5.12: Time domain representation of interference frame 'IF3.' (a) Extracted IF 3, (b) subset of the VR MIMO sequence, (c) interference in the short time.

Due to interference being a slow chirp sequence, only two out of the four VR chirps in a MIMO frame are interfered with for IF3, as shown in Figure 5.12 (b) and (c).



(a) (b) (c)

Figure 5.13: Time domain representation of interference frame 'IF4.' (a) Extracted IF 4, (b) subset of the VR MIMO sequence, (c) interference in the short time.

The interference pulses for IF4 also overlap in time across the VR MIMO frame.

All the VR chirps in the extracted IF interfere in the fast chirp sequence. However, this is not true for a slow chirp sequence such as IF3 in Figure 5.12 (b).

For each IF, depending upon the waveform parameters, a different number of interference pulses have been observed within each VR chirp, as shown in Figure 5.10 – Figure 5.13. Based on this feature, interference parameters have been estimated for each IF. The stages to estimate interference parameters have been presented in Figure 5.14.

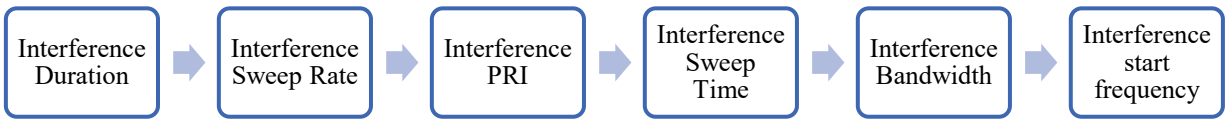


Figure 5.14: Steps used to estimate interference waveform parameters.

The interference duration (T_{INT}) for each interference source is first estimated from the envelope of the interference pulse. The slope of interference (K_{INT}) is then estimated using:

$$K_{INT} = K_V - \frac{2F_{LPF}}{T_{INT}} \tag{5-4}$$

where, F_{LPF} = 10 MHz is the cut-off frequency of the VR's LPF in the used sensor suite. Interference pulse-to-pulse distance (I_{PP}) is estimated from the time series plot of the MIMO frame, as shown in Figure 5.15 (a) and (b) for fast chirp and slow chirp interference sequences, respectively.

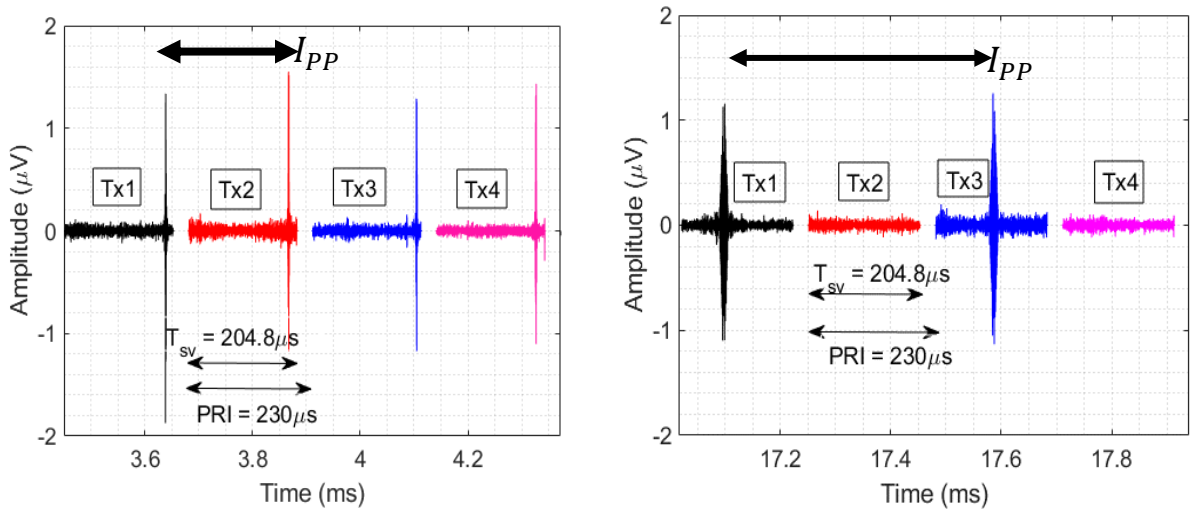


Figure 5.15: Interference pulse to pulse distance (I_{PP}): (a) fast chirp, (b) slow chirp.

Using this, the PRI of interference (PRI_{INT}) has been estimated next.

$$N_{Rx-FPA} = N_{Tx-MIMO} \cdot N_{Rx-MIMO} \tag{5-5}$$

The sweep time of interference (T_{sint}) is then estimated using the following:

$$T_{\text{sint}} = PRI_{INT} - T_{Idle} \tag{5-6}$$

where, T_{idle} is the idle time between chirps equal to 8 μs [265]. The bandwidth of interference has been estimated from:

$$B_{\text{sint}} = K_{INT} T_{\text{sint}} \tag{5-7}$$

The interference chirp sequence has been reconstructed using the estimated sweep time and bandwidth to estimate the start frequency of the interference. The start frequency of the interference is varied between the following ranges through an iterative process:

$$F_{\text{cint}} = F_{cv} - B_{\text{sint}} \text{ to } F_{cv} + B_{\text{sint}} \tag{5-8}$$

For each value of F_{cint},

- The instantaneous time of interference occurrence, which indicates the temporal position of interference $\left(P_{INT-x}\right)$, has been estimated using the mid-value of the envelope of each interference pulse.
- P_{INT-x} has been compared with the measured interference temporal position $\left(P_{INT-M}\right)$.
- The error has been estimated between the two, given as:

$$E = P_{INT-M} - P_{INT-X} \tag{5-9}$$

The value for which *E* is minimum has been used as F_{cint}.

Based on the discussed methodology, the estimated interference parameters have been mentioned in Table 5.1.

Table 5.1. Estimated interference parameters from various interfering sources[17].

Parameter	**IF1**	**IF2**	**IF3**	**IF4**
Interference Duration (μs)	2.8	1.1	16.7	1
Estimated Interference Slope (MHz/μs)	2.26	13.3	3.7	15.1
Pulse repetition interval (μs)	228	30.8	256	24.4
Sweep Time (μs)	220	22.8	248	16.4
Sweep Bandwidth (MHz)	500	300	920	250
Start frequency (GHz)	76.5	76.65	76	76.5
Victim chirps with interference N_{VInt} – Estimated from the time series of each IF	115	62	512	60
Interference frame duration $\left(N_{VInt} PRI_{VR}\right)$ (ms)	26.45	14.26	118	13.8

[17] The estimated waveform parameters of unknown sources of interference have been verified using the developed simulator, discussed in Appendix 12.

Along with estimating the interference waveform parameters, i.e., bandwidth and sweep time, the PRI_{INT} and interference frame duration has also been estimated using the presented methodology. This provides greater degrees of freedom for interference avoidance/ suppression using cognitive mitigation described in the following section.

5.3 Cognitive Interference Avoidance/ Mitigation

With the estimated parameters of interfering waveforms from different sources and potentially different orientations such as forward-looking, corner-looking, and side-looking, cognitive interference mitigation has been performed to either avoid interference or reduce the impact of interference.

5.3.1 Impact of Interference

It is essential to estimate the impact of interference before its mitigation. For example, if the impact of interference is inconsiderable, no mitigation would be required, or it can be assigned a lower priority compared to the case when interference impact is high.

After detecting interference and representing it as the augmented range profile, the following have been estimated:

1. Mean interference power (floor) across the interfered VR chirps for each extracted IF.
2. Interference to noise ratio (INR) for each IF.

As an example, based on the test scenes in Figure 5.6 and results in Figure 5.8, the mean interference power and the INR have been mentioned in Table 5.2.

Table 5.2. Mean interference power and interference to noise ratio (INR). IF represents interference frames, identified in Figure 5.8.

Parameter	IF1	IF2	IF3	IF4
Mean interference power (dBm)	-71	-79	-73	-78
INR (dB)	22	14	20	15

The IFs have been prioritised using the estimated power level and the INR. Next, the impact of each IF has been determined using the INR heatmap discussed in detail in section 8.3.2 and shown in Figure 5.16. The INR heatmap shows the INR as a function of waveform parameters of the VR and IR at the input of the radar detector after the 3D-FFT. When the INR is high, interference will significantly affect target detection due to its higher power.

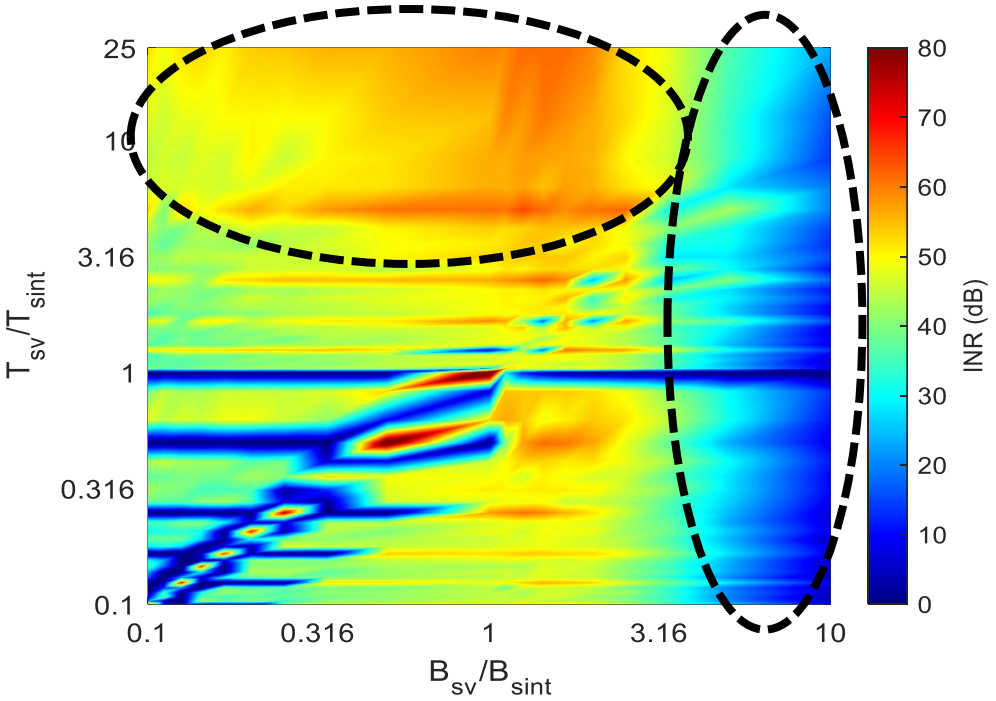


Figure 5.16: Interference to noise ratio (INR) heatmap to estimate interference impact.

If interference appears in the 'low impact region' (right side of the INR heatmap), the interference floor is close to the receiver thermal noise floor after signal processing. In this case, cognitive mitigation has not been performed. For IFs with substantial impacts, such as appearing on the top side of the INR heatmap, the VR waveform parameters have been changed to avoid or suppress interference.

For the cases where interference avoidance is not possible, especially in the background of interference from multiple sources or a higher interference frame duration, the VR parameters have been changed so that the INR is shifted to the 'low impact region' of the heatmap with a reduced interference floor.

5.3.2 Methodology

The bandwidth and sweep time of the VR directly affects its performance, such as the range resolution and the unambiguous range. Therefore, for cognitive avoidance/ mitigation, the variation in idle time between chirps and the start frequency of the VR has been the preferred option in the simulator.

An example of interference avoidance has been shown in Figure 5.17 for IF1, where the idle time variation between the VR chirps has been used to eliminate the chirp signal overlaps between the VR and IR.

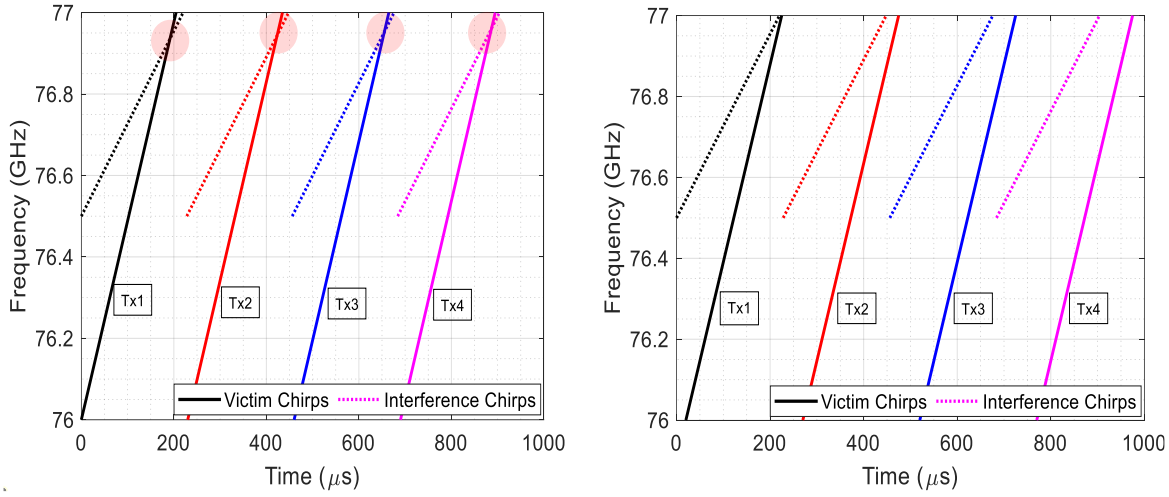


Figure 5.17: Cognitive interference avoidance using idle time variation. The red highlighted region indicates victim and interference chirp overlap.

The proposed methodology can be used to detect and avoid interference signals with a comparatively weaker amplitude, such as in the case where the source of interference is located at a larger distance from the VR. Therefore, the optimum VR parameters can be estimated to avoid interference beforehand during approaches closer to the VR where a greater impact is expected.

Next, the two pre-detection interference mitigation techniques based on windowing and waveform randomisation have been discussed.

5.4 Windowing for Interference Mitigation[18]

In traditional radar processing, an appropriate window is applied to the signal before each FFT to minimise the spectral leakage that appears as sidelobes in other frequency bins (section 2.3.4.IV) [146]. The use of window can be extended to suppress interference in the time domain and has been discussed in this section[19].

In the time domain, interference appears as high-amplitude pulses. Depending upon the instantaneous occurrence time of interference pulse within each VR chirp, some amount of interference can be suppressed due to the applied window before range compression.

As an example, a VR operating in TDM-MIMO mode with T_{sv} = 100 µs, B_{sv} = 0.5 GHz, and F_{cv} = 76 GHz, based on the INRAS Radarlog configuration with 4 transmit and 16 receive elements has been used. The VR interferes with a periodic CW interference with 76.05 GHz, 76.15 GHz, and 76.25 GHz. This results in different temporal locations of the interference pulse within the VR chirp. A reference target with an RCS of 10 dBsm has been positioned at 50 m, 0^o from the VR, with collocated interference. For the Doppler compression, 64 VR chirps have been integrated.

The overlayed time domain plot for different frequencies of CW interference is shown in Figure 5.18 alongside the responses of the Blackman Harris, Hann, and Kaiser windows for comparison. For illustration purposes, the window response has been normalised to the maximum interference amplitude.

[18] Windowing is a signal processing step inherently used while processing the signal. This section presents an analysis of how windowing affects the radar performance in an interference background.

[19] It needs to be noted that the windowing function also widens the effective resolution in each frequency bin, with a commensurate increase in the thermal noise floor.

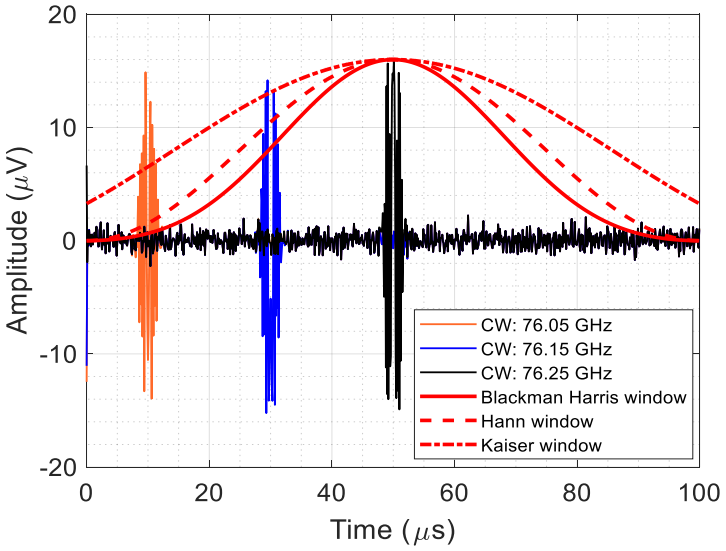


Figure 5.18: Time domain response for different interference temporal locations with different spectral windows.

As the temporal location of interference approaches the start (or the end) of the VR chirp, the amount of attenuation due to the applied window increases. This is true for all the windows in Figure 5.18. In contrast, minimum attenuation is expected when an interference pulse appears in the centre of the victim's chirp. Moreover, by comparing the response of different windows, the Blackman-Harris window has the best interference suppression due to a sharper roll-off [159]. Therefore, it has been used before range compression in the subsequent results.

The Blackman Harris window has been generated using the following:

$$w_{Blackmann}(n) = 0.42 - 0.5\cos\left(\frac{2\pi n}{L-1}\right) + 0.08\cos\left(\frac{4\pi n}{L-1}\right) \tag{5-10}$$

where, L is the length of the window, and

$$\begin{aligned} &n = 0 : M-1, \\ &\mathrm{M} = \frac{L}{2} \qquad \mathrm{L\ is\ even} \\ &\mathrm{M} = \frac{L+1}{2} \qquad \mathrm{L\ is\ odd} \end{aligned} \tag{5-11}$$

The corresponding modelled radar plots in the time domain, range profile, range-Doppler, and range-azimuth for no interference case, and unmodulated CW interference at 76.05 GHz,

76.15 GHz, and 76.25 GHz have been shown in Figure 5.19 (a), (b) and (c), respectively. The Hann window has been applied before the Doppler and spatial compression.

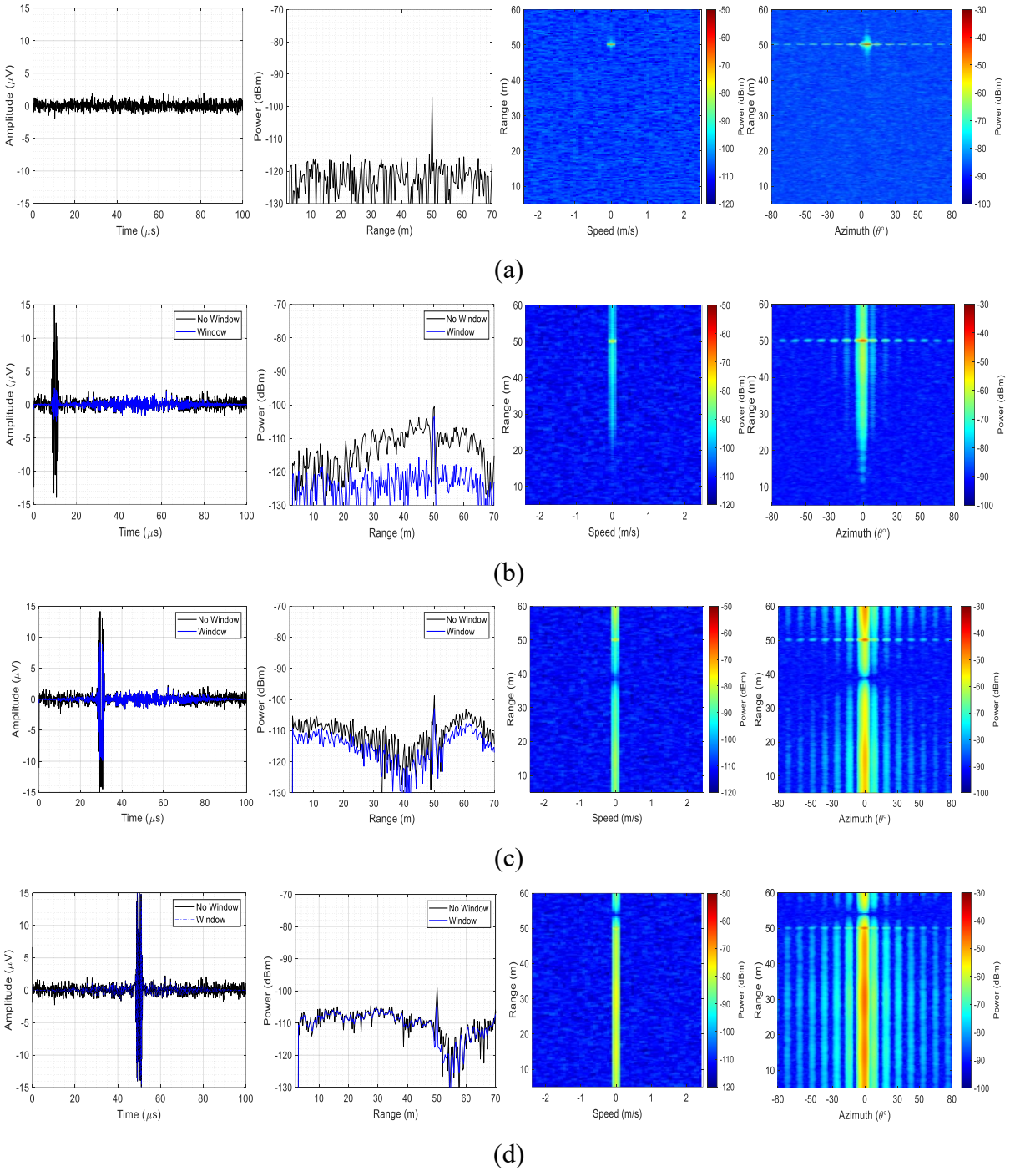


Figure 5.19: Modelled radar plots after interference mitigation due to windowing applied before FFT across the fast-time: (a) no interference, (b) CW interference at 76.05 GHz, (c) CW interference at 76.15 GHz, (d) CW interference at 76.25 GHz. The blue plot in the time domain is the received signal after the window.

As expected, minimum attenuation has been observed when the interference pulse appears at the centre of the VR chirp (Figure 5.19 (d)). Due to higher interference power, target detectability in range-Doppler and range-azimuth domains might be affected. As the temporal interference location is away from the centre of the victim chirp, the attenuation due to the applied window increases. Consequently, the SINR improvement has been observed and summarised in Table 5.3 for the discussed examples.

The SINR gain $\left(G_{SINR}\right)$ after range compression due to the applied fast-time window has been estimated as:

$$G_{SINR} \approx 20\log_{10}\left(\frac{V_{Windowed}}{V_{No-Window}}\right) \tag{5-12}$$

where, $V_{No-Window}$ and $V_{Windowed}$ are the mean interference amplitude in the time domain before and after applying the window, respectively. Due to the inherent characteristics of the window, the echo signal power has also been reduced by ~ 4 dB after the Blackman-Harris window [146]. Therefore, an SINR loss of 4 dB has also been observed.

Table 5.3. The SINR after range compression and the SINR improvement due to the applied spectral window.

Condition	**SINR**	**SINR Improvement (Compared to no window case)**
No Interference	23 dB	NA
After Applying Blackman Harris Window		
Case A: CW Interference: 76.05 GHz	17 dB	15 dB
Case B: CW Interference: 76.15 GHz	10 dB	6 dB
Case C: CW Interference: 76.25 GHz	3 dB	0 dB

As the unmodulated CW interference is periodic, after the Doppler and spatial compression, no SINR gain has been observed due to a similar increase in the interference power and the echo signal power (section 4.4.3).

The frequency characteristics of the window have a continuous spectrum with a main lobe and several sidelobes. The main lobe of the window is centred at each frequency content of the echo signal, which is focused on a single or a limited number of the frequency bins. In contrast, as interference spreads across the multiple frequency bins (section 3.4), additional interference suppression has not been observed due to the window applied before the Doppler and spatial compression.

5.5 Randomisation for Interference Reduction

It has been shown in Chapter 4 that aperiodic interference – the most common type of interference – exhibits statistical characteristics similar to AWGN. Therefore, existing coherent integration and detection techniques [272] can be used for target detection in the background of aperiodic interference. In contrast, synchronous, semi-synchronous, and periodic interference identified as the critical cases from the NRMSE heatmap in Figure 4.9 (b) have a high correlation between interference pulses. Consequently, they show a deviation from Gaussian statistics, and an increase in the power is comparable to the echo signal's power after signal processing across the VR (section 4.4.3).

In this section, randomisation of the VR waveform parameters, a pre-detection mitigation technique, has been proposed to decorrelate interference pulses for the identified critical cases to make their statistics comparable to AWGN with an improvement in the SINR.

5.5.1 Randomisation Parameters

An FMCW radar transmits a sequence of chirps as a frame during the CPI, as demonstrated in Figure 5.20. Each frame has a succeeding off time before the radar can begin with the transmission of a new frame. This time has been called the inter-frame off-time. Moreover, the consecutive chirps have an inherent idle time between them to allow enough time for the ADCs and oscillators to reset [265].

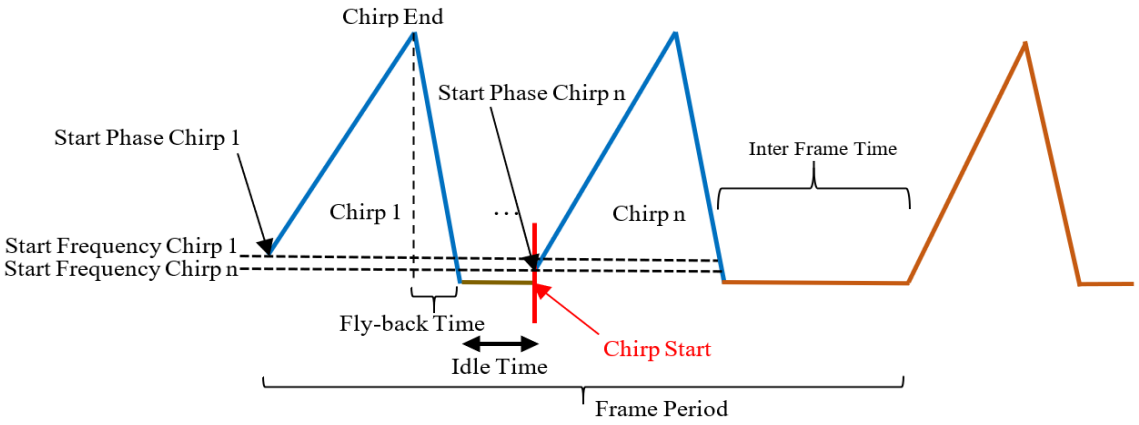


Figure 5.20: FMCW chirp sequence with scalable parameters for chirp randomisation.

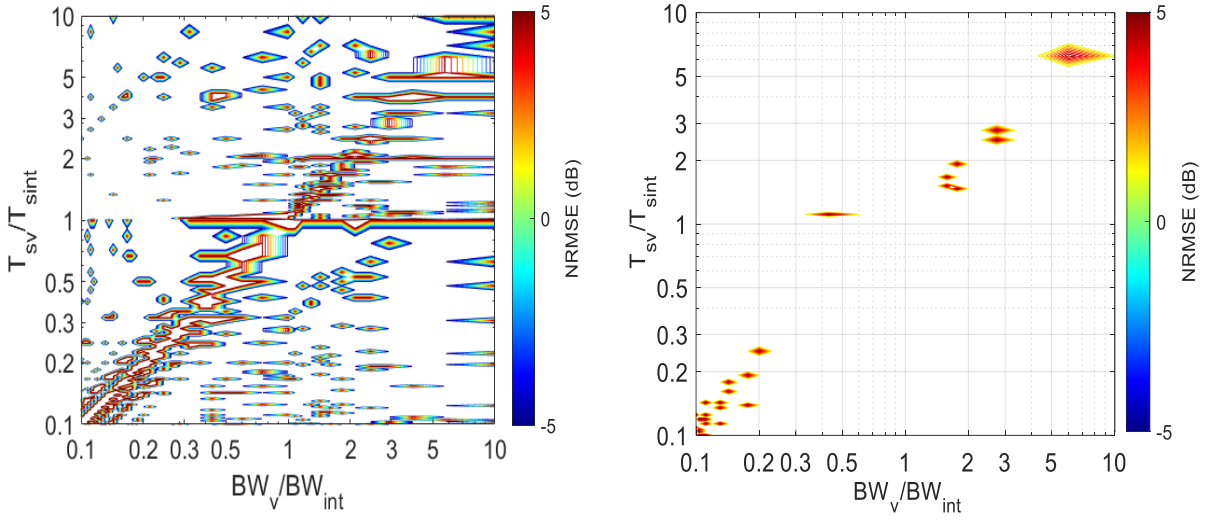
As indicated in Figure 5.20, the waveform parameters that can potentially be randomised without affecting radar performance are the start frequency, the initial phase of the VR chirps, and the idle time between radar chirps $\left(\Delta\tau_j\right)$. In modern automotive radars, these parameters are often configurable within the software [265] and have been used as scalable waveform parameters in this section. As a result of scalable waveform parameters of the VR chirps, the received interference pulses across these chirps are randomised. This reduces the correlation between them, eliminating the probability of synchronous, asynchronous, or periodic interference, and has been assessed in the subsequent section.

5.5.2 Effect of Randomisation on Interference Statistics

For the identified critical cases in Chapter 4, randomisation in the VR has been applied using the parameters stated below. For each case, radar performance has been evaluated.

1. The idle time between the VR chirps is uniformly distributed from 1 – 10 µs.
2. The start frequency of the VR chirps is varied between $F_{cv} \pm \Delta F_j$. Uniformly distributed ΔF_j values have been used in the range of 1 – 50 MHz.
3. The initial phase of the VR chirps $\left(\Delta\theta_j\right)$ has been randomly selected from the set $\left[0^o, 45^o, 90^o, 180^o\right]$.

NRMSE contour maps for the critical cases with NRMSE > -5 dB before and after applying the idle-time randomisation have been presented in Figure 5.21 (a) and (b), respectively.



(a) (b)

Figure 5.21: NRMSE contour maps; (a) No randomisation, (b) Idle time randomisation.

For most of the cases, the NRMSE value has been reduced after randomisation. These cases mainly belong to the periodic and semi-periodic interference. The remaining critical values correspond to some synchronous and semi-synchronous interference, where interference chirps remain within the VR receiver bandwidth after randomisation.

This has been explained by the range-Doppler maps in Figure 5.22 (a) and (b) before and after applying idle-time randomisation, respectively. No target has been considered, and one IR with the same waveform parameters as the VR had been positioned at 50 m from the VR. As expected, a ghost target appears in Figure 5.22 (a) at 25 m (half the true range of interferer due to one-way propagation) due to synchronous interference.

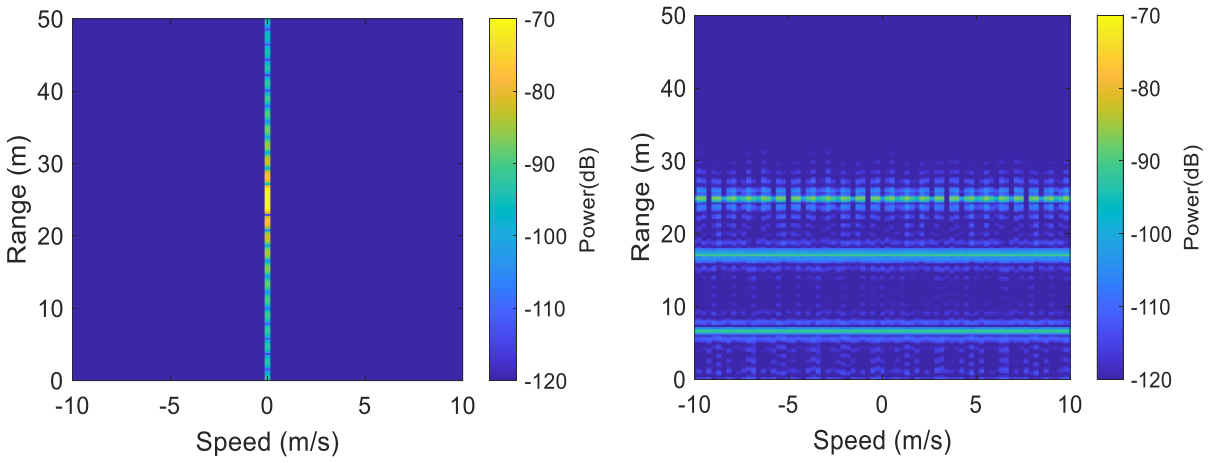


Figure 5.22: Range-Doppler map of synchronous interference: (a) before randomisation, (b) after idle-time randomisation.

After idle time randomisation, each VR chirp will have a different delay with respect to the interference chirp. However, depending upon the value of the idle time, in some of the VR chirps, interference remains within the VRs' LPF band and is still synchronised with the victim chirps. Due to applied randomisation, the phase difference between the IR and VR chirps randomly walks within each CPI. This leads to the ghost target appearance across multiple range bins. Moreover, a broad Doppler shift has been observed due to a random phase shift of the interference across the multiple VR chirps. Consequently, a single ghost target before randomisation has been replaced with multiple smaller amplitude targets with energy spread along range-Doppler axes (Figure 5.22 (b)). A similar trend has been observed for semi-synchronous interference, where the interference pedestal spreads along the Doppler axis after idle time randomisation.

5.5.3 Performance Analysis

The performance analysis of randomisation techniques has been based on the following two parameters:

1. Mean NRMSE $\left(\overline{NRMSE}\right)$ of the critical cases estimated using the following:

$$\overline{NRMSE} = \frac{\sum_{n=1}^{N_C} NRMSE(n)}{N_C} \tag{5-13}$$

where N_C is the total number of critical cases and,

2. Parameter '*P,*' which is the ratio of the number of critical cases and total cases under consideration and presented as a percent ratio.

The estimated $\overline{NRMSE}$ and $P\,\%$ values for different randomisation techniques have been given in Table 5.4. Idle time and start frequency randomisation have similar reductions. Nevertheless, no further improvement has been achieved by combining randomisation techniques as interference pulses are already decorrelated.

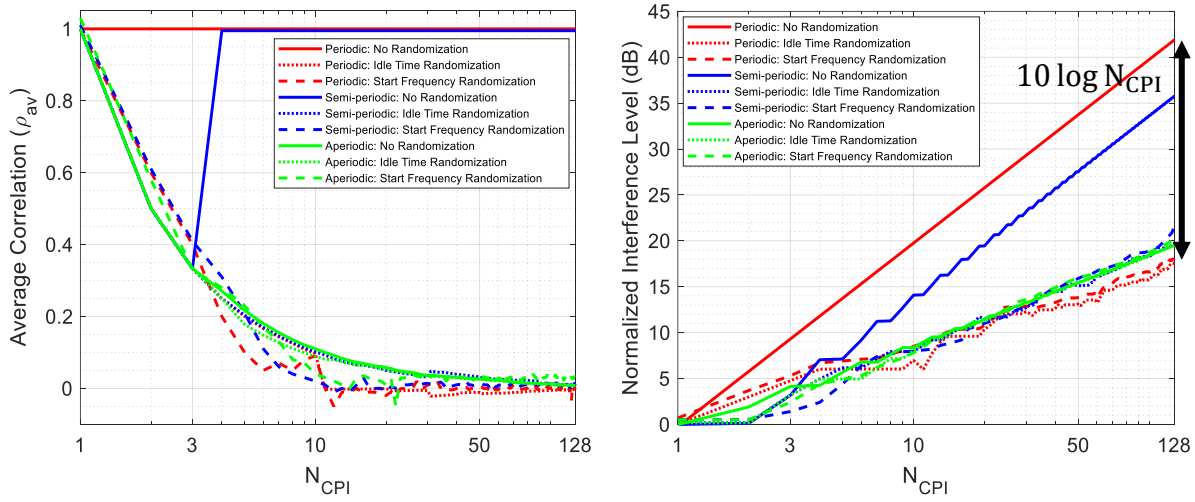
Table 5.4. Performance comparison of randomisation techniques, $\overline{NRMSE}$ value is in dB.

Randomisation Technique	***P(%)***	$\overline{\boldsymbol{NRMSE}}$	**Randomisation Technique**	***P(%)***	$\overline{\boldsymbol{NRMSE}}$
No Randomisation	14.7	-1			
Idle Time	5.9	-6	Idle time + start frequency	8.1	-5
Start Frequency	8.6	-5	Idle time + initial phase	9.8	-5.6
Initial Phase	12.8	0.9	Start frequency + initial phase	11.2	-5

For most cases, randomisation is an effective technique to decorrelate interference pulses and reduce $\overline{NRMSE}$. Idle time randomisation is the most efficient yet technically simple solution to reduce the number of critical cases. In contrast, initial phase randomisation does not significantly reduce the number of critical cases due to the limited phase values available. Therefore, idle time and start frequency randomisations have been discussed in the remainder of this section.

For further analysis, a) average correlation coefficient (ρ_{av}) discussed in section 4.4.2 and b) interference level trend during the CPI have been estimated and presented in Figure 5.23 (a) and (b), respectively, for different types of interference, before and after applying

randomisation. A VR with B_{sv} = 0.3 GHz, and T_{sv} = 100 µs has been used. For the interfering radar, B_{sint} = 0.15 GHz, and T_{sint} = 100 µs, 150 µs, and 151 µs, to generate periodic, semi-periodic, and aperiodic interference, respectively. The average interference level within the unambiguous range of the VR was obtained for each chirp during a CPI and then normalised to the interference level at the first VR chirp.



(a) (b)

Figure 5.23: Effect of randomisation on different interference cases: (a) average correlation, (b) normalised interference level.

After applying idle time randomisation, the value of ρ_{av} for the periodic interference has been significantly reduced. Consequently, the interference level reduces with $\sim 10\log(N_{CPI})$ improvement in SIR. For semi-periodic interference, $< 10\log(N_{CPI})$ SIR improvement has been achieved. As it is inherently uncorrelated, no difference has been observed for aperiodic interference. The start frequency randomisation has a similar trend to the idle time randomisation but is less efficient in terms of statistical characteristics (Table 5.4).

The effect of idle time randomisation on the echo signal and the range of idle time values on radar performance have been discussed in Appendix 8 and Appendix 9, respectively.

Next, the effect of randomisation on radar detector has been analysed for discussed cases.

5.5.4 Detection Characteristics

The distribution characteristics and detection curves for periodic CW interference before and after applying randomisation using parameters in Table A7.1 and the measurement scenario in Appendix 7 are given in Figure 5.24. Start frequency randomisation has been used due to the flexibility of the available radar chipset in setting the start frequencies of each VR chirp.

The start frequency of the VR (AWR1243EVM [38]) has been changed within the range of 1 kHz – 100 kHz. After applying randomisation, a close Gaussian approximation has been observed with detection characteristics close to that of AWGN.

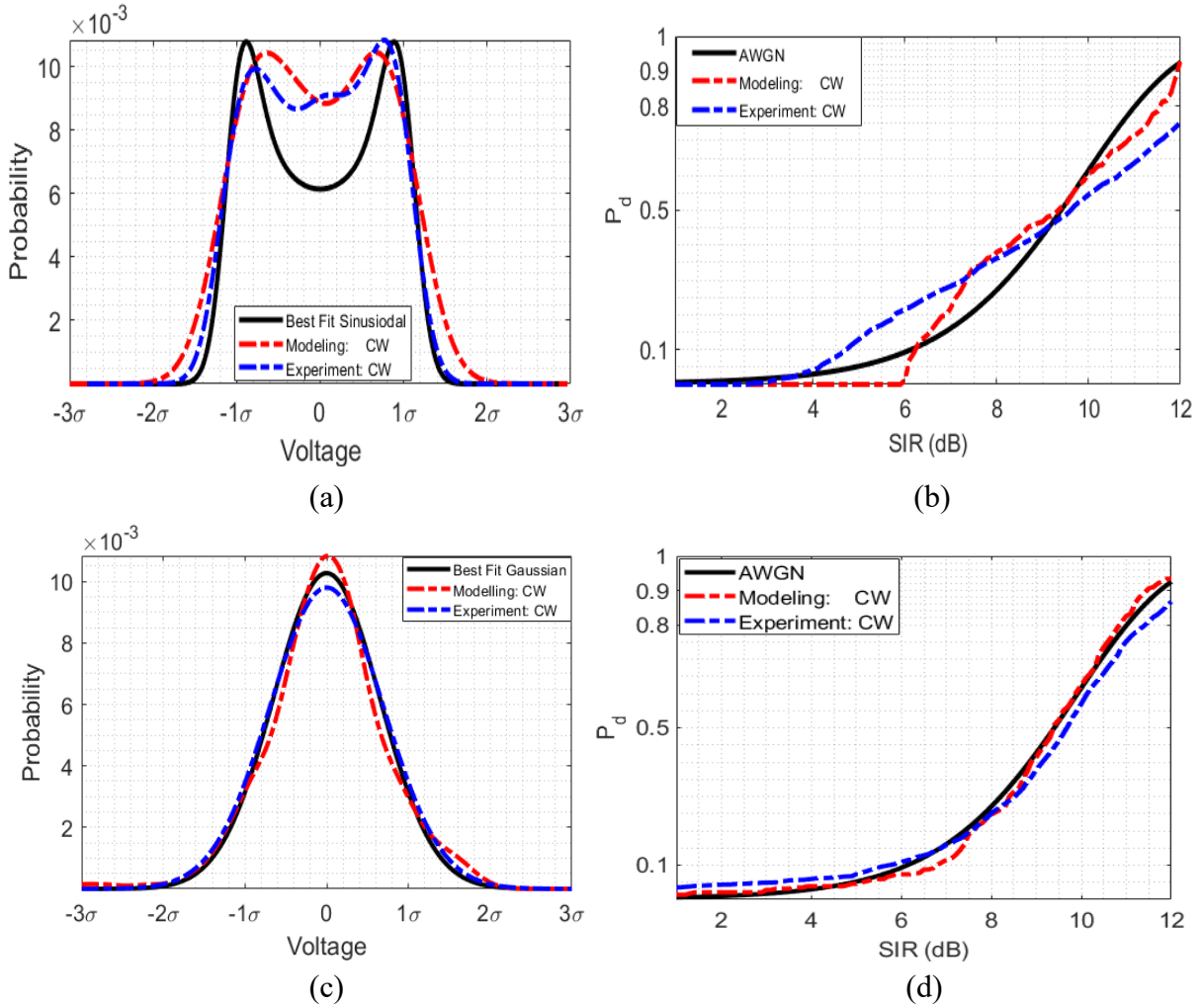


Figure 5.24: Validation of statistical and detection characteristics of periodic continuous wave (CW) interference: (a) distribution before randomisation, (b) probability of detection vs. SIR before randomisation, (c) distribution after randomisation, (d) probability of detection vs. SIR after randomisation.

Randomisation decorrelates interference pulses and ensures that pre-existing detection techniques remain optimal for target detection in an interference background. It also reduces the interference floor for the periodic and semi-periodic interference, the critical interference cases.

5.6 Summary

Various pre-detection and post-detection techniques to mitigate radar interference have been discussed in this chapter. Firstly, methodologies to detect the presence of interference in the time and time-frequency domains have been investigated. The proposed techniques can identify interference in the presence of short-range targets, that have a comparatively stronger return, or the cases where the interference power is less. These techniques play a crucial role in interference mitigation, as discussed in this chapter and the subsequent chapters.

The methodology to estimate the waveform parameters of a-priori unknown interference signals has been presented based on the amplitude and spectral characteristics of the interference. These parameters have been used to cognitively avoid or suppress the impact of interference by changing the waveform parameters of the VR. The methodology has been validated by measurements performed in various real-road scenarios with slow and fast chirp interference sequences and weaker amplitude interference.

Interference mitigation using windowing, which is inherently included in the radar processing chain to minimise spectral leakage, has also been discussed. Depending upon the instantaneous position of the interference pulse, the SINR improvement of up to 15 dB has been achieved. Additionally, the VR waveform parameters randomisation has been evaluated to decorrelate interference pulses with an SINR improvement up to $10\log\left(N_{CPI}\right)$. Moreover, this reduces the deviation between the statistics of critical interference cases and random Gaussian

noise and improves the detector's performance. Nevertheless, as randomisation does not require costly hardware upgrades, it can easily be integrated into modern automotive radars. However, it only applies to cases exhibiting a high correlation between interference pulses. Randomisation can therefore be used in conjunction with other mitigation techniques.

The current mitigation techniques might be suitable for contemporary road scenarios. However, with an increase in the RPR, robust mitigation would be required either by itself or in combination with other mitigation techniques. This has been investigated in the subsequent chapters.

Chapter 6. MITIGATION IN THE SPATIAL DOMAIN

For the interoperability of radars with robust performance, interference mitigation techniques have been proposed in the temporal [227], spectral [274], and spatial domains [191]. Mitigation in the temporal and spectral domains is well-presented in literature [145], [173], [188], [190], [229].

Mitigation in the spatial domain is also not a new area of radar technology. Adaptive beamforming for null steering is one of the proposed methodologies to suppress energy from the direction of interference. This is particularly useful because it does not rely on the waveform parameters, as discussed in Chapter 5, or the signal's modulation schemes. Instead, it depends upon the hardware characteristics of the radar with specialised signal processing to direct an adaptive null towards the source of the interference.

However, as discussed in Table 2.6, the applicability of spatial domain mitigation, especially in an automotive scenario, is accompanied by various limitations and drawbacks. The presented literature has been focused on a limited number of interferers and well-separated targets and interferers [164], [192], [193], [216]. Moreover, the analysis of interference and its mitigation in MIMO and full phased array (FPA) – the two main modes of signal transmission in SoA automotive sensors – has not been discussed in the literature.

This chapter focuses on the effectiveness of spatial domain mitigation in congested automotive scenarios for various road conditions and radar configurations. The significant contributions of this chapter include the following:

- The severity of radar interference and the motivation behind investigating interference mitigation in the spatial domain.
- Analysis and mitigation of radar interference in the spatial domain.
- Comparative analysis of blind and trained spatial mitigation techniques.
- Performance evaluation of spatial domain mitigation by computing the peak to highest side lobe levels (PHSLLs) and the SINR as performance metrics. These parameters have been estimated for various road scenarios and radar configurations as a function of spatial separation between the target and the interferer.
- Qualitative and quantitative comparison of adaptive beamformers performance in MIMO and traditional FPA based radars.
- Comparative analysis of spatial and temporal domain mitigation.
- SoA sensor limitations for spatial domain interference mitigation.

6.1 Interference in the Spatial Domain

The VR can receive interference from a variety of possible angles within its FoV. An example of a typical road scenario has been illustrated in Figure 6.1 (a), with 4 vehicles travelling in close proximity. The radar installed on the vehicle shown in blue is the VR. The VR in this example has been configured based on TI AWR1243 [250] automotive chipset with 3 transmit and 4 receive elements. The remaining three vehicles (red) have IRs. For ease of illustration, only the forward-looking radars have been considered. Figure 6.1 (b) shows the modelled MIMO beamformed range-cross range plot in the absence of interference. Each of the three echoes from the nearby vehicles has a reasonable SNR. However, a large part of the VR's FoV has been masked due to interference from these vehicles, shown in Figure 6.1 (c). This leaves the targets undetectable.

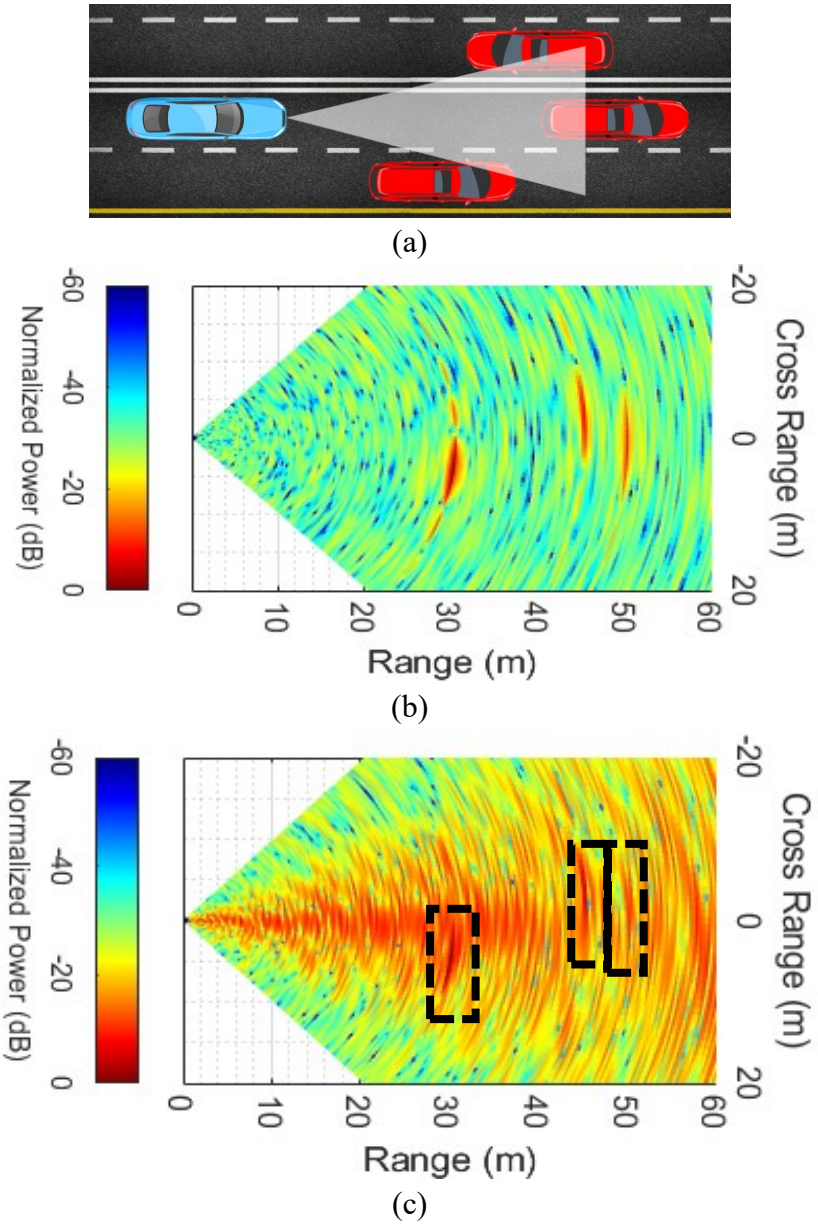


Figure 6.1: Severity of radar interference: (a) typical roadside scenario, (b) modelled azimuth response without interference, (c) modelled azimuth response with interference from radars on the nearby vehicles.

Furthermore, as the linear cross-range resolution degrades with an increase in the range [92], the targets at a larger range from the VR might be masked even if they have a reasonable angular separation from the source of interference. In the absence of mitigation, this can lead to losing substantial information about targets and potentially fatal accidents, especially when interfering sources are closer to the VR and transmit a higher power.

6.2 Mathematical Model

The block-level representation of the processing chain used to analyse and mitigate interference in the spatial domain has been demonstrated in Figure 6.2.

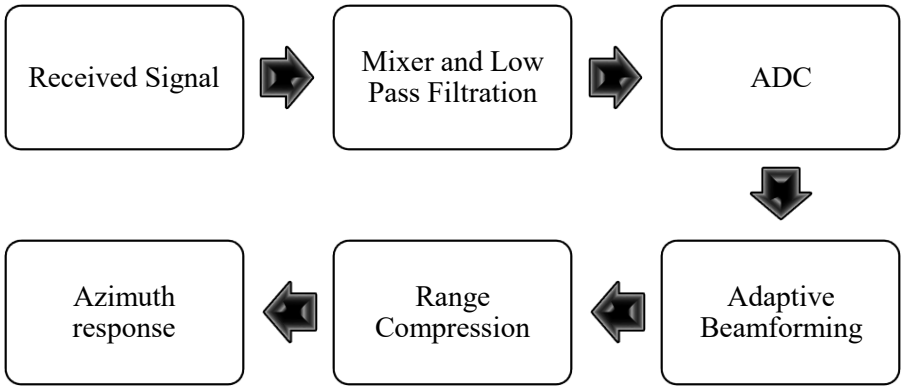


Figure 6.2: The victim receiver's signal processing chain for interference mitigation in the spatial domain.

The signals received across the consecutive array elements have a phase difference $\psi = kd\sin\left(\theta_{AoA}\right)$ between them where θ_{AoA} is the AoA of the received signal. The steering vector (SV) across each target or interferer direction $SV\left(\theta_{AoA}\right)$ can be expressed as follows:

$$SV\left(\theta_{AoA}\right) = \left[1 \; e^{j\psi} \; e^{j2\psi} \; \ldots \; e^{j(N_{Rx}-1)\psi}\right]^T \tag{6-1}$$

where, T represents the transpose operation. The received signal $X\left(t\right)$ can therefore be expressed as follows:

$$X\left(t\right) = \sum_{l=1}^{L} S_{RxT}^{l}\left(t\right)\cdot SV\left(\theta_{AoA_l}\right) + \sum_{m=1}^{M} S_{RxI}^{m}\left(t\right)\cdot SV\left(\theta_{AoA_m}\right) + n\left(t\right) \tag{6-2}$$

where, L and M are the number of targets and interferers, respectively, $S_{RxT}^{l}\left(t\right)$ and $S_{RxI}^{m}\left(t\right)$ are the signals received from the l^{th} target and m^{th} interferer, respectively, θ_{AoA_l} and θ_{AoA_m} are the AoA from l^{th} target and m^{th} interferer, respectively, and $n\left(t\right)$ is the VR receiver's thermal noise.

6.2.1 Echo Signal Reception

In a MIMO radar, the echo signal at the receiving elements of the VR corresponds to the signal transmitted by the same radar. After appropriate signal processing, a beam according to the virtual aperture is formed in the direction of the target (section 3.5).

The echo signal from target 'l' $\left(S_{RxT}^{l}\right)$ across the virtual elements of the VR $\left(N_{Tx}N_{Rx}\right)$ is expressed as:

$$S_{RxT}^{l} = \left[S_{1,1}^{l} \; S_{1,2}^{l} \; \cdots \; S_{1,N_{Rx}}^{l} \; \cdots \; S_{N_{Tx},1}^{l} \; S_{N_{Tx},2}^{l} \cdots S_{N_{Tx},N_{Rx}}^{l} \right] \tag{6-3}$$

where the first and second indices of the subscript with S represent the transmit and receive element of the VR, respectively. The steering vector for the echo signal from target 'l', represented as $SV\left(\theta_{AoA_l}\right)$, can be expressed as follows:

$$SV\left(\theta_{AoA_l}\right) = \left[1 \; e^{jkd\sin\theta_{AoA_l}} \; e^{j2kd\sin\theta_{AoA_l}} \; \ldots \; e^{jkd\left(N_{Rx}\cdot N_{Tx}-1\right)\sin\theta_{AoA_l}} \right]^{T} \tag{6-4}$$

6.2.2 Interference Reception

As discussed in section 3.5, the angular resolution of interference depends upon the waveform parameters of the VR and IR.

Synchronous and asynchronous periodic interference are quasi-coherent with the VR's transmit signal [144]. Therefore, the antenna pattern is formed according to the virtual aperture, and this interference follows a resolution similar to the echo signal. The received interference from the 'm^{th}' interferer $\left(S_{RxI-Coh}^{m}\right)$ and the corresponding steering vector $SV\left(\theta_{AoA_m}\right)$, for these interference can be estimated as follows:

$$S_{RxI-Coh}^{m} = \left[S_{1,1}^{m} \; S_{1,2}^{m} \; \cdots \; S_{1,N_{Rx}}^{m} \; \cdots \; S_{N_{Tx},1}^{m} \; S_{N_{Tx},2}^{m} \cdots S_{N_{Tx},N_{Rx}}^{m} \right] \tag{6-5}$$

$$SV\left(\theta_{AoA_m}\right) = \left[1 \; e^{jkd\sin\theta_{AoA_m}} \; e^{j2kd\sin\theta_{AoA_m}} \; \ldots \; e^{jkd\left(N_{Rx}N_{Tx}-1\right)\sin\theta_{AoA_m}} \right]^{T} \tag{6-6}$$

An unmodulated CW signal has been used at the experimental stage as an example of quasi-coherent (periodic) interference in the following discussion.

For non-coherent interference pulses, after beamforming, the array pattern with a real aperture of N_{Rx} elements has been formed for this interference. The received interference $\left(S^{m}_{RxI-NonCoh}\right)$, in this case, is expressed as follows:

$$S^{m}_{RxI-NonCoh} = [S^{m}_{1} \; S^{m}_{2} \; \cdots \; S^{m}_{N_{Rx}}] \tag{6-7}$$

whereas the corresponding steering vector $SV\left(\theta_{AoA_m}\right)$ is expressed as:

$$SV\left(\theta_{AoA_m}\right) = \left[1 \; e^{jkd\sin\theta_{AoA_m}} \; e^{j2kd\sin\theta_{AoA_m}} \; \ldots \; e^{jkd\left(N_{Rx}-1\right)\sin\theta_{AoA_m}}\right]^{T} \tag{6-8}$$

By comparing (6-6) and (6-8), the steering vector (SV) of aperiodic interference depends upon the receive array only. Therefore, the angular resolution is broader in contrast to the periodic interference cases.

To assess the angular resolution of different types of interference relative to the echo signal resolution, the ratio of angular resolutions of the echo signal and quasi-coherent interference $\left(\eta_{Coh}\right)$ and non-coherent interference $\left(\eta_{NonCoh}\right)$ have been estimated and given as:

$$\eta_{Coh} = \frac{\Delta\theta_t}{\Delta\theta_i} = \frac{N_{Tx}\cdot N_{Rx}}{N_{Tx}\cdot N_{Rx}} = 1 \tag{6-9}$$

$$\eta_{NonCoh} = \frac{\Delta\theta_t}{\Delta\theta_i} = \frac{N_{Tx}\cdot N_{Rx}}{N_{Rx}} = N_{Tx} \tag{6-10}$$

Therefore, $\eta_{Coh} = N_{Tx}\eta_{NonCoh}$ indicating that the resolution of non-coherent interference is N_{Tx} times worse than the echo signal and hence the quasi-coherent interference.

Measurements have been performed in an anechoic chamber to validate the appearance of different types of interference. The details have been presented in Appendix 10.

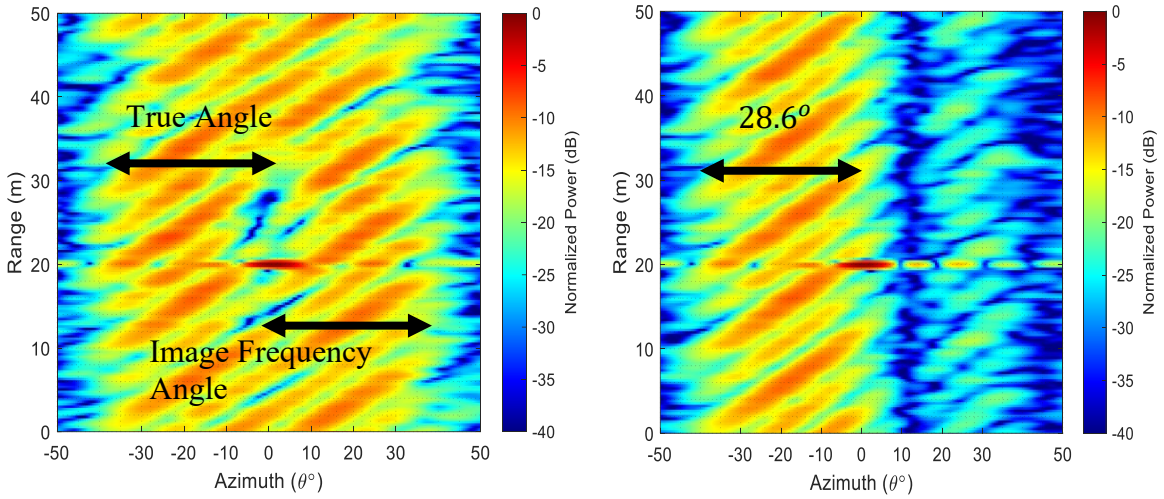
For the majority of the practical automotive scenarios, due to a low correlation between the interference pulses [247], interference resolution in MIMO radars will be much lower in comparison to the target's resolution. Therefore, a larger FoV of the VR will be affected by interference. This makes the problem of interference mitigation even more critical.

6.3 Interference in Single Channel and Dual Channel Receivers

SoA automotive sensors have been developed with either a single (real) channel receiver, such as the INRAS Radarbook [40], or with an optional dual (in phase-quadrature) channel receiver, such as TI AWR1243 [250]. The receiver configurations have been discussed in detail in Appendix 6. In both the receiver configurations, the target can be efficiently detected. However, the radar's receiver structure has an essential effect on the appearance and mitigation of interference. Furthermore, as discussed in Appendix 4, the receiver configuration affects all types of asynchronous interference, including coherent (periodic), partially coherent (semi-periodic), and non-coherent (aperiodic) interference.

In a single channel receiver, each interferer corresponds to two AoA: one towards its actual direction (θ_{AoA}), and one towards $-\theta_{AoA}$ due to the image frequency components (Appendix 4). However, a dual 'I/Q' channels receiver filters the image frequency after the LPF (see Figure 6.2), resulting in only one actual AoA after beamforming. Figure 6.3 (a) and (b) show the modelled range-azimuth plots for a single channel and dual channels receiver, respectively. The simulator was set based on the TI AWR1243 chipset [250] (that has both single and dual channel capability) with $N_{Tx} = 3$, and $N_{Rx} = 4$. $T_{sv} = 51.2$ µs, $B_{sv} = 0.5$ GHz. An FMCW interference with $T_{\text{sint}} = 1000$ µs, $B_{\text{sint}} = 0.3$ GHz has been used. The target (RCS 10 dBsm) has been positioned at 20 m, 0^o from the VR, whereas interference has been positioned in the first side lobe of the target at 20 m, -16^o. Two AoAs at $\pm 16^o$ have been

observed in a single channel receiver that masks a larger portion of the VR's FoV compared to the I/Q channels receiver.



(a) (b)

Figure 6.3: Range-azimuth plots for different receiver configurations: (a) single channel, (b) dual 'I/Q' channels.

Due to a wider region of the VR's FoV masked by interference, spatial mitigation in a single channel receiver becomes even more challenging, investigated in section 6.5.

6.4 Interference in MIMO and Full Phased Array

There is a modern trend of using MIMO technology in automotive radars [116]. These radars gained importance as an alternative to conventional FPA radars [238]. However, as shown in this section, in the background of interference, the performance of MIMO radar degrades compared to a FPA with the same angular resolution.

For MIMO and FPA performance evaluation, the echo signal's angular resolution, side lobe level (SLL), and available DoF have been considered to define the respective array sizes. The array sizes have been chosen to obtain a similar two-way echo signal's angular resolution and SLL in both the arrays. To achieve this, an FPA with a single transmit element and receive array equivalent to the number of virtual elements of the corresponding MIMO array has been

used, unless stated otherwise. This results in normalised SLL ~ -13 dB for both arrays, and angular resolution of $2/N$ radians, where N represents the number of virtual channels in the MIMO array.

The ratio of angular resolutions of the MIMO array $(\Delta\theta_{MIMO})$ and the FPA $(\Delta\theta_{FPA})$ for target (η_T) and interference (η_I) can be estimated as follows:

$$\eta_T = \frac{\Delta\theta_{MIMO-T}}{\Delta\theta_{FPA-T}} = \frac{N_{Rx-FPA}}{N_{Tx-MIMO} \cdot N_{Rx-MIMO}} \tag{6-11}$$

$$\eta_I = \frac{\Delta\theta_{MIMO-I}}{\Delta\theta_{FPA-I}} = \frac{N_{Rx-FPA}}{N_{Rx-MIMO}} \tag{6-12}$$

Subscripts T and I represent target and interferer, respectively, $N_{Tx-MIMO}$ and $N_{Rx-MIMO}$ represent the number of transmit and receive elements in the MIMO array, and N_{Rx-FPA} represent the number of receive elements in the FPA. According to the defined criterion, $\Delta\theta_{MIMO-T} = \Delta\theta_{FPA-T}$, which gives η_T = 1. Using (6-11), to achieve this, the following array size would be required for the FPA:

$$N_{Rx-FPA} = N_{Tx-MIMO} \cdot N_{Rx-MIMO} \tag{6-13}$$

Using this in (6-12),

$$\Delta\theta_{MIMO-I} = N_{Tx-MIMO} \cdot \Delta\theta_{FPA-I} \tag{6-14}$$

Therefore, after beamforming, the MIMO array will form a beam towards the direction of interference with a lower resolution compared to the FPA counterpart, where the beam will be formed with a larger receive array and a better resolution. Consequently, interference will affect a larger FoV of the MIMO VR.

A TDM-MIMO radar [6] with $N_{Tx-MIMO}$ = 3, $N_{Rx-MIMO}$ = 4 and a FPA with N_{Tx-FPA} = 1, N_{Rx-FPA} = 12 have been modelled. The respective array sizes result in $\eta_I = 3$ and

$\Delta\theta_{MIMO-I} = 3\Delta\theta_{FPA-I}$. A VR with T_{sv} = 204.8 µs, B_{sv} = 2 GHz, and an interfering source with T_{sint} = 150 µs and B_{sint} = 1.9 GHz have been used, corresponding to the asynchronous aperiodic interference case. The modelled scenario is demonstrated in Figure 6.4 with a target and interfering source in adjacent lanes in front of the VR. After beamforming in the MIMO array, the AoA of the interfering source appears in the first sidelobe of the target.

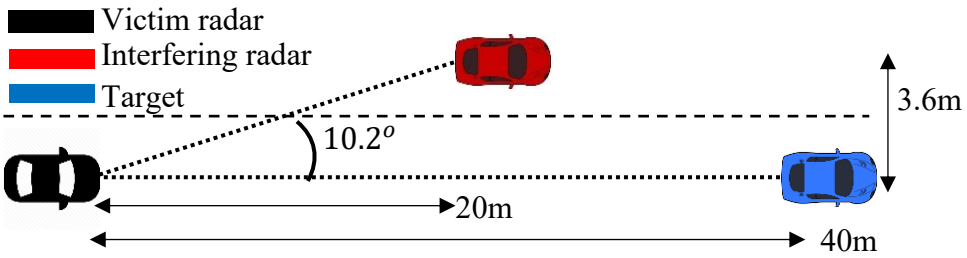


Figure 6.4: An automotive scenario with a close spatial separation between the target and the interferer.

The corresponding signal processing results have been demonstrated in Figure 6.5. The target at 40 m is fully masked by the interference floor in the modelled range profile in Figure 6.5 (a). The beamformed range-azimuth plots for MIMO and FPA in the absence of interference have been shown in Figure 6.5 (b). Due to similar resolution and SLL, the target appears similar in both arrays. Modelled range-azimuth plots in the background of interference for MIMO and FPA have been presented in Figure 6.5 (c) and (d), respectively, for dual ('I/Q') channels receiver. For the target, the antenna pattern in the MIMO and FPA coincides with a 9.5^o angular resolution and a 13 dB SLL. For the defined configuration, η_I = 3, $\Delta\theta_{FPA-I} = 9.5^o$ and $\Delta\theta_{MIMO-I} = 28^o$. Therefore, interference in the MIMO array has a broader beam than in the FPA. However, a narrow interference beam has been observed in the FPA case. Therefore, a virtual MIMO aperture does not give any additional advantage in the background of interference as it does for the echo signal.

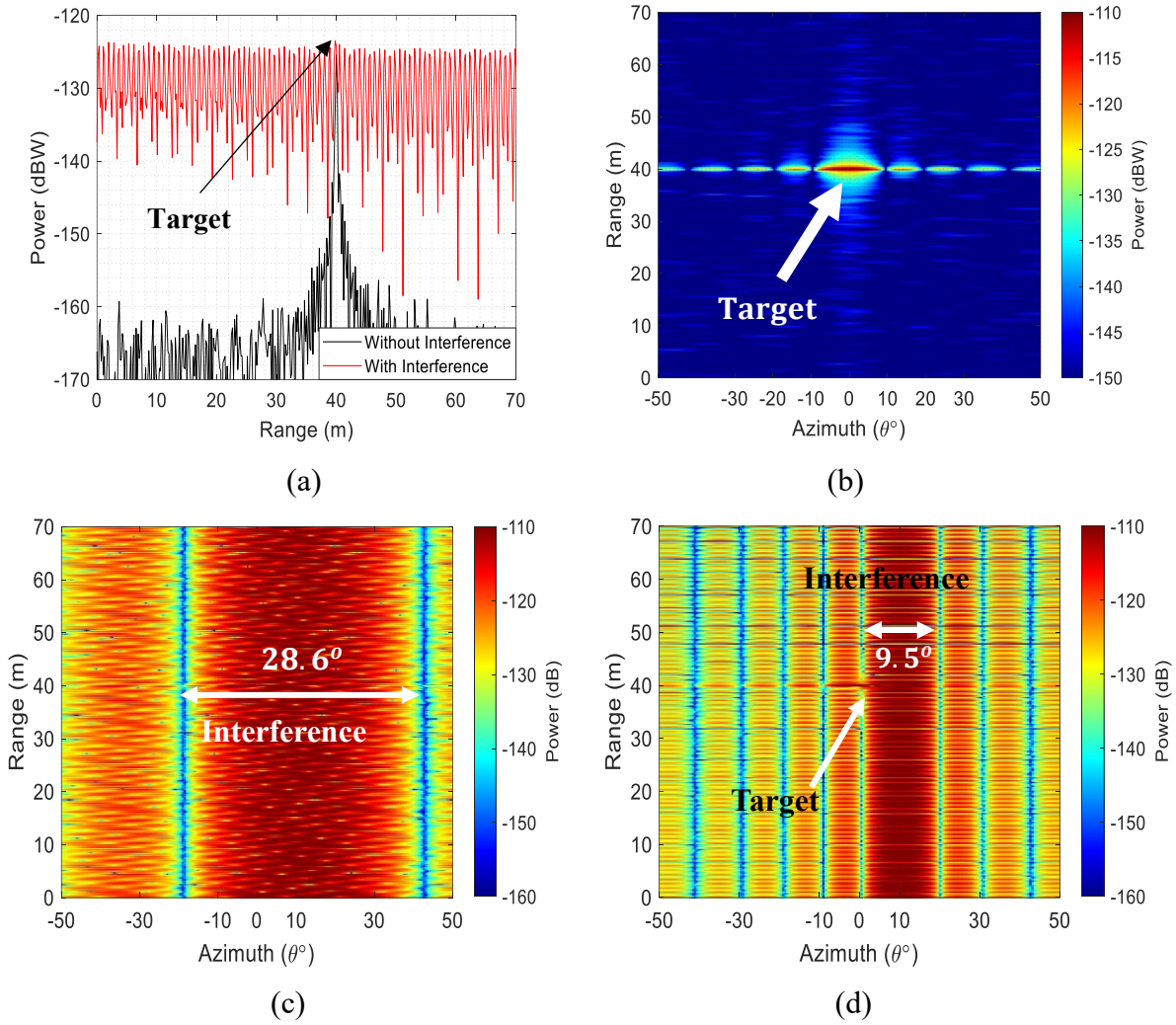


Figure 6.5: Modelled results for the example scenario in Figure 6.4: (a) range profile with and without interference, (b) range-azimuth plot for the MIMO array and FPA without interference, (c) range-azimuth plot for the MIMO array with interference, (d) range-azimuth plot for the full phased array with interference.

For effective target detection, appropriate interference suppression is required in both cases. Even if a large MIMO array is used, the interference beam would still be much broader than the target beam and would have a detrimental effect on the VR's FoV and performance.

Periodic or synchronous interference is quasi-coherent across the VR's transmit elements [144], resulting in $\eta_T = \eta_I$. However, aperiodic interference is more common in practical automotive scenarios [247] and has been discussed in this chapter.

6.5 Spatial Mitigation of Interference

One of the solutions to the mutual interference problem is adaptive digital beamforming (ADBF) [191], [192]. ADBF exploits an antenna array to receive maximum signal power from a specified direction while rejecting signals from other directions. This is achieved by varying the weights of array elements $\left(\mathbf{w}_i^*\right)$, as illustrated in Figure 6.6. The received signal is multiplied by a complex weight vector, due to which the resulting antenna pattern has a notch in the interferer's direction, suppressing the interfering signal's energy at the output of the adaptive beamformer.

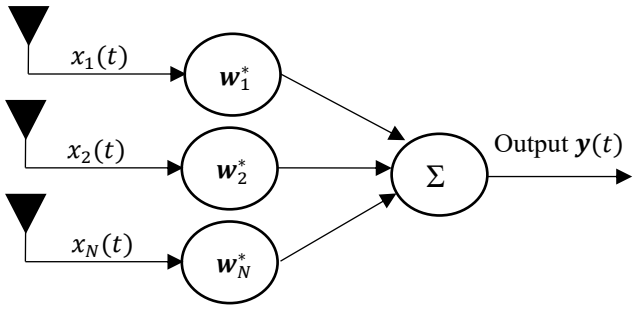


Figure 6.6: The methodology of adaptive digital beamforming.

In the background of multiple targets and interfering sources, the objective function of an adaptive beamformer $\left(SV\left(\theta_{Adaptive}\right)\right)$ has been defined as:

$$SV(\theta_{Adaptive}) = \sum_{l=1}^{L} SV(\theta_{AoA_l}) - \sum_{m=1}^{M} SV(\theta_{AoA_m}) \tag{6-15}$$

where, $SV\left(\theta_{AoA_l}\right)$ represents the SV for the received echo from target '*l*', $SV\left(\theta_{AoA_m}\right)$ represents the SV for interferer '*m,*' and *N* and *M* represent the number of targets and interferers, respectively. The equivalent array pattern $E\left(\theta_{Adaptive}\right)$ has then been estimated as:

$$E\left(\theta_{Adaptive}\right) = \sum_{n=0}^{K-1} w_n{}^* SV\left(\theta_{Adaptive}\right) \tag{6-16}$$

where, *K* represents the number of array elements, and the weight vector is expressed as:

$$\boldsymbol{w} = [\boldsymbol{w}_o \ \boldsymbol{w}_1 \ \ldots \ \boldsymbol{w}_{K-1}] \tag{6-17}$$

One of the challenging aspects is the precise estimation of these adaptive weights, which meets the defined objective function. For this, various techniques have been discussed next.

6.5.1 Types of Mitigation Techniques

The two major categories of adaptive mitigation techniques discussed in the literature are the trained and blind adaptive algorithms [275]. Trained adaptive algorithms use a training, interference-free, signal to update the adaptive weight vector. In contrast, the blind algorithms do not require any training sequence [276] and entirely depend upon the received signal's characteristics to estimate the adaptive weight vector. However, to achieve the desired response, the convergence factor of blind mitigation techniques is susceptible to the type of interference [247] and its power. Various trained and blind mitigation techniques have been summarised in Figure 6.7, which were initially investigated and assessed to select the appropriate mitigation methodology in the discussed work.

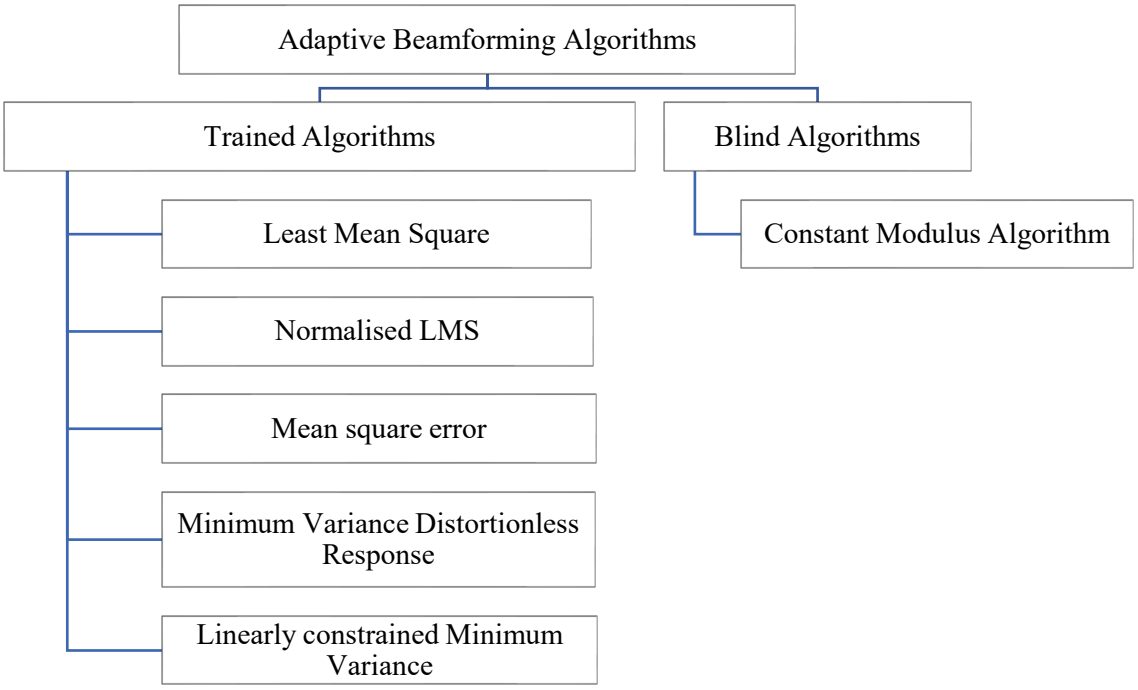


Figure 6.7: Types of adaptive digital beamforming techniques assessed for the spatial domain mitigation of interference.

The comparison of blind and trained mitigation has been performed using SLL as the performance metric for the following scenarios:

1. Well-separated target and interferer, and
2. Closely spaced target and interferer.

The investigated techniques include least mean square (LMS) [193], normalized-LMS (N-LMS) [216], constant modulus algorithm (CMA) [277], mean square error (MSE) [164], minimum variance distortion-less response (MVDR) [278], and linearly constrained minimum variance (LCMV) [279], [280] beamformers. With a different base algorithm, all the techniques maximize the SINR by minimizing the error between the desired signal (interference-free signal) and the received signal with interference. ADBF with LMS (trained) and CMA (blind) techniques have been summarised in Figure 6.8 (a) and (b), respectively.

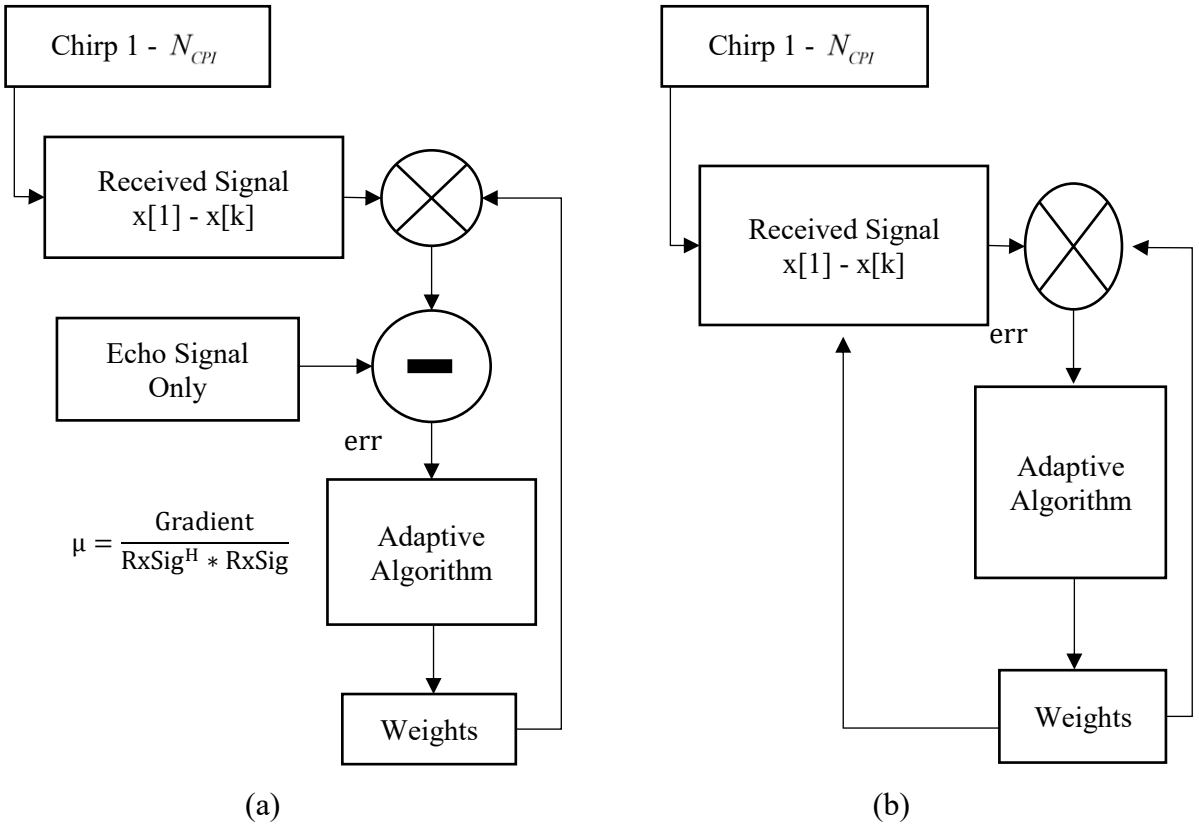


Figure 6.8: Examples of adaptive mitigation techniques: (a) least mean square, (b) constant modulus algorithm.

In the CMA algorithm, the error '*err*' has been estimated as follows:

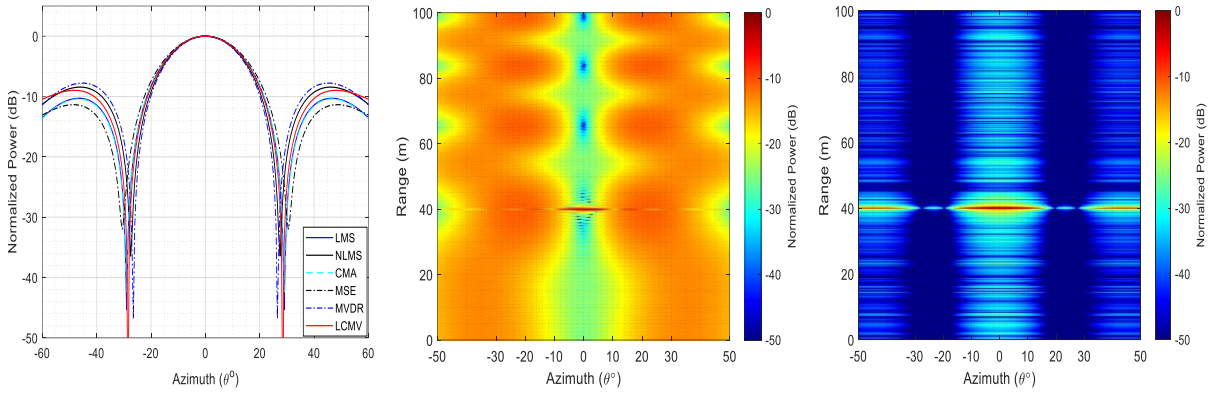
$$err = \frac{ADBF_{Out}}{\sum ADBF_{Out}} - ADBF_{Out} \tag{6-18}$$

where, $ADBF_{Out}$ represents the beamformers output signal after applying estimate weights during each iteration. After each iteration, the adaptive process minimises the beamformer's output error (*err*). For each iteration, the updated weight vector has been estimated as follows:

$$\boldsymbol{w}(k+1) = \boldsymbol{w}(k) + \mu \cdot err \cdot \boldsymbol{Sig}_{Rx}(k) \tag{6-19}$$

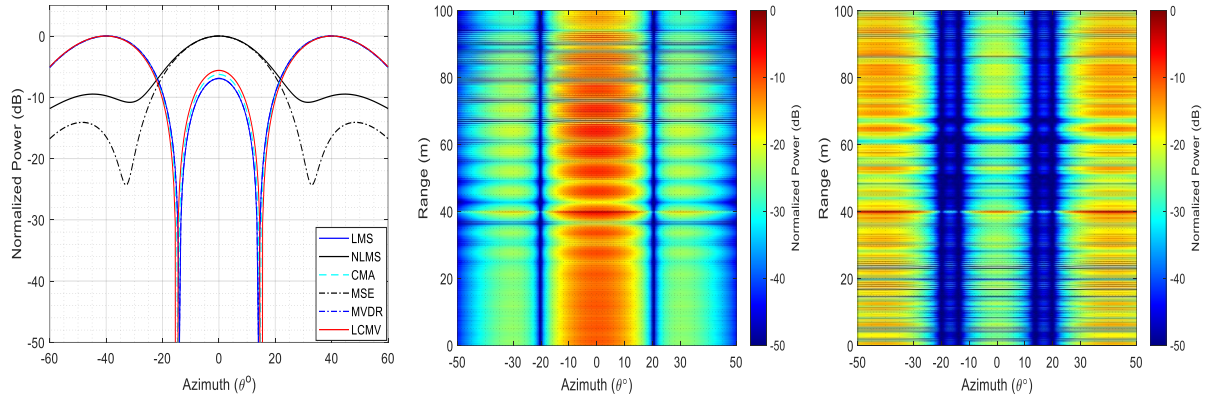
where, *k* represents the number of fast-time samples, $\boldsymbol{Sig}_{Rx}$ is the received signal, and $\mu = 1$.

First, a simplified case is considered where a single Tx element VR with T_{sv} = 102.4 μs, B_{sv} = 0.5 GHz illuminates the radar FoV. The echo signal is received by a full Rx array of 4 elements having a single (real only) channel receiver configuration. The target has been positioned at 40 m, 0^o from the VR. For the well-separated case, interference has been positioned at 40 m, 27^o from the VR (within the side lobe of the target). In contrast, for the closely spaced case, interference has been positioned at 40 m, 14^o (within the main lobe of the target). The adaptive array response for the aforementioned mitigation techniques has been shown in Figure 6.9 (a). The beamformed range-azimuth plot with LCMV-based adaptive weights (used for the detailed analysis in the presented work) for the well-separated case before and after spatial mitigation has been presented in Figure 6.9 (b) and (c), respectively. The array response after applying adaptive weights in the case of closely spaced target and interferer has been shown in Figure 6.10 (a). The range-azimuth plot after MSE and LCMV techniques have been shown in Figure 6.10 (b) and (c), respectively.



(a) (b) (c)

Figure 6.9: Spatial mitigation results for a well-separated target and interferer: (a) array response using adaptive weight, (b) range-azimuth plot before mitigation, (c) range-azimuth plot with LCMV-based adaptive weights.



(a) (b) (c)

Figure 6.10: Spatial mitigation for closely spaced target and interferer: (a) array response using adaptive weights, (b) range-azimuth plot with MSE-based adaptive weights, (c) range-azimuth plot with LCMV-based adaptive weights.

For the two discussed scenarios, the SLL after applying each spatial mitigation technique has been presented in Table 6.1. SLL has been estimated using the following:

$$SLL(\text{dB}) = P_{Echo}(\text{dB}) - P_{SideLobe}(\text{dB}) \tag{6-20}$$

where, P_{Echo} represents the power of the main lobe in the target's direction, and $P_{SideLobe}$ represents the power of the highest sidelobe. In this context, a negative SLL indicates a sidelobe level greater than the main lobe towards the target.

Table 6.1: Side lobe level (SLL) for well-separated and closely spaced target and interferer.

Technique	**SLL (dB)**	
	Well-separated target and interferer	Closely spaced target and interferer
LMS	10	-6.4 dB
NLMS	8	9.8 dB
CMA	10	-6.1 dB
MSE	11	14 dB
MVDR	7.9	-6.4 dB
LCMV	9.8	-6 dB

For well-separated case, applied techniques suppress interference with a reasonable SLL, as shown in Table 6.1. In the case when the target and interferer have a small spatial separation between them, the following observations have been made from Figure 6.10 and results presented in Table 6.1:

- A few techniques, such as NLMS and MSE, show reasonably high SLL because the adaptive weights could not fully converge after the iterative process. Therefore, the null could not be placed in the direction of the interferer to suppress its power while maximising the SINR. This has been shown in Figure 6.10 (b) for the MSE algorithm. Consequently, the reliability of these techniques in a congested dynamic scenario would be questionable due to rapidly changing interferer position and a high possibility of adaptive beamformers not converging in this short time span.
- The techniques that place a null in the direction of interference result in higher sidelobes, often stronger than the main lobe towards the target. An example after the LCMV beamformer has been shown in Figure 6.10 (c), where interferer energy spreads in the sidelobes. This results in a significant reduction in the SINR and makes target detection ambiguous.

Therefore, spatial domain mitigation is particularly challenging, especially in a congested scenario with closely spaced targets and interferers. This has been further investigated in the subsequent sections.

Further in this chapter, without loss of generality, the LCMV beamformer has been used for the detailed analysis due to the following:

1. Better SINR while achieving comparatively lower sidelobes.
2. Trained mitigation technique, which provides the capability of using additional constraints to maximise power from the echo signal's direction and minimise power reception along the direction of the interferer.

The LCMV beamformer minimises the interfering signal, keeping the echo signal undistorted. Furthermore, by imposing several linear constraints to minimise the output variance, the LCMV beamformer offers improved robustness against inaccurate AoA estimates [281].

6.5.2 LCMV Beamformer

The LCMV beamformer uses the AoA of the target(s) and interferer(s) as constraints to compute the adaptive weights. After applying these weights to the received signal, the received power from potential targets is preserved, whereas the interference power and variance are minimised by directing nulls toward these directions. Each constrained direction ϕ has a corresponding SV SV_ϕ. The array response to SV_ϕ can be defined as:

$$\boldsymbol{r}_\phi = \boldsymbol{S}\boldsymbol{V}_\phi^{\,H}\boldsymbol{w} \tag{6-21}$$

where, $\boldsymbol{w}$ represents the complex array weights, and H is the Hermitian operation. With k constraints, the response vector is expressed as:

$$\boldsymbol{R} = [\boldsymbol{r}_{\phi 1}\ \boldsymbol{r}_{\phi 2} \ldots \boldsymbol{r}_{\phi k}] \tag{6-22}$$

The echo signal power is maximised by equating the response from its direction to unity, whereas the interference power is minimised by equating the response from its direction to zero. Adaptive weights are then computed using the following:

$$\boldsymbol{w} = R_{xx}^{-1}\boldsymbol{SV}\left(\boldsymbol{SV}^{H}R_{xx}^{-1}\boldsymbol{SV}\right)^{-1}\boldsymbol{R} \tag{6-23}$$

where, R_{xx} is the spatial correlation matrix of the received signal [282], and

$$\boldsymbol{SV} = \left[\boldsymbol{SV}_{\phi 1}\ \boldsymbol{SV}_{\phi 2}\ \ldots \boldsymbol{SV}_{\phi k}\right] \tag{6-24}$$

If the received signal for chirp '*j*' is represented by x_j, the beamformed signal has been estimated using:

$$\boldsymbol{y}(i,j) = \boldsymbol{w}^{H} \cdot \boldsymbol{x}_j \tag{6-25}$$

where, $\boldsymbol{w} = [\boldsymbol{w}_o\ \boldsymbol{w}_1\ \ldots\ \boldsymbol{w}_{M-1}]$, and M is the number of virtual array elements for the MIMO array and receive elements for the FPA. After applying adaptive weights, the output variance (σ_b) calculated as follows is minimised.

$$\sigma_b = \boldsymbol{w}^{H}R_{xx}\boldsymbol{w} \tag{6-26}$$

This results in the suppression of signal from the constrained direction (direction of interference in the considered case).

The methodology to estimate adaptive weights using an LCMV beamformer has been summarised in Figure 6.11.

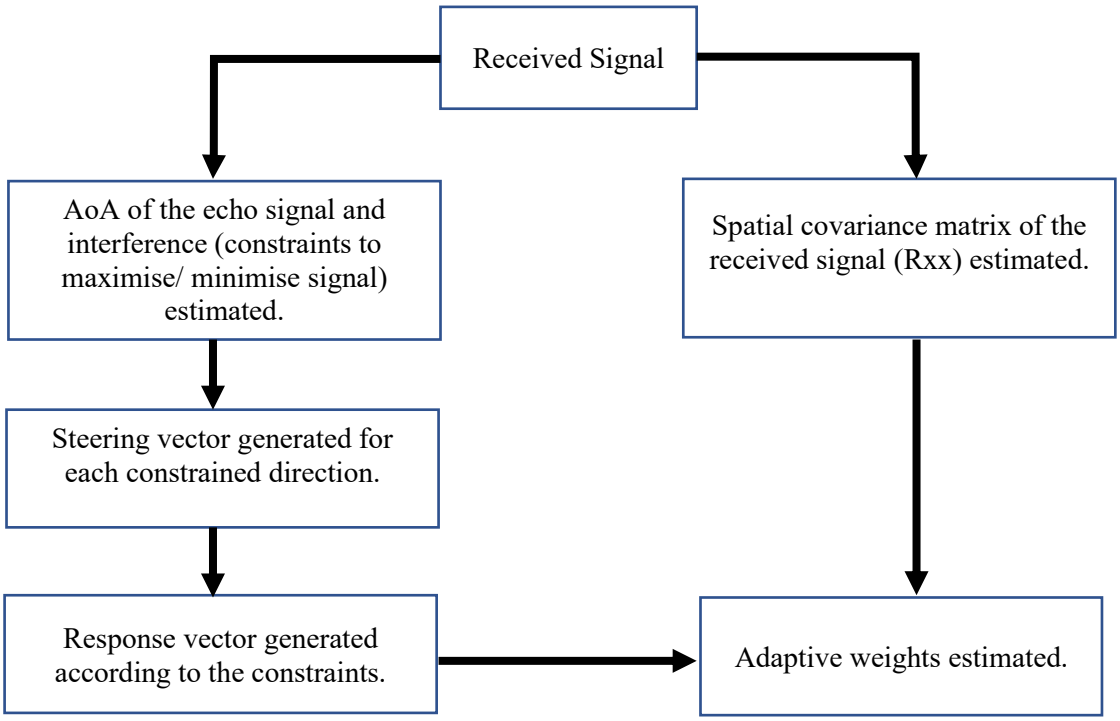


Figure 6.11: Adaptive weight estimation using LCMV beamformer.

To estimate the constraints for LCMV beamformer (AoA of targets and interferers), interference has first been detected using the power detector, discussed in section 5.1.1, followed by the estimation of AoA of the target(s) and interferer(s).

I. AoA of Targets

To determine the AoA of the target(s) (constrained to maximise response), firstly, interference-free samples are detected using power detection methodology in section 5.1.1. Based on this, two techniques have been developed.

1. If the interference-free samples include more than 20% of the total fast-time samples, they are extracted from the received signal across all the antenna elements (samples with amplitude less than the estimated threshold (see section 5.1.1). This is followed by range compression and beamforming (section 2.3.4.III). Finally, a CA-CFAR (section 2.3.4.V) has been applied to estimate the target's AoA.

2. If the interference-free samples include fewer than 20% of the total fast-time samples, the beamformer does not give reliable results due to limited samples. In this case, 256 chirps are transmitted in a frame, and an interference-free chirp is collected across all the antenna elements. Considering the probability of interference in the VR [205] and the results presented in Figure 5.8, there is a good chance of interference-free chirps within a frame of the VR. This is followed by the range compression and beamforming, and finally, CA-CFAR to estimate the target's AoA. This case might occur if a) multiple interference pulses appear within each VR chirp (such as fast chirp interference sequence), or b) interference is semi-synchronous, occupying the most samples of the received signal.

II. AoA of Interferers

Depending upon the number of interferers in the VR's FoV and interference power relative to the echo signal power, the AoA of the interference (constrained to minimise response) has been estimated using the following two techniques:

1. If a single interference pulse appears in the VR chirp with sufficient interfered samples $(> 20\%)$, the samples are identified across the VR's antenna elements. This is followed by high-pass filtering to attenuate the response from the echo signal. The range compression, beamforming, and CA-CFAR are then used to estimate AoA of interferer.
2. In the case of multiple interference pulses within the VR chirp or when interference power is not dominant (left undetected in threshold estimation), the VR is configured to operate in passive 'listening' mode for a duration of one frame, as discussed in section 5.1.2. Any signal received during this period corresponds to interference(s). The range compression, beamforming, and CA-CFAR are then used to estimate the AoA of the interferer. This method also helps to estimate interference power relative to the echo power when the radar is switched back to active mode.

III. Range-Azimuth after Adaptive Beamformer

The following steps have been used to generate the range-azimuth plot with adaptive weights:

1. Normalised array response $\boldsymbol{R}(\theta)$ has been estimated for azimuth angles (θ) within the VR FoV using the following:

$$\boldsymbol{R}(\theta) = \exp\left(-j2\pi d\left(0-(M-1)\right)\frac{\sin(\theta)}{\lambda\sqrt{M}}\right) \tag{6-27}$$

where, M is the number of array elements,

2. The beamformed response $\boldsymbol{R}'(\theta)$ has then been determined by:

$$\boldsymbol{R}'(\theta) = \boldsymbol{w}^{*}\boldsymbol{R}(\theta) \tag{6-28}$$

3. The beamformed signal $\boldsymbol{SB}(i,\theta,j)$ has been estimated using:

$$\boldsymbol{SB}(i,\theta,j) = \boldsymbol{x}(i,j)\boldsymbol{R}'(\theta) \tag{6-29}$$

where, $\boldsymbol{x}$ represents the received signal, and i and j represent the fast-time and the slow-time samples, respectively.

Range compression on $\boldsymbol{SB}(i,\theta,j)$ across the fast-time samples 'i' has been performed to generate the adaptive beamformed range-azimuth plots presented later in the chapter.

6.6 Mitigation in Congested Environment

An automotive environment is inherently congested with multiple targets and interferers having a small angular separation. Moreover, due to the limited DoF in the SoA sensors to suppress interference completely while ensuring the maximum SINR, spatial mitigation is often ambiguous and a subject of discussion in this section.

An example demonstrating array response with LCMV-based adaptive weights has been shown in Figure 6.12. The VR with dual channels receiver and array sizes of 4 and 12 elements have been considered with four interfering sources at 10^o, 25^o, -20^o and -35^o, with a target at 0^o.

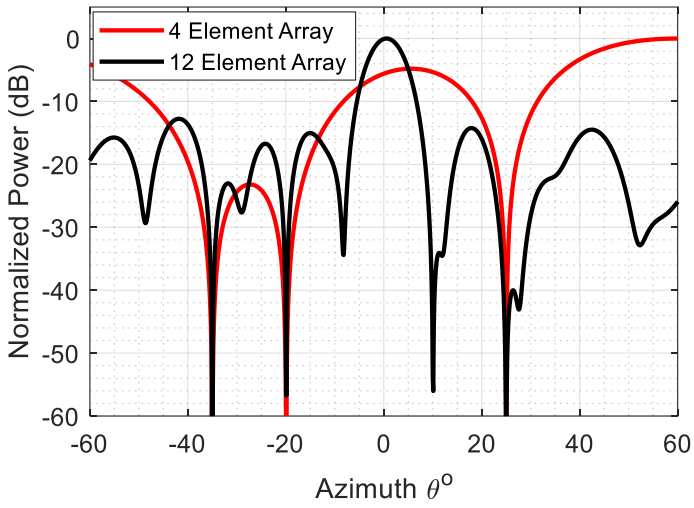
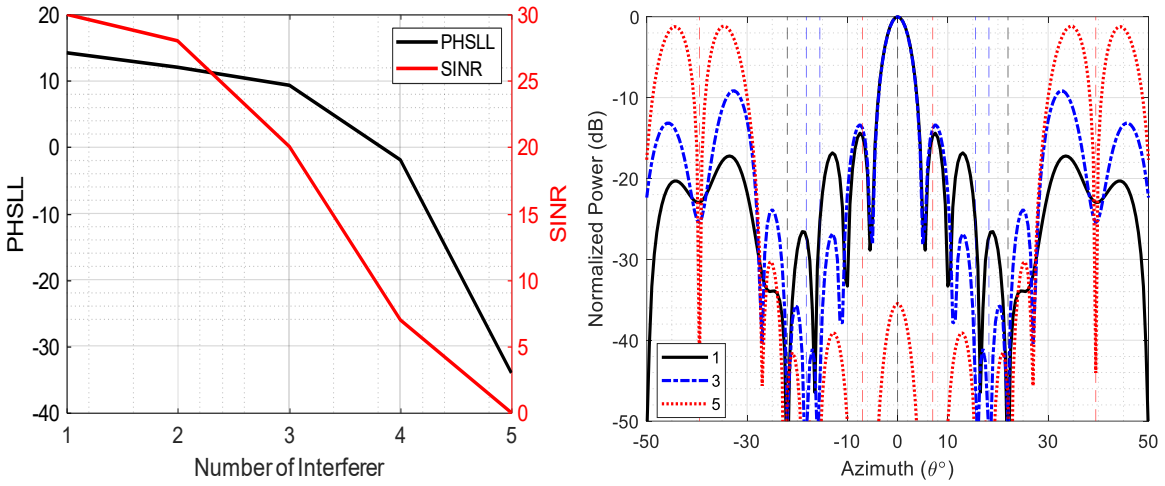


Figure 6.12: Spatial mitigation using LCMV weights showing limited degrees for freedom to suppress all interferers.

In the 12-element array, with potentially 11 DoF, nulls have been placed in the directions of all interferers. However, the interferer at 10^o has not been suppressed in a 4-element array due to limited DoF (3 in this example). Moreover, the SLL is greater than the main lobe, which affects target detectability.

Figure 6.13 (a) gives the PHSLL and SINR as a function of the number of interferers after spatial mitigation. The interferers were randomly positioned in the FoV of the VR. In all the cases, a single target has been positioned at 20 m, 0^o from the VR. A MIMO-based VR with a single channel receiver, $N_{Tx} = 3$, $N_{Rx} = 4$, $T_{sv} = 100\mu s$, $B_{sv} =$ 0.5 GHz, and IR with $T_{\text{sint}} = 27\mu s$, and $B_{\text{sint}} = 0.5$ GHz have been used. The array responses after beamforming with adaptive weights for 1, 3, and 5 interferers are demonstrated in Figure 6.13 (b). The black dotted

line at 0^o shows the target direction, while the remaining dotted lines show the additional direction of nulls for each case, e.g., with 5 interferers, a total of 10 nulls are required for interference suppression.



(a) (b)

Figure 6.13: Interference mitigation in the spatial domain for different numbers of interferers. (a) The PHSLL and SINR as a function of the number of interferers. The PHSLL and SINR values are in dB. (b) Array response after beamforming using adaptive weights for a different number of interferers.

The SINR and PHSLL reduce as the number of interferers increases until a point at which the target at 0^o is no longer detectable. Considering a SINR value of 10 dB for effective target detection, in the demonstrated example, the system performance is dramatically reduced for the number of interferers > 2. Moreover, a large number of nulls leaves an essential portion of the VR's FoV unusable for target detection ($\pm 20^o$ to $\pm 10^o$ in this case).

To validate the developed model, spatial suppression has been performed in an outdoor scenario with multiple targets and interferers in the VR's FoV and presented in Appendix 14. As discussed, spatial mitigation effectiveness degraded in the presence of multiple interferers in the FoV of the VR, thus, deteriorating the radar performance.

6.7 Spatial Mitigation in MIMO and FPA Radar

As discussed earlier, interference in a MIMO array follows the real aperture and spreads over a large FoV. Therefore, a virtual MIMO aperture does not give any additional advantage in the background of interference, as it does for the echo signal where resolution is enhanced.

Interference suppression using LCMV adaptive weights for the case and parameters in section 6.4 has been performed in this section. The primary focus has been on the comparative analysis of adaptive beamformers' performance in MIMO and FPA for which the peak to highest SLL (PHSLL) and SINR have been considered as the evaluation metrics.

Interference suppression in a MIMO radar with well-separated target and interferer has been presented in [192], [216] demonstrating a reasonable performance. However, due to the MIMO array's inherent peculiarity, i.e., a smaller number of N_{Rx} compared to a FPA (with the same angular resolution) and one-way antennas SLL, the performance of an adaptive beamformer for spatial interference suppression becomes less effective. This is especially significant in the scenario with a small spatial separation between the targets and interferers and, at the same time, less investigated.

An example scenario discussed in this section has been demonstrated in Figure 6.4. For a 3 transmit and 4 receive element MIMO radar (used in a specific automotive chipset [39]) with the virtual angular resolution of 9.5^o, the AoA of the interfering source will be in the first sidelobe of the target after beamforming. Placing an adaptive spatial null for interference suppression will be accompanied by various limitations in a MIMO array, which have been evaluated and compared to that of a FPA counterpart.

6.7.1 Dual (I/Q) Channel Receiver

In the I/Q channel receiver, each interferer corresponds to one AoA after beamforming. This configuration is used in a number of COTS chipsets [38].

The radar plots after spatial suppression in the I/Q channels receiver have been presented in Figure 6.14. The AoA normalized by the peak power after beamforming before and after interference suppression for MIMO and FPA has been shown in Figure 6.14 (a) and (b), respectively. Figure 6.14 (c) and (d) show the range-azimuth plot for MIMO and FPA after interference spatial suppression, respectively.

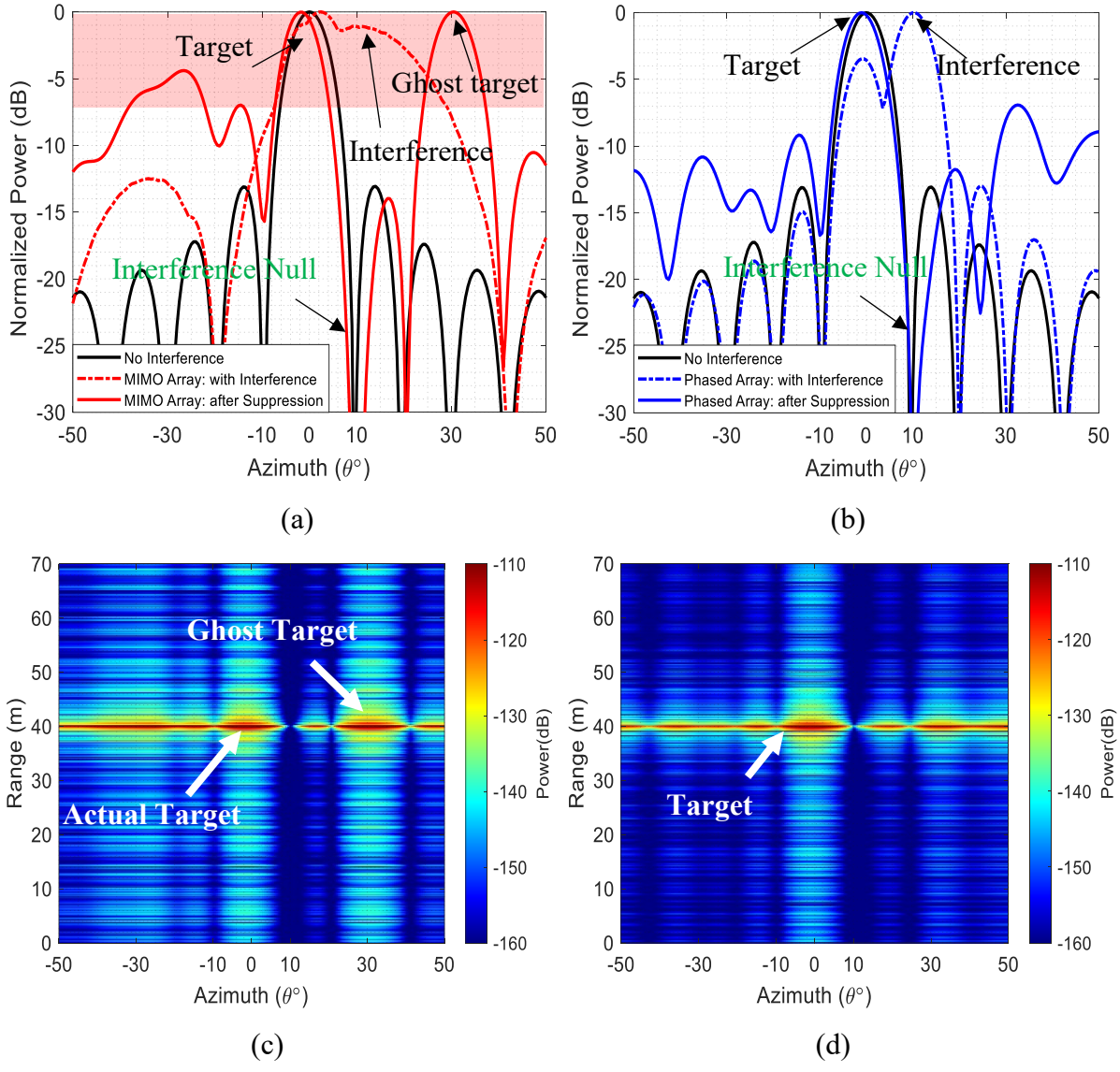


Figure 6.14: Interference suppression using LCMV weights for I/Q channel receiver. The red highlighted region shows MIMO sidelobes greater than FPA sidelobes: (a) AoA for the MIMO array, (b) AoA for the full phase array, (c) range-azimuth plot after spatial suppression for the MIMO array, (d) range-azimuth plot after spatial suppression for the full phased array.

As interference follows the real aperture in the MIMO array, a broader null is directed toward the direction of the interference resulting in higher sidelobes (to conserve the total power distribution) with PHSLL = 0 dB. This makes target detection at 0^o ambiguous. In contrast, the FPA with PHSLL = 7 dB outperforms the MIMO counterpart. The target at 0^o is detectable after suppression. However, a ghost target at 30^o (due to a high SLL) appears in the MIMO array (Figure 6.14 (c)). In comparison, the FPA (Figure 6.14 (d)) has a clear target at 0^o with a reasonable SINR of 7 dB.

Compared to Figure 6.5 (c) and (d), adaptive beamforming by spatial nulls in the interference direction reduces interference by ~40 dB with the suppressed interference floor comparable to the receiver thermal noise floor.

6.7.2 Single (Real only) Channel Receiver

In a single (real) channel receiver, which is also used in a number of COTS chipsets [39], interference corresponds to two AoA's: one towards its true direction, and another one towards the image direction (Appendix 4). This requires two nulls to suppress each interference completely.

Radar plots for this case have been presented in Figure 6.15. Normalized AoA before and after suppression for the MIMO and FPA radars have been given in Figure 6.15 (a) and (b), respectively. In the MIMO array, due to broader interference beams at $\pm\theta$, a further increase in the VR's FoV masked by interference is observed as compared to the I/Q channels receiver case (see Figure 6.15 (c)). Figure 6.15 (c) and (d) shows range-azimuth plots for MIMO and FPA. For the MIMO array, the target at 0^o has been sandwiched between the adjacent wide nulls and suffers a degradation in target echo power after spatial suppression. Interference energy appears in the sidelobes for the MIMO array case and does not reduce to the level of thermal noise floor after mitigation (Figure 6.15 (c)).

Furthermore, due to multiple wide nulls to suppress interference, SLL is even higher in amplitude than the target at 0^o, resulting in ghost targets in the range-azimuth plot at 40 m (Figure 6.15 (c)). However, in the FPA, due to finer $\Delta\theta_{FPA-I}$, lower sidelobes are observed after suppression, and the target is detectable after beamforming with SINR = 12 dB (Figure 6.15 (d), see colour bar). Interference is suppressed to the thermal noise floor in this case.

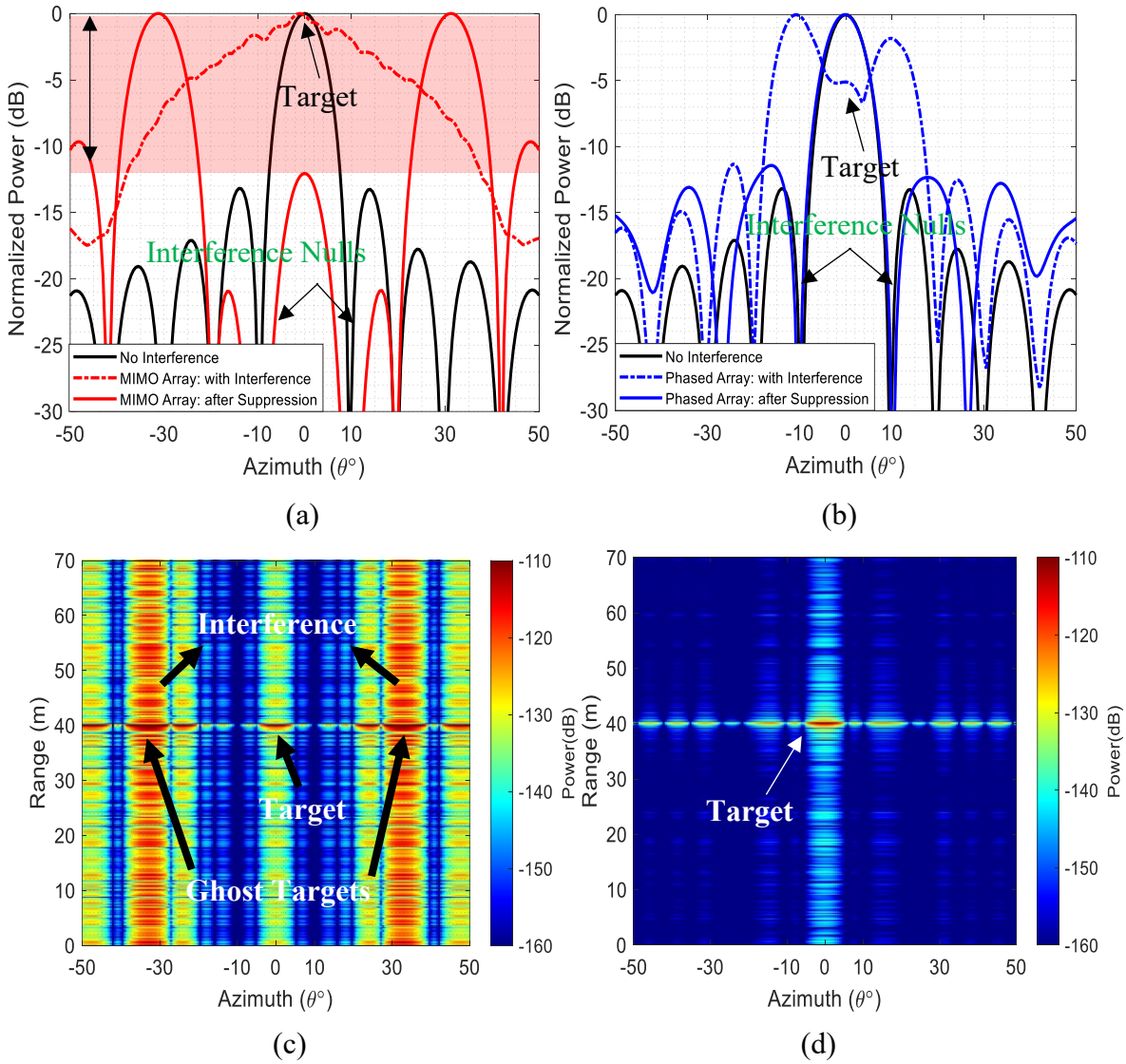


Figure 6.15: Interference suppression using LCMV spatial weights for a single channel victim receiver. Red highlighted region shows MIMO sidelobes greater than FPA sidelobes: (a) AoA for MIMO array, (b) AoA for full phased array (FPA), (c) range-azimuth plot after spatial suppression in MIMO array, (d) range-azimuth plot after spatial suppression in FPA.

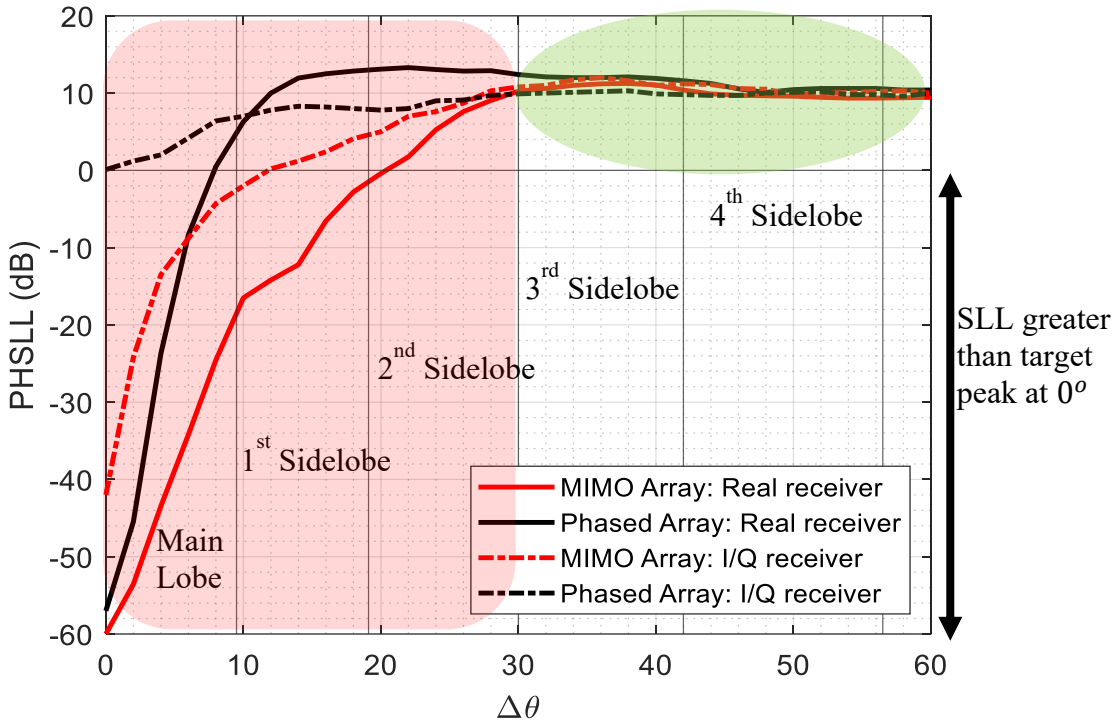
6.7.3 The PHSLL and SINR after Spatial Mitigation

As observed in the preceding sub-section, placing a null closer to the target's angular position in a MIMO array results in higher sidelobes (Figure 6.14 (c) and Figure 6.15 (c)) compared to the FPA (Figure 6.14 (d) and Figure 6.15 (d)). Depending upon the interferer position, sidelobes result in the appearance of ghost targets after spatial filtering. Consequently, target detection becomes ambiguous. Figure 6.16 (a) and (b) show the PHSLL and SINR as a function of the angular separation between the target and interferer ($\Delta\theta$), respectively.

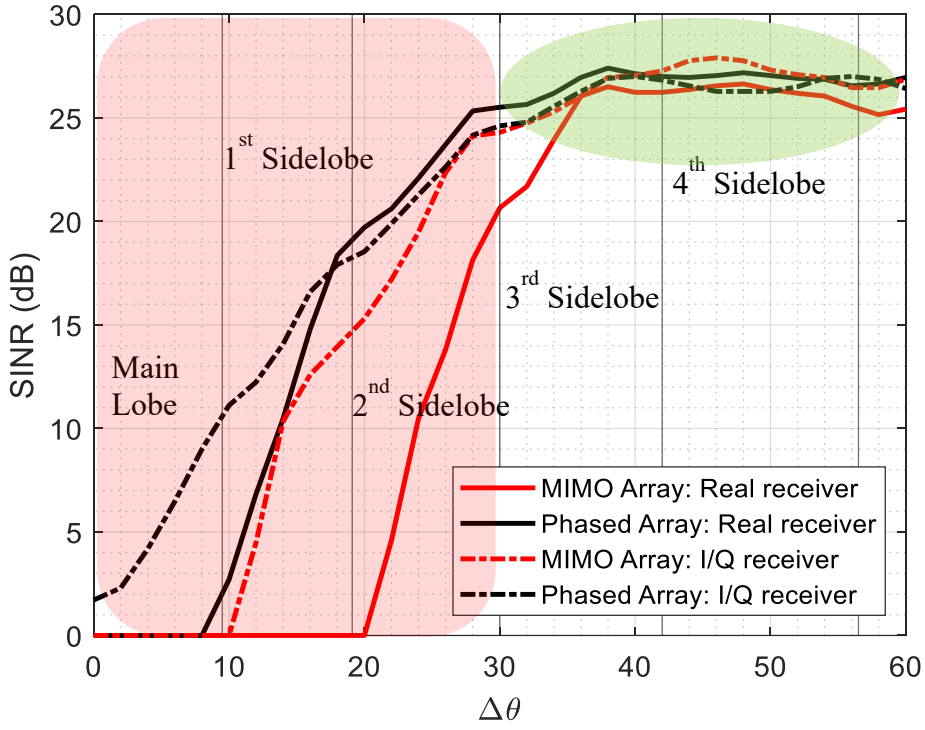
For simplicity, but without loss of generality, a single target and interferer have been considered to generate the results. The target position is fixed at 20 m, 0^o whereas, the interferer position has been changed from 20 m, 0^o to 20 m, 60^o. The range to the interferer is fixed at 20 m to keep its power constant at the VR's antenna input. Maximal power corresponds to the power of the target at 0^o in all cases. The victim and interferer waveform parameters are the same as in section 6.4.

For well-separated targets and interferers with a broader $\Delta\theta$ (interferer in the third sidelobe in the considered case), interference mitigation in the spatial domain with a MIMO array and FPA are comparable in performance. However, as $\Delta\theta$ reduces, especially with interference in the second sidelobe or closer to the target beam – a common automotive scenario, FPA outperforms a MIMO array.

Moreover, in a single channel receiver, with both MIMO and FPA, due to adjacent nulls around the target at 0^o, SLL increases beyond the target beam when a null is placed to suppress interference. In a MIMO array, a blind region is observed from $0^o - 10^o$ with a dual channel receiver (interferer in the main lobe), whereas from $0^o - 20^o$ with a single channel receiver (interferer in the first side lobe).



(a)



(b)

Figure 6.16: (a) Peak to highest sidelobe level (PHSLL) as a function of spatial separation $(\Delta\theta)$ between the target and interferer. (b) SINR vs. spatial separation $(\Delta\theta)$ between target and interferer. Negative PHSLL indicates a sidelobe greater than the target peak.

A broader null to suppress interference in the MIMO array results in a large blind FoV. Any targets in this region might not be detected with a reasonable SINR. Due to one spatial null required in an I/Q channel receiver for complete interference suppression, it has better SLL than a real channel VR, especially when $\Delta\theta$ is close to 0. Additionally, directing a null in the main lobe of the target results in much higher sidelobes and even complete target masking.

The performance of interference suppression in MIMO and FPA radars has been summarised in Figure 6.17 with interference in the main lobe at 8^o, the first sidelobe at 14^o, and the second sidelobe at 28^o of the target beam.

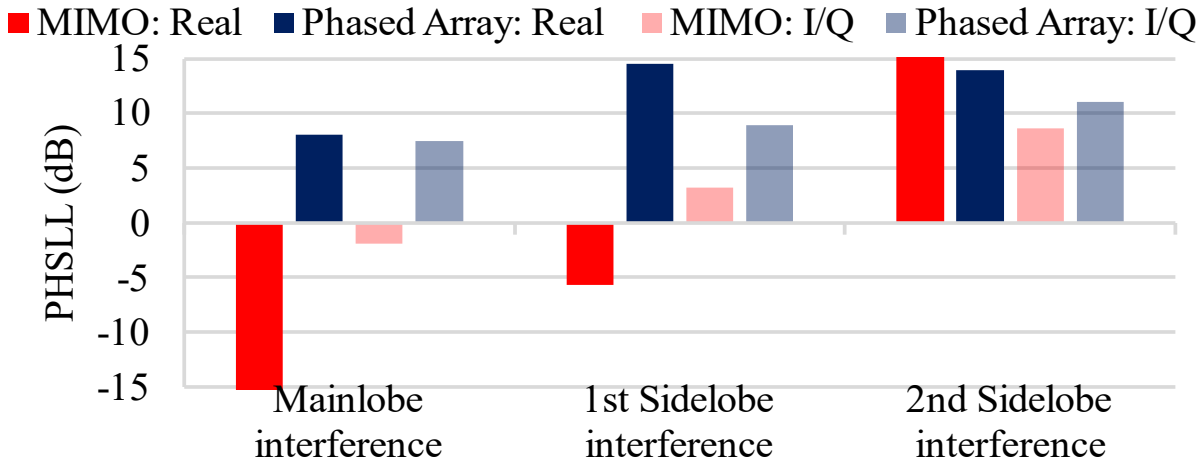


Figure 6.17: Performance analysis of MIMO and full phased arrays.

In terms of interference beamwidth and spatial interference suppression, FPA is more effective than a MIMO array, especially when the interferer is closer to the target.

Although the waveform diversity provided by independent transmit beams offers additional DoF in a MIMO radar, these are not provided in the background of interference, making the MIMO configuration ineffective. Even if a large MIMO array is used, the interference beam (defined by the number of elements in the receive array only) will still be much broader than the target beam, resulting in detrimental effects on the radar's FoV.

In the presented analysis, a single transmit element has been considered for the FPA to match its antenna pattern SLL with the MIMO array. However, increasing the number of transmit elements for the phased array will further reduce the SLL after suppression.

6.8 Limitations of Spatial Domain Mitigation

Adaptive beamforming suppresses the interference to enhance the SINR for precise echo signal detection. However, as discussed in this section, it is more effective in certain scenarios with specific radar configurations. In other cases, it has detrimental effects on radar performance, which have been elaborated on in Appendix 15. Summarising here, spatial domain mitigation is less effective, specifically in automotive conditions, due to the following:

1. Limited degrees of freedom (DoFs) in the SoA automotive radar chipsets to place nulls in the directions of all interferers, especially in congested scenarios.
2. Higher computational complexity and requirement to converge within the radar frame time.
3. Difficult to implement in dynamic road scenarios where AoA of interferers might rapidly change or new interferes might appear. Consequently, the antenna pattern nulls created at the end of frame duration cannot consider these new AoA or interference signals, leading to SINR degradation.
4. Multiple targets and interferers: In the presence of multiple targets and interferers, considering that DoFs are sufficient to place the required number of nulls, any target that is also a source of interference will have a null directed towards it. This suppresses the echo energy, leading to SINR degradation. The effect of the number of interferers on the interference mitigation performance has been analysed and shown in Figure 6.13. A negative PHSLL indicated SLL greater than the main lobe. As observed, spatial domain mitigation is effective only when the number of interferers is small and with a wider separation between the target and the interferer.

6.9 Performance Comparison of Mitigation Techniques

To evaluate the performance of ADBF, the PHSLL and SINR values obtained by spatial mitigation and time domain mitigation have been compared and presented in Table 6.2.

For time domain mitigation, interference has first been detected (section 5.1.1), and then the appropriate time intervals have been replaced by zeros. The VR with $N_{Tx} = 3$, $N_{Rx} = 4$, operating in TDM-MIMO mode with a single channel receiver, $T_{sv} = 102.4$ µs, $B_{sv} = 0.5$ GHz, and 1 ms CPI has been used. A target with 10 dBsm RCS has been positioned at 40 m, 0^o from the VR. Three interference sources with sweep times ∞ (CW), 23 µs, and 1000 µs, and sweep bandwidths 0, 0.5, and 0.2 GHz, respectively, have been positioned at 30 m 7.5^o, 40 m 14^o, and 21 m 22^o from the VR. The interferers appeared in the main lobe, first side lobe, and second sidelobe, respectively. For a single interferer case, the interferer with a sweep time of 1000 µs and bandwidth of 0.2 GHz has been used (21 m, 22^o).

Table 6.2: Performance comparison of time domain and spatial domain mitigation

Performance Metric	**Number of Interferer**	**Value**	
	Before Mitigation		
PHSLL (dB)	0	13.4	
	1	7.3	
	3	5.9	
SINR (dB)	0	32	
	1	7	
	3	5	
	After Mitigation		
		Time Domain	Spatial Domain
PHSLL (dB)	1	12.9	13.4
	3	12.7	-5
SINR (dB)	1	29	30
	3	26	0

The PHSLL and SINR after time domain and spatial domain mitigation are comparable for a single and well-separated interferer. However, as the number of interferers increases, time domain mitigation outperforms spatial domain with much higher PHSLL and SINR.

6.10 Summary

The interference suppression performance of ADBF has been evaluated using the SINR and PHSLL as the performance metrics in the MIMO and FPA configurations. It has been shown that an interfering signal does not follow the virtual aperture and forms a broader beam according to the receive aperture size of the MIMO radar. Thus, after beamforming, ADBF affects interference only with the real aperture size, leading to broader nulls for interference cancellation.

Additionally, it has been discussed that spatial suppression in contemporary MIMO radars works well only for well-separated targets and interferers and matches in performance to the traditional FPA. In the case of a small spatial separation between the target and interferer, due to a broader interference beam in the MIMO array, ADBF performance in the FPA outperforms that in the MIMO array. Consequently, the MIMO array might not give an advantage in the background of interference as it does for the echo signal (resolution enhancement). The performance of ADBF degrades in a typical roadside scenario, with multiple and congested targets and interferers due to limited DoF in the SoA automotive sensors [283].

The ADBF works with both real and I/Q receiver configurations. However, due to the image band fold-back in real channel receivers, complete interference suppression requires more DoF (additional notches in the receiving array pattern) than needed for the I/Q channels receivers. The additional notches in the antenna pattern may lead to SINR degradation.

Lastly, performance evaluation of spatial domain mitigation with the temporal domain mitigation indicated that with a larger number of interferers in the VR's FoV, mitigation in the temporal domain is more effective with better SINR and PHSLL than the spatial domain.

Therefore, it can be concluded that interference mitigation in the spatial domain is highly sensitive to the relative position of the target and interferer, and the available DoF. In an automotive scenario, potential targets such as vehicles are also sources of interference due to the radars installed on them. After implementing spatial domain mitigation, the echo signal energy from these targets is also suppressed and these targets could be lost due to a blind FoV created in the array pattern making target detection ambiguous. Consequently, a reduction in the SINR is expected. Thus, applications of interference mitigation in the spatial domain may be recommended for the following scenarios:

- Non-radiating targets, e.g., pedestrian, roadside clutter and infrastructure, etc. and
- Interference received from directions well outside of an area of radar observation.

Chapter 7. SINR ALONG THE RADAR PROCESSING STAGES

To understand the effect of radar architecture and traffic density conditions on interference detection/ mitigation, it is essential to investigate the SINR enhancement/ degradation as the received signal is processed by the VR. This is the subject of study in this chapter. In general, as discussed in Chapter 3 and Chapter 4, the mean interference power depends on the waveform parameters of the VR and IR and the specific signal processing methodology employed at the VR.

Based on the characteristics of interference identified previously in the presented work, interference power for various radar parameters and configurations using real-road measured data has been estimated across the radar's processing chain. The main contributions of this chapter are:

- A systematic analysis of the SINR at each step of the signal processing chain of the VR. This includes the analogue and digital signal processing stages.
- Demonstrating the SINR improvement using real-time measured data for different orientations of the interfering sensors.
- Assessing the SINR and INR values for various SoA automotive radar chipsets, sensor parameters, configurations, and scenarios.

7.1 MIMO FMCW Processing

The MIMO-FMCW signal processing chain and its effect on interference have been described in detail in sections 3.1 and 3.5. A summary is included in the subsequent paragraphs.

FMCW radar transmits a chirp signal of duration T_{sv} during each PRI. Depending upon the RCS of the target, some part of the incident signal is reflected towards the radar and received by the collocated receiver. A sequence of N_{CPI} chirps is conditionally transmitted from each transmit element of the radar as a Doppler frame with duration $\left(N_{CPI} \cdot PRI\right)$. The phase variation across chirps within a Doppler frame is used to estimate the relative speed of the targets. Moreover, by integrating the chirps returned from the targets, the receiver's dynamic range is enhanced. To resolve the targets along the spatial direction (azimuth angle or cross-range), the radar transmits a signal from multiple transmit elements using either the traditional phased array configuration or the modern MIMO configuration. In MIMO mode, orthogonal signals are transmitted through multiple transmit elements. A synthesized virtual array at the receiver side increases the resolution to $\sim 2/\left(N_{Tx}N_{Rx}\right)$ radians using $N_{Tx}+N_{Rx}$ elements.

As the received signal is processed by the radar, the noise contribution of each stage is added to the signal. The main types of noise in the receiver are thermal noise, quantisation noise at the ADC, and jitter of the quantisation clock [284]. Thermal noise – the most significant noise – is caused by the thermal excitation of the receiver input stages and has a white Gaussian distribution. It has been considered the main contributor to the noise in this chapter.

7.1.1 Block Diagram of Radar Processing Chain

The received signal, composed of echoes and interference, is first processed at the analogue front end (AFE), and then digitised at the ADC. The signal after the ADC has been called the receiver output signal in the presented work. The DSP follows this, where a 3D-FFT has been performed to extract the range, relative speed, and spatial location of the targets.

The simplified block-level diagram of a typical radar receiver used to evaluate the impact of interference along each stage is shown in Figure 7.1. The block diagram represents various

sections of the AFE where the analogue signal is processed followed by the DSP. The range profile, range-Doppler, and range-azimuth have been obtained after estimating the phase variation across each dimension of the radar data cube (section 2.3.4.II).

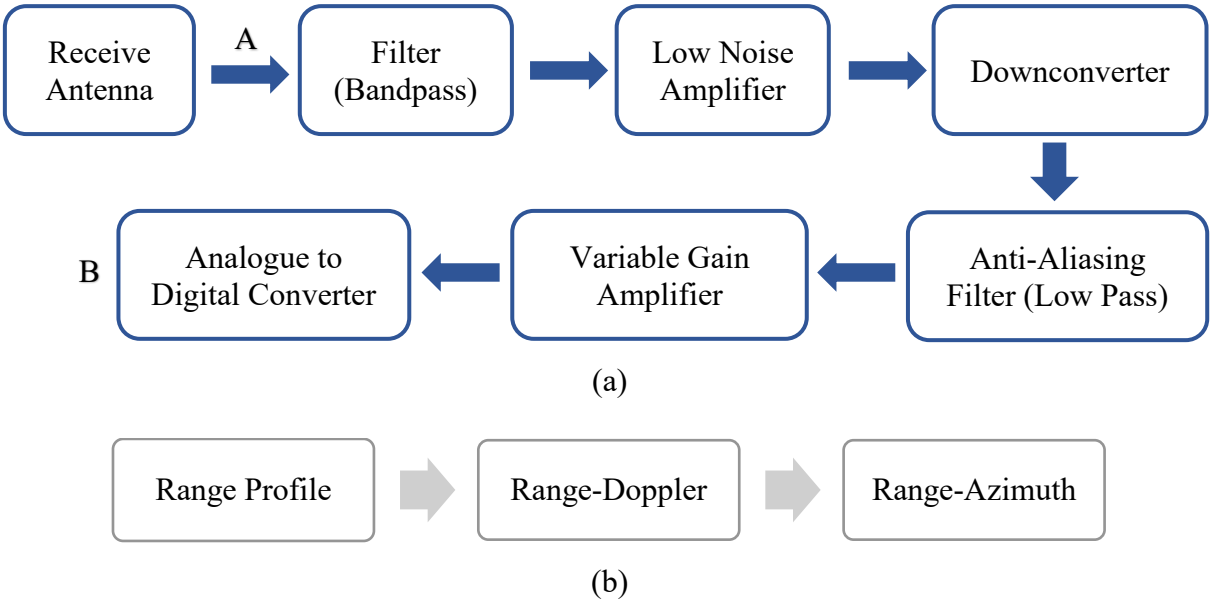


Figure 7.1: Block diagram of a typical radar system with processing steps: (a) analogue front end, (b) digital signal processing.

7.2 SINR Improvement

It has been discussed in Chapter 4 that for most of the types of interference, the echo signal and interfering signal have different statistics which depends upon the waveform parameters of the VR and IR. For most practical road scenarios, the statistics of interference are more comparable to the random Gaussian noise (Figure 4.9). Consequently, the effect of each processing stage on the echo signal and interference will be different and assessed in this section.

7.2.1 Receiver Input

At the input of the VR receiver, shown as point 'A' in Figure 7.1 (a), considering free-space propagation, the echo signal received from a point target located at (θ,φ) where θ and

φ are the azimuth and elevation angles of the target with respect to the VR, respectively, is given as follows:

$$P_R(\theta,\varphi)=\frac{P_{Tx}G_{Tx}(\theta,\varphi)\cdot G_{Rx}(\theta,\varphi)\lambda^2\sigma}{(4\pi)^3 R_T{}^4 L_P} \tag{7-1}$$

where, P_{Tx} is the transmitted power of the VR, $G_{Tx}(\theta,\varphi)$ and $G_{Rx}(\theta,\varphi)$ are the transmit and receive antenna gains of the VR as a function of the target's position in space, respectively, σ is the RCS of a non-fluctuating target, R_T is the range to the target, and L_p accounts for additional propagation losses including the loss due to improper alignment of the VR and the target.

Interference received at the VR has a one-way propagation path from the source of interference located at $(\theta_{\text{int}},\varphi_{\text{int}})$, where θ_{int} and φ_{int} are the azimuth and elevation angles of the interferer with respect to the VR. The interference power (P_{RInt}) at the VR's receiver input is given as:

$$P_{RInt}(\theta_{Int},\varphi_{Int})=\frac{P_{TxInt}\cdot G_{TxInt}(\theta_{Int},\varphi_{Int})\cdot G_{Rx}(\theta_{Int},\varphi_{Int})\cdot\lambda^2}{(4\pi R_I)^2\cdot L_P} \tag{7-2}$$

where, P_{TxInt} is the transmitted power of the IR, $G_{TxInt}(\theta_{Int},\varphi_{Int})$ is the transmit antenna gain of the interferer transmitter as a function of its position, $G_{RxInt}(\theta_{Int},\varphi_{Int})$ is the receive antenna gain of the VR as a function of interferer position, and R_I is the range to interferer.

The signal to interference ratio (SIR) at the input of receiver (SIR_A) is estimated as:

$$SIR_A=\frac{P_R(\theta,\varphi)}{P_{RInt}(\theta_{Int},\varphi_{Int})}=\frac{P_{Tx}G_{Tx}(\theta,\varphi)G_{Rx}(\theta,\varphi)\sigma R_{\text{I}}^2}{4\pi R_T{}^4 P_{TxInt}G_{TxInt}(\theta_{Int},\varphi_{Int})G_{Rx}(\theta_{Int},\varphi_{Int})} \tag{7-3}$$

Due to the one-way propagation loss of interference compared to the two-way echo signal loss, interference power in most cases will be stronger.

7.2.2 Receiver Output

The signal (plus interference) at the receiver output, point '*B'* in Figure 7.1 (a), passes through multiple stages of the AFE, where the signal is amplified, filtered, down-converted, and then digitised. Each stage also contributes to the total noise power level.

The approximate power contribution of the AFE $\left(P_{AFE}\right)$ has been estimated as follows:

$$P_{AFE} = G_{LNA} + G_{VGA} + L_{Mixer} + P_{FS} + G_{ADC} \tag{7-4}$$

where, G_{LNA} and G_{VGA} are the gains of the low noise amplifier (LNA) and the variable gain amplifier (VGA), respectively, $L_{Mixer} = 20\log\left(0.5\right)$ is the loss due to double sideband to single sideband conversion at the mixer, P_{FS} represents the full-scale ADC input power after which the signal's power is clipped. The ADC gain is estimated as [285] follows:

$$G_{ADC} = 6.02N_{ADC} + 1.74 \tag{7-5}$$

where N_{ADC} is the number of ADC bits.

Through the AFE, the echo signal and interference appear as well-defined sinusoidal and chirp-like LFM signals, respectively. Therefore, the AFE has a similar effect on the echo signal and interference. Consequently, the equivalent gain in SIR is close to 0, resulting in $SIR_B = SIR_A$, where SIR_B represents SIR at the output of the receiver.

The power spectral density (PSD) of noise at the output of the receiver per Hz bandwidth is defined as follows:

$$P_{Noise} = kT_{Eff} \tag{7-6}$$

where, k is the Boltzmann constant, $T_{Eff} = T_{Ant} \cdot N_F$ is the effective noise temperature at the output of the receiver in Kelvin, T_{Ant} is the noise temperature at the antenna in Kelvin, and N_F

is the combined noise figure of the receiver AFE. The noise figure of the LNA will have the most significant contribution as it is the first stage of the AFE [286].

In most cases, interference power dominates the receiver noise i.e., $INR \gg 1$, and is the main contributor in defining the INR at the subsequent stages of a victim receiver. Consequently, $SINR = SIR$. However, if $INR < 1$, the interference power will be smaller than the noise power, leaving $SINR = SNR$. In the forthcoming discussion, it has been assumed that the received interference power is stronger than the noise power i.e., $P_{RInt}\left(\theta_{Int},\varphi_{Int}\right) > P_{Noise}$.

Based on these, SNR_B, $SINR_B$, INR_B at the output of the receiver have been estimated as follows:

$$\begin{aligned} SNR_B &= \frac{P_R(\theta,\varphi)\cdot P_{AFE}}{P_{Noise}} = \frac{P_{Tx}G_{Tx}(\theta,\varphi)G_{Rx}(\theta,\varphi)\lambda^2\sigma\cdot P_{AFE}}{(4\pi)^3 R_T{}^4 L_P k T_{Eff}} \\ SINR_B &= \frac{P_R(\theta,\varphi)\cdot P_{AFE}}{P_{RInt}\left(\theta_{Int},\varphi_{Int}\right)\cdot P_{AFE}} = \frac{P_{Tx}G_{Tx}(\theta,\varphi)G_{Rx}(\theta,\varphi)\sigma R_I^2}{4\pi R_T{}^4 P_{TxInt}G_{TxInt}\left(\theta_{Int},\varphi_{Int}\right)G_{Rx}\left(\theta_{Int},\varphi_{Int}\right)} \\ INR_B &= \frac{P_{RInt}\left(\theta_{Int},\varphi_{Int}\right)\cdot P_{AFE}}{P_{Noise}} = \frac{P_{TxInt}G_{TxInt}\left(\theta_{Int},\varphi_{Int}\right)G_{Rx}\left(\theta_{Int},\varphi_{Int}\right)\lambda^2\cdot P_{AFE}}{(4\pi R_I)^2 L_P k T_{Eff}} \end{aligned} \quad (7\text{-}7)$$

During the first step of pulse compression, the received signal is mixed with the transmitted signal to form an intermediate frequency signal, as shown in (3-18) and (3-22) for the echo signal and interference, respectively. After this, a LPF attenuates the higher frequencies and also limits the interference duration.

After being processed at the AFE, the received radar data is organized as a radar data cube. In the digital domain, the 3D-FFT has been performed on the radar data cube to generate the radar imagery in each domain (range, range-Doppler, range-azimuth). The DSP has been discussed in the following sections based on the real-road radar data collected during a series of experiments according to the defined use-cases detailed in Appendix 11.

7.3 Use-Cases for the SINR Assessment

The example cases have been presented in this section where the SINR after each processing stage of the VR is analysed for the two interference sources:

1. Radar 1: Forward-looking TI AWR1243 radar [38], and
2. Radar 2: Corner-looking NXP Dolphin radar [39].

The interfering radars have different orientations and waveform parameters wrt. the VR. At a time, only one interfering radar has been switched on to estimate the effect of the IR orientation and its waveform parameters on the performance of the VR. The VR is a forward-looking INRAS Radarlog RDL-77G-TX4RX16-D02 [91], operating in TDM-MIMO mode. The measurement setup is shown in Figure 7.2. In the designed setup, the vehicle with interfering radars is parked at 11.5 m from the VR in the adjacent lane with a lane width of 3.6 m.

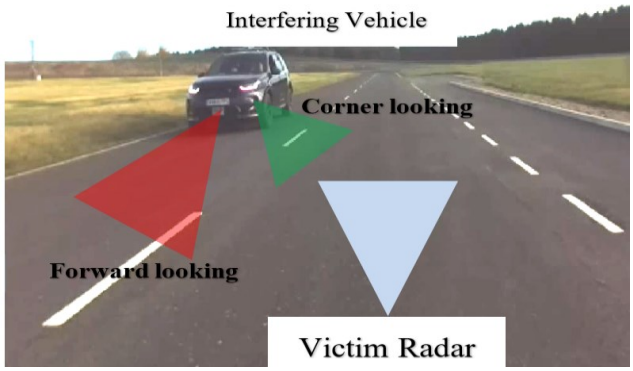


Figure 7.2: Measurement setup for the SINR analysis in real road conditions.

For the considered example, each VR frame has been generated after 128 ms of data collection, where 512 victim chirps are transmitted sequentially from the 4 transmit elements of the VR. 128 chirps have been used for the Doppler processing (Doppler frame). For Radarlog, the virtual array of 64 elements is formed. However, the antenna elements arrangement is such that the synthesised virtual array has 3 overlapping antenna elements. After removing these elements, an equivalent virtual array of 61 channels has been formed. This constitutes an azimuth/ beamform frame over which beamforming has been performed.

The parameters and configurations of the victim and interfering sensors used for the SINR estimation have been given in Table 7.1.

Table 7.1: Sensor parameters for the SINR analysis.

Parameter	Value	Unit
L_p + Alignment Errors	5	dB
Victim Radar		
Centre Frequency	76.5	GHz
Wavelength	0.0039	m
Peak transmit power: P_{Tx}	10	dBm
Transmit antenna gain: G_{Tx}	14	dBi
Receive antenna gain: G_{Rx}	14	dBi
G_{LNA}	42	dB
G_{VGA}	20	dB
N_{ADC}	12+4	bits
ADC Gain: G_{ADC}	98.06	dB
Mixer Loss	20log(0.5) = - 6	dB
V_{FS}	$\pm 1V$	peak to peak
P_{FS} (1V peak full-scale amplitude to W)	$\frac{\left(\frac{1}{\sqrt{2V_{pk}}}\right)^2}{50}$ = - 20 dBW	W/50ohm
P_{AFE}	164	dBm
Array Configuration	4 Tx* 16 Rx	Elements
Configuration	TDM-MIMO	
Receiver Type	Real Channel	
N_F	14	dB
Sweep Time	204.8	µs
Bandwidth	1	GHz
$N_{FastFFT}$	2048	points
$N_{SlowFFT}$	128	points
N_{AzFFT}	512	points
T_{Ant}	290	K
Window: Fast-Time	Blackman Harris	
Window: Slow-Time	Hann	
Window: Azimuth	Hann	

Interferer Radar			
	Radar 1 (IR1)	Radar 2 (IR2)	Unit
Peak transmit power: P_{TxInt}	10	10	dBm
Centre Frequency	76.5	76.5	GHz
Wavelength	0.0039	0.0039	m
Transmit antenna gain (Considering antenna orientation in VR direction)	9	5	dBi
Receive antenna gain (Considering antenna orientation in IR direction)	14.4	10	dBi
Sweep Time	250	102.4	µs
Bandwidth	0.95	1	GHz
Measured T_{INT}	16	3.3	us
Active duty-cycle	98	48	%
$W^{*}_{Fast-FFT}$	13	10	dB

A comparatively lower value of the probability of interference occurrence $\left(PR_{\text{int}}\right)$ has been observed for both the interfering sensors. Various factors impact PR_{int}, which includes a random idle time between the chirps and frames (configurable in the software [288]), potential frequency and sweep time jitter, time to reset ADCs before each new transmission, switching time between the transmit antenna elements in MIMO configuration [265], a limited active-duty cycle to ensure smooth data transfer from the radar to the capturing PC.

Due to a relatively low active duty cycle of radar 2 (Table 7.1), PR_{int} for IR2 is smaller compared to the interference received from radar 1. With the defined parameters of the interfering radars, the probability of occurrence of interference $\left(PR_{\text{int}}\right)$, averaged over 10 VR frames, has been given in Table 7.2. For comparison, the modelled PR_{int} for the two interfering sensors is also shown.

Table 7.2: Probability of occurrence of interference $\left(PR_{\text{int}}\right)$.

	Radar 1		**Radar 2**	
	Model	Measurement	Model	Measurement
Full frame: 512 chirps (% interfered chirps)	180 (35%)	176 (34%)	152 (29%)	147 (28.7%)
Doppler Frame: 128 chirps (% interfered chirps)	52 (40%)	49 (38%)	35 (27%)	31 (24%)
Azimuth Frame: 61 chirps (% interfered chirps)	28 (43%)	25 (39%)	19 (29%)	17 (26%)

As expected, the probability of interference is reasonably small for both the interfering sources. Next, the results in different domains have been presented and assessed.

7.3.1 Range Profile of Interference

Each VR chirp of duration 204.8 µs is sampled with F_s = 10 MSps. Therefore, each PRI contains 2048 samples, over which range compression has been performed.

After the FFT, the usable frequency range can be expressed as: 0 - F_{Max}, where F_{Max} in a single (real only) channel receiver is $F_{Max} = F_s/2$ [289]. In the absence of spectral windowing, the resolution of each frequency bin $\left(FFT_{BW}\right)$ is defined by $F_s/N_{FastFFT}$ [20], that sweeps across the entire frequency spectrum where $N_{FastFFT}$ is the number of fast-time FFT points. Therefore, the FFT processing gain $\left(G_{FFT}\right)$ can be estimated as follows:

$$G_{FFT} = \frac{F_{Max}}{FFT_{BW}} = \frac{\frac{F_s}{2}}{\frac{F_s}{N_{FastFFT}}} = \frac{N_{FastFFT}}{2} \tag{7-8}$$

[20] Windowing function widens the FFT bin and reduces the resolution as discussed in section 2.3.4.IV.

As shown in (3-18), the beat frequency corresponding to the echo signal is a constant frequency tone. Depending upon the FFT resolution, it generally occupies a single frequency (range) bin in the range profile. In contrast, for a majority of the cases, interference being time-limited spreads across multiple frequency bins. The spread of interference in the frequency domain depends upon the waveform parameters of the VR and IR (section 3.4). This is defined by the time-dependent second term in (3-22), expressed as $\left(K_v - K_{\text{int}}\right)t$.

Based on this, the number of frequency bins with interference $\left(N_{INT}\right)$ times the FFT resolution $\left(1/T_{sv}\right)$ should be equal to $\left(K_v - K_{\text{int}}\right)T_{sv}$. Therefore,

$$N_{INT} \cdot \frac{1}{T_{sv}} = (K_v - K_{\text{int}}) \cdot T_{sv} \qquad (7\text{-}9)$$

$$N_{INT} = (K_v - K_{\text{int}}) \cdot {T_{sv}}^2$$

$$N_{INT} = \left(K_v - K_{\text{int}}\right) \cdot {T_{sv}}^2 \qquad (7\text{-}10)$$

For a larger value of N_{INT} , interference spreads over a larger number of frequency bins and, therefore, has a wide spectrum but with a reduced mean interference power.

Furthermore, the window has also been applied across the fast-time (the Blackman-Harris window) to reduce the spectral leakage due to signal discontinuities. As discussed in section 5.4, if the instantaneous time of interference occurrence is other than the centre of a victim chirp, depending upon the temporal position of interference, interference power is also attenuated due to the applied window to the time domain signal. This loss has been expressed by $W^*_{FastFFT}$.

The white thermal noise spreads across all the frequency bins, and the equivalent noise power per frequency bin depends upon the frequency resolution [290], that in a real-only channel receiver is defined as:

$$P_{Noise} = kT_{Eff}\left(\frac{N_{FFT}}{2}\right).\frac{1}{T_{sv}} \tag{7-11}$$

where, $1/T_{sv}$ is the noise bandwidth per FFT bin [291], and kT_{Eff}/T_{sv} defines the thermal noise floor level.

The SINR and INR in the range profile, represented as $SINR_R$ and INR_R, respectively are given as:

$$\begin{aligned} SINR_R &= SINR_B.\frac{G_{FFT}}{\frac{G_{FFT}}{N_{INT}\cdot W^*_{FastFFT}}} = SINR_B \cdot N_{INT} \cdot W^*_{FastFFT} \\ INR_R &= INR_B \frac{\frac{G_{FFT}}{N_{INT}\cdot W^*_{FastFFT}}}{\frac{G_{FFT}}{T_{sv}}} = INR_B \frac{T_{sv}}{N_{INT}\cdot W^*_{FastFFT}} \end{aligned} \tag{7-12}$$

An example of the range profile for one victim chirp across one receive channel and augmented range-time plot for the VR frame of 128 ms in the background of interference from radar 1 (TI AWR1243) have been shown in Figure 7.3 (a) and (b), respectively. Similar plots in the background of interference from radar 2 (NXP Dolphin) have been shown in Figure 7.3 (c) and (d), respectively.

Compared to the interference from radar 2, due to a higher active frame duration from radar 1, PR_{INT} from IR1 is higher, as can be visually seen in Figure 7.3 (b) and (d), and presented in Table 7.2. Moreover, the interference floor defined by IR1 is higher (~ -64 dBm mean interference power) compared to that defined by IR2 (~ -72 dBm mean interference power) due to the forward-looking orientation of IR1.

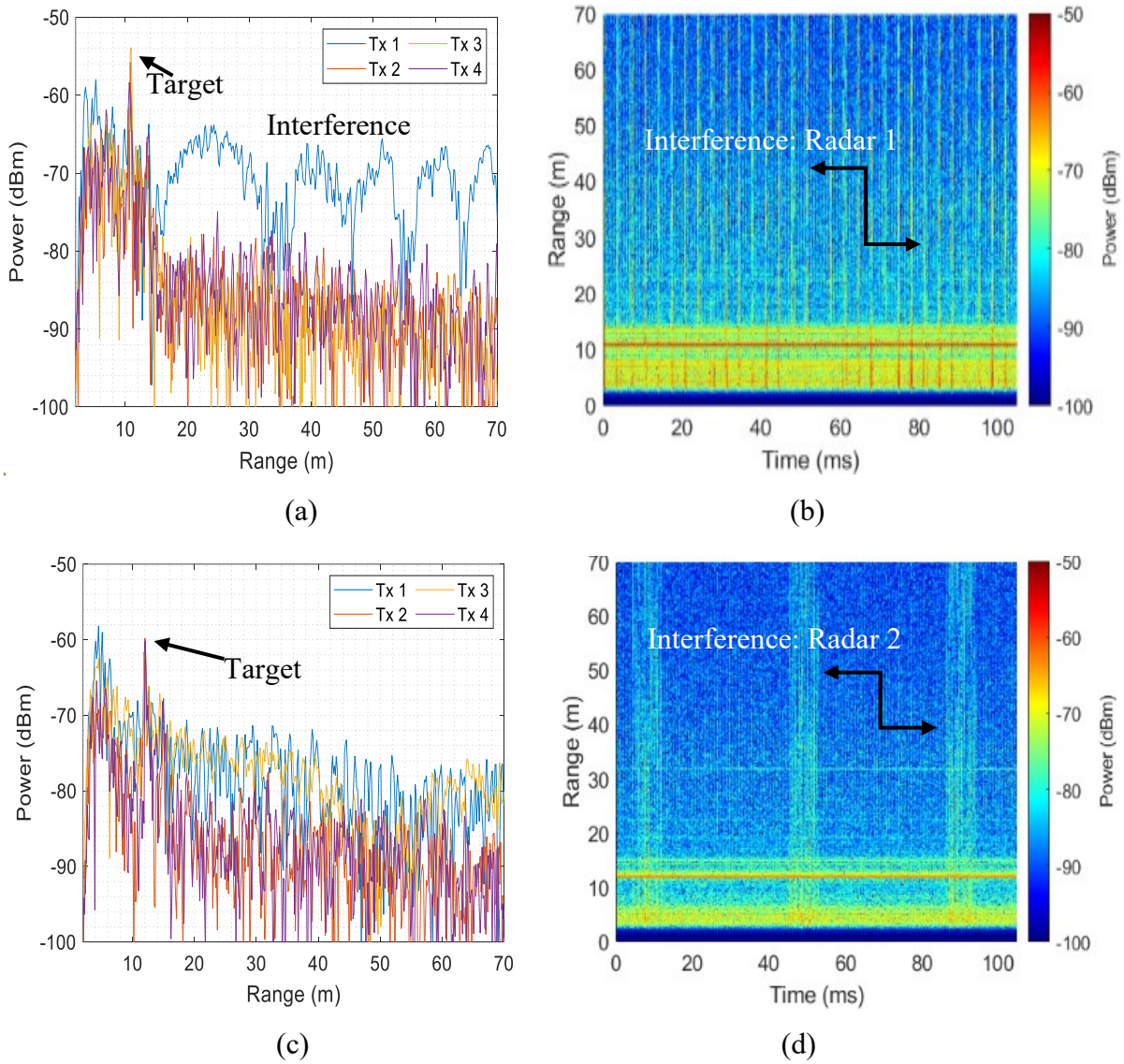


Figure 7.3: Radar plots in the range domains for the defined use cases: (a) range profile of interference from radar 1, (b) range time of interference from radar 1, (c) range profile of interference from radar 2, (d) range time of interference from radar 2.

In the I/Q channels receiver, an interference power reduction by a factor of 2 is expected (Appendix 6). In the forthcoming discussion, without loss of generality, a single (real-only) channel receiver has been considered.

7.3.2 Range-Doppler Representation of Interference

The received chirps are integrated over a CPI during the Doppler compression. After integration, the echo signal power increases by N_{CPI}^2 times if it is coherent across the integrated

chirps within a Doppler frame. The noise, being a random process, is non-coherent across the chirps. Therefore, its power increases by N_{CPI} times.

As discussed in Chapter 4, for a majority of the cases, interference is non-coherent across the victim chirps within a Doppler frame (Figure 4.9). Therefore, similar to noise, interference power should increase by N_{CPI} times if all the victim chirps within the CPI are interfered with.

However, in a realistic automotive scenario, as shown in Table 7.2 and Figure 7.3, due to the factors such as multiple radar manufacturers – leading to different hardware configurations and waveform parameters, – the chirps from the interference source interfere with only a subset of N_{CPI} within each Doppler frame, represented as $N_{CPI-INT}$. $N_{CPI-INT}$ is the number of VR chirps within a Doppler frame that are being interfered with, and $N_{CPI-INT} \leq N_{CPI}$. This defines the probability of interference occurrence in a Doppler frame $\left(P_{INT}\left(CPI\right)\right)$, defined as:

$$P_{INT}(CPI) = \frac{N_{CPI-INT}}{N_{CPI}} \tag{7-13}$$

Based on $P_{INT}\left(CPI\right)$, the following cases can occur:

1. If $P_{INT}\left(CPI\right) = 0$, none of the VR chirps within a Doppler frame has interference. This results in zero interference power and SINR = SNR.
2. When $P_{INT}\left(CPI\right) = 1$, $N_{CPI-INT} = N_{CPI}$, and all the VR chirps within a Doppler frame interfere. This results in maximum interference power in the range-Doppler profile.
3. In most cases, $N_{CPI-INT} < N_{CPI}$.

The SINR and INR in the range-Doppler profile, represented as $SINR_{RD}$ and INR_{RD}, respectively have been estimated as:

$$SINR_{RD} = SINR_R \cdot \frac{N_{CPI}^{\ 2}}{P_{INT}(CPI) \cdot N_{CPI}} = SINR_R \cdot \frac{N_{CPI}}{P_{INT}(CPI)}$$
$$INR_{RD} = INR_R \cdot \frac{P_{INT}(CPI) \cdot N_{CPI}}{N_{CPI}} = INR_R \cdot P_{INT}(CPI) \quad (7\text{-}14)$$

The range-Doppler maps for the discussed use cases have been shown in Figure 7.4 (a) and (b) for interference from radar 1 and 2, respectively. Due to different orientations and radar parameters of radar 1 (forward-looking) and radar 2 (corner-looking) with respect to the VR, average interference powers of -54 dBm and -63 dBm have been observed for interference received from radar 1 and radar 2, respectively.

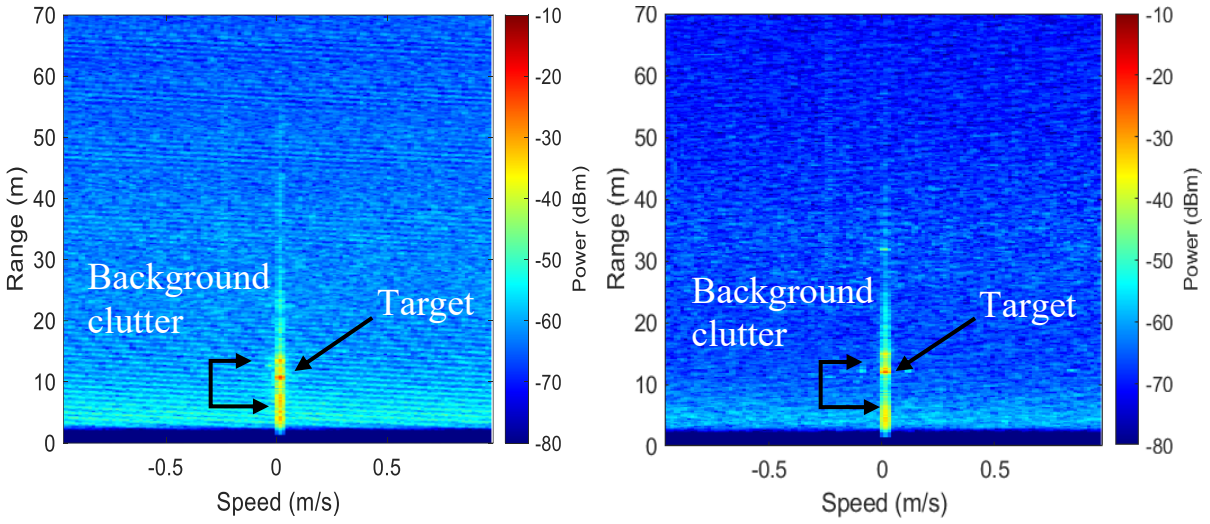


Figure 7.4: Range-Doppler plots for the SINR analysis: (a) radar 1, (b) radar 2.

7.3.3 Spatial Domain Representation of Interference

Spatial compression is performed across the VR antenna elements to a) resolve targets along the spatial axis and b) estimate the spatial position of the targets.

The echo signals and interfering signals are received by multiple receive elements of the VR (with a different phase shift, depending upon the AoA). Therefore, at the VR with a single transmit and N_{Rx} receive elements, the signal and interference power increases coherently after

beamforming (spatial compression) by N_{Rx}^2 times. However, SoA radars have multiple transmit elements to improve the azimuth resolution of the targets and enhance the SNR.

As discussed in Chapter 6, there are two main antenna configurations: a) phased array and b) MIMO array. Depending upon the mode of signal transmission, the interference power after beamforming varies and is discussed next.

I. Phased Array Configuration

In the phased array configuration, the beam resolution is defined by the receive elements of the VR only. Therefore, the echo signal power increases by N_{Rx}^2 times after beamforming. The noise being incoherent across the receive channels has N_{Rx} times increase in power.

The receive channels of the VR receive interference coherently. This has been explained in Table 7.3 for the typical automotive radar parameters [235], [265].

Table 7.3: Time shift and sampling interval for long and short-range radar.

Parameter	**Long Range Radar**	**Short Range Radar**
Maximum Detection Range (*d*)	200 m	40 m
Field of view (ϕ)	$\pm 5^o$	$\pm 80^o$
Time shift across antenna element $(d\sin(\phi)/c)$	58 ns	131 ns
Sampling Frequency (F_s)	16 MSps	5 MSps
Sampling Interval $(1/F_s)$	63 ns	200 ns

The sampling intervals for both the LRR and SRR are greater than the time shift across the antenna element. Therefore, it can be assumed that interference will be received at a similar time sample of each chirp within the azimuth frame, but with a different phase shift. Therefore, for the azimuth frame, the probability of interference occurrence in the azimuth frame $(P_{INT-PA}(Az))$ is binary, i.e., either all the victim chirps have interference, or no victim chirp has interference. This can be expressed as follows:

$$P_{INT-PA}(Az) = \begin{cases} 0 & \mathrm{N_{INT\text{-}PA}} = 0 \quad \text{No interference} \\ 1 & \mathrm{N_{INT\text{-}PA}} = \mathrm{N_{Rx}} \quad \text{Interference across all receive channels} \end{cases} \tag{7-15}$$

where N_{INT-PA} represents the number of VR chirps within an azimuth frame with interference. Interference power increases by N_{INT-PA}^2 after beamforming for $P_{INT-PA}(Az) = 1$. For $P_{INT-PA}(Az) = 0$, interference power will be zero and SINR = SNR, whereas INR = 0.

Moreover, in a single (real only) channel receiver, the interference power spreads along two angles. Consequently, the interference power is reduced by a factor of 2 towards the true AoA. In the I/Q channels receiver, as interference energy is focused on the actual AoA only, this additional reduction in interference power is not observed.

The SINR and INR for $P_{INT-PA}(Az) = 1$, in a phased array configuration, expressed as $SINR_{RA-PA}$ and INR_{RA-PA}, respectively are expressed as follows:

$$\begin{aligned} SINR_{RA-PA} &= SINR_{RD} . \frac{N_{Rx}^{\ 2}}{\frac{N_{Rx}^{\ 2}}{2}} = SINR_{RD} \cdot 2 \\ INR_{RA-PA} &= INR_{RD} . \frac{\frac{N_{Rx}^{\ 2}}{2}}{N_{Rx}} = INR_{RD} . \frac{N_{Rx}}{2} \end{aligned} \tag{7-16}$$

II. MIMO Configuration

In the MIMO array configuration, to achieve orthogonality between the transmit signals, SoA automotive radars use two approaches [292]:

a) BPM – MIMO

In the binary phase modulation (BPM) MIMO, the transmit elements of the VR transmit simultaneously from each transmit element, but with a different phase shift. This results in orthogonality between transmit signals and the received signal corresponding to each transmitter can be identified. Similar to TDM-MIMO, the beam resolution is defined by the

virtual elements of the VR, and each azimuth frame consists of $N_{Tx}N_{Rx}$ elements. After beamforming, the echo signal power increases by $\left(N_{Tx}N_{Rx}\right)^2$ times. The noise power after the spatial compression increases by $N_{Tx}N_{Rx}$ times due to noise samples being incoherent across the azimuth frame.

As the chirps from multiple transmitters are transmitted in a similar time slot, after virtual array formation, it can be assumed that interference is received coherently across the VR chirps (Table 7.3). Similar to the phased array configuration, the probability of interference occurrence $\left(P_{INT-BPM-MIMO}\left(Az\right)\right)$ is binary in this case as well, and expressed as follows:

$$P_{INT-BPM-MIMO}(Az)=\begin{cases}0 & \mathrm{N_{Int\text{-}BPM\text{-}MIMO}}=0 \quad \text{No interference received}\\ 1 & \mathrm{N_{Int\text{-}BPM\text{-}MIMO}}=\mathrm{N}_{Tx}\mathrm{N}_{Rx} \quad \text{Interference across all channels}\end{cases} \tag{7-17}$$

Therefore, if $P_{INT-BPM-MIMO}\left(Az\right)$ = 1, interference power increases by $N^2_{INT-BPM-MIMO}$ after beamforming.

The SINR and INR for $P_{INT-BPM-MIMO}\left(Az\right)=1$ in the BPM-MIMO configuration, represented by $SINR_{RA-BPM-MIMO}$ and $INR_{RA-BPM-MIMO}$, respectively can then be expressed as:

$$\begin{aligned} SINR_{RA-BPM-MIMO} &= SINR_{RD}.\frac{\left(N_{Tx}N_{Rx}\right)^2}{\frac{\left(N_{Tx}N_{Rx}\right)^2}{2}} = SINR_{RD}\cdot 2 \\ INR_{RA-BPM-MIMO} &= INR_{RD}.\frac{\frac{\left(N_{Tx}N_{Rx}\right)^2}{2}}{N_{Tx}N_{Rx}} = INR_{RD}.\frac{N_{Tx}N_{Rx}}{2} \end{aligned} \tag{7-18}$$

An additional factor of 2 has been included in (7-18) due to a single (real) channel receiver.

b) TDM – MIMO

In TDM-MIMO, the transmit elements of the VR transmit at different time intervals to achieve orthogonality. This time is equal to $T_{TDM}=T_{sv}+T_{Idle}$ where T_{Idle} is the idle time between

two consecutive chirps. After virtual array formation, the beam resolution for the echo signal is defined by $N_{Tx}N_{Rx}$ elements. After beamforming, the echo signal being coherent across the virtual elements, has $\sim\left(N_{Tx}N_{Rx}\right)^2$ times increase in power.

As discussed in section 3.5, the received interference is incoherent across the VR transmit elements. Therefore, the interference beam resolution is defined by only N_{Rx} elements. Furthermore, due to the different time slots of the transmitted waveforms, only a subset of the corresponding received chirps in the azimuth frame will be affected by interference (Table 7.2). This defines the probability of interference occurrence $\left(P_{INT-TDM-MIMO}\left(Az\right)\right)$, given as follows:

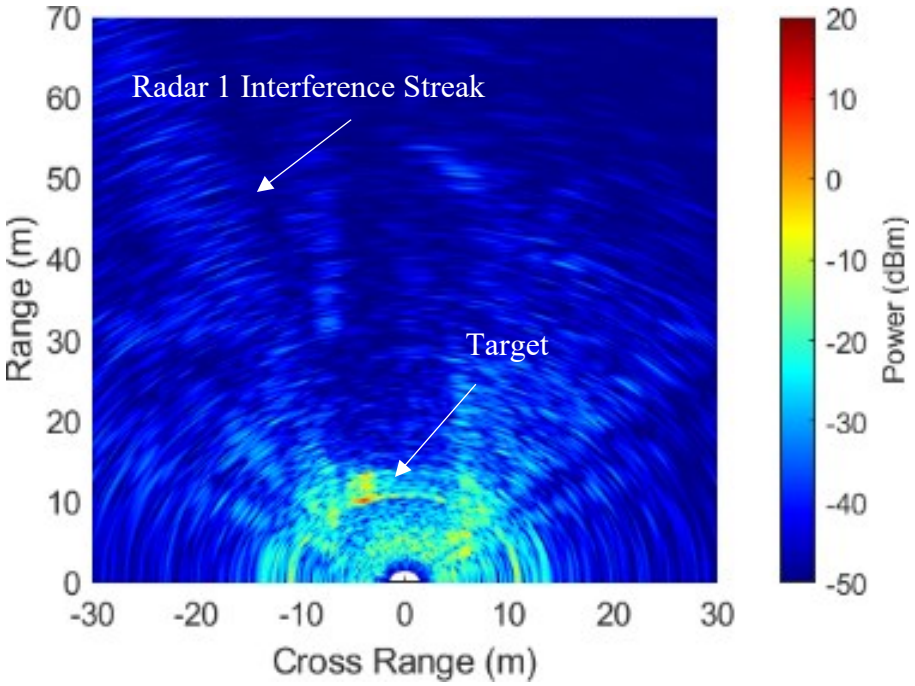
$$P_{INT-TDM-MIMO}(Az)=\frac{N_{Int-MIMO}}{N_{Tx}N_{Rx}} \tag{7-19}$$

where, $N_{INT-MIMO}$ represents the number of chirps within the azimuth frame with interference, and $N_{INT-MIMO}\le N_{Tx}N_{Rx}$.

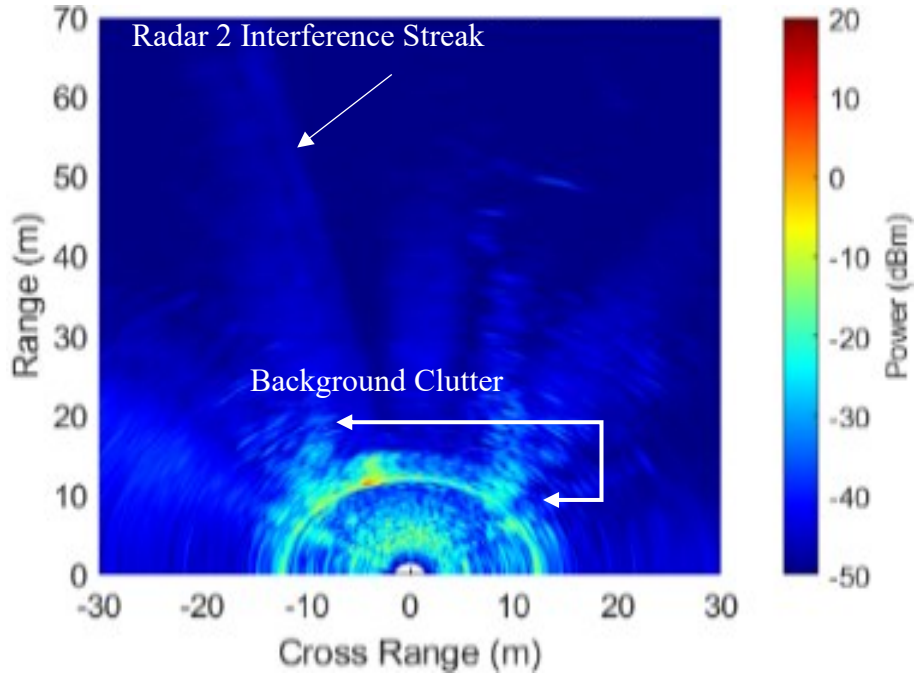
The SINR and INR after beamforming $SINR_{RA-TDM-MIMO}$ and $INR_{RA-TDM-MIMO}$, respectively are given as follows:

$$\begin{aligned} SINR_{RA-TDM-MIMO} &= SINR_{RD}\cdot\frac{\left(N_{Tx}N_{Rx}\right)^2}{\frac{P_{Int-TDM-MIMO}(Az)\cdot N_{Tx}N_{Rx}}{2}}=SINR_{RD}\cdot\frac{2N_{Tx}N_{Rx}}{P_{Int-TDM-MIMO}(Az)} \\ INR_{RA-TDM-MIMO} &= INR_{RD}.\frac{\frac{P_{Int-TDM-MIMO}(Az)\cdot N_{Tx}N_{Rx}}{2}}{N_{Tx}N_{Rx}}=INR_{RD}.\frac{P_{Int-TDM-MIMO}(Az)}{2} \end{aligned} \tag{7-20}$$

Therefore, in contrast to phased array and BPM-MIMO configurations, TDM-MIMO provides an SINR gain after beamforming. The range cross-range maps after the 3D-FFT according to the parameters defined in Table 7.1 have been demonstrated in Figure 7.5 (a) and (b) for the interference from radar 1 and radar 2, respectively.



(a)



(b)

Figure 7.5: Range cross-range for the SINR analysis: (a) interference from radar 1, (b) interference from radar 2.

Average (processed) interference powers of -40 dBm and -52 dBm have been observed from radar 1 and radar 2, respectively. In both cases, the interference received from a collocated target at 11.1 m is significantly reduced after the processing stages at the VR.

7.4 Performance Evaluation

For defined configurations and orientations of the interfering radars, the SINR and INR improvements along each step of the VR's processing chain are demonstrated in Figure 7.6. An SINR improvement of 46 dB for the interference from radar 1 and 50 dB for the interference from radar 2 have been observed in the discussed case.

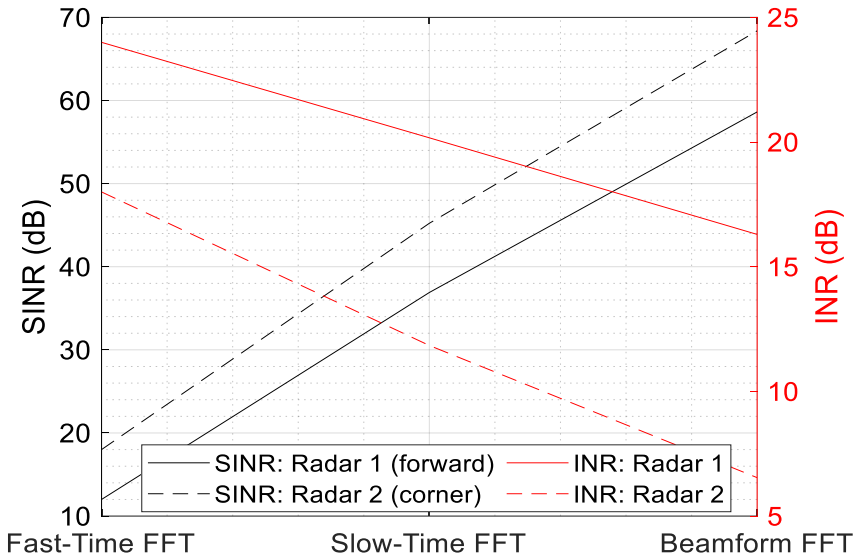


Figure 7.6: The SINR and INR along the radar processing stages.

It is worth mentioning that the results are reproducible in case of multiple sources of interference. The interference floor will still be defined by the received interference with maximum power. The remaining interference will, however, make the interference floor more random due to different statistics [247].

7.5 Summary

It has been demonstrated that in real automotive scenarios, due to uncorrelated interference pulses and a comparatively lower probability of interference occurrence, a significant improvement in the SINR is observed as the received signal is processed by the processing stages at the VR. This has been achieved without incorporating dedicated

interference detection or mitigation techniques in the radar's processing chain. The estimated SINR and INR after each stage of the VR have been summarised in Table 7.4.

Table 7.4: The estimated SINR and INR after victim radar processing stages.

Processing Stage		SINR	INR
Receiver Output X_B		$\frac{P_{Tx}G_{Tx}(\theta,\varphi)G_{Rx}(\theta,\varphi)\sigma R_1^2}{4\pi R_T^4 P_{TxInt}G_{TxInt}(\theta_{Int},\varphi_{Int})G_{Rx}(\theta_{Int},\varphi_{Int})}$	$\frac{P_{TxInt}G_{TxInt}(\theta_{Int},\varphi_{Int})G_{Rx}(\theta_{Int},\varphi_{Int})\lambda^2 P_{AFE}}{(4\pi R_1)^2 L_P k T_{Eff}}$
Range Profile X_R		$SINR_B \cdot N_{INT} \cdot W^*_{FastFFT}$	$INR_B \frac{T_{sv}}{N_{INT} \cdot W^*_{FastFFT}}$
Range Doppler X_{RD}		$SINR_R \cdot \frac{N_{CPI}}{P_{INT}(CPI)}$	$INR_R \cdot P_{INT}(CPI)$
Azimuth FFT	Phased Array	$SINR_{RD} \cdot 2$	$INR_{RD} \cdot \frac{N_{Rx}}{2}$
	BPM-MIMO	$SINR_{RD} \cdot 2$	$INR_{RD} \cdot \frac{N_{Tx}N_{Rx}}{2}$
	TDM-MIMO	$SINR_{RD} \cdot \frac{2N_{Tx}N_{Rx}}{P_{Int-TDM-MIMO}(Az)}$	$INR_{RD} \cdot \frac{P_{Int-TDM-MIMO}(Az)}{2}$

*X represents either of the following: SINR, INR.

Although the SINR improves as the echo signal and received interference are processed by the radar, this does not eliminate the requirement for interference mitigation techniques. For example, interference suppression is required in the presence of targets with a low RCS or to achieve a wide dynamic range to detect targets with varying RCS values.

Chapter 8. DOPPLER BEAM SHARPENING FOR INTERFERENCE MITIGATION

Interference mitigation techniques exploiting the time, spectral, and spatial domains have been discussed in Chapters 5 and 6 to improve the SINR for reliable target detection. However, as discussed, the implementation of these techniques in real road scenarios is challenging. For example, some of the techniques are computationally complex and may not be effective in congested scenarios, such as an urban city road, where closely spaced targets and interfering signals are expected, and interference might be received from a direct path or an indirect path after being reflected from the roadside infrastructure. Moreover, interference mitigation often results in the degradation of the echo signal power, especially when interference is received from multiple interfering sources or from a source collocated with the source of the echo signal.

Considering this, it seems essential to investigate innovative mitigation strategies that do not require any significant hardware upgrade in the SoA sensors, add computational load on the processor, or have an undesired effect in certain road conditions, such as when there is a close spatial separation between the desired target and interferer where traditional MIMO or adaptive MIMO beamformed imagery degrades [238].

For real-time sensing, the radar sensor must provide fine resolution and a high SINR while achieving fast data acquisition and processing times. However, to achieve image-like resolution in the next-generation radars, the MIMO array alone is not sufficient to provide the required resolution due to the limited space available for the sensors [74]. Moreover, in the MIMO configuration, the resulting antenna pattern is equal to the one-way beam pattern of the virtual array, which determines the angular resolution and side-lobe levels. This puts MIMO at a disadvantage, particularly in the scenes requiring a high dynamic range, where targets with a

small RCS must be separated from targets with a much higher RCS, and to resolve targets with a small cross-range separation. This indicates the requirement of:

1. Resolution enhancement algorithms to enhance the performance of traditional MIMO-based automotive radars, meeting the requirements for vehicle autonomy [69], [293].
2. A combination of these algorithms with MIMO beamforming (currently used technology in SoA radar chipsets) for precise imaging and scene mapping.

The focus of this chapter is the exploitation of synthetic aperture radar (SAR), specifically Doppler beam sharpening (DBS), to enhance the radar resolution for echo signal detection in MIMO radars, and to suppress interference at the same time. The significant contributions of this chapter are as follows:

- Investigating DBS to enhance the imaging capabilities of MIMO radars.
- Phenomenology of DBS for the echo signal and received interference.
- Implementing DBS as a technique to mitigate radar interference.
- Developing the INR heatmaps to evaluate the effectiveness of DBS for various interference types.
- Quantitative and qualitative analysis of the VR and IR waveform parameters on the effectiveness of DBS for interference suppression.
- Comparative analysis of DBS and temporal domain interference mitigation to highlight the suitability of DBS in a complex automotive scenario with multiple interferers.

8.1 State of the Art

SAR and DBS are well-known technologies in the airborne radars [294], the shipborne radars [295], and the missile systems [295] to enhance the resolution for precise imaging [295]–[297], ground mapping and clutter discrimination [298], and for deception jamming [298],

[299]. However, their applications for automotive sensing are currently limited and primarily focused on parking lot detection [300], [301], object height finding [302], [303], and the enhancement of azimuth and cross-range resolution [92].

DBS as a tool for automotive radar interference mitigation and the phenomenology of MIMO-DBS in an interference background is missing in the literature and discussed in this chapter. Moreover, as DBS can be performed in the order of milliseconds, which is comparable to the frame duration of typical automotive radars [21], [298], it is a suitable choice for automotive applications.

8.2 Phenomenology of Doppler Beam Sharpening

In conventional signal processing, the physical beam in the scanning radars [304] or the virtual beam in the MIMO radars [116] is used for scene mapping. The cross-range resolution of the radar (ΔCR) depends upon the slant range (R) and number of antenna elements (N), estimated as [305]:

$$\Delta CR = R\theta_{MB} \approx R\frac{2}{N} \tag{8-1}$$

where, θ_{MB} is the 3-dB azimuth beamwidth. Equation (8-1) indicates that the azimuth angle (θ_{MB}) and cross range (CR) are interchangeable and ΔCR degrades at a longer slant range. Consequently, the degradation of spatial resolution is expected for targets located away from the radar which affects the target detection and classification.

To achieve fine azimuth (polar representation) and cross-range (Cartesian representation) resolutions, a larger array is required. However, as automotive radar has to be installed behind a bumper fascia [306], and with up to 12 radar sensors per vehicle [37], the array size is restricted by the physical constraints.

Figure 8.1 demonstrates ΔCR degradation for an example road scenario with two vehicles in the adjacent lanes at 10 m and 50 m from the radar, modelled based on the INRAS Radarbook sensor [40] with 4 transmit and 8 receive elements (4^o virtual MIMO resolution).

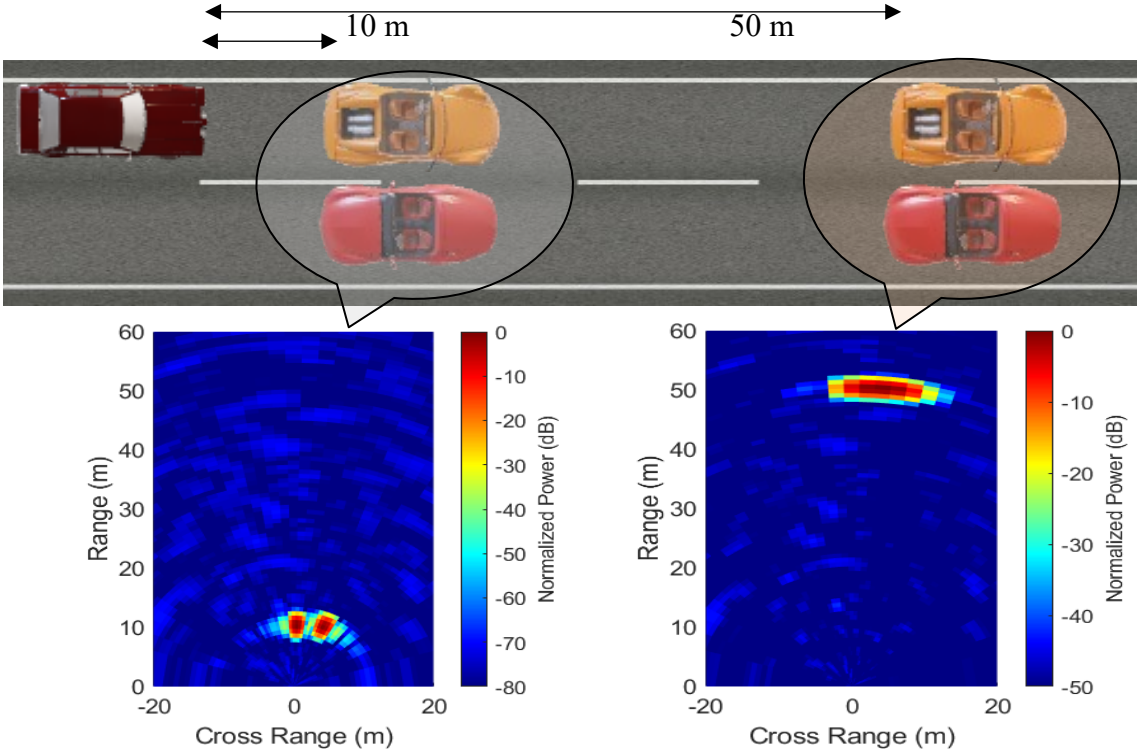


Figure 8.1: Degradation in target detection as a function of range from the radar.

With traditional MIMO beamforming, the two vehicles at 50 m from the radar cannot be resolved across the cross-range. Therefore, resolution enhancement is required to achieve the desired resolutions for vehicle navigation.

DBS provides a computationally efficient way of improving the cross-range resolution of radar by using the Doppler domain to resolve targets rather than just using the real or virtual beam of the radar. Based on the difference in the Doppler frequency shift between the targets located at different azimuth angles, a larger effective antenna aperture is synthesised, which narrows the antenna beam without any additional computation load on the processor [296], [301], [307].

In this work, DBS has been implemented by partitioning the main beam into narrow sub-beams, as illustrated in Figure 8.2 (a) and (b). The different radial velocity (hence the Doppler frequency) of each sub-beam (bin) with respect to the moving VR has been used to map each bin into the corresponding azimuth angle. This provides an independent technique to estimate the azimuth position of the targets.

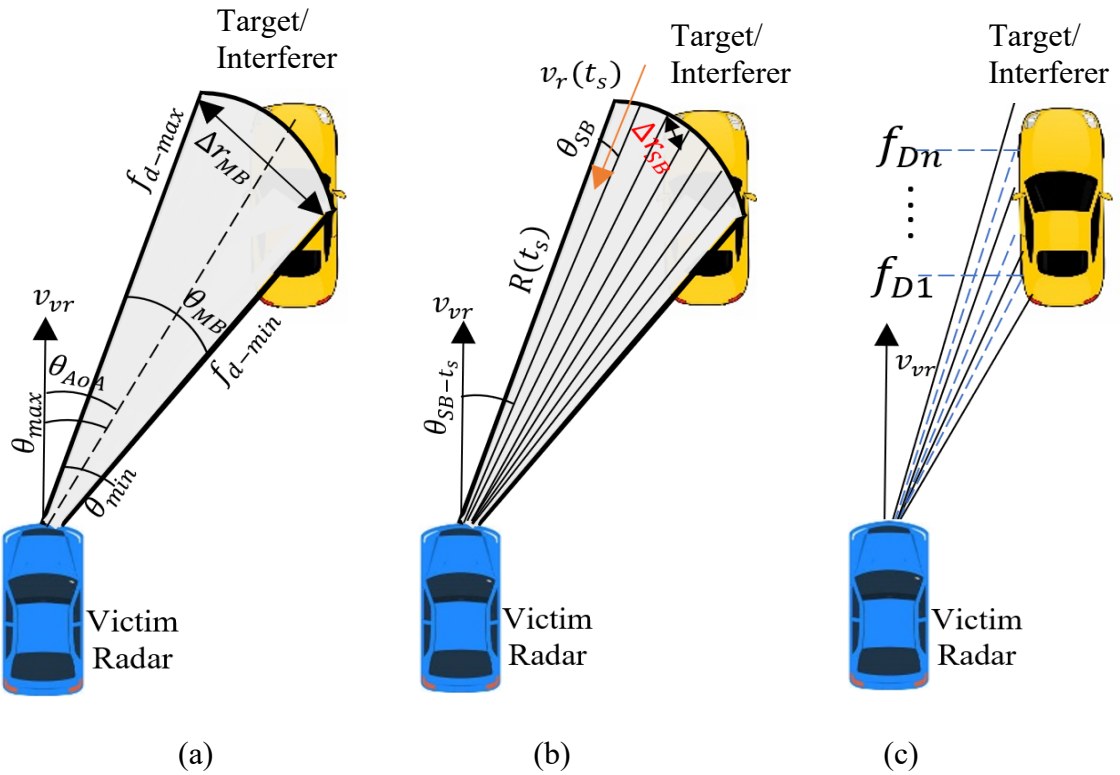


Figure 8.2: Doppler beam sharpening illustration: (a) main beam, (b) sub-beam formation due to a moving victim radar, (c) The Doppler frequency of each sub-beam.

The Doppler frequency difference across the sub-beams in Figure 8.2 has been estimated by applying narrowband filters across these sub-beams such that:

1. The centre frequency (Doppler shift) of each filter matches the Doppler centroid of each sub-beam along the azimuth direction (blue dotted line in Figure 8.2 (c)), and
2. The bandwidth matches the width of the main beam (Figure 8.2 (a)) such that it covers the Doppler frequencies induced by all the targets.

This results in the detection of targets located along different sub-beams with a high resolution compared to the traditional MIMO beamformed imagery with the same physical aperture size.

To demonstrate the phenomenology of DBS for the echo signal and interference, an example case has been considered where a radar sensor moves with a velocity v_{vr} and observes a stationary target/ interferer. For simplification, the scene is assumed to be two-dimensional with an elevation angle of both target and interferer equal to 0^o with respect to the VR.

8.2.1 DBS for the Echo Signal

The phase of the down-converted echo signal $\left(\varphi_{IF-t}\right)$ in the FMCW VR is expressed as:

$$\varphi_{IF-t}\left(t,t_s\right)=-K_v\tau_v^2\left(t_s\right)+2K_vt\tau_v\left(t_s\right)+2F_{cv}\tau_v\left(t_s\right) \tag{8-2}$$

where t and t_s represents the fast-time and slow-time samples, respectively. As the VR moves, depending upon v_{vr}, the target traverses across multiple Doppler sub-beams (Figure 8.2 (b)). The phase difference between the signal transmitted from the VR and the received echo across each sub-beam (slow-time sample) is expressed as:

$$\varphi_t\left(t_s\right)=-2R_T\left(t_s\right)\frac{2\pi}{\lambda} \tag{8-3}$$

where $R_T\left(t_s\right)$ represents the distance between the VR and target for each sub-beam and a factor of 2 is included due to the two-way propagation of the echo signal. With a change in the azimuth angle of the target, the radial velocity of the echo signal also changes and is expressed as:

$$v_r\left(t_s\right)=\frac{dR_T\left(t_s\right)}{dt_s} \tag{8-4}$$

Therefore, (8-3) and (8-4) gives:

$$\frac{d\varphi_t\left(t_s\right)}{dt_s}=-\frac{4\pi}{\lambda}v_r\left(t_s\right) \tag{8-5}$$

Depending upon the platform velocity and the azimuth location of the target, the radial velocity is estimated as follows:

$$v_r\left(t_s\right) = -v_{vr}\cos\left(\theta_{SB-t_s}\right) \tag{8-6}$$

where, θ_{SB-t_s} is the AoA of the signal received from a specific sub-beam at a slow-time 't_s' (Figure 8.2 (b)). Hence, the Doppler shift of the echo signals $f_{D-t}\left(t_s\right)$ is expressed as:

$$f_{D-t}(t_s) = \frac{1}{2\pi}\frac{d\varphi_t(t_s)}{dt_s} = -2\frac{v_r(t_s)}{\lambda} = 2\frac{v_{vr}}{\lambda}\cos(\theta_{SB-t_s}) \tag{8-7}$$

$f_{D-t}\left(t_s\right)$ is the centre frequency of a specific sub-beam at a slow-time t_s. The echo signal, therefore, has a well-defined Doppler frequency across each sub-beam, which is a function of v_{vr} and the spatial position of the target. After axis manipulation, the radial velocity is mapped into the corresponding azimuth angle.

Using (8-7), the minimum $\left(f_{D-\min}\right)$ and maximum $\left(f_{D-\max}\right)$ Doppler frequencies over which the sub-beams are defined (Figure 8.2) can be estimated as:

$$\begin{aligned} f_{d-\min}(t_s = 1) &= 2\frac{v_{vr}}{\lambda}\cos(\theta_{\min}); \quad \theta_{\min} = \theta_{AoA} + \theta_{MB}/2 \\ f_{d-\max}(t_s = N_{SB}) &= 2\frac{v_{vr}}{\lambda}\cos(\theta_{\max}); \quad \theta_{\max} = \theta_{AoA} - \theta_{MB}/2 \end{aligned} \tag{8-8}$$

where, N_{SB} is the number of sub-beams that is equivalent to the number of VR chirps across the slow-time.

8.2.2 Block Level Representation of Signal Processing Chain

In the presented work, an FFT-based DBS algorithm combined with axis manipulations involving trigonometric functions and inverse trigonometric functions have been used for DBS beamforming. As most SoA automotive radar chipsets are based on MIMO configuration, the output of DBS beamforming and MIMO beamforming is combined using interpolation to get

the integrated MIMO-DBS beamforming. In the integrated map, the two independent angle estimates, from MIMO and DBS, are combined to provide an enhanced resolution whilst achieving a lower SLL. The block level diagram of the traditional FMCW processing chain has been shown in Figure 8.3 (a), and MIMO beamforming and MIMO-DBS beamforming processing chains have been presented in Figure 8.3 (b) and Figure 8.3 (c), respectively.

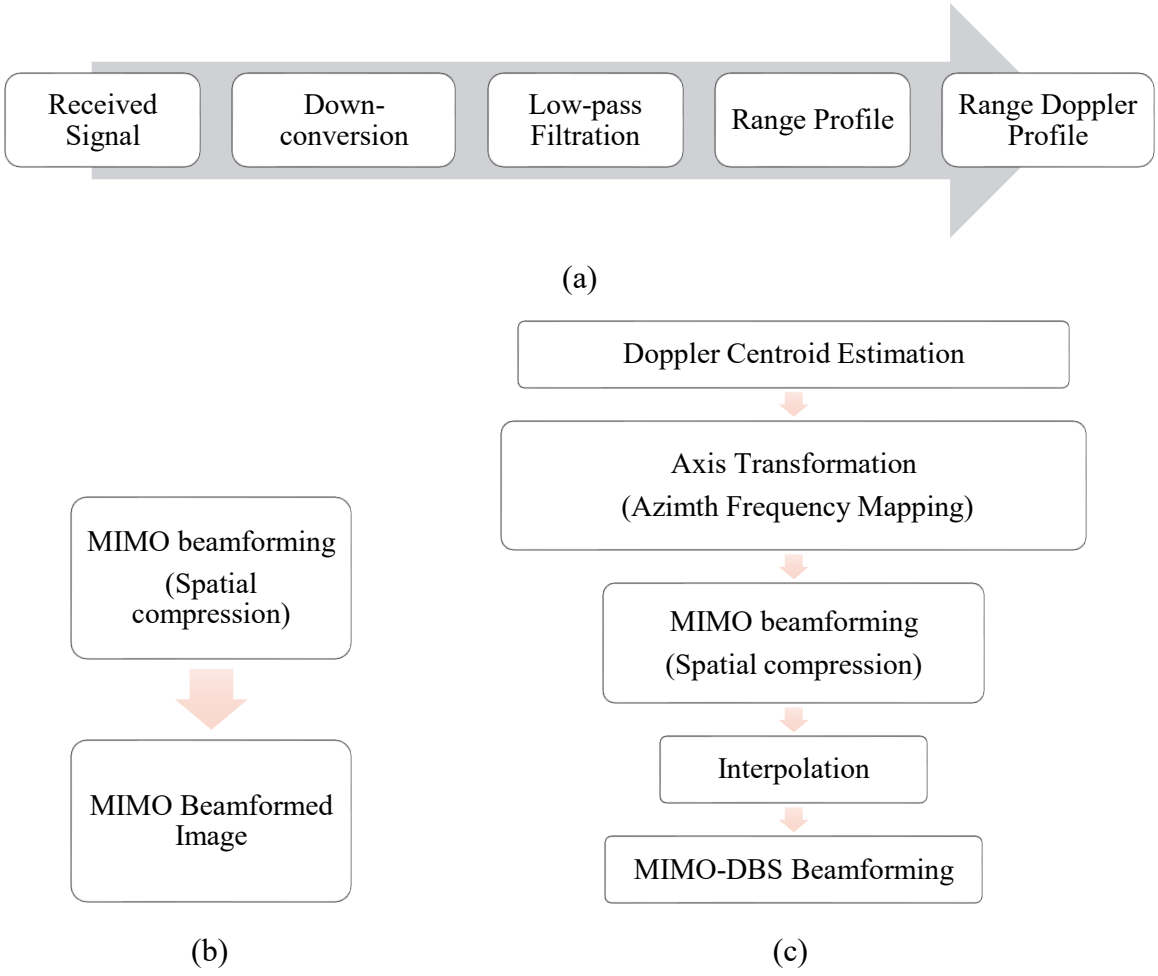


Figure 8.3: Block level representation of signal processing chain: (a) common for FMCW-based victim radar, (b) MIMO beamforming, (c) MIMO-DBS beamforming.

The traditional signal processing to achieve MIMO beamformed results has been discussed earlier in the presented work (section 3.1). To perform MIMO-DBS beamforming, the following methodology has been used.

1. The Doppler centroid of each Doppler bin has been estimated, which forms the centre of each sub-beam.
2. For DBS-only beamforming, axis mapping has been performed where, $f_{D-t}(t_s)$ from (8-7) is mapped to the azimuth centre of each sub-beam to get the following [308]:

$$\theta_{SB-t_s} = \cos^{-1}\left(f_{D-t}(t_s)\frac{\lambda}{2v_{vr}} \right) \tag{8-9}$$

3. This is followed by the spatial compression to get the MIMO beamformed imagery.
4. Finally, the interpolation of DBS and MIMO angles obtained from steps (2) and (3) has been performed to generate the MIMO-DBS beamformed results.

In MIMO radars, an additional phase is also induced due to the motion of the VR, which results in an inaccurate estimate of the spatial position of targets/ interferer hence incorrect angle estimate. Therefore, phase compensation has been performed to compensate for the motion-induced phase shift across the transmit antenna elements of the radar [309], [310] before performing Doppler (DBS) processing.

8.2.3 Resolution Enhancement

With DBS processing, the echo signal's resolution has been enhanced over the observation interval defined by the frame duration (T_F) of the VR. Therefore, the width of each sub-beam Δf_{SB} formed during the observation interval is $1/T_F$ and the number of sub-beams N_{SB} can be estimated as [92]:

$$N_{SB} = \frac{f_{d-BW}}{\Delta f_{SB}} \tag{8-10}$$

where, f_{d-BW} is the difference of $f_{D-\min}$ and $f_{D-\max}$ in (8-8). After solving (8-10),

$$N_{SB} = 4\frac{v_{vr}}{\lambda} T_F \sin(\theta_{AoA}) \sin\left(\frac{\theta_{MB}}{2}\right) \tag{8-11}$$

Based on this, after applying MIMO-DBS beamforming, the echo signal's azimuth resolution (θ_{SB}) and cross-range resolution (Δr_{SB}), respectively have been enhanced by:

$$\theta_{SB} = \frac{\theta_{MB}}{N_{SB}} \tag{8-12}$$

$$\Delta r_{SB} = \frac{\Delta r_{MB}}{N_{SB}} \tag{8-13}$$

It is worth mentioning that DBS exploits the change in the Doppler frequency due to the motion of the VR to achieve azimuth refinement and interference suppression. Therefore, it is not effective in a static scenario where $v_{vr} = 0$.

After applying MIMO-DBS beamforming on the scenario in Figure 8.1, the two targets at 50 m have been resolved, as shown in Figure 8.4.

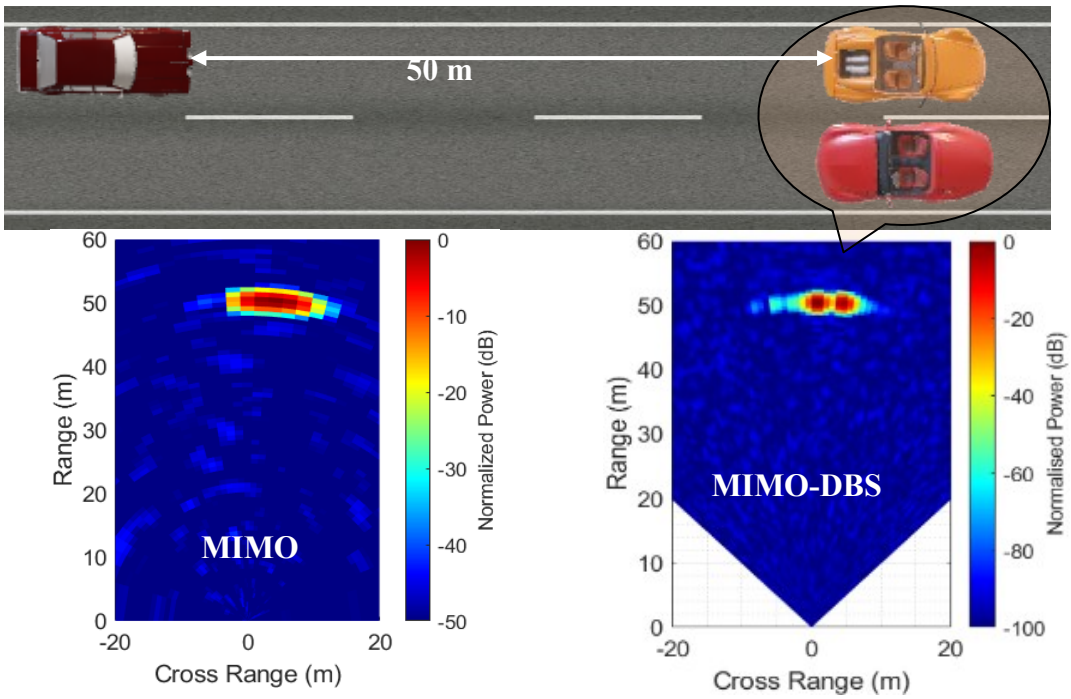


Figure 8.4: Enhancement in target resolution after applying MIMO-DBS beamforming.

In the presented details, the TDM-MIMO configuration has been used for signal transmission. However, without a loss of generality, the results are equally valid for other techniques to achieve orthogonality in MIMO radars.

8.2.4 DBS Processing in an Interference Background

The motivation for using DBS processing for interference mitigation comes from the fact that:

1. Interference has a one-way propagation delay as compared to the two-way propagation delay of the echo signal (Chapter 3).
2. In the majority of the cases, interference pulses are incoherent at the VR (Chapter 4).

Consequently, interference often appears in a Doppler bin which differs from that of a true target at the same spatial location. Therefore, the resolution of the echo signal is enhanced after DBS beamforming, and at the same time, interference suppression is achieved, as discussed in the subsequent sections.

FMCW-based VR in the background of FMCW interference has been considered in the presented work as it is the most widely used modulation scheme in SoA automotive sensors [311]. The phase of down-converted interference $\left(\varphi_{IF-i}\right)$ can be expressed as [175]:

$$\varphi_{IF-i}\left(t,t_s\right)=\Delta K t^2+2K_{\text{int}}t\tau_{\text{int}}\left(t_s\right)+2\Delta F t-K_{\text{int}}\tau_{\text{int}}^2\left(t_s\right)+2F_{\text{cint}}\tau_{\text{int}} \tag{8-14}$$

where, $\Delta K=K_v-K_{\text{int}}$, τ_{int} is the propagation delay of the interference signal, $\Delta F=F_{cv}-F_{c\text{int}}$. The intermediate frequency of interference can be estimated as:

$$f_{IF-i}=\frac{1}{2\pi}\left(\frac{d\varphi_{IF-i}}{dt}\right) \tag{8-15}$$

After simplification,

$$f_{IF-i}\left(t,t_s\right)=\Delta K t+K_{\text{int}}\tau_{\text{int}}\left(t_s\right) \tag{8-16}$$

Due to the time dependence of f_{IF-i}, a corresponding phase shift $\left(\varphi_{\text{int}}\left(t_s\right)\right)$ is incorporated across each slow-time. Therefore, with one-way propagation delay of the received interference, the phase difference between interference and the signal transmitted from the VR becomes:

$$\varphi_i(t_s) = -R_I(t_s)\frac{2\pi}{\lambda} + \phi_{\text{int}}(t_s) \tag{8-17}$$

where, R_I is the distance between the VR and IR. With the same relation for the radial velocity as used for the echo signal in (8-4), the Doppler shift of interference $f_{D-i}(t_s)$ can be expressed as:

$$f_{D-i}(t_s) = \frac{v_{vr}}{\lambda}\cos(\theta_{SB-t_s}) + \frac{d\phi_{\text{int}}(t_s)}{dt_s} \tag{8-18}$$

From (8-7) and (8-18), the following observations have been made:

- The Doppler frequency of induced interference from each sub-beam is different from that observed for the echo signal. This results in interference suppression after MIMO-DBS beamforming, as discussed in the subsequent section.
- Equations (8-16) and (8-18) indicate that the intermediate and the Doppler frequency of interference depends upon the waveform parameters of the VR and IR.
- If the induced Doppler shift in (8-18) is beyond the FoV of the VR defined by f_{d-BW}, interference is completely removed from the FoV of the VR after MIMO-DBS processing.
- Even in the absence of a random interference phase shift across the synthesised sub-beams in (8-18), interference will be suppressed due to one-way propagation of interfering signal. This is because the Doppler to azimuth mapping of interference signal results in a different azimuth position compared to that obtained after MIMO beamforming and interpolation of MIMO and DBS angles in this case will result in interference suppression.

8.3 Interference Suppression with MIMO-DBS Beamforming

As discussed in section 8.2, in the background of interference, the Doppler frequency of interference is different from that used to enhance the azimuth and cross-range resolution of the echo signal. This holds valid even for the cases when $R_T = R_I$ (target and interference are

collocated). Therefore, a non-focused interference beam along with the spread of interference has been observed across the sub-beams after applying DBS beamforming. This has been quantitatively analysed in this section for the various VR and IR configurations and types of interference.

8.3.1 The Doppler Characteristics of Different Types of Interference

It has been shown in section 8.2.4 that the Doppler frequency and resulting phase variation across the slow-time samples of the VR in an interference background depends upon the waveform parameters of the VR and IR. Based on these parameters, interference has been previously classified as synchronous, semi-synchronous, and asynchronous (periodic, semi-periodic, and aperiodic) interference. As each type of interference manifests differently in the VR (Appendix 4), DBS beamforming affects them in a distinct way.

The range-Doppler maps of these interference types have been shown in Figure 8.5 for the VR with $T_{sv} = 50\mu s$, $B_{sv} = 0.5$ GHz, single (real) channel receiver. The VR and IR have the same starting frequency. For the presented example, the collocated static target and interferer have been considered at 50 m, 10^o from the VR travelling at 40 km/h.

Due to a single (real) channel receiver, interference affects both positive and negative Doppler bins (Appendix 6). It has been observed that even for the same spatial location of target and interferer, they appear in different Doppler bins due to the following:

- A random phase shift of interference across the slow-time samples (the second term in (8-18)). This results in interference spread across all the Doppler bins (aperiodic interference in Figure 8.5).
- An additional phase shift of interference due to different K_v and K_{int}. This affects a few Doppler bins (periodic and semi-periodic interference in Figure 8.5).

- No random phase shift in (8-18), but a one-way propagation delay of interference. This concentrates the interference energy at half the Doppler bin as that of the target (synchronous and semi-synchronous interference in Figure 8.5).

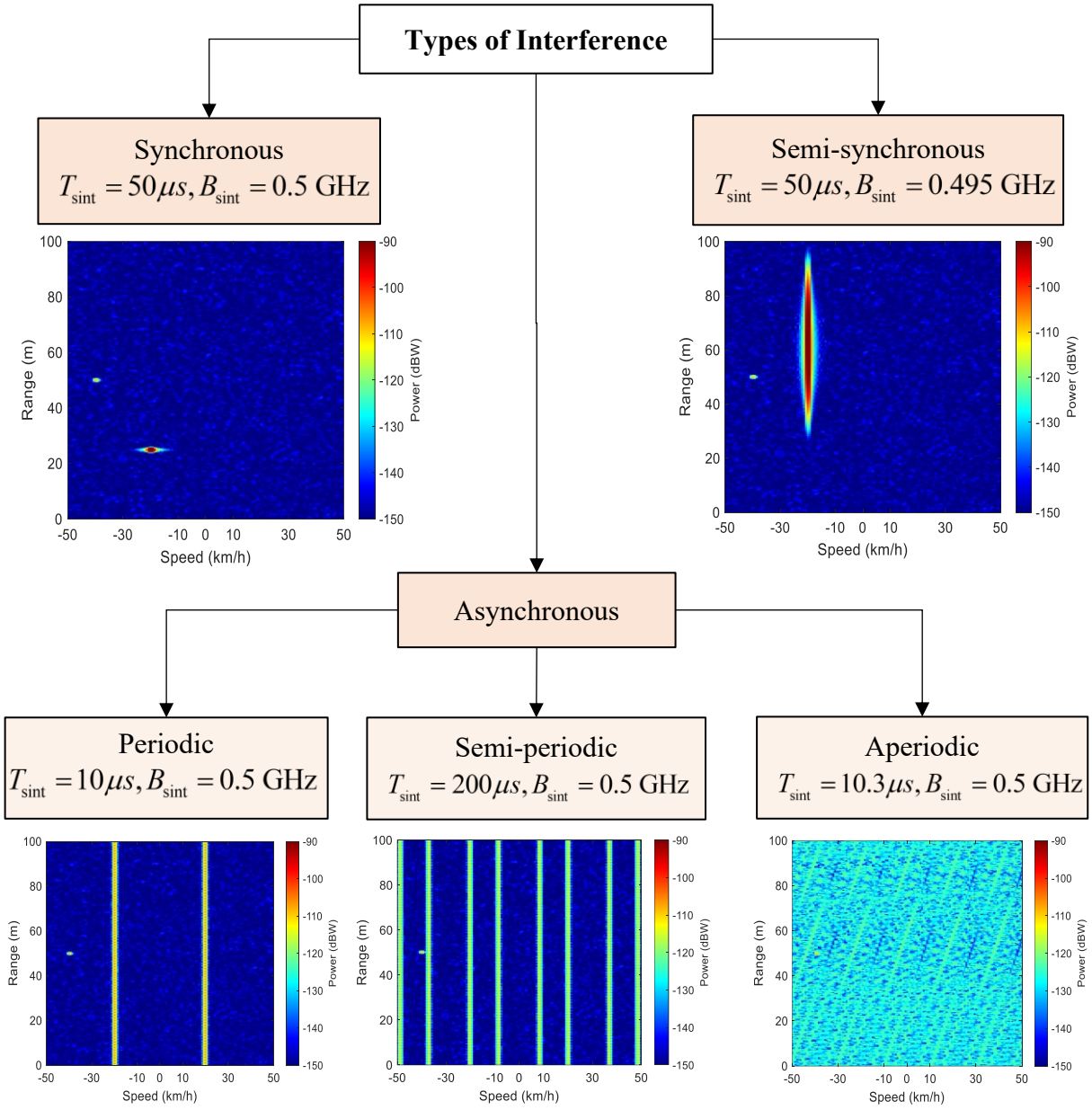


Figure 8.5: Range-Doppler maps of each interference type for the analysis of DBS beamforming.

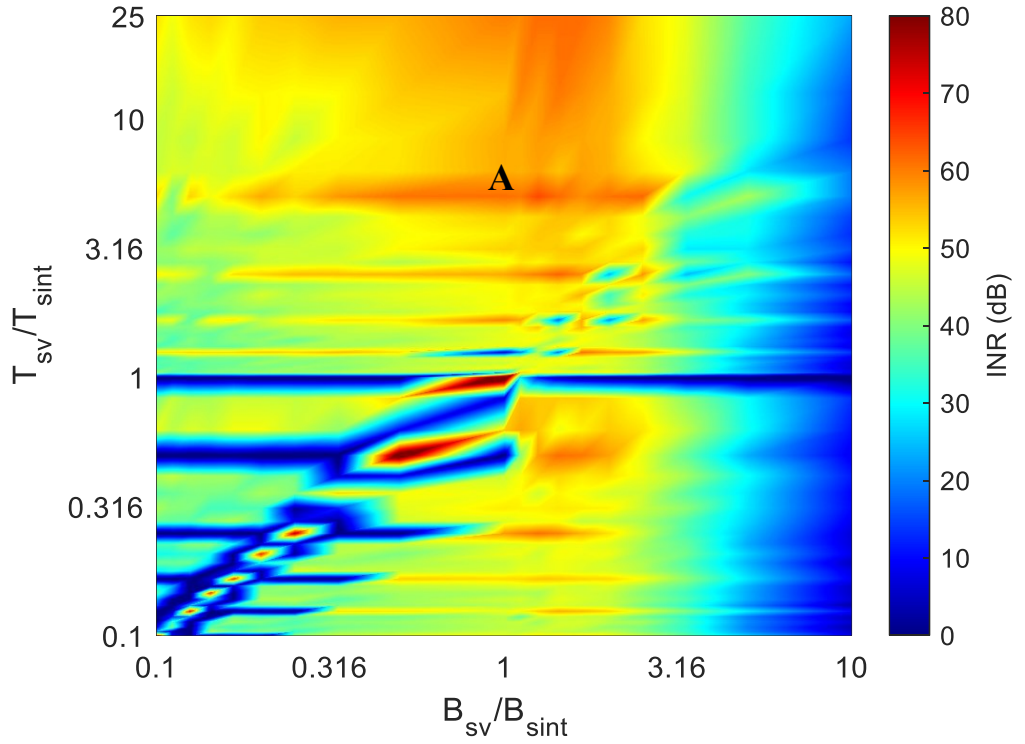
As the Doppler bins are mapped into azimuth locations, due to different interference Doppler bins than that of the echo signal, the mapping required to focus interference is different

from that used to enhance the azimuth and cross-range resolution of the echo signal. Moreover, the estimated azimuth angle of interference obtained after DBS beamforming and MIMO beamforming is different. Therefore, interference is suppressed after the combined MIMO-DBS beamforming.

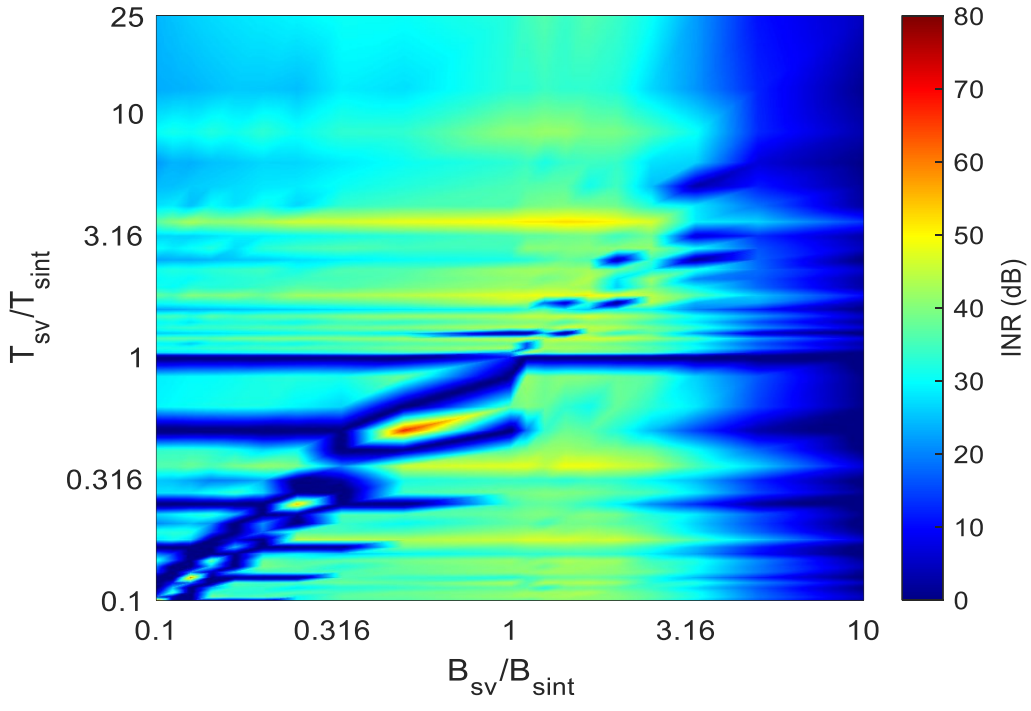
8.3.2 SINR Improvement after MIMO-DBS Processing

After MIMO beamforming, the interference floor and angular resolution depend upon the waveform parameters of the VR and IR. The same has been established for MIMO-DBS earlier in this chapter, where different types of interference have a distinct effect on the Doppler bins.

To compare the performance of MIMO and MIMO-DBS beamforming, the INR at the output of the beamformer has been estimated as a function of B_{sv}/B_{sint} and T_{sv}/T_{sint} after MIMO, and MIMO-DBS beamforming, and presented in Figure 8.6 (a) and (b), respectively. To generate the INR heatmaps, the VR parameters have been fixed, and the waveform parameters of the IR have been varied to generate different types of interference. The VR moving at 40 km/h, with 4 transmit and 8 receive elements based on the INRAS Radarbook configuration with $T_{sv} = 50\mu s$, B_{sv} = 0.5 GHz and CPI = 10 ms has been modelled such that $PRF > f_{d-BW}$. The IR has been positioned at 20m, 0^o from the VR. In all the cases, a target at 50m, 0^o from the VR has been used for reference. It is to be mentioned that closer to the radar's boresight at 0^o, the smallest cross-range resolution enhancement is observed for the echo signal [92].



(a)



(b)

Figure 8.6: The heatmaps for interference to noise ratio (INR) analysis as a function of victim and interferer radars waveform parameters. (a) MIMO beamforming, (b) MIMO-DBS beamforming.

In most cases, the INR has been significantly suppressed after MIMO-DBS beamforming. The INR heatmaps have further been analysed for the periodic and aperiodic interference types.

I. Periodic Interference

The MIMO and MIMO-DBS beamformed plots for periodic interference with $T_{sv}/T_{\text{sint}} = 5$ and $B_{sv}/B_{\text{sint}} = 1$ (region 'A' in Figure 8.6 (a)) have been shown in Figure 8.7 (a) and (b), respectively.

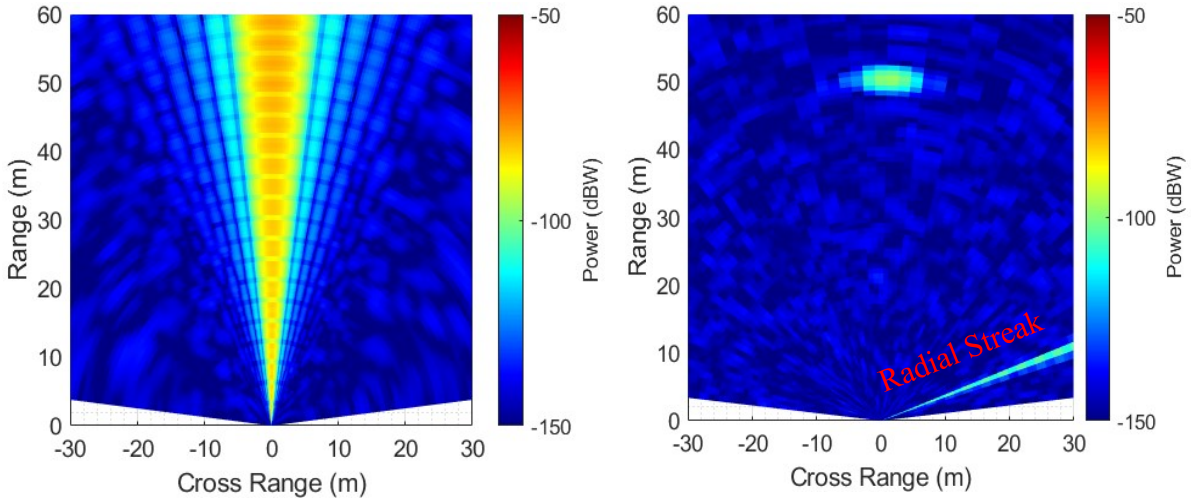


Figure 8.7: Range-cross range plot for periodic interference with $T_{sv}/T_{\text{sint}} = 5$, $B_{sv}/B_{\text{sint}} = 1$. (a) MIMO beamforming, (b) MIMO-DBS beamforming.

Interference has been significantly suppressed with a radial interference streak in Figure 8.7 (b) due to the image Doppler bin in this case. The additional phase term in (8-18) is fixed for periodic interference. Therefore, the interference streak is focused but well separated from the echo signal after MIMO-DBS beamforming. Consequently, target detection techniques such as the CFAR algorithm can be efficiently used to detect the presence of a target.

II. Aperiodic Interference

As shown in Figure 8.5, aperiodic interference uniformly spreads across all the Doppler bins due to the random phase shift in (8-18). Therefore, after the Doppler to azimuth mapping,

an interference streak according to the VR real aperture (defined by N_{Rx}) has been observed along 0 cross-range in Figure 8.8. A reduction in interference power is observed after MIMO-DBS beamforming due to the spread of interference across the Doppler bins and a non-focused interference beam due to interference incoherence across the Doppler bins.

The MIMO beamformed and MIMO-DBS beamformed plots for aperiodic interference example with $B_{sv}/B_{\text{sint}} = 1$ and $T_{sv}/T_{\text{sint}} = 2.1$ have been shown in Figure 8.8 (a) and (b), respectively.

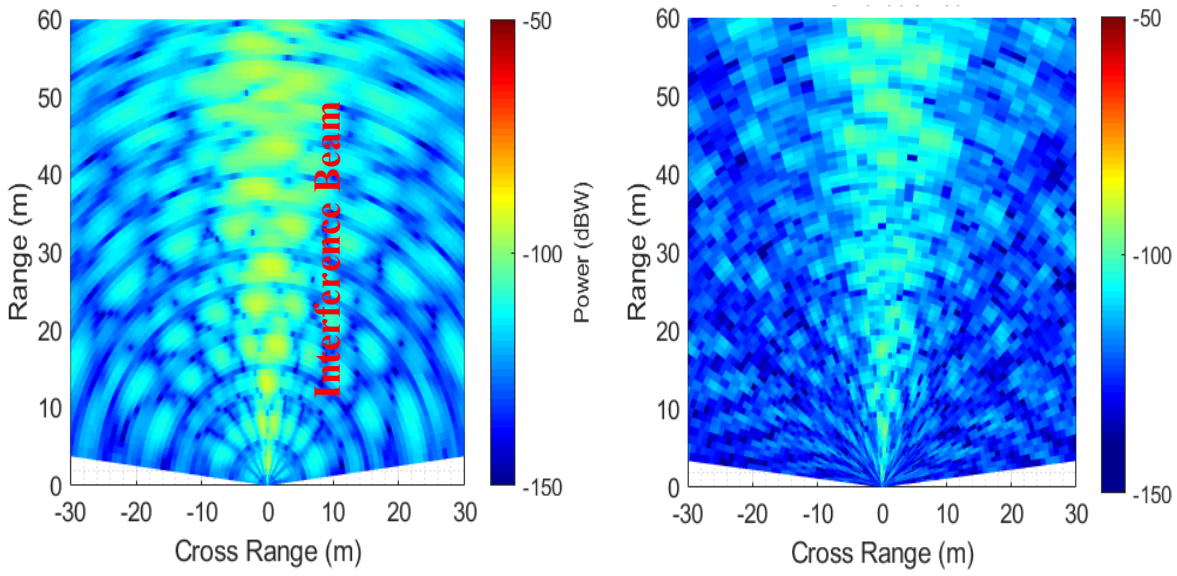


Figure 8.8: Range-cross range plot for aperiodic interference with T_{sv}/T_{sint} = 2.1 and B_{sv}/B_{sint} = 1 and a single channel receiver: (a) MIMO beamforming, (b) MIMO-DBS beamforming.

It has been shown that DBS utilises a different Doppler frequency of interference compared to the echo signal to improve radar performance in the background of interference. The factors affecting the amount of interference suppression and conditions under which interference will be outside the VR FoV have been discussed in the following sub-sections.

8.3.3 Effect of Platform Velocity

As shown in (8-7) and (8-18), the Doppler shift of the echo signal and interference depends upon the radial velocities for a fixed set of VR and IR parameters. At a higher speed, the change in the Doppler frequency at a larger angle (θ_{AoA}) increases, which limits the FoV of the VR for unambiguous echo signal detection. Furthermore,

- When interference appears in a Doppler bin closer to 0, it is mapped to the farthest angle, which often appears outside the VR FoV after DBS beamforming.
- When interference appears in a Doppler bin closer to the VR unambiguous Doppler, it is mapped to a cross-range of ~ 0 m.

Figure 8.9 shows the INR as a function of v_{vr}. The VR parameters are the same as used in section 8.3.2. Periodic interference with $T_{\text{sint}} = 10\mu s$ and semi-periodic interference with $T_{\text{sint}} = 200\mu s$ has been used. $B_{\text{sint}} = 0.5$ GHz for both the cases.

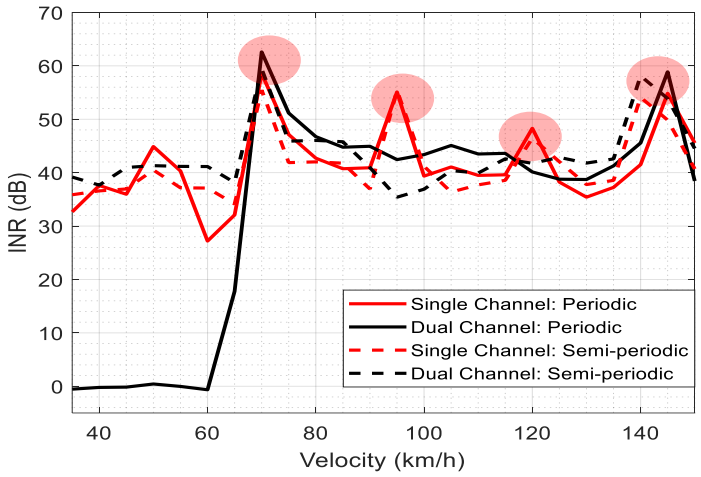


Figure 8.9: Interference to noise ratio (INR) as a function of the VR velocity.

For the I/Q channels receiver, at a smaller velocity, due to the absence of interference image Doppler frequency, it appears outside the FoV of the VR. As the velocity increases, the interference streak remains within the FoV of the VR after axis mapping. The highest INR (red highlighted regions in Figure 8.9) has been observed for the following reasons:

- Interference appears in a Doppler bin closer to the unambiguous velocity of the VR.
- Interference appears in the same Doppler bin as the echo signal. Interference, in this case, is focused like the echo signal after DBS as its Doppler frequency is closer to the Doppler centroid of a particular sub-beam.

Therefore, interference suppression with MIMO-DBS beamforming largely depends upon the velocity of the VR.

8.4 Performance Analysis

To evaluate the performance of MIMO-DBS beamforming, the INR values obtained after MIMO beamforming and MIMO beamforming combined with time domain interference mitigation have been compared with MIMO-DBS beamforming and MIMO-DBS beamforming combined with time domain mitigation. Interference zeroing has been used for time domain mitigation. The results are presented in Table 8.1.

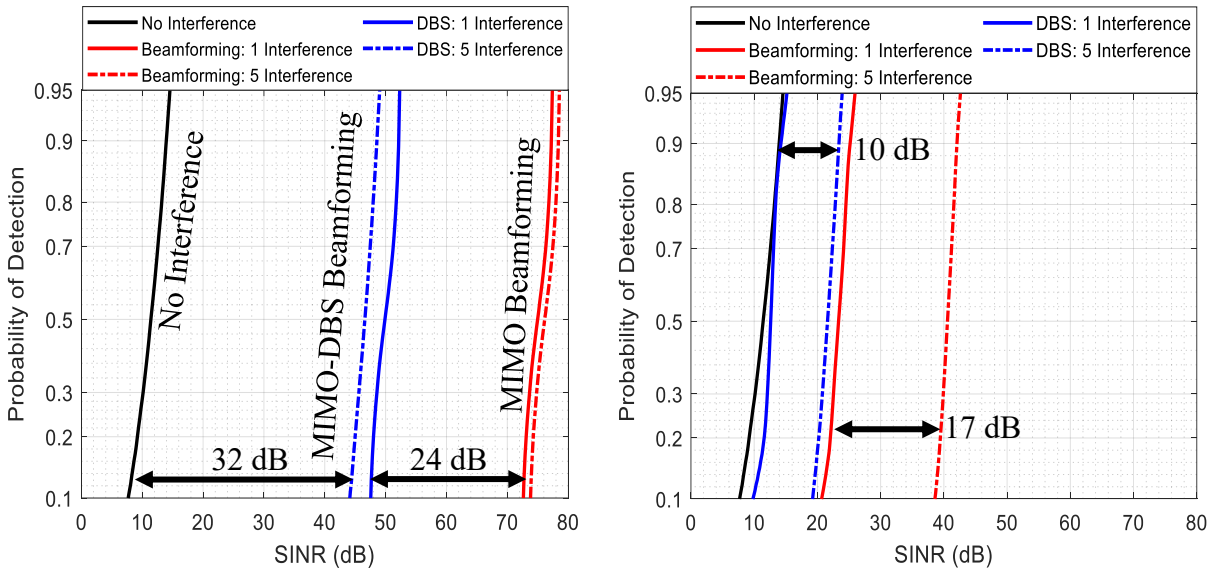
A TDM-MIMO VR with $N_{Tx} = 4,\ N_{Rx} = 8,\ T_{sv} = 50\ \mu s,\ B_{sv} = 0.5$ GHz, $v_{vr} = 40$ km/h has been used. Five interfering sources with sweep times ∞, 10 µs, 41.3 µs, 200 µs, and 800 µs and sweep bandwidths 0, 0.5 GHz, 0.5 GHz, 0.5 GHz, and 0.2 GHz have been placed at 20 m 40^o, 25 m 30^o, 30 m 15^o, 35 m 7^o, and 40 m 2^o from the VR, respectively.

Table 8.1: Performance comparison of MIMO beamforming, time domain interference zeroing, and MIMO-DBS beamforming.

No. of Interferers	**1**	**3**	**5**
		INR (dB)	
MIMO Beamforming	62	65	66
MIMO Beamforming + Zeroing	12	20	28
MIMO-DBS Beamforming	37	34	31
MIMO-DBS Beamforming + Zeroing	1	8	11

Based on the results in Table 8.1, MIMO-DBS beamforming outperforms traditional MIMO beamforming in the background of interference with up to 35 dB greater interference suppression. Moreover, interference zeroing combined with MIMO-DBS gives an interference suppression of up to 60 dB. Therefore, DBS is especially effective in the background of multiple interferers where the performance of time and spatial mitigation techniques degrade, as discussed in Chapter 6.

The detection curves for the discussed cases in Table 8.1 in the background of single and multiple interferers have been shown in Figure 8.10 (a) and (b). The probability of false alarm is 10^{-6}.



(a) (b)

Figure 8.10: Probability of detection as a function of the SINR. (a) MIMO beamforming and MIMO-DBS beamforming without interference zeroing. (b) MIMO beamforming and MIMO-DBS beamforming with interference zeroing.

Figure 8.10 highlights the effectiveness of DBS for optimising the radar performance in the background of interference. MIMO-DBS beamforming performs reasonably well, with the interference floor reduced to the thermal noise floor level in certain cases.

It is to be noted that according to the principles of DBS, it is not effective to improve the resolution of targets close to 0^o because the change in the Doppler frequency due to the VR motion is minimal in this case. However, interference located close to 0^o is still suppressed due to its different Doppler bin than the echo signal.

8.5 MIMO-DBS Beamforming - Validation

To demonstrate the practical implementation of MIMO-DBS beamforming, measurements have been conducted in real-road conditions using SoA automotive radar chipsets. The measurement setup is shown in Figure 8.11. The interferer vehicle is parked in the adjacent lane of the VR at 9 m. A pedestrian is in the LoS of the VR at 6.6 m. To conduct the measurements, an INRAS Radarlog VR with T_{sv} = 204.8 µs, B_{sv} = 1 GHz, 4 transmit and 8 receive element arrays operating in TDM-MIMO configuration has been installed as a forward-looking VR. The VR receives aperiodic interference from the forward-looking TI AWR1243 radar with T_{sint} = 250 µs and B_{sint} = 0.95 GHz. The onboard inertial measurement unit has been used for the precise estimation of vehicle velocity. This enables the practical application of DBS for automotive environment possible. The MIMO and MIMO-DBS beamformed plots are shown in Figure 8.11 (b) and (c), respectively.

As shown, MIMO-DBS beamforming reduces the interference level and, at the same time, improves the cross-range resolution for enhanced target detection. As expected and discussed in section 8.3.2.II, for aperiodic interference, an interference streak appears towards the direction of interference. However, with an interference suppression of 12 dBs in the discussed case. Moreover, the MIMO sidelobes have also been significantly reduced after MIMO-DBS beamforming.

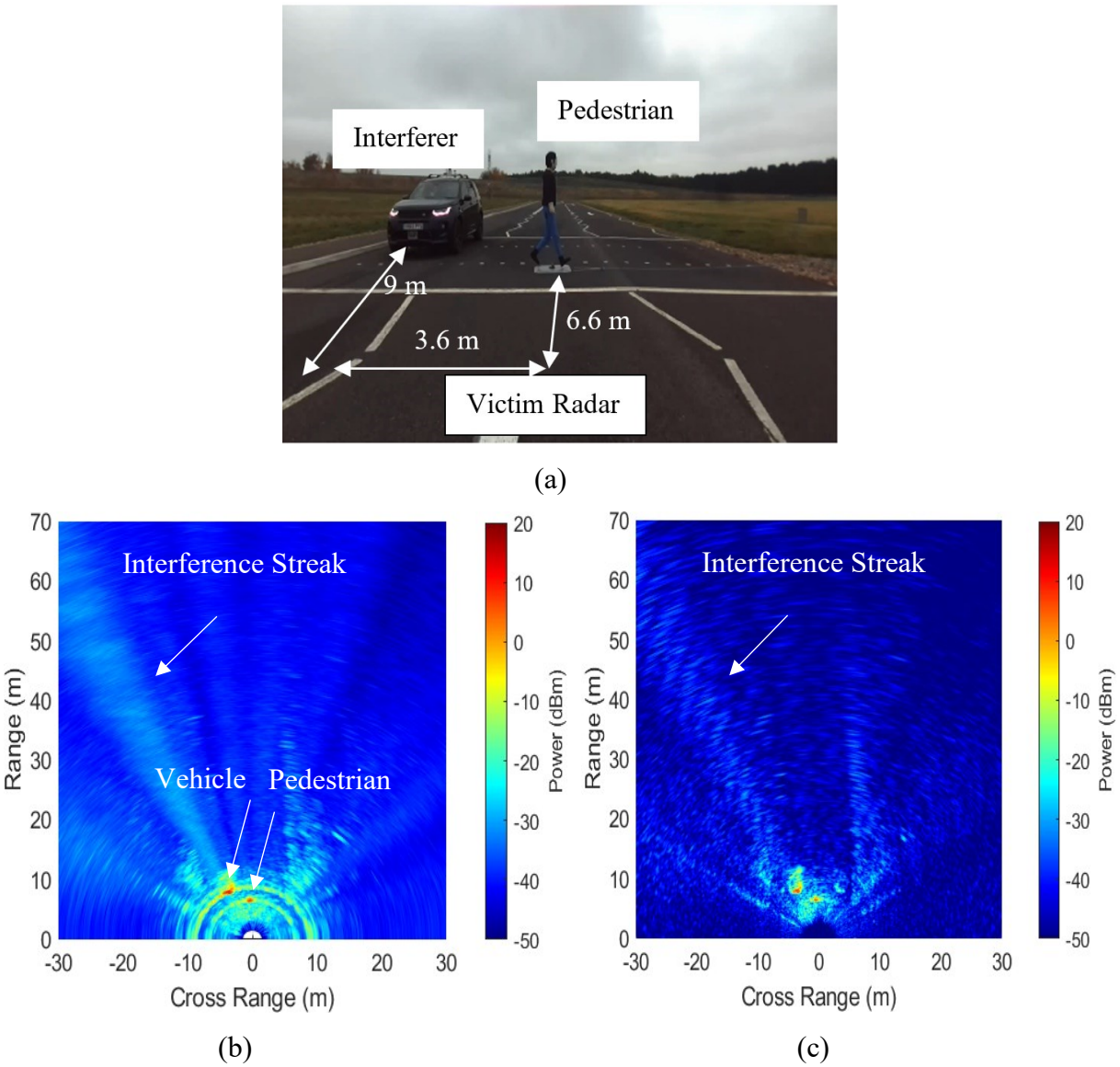


Figure 8.11: Measured results for the comparison of MIMO and MIMO-DBS imagery: (a) measurement setup, (b) MIMO beamforming, (c) MIMO-DBS beamforming.

8.6 Summary

In the presented analysis, DBS has been used for interference suppression by exploiting the difference in Doppler frequency between the target and the interferer. As the Doppler frequency of interference is, in most cases, located at a different Doppler bin than the echo signal, interference is not focused after DBS.

The effectiveness of DBS to suppress all types of interference has been shown by developing the INR heatmaps after MIMO and MIMO-DBS beamforming. Moreover, depending upon the waveform parameters of interfering radars, complete removal of interference from the radar's FoV has been observed in some cases.

Therefore, compared to temporal and spatial mitigation techniques, which often have an adverse effect on the echo signal, DBS suppresses interference while achieving enhanced azimuth/ cross-range resolutions for the echo signal. Additionally, it functions well in the background of multiple interfering signals.

The presented analysis has been validated in an actual automotive scenario to show the applicability of MIMO-DBS processing in SoA sensors. The implementation of DBS does not require any hardware upgrade or additional computational requirements, making it an ideal choice for modern radar systems.

Chapter 9. CONCLUSIONS AND OUTLOOK

The radar sensors are designed to use a wide range of specifications and waveform parameters according to the industry requirements. For increased automation and traffic safety, they should deliver full scene mapping around the car. To achieve this, each vehicle is expected to have up to 12 radars. In a coexistence scenario, the chances of overlapping bandwidths between the radars increase, which leads to interference between them. The motivation behind the presented work is to characterise radar interference and provide mitigation strategies that could be incorporated into SoA automotive radar chipsets with reliable performance.

This work presented a detailed study of the mutual interference in FMCW radars by investigating the methodologies to identify, classify, detect, reconstruct, avoid, and mitigate interference in automotive applications. The developed techniques would also be applicable to counter the impact of interference in other scenarios.

9.1 Conclusions

A system-level mathematical model has initially been developed to analyse interference in an FMCW automotive radar. This laid the foundation to estimate the impact of interference on radar performance. It has been shown that interference signals within the receiver band of radar can degrade its detection capability, leading to missed detections and, in rare cases, false targets. To understand the effect of interference on a radar detection characteristics, the statistics of interference have been determined and compared with the AWGN. The statistics of most types of interference are Gaussian-like and hence will not require developing new detection techniques. However, certain cases show a deviation from Gaussian statistics indicating the

requirement of optimal detection techniques. As the interference floor is much higher than the AWGN floor, it affects the SINR and requires appropriate mitigation before target detection.

Effective interference mitigation requires a thorough understanding of how interference manifests itself along the signal-processing stages of a radar. For this, a qualitative and quantitative comparison of the characteristics of interference and the SINR along the processing stages of the VR have been evaluated. This has been used as a groundwork to develop interference mitigation in different domains, including:

- Time domain – where interference parameters of an unknown interfering signal have been estimated and used to avoid interference or suppress its impact using the sense and avoid approach.
- Spatial domain – where interference has been suppressed by directing an adaptive null towards the direction of incoming interference for MIMO and full-phased array configurations. Spatial domain mitigation performs reasonably well for well-separated targets and interferers. However, its applicability in congested automotive scenarios is questionable, considering the limited degrees of freedom in SoA radar chipsets. Additionally, mitigation in the spatial domain compromises the performance of radar with higher sidelobes, causing false detections and limiting radar dynamic range.
- Doppler and spatial domains – where the Doppler and spatial characteristics of the interfering signal have been combined using MIMO-DBS beamforming to mitigate interference. A significant reduction in interference has been achieved. In specific scenarios, interference has been completely removed from the FoV of radar without degrading radar performance. Implementing DBS as a software upgrade in sensors can significantly reduce interference while minimising radar development costs.

- Additionally, techniques such as waveform randomisation have been proposed to decorrelate interference pulses and reduce their impact. A significant improvement in the SINR has been achieved for uncorrelated interference as the radar processes it.

The novel aspects of the presented research are summarised as follows:

1. Analysis of the impact of the LPF parameters, especially its order, on the appearance of interference, duration of interference, and radar detector's performance in SoA automotive radar chipsets.
2. Classification of interference with respect to the mutual automotive radar parameters: synchronous, semi-synchronous, asynchronous interference.
3. Statistical analysis of interference and the effect of various types of interference on detectors' performance.
4. Methodology to detect interference when its power level is comparable to the received echo signal.
5. Methodology to estimate the waveform parameters of an 'a-priori' unknown interference.
6. Interference mitigation based on the cognitive adaption of the VR waveform parameters without compromising the radar performance.
7. Randomisation as a technique to reduce the impact of interference at the VR.
8. Mitigation of radar interference by exploiting spatial domain features in MIMO and traditional full phased array.
9. Qualitative and quantitative analysis of interference along the processing stages of radar employing the SINR as the performance metric.
10. MIMO-DBS beamforming as a technique to mitigate radar interference.
11. Development of a holistic simulator to model radar and environment interactions and test advanced algorithms before implementing them in robust sensors.

Based on the developed models for radar analysis and performance evaluation in coexistence scenarios, an experimentally verified holistic end-to-end simulator has been developed, accounting for sensor configuration and sensed scene representation in different formats. The simulator has been validated using data recorded by a multi-sensory suite during a series of specifically designed real-road automotive trials. Radar-environment interactions have been demonstrated for extended targets, clutter, and transmissions from nearby sensors – radar interference. Moreover, various aspects of sensor configuration and signal processing according to radars' hardware and software capabilities have been investigated. The models could bring real-world conditions into the software by modelling various propagation scenarios and processing the data with various radar configurations, penetration rates, and types of interference. Based on the sensed scene, various mitigation strategies can be applied to counter the impacts of the environment. The simulator will be an effective tool for analysing the performance of radar chipsets in realistic road conditions and understanding radar–environment interactions. Moreover, it would facilitate a comparative analysis of the performance of sensors currently expected to be used for ADAS, acting as a guide toward the development of robust radar sensors.

9.2 Outlook

The prospects of the presented work have been summarised in this section.

9.2.1 Resolution Enhancement with DBS Beamforming

Conventional DBS processing is based on the Doppler compression followed by axes manipulations to provide an enhanced azimuth resolution with a lower SLL. Prospects of super-resolution DBS imaging methods [312] can further enhance the angular resolution. However, DBS relies on the relative speed information of the radar and target. Therefore, its application

is limited to a moving platform with a static target(s). The application of DBS beamforming in a dynamic environment with multiple targets is a subject of further study.

9.2.2 Digital Radars

A modern trend in automotive radar is the use of digital radars such as with code division multiplexing (CDM) [313], orthogonal frequency division multiplexing (OFDM) [233], [314], and digital code modulation (DCM) [315]–[317]. Digital waveforms provide more flexibility and adaptability to radar functionality. The basic idea is to generate multi-carrier wideband signals with anti-interference capability digitally. DCM-based automotive radars are claimed to have no interference from other DCM radars [316]. However, their interaction with SoA radars using other modulation schemes, typically FMCW and PMCW, is yet to be investigated. Moreover, a more detailed investigation of radar interaction in specifically designed road scenarios, especially congested environments, is required.

9.2.3 Radar Communication

Currently, automotive radar sensors operate in a non-cooperative mode without communicating with each other. Radar Communications (RadCom) is another modern approach for automotive sensing where radar hardware would be utilised for communication purposes, allowing a fusion between communication nodes and radar sensors. This paves the way for using under-utilised FMCW radar bandwidth for communication purposes [105], [318]–[322] using dynamic frequency allocation. This reduces the probability of spectrum overlaps between coexisting radars, thus, reducing interference between them [205], [319], [323]–[325].

9.2.4 Cognitive Radar

Cognitive radars are the next-generation sensors. The necessity for enhanced performance of cognitive radars has been discussed in the literature [326]. However, its application for

automotive sensing, specifically interference suppression, is a relatively new research area [327], [328]. Cognitive radar could sense the environment and make optimal decisions such as using unique waveform modulations – OFDM in [328], PC-FMCW in [245], adapting waveform parameters [329], [330], or resources re-allocation [331] to reduce susceptibility to interference. However, future work in this area should be an experimental analysis of proposed techniques in congested automotive scenarios, where radars from different manufacturers with different waveform modulations are expected.

9.2.5 Standardisation and Resource Allocation Mechanism

One of the foremost requirements in solving the problem of interference between coexisting radars is industry-wide coordination to develop pertinent regulations and standards for automotive radars. Standardisation will allow frequency planning, waveform modulations, time slot management, and polarisation assignment based on radar orientation for robust radar operation. This is particularly essential for the attainment of techniques like RadCom [332]–[335]. However, this requires an agreement between manufacturers and Tier-1 and Tier-2 suppliers. Additionally, individual mitigation techniques are often suitable for particular scenarios only. Therefore, to achieve optimum radar performance, a combination of multiple interference mitigation techniques would be needed to mitigate interference efficiently without any additional complexity in terms of signal processing, radar form factor, or mitigation duration.

9.3 Radar Interference From Author's Perspective

The future of the automotive industry is a fully autonomous car that can drive itself without requiring any driver assistance. This however needs a solution to all the underlying challenges and one of them is the interference between automotive radars. Interference is although a challenging phenomenon and a current area of research, however, at the same time

it's unique behaviour makes it interesting. Interference occurs when two or more radar signals access the same portion of the frequency spectrum, and their waves interact. To achieve a broad FoV with 360^o sensing around the vehicle and to obtain high range, speed, and azimuth resolutions, industry trends have demonstrated the use of higher bandwidth and higher active duty cycles with multiple sensors per vehicle. However, this leads to a higher probability of victim and interfering signals overlapping in temporal, frequency, and spatial domains.

Vehicles moving in opposite directions, the same direction, and through crossings can cause interference and the impact of interference is significantly affected by the orientation of radar sensors. For example, consider the following cases:

- Case 1: The two radars are facing each other, such as a scene expected in a typical highway scenario where the forward-looking radar of one vehicle will interfere with the backward-looking radar of the other vehicle. In this case, the main lobes of the two radars will interfere leading to a much stronger impact of interference. This has been illustrated in Figure 9.1(a).
- Case 2: The vehicle at the back decides to overtake the vehicle at the front. As soon as the vehicle starts to manoeuvre to the second lane, the impact of interference from the backward-looking radar of front vehicle will start decreasing while the interference from the corner-looking radar will start increasing. In this case, there will be multiple interference scenarios such as interference between the forward and corner looking radars, between the two corner-looking radars. In certain instances, depending upon the position of each vehicle, interference might also happen through the sidelobes of the array pattern. This has been illustrated in Figure 9.1 (b).
- Case 3: When the vehicles are next to each other, interference will predominantly happen between the two side-looking radars. Interference might also occur between the backward-

looking radar of one vehicle and the corner-looking radar of the other vehicle. This will however have a smaller impact due to the orientation of interfering radars. This has been illustrated in Figure 9.1 (c).

- Case 4: In the next scene, consider a cross-traffic scenario where two vehicles are waiting at a traffic light or a junction. The interference will occur between the forward-looking radars of two vehicles, mainly through the sidelobes, and between the corner-looking radars through the main lobes. This has been illustrated in Figure 9.1 (d).
- Case 5: In this case, the source of interference is off-road, such as an intentional jamming towards the radar, or a radar for another purpose such as to measure the speed of vehicles. This has been illustrated in Figure 9.1 (e).

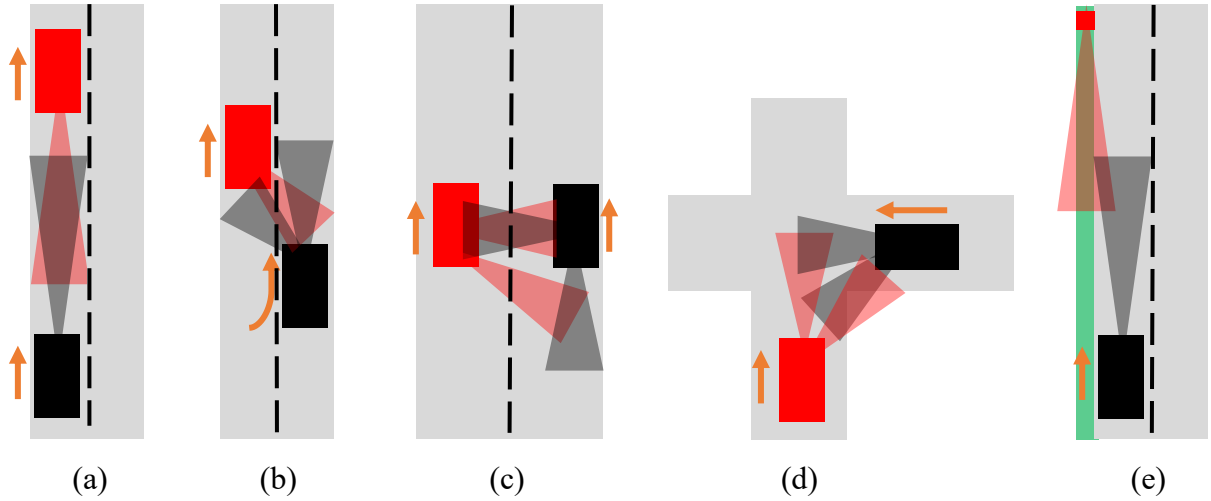


Figure 9.1: Interference scenarios. (a) Vehicles facing each other. (b) The vehicle in black is about to overtake the vehicle in red. (c) Vehicles next to each other in different lanes. (d) Vehicles waiting at a junction. (e) Off-road source of interference. The black and red blocks represent the vehicles, and the corresponding beams show the orientation of each radar sensor.

In the above scenarios, the effect of waveform parameters has not been included. However, distinct waveform interactions with different impacts are expected with a slight change in the waveform parameters of the interfering radars.

Therefore, a variety of possible interference cases can occur in an automotive environment. In environments such as a highway or a countryside road, as the vehicles will be in the proximity of each other for a long time, interference will be long-lived compared to scenarios such as a busy road where the relative position of vehicles changes rapidly, making interference between two specific radars a short-lived phenomenon.

Considering the logistics and planning behind organising and conducting the field trials and processing the recorded data, it will be impossible to test all the real road scenarios, with the available SoA radar chipsets, and understand the phenomena of interference between them. Therefore, as part of this research, an experimentally verified simulator has been developed, which can be used to understand the impact of interfering in different off-road and on-road scenarios, and also evaluate the impact of radar parameters on interference.

Based on the aforementioned scenarios, a variety of mitigation techniques or their combination might be needed to suppress interference. For example, referring back to Figure 3.1, in a countryside road, where the number of interfering sources are expected to be less, time domain mitigation of interference such as interference zeroing might be a suitable choice to suppress interference. Spatial domain mitigation using adaptive beamforming to direct spatial nulls might be suitable when the source of interference is off-road (Figure 9.1 (e)). However, as soon the road scene becomes congested, time domain or spatial domain mitigations alone are no more suited due to an increase in the number of interfering sources, and the target being a source of interference. In these cases, imaging techniques such as Doppler beam sharpening are more suited as they can suppress interference and at the same time enhance the performance of the radar.

As part of future work, multi-modal distributed sensing would be a useful way of suppressing the impact of interference. In this case, as each sensor (installed at a different

orientation) will observe the scene from a different perspective, the integrated images will provide an enhanced SINR. Digital modulation schemes are also expected to provide robustness against interference. Lastly, it is essential and the need of time for automotive manufacturers to sit together and decide on the regulatory limitations and allocation of the resources for better coordination between the vehicles (such as radar-communication).

REFERENCES

[1] M. V. Rajasekhar and A. K. Jaswal, 'Autonomous vehicles: The future of automobiles', in *2015 IEEE International Transportation Electrification Conference (ITEC)*, Aug. 2015, pp. 1–6. doi: 10.1109/ITEC-India.2015.7386874.

[2] Y. Ji, X. Zhu, T. Zhao, L. Wu, and M. Sun, 'Revealing Technology Innovation, Competition and Cooperation of Self-Driving Vehicles From Patent Perspective', *IEEE Access*, vol. 8, pp. 221191–221202, 2020, doi: 10.1109/ACCESS.2020.3042019.

[3] K. Dalal, Z. Lin, M. Gifford, and L. Svanström, 'Economics of Global Burden of Road Traffic Injuries and Their Relationship with Health System Variables', *Int. J. Prev. Med.*, vol. 4, no. 12, pp. 1442–1450, Dec. 2013.

[4] 'Road traffic injuries'. https://www.who.int/news-room/fact-sheets/detail/road-traffic-injuries (accessed Jul. 05, 2021).

[5] 'Global road safety statistics', *Brake*. https://www.brake.org.uk/get-involved/take-action/mybrake/knowledge-centre/global-road-safety (accessed Nov. 21, 2022).

[6] M. Stevenson and J. Thompson, 'On the road to prevention: Road injury and health promotion', *Health Promot. J. Aust. Off. J. Aust. Assoc. Health Promot. Prof.*, vol. 25, pp. 4–7, Apr. 2014, doi: 10.1071/HE13075.

[7] 'Estimated number of road traffic deaths'. https://www.who.int/data/gho/data/indicators/indicator-details/GHO/estimated-number-of-road-traffic-deaths (accessed Jul. 05, 2021).

[8] B. Crew, 'Driverless Cars Could Reduce Traffic Fatalities by Up to 90%, Says Report', *ScienceAlert*. https://www.sciencealert.com/driverless-cars-could-reduce-traffic-fatalities-by-up-to-90-says-report (accessed Jul. 05, 2021).

[9] B. C. Zanchin, R. Adamshuk, M. M. Santos, and K. S. Collazos, 'On the instrumentation and classification of autonomous cars', in *2017 IEEE International Conference on Systems, Man, and Cybernetics (SMC)*, Oct. 2017, pp. 2631–2636. doi: 10.1109/SMC.2017.8123022.

[10] M. I. November 05 and 2020, ‘What Are the Levels of Automated Driving?’, *Aptiv*. https://www.aptiv.com/en/insights/article/what-are-the-levels-of-automated-driving (accessed Jul. 28, 2023).

[11] ‘The 6 Levels of Vehicle Autonomy Explained | Synopsys Automotive’. https://www.synopsys.com/automotive/autonomous-driving-levels.html (accessed Jul. 28, 2023).

[12] ‘Automotive Radar Market Forecast 2024 - Global Industry Report’, *Global Market Insights Inc.* https://www.gminsights.com/industry-analysis/automotive-radar-market (accessed Nov. 21, 2022).

[13] S. M. Patole, M. Torlak, D. Wang, and M. Ali, ‘Automotive radars: A review of signal processing techniques’, *IEEE Signal Process. Mag.*, vol. 34, no. 2, pp. 22–35, Mar. 2017, doi: 10.1109/MSP.2016.2628914.

[14] B. Clarke, S. Worrall, G. Brooker, J. Martinez, and E. Nebot, ‘Improving situational awareness with radar information’, in *2012 IEEE Intelligent Vehicles Symposium*, Jun. 2012, pp. 535–540. doi: 10.1109/IVS.2012.6232211.

[15] I. Bilik, ‘Comparative Analysis of Radar and Lidar Technologies for Automotive Applications’, *IEEE Intell. Transp. Syst. Mag.*, vol. 15, no. 1, pp. 244–269, Jan. 2023, doi: 10.1109/MITS.2022.3162886.

[16] J. Vargas, S. Alsweiss, O. Toker, R. Razdan, and J. Santos, ‘An Overview of Autonomous Vehicles Sensors and Their Vulnerability to Weather Conditions’, *Sensors*, vol. 21, no. 16, Art. no. 16, Jan. 2021, doi: 10.3390/s21165397.

[17] Z. Hong, Y. Petillot, and S. Wang, ‘RadarSLAM: Radar based Large-Scale SLAM in All Weathers’, in *2020 IEEE/RSJ International Conference on Intelligent Robots and Systems (IROS)*, Oct. 2020, pp. 5164–5170. doi: 10.1109/IROS45743.2020.9341287.

[18] A. Bourdoux, K. Parashar, and M. Bauduin, ‘Phenomenology of mutual interference of FMCW and PMCW automotive radars’, in *2017 IEEE Radar Conference (RadarConf)*, May 2017, pp. 1709–1714. doi: 10.1109/RADAR.2017.7944482.

[19] F. Engels, P. Heidenreich, A. M. Zoubir, F. K. Jondral, and M. Wintermantel, ‘Advances in Automotive Radar: A framework on computationally efficient high-resolution

frequency estimation', *IEEE Signal Process. Mag.*, vol. 34, no. 2, pp. 36–46, Mar. 2017, doi: 10.1109/MSP.2016.2637700.

[20] A. Pirkani, S. Cassidy, F. Norouzian, M. Gashinova, and M. Cherniakov, 'Doppler Beam Sharpening for Enhanced MIMO Imagery in the Presence of Automotive Interference', in *2021 18th European Radar Conference (EuRAD)*, Apr. 2022, pp. 417–420. doi: 10.23919/EuRAD50154.2022.9784499.

[21] S. Alland, W. Stark, M. Ali, and M. Hegde, 'Interference in Automotive Radar Systems: Characteristics, Mitigation Techniques, and Current and Future Research', *IEEE Signal Process. Mag.*, vol. 36, no. 5, pp. 45–59, Sep. 2019, doi: 10.1109/MSP.2019.2908214.

[22] 'Advancements in Automotive Radars', *FutureBridge*, Sep. 20, 2019. https://www.futurebridge.com/blog/advancements-in-automotive-radars/ (accessed Nov. 23, 2022).

[23] R. and Markets, 'Insights on the Automotive Radar Global Market to 2027 - Technological Advancements in Vehicle Safety and Security Presents Opportunities'. https://www.prnewswire.com/news-releases/insights-on-the-automotive-radar-global-market-to-2027---technological-advancements-in-vehicle-safety-and-security-presents-opportunities-301522761.html (accessed Nov. 23, 2022).

[24] 'Automotive Radar: Golden Era of Innovation and Growth', *IDTechEx*, Jul. 14, 2020. https://www.idtechex.com/en/research-article/automotive-radar-golden-era-of-innovation-and-growth/21210 (accessed Nov. 23, 2022).

[25] S. Salehian, 'Council Post: How Advancements In Vehicle Safety Technology Can Eliminate Traffic Fatalities', *Forbes*. https://www.forbes.com/sites/forbestechcouncil/2022/10/31/how-advancements-in-vehicle-safety-technology-can-eliminate-traffic-fatalities/ (accessed Nov. 23, 2022).

[26] 'Advancements in Radar Sensors, CMOS Image Sensors, Connected or Autonomous Vehicles, ADAS, Parking Space Detection, and Cyber Security', *Store.Frost.com*. https://store.frost.com/advancements-in-radar-sensors-cmos-image-sensors-connected-or-autonomous-vehicles-adas-parking-space-detection-and-cyber-security.html (accessed Nov. 23, 2022).

[27] J. Kocić, N. Jovičić, and V. Drndarević, ‘Sensors and Sensor Fusion in Autonomous Vehicles’, in *2018 26th Telecommunications Forum (TELFOR)*, Nov. 2018, pp. 420–425. doi: 10.1109/TELFOR.2018.8612054.

[28] D. Das, N. Adhikary, and S. Chaudhury, ‘Sensor fusion in autonomous vehicle using LiDAR and camera Sensor’, in *2022 IEEE 10th Region 10 Humanitarian Technology Conference (R10-HTC)*, Sep. 2022, pp. 336–341. doi: 10.1109/R10-HTC54060.2022.9929588.

[29] J. Hasch, E. Topak, R. Schnabel, T. Zwick, R. Weigel, and C. Waldschmidt, ‘Millimeter-Wave Technology for Automotive Radar Sensors in the 77 GHz Frequency Band’, *IEEE Trans. Microw. Theory Tech.*, vol. 60, no. 3, pp. 845–860, Mar. 2012, doi: 10.1109/TMTT.2011.2178427.

[30] I. Bilik *et al.*, ‘Automotive MIMO radar for urban environments’, in *2016 IEEE Radar Conference (RadarConf)*, May 2016, pp. 1–6. doi: 10.1109/RADAR.2016.7485215.

[31] F. Engels, M. Wintermantel, and P. Heidenreich, ‘Automotive MIMO radar angle estimation in the presence of multipath’, in *2017 European Radar Conference (EURAD)*, Oct. 2017, pp. 82–85. doi: 10.23919/EURAD.2017.8249152.

[32] M. Kunert, H. Meinel, C. Fischer, and M. Ahrholdt, ‘Report on interference density increase by market penetration forecast’, MOSARIM consortium CNTR 248 231, Sep. 2010. [Online]. Available: www.mosarim.eu

[33] H. H. Meinel and J. Dickmann, ‘Automotive Radar: From Its Origins to Future Directions’, *Microw. J.*, vol. 56, no. 9, pp. 24–57, 2013.

[34] H. H. Meinel, ‘Evolving automotive radar — From the very beginnings into the future’, in *The 8th European Conference on Antennas and Propagation (EuCAP 2014)*, Apr. 2014, pp. 3107–3114. doi: 10.1109/EuCAP.2014.6902486.

[35] ‘Automotive Radars Could Soon Face Significant Interference’, *EE Times Asia*, May 02, 2021. https://www.eetasia.com/automotive-radars-could-soon-face-significant-interference/ (accessed Nov. 23, 2022).

[36] K. Field, ‘As radar technology on cars proliferates, so do interference concerns’, *Fierce Electronics*, Dec. 30, 2019. https://www.fierceelectronics.com/electronics/as-radar-technology-cars-proliferates-so-do-interference-concerns (accessed Nov. 23, 2022).

[37] C. Waldschmidt, J. Hasch, and W. Menzel, 'Automotive Radar — From First Efforts to Future Systems', *IEEE J. Microw.*, vol. 1, no. 1, pp. 135–148, winter 2021, doi: 10.1109/JMW.2020.3033616.

[38] 'AWR1243BOOST AWR1243 76-GHz to 81-GHz high-performance automotive MMIC evaluation module | TI.com'. https://www.ti.com/tool/AWR1243BOOST (accessed Aug. 07, 2020).

[39] 'TEF810X Fully-Integrated 77 GHz Radar Transceiver | NXP'. https://www.nxp.com/products/rf/radar-transceivers/tef810x-fully-integrated-77-ghz-radar-transceiver:TEF810X (accessed Mar. 30, 2020).

[40] 'INRAS Products - Radarbook'. http://www.inras.at/en/products/radarbook.html (accessed May 28, 2020).

[41] T. Schipper, M. Harter, L. Zwirello, T. Mahler, and T. Zwick, 'Systematic approach to investigate and counteract interference-effects in automotive radars', in *2012 9th European Radar Conference*, Oct. 2012, pp. 190–193.

[42] M. Dudek, R. Wahl, D. Kissinger, R. Weigel, and G. Fischer, 'Millimeter wave FMCW radar system simulations including a 3D ray tracing channel simulator', in *2010 Asia-Pacific Microwave Conference*, Dec. 2010, pp. 1665–1668.

[43] M. I. Skolnik, *Introduction to radar systems*, 2d ed. New York: McGraw-Hill, 1980.

[44] A. Lazaro, M. Lazaro, R. Villarino, and P. De Paco, 'New Radar Micro-Doppler Tag for Road Safety Based on the Signature of Rotating Backscatters', *IEEE Sens. J.*, vol. 21, no. 6, pp. 8604–8612, Mar. 2021, doi: 10.1109/JSEN.2020.3048081.

[45] S. Duong, D. Kahrizi, S. Mettler, and C. Klöck, 'Moving Target Classification with a Dual Automotive FMCW Radar System Using Convolutional Neural Networks', in *2021 21st International Radar Symposium (IRS)*, Jun. 2021, pp. 1–9. doi: 10.23919/IRS51887.2021.9466195.

[46] L. Senigagliesi, G. Ciattaglia, D. Disha, and E. Gambi, 'Classification of Human Activities based on Automotive Radar Spectral Images Using Machine Learning Techniques: A Case Study', in *2022 IEEE Radar Conference (RadarConf22)*, Mar. 2022, pp. 1–6. doi: 10.1109/RadarConf2248738.2022.9764217.

[47] P. D. Mark A. Richards, *Fundamentals of Radar Signal Processing, Second Edition*. McGraw-Hill Education: New York, Chicago, San Francisco, Athens, London, Madrid, Mexico City, Milan, New Delhi, Singapore, Sydney, Toronto, 2014. Accessed: Feb. 03, 2020. [Online]. Available: /content/book/9780071798327

[48] C. Diehl, E. Feicho, A. Schwambach, T. Dammeier, E. Mares, and T. Bertram, 'Radar-based Dynamic Occupancy Grid Mapping and Object Detection', in *2020 IEEE 23rd International Conference on Intelligent Transportation Systems (ITSC)*, Sep. 2020, pp. 1–6. doi: 10.1109/ITSC45102.2020.9294626.

[49] T. Grebner, P. Schoeder, V. Janoudi, and C. Waldschmidt, 'Radar-Based Mapping of the Environment: Occupancy Grid-Map Versus SAR', *IEEE Microw. Wirel. Compon. Lett.*, vol. 32, no. 3, pp. 253–256, Mar. 2022, doi: 10.1109/LMWC.2022.3145661.

[50] 'Radar - History of radar', *Encyclopedia Britannica*. https://www.britannica.com/technology/radar (accessed Jul. 06, 2021).

[51] 'The Birth of Radar and the 2nd World War', *RAF Air Defence Radar Museum*. https://www.radarmuseum.co.uk/history/world-war-two/ (accessed Jul. 30, 2023).

[52] 'History of Ionospheric Radars', *URSI Radio Sci. Bull.*, vol. 2019, no. 370, pp. 69–69, Sep. 2019, doi: 10.23919/URSIRSB.2019.8956155.

[53] H. A. H. Boot and J. T. Randall, 'Historical notes on the cavity magnetron', *IEEE Trans. Electron Devices*, vol. 23, no. 7, pp. 724–729, Jul. 1976, doi: 10.1109/T-ED.1976.18476.

[54] V. Clarkson and B. Ng, 'A Radar Revolution', *IEEE Potentials*, vol. 38, no. 4, pp. 6–8, Jul. 2019, doi: 10.1109/MPOT.2019.2913941.

[55] Z. Feng, M. Stolz, M. Li, M. Kunert, and W. Wiesbeck, 'Verification of a Lane Detection Method with Automotive Radar based on a New Type of Road Marking', in *2018 IEEE MTT-S International Conference on Microwaves for Intelligent Mobility (ICMIM)*, Apr. 2018, pp. 1–4. doi: 10.1109/ICMIM.2018.8443513.

[56] H. H. Meinel and W. Bösch, 'Radar Sensors in Cars', in *Automated Driving: Safer and More Efficient Future Driving*, D. Watzenig and M. Horn, Eds., Cham: Springer International Publishing, 2017, pp. 245–261. doi: 10.1007/978-3-319-31895-0_10.

[57] H. H. Meinel, ‘Evolving automotive radar — From the very beginnings into the future’, in *The 8th European Conference on Antennas and Propagation (EuCAP 2014)*, Apr. 2014, pp. 3107–3114. doi: 10.1109/EuCAP.2014.6902486.

[58] L. H. Eriksson and B.-O. As, ‘Automotive radar for adaptive cruise control and collision warning/avoidance’, in *Radar 97 (Conf. Publ. No. 449)*, Oct. 1997, pp. 16–20. doi: 10.1049/cp:19971623.

[59] C. Eckersten and B.-O. As, ‘A high performance automotive radar for adaptive cruise control and collision warning/avoidance’, in *Proceedings of Conference on Intelligent Transportation Systems*, Nov. 1997, pp. 446–451. doi: 10.1109/ITSC.1997.660516.

[60] J. D. Woll, ‘Monopulse Doppler radar for vehicle applications’, in *Proceedings of the Intelligent Vehicles ’95. Symposium*, Sep. 1995, pp. 42–47. doi: 10.1109/IVS.1995.528255.

[61] M. Schneider, ‘Automotive radar: Status and trends’, in *In Proceedings of the German Microwave Conference GeMIC 2005*, 2005, pp. 144–147.

[62] H. Meinel and B. R. Bold, ‘Commercial and scientific applications of millimetric and sub-millimetric waves’, *Radio Electron. Eng.*, vol. 49, no. 7, pp. 351–360, Dec. 1979, doi: 10.1049/ree.1979.0068.

[63] H. H. Meinel, ‘Millimeter-wave systems and applications in Europe’, in *1988., IEEE MTT-S International Microwave Symposium Digest*, May 1988, pp. 649–653 vol.2. doi: 10.1109/MWSYM.1988.22117.

[64] P. Kalyan, ‘System Modeling of Next Generation Digitally Modulated Automotive RADAR (DMR)’, p. 92.

[65] L. P. Goetz and J. D. Albright, ‘Airborne Pulse-Doppler Radar’, *IRE Trans. Mil. Electron.*, vol. MIL–5, no. 2, pp. 116–126, Apr. 1961, doi: 10.1109/IRET-MIL.1961.5008329.

[66] M. A. Adnan, N. Sulaiman, N. I. Zainuddin, and T. B. H. T. Besar, ‘Vehicle speed measurement technique using various speed detection instrumentation’, in *2013 IEEE Business Engineering and Industrial Applications Colloquium (BEIAC)*, Apr. 2013, pp. 668–672. doi: 10.1109/BEIAC.2013.6560214.

[67] ‘M.2057 : Systems characteristics of automotive radars operating in the frequency band 76-81 GHz for intelligent transport systems applications’. https://www.itu.int/rec/R-REC-M.2057-0-201402-S/en (accessed Aug. 05, 2021).

[68] J. Steinbaeck, C. Steger, G. Holweg, and N. Druml, ‘Next generation radar sensors in automotive sensor fusion systems’, in *2017 Sensor Data Fusion: Trends, Solutions, Applications (SDF)*, Oct. 2017, pp. 1–6. doi: 10.1109/SDF.2017.8126389.

[69] J. Dickmann *et al.*, ‘Automotive radar the key technology for autonomous driving: From detection and ranging to environmental understanding’, in *2016 IEEE Radar Conference (RadarConf)*, May 2016, pp. 1–6. doi: 10.1109/RADAR.2016.7485214.

[70] S. Sun, A. P. Petropulu, and H. V. Poor, ‘MIMO Radar for Advanced Driver-Assistance Systems and Autonomous Driving: Advantages and Challenges’, *IEEE Signal Process. Mag.*, vol. 37, no. 4, pp. 98–117, Jul. 2020, doi: 10.1109/MSP.2020.2978507.

[71] K. Ramasubramanian and K. Ramaiah, ‘Moving from Legacy 24 GHz to State-of-the-Art 77-GHz Radar’, *ATZelektronik Worldw.*, vol. 13, no. 3, pp. 46–49, Jun. 2018, doi: 10.1007/s38314-018-0029-6.

[72] J. Wenger, ‘Automotive radar - status and perspectives’, in *IEEE Compound Semiconductor Integrated Circuit Symposium, 2005. CSIC ’05.*, Oct. 2005, p. 4 pp.-. doi: 10.1109/CSICS.2005.1531741.

[73] M. M. Vazquez, ‘Radar For Automotive: Why Do We Need Radar?’, *Semiconductor Engineering*, Mar. 24, 2022. https://www.renesas.com/us/en/blogs/radar-transceivers-key-component-adas-autonomous-driving-blog-1-why-do-we-need-radar (accessed Jul. 30, 2023).

[74] S. Sun, A. P. Petropulu, and H. V. Poor, ‘MIMO Radar for Advanced Driver-Assistance Systems and Autonomous Driving: Advantages and Challenges’, *IEEE Signal Process. Mag.*, vol. 37, no. 4, pp. 98–117, Jul. 2020, doi: 10.1109/MSP.2020.2978507.

[75] H. J. Ng, R. Feger, and A. Stelzer, ‘A Fully-Integrated 77-GHz UWB Pseudo-Random Noise Radar Transceiver With a Programmable Sequence Generator in SiGe Technology’, *IEEE Trans. Circuits Syst. Regul. Pap.*, vol. 61, no. 8, pp. 2444–2455, Aug. 2014, doi: 10.1109/TCSI.2014.2309774.

[76] H. Veenstra, E. van der Heijden, M. Notten, and G. Dolmans, 'A SiGe-BiCMOS UWB Receiver for 24 GHz Short-Range Automotive Radar Applications', in *2007 IEEE/MTT-S International Microwave Symposium*, Jun. 2007, pp. 1791–1794. doi: 10.1109/MWSYM.2007.380095.

[77] 'Automotive Radar – A Tale of Two Frequencies', *ST life.augmented Blog*, Aug. 19, 2016. https://blog.st.com/automotive-radar-tale-two-frequencies/ (accessed Jul. 07, 2021).

[78] M. Goppelt, H.-L. Blöcher, and W. Menzel, 'Automotive radar - investigation of mutual interference mechanisms', *Adv. Radio Sci.*, vol. 8, pp. 55–60, Sep. 2010, doi: 10.5194/ars-8-55-2010.

[79] '79 GHz High Resolution Short Range Automotive Radar Evolution | 2013-09-15 | Microwave Journal'. https://www.microwavejournal.com/articles/20473-ghz-high-resolution-short-range-automotive-radar-evolution?v=preview (accessed Jul. 07, 2021).

[80] R. Schneider, H.-L. Blocher, and K. M. Strohm, 'KOKON - automotive high frequency technology at 77/79 GHz', in *2007 European Microwave Conference*, Oct. 2007, pp. 1526–1529. doi: 10.1109/EUMC.2007.4405497.

[81] 'ARS30X-Datasheet-EN.pdf.pdf'. Accessed: Aug. 25, 2021. [Online]. Available: https://www.continental-automotive.com/getattachment/9b6de999-75d4-4786-bb18-8ab64fd0b181/ARS30X-Datasheet-EN.pdf.pdf

[82] '120903_LRR3_EN_V05_final.pdf'. Accessed: Aug. 25, 2021. [Online]. Available: https://www.bosch-engineering.jp/media/jp/pdfs_3/einsatzgebiete_4/produktdatenblaetter_2/120903_LRR3_EN_V05_final.pdf

[83] '76 GHz to 81 GHz car RADAR transceiver', vol. 2019, p. 13, 2019.

[84] 'TEF810x Fully-Integrated 77 GHz Radar Transceiver | NXP Semiconductors'. https://www.nxp.com/products/radio-frequency/radar-transceivers/tef810x-fully-integrated-77-ghz-radar-transceiver:TEF810X (accessed Aug. 25, 2021).

[85] 'MR2001 Multi-channel 77GHz Radar Transceiver | NXP Semiconductors'. https://www.nxp.com/products/no-longer-manufactured/mr2001-multi-channel-77-ghz-radar-transceiver-chipset:MR2001 (accessed Aug. 25, 2021).

[86] I. T. AG, ‘Radar sensors for automotive - Infineon Technologies’. https://www.infineon.com/cms/en/product/sensor/radar-sensors/radar-sensors-for-automotive/ (accessed Aug. 25, 2021).

[87] I. T. AG, ‘Automotive 77 GHz radar system - Infineon Technologies’. https://www.infineon.com/cms/en/applications/automotive/chassis-safety-and-adas/automotive-77-ghz-radar-system/ (accessed Aug. 25, 2021).

[88] ‘mmWave radar sensors for automotive applications | Overview | Automotive Radar Sensors | TI.com’. https://www.ti.com/sensors/mmwave-radar/automotive/overview.html (accessed Aug. 25, 2021).

[89] ‘TIDEP-01012 reference design | TI.com’. https://www.ti.com/tool/TIDEP-01012 (accessed Nov. 02, 2022).

[90] ‘INRAS Products - Radarbook’. http://www.inras.at/en/products/radarbook.html (accessed Jul. 21, 2021).

[91] ‘INRAS Products - RadarLog - RF-Frontends’. http://www.inras.at/en/products/new-radarlog/rf-frontends.html (accessed Aug. 25, 2021).

[92] L. Daniel *et al.*, ‘Application of Doppler beam sharpening for azimuth refinement in prospective low-THz automotive radars’, *IET Radar Sonar Navig.*, vol. 12, no. 10, pp. 1121–1130, 2018, doi: 10.1049/iet-rsn.2018.5024.

[93] D. Jasteh, E. G. Hoare, M. Cherniakov, and M. Gashinova, ‘Experimental Low-Terahertz Radar Image Analysis for Automotive Terrain Sensing’, *IEEE Geosci. Remote Sens. Lett.*, vol. 13, no. 4, pp. 490–494, Apr. 2016, doi: 10.1109/LGRS.2016.2518579.

[94] World Radiocommunication Conference and International Telecommunication Union, Eds., *Final acts WRC-15: World Radiocommunication Conference (Geneva, 2015).* 2016.

[95] ‘ECC Report 262,’ Accessed: Jul. 06, 2021. [Online]. Available: https://docdb.cept.org/download/1292

[96] H. Rohling and M.-M. Meinecke, ‘Waveform design principles for automotive radar systems’, in *2001 CIE International Conference on Radar Proceedings (Cat No.01TH8559)*, Oct. 2001, pp. 1–4. doi: 10.1109/ICR.2001.984612.

[97] H. Rohling and C. Moller, ‘Radar waveform for automotive radar systems and applications’, in *2008 IEEE Radar Conference*, May 2008, pp. 1–4. doi: 10.1109/RADAR.2008.4721121.

[98] S. Khobahi, A. Bose, and M. Soltanalian, ‘Deep Radar Waveform Design for Efficient Automotive Radar Sensing’, in *2020 IEEE 11th Sensor Array and Multichannel Signal Processing Workshop (SAM)*, Jun. 2020, pp. 1–5. doi: 10.1109/SAM48682.2020.9104367.

[99] A. G. Stove, ‘Linear FMCW radar techniques’, *IEE Proc. F - Radar Signal Process.*, vol. 139, no. 5, pp. 343–350, Oct. 1992, doi: 10.1049/ip-f-2.1992.0048.

[100] D. Guermandi *et al.*, ‘19.7 A 79GHz binary phase-modulated continuous-wave radar transceiver with TX-to-RX spillover cancellation in 28nm CMOS’, in *2015 IEEE International Solid-State Circuits Conference - (ISSCC) Digest of Technical Papers*, Feb. 2015, pp. 1–3. doi: 10.1109/ISSCC.2015.7063072.

[101] F. Uysal, ‘Phase-Coded FMCW Automotive Radar: System Design and Interference Mitigation’, *IEEE Trans. Veh. Technol.*, vol. 69, no. 1, pp. 270–281, Jan. 2020, doi: 10.1109/TVT.2019.2953305.

[102] H. Gruchalla-Wesierski, M. Czyzewski, and A. Slowik, ‘The analysis of frequency modulated signals based on the IFM receiver’, in *MIKON 2008 - 17th International Conference on Microwaves, Radar and Wireless Communications*, May 2008, pp. 1–4.

[103] A. Pirkani, F. Norouzian, E. Hoare, M. Cherniakov, and M. Gashinova, ‘Automotive interference statistics and their effect on radar detector’, *IET Radar Sonar Navig.*, vol. 16, no. 1, pp. 9–21, 2022, doi: 10.1049/rsn2.12132.

[104] D. Guermandi *et al.*, ‘A 79GHz 2×2 MIMO PMCW radar SoC in 28nm CMOS’, in *2016 IEEE Asian Solid-State Circuits Conference (A-SSCC)*, Nov. 2016, pp. 105–108. doi: 10.1109/ASSCC.2016.7844146.

[105] M. Bekar, C. J. Baker, E. G. Hoare, and M. Gashinova, ‘Joint MIMO Radar and Communication System Using a PSK-LFM Waveform With TDM and CDM

Approaches', *IEEE Sens. J.*, vol. 21, no. 5, pp. 6115–6124, Mar. 2021, doi: 10.1109/JSEN.2020.3043085.

[106] Ó. F. García, 'Signal Processing for mmWave MIMO Radar', p. 259.

[107] H.-P. Beise, T. Stifter, and U. Schröder, 'Virtual interference study for FMCW and PMCW radar', in *2018 11th German Microwave Conference (GeMiC)*, Mar. 2018, pp. 351–354. doi: 10.23919/GEMIC.2018.8335102.

[108] M. Raymond, 'Multiple Target Tracking using FMCW Radar', *undefined*, 2018, Accessed: Jul. 07, 2021. [Online]. Available: https://www.semanticscholar.org/paper/Multiple-Target-Tracking-using-FMCW-Radar-Raymond/6fc20645fe4ee74ac4acc89a98d9065aaad9c1a6

[109] J.-J. Lin, Y.-P. Li, W.-C. Hsu, and T.-S. Lee, 'Design of an FMCW radar baseband signal processing system for automotive application', *SpringerPlus*, vol. 5, no. 1, p. 42, Dec. 2016, doi: 10.1186/s40064-015-1583-5.

[110] I. V. Komarov, S. Smolskiy, and D. K. Barton, 'Fundamentals of Short-Range Fm Radar', *undefined*, 2003, Accessed: Jul. 07, 2021. [Online]. Available: https://www.semanticscholar.org/paper/Fundamentals-of-Short-Range-Fm-Radar-Komarov-Smolskiy/96377a9051b8ab14171b7f333aaf6eb7a2457ced

[111] N. Levanon and B. Getz, 'Comparison between linear FM and phase-coded CW radars', *Radar Sonar Navig. IEE Proc.* -, vol. 141, pp. 230–240, Sep. 1994, doi: 10.1049/ip-rsn:19941233.

[112] M.-M. Meinecke, H. Rohling, and M. Rohling, 'Combination Of Lfmcw And Fsk Modulation Principles For Automotive Radar Systems'. 2000.

[113] S. M. Patole, M. Torlak, D. Wang, and M. Ali, 'Automotive radars: A review of signal processing techniques', *IEEE Signal Process. Mag.*, vol. 34, no. 2, pp. 22–35, Mar. 2017, doi: 10.1109/MSP.2016.2628914.

[114] S. W. Alland, J. P. Bordes, C. Davis, and M. Ali, 'Virtual radar configuration for 2D array', US9869762B1, Jan. 16, 2018 Accessed: Jul. 07, 2021. [Online]. Available: https://patents.google.com/patent/US9869762B1/en

[115] F. Meinl, M. Stolz, M. Kunert, and H. Blume, ‘An experimental high performance radar system for highly automated driving’, in *2017 IEEE MTT-S International Conference on Microwaves for Intelligent Mobility (ICMIM)*, Mar. 2017, pp. 71–74. doi: 10.1109/ICMIM.2017.7918859.

[116] A. A. Pirkani, S. Pooni, and M. Cherniakov, ‘Implementation of MIMO Beamforming on an OTS FMCW Automotive Radar’, in *2019 20th International Radar Symposium (IRS)*, Jun. 2019, pp. 1–8. doi: 10.23919/IRS.2019.8768103.

[117] X. Gao, G. Xing, S. Roy, and H. Liu, ‘Experiments with mmWave Automotive Radar Test-bed’, *ArXiv191212566 Cs Eess*, Sep. 2020, doi: 10.1109/IEEECONF44664.2019.9048939.

[118] E. Fishler, A. Haimovich, R. S. Blum, L. J. Cimini, D. Chizhik, and R. A. Valenzuela, ‘Spatial Diversity in Radars—Models and Detection Performance’, *IEEE Trans. Signal Process.*, vol. 54, no. 3, pp. 823–838, Mar. 2006, doi: 10.1109/TSP.2005.862813.

[119] E. Fishler, A. Haimovich, R. Blum, R. Cimini, D. Chizhik, and R. Valenzuela, ‘Performance of MIMO radar systems: advantages of angular diversity’, in *Conference Record of the Thirty-Eighth Asilomar Conference on Signals, Systems and Computers, 2004.*, Nov. 2004, pp. 305-309 Vol.1. doi: 10.1109/ACSSC.2004.1399142.

[120] J. J. M. de Wit, W. L. van Rossum, and A. J. de Jong, ‘Orthogonal waveforms for FMCW MIMO radar’, in *2011 IEEE RadarCon (RADAR)*, May 2011, pp. 686–691. doi: 10.1109/RADAR.2011.5960625.

[121] Y. Shrestha and Y. Zhang, ‘Orthogonality using frequency division multiplexing to enable multiple input multiple output in an automotive radar’, vol. 11408, p. 1140813, Apr. 2020, doi: 10.1117/12.2558263.

[122] Y. Sun, M. Bauduin, and A. Bourdoux, ‘Enhancing Unambiguous Velocity in Doppler-Division Multiplexing MIMO Radar’, in *2021 18th European Radar Conference (EuRAD)*, Apr. 2022, pp. 493–496. doi: 10.23919/EuRAD50154.2022.9784545.

[123] O. Bialer, A. Jonas, and T. Tirer, ‘Code Design For Automotive MIMO Radar’, in *2021 29th European Signal Processing Conference (EUSIPCO)*, Aug. 2021, pp. 1765–1769. doi: 10.23919/EUSIPCO54536.2021.9616288.

[124] K. Rambach and B. Yang, ‘MIMO radar: Time division multiplexing vs. code division multiplexing’, in *International Conference on Radar Systems (Radar 2017)*, Oct. 2017, pp. 1–5. doi: 10.1049/cp.2017.0383.

[125] R. Feger, C. Wagner, S. Schuster, S. Scheiblhofer, H. Jager, and A. Stelzer, ‘A 77-GHz FMCW MIMO Radar Based on an SiGe Single-Chip Transceiver’, *IEEE Trans. Microw. Theory Tech.*, vol. 57, no. 5, pp. 1020–1035, May 2009, doi: 10.1109/TMTT.2009.2017254.

[126] T. Fickenscher, A. Gupta, J. Hinz, M. Holters, and U. Zölzer, ‘MIMO surface wave radar using time staggered FMCW chirp signals’, in *2011 8th European Radar Conference*, Oct. 2011, pp. 69–72.

[127] D. Patrick, Y. Huang, and P. V. Brennan, ‘FMCW BASED MIMO IMAGING RADAR’, p. 22, 2014.

[128] P. van Dorp, ‘LFMCW based MIMO imaging processing with keystone transform’, in *2013 European Microwave Conference*, Oct. 2013, pp. 1779–1782. doi: 10.23919/EuMC.2013.6687023.

[129] I. Bekkerman and J. Tabrikian, ‘Target Detection and Localization Using MIMO Radars and Sonars’, *IEEE Trans. Signal Process.*, vol. 54, no. 10, pp. 3873–3883, Oct. 2006, doi: 10.1109/TSP.2006.879267.

[130] F. C. Robey, S. Coutts, D. Weikle, J. C. McHarg, and K. Cuomo, ‘MIMO radar theory and experimental results’, in *Conference Record of the Thirty-Eighth Asilomar Conference on Signals, Systems and Computers, 2004.*, Nov. 2004, pp. 300-304 Vol.1. doi: 10.1109/ACSSC.2004.1399141.

[131] M. S. Davis, G. A. Showman, and A. D. Lanterman, ‘Coherent MIMO radar: The phased array and orthogonal waveforms’, *IEEE Aerosp. Electron. Syst. Mag.*, vol. 29, no. 8, pp. 76–91, Aug. 2014, doi: 10.1109/MAES.2014.130148.

[132] J. Li and P. Stoica, ‘MIMO Radar with Colocated Antennas’, *IEEE Signal Process. Mag.*, vol. 24, no. 5, pp. 106–114, Sep. 2007, doi: 10.1109/MSP.2007.904812.

[133] C. Kärnfelt, A. Péden, A. Bazzi, G. El Haj Shhadé, M. Abbas, and T. Chonavel, ‘77 GHz ACC radar simulation platform’, in *2009 9th International Conference on*

Intelligent Transport Systems Telecommunications, (ITST), Oct. 2009, pp. 209–214. doi: 10.1109/ITST.2009.5399354.

[134] E. Hyun and J.-H. Lee, 'A meothod for multi-target range and velocity detection in automotive FMCW radar', in *2009 12th International IEEE Conference on Intelligent Transportation Systems*, Oct. 2009, pp. 1–5. doi: 10.1109/ITSC.2009.5309873.

[135] K. Pourvoyeur, R. Feger, A. Haderer, C. Wagner, A. Stelzer, and L. Maurer, 'A highly modular 77-GHz FMCW radar sensor prototype for multi target tracking applications', in *2008 European Radar Conference*, Oct. 2008, pp. 455–458. doi: 10.1109/EUMC.2008.4751780.

[136] T. Wagner, R. Feger, and A. Stelzer, 'Wide-band range-Doppler processing for FMCW systems', in *2013 European Radar Conference*, Oct. 2013, pp. 160–163.

[137] V. Winkler, 'Range Doppler detection for automotive FMCW radars', in *2007 European Microwave Conference*, Oct. 2007, pp. 1445–1448. doi: 10.1109/EUMC.2007.4405477.

[138] S. Rahman and D. A. Robertson, 'Radar micro-Doppler signatures of drones and birds at K-band and W-band', *Sci. Rep.*, vol. 8, no. 1, p. 17396, Nov. 2018, doi: 10.1038/s41598-018-35880-9.

[139] D. Tahmoush and J. Silvious, 'Radar Measurement of Human Polarimetric Micro-Doppler', *J. Electr. Comput. Eng.*, vol. 2013, p. e804954, Nov. 2013, doi: 10.1155/2013/804954.

[140] M. G. Amin, Y. D. Zhang, F. Ahmad, and K. C. D. Ho, 'Radar Signal Processing for Elderly Fall Detection: The future for in-home monitoring', *IEEE Signal Process. Mag.*, vol. 33, no. 2, pp. 71–80, Mar. 2016, doi: 10.1109/MSP.2015.2502784.

[141] T. Wagner, R. Feger, and A. Stelzer, 'Wide-band range-Doppler processing for FMCW systems', in *2013 European Radar Conference*, Oct. 2013, pp. 160–163.

[142] E. Hyun, Y.-S. Jin, and J.-H. Lee, 'A Pedestrian Detection Scheme Using a Coherent Phase Difference Method Based on 2D Range-Doppler FMCW Radar', *Sensors*, vol. 16, no. 1, Art. no. 1, Jan. 2016, doi: 10.3390/s16010124.

[143] M. Song, J. Lim, and D.-J. Shin, 'The velocity and range detection using the 2D-FFT scheme for automotive radars', in *2014 4th IEEE International Conference on Network Infrastructure and Digital Content*, Sep. 2014, pp. 507–510. doi: 10.1109/ICNIDC.2014.7000356.

[144] A. Pirkani, F. Norouzian, E. Hoare, M. Cherniakov, and M. Gashinova, 'Analysis of Automotive Radar Interference in Spatial Domain', in *2021 21st International Radar Symposium (IRS)*, Jun. 2021, pp. 1–8. doi: 10.23919/IRS51887.2021.9466171.

[145] S. Neemat, O. Krasnov, and A. Yarovoy, 'An Interference Mitigation Technique for FMCW Radar Using Beat-Frequencies Interpolation in the STFT Domain', *IEEE Trans. Microw. Theory Tech.*, vol. 67, no. 3, pp. 1207–1220, Mar. 2019, doi: 10.1109/TMTT.2018.2881154.

[146] F. J. Harris, 'On the use of windows for harmonic analysis with the discrete Fourier transform', *Proc. IEEE*, vol. 66, no. 1, pp. 51–83, Jan. 1978, doi: 10.1109/PROC.1978.10837.

[147] J. Bechter, F. Roos, and C. Waldschmidt, 'Compensation of Motion-Induced Phase Errors in TDM MIMO Radars', *IEEE Microw. Wirel. Compon. Lett.*, vol. PP, pp. 1–3, Sep. 2017, doi: 10.1109/LMWC.2017.2751301.

[148] B. Major *et al.*, 'Vehicle Detection With Automotive Radar Using Deep Learning on Range-Azimuth-Doppler Tensors', in *2019 IEEE/CVF International Conference on Computer Vision Workshop (ICCVW)*, Seoul, Korea (South): IEEE, Oct. 2019, pp. 924–932. doi: 10.1109/ICCVW.2019.00121.

[149] J. Mun, H. Kim, and J. Lee, 'A Deep Learning Approach for Automotive Radar Interference Mitigation', *ArXiv190306380 Eess*, Nov. 2019, Accessed: Jul. 07, 2021. [Online]. Available: http://arxiv.org/abs/1903.06380

[150] A. Stroescu, M. Cherniakov, and M. Gashinova, 'Classification of High Resolution Automotive Radar Imagery for Autonomous Driving Based on Deep Neural Networks', in *2019 20th International Radar Symposium (IRS)*, Jun. 2019, pp. 1–10. doi: 10.23919/IRS.2019.8768156.

[151] A. Stroescu, L. Daniel, D. Phippen, M. Cherniakov, and M. Gashinova, 'Object Detection on Radar Imagery for Autonomous Driving Using Deep Neural Networks',

in *2020 17th European Radar Conference (EuRAD)*, Jan. 2021, pp. 120–123. doi: 10.1109/EuRAD48048.2021.00041.

[152] A. Stroescu, L. Daniel, and M. Gashinova, 'Combined Object Detection and Tracking on High Resolution Radar Imagery for Autonomous Driving Using Deep Neural Networks and Particle Filters', in *2020 IEEE Radar Conference (RadarConf20)*, Sep. 2020, pp. 1–6. doi: 10.1109/RadarConf2043947.2020.9266686.

[153] S. M. Sabery, A. Bystrov, P. Gardner, A. Stroescu, and M. Gashinova, 'Road Surface Classification Based on Radar Imaging Using Convolutional Neural Network', *IEEE Sens. J.*, vol. 21, no. 17, pp. 18725–18732, Sep. 2021, doi: 10.1109/JSEN.2021.3087336.

[154] C. Fischer, H. L. Blöcher, J. Dickmann, and W. Menzel, 'Robust detection and mitigation of mutual interference in automotive radar', in *2015 16th International Radar Symposium (IRS)*, Jun. 2015, pp. 143–148. doi: 10.1109/IRS.2015.7226239.

[155] P. Anjaneyulu, N. Pallavi, P. B. Reddy, V. Mahendra, and R. Karthik, 'Implementation of digital beam former for phased array radar', in *2017 International conference of Electronics, Communication and Aerospace Technology (ICECA)*, Apr. 2017, pp. 242–244. doi: 10.1109/ICECA.2017.8212807.

[156] M. U. Shahid, M. Nauman, D. Haider, and Y. Imran, 'Comparative analysis between direction of arrival algorithms', in *2017 International Conference on Infocom Technologies and Unmanned Systems (Trends and Future Directions) (ICTUS)*, Dec. 2017, pp. 451–454. doi: 10.1109/ICTUS.2017.8286051.

[157] JunHyeok. Choi, JeongHo. Park, and DongJin. Yeom, 'High angular resolution estimation methods for vehicle FMCW radar', in *Proceedings of 2011 IEEE CIE International Conference on Radar*, Oct. 2011, pp. 1868–1871. doi: 10.1109/CIE-Radar.2011.6159937.

[158] H. Steyskal, 'Digital beamforming-an emerging technology', in *MILCOM 88, 21st Century Military Communications - What's Possible?'. Conference record. Military Communications Conference*, Oct. 1988, pp. 399–403 vol.2. doi: 10.1109/MILCOM.1988.13422.

[159] A. V. Oppenheim, R. W. Schafer, and J. R. Buck, *Discrete-time signal processing (2nd ed.)*. USA: Prentice-Hall, Inc., 1999.

[160] M. Cerna and A. F. Harvey, 'The Fundamentals of FFT-Based Signal Analysis and Measurement', National Instruments, Application Note, 2000. [Online]. Available: http://online.fliphtml5.com/yhdq/qcqt/#p=1

[161] 'Adaptive Array Systems: Fundamentals and Applications | Wiley', *Wiley.com*. https://www.wiley.com/en-gb/Adaptive+Array+Systems%3A+Fundamentals+and+Applications-p-9780470861899 (accessed Feb. 10, 2020).

[162] M. Cerna and A. F. Harvey, 'The Fundamentals of FFT-Based Signal Analysis and Measurement', p. 20.

[163] H. Rohling, 'Radar CFAR Thresholding in Clutter and Multiple Target Situations', *IEEE Trans. Aerosp. Electron. Syst.*, vol. AES-19, no. 4, pp. 608–621, Jul. 1983, doi: 10.1109/TAES.1983.309350.

[164] J. Bechter, A. Demirlika, P. Hügler, F. Roos, and C. Waldschmidt, 'Blind Adaptive Beamforming for Automotive Radar Interference Suppression', in *2018 19th International Radar Symposium (IRS)*, Jun. 2018, pp. 1–10. doi: 10.23919/IRS.2018.8447965.

[165] A. Al-Hourani, R. J. Evans, S. Kandeepan, B. Moran, and H. Eltom, 'Stochastic Geometry Methods for Modeling Automotive Radar Interference', *IEEE Trans. Intell. Transp. Syst.*, vol. 19, no. 2, pp. 333–344, Feb. 2018, doi: 10.1109/TITS.2016.2632309.

[166] M. Hischke, 'Collision warning radar interference', in *Proceedings of the Intelligent Vehicles '95. Symposium*, Sep. 1995, pp. 13–18. doi: 10.1109/IVS.1995.528250.

[167] 'Analysis of Mutual Interference between Automotive Radar Systems', *Int. Radar Symp. IRS 2005*, vol. 1998, pp. 83–90, 1998.

[168] G. M. Brooker, 'Mutual Interference of Millimeter-Wave Radar Systems', *IEEE Trans. Electromagn. Compat.*, vol. 49, no. 1, pp. 170–181, Feb. 2007, doi: 10.1109/TEMC.2006.890223.

[169] M. Goppelt, H.-L. Blöcher, and W. Menzel, ‘Analytical investigation of mutual interference between automotive FMCW radar sensors’, in *2011 German Microwave Conference*, Mar. 2011, pp. 1–4.

[170] B.-E. Tullsson, ‘Topics in FMCW radar disturbance suppression’, in *Radar 97 (Conf. Publ. No. 449)*, Oct. 1997, pp. 1–5. doi: 10.1049/cp:19971620.

[171] The MOSARIM Consortium, ‘Generation of an interference susceptibility model for the different radar principles’, Workpackage: General Interference Risk Assessment, Jun. 2010. [Online]. Available: https://trimis.ec.europa.eu/sites/default/files/project/documents/20121024_170826_81467_Deliverable_2.2_V1.2.pdf

[172] J. Bechter, K. D. Biswas, and C. Waldschmidt, ‘Estimation and cancellation of interferences in automotive radar signals’, in *2017 18th International Radar Symposium (IRS)*, Jun. 2017, pp. 1–10. doi: 10.23919/IRS.2017.8008126.

[173] M. Barjenbruch, D. Kellner, K. Dietmayer, J. Klappstein, and J. Dickmann, ‘A method for interference cancellation in automotive radar’, in *2015 IEEE MTT-S International Conference on Microwaves for Intelligent Mobility (ICMIM)*, Apr. 2015, pp. 1–4. doi: 10.1109/ICMIM.2015.7117925.

[174] T. Schipper, M. Harter, T. Mahler, O. Kern, and T. Zwick, ‘Discussion of the operating range of frequency modulated radars in the presence of interference’, *Int. J. Microw. Wirel. Technol.*, vol. 6, no. 3–4, pp. 371–378, Jun. 2014, doi: 10.1017/S1759078714000221.

[175] S. Sanka, ‘Radar to radar interference for 77GHz automotive radar’, 2017, Accessed: Feb. 05, 2020. [Online]. Available: https://repository.tudelft.nl/islandora/object/uuid%3A6f4231ff-49ce-4f46-944a-3c15f86c50b4

[176] S. Lee, J.-Y. Lee, and S.-C. Kim, ‘Mutual Interference Suppression Using Wavelet Denoising in Automotive FMCW Radar Systems’, *IEEE Trans. Intell. Transp. Syst.*, vol. 22, no. 2, pp. 887–897, Feb. 2021, doi: 10.1109/TITS.2019.2961235.

[177] T. Schipper, S. Prophet, M. Harter, L. Zwirello, and T. Zwick, ‘Simulative Prediction of the Interference Potential Between Radars in Common Road Scenarios’, *IEEE Trans.*

Electromagn. Compat., vol. 57, no. 3, pp. 322–328, Jun. 2015, doi: 10.1109/TEMC.2014.2384996.

[178] M. Dudek, D. Kissinger, R. Weigel, and G. Fischer, 'A millimeter-wave FMCW radar system simulator for automotive applications including nonlinear component models', in *2011 8th European Radar Conference*, Oct. 2011, pp. 89–92.

[179] T. Schipper, S. Prophet, L. Zwirello, M. Harter, L. Reichardt, and T. Zwick, 'Simulation framework for the estimation of future interference situations between automotive radars', in *2013 IEEE Antennas and Propagation Society International Symposium (APSURSI)*, Jul. 2013, pp. 2103–2104. doi: 10.1109/APS.2013.6711710.

[180] H. Rohling and M.-M. Meinecke, 'Waveform design principles for automotive radar systems', in *2001 CIE International Conference on Radar Proceedings (Cat No.01TH8559)*, Oct. 2001, pp. 1–4. doi: 10.1109/ICR.2001.984612.

[181] T.-N. Luo, C.-H. E. Wu, and Y.-J. E. Chen, 'A 77-GHz CMOS Automotive Radar Transceiver With Anti-Interference Function', *IEEE Trans. Circuits Syst. Regul. Pap.*, vol. 60, no. 12, pp. 3247–3255, Dec. 2013, doi: 10.1109/TCSI.2013.2265974.

[182] X. Hu, Y. Li, M. Lu, Y. Wang, and X. Yang, 'A Multi-Carrier-Frequency Random-Transmission Chirp Sequence for TDM MIMO Automotive Radar', *IEEE Trans. Veh. Technol.*, vol. 68, no. 4, pp. 3672–3685, Apr. 2019, doi: 10.1109/TVT.2019.2900357.

[183] Y. Kitsukawa, M. Mitsumoto, H. Mizutani, N. Fukui, and C. Miyazaki, 'An Interference Suppression Method by Transmission Chirp Waveform with Random Repetition Interval in Fast-Chirp FMCW Radar', in *2019 16th European Radar Conference (EuRAD)*, Oct. 2019, pp. 165–168.

[184] Z. Xu and Q. Shi, 'Interference Mitigation for Automotive Radar Using Orthogonal Noise Waveforms', *IEEE Geosci. Remote Sens. Lett.*, vol. 15, no. 1, pp. 137–141, Jan. 2018, doi: 10.1109/LGRS.2017.2777962.

[185] J. Sanmartin-Jara, M. Burgos-Garcia, and J. Retamose-Sanchez, 'SS-FH signals used for very low interference in vehicular cruising control systems', in *Gateway to 21st Century Communications Village. VTC 1999-Fall. IEEE VTS 50th Vehicular Technology Conference (Cat. No.99CH36324)*, Sep. 1999, pp. 819–823 vol.2. doi: 10.1109/VETECF.1999.798443.

[186] Z. Jian-Hui, L. Guo-Sui, G. Hong, and S. Wei-Min, 'A novel transmit signal based on high range-resolution concept for FLAR or AICC system applications', in *2001 CIE International Conference on Radar Proceedings (Cat No.01TH8559)*, Oct. 2001, pp. 81–84. doi: 10.1109/ICR.2001.984628.

[187] S. Skaria, A. Al-Hourani, R. J. Evans, K. Sithamparanathan, and U. Parampalli, 'Interference Mitigation in Automotive Radars Using Pseudo-Random Cyclic Orthogonal Sequences', *Sensors*, vol. 19, no. 20, Art. no. 20, Jan. 2019, doi: 10.3390/s19204459.

[188] J. Bechter and C. Waldschmidt, 'Automotive radar interference mitigation by reconstruction and cancellation of interference component', in *2015 IEEE MTT-S International Conference on Microwaves for Intelligent Mobility (ICMIM)*, Apr. 2015, pp. 1–4. doi: 10.1109/ICMIM.2015.7117954.

[189] T. Nozawa *et al.*, 'An anti-collision automotive FMCW radar using time-domain interference detection and suppression', in *International Conference on Radar Systems (Radar 2017)*, Oct. 2017, pp. 1–5. doi: 10.1049/cp.2017.0366.

[190] F. Jin and S. Cao, 'Automotive Radar Interference Mitigation Using Adaptive Noise Canceller', *IEEE Trans. Veh. Technol.*, vol. 68, no. 4, pp. 3747–3754, Apr. 2019, doi: 10.1109/TVT.2019.2901493.

[191] J. Bechter, M. Rameez, and C. Waldschmidt, 'Analytical and Experimental Investigations on Mitigation of Interference in a DBF MIMO Radar', *IEEE Trans. Microw. Theory Tech.*, vol. 65, no. 5, pp. 1727–1734, May 2017, doi: 10.1109/TMTT.2017.2668404.

[192] J. Bechter, K. Eid, F. Roos, and C. Waldschmidt, 'Digital beamforming to mitigate automotive radar interference', in *2016 IEEE MTT-S International Conference on Microwaves for Intelligent Mobility (ICMIM)*, May 2016, pp. 1–4. doi: 10.1109/ICMIM.2016.7533914.

[193] M. Rameez, M. Dahl, and M. I. Pettersson, 'Experimental Evaluation of Adaptive Beamforming for Automotive Radar Interference Suppression', in *2020 IEEE Radio and Wireless Symposium (RWS)*, Jan. 2020, pp. 183–186. doi: 10.1109/RWS45077.2020.9049982.

[194] M. Umehira, T. Okuda, X. Wang, S. Takeda, and H. Kuroda, 'An Adaptive Interference Detection and Suppression Scheme Using Iterative Processing for Automotive FMCW Radars', in *2020 IEEE Radar Conference (RadarConf20)*, Sep. 2020, pp. 1–5. doi: 10.1109/RadarConf2043947.2020.9266712.

[195] S. Murali, K. Subburaj, B. Ginsburg, and K. Ramasubramanian, 'Interference detection in FMCW radar using a complex baseband oversampled receiver', in *2018 IEEE Radar Conference (RadarConf18)*, Apr. 2018, pp. 1567–1572. doi: 10.1109/RADAR.2018.8378800.

[196] K.-J. You, H.-E. Jeon, and H.-C. Shin, 'Radar Modulation Identification Using Inequality Measurement in Frequency Domain', *IEICE Trans Fundam Electron Commun Comput Sci*, 2017, doi: 10.1587/TRANSFUN.E100.A.975.

[197] R. Zhang and S. Cao, 'Support vector machines for classification of automotive radar interference', in *2018 IEEE Radar Conference (RadarConf18)*, Apr. 2018, pp. 0366–0371. doi: 10.1109/RADAR.2018.8378586.

[198] J. Kim, S. Lee, and S.-C. Kim, 'Modulation type classification of interference signals in automotive radar systems', *Sonar Navig. IET Radar*, vol. 13, no. 6, pp. 944–952, 2019, doi: 10.1049/iet-rsn.2018.5521.

[199] T.-N. Luo, C.-H. E. Wu, and Y.-J. E. Chen, 'A 77-GHz CMOS FMCW Frequency Synthesizer With Reconfigurable Chirps', *IEEE Trans. Microw. Theory Tech.*, vol. 61, no. 7, pp. 2641–2647, Jul. 2013, doi: 10.1109/TMTT.2013.2264685.

[200] M. A. Hossain, I. Elshafiey, and A. Al-Sanie, 'Waveform diversity for mutual interference mitigation in automotive radars under realistic traffic environments', *Signal Image Video Process.*, vol. 13, no. 1, pp. 1–8, Feb. 2019, doi: 10.1007/s11760-018-1321-x.

[201] M. Umehira, Y. Makino, T. Okuda, X. Wang, S. Takeda, and H. Kuroda, 'Inter-Radar Interference Analysis and Concept of Scalable Fast Chirp FMCW Radar for Automotive Applications', in *2019 20th International Radar Symposium (IRS)*, Jun. 2019, pp. 1–8. doi: 10.23919/IRS.2019.8768092.

[202] Y.-S. Son, H.-K. Sung, and S. W. Heo, 'Automotive Frequency Modulated Continuous Wave Radar Interference Reduction Using Per-Vehicle Chirp Sequences', *Sensors*, vol. 18, no. 9, Aug. 2018, doi: 10.3390/s18092831.

[203] M. A. Hossain, I. Elshafiey, and A. Al-Sanie, 'Mutual interference mitigation in automotive radars under realistic road environments', in *2017 8th International Conference on Information Technology (ICIT)*, May 2017, pp. 895–900. doi: 10.1109/ICITECH.2017.8079965.

[204] M. Umehira, Y. Watanabe, X. Wang, S. Takeda, and H. Kuroda, 'Inter-radar interference in automotive FMCW radars and its mitigation challenges', in *2020 IEEE International Symposium on Radio-Frequency Integration Technology (RFIT)*, Sep. 2020, pp. 220–222. doi: 10.1109/RFIT49453.2020.9226222.

[205] C. Aydogdu, N. Garcia, L. Hammarstrand, and H. Wymeersch, 'Radar Communications for Combating Mutual Interference of FMCW Radars', in *2019 IEEE Radar Conference (RadarConf)*, Apr. 2019, pp. 1–6. doi: 10.1109/RADAR.2019.8835744.

[206] W. Machowski, G. S. Koutsogiannis, and P. A. Ratliff, 'Novel pulse-sequences design enables multi-user collision-avoidance vehicular radar', in *2007 International Waveform Diversity and Design Conference*, Jun. 2007, pp. 155–159. doi: 10.1109/WDDC.2007.4339400.

[207] M. Kunert *et al.*, 'D1.5 - Study on the state-of-the-art interference mitigation technique, MOre Safety for All by Radar Interference Mitigation (MOSARIM) project'. Robert Bosch GmbH, 2010., 2010.

[208] I. Pasya, H. Kato, and T. Kobayashi, 'Interference Suppression Performance of Automotive UWB Radars Using Pseudo Random Sequences', *Radioengineering*, vol. 24, no. 4, pp. 932–939, Sep. 2015, doi: 10.13164/re.2015.0932.

[209] J.-G. Kim, S.-H. Sim, S. Cheon, and S. Hong, '24 GHz circularly polarized Doppler radar with a single antenna', in *2005 European Microwave Conference*, Oct. 2005, p. 4 pp. – 1386. doi: 10.1109/EUMC.2005.1610194.

[210] T.-H. Liu, M.-L. Hsu, and Z.-M. Tsai, 'Mutual interference of pseudorandom noise radar in automotive collision avoidance application at 24 GHz', in *2016 IEEE 5th*

Global Conference on Consumer Electronics, Oct. 2016, pp. 1–2. doi: 10.1109/GCCE.2016.7800400.

[211] L. Sakkila, Y. Elhillali, A. Rivenq, C. Tatkeu, and J.-M. Rouvaen, 'Short range automotive radar based on UWB pseudo-random coding', in *2007 7th International Conference on ITS Telecommunications*, Jun. 2007, pp. 1–6. doi: 10.1109/ITST.2007.4295848.

[212] H. H. Meinel, 'Evolving automotive radar — From the very beginnings into the future', in *The 8th European Conference on Antennas and Propagation (EuCAP 2014)*, Apr. 2014, pp. 3107–3114. doi: 10.1109/EuCAP.2014.6902486.

[213] M. Umehira, T. Nozawa, Y. Makino, X. Wang, S. Takeda, and H. Kuroda, 'A Novel Iterative Inter-Radar Interference Reduction Scheme for Densely Deployed Automotive FMCW Radars', in *2018 19th International Radar Symposium (IRS)*, Jun. 2018, pp. 1–10. doi: 10.23919/IRS.2018.8448223.

[214] O. A. Krasnov, G. P. Babur, L. P. Ligthart, and F. van der Zwan, 'Basics and first experiments demonstrating isolation improvements in the agile polarimetric FM-CW radar — PARSAX', in *2009 European Radar Conference (EuRAD)*, Sep. 2009, pp. 13–16.

[215] G. Babur, Z. Wang, O. A. Krasnov, and L. P. Ligthart, 'Design and implementation of cross-channel interference suppression for polarimetric LFM-CW radar', in *Photonics Applications in Astronomy, Communications, Industry, and High-Energy Physics Experiments 2010*, International Society for Optics and Photonics, Sep. 2010, p. 774520. doi: 10.1117/12.872225.

[216] M. Rameez, M. Dahl, and M. I. Pettersson, 'Adaptive digital beamforming for interference suppression in automotive FMCW radars', in *2018 IEEE Radar Conference (RadarConf18)*, Apr. 2018, pp. 0252–0256. doi: 10.1109/RADAR.2018.8378566.

[217] C. Fischer, M. Goppelt, H.-L. Blöcher, and J. Dickmann, 'Minimizing interference in automotive radar using digital beamforming', in *Advances in Radio Science*, Copernicus GmbH, Jul. 2011, pp. 45–48. doi: https://doi.org/10.5194/ars-9-45-2011.

[218] T. M. K. Jr, R. G. Aeder, and W. G. Woodington, ‘System and method for reducing the effect of a radar interference signal’, US7683827B2, Mar. 23, 2010 Accessed: Aug. 09, 2021. [Online]. Available: https://patents.google.com/patent/US7683827/en

[219] J. Bechter, C. Sippel, and C. Waldschmidt, ‘Bats-inspired frequency hopping for mitigation of interference between automotive radars’, in *2016 IEEE MTT-S International Conference on Microwaves for Intelligent Mobility (ICMIM)*, May 2016, pp. 1–4. doi: 10.1109/ICMIM.2016.7533928.

[220] L. Mu, T. Xiangqian, S. Ming, and Y. Jun, ‘Research on key tchnologies for collision avoidance automotive radar’, in *2009 IEEE Intelligent Vehicles Symposium*, Jun. 2009, pp. 233–236. doi: 10.1109/IVS.2009.5164283.

[221] J. Rock, M. Toth, P. Meissner, and F. Pernkopf, ‘Deep Interference Mitigation and Denoising of Real-World FMCW Radar Signals’, in *2020 IEEE International Radar Conference (RADAR)*, Apr. 2020, pp. 624–629. doi: 10.1109/RADAR42522.2020.9114627.

[222] J. Mun, S. Ha, and J. Lee, ‘Automotive Radar Signal Interference Mitigation Using RNN with Self Attention’, in *ICASSP 2020 - 2020 IEEE International Conference on Acoustics, Speech and Signal Processing (ICASSP)*, May 2020, pp. 3802–3806. doi: 10.1109/ICASSP40776.2020.9053013.

[223] J. Rock, M. Toth, E. Messner, P. Meissner, and F. Pernkopf, ‘Complex Signal Denoising and Interference Mitigation for Automotive Radar Using Convolutional Neural Networks’. arXiv, Jun. 25, 2019. doi: 10.48550/arXiv.1906.10044.

[224] N.-C. Ristea, A. Anghel, and R. T. Ionescu, ‘Fully Convolutional Neural Networks for Automotive Radar Interference Mitigation’, in *2020 IEEE 92nd Vehicular Technology Conference (VTC2020-Fall)*, Nov. 2020, pp. 1–5. doi: 10.1109/VTC2020-Fall49728.2020.9348690.

[225] J. Wang, ‘CFAR-Based Interference Mitigation for FMCW Automotive Radar Systems’, *ArXiv210101257 Eess*, Jan. 2021, Accessed: Aug. 09, 2021. [Online]. Available: http://arxiv.org/abs/2101.01257

[226] H. Rohling and R. Mende, 'OS CFAR performance in a 77 GHz radar sensor for car application', in *Proceedings of International Radar Conference*, Oct. 1996, pp. 109–114. doi: 10.1109/ICR.1996.573784.

[227] F. Uysal and S. Sanka, 'Mitigation of automotive radar interference', in *2018 IEEE Radar Conference (RadarConf18)*, Apr. 2018, pp. 0405–0410. doi: 10.1109/RADAR.2018.8378593.

[228] J. Bechter and C. Waldschmidt, 'Automotive radar interference mitigation by reconstruction and cancellation of interference component', in *2015 IEEE MTT-S International Conference on Microwaves for Intelligent Mobility (ICMIM)*, Apr. 2015, pp. 1–4. doi: 10.1109/ICMIM.2015.7117954.

[229] J. Bechter, F. Roos, M. Rahman, and C. Waldschmidt, 'Automotive radar interference mitigation using a sparse sampling approach', in *2017 European Radar Conference (EURAD)*, Oct. 2017, pp. 90–93. doi: 10.23919/EURAD.2017.8249154.

[230] Norouzian, F., et al.: Phenomenology of automotive radar interference. IET Radar Sonar Navig. 15(9), 1045– 1060 (2021). https://doi.org/10.1049/rsn2.12096.

[231] Y. Kim, 'Identification of FMCW radar in mutual interference environments using frequency ramp modulation', in *2016 10th European Conference on Antennas and Propagation (EuCAP)*, Apr. 2016, pp. 1–3. doi: 10.1109/EuCAP.2016.7481567.

[232] C. Aydogdu *et al.*, 'Radar Interference Mitigation for Automated Driving', *ArXiv190909441 Eess*, Sep. 2019, Accessed: Feb. 06, 2020. [Online]. Available: http://arxiv.org/abs/1909.09441

[233] 'Automotive Radar Sensors and Congested Radio Spectrum: An Urban Electronic Battlefield? | Analog Devices'. https://www.analog.com/en/analog-dialogue/articles/automotive-radar-sensors-and-congested-radio-spectrum-an-urban-electronic-warfare.html# (accessed May 04, 2020).

[234] M. Wintermantel and H. Goelz, 'Radar system for detecting the surroundings with compensation of interfering signals', US20100085233A1, Apr. 08, 2010 Accessed: May 04, 2020. [Online]. Available: https://patents.google.com/patent/US20100085233/en

[235] ‘ECC report 262’. Jan. 2017. [Online]. Available: https://docdb.cept.org/download/1292

[236] Z. Yang and A. Mani, ‘Interference Mitigation For AWR/IWR Devices’, Texas Instruments, Application Report SWRA662, Jan. 2020. [Online]. Available: http://www.ti.com/lit/an/swra662/swra662.pdf

[237] I. P. Gravas, Z. D. Zaharis, T. V. Yioultsis, P. I. Lazaridis, and T. D. Xenos, ‘Adaptive Beamforming With Sidelobe Suppression by Placing Extra Radiation Pattern Nulls’, *IEEE Trans. Antennas Propag.*, vol. 67, no. 6, pp. 3853–3862, Jun. 2019, doi: 10.1109/TAP.2019.2905709.

[238] A. Pirkani, F. Norouzian, E. Hoare, M. Cherniakov, and M. Gashinova, ‘Automotive Interference Suppression in MIMO and Phased Array Radar’, in *2021 18th European Radar Conference (EuRAD)*, Apr. 2022, pp. 413–416. doi: 10.23919/EuRAD50154.2022.9784453.

[239] M. S. Greco, ‘Automotive Radar’, *IEEE Radar Conf.*, p. 26, 2012.

[240] R. E. Crochiere and L. R. Rabiner, ‘Interpolation and decimation of digital signals—A tutorial review’, *Proc. IEEE*, vol. 69, no. 3, pp. 300–331, Mar. 1981, doi: 10.1109/PROC.1981.11969.

[241] H. Eugin and J. Lee, ‘Hardware architecture design and implementation for FMCW radar signal processing algorithm’, in *Proceedings of the 2014 Conference on Design and Architectures for Signal and Image Processing*, Oct. 2014, pp. 1–6. doi: 10.1109/DASIP.2014.7115643.

[242] K. Lin, Y. E. Wang, C.-K. Pao, and Y.-C. Shih, ‘A Ka-Band FMCW Radar Front-End With Adaptive Leakage Cancellation’, *IEEE Trans. Microw. Theory Tech.*, vol. 54, no. 12, pp. 4041–4048, Dec. 2006, doi: 10.1109/TMTT.2006.885882.

[243] V. Winkler, ‘Range Doppler detection for automotive FMCW radars’, in *2007 European Radar Conference*, Oct. 2007, pp. 166–169. doi: 10.1109/EURAD.2007.4404963.

[244] X. Li, X. Wang, Q. Yang, and S. Fu, ‘Signal Processing for TDM MIMO FMCW Millimeter-Wave Radar Sensors’, *IEEE Access*, vol. 9, pp. 167959–167971, 2021, doi: 10.1109/ACCESS.2021.3137387.

[245] U. Kumbul, F. Uysal, C. S. Vaucher, and A. Yarovoy, ‘Automotive radar interference study for different radar waveform types’, *IET Radar Sonar Navig.*, vol. n/a, no. n/a, doi: 10.1049/rsn2.12203.

[246] M. Selvaganesh and H. Mangalam, ‘Computation of range velocity and direction of arrival in FMCW radar’, *Mater. Today Proc.*, vol. 62, pp. 4946–4952, Jan. 2022, doi: 10.1016/j.matpr.2022.03.686.

[247] A. Pirkani, F. Norouzian, E. Hoare, M. Gashinova, and M. Cherniakov, ‘Statistical Analysis of Automotive Radar Interference’, in *2020 IEEE Radar Conference (RadarConf20)*, Sep. 2020, pp. 1–6. doi: 10.1109/RadarConf2043947.2020.9266653.

[248] D. K. Barton, *Radars: Pulse compression*. Artech House, 1974.

[249] S. K. Mitra, *Digital signal processing: a computer-based approach / Sanjit K. Mitra.*, 4th ed. New York, NY: McGraw-Hill, 2011.

[250] T. Instruments, ‘AWR1243 Single-Chip 77- and 79-GHz FMCW Transceiver’. May 2017. [Online]. Available: https://www.ti.com/lit/ds/symlink/awr1243.pdf?ts=1611145813889&ref_url=https%253A%252F%252Fwww.google.com%252F

[251] ‘Radarbook2 – INRAS’. https://inras.at/en/radarbook2/ (accessed May 06, 2022).

[252] ‘How Wide Is a Car?’, *Driveways Nottingham*, Jul. 23, 2022. https://www.drivewaysnottingham.org.uk/how-wide-is-a-car/ (accessed Jul. 29, 2023).

[253] C. Aydogdu, M. F. Keskin, N. Garcia, H. Wymeersch, and D. W. Bliss, ‘RadChat: Spectrum Sharing for Automotive Radar Interference Mitigation’, *IEEE Trans. Intell. Transp. Syst.*, vol. 22, no. 1, pp. 416–429, Jan. 2021, doi: 10.1109/TITS.2019.2959881.

[254] G. Lindgren, ‘Lectures on Stationary Stochastic Processes’. Lund University, Oct. 2006. [Online]. Available: http://www.maths.lth.se/matstat/staff/georg/Publications/lecture2006.pdf

[255] M. I. Skolnik, ‘Detection of Signal in Noise, Chapter 5’, in *Introduction to Radar Systems*, 3rd Edition.McGraw-Hall, 2001, p. 772. Accessed: Mar. 24, 2020. [Online]. Available: https://www.abebooks.com/Introduction-Radar-Systems-Third-Edition-Merrill/11764089612/bd

[256] S. G. Kwak and J. H. Kim, ‘Central limit theorem: the cornerstone of modern statistics’, *Korean J. Anesthesiol.*, vol. 70, no. 2, pp. 144–156, Apr. 2017, doi: 10.4097/kjae.2017.70.2.144.

[257] J. Overdevest, F. Jansen, F. Laghezza, F. Uysal, and A. Yarovoy, ‘Uncorrelated Interference in 79 GHz FMCW and PMCW Automotive Radar’, in *2019 20th International Radar Symposium (IRS)*, Jun. 2019, pp. 1–8. doi: 10.23919/IRS.2019.8768181.

[258] G. Antonini, G. Fedele, P. Repaci, and F. A. Studer, ‘Performance comparison of radar receivers subject to amplitude and frequency modulated audio interference’, in *Proceedings International Radar Conference*, May 1995, pp. 233–238. doi: 10.1109/RADAR.1995.522551.

[259] T. Schipper, M. Harter, T. Mahler, O. Kern, and T. Zwick, ‘Discussion of the operating range of frequency modulated radars in the presence of interference’, 2014. doi: 10.1017/S1759078714000221.

[260] F. E. Nathanson and J. P. Reilly, ‘Statistical relationships for various detection processes’, in *Radar design principles*, 2nd ed.McGraw Hill, pp. 77–106.

[261] M. A. Richards, ‘Detection Fundamentals, Chapter 6’, in *Fundamentals of Radar Signal Processing*, Second Edition.McGraw-Hill Education, 2014. [Online]. Available: https://www.accessengineeringlibrary.com/content/book/9780071798327/chapter/chapter6

[262] G.-T. Gil, J. Y. Lee, and D.-H. Cho, ‘Estimation of Path Loss Parameters of a Sub-Terahertz Wireless Channel Using Monostatic Radar’, *IEEE Access*, vol. 9, pp. 52654–52663, 2021, doi: 10.1109/ACCESS.2021.3070378.

[263] H. Akoglu, ‘User’s guide to correlation coefficients’, *Turk. J. Emerg. Med.*, vol. 18, no. 3, pp. 91–93, Sep. 2018, doi: 10.1016/j.tjem.2018.08.001.

[264] F. Norouzian, A. Pirkani, E. Hoare, M. Cherniakov, and M. Gashinova, ‘Automotive Radar Waveform Parameters Randomisation for Interference Level Reduction’, in *2020 IEEE Radar Conference (RadarConf20)*, Sep. 2020, pp. 1–5. doi: 10.1109/RadarConf2043947.2020.9266375.

[265] V. Dham, ‘Programming Chirp Parameters in TI Radar Devices’, p. 16, 2017.

[266] J. Granderson and P. N. Price, ‘Development and application of a statistical methodology to evaluate the predictive accuracy of building energy baseline models’, *Energy*, vol. 66, pp. 981–990, Mar. 2014, doi: 10.1016/j.energy.2014.01.074.

[267] G. L. Turin, ‘An introduction to digitial matched filters’, *Proc. IEEE*, vol. 64, no. 7, pp. 1092–1112, Jul. 1976, doi: 10.1109/PROC.1976.10274.

[268] J.-H. Park, M.-H. Kim, D.-C. Hwang, and J. Han, ‘Analysis on Preamble Detection and False Alarm Probabilities of ICPC Method’, in *2015 IEEE 82nd Vehicular Technology Conference (VTC2015-Fall)*, Sep. 2015, pp. 1–5. doi: 10.1109/VTCFall.2015.7390844.

[269] B. R. Mahafza, *Radar Signal Analysis and Processing Using MATLAB, Chapter 7*, 1st ed. Chapman and Hall/CRC, 2016. Accessed: Mar. 12, 2020. [Online]. Available: https://uk.mathworks.com/academia/books/radar-signal-analysis-and-processing-using-matlab-mahafza.html

[270] J. Brownlee, ‘Moving Average Smoothing for Data Preparation and Time Series Forecasting in Python’, *MachineLearningMastery.com*, Dec. 27, 2016. https://machinelearningmastery.com/moving-average-smoothing-for-time-series-forecasting-python/ (accessed Nov. 17, 2022).

[271] T. Murakami, N. Hasegawa, Y. Utagawa, T. Arai, and S. Yamaura, ‘A 9 dB Noise Figure Fully Integrated 79 GHz Automotive Radar Receiver in 40 nm CMOS Technology’, in *2019 IEEE Radio Frequency Integrated Circuits Symposium (RFIC)*, Jun. 2019, pp. 307–310. doi: 10.1109/RFIC.2019.8701748.

[272] W. Woodington, M. Delcheccolo, J. Pleva, M. Russell, and H. Rees, ‘Radar detection method and apparatus’, US20020044082A1, Apr. 18, 2002 Accessed: May 19, 2020. [Online]. Available: https://patents.google.com/patent/US20020044082/en

[273] C. Katzlberger, ‘Object Detection with Automotive Radar Sensors using CFAR Algorithms’, p. 26.

[274] M. Wagner, F. Sulejmani, A. Melzer, P. Meissner, and M. Huemer, ‘Threshold-Free Interference Cancellation Method for Automotive FMCW Radar Systems’, in *2018 IEEE International Symposium on Circuits and Systems (ISCAS)*, May 2018, pp. 1–4. doi: 10.1109/ISCAS.2018.8351077.

[275] O. Abu-Ella and B. El-Jabu, *Adaptive Beamforming Algorithm Using a Pre-filtering System*. IntechOpen, 2010. doi: 10.5772/7167.

[276] R. Thakur and K. S. Mourya, 'Performance Comparison of Blind and Non Blind Adaptive Beamforming Algorithms in Mobile Communication', 2017. /paper/Performance-Comparison-of-Blind-and-Non-Blind-in-Thakur-Mourya/4d61b3ee73093568bebfc827a285a7f7d1792639 (accessed Jun. 17, 2021).

[277] X. Qiu and Y. Gao, 'A step-varied CMA blind equalization algorithm based on autocorrelation of error signal', in *Proceedings of the 29th Chinese Control Conference*, Jul. 2010, pp. 2171–2174.

[278] M. D. Zoltowski, 'On the performance analysis of the MVDR beamformer in the presence of correlated interference', *IEEE Trans. Acoust. Speech Signal Process.*, vol. 36, no. 6, pp. 945–947, Jun. 1988, doi: 10.1109/29.1614.

[279] E. A. P. Habets, J. Benesty, S. Gannot, P. A. Naylor, and I. Cohen, 'On the application of the LCMV beamformer to speech enhancement', in *2009 IEEE Workshop on Applications of Signal Processing to Audio and Acoustics*, Oct. 2009, pp. 141–144. doi: 10.1109/ASPAA.2009.5346463.

[280] M. Souden, J. Benesty, and S. Affes, 'A Study of the LCMV and MVDR Noise Reduction Filters', *IEEE Trans. Signal Process.*, vol. 58, no. 9, pp. 4925–4935, Sep. 2010, doi: 10.1109/TSP.2010.2051803.

[281] J. Xu, G. Liao, S. Zhu, and L. Huang, 'Response Vector Constrained Robust LCMV Beamforming Based on Semidefinite Programming', *IEEE Trans. Signal Process.*, vol. 63, pp. 1–1, Nov. 2015, doi: 10.1109/TSP.2015.2460221.

[282] D. H. Johnson and D. E. Dudgeon, *Array Signal Processing: Concepts and Techniques*. P T R Prentice Hall, 1993.

[283] C. Quispe and H. Orlando, 'Implementation of null steering algorithms in a compact analog array', Thesis, Montana State University - Bozeman, College of Engineering, 2014. Accessed: Aug. 11, 2021. [Online]. Available: https://scholarworks.montana.edu/xmlui/handle/1/3344

[284] A. W. Doerry, 'Noise and Noise Figure for Radar Receivers.', SAND2016-9649, 1562649, Sep. 2016. doi: 10.2172/1562649.

[285] W. Kester, ‘Understand SINAD, ENOB, SNR, THD, THD + N, and SFDR so You Don’t Get Lost in the Noise Floor’, Analog Devices, Tutorial MT-003.

[286] S. Prasad, M. Meenakshi, and P. H. Rao, ‘Noise figure analysis of beamforming systems’, in *2019 URSI Asia-Pacific Radio Science Conference (AP-RASC)*, Mar. 2019, pp. 1–4. doi: 10.23919/URSIAP-RASC.2019.8738248.

[287] F. Norouzian, A. Pirkani, E. Hoare, M. Cherniakov, and M. Gashinova, ‘A Graphical Heatmap Tool to Analyse the Effects of Interference in Automotive Radar’, in *2020 IEEE Radar Conference (RadarConf20)*, Sep. 2020, pp. 1–6. doi: 10.1109/RadarConf2043947.2020.9266353.

[288] V. Dham, ‘Programming Chirp Parameters in TI Radar Devices’, Texas Instruments, Application Report SWRA553A, Feb. 2020.

[289] W. Kester, ‘Understand SINAD, ENOB, SNR, THD, THD + N, and SFDR so You Don’t Get Lost in the Noise Floor’, p. 8.

[290] F. F. Digham, M.-S. Alouini, and M. K. Simon, ‘On the Energy Detection of Unknown Signals Over Fading Channels’, *IEEE Trans. Commun.*, vol. 55, no. 1, pp. 21–24, Jan. 2007, doi: 10.1109/TCOMM.2006.887483.

[291] G. Brooker, *Introduction to Sensors for Ranging and Imaging*. IET Digital Library, 2009. doi: 10.1049/SBRA014E.

[292] S. Rao, ‘MIMO Radar’. Texas Instruments, May 2017. [Online]. Available: http://www.ti.com/lit/an/swra554a/swra554a.pdf?ts=1588623508846

[293] I. Bilik, O. Longman, S. Villeval, and J. Tabrikian, ‘The Rise of Radar for Autonomous Vehicles: Signal Processing Solutions and Future Research Directions’, *IEEE Signal Process. Mag.*, vol. 36, no. 5, pp. 20–31, Sep. 2019, doi: 10.1109/MSP.2019.2926573.

[294] D. K. Jayaram, A. Gopalakrisnan, S. Sharan, ‘To Improve the Azimuth Resolution in Ground Mapping Radar using Doppler Beam Sharpening Technique,’ in *IJRSI*, Vol III, Issue V, May 2016, Accessed: Jul. 21, 2021. [Online]. Available: https://www.rsisinternational.org/IJRSI/Issue27/100-105.pdf

[295] K. H. Kim, S. G. Kim, and J. W. Yi, ‘Detection of ship targets near coastline by using Doppler Beam Sharpening technique’, in *2011 3rd International Asia-Pacific Conference on Synthetic Aperture Radar (APSAR)*, Sep. 2011, pp. 1–4.

[296] F. Zhang, A. Yu, F. He, and Z. Dong, ‘An improved DBS algorithm based on Doppler localization equations’, in *2013 IEEE China Summit and International Conference on Signal and Information Processing*, Jul. 2013, pp. 607–611. doi: 10.1109/ChinaSIP.2013.6625413.

[297] G. Pietrzyk, P. Samczyński, A. Gorzelańczyk, and K. Kulpa, ‘Real-time implementation of doppler beam sharpening technique with simple motion estimation’, *First Eur. Radar Conf. 2004 EURAD*, 2004.

[298] G. Frazer, A. Balleri, and G. Jacob, ‘Deception Jamming Against Doppler Beam Sharpening Radars’, *IEEE Access*, vol. 8, pp. 32792–32801, 2020, doi: 10.1109/ACCESS.2020.2973191.

[299] G. Frazer, A. Balleri, and G. Jacob, ‘Simulations of Repeat Jamming against Anti-Ship Missile Seekers Which Use Doppler Beam Sharpening Modes’, in *2017 Sensor Signal Processing for Defence Conference (SSPD)*, Dec. 2017, pp. 1–5. doi: 10.1109/SSPD.2017.8233265.

[300] H. Wu and T. Zwick, ‘Automotive SAR for Parking Lot Detection’, in *2009 German Microwave Conference*, Mar. 2009, pp. 1–8. doi: 10.1109/GEMIC.2009.4815910.

[301] J. Mure-Dubois, F. Vincent, and D. Bonacci, ‘Sonar and radar SAR processing for parking lot detection’, in *2011 12th International Radar Symposium (IRS)*, Sep. 2011, pp. 471–476.

[302] A. Laribi, M. Hahn, J. Dickmann, and C. Waldschmidt, ‘A new height-estimation method using FMCW radar Doppler beam sharpening’, in *2017 25th European Signal Processing Conference (EUSIPCO)*, Aug. 2017, pp. 1932–1396. doi: 10.23919/EUSIPCO.2017.8081546.

[303] A. Laribi, M. Hahn, J. Dickmann, and C. Waldschmidt, ‘Vertical Doppler beam sharpening goes self parking’, in *2018 IEEE Radar Conference (RadarConf18)*, Apr. 2018, pp. 0383–0388. doi: 10.1109/RADAR.2018.8378589.

[304] S. Gishkori, L. Daniel, M. Gashinova, and B. Mulgrew, 'Imaging for a Forward Scanning Automotive Synthetic Aperture Radar', *IEEE Trans. Aerosp. Electron. Syst.*, vol. 55, no. 3, pp. 1420–1434, Jun. 2019, doi: 10.1109/TAES.2018.2871436.

[305] H.-J. Li and Y.-W. Kiang, 'Radar and Inverse Scattering', in *The Electrical Engineering Handbook*, Chapter 10, W.-K. Chen, Burlington: Academic Press, 2005, pp. 671–690. doi: 10.1016/B978-012170960-0/50047-5.

[306] R. J. Marhefka, B. A. Baertlein, M. Rao, and K. Prakah-Asante, 'Modeling the performance of automotive bumper mounted antennas', in *IEEE Antennas and Propagation Society International Symposium (IEEE Cat. No.02CH37313)*, Jun. 2002, pp. 316–319 vol.3. doi: 10.1109/APS.2002.1018218.

[307] J. Yang, C. Liu, and Y. Wang, 'Real-time DBS imaging algorithm based on chirp z-transform', *IEICE Electron. Express*, vol. 9, pp. 1660–1665, Nov. 2012, doi: 10.1587/elex.9.1660.

[308] L. Daniel *et al.*, 'Doppler Beam Sharpening for Angular Refinement at 150 GHz – Initial Experimentation', in *2018 19th International Radar Symposium (IRS)*, Jun. 2018, pp. 1–7. doi: 10.23919/IRS.2018.8448091.

[309] Y. Lin, K.-P. Yang, M. Guo, and Y. Fu, 'Elimination of Motion-Induced Phase Based on Double-Time Switching Scheme for SAA FMCW Radar', 2019, doi: 10.3390/ELECTRONICS8070786.

[310] J. Bechter, F. Roos, and C. Waldschmidt, 'Compensation of Motion-Induced Phase Errors in TDM MIMO Radars', *IEEE Microw. Wirel. Compon. Lett.*, vol. 27, no. 12, pp. 1164–1166, Dec. 2017, doi: 10.1109/LMWC.2017.2751301.

[311] J.-J. Lin, Y.-P. Li, W.-C. Hsu, and T.-S. Lee, 'Design of an FMCW radar baseband signal processing system for automotive application', *SpringerPlus*, vol. 5, no. 1, p. 42, Jan. 2016, doi: 10.1186/s40064-015-1583-5.

[312] Y. Kang, Y. Zhang, D. Mao, X. Tuo, Y. Zhang, and Y. Huang, 'Super-resolution Doppler Beam Sharpening based on Online Tikhonov Regularization', in *2019 6th Asia-Pacific Conference on Synthetic Aperture Radar (APSAR)*, Nov. 2019, pp. 1–4. doi: 10.1109/APSAR46974.2019.9048298.

[313] V. Giannini *et al.*, '9.2 A 192-Virtual-Receiver 77/79GHz GMSK Code-Domain MIMO Radar System-on-Chip', in *2019 IEEE International Solid- State Circuits Conference - (ISSCC)*, Feb. 2019, pp. 164–166. doi: 10.1109/ISSCC.2019.8662386.

[314] C. Knill, J. Bechter, and C. Waldschmidt, 'Interference of chirp sequence radars by OFDM radars at 77 GHz', in *2017 IEEE MTT-S International Conference on Microwaves for Intelligent Mobility (ICMIM)*, Mar. 2017, pp. 147–150. doi: 10.1109/ICMIM.2017.7918878.

[315] 'Digital Code Modulation MIMO Radar Improves Automotive Safety | 2019-08-10 | Microwave Journal'. https://www.microwavejournal.com/articles/32668-digital-code-modulation-mimo-radar-improves-automotive-safety (accessed Nov. 20, 2022).

[316] W. Stark, M. Ali, and M. Maher, 'Digital Code Modulation (DCM) Radar for Automotive Applications', Jan. 2020. Accessed: Nov. 20, 2022. [Online]. Available: https://www.semanticscholar.org/paper/DIGITAL-CODE-MODULATION-(DCM)-RADAR-FOR-AUTOMOTIVE-White/b1c86d9adaaf77ae274d2aed6ea8c30f8d9adda5

[317] 'Uhnder Digital Radar Advances Automotive ADAS, Uses Micron Memory'. https://www.micron.com/insight/uhnder-digital-radar-advances-automotive-adas-uses-micron-memory (accessed Nov. 20, 2022).

[318] C. D. Ozkaptan, E. Ekici, and O. Altintas, 'Enabling Communication via Automotive Radars: An Adaptive Joint Waveform Design Approach', in *IEEE INFOCOM 2020 - IEEE Conference on Computer Communications*, Jul. 2020, pp. 1409–1418. doi: 10.1109/INFOCOM41043.2020.9155527.

[319] A. Hassanien, B. Himed, and M. G. Amin, 'Transmit/receive beamforming design for joint radar and communication systems', in *2018 IEEE Radar Conference (RadarConf18)*, Apr. 2018, pp. 1481–1486. doi: 10.1109/RADAR.2018.8378784.

[320] J. Khoury, R. Ramanathan, D. McCloskey, R. Smith, and T. Campbell, 'RadarMAC: Mitigating Radar Interference in Self-Driving Cars', in *2016 13th Annual IEEE International Conference on Sensing, Communication, and Networking (SECON)*, Jun. 2016, pp. 1–9. doi: 10.1109/SAHCN.2016.7733011.

[321] E. BouDaher, A. Hassanien, E. Aboutanios, and M. G. Amin, 'Towards a dual-function MIMO radar-communication system', in *2016 IEEE Radar Conference (RadarConf)*, May 2016, pp. 1–6. doi: 10.1109/RADAR.2016.7485316.

[322] Y. Yao, J. Zhao, and L. Wu, 'Adaptive Waveform Design for MIMO Radar-Communication Transceiver', *Sensors*, vol. 18, no. 6, p. 1957, Jun. 2018, doi: 10.3390/s18061957.

[323] W. Wang and H. Shao, 'Radar-to-Radar Interference Suppression for Distributed Radar Sensor Networks', *Remote Sens*, 2014, doi: 10.3390/rs6010740.

[324] 'Combined Radar-Based Communication and Interference Mitigation for Automotive Applications - Högskolan i Halmstad'. https://www.hh.se/english/research/our-research/research-at-the-school-of-information-technology/technology-area-smart-electronic-systems/research-projects-within-smart-electronic-systems/combined-radar-based-communication-and-interference-mitigation-for-automotive-applications.html (accessed Nov. 20, 2022).

[325] A. Bose, B. Tang, M. Soltanalian, and J. Li, 'Mutual Interference Mitigation for Multiple Connected Automotive Radar Systems', *IEEE Trans. Veh. Technol.*, vol. PP, pp. 1–1, Aug. 2021, doi: 10.1109/TVT.2021.3108714.

[326] J. Ender and S. Brüggenwirth, 'Cognitive radar - enabling techniques for next generation radar systems', in *2015 16th International Radar Symposium (IRS)*, Jun. 2015, pp. 3–12. doi: 10.1109/IRS.2015.7226395.

[327] M. Steck, C. Neumann, and M. Bockmair, 'Cognitive Radar Principles and Application to Interference Reduction', in *2018 19th International Radar Symposium (IRS)*, Jun. 2018, pp. 1–10. doi: 10.23919/IRS.2018.8448217.

[328] G. Hakobyan, K. Armanious, and B. Yang, 'Interference-Aware Cognitive Radar: A Remedy to the Automotive Interference Problem', *IEEE Trans. Aerosp. Electron. Syst.*, vol. 56, no. 3, pp. 2326–2339, Jun. 2020, doi: 10.1109/TAES.2019.2947973.

[329] A. Pirkani, F. Norouzian, M. Cherniakov, and M. Gashinova, 'Automotive Radar Parameter Estimation for Cognitive Interference Mitigation', in *2022 19th European Radar Conference (EuRAD)*, Sep. 2022, pp. 161–164. doi: 10.23919/EuRAD54643.2022.9925005.

[330] Z. Slavik and K. V. Mishra, ‘Cognitive Interference Mitigation in Automotive Radars’, in *2019 IEEE Radar Conference (RadarConf)*, Apr. 2019, pp. 1–6. doi: 10.1109/RADAR.2019.8835643.

[331] S. Haykin, ‘Cognitive radar: a way of the future’, *IEEE Signal Process. Mag.*, vol. 23, no. 1, pp. 30–40, Jan. 2006, doi: 10.1109/MSP.2006.1593335.

[332] J. Rong, F. Liu, and Y. Miao, ‘Integrated Radar and Communications Waveform Design Based on Multi-Symbol OFDM’, *Remote Sens.*, vol. 14, no. 19, Art. no. 19, Jan. 2022, doi: 10.3390/rs14194705.

[333] K. Wu, J. A. Zhang, X. Huang, Y. J. Guo, and R. W. Heath, ‘Waveform Design and Accurate Channel Estimation for Frequency-Hopping MIMO Radar-Based Communications’, *IEEE Trans. Commun.*, vol. 69, no. 2, pp. 1244–1258, Feb. 2021, doi: 10.1109/TCOMM.2020.3034357.

[334] J. Lee, D. Niyato, Y. L. Guan, and D. I. Kim, ‘Learning to Schedule Joint Radar-Communication With Deep Multi-Agent Reinforcement Learning’, *IEEE Trans. Veh. Technol.*, vol. 71, no. 1, pp. 406–422, Jan. 2022, doi: 10.1109/TVT.2021.3124810.

[335] T. D. Çaha and L. D. Ata, ‘Time Resource Management in Cognitive Radars Based on Parameter Optimization’, in *2022 30th Signal Processing and Communications Applications Conference (SIU)*, May 2022, pp. 1–4. doi: 10.1109/SIU55565.2022.9864811.

[336] M. Kunert, *The EU project MOSARIM: A general overview of project objectives and conducted work*. 2012, p. 5.

[337] C. Fischer, M. Barjenbruch, H. L. Bloecher, and W. Menzel, ‘Detection of pedestrians in road environments with mutual interference’, in *2013 14th International Radar Symposium (IRS)*, Jun. 2013, pp. 746–751.

[338] L. Reichardt, J. Maurer, T. Fugen, and T. Zwick, ‘Virtual Drive: A Complete V2X Communication and Radar System Simulator for Optimization of Multiple Antenna Systems’, *Proc. IEEE*, vol. 99, no. 7, pp. 1295–1310, Jul. 2011, doi: 10.1109/JPROC.2011.2124430.

[339] W. Buller, J. Garbarino, B. Wilson, and J. Kelly, ‘Estimating Expected Levels of Mutual Interference in Automotive Radar and Simulating System Impacts’, 2019.

https://www.semanticscholar.org/paper/Estimating-Expected-Levels-Of-Mutual-Interference-Buller-Garbarino/ba35667eef52c6f8d7c00666c7b773ef76b99cde (accessed Aug. 04, 2021).

[340] 'IMIKO radar - microelectronics research'. https://www.elektronikforschung.de/projekte/imiko-radar (accessed Aug. 04, 2021).

[341] B. Nuß, 'KIT - IHE - Radar Systems - IMIKO', Nov. 20, 2021. https://www.ihe.kit.edu/4977_4347.php (accessed Nov. 30, 2022).

[342] A. Ossowska, L. Sit, S. Manchala, T. Vogler, K. Krupinski, and U. Luebbert, 'IMIKO-Radar Project: Laboratory Interference Measurements of Automotive Radar Sensors', in *2020 21st International Radar Symposium (IRS)*, Oct. 2020, pp. 334–338. doi: 10.23919/IRS48640.2020.9253845.

[343] F. Norouzian, A. Pirkani, E. Hoare, M. Cherniakov, and M. Gashinova, 'Automotive Radar Waveform Parameters Randomisation for Interference Level Reduction', in *2020 IEEE Radar Conference (RadarConf20)*, Sep. 2020, pp. 1–5. doi: 10.1109/RadarConf2043947.2020.9266375.

[344] F. Norouzian, A. A. Pirkani, E. G. Hoare, M. Cherniakov, and M. Gashinova, 'Characterization of the Effect of Low Pass Filter Response on the Interference in FMCW Automotive Radar', in *2021 21st International Radar Symposium (IRS)*, Jun. 2021, pp. 1–6. doi: 10.23919/IRS51887.2021.9466189.

[345] A. Pirkani *et al.*, 'SINR Improvement Across the Automotive Radar Signal Processing Chain', in *2022 19th European Radar Conference (EuRAD)*, Sep. 2022, pp. 5–8. doi: 10.23919/EuRAD54643.2022.9924759.

[346] A. Pirkani *et al.*, 'COSMOS dataset for co-existence/ interference analysis and simultaneous scene representation by automotive radar and video with GPS/IMU ground truth'. University of Birmingham, Jan. 19, 2022. doi: 10.25500/edata.bham.00000777.

[347] A. Pirkani *et al.*, 'COSMOS dataset for co-existence/ interference analysis and simultaneous scene representation by automotive radar and video with GPS/IMU ground truth - Sub-Dataset B'. University of Birmingham, Jan. 30, 2022. doi: 10.25500/edata.bham.00000785.

[348] A. Pirkani *et al.*, ‘COSMOS dataset for co-existence/ interference analysis and simultaneous scene representation by automotive radar and video with GPS/IMU ground truth - Sub-Dataset C’. University of Birmingham, Jan. 30, 2022. doi: 10.25500/edata.bham.00000786.

[349] A. Pirkani *et al.*, ‘COSMOS dataset for co-existence/ interference analysis and simultaneous scene representation by automotive radar and video with GPS/IMU ground truth - Sub-Dataset D’. University of Birmingham, Jan. 30, 2022. Accessed: Apr. 24, 2022. [Online]. Available: https://edata.bham.ac.uk/787/?_ga=2.35144482.2000380920.1650820948-2035368691.1636062447

[350] A. Pirkani *et al.*, ‘COSMOS dataset for co-existence/ interference analysis and simultaneous scene representation by automotive radar and video with GPS/IMU ground truth - Sub-Dataset E’. University of Birmingham, Jan. 30, 2022. doi: 10.25500/edata.bham.00000788.

[351] A. Pirkani and M. Gashinova, ‘COSMOS “Adaptive Cruise Control (ACC) dataset” for co-existence/ interference analysis and simultaneous scene representation by automotive radar and video’. University of Birmingham, Mar. 01, 2022. doi: 10.25500/edata.bham.00000800.

[352] A. Pirkani and M. Gashinova, ‘COSMOS “Cross Traffic Alert (CTA) dataset” for co-existence/ interference analysis and simultaneous scene representation by automotive radar and video.’ University of Birmingham, Mar. 01, 2022. doi: 10.25500/edata.bham.00000801.

[353] ‘ESI CEM One 2018 Facilitates the Integration of Sensors in their Operating Environment | myESI’. https://myesi.esi-group.com/jp/resources/press-releases/esi-cem-one-2018-facilitates-integration-sensors-their-operating (accessed Sep. 18, 2022).

[354] ‘CST Studio Suite 3D EM simulation and analysis software’. https://www.3ds.com/products-services/simulia/products/cst-studio-suite/ (accessed Sep. 18, 2022).

[355] ‘Automotive Simulation Models’. https://www.dspace.com/en/inc/home/products/sw/automotive_simulation_models.cfm (accessed May 16, 2022).

[356] ‘VTD - Enabling safety validation in autonomous driving and ADAS system simulation’, *VTD*. https://vires.mscsoftware.com/ (accessed May 16, 2022).

[357] ‘Active Safety System Simulation | Siemens Software’, *Siemens Digital Industries Software*. https://www.plm.automation.siemens.com/global/en/products/simulation-test/active-safety-system-simulation.html (accessed May 16, 2022).

[358] ‘Automated Driving Toolbox Documentation - MathWorks United Kingdom’. https://uk.mathworks.com/help/driving/index.html?s_tid=srchtitle_automated%20driving%20toolbox_1 (accessed May 16, 2022).

[359] H. Ling, R.-C. Chou, and S.-W. Lee, ‘Shooting and bouncing rays: calculating the RCS of an arbitrarily shaped cavity’, *IEEE Trans. Antennas Propag.*, vol. 37, no. 2, pp. 194–205, Feb. 1989, doi: 10.1109/8.18706.

[360] J. Maurer, T. Fuegen, and W. Wiesbeck, ‘A Ray-Optical Channel Model for Vehicular Ad-Hoc Networks’, in *11th European Wireless Conference 2005 - Next Generation wireless and Mobile Communications and Services*, Apr. 2006, pp. 1–7.

[361] T. Schipper, J. Schlichenmaier, D. Ahbe, T. Mahler, J. Kowalewski, and T. Zwick, ‘A simulator for multi-user automotive radar scenarios’, in *2015 IEEE MTT-S International Conference on Microwaves for Intelligent Mobility (ICMIM)*, Apr. 2015, pp. 1–4. doi: 10.1109/ICMIM.2015.7117928.

[362] M. Schoeman and U. Jakobus, ‘Efficient analysis of integrated windscreen antennas’, Jan. 2009.

[363] R. Wahl, M. Layh, and T. F. Eibert, ‘Wave Propagation Inside and Around Vehicles in Dynamic Time Variant Scenarios’, in *2006 IEEE 63rd Vehicular Technology Conference*, May 2006, pp. 2883–2886. doi: 10.1109/VETECS.2006.1683395.

[364] N. Hirsenkorn *et al.*, ‘A ray launching approach for modeling an FMCW radar system’, in *2017 18th International Radar Symposium (IRS)*, Jun. 2017, pp. 1–10. doi: 10.23919/IRS.2017.8008120.

[365] R. Pell, ‘Automotive radar test solution advances autonomous driving safety Smart2.0’, *EENewsEurope*, Mar. 09, 2018. https://www.smart2zero.com/en/automotive-radar-test-solution-advances-autonomous-driving-safety/ (accessed Sep. 18, 2022).

[366] S. Scheiblhofer, M. Treml, S. Schuster, R. Feger, and A. Stelzer, ‘A versatile FMCW Radar System Simulator for Millimeter-Wave Applications’, in *2008 38th European Microwave Conference*, Oct. 2008, pp. 1604–1607. doi: 10.1109/EUMC.2008.4751778.

[367] ‘Enable S3 – Enable S3 official page’. https://enable-s3.eu/ (accessed Aug. 04, 2021).

[368] ‘About PEGASUS - pegasus-EN’. https://www.pegasusprojekt.de/en/about-PEGASUS (accessed Aug. 04, 2021).

[369] S. B. Jayapal Gowdu, A. Schwind, R. Stephan, and M. A. Hein, ‘Monostatic RCS measurements of a passenger car mock-up at 77 GHz frequency in virtual environment’, in *2019 16th European Radar Conference (EuRAD)*, Oct. 2019, pp. 361–364.

[370] K. Ramasubramanian, ‘Using a complex-baseband architecture in FMCW radar systems’, p. 10, 2017.

[371] ‘AWR1243 data sheet, product information and support | TI.com’. https://www.ti.com/product/AWR1243 (accessed Oct. 02, 2021).

[372] L. W. C. II, *Digital and Analog Communication Systems: International Edition*, 6th edition. Upper Saddle River, N.J: Pearson, 2020.

[373] ‘Millimeter wave components and systems, waveguide antennas, standard gain horns, MM wave radars - ELVA-1’. http://elva-1.com/ (accessed Mar. 30, 2020).

[374] ‘AWR1243BOOST AWR1243 76-GHz to 81-GHz high-performance automotive MMIC evaluation module | TI.com’. https://www.ti.com/tool/AWR1243BOOST (accessed Aug. 07, 2020).

[375] ‘ASSURED CAV City - Proving Ground’. https://www.vehicletesting.solutions/proving-ground-surfaces/city-circuit/ (accessed May 04, 2022).

[376] ‘Define Road Layouts Programmatically - MATLAB & Simulink - MathWorks United Kingdom’. https://uk.mathworks.com/help/driving/ug/define-road-layouts.html (accessed Dec. 01, 2022).

[377] ‘Add road to driving scenario or road group - MATLAB road - MathWorks United Kingdom’. https://uk.mathworks.com/help/driving/ref/drivingscenario.road.html (accessed Dec. 01, 2022).

[378] ‘Design driving scenarios, configure sensors, and generate synthetic data - MATLAB - MathWorks United Kingdom’. https://uk.mathworks.com/help/driving/ref/drivingscenariodesigner-app.html (accessed Sep. 18, 2022).

[379] M. Buhren and B. Yang, ‘Simulation of Automotive Radar Target Lists using a Novel Approach of Object Representation’, in *2006 IEEE Intelligent Vehicles Symposium*, Jun. 2006, pp. 314–319. doi: 10.1109/IVS.2006.1689647.

[380] L. Daniel, D. Phippen, E. Hoare, M. Cherniakov, and M. Gashinova, ‘Image Segmentation in Real Aperture Low-THz Radar Images’, in *2019 20th International Radar Symposium (IRS)*, Jun. 2019, pp. 1–8. doi: 10.23919/IRS.2019.8768106.

[381] L. Daniel and M. Gashinova, ‘Sub-THz Radar Imagery for Automotive Application’, in *2022 19th European Radar Conference (EuRAD)*, Sep. 2022, pp. 261–264. doi: 10.23919/EuRAD54643.2022.9924931.

[382] S. M. Sabery, A. Bystrov, M. Navarro-Cía, P. Gardner, and M. Gashinova, ‘Study of Low Terahertz Radar Signal Backscattering for Surface Identification’, *Sensors*, vol. 21, no. 9, Art. no. 9, Jan. 2021, doi: 10.3390/s21092954.

[383] Y. Xiao, L. Daniel, and M. Gashinova, ‘Image Segmentation and Region Classification in Automotive High-Resolution Radar Imagery’, *IEEE Sens. J.*, vol. 21, no. 5, pp. 6698–6711, Mar. 2021, doi: 10.1109/JSEN.2020.3043586.

[384] Z. Zheng, Y. Zheng, W.-Q. Wang, and H. Zhang, ‘Covariance Matrix Reconstruction With Interference Steering Vector and Power Estimation for Robust Adaptive Beamforming’, *IEEE Trans. Veh. Technol.*, vol. 67, no. 9, pp. 8495–8503, Sep. 2018, doi: 10.1109/TVT.2018.2849646.

[385] Z. hongwei, L. Baowang, and F. Juan, ‘Adaptive Beamforming Algorithm for Interference Suppression in GNSS Receivers’, *Int. J. Comput. Sci. Inf. Technol.*, vol. 3, no. 5, pp. 17–28, Oct. 2011, doi: 10.5121/ijcsit.2011.3502.

[386] I. P. Gravas, Z. D. Zaharis, T. V. Yioultsis, P. I. Lazaridis, and T. D. Xenos, ‘Adaptive Beamforming With Sidelobe Suppression by Placing Extra Radiation Pattern Nulls’, *IEEE Trans. Antennas Propag.*, vol. 67, no. 6, pp. 3853–3862, Jun. 2019, doi: 10.1109/TAP.2019.2905709.

[387] A. De Maio, Y. C. Eldar, and A. M. Haimovich, Eds., *Compressed Sensing in Radar Signal Processing*. Cambridge: Cambridge University Press, 2019. doi: 10.1017/9781108552653.

[388] J. Yang, J. Lu, X. Liu, and G. Liao, ‘Robust Null Broadening Beamforming Based on Covariance Matrix Reconstruction via Virtual Interference Sources’, *Sensors*, vol. 20, no. 7, p. 1865, Mar. 2020, doi: 10.3390/s20071865.

APPENDICES

Appendix 1. Industry-Led Projects on Automotive Radar Interference

Since the last decade, the issue of radar interference has gained significant attention leading to industry-based projects dedicated to its analysis.

- MOSARIM

The project MOSARIM (MOre Safety for All by Radar Interference Mitigation) [171], [207], [336] was funded by the EU, and started in 2010. It is the foremost industry-led research to explore the impact of mutual interference using real-road measurements [41], [179], [259], [337]. Various tests, simulations, and analyses were performed to get an overview of the interference situation between automotive radars. The simulation tools to predict future interference situations were also discussed [128],[130],[167]. Moreover, various countermeasures and interference mitigation techniques were investigated and assessed with general guidelines and recommendations. It was concluded that to attain an INR of 0 to 10 dB, reliable mitigation techniques are required, with a capability of providing up to 50 dB interference suppression in specific scenarios [32], [336].

The MOSARIM project assessed numerous road scenarios. However, the study was limited to slow-chirp and triangular FMCW waveforms. The mutual interference was analysed between a) FMCW-FMCW radars and b) FMCW-pulse radars [78]. Though, pulse radar is rarely used for automotive applications due to its limited transmitted energy.

- NHSTA

National Highway Traffic Safety Administration (NHSTA) funded ‘Radar Congestion Study’ [339] provided simplified expressions to estimate scenarios in which automotive radars

must operate as the RPR increase. Based on the theoretical estimation and modelling, the received interference level and its impact on the radar's performance have been evaluated.

The research concluded that interference levels based on the functionality of current automotive sensors would be significant, especially in congested environments. However, the presented approach does not consider the effect of radar parameters, hardware configurations, and radar processing chain on the overall impact of interference.

- IMIKO

The German Federal Ministry of Education and Research funded project IMIKO (Interference Mitigation by Cooperation in Radar for Autonomous Electric Cars) started in late 2018 and is ongoing at the time of writing this thesis. The mutual interference and mitigation possibilities [340]–[342] have been investigated alongside the formulation of requirements on radar-based automotive systems, cooperative methods, and an evaluation of investigated solutions.

- COSMOS

The Innovate UK-funded project COSMOS (CO-existence Simulation MOdelling of radars for Self-driving) started in early 2018. The project goal was to develop an experimentally verified simulator with a whole sensing loop, where sensors, control system, signal processing, and environment will interact to emulate different driving scenarios. The developed simulator investigated and mitigated mutual interference between sensors to ensure traffic safety.

The project outcome was a holistic simulator with a physics-based sensor level modelling, where each part of the sensor such as sensor configuration, environment and propagation channels, interference and co-existence effects, signal processing chain according to the hardware and software capabilities of automotive radar chipsets have been modelled [20], [103], [144], [230], [247], [287], [343]–[345]. The simulator also provided verifiable

performance metrics used to develop and analyse the performance of various developed interference mitigation strategies. The multi-sensor raw data [346]–[350] and processed radar data [351], [352] collected after extensive field trials in various road scenarios are made available for offline processing and advanced algorithm implementation.

Appendix 2. Literature Survey on Radar Simulators

The existing radar simulators have been categorised as follows:

1. ADAS simulators to model the environment. These have been summarised in Table A2.1.
2. EM simulators to model propagation through materials [353], and
3. Radiation simulators [354].

Table A2.1: ADAS simulators to model environment

Simulator	Application	Remarks
ASM (D-Space) [355]	Used for hardware in the loop test.	Not suitable for radar sensing simulations
Vires VTD [356]	Modular toolset to test and develop ADAS and active safety.	No radar sensing element
TASS Pre-Scan [357]	ADAS simulation package.	Physics-based modelling has been used for a limited number of surfaces. Limited to the number of scenes and not flexible with sensor parameters. Mainly used for camera simulation.
MATLAB Automated Driving Toolbox [358]	Automated Driving Toolbox provides algorithms and tools to design, simulate, and test ADAS and autonomous driving systems.	Single point return from target with some elements of RCS and waveform models. Sensors only on host vehicle but can be expanded.

Another category of simulators includes the ray tracing models (RTM) where the EM wave propagation is simulated by means of geometrical or physical optics approximations [359]. This includes an evaluation of the complex car-to-car communication scenarios [360] and RTM with scenario-specific simulation environments [42], [42], [177], [361], [362], [363], [41]. At higher frequencies, the approach with full wave methods requires an enormous effort in terms of computational requirements and memory resources.

Based on ray tracking, a simulator called “Virtual Drive” has been discussed in [338] that consists of an environment and a realistic traffic model and calculates the multipath propagation. The models do not consider various radar parameters and interference received from roadside radars in a dynamic environment. RTM can simulate different physical phenomena, including multipath propagation and interference [364]. However, they have some limitations, discussed below:

- Their application in real-time is constrained due to high computational time and complexity.
- The geometry and properties of the radar’s environment, including statics and dynamic road actors and clutter must be modelled with high precision, making these models more challenging.
- For precisely calibrated results, RTM should implement all the steps in a radar’s pipeline. However, they are often proprietary for the commercial radar chipsets.

The simulators based on hardware in the loop, software in the loop, and target in the loop address either the sensor design, the hardware components, or the signal processing. Such simulators are usually dedicated to a specific problem, such as waveform optimisation or modelling the response from a target. However, the can only model part of the mmWave sensor and the environment. Examples of such simulators include Keysight automotive radar test solution and Keysight’s premiere System Vue automotive radar library (W1908). These tools present various solutions to optimise FMCW signals and sensor design [365]. In [366], a flexible model has been discussed that considers the aspects of hardware simulation and also the influence of system control, such as the sweep parameters, on sensor performance. However, the impact of radar interference and co-existence have not been considered.

Several other research projects including ENABLE-S3 [367] and PEGASUS [368] have also been aimed to establish the testing methods to assure traffic safety. These simulators rely on the modelling-based approach for the validation of expected results. Additionally, they have the capability to incorporate more physical components into the final system.

Interference-based simulators have been discussed in [41], [179]. A multisystem radar simulator presented in [41] focuses on interference investigation and mitigation, including a scenario editing tool, a wave propagation simulator, and the data post-processing. Moreover, a method to predict future interference conditions between automotive radars has been introduced in [179].

Appendix 3. Interference Classification

Example parameters for each interference type used to generate radar plots in this section have been given in Table A3.1.

Table A3.1: Example interference parameters classified based on the sweep rate difference.

Interference	Sub-Types	Description	Cases	T_{sint}, B_{sint}
Synchronous $B_{IF-I} \leq B_{Rx}$ for the entire victim chirp duration		$K_v = K_{\text{int}}$	1	102.4 µs, 0.3 GHz
Semi-Synchronous $B_{IF-i} \leq B_{Rx}$ for the entire victim chirp duration	--	$K_v \approx K_{\text{int}}$	2a	102.4 µs, 0.299 GHz
			2b	102.39 µs, 0.3 GHz
Asynchronous $K_v \neq K_{\text{int}}$ $B_{IF-i} \leq B_{Rx}$ for some part(s) of victim chirp duration	Periodic	Fast Chirp $mT_{\text{sint}} = T_{sv}$ for m = 1,2,3, …	3a	25.6 µs
		Slow Chirp $T_{\text{sint}} = mT_{sv}$ for m = 2,3, …	3b	CW
	Semi-Periodic	$mT_{\text{sint}} = nT_{sv}$ for m = 2,3, … n = 2,3, …	4	153.6 µs
	Aperiodic	$mT_{\text{sint}} \neq T_{sv}$ and $mT_{\text{sint}} \neq nT_{sv}$ For any value of m and n	5a	27 µs
			5b	423 µs

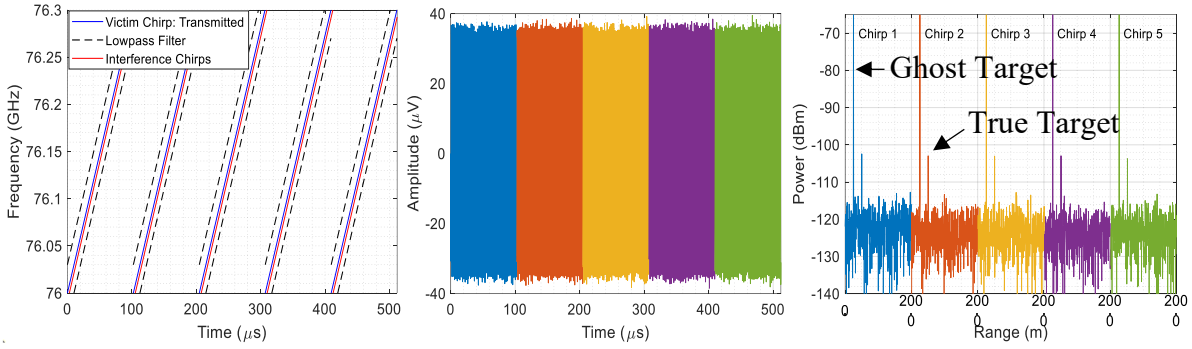
In a typical automotive scenario, majority of the interference types are asynchronous and aperiodic [103]. However, as interference fundamentally appear as stochastic processes, all kinds of interference have been investigated in this work.

A3.1. Synchronous Interference

When two radars with identical waveform parameters interfere such that $K_v = K_{\text{int}}$, and $F_{cv} - \frac{F_{LPF}}{2} \leq F_{ci} \leq F_{cv} + \frac{F_{LPF}}{2}$, the interference signal chirp is completely synchronised with the

VR chirp, however, with a delay. The entire interferer chirp is within the LPF band of the VR, similar to the return from a target. The down-converted synchronous interference contribution to the beat signal in (3-22) is monotonic and expressed as: $f_{IF-Synchronous} = K_{\text{int}}\tau_{\text{int}}$.

After signal processing, a ghost target appears at an arbitrary distance. The chirp overlap plot, time domain, and frequency domain representation of synchronous interference have been shown in Figure A3.1. Compared to the echo signal (Figure 3.13), a higher interference power is received due to a one-way propagation delay, causing false alarms at the detection stage.



(a) (b) (c)

Figure A3.1: Synchronous interference: (a) chirp plot, (b) time domain, (c) range profile.

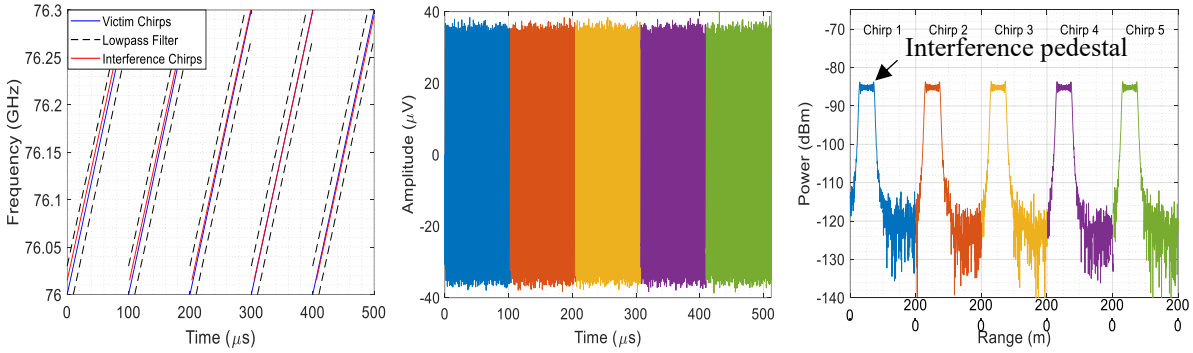
Synchronous interference can also occur if the VR's signal is received through the multipath reflections, such as in the tunnels, highways with guard rails, car parks, etc. Consequently, ghost targets appear at arbitrary distances and directions that depends upon the distance between the radar and the reflecting surface.

A3.2. Semi-Synchronous Interference

The sweep rates of VR and IR for semi-synchronous interference are similar but not identical $\left(K_v \approx K_{\text{int}}\right)$. Analogous to synchronous interference, semi-synchronous interference remains within the entire duration of the victim's chirp. However, the time-dependent term in (3-22) is non-zero, resulting in interference spread across multiple frequency (range) bins. Two types of semi-synchronous interference have been observed based on the IR parameters.

- Case 2 (a): Table A3.1

For the similar VR and IR sweep times, with a small bandwidth difference, a chirp-like interference pattern has been observed in the down-converted signal. Therefore, interference spreads across limited range bins with a higher power, forming a pedestal-like interference floor. The position and width of the pedestal depend upon the VR and IR waveform parameters. Radar plots of semi-synchronous interference for Case 2 (a) have been given in Figure A3.2. Compared to the echo signal (Figure 3.13), a higher interference power is received due to a one-way propagation delay, which masks the target at 50 m in all the VR chirps.

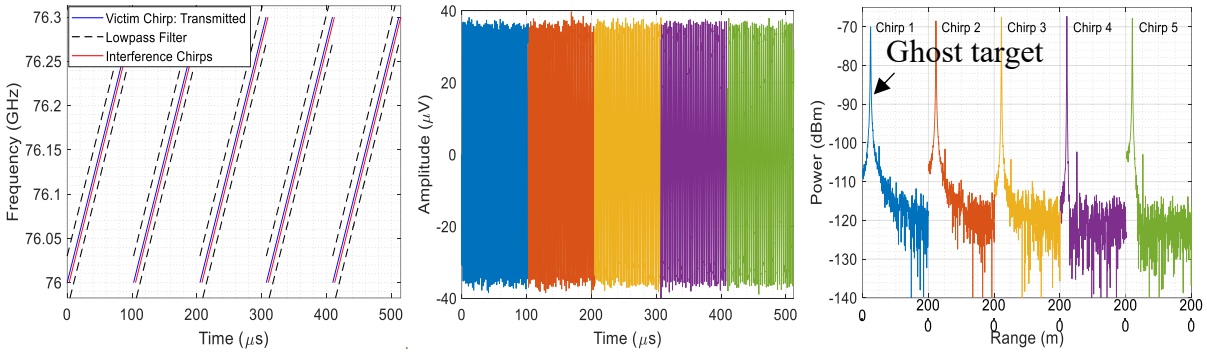


(a) (b) (c)

Figure A3.2: Semi-synchronous interference, Case 2(a): (a) chirp plot, (b) time domain, (c) range profile.

- Case 2 (b): Table A3.1

For the similar bandwidth of VR and IR waveforms but a slight difference in sweep time, there is an absence of complete coherence between the VR and IR chirps. Therefore, interference appears like a ghost target but with a broad peak (and broader resolution) centred around frequency $K_{\text{int}}\tau_{\text{int}}$ rather than a sharp peak, as observed for the echo signals in Figure 3.13. Radar plots of semi-synchronous interference for Case 2 (b) have been presented in Figure A3.3.



(a) (b) (c)

Figure A3.3: Semi-synchronous interference, Case 2 (b): (a) chirp plot, (b) time domain, (c) range profile.

Synchronous and semi-synchronous interference are unlikely to occur in real-road automotive scenes because they need full synchronisation between the VR and IR waveforms. However, they cannot be completely ruled out, particularly on highways where numerous radars operate simultaneously for extended periods of time. Therefore, even low probability radar interaction might occur, and must be taken into account while developing appropriate models.

A3.3. Asynchronous Interference

In a typical automotive scenario, radars from various manufacturers, different waveform parameters, and configurations will be present. Interference between them gives rise to asynchronous interference, a more common type. It occurs when the waveforms of two interfering radars have different sweep rates such that $K_v \neq K_{\text{int}}$.

The interference signal, in this case, lies within the LPF band of the VR at a few locations. This depends upon the waveform parameters of radars. Consequently, unlike synchronous and semi-synchronous interference, which is more focused with spread across a limited number of frequency (range) bins, asynchronous interference is time limited. Therefore, it spreads over a large number of frequency bins after FFT across the fast-time. This leads to a uniform interference pattern. The increased noise floor would degrade radar detection sensitivity by

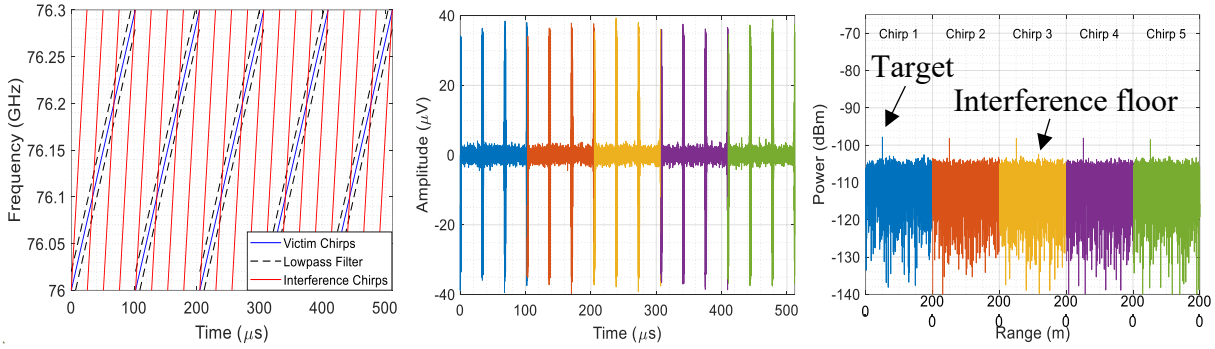
lowering the SINR and might result in missed targets. Asynchronous interference has further been further divided into three sub-groups: periodic, semi-periodic, and aperiodic interference. For understanding, the fractional times of interference occurrence within each VR chirp have been defined as a vector: $t_{\text{int}} = [t_1, t_2, ..., t_M]$, where M represents the number of interference pulses within each VR chirp.

I. Periodic Interference

Periodic interference occurs when the interference pattern across each the VR chirp is similar. The following cases have been observed based on the number of interference pulses in each VR chirp.

- Case 3 (a) from Table A3.1 – Fast Chirp Periodic Interference:

In this case, t_{int} vector across all the VR chirps is similar. The radar plots for Case 3 (a) have been given in Figure A3.4.



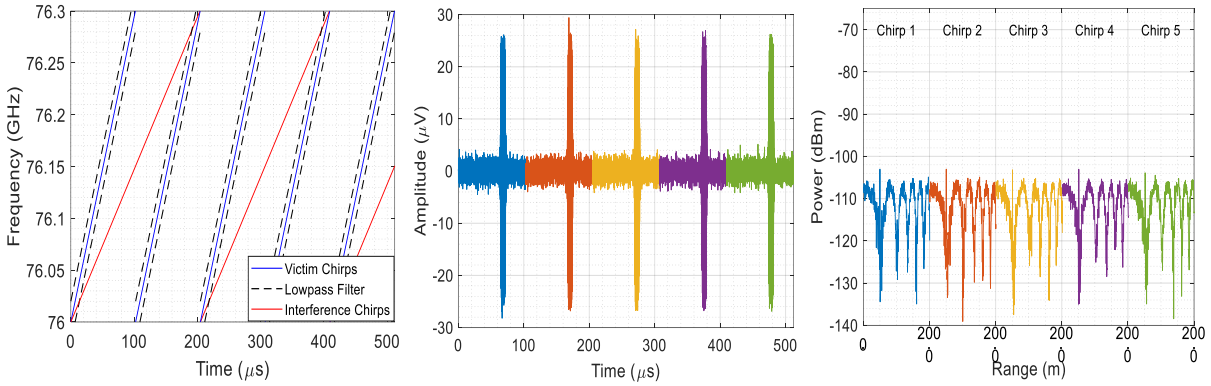
(a) (b) (c)

Figure A3.4: Fast chirp periodic interference: (a) chirp plot, (b) time domain, (c) range profile.

Due to the appearance of multiple interference pulses within each VR chirp (M in (3-39) is 4) with different time of occurrence of each interference pulse, random peaks and nulls appear in the interference floor after FFT across the fast-time with a uniform spread. This has been demonstrated in Figure A3.4 (c).

- Case 3(b) from Table A3.1 – Slow Chirp Periodic Interference:

Each VR chirp has at most one interference pulse; therefore, *M* in (3-39) is 1. Moreover, the fractional time of occurrence of interference pulse is similar across all the VR chirps. CW interference has been considered as an example to generate periodic slow chirp interference in the presented work. The radar plots for Case 3 (b) have been given in Figure A3.5.



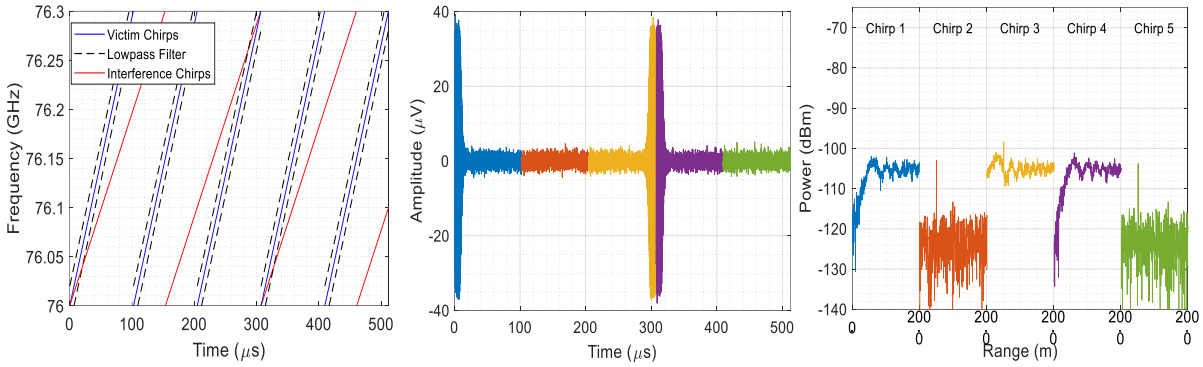
(a) (b) (c)

Figure A3.5: Slow chirp periodic interference: (a) chirp plot, (b) time domain, (c) range profile.

A linear phase relationship between the interference samples of each pulse causes well-defined bows and nulls in the spectrum.

II. Semi-Periodic Interference

For semi-periodic interference, the interference sequence appears randomly for a few victim chirps, then repeats for the remainder of the VR chirps during a CPI. Therefore, the fractional times of interference occurrence for the first few victim chirps are different, and then they start to repeat, so that $mT_{\text{sint}} = nT_{sv}$ for an integer $m \geq 2$. The radar plots are given in Figure A3.6.



(a) (b) (c)

Figure A3.6: Semi-periodic interference: (a) chirp plot, (b) time domain, (c) range profile.

In particular, for the semi-periodic interference case mentioned in Table A3.1 and Figure A3.6, at most, one interference pulse appears per each VR chirp, and the interference sequence repeats after every 3 VR chirps. This results in bows and nulls after FFT across the fast-time. However, in this example, as each VR chirp has a single-sided interference pulse, bows and nulls are not well-defined compared to periodic interference. The second and fifth VR chirp has no interference appearance due to the non-overlapping VR and IR chirps.

III. Aperiodic Interference

For aperiodic interference, the interference sequence across each VR chirp during the CPI is random. Therefore, the vector t_{int} is unique for each victim chirp. Depending upon the number of interference pulses within each victim chirp, aperiodic interference has further been divided into fast and slow chirp sequences. These have been discussed in section 3.6.1.

Interference examples in Table A3.1 show a distinct behaviour in the frequency domain. Synchronous and semi-synchronous interference can be called narrowband interference, as they affect a small portion of the frequency spectrum. Asynchronous interference can be called broadband interference as it affects a larger portion of the VR's frequency band. At the output of Doppler compression, the echo signal and interference are further averaged over the integration time. Therefore, the interference spectrum spread becomes even more uniform. This has been discussed in section 3.7.

Appendix 4. Interference Representation in Each Domain – Use Cases

To analyse the characteristics of interference, examples for synchronous, semi-synchronous, and asynchronous interference have been given in Table A4.1 for the VR with $T_{sv} = 50$ µs, $B_{sv} = 0.5$ GHz, and $F_{cv} = F_{\text{cint}} = 76$ GHz. A target with an initial position of 50 m, 10^o from the VR has been driving at 4 m/s toward the static VR. The target is also a source of interference with forward-looking IR. The target and interferer are therefore collocated. The RCS of the target is 10 dBsm, which is a typical RCS value for a normal-sized car [369]. Both the VR and IR operate in TDM-MIMO mode with $N_{Tx} = 4$, $N_{Rx} = 16$ based on the INRAS Radarlog chipset [91].

The target's speed has been selected to keep the relative speed between the VR and target within the VR unambiguous velocity: $\pm\lambda/4T_{MIMO} = \pm 4.9$ m/s, where $T_{MIMO} = N_{Tx}T_{sv}$. With the defined array configuration, virtual array resolution is 1.9^o whereas resolution defined by the real aperture (16 receive elements) is 7.2^o. The Blackman-Harris window has been applied across fast-time to achieve better sidelobe suppression while the Hann window across slow-time and array elements to achieve lesser resolution degradation after windowing.

Table A4.1. Types of interference and waveform parameters for the analysis in frequency and spatial domains.

Interference Type	**Sub-Types**		**Case**	**Interference Parameters**
Synchronous			1	50 µs, 0.5 GHz
Semi-Synchronous			2	50 µs, 0.499 GHz
Asynchronous	Periodic	Fast Chirp	3a	10 µs, 0.5 GHz
		Slow Chirp	3b	CW at 76.2 GHz
	Semi-Periodic		4	150 µs, 0.5 GHz
	Aperiodic	Fast Chirp	5a	10.3 µs, 0.5 GHz
		Slow Chirp	5b	423 µs, 0.5 GHz

The analyses of these types of interference in different domains have been presented here.

A4.1. Range Profiles

The range profiles of interference examples in Table A4.1 have been estimated after the range compression and presented in Figure A4.1.

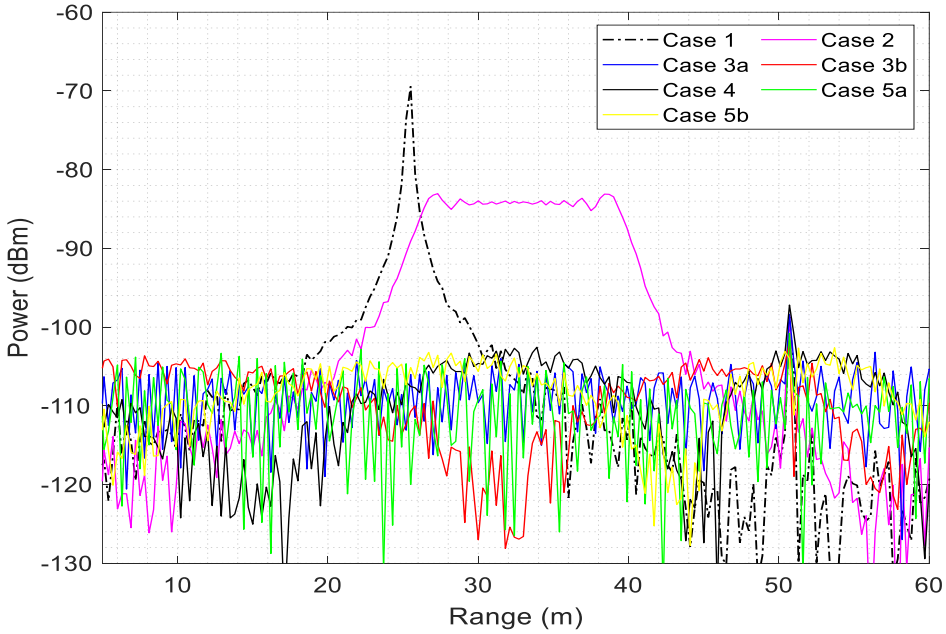


Figure A4.1: Range profile of the types of interference stated in Table A4.1.

The following observations have been made for different types of interference:

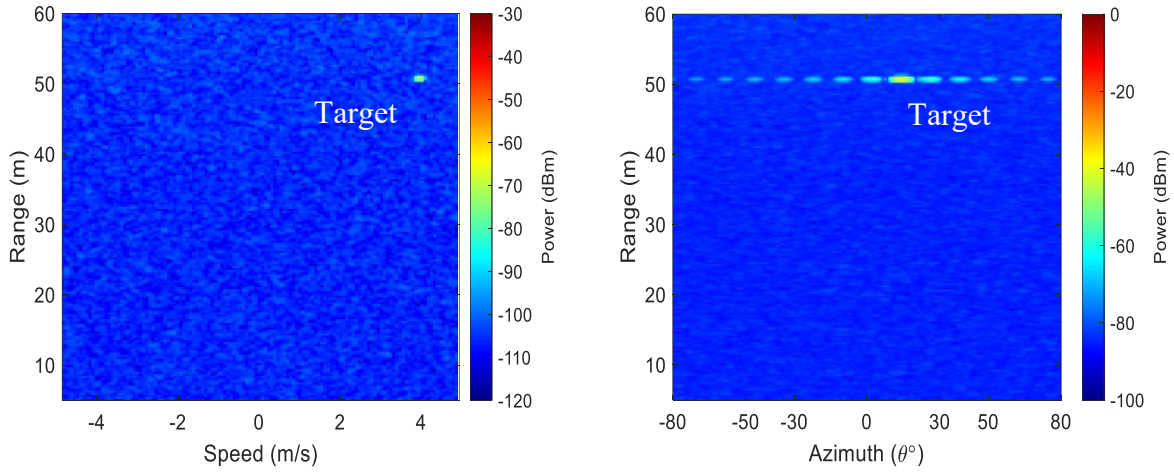
- Synchronous interference causes a ghost target in the range profile [168].
- Semi-synchronous interference has a non-uniform pedestal-like interference floor with a higher power.
- Asynchronous interference has a uniform interference floor over all the range (frequency) bins, such as, cases 3 – 5 in Table A4.1.
- When only one interference pulse appears within each VR chirp $\left(T_{\text{sint}} > T_{sv}\right)$, such as in cases 3b, 4, and 5b in Table A4.1, there is a linear phase relationship between samples of each interference pulse. Consequently, a 'scalloping pattern' with periodic bows and nulls has been observed in the spectrum.

- For the cases with $T_{\text{sint}} < T_{sv}$, multiple interference pulses appear within each VR chirp – cases 3a and 5a in Table A4.1. Therefore, a distinct phase relationship between the samples of different interference pulses in each VR chirp replaces the well-defined bows and nulls with random peaks and nulls.

A4.2. Range-Doppler and Range-Azimuth Profiles

The characteristics of the received signal after FFT across the slow-time to generate the range-Doppler map and after beamform FFT to generate the range-azimuth map have been discussed next. At the output of FFT across the slow-time, the received signal, composed of the echo signal and interference, is further averaged over the CPI. Therefore, the interference spectrum spread becomes more uniform compared to the range profile.

The modelled radar plots in an ideal scenario when IR is not transmitting have been shown in Figure A4.2. Target is at 50 m, 10^o, travelling at 4 m/s with an SNR ~ 35 dB and ~ 43 dB after the Doppler and spatial compression, respectively. The 3 dB angular resolution after beamforming is 2.5^o (Hann windowed). A CPI of 25 ms has been used, resulting in 128 victim chirps integrated within CPI.



(a) (b)

Figure A4.2: Radar plots in absence of interference: (a) range-Doppler, (b) range-azimuth.

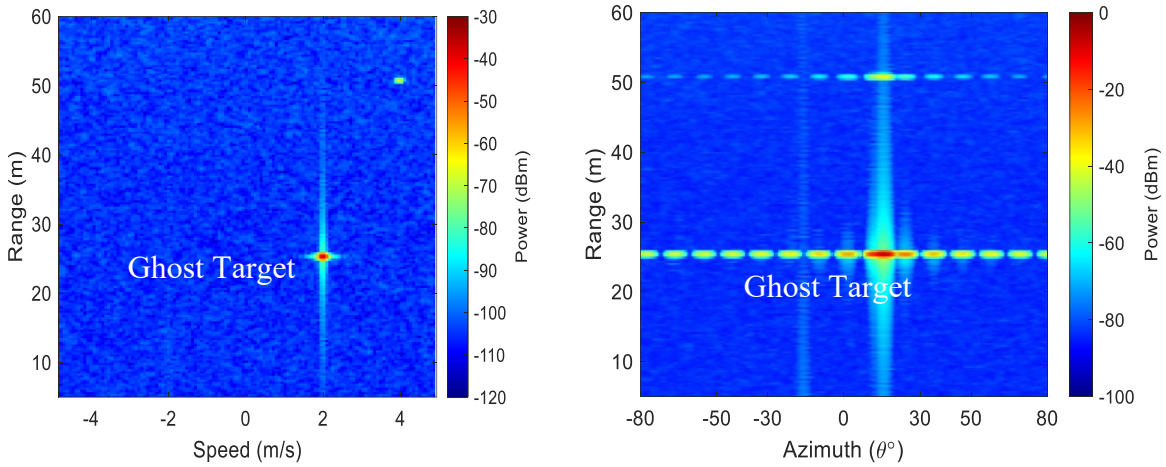
The range-Doppler and range-azimuth maps of different types of interference mentioned in Table A4.1 have been shown in Figure A4.3 to Figure A4.7. The results are presented for the two receiver configurations used in SoA automotive radar chipsets, the single channel receiver and the dual (I/Q) channels receiver. The details of both receiver configurations have been discussed in Appendix 6. Summarising in this section, in a single channel receiver, due to image frequency foldback towards usable frequency band [370],

- In the range-Doppler domain, interference affects both the positive and negative Doppler bins. One indicates the expected interference Doppler bin, and the other is due to the image frequency.
- In the range-azimuth plot, each interferer appears at two AoAs: one towards its actual direction (θ_{AoA}), and one towards $-\theta_{AoA}$ due to image frequency components.

The dual-channel receiver filters the image frequency component after the LPF. Therefore, a correct Doppler bin and one actual AoA have been observed after beamforming.

I. Synchronous Interference

The range-Doppler and range-azimuth maps of synchronous interference have been shown in Figure A4.3. A ghost target appears at 25 m, 2 m/s in this example. Additionally, interference is coherent across the VR's virtual elements due to the VR and IR synchronised waveforms. Therefore, similar to an echo signal, a beam toward the ghost target is according to the full MIMO virtual aperture with $\sim 2.5^{o}$ angular resolution. Higher interference power (one-way propagation) might trigger a false alarm in the detection process, which has been discussed in Chapter 4.



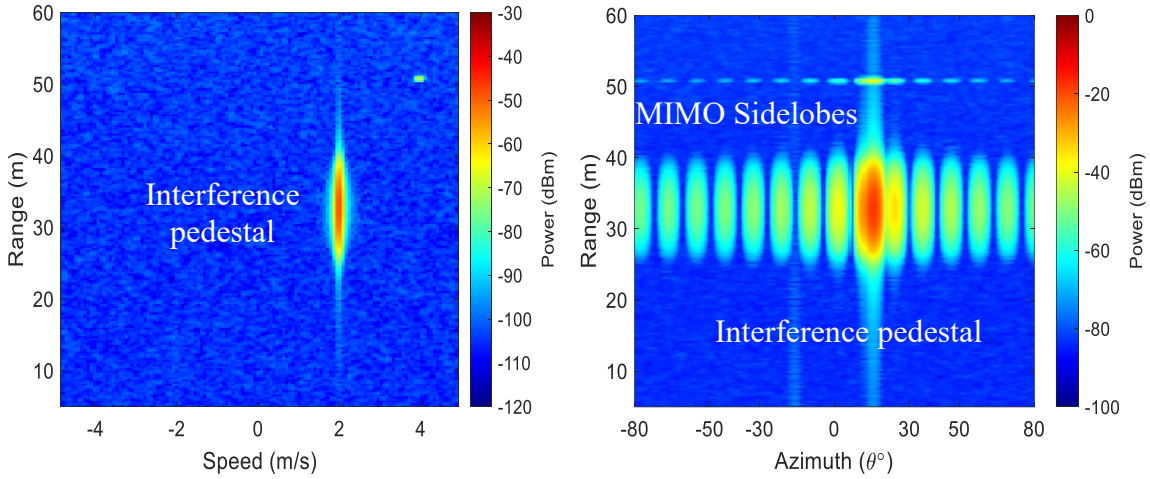
(a) (b)

Figure A4.3: Synchronous interference plots: (a) range-Doppler, (b) range-azimuth.

II. Semi Synchronous Interference

The range-Doppler and ranger azimuth maps of semi-synchronous interference have been shown in Figure A4.4. Depending upon the interference parameters, the following behaviour has been observed:

- Interference spreads across limited range bins with a higher mean power. This forms a pedestal-like floor whose position and width depend on the waveform parameters of IR.
- The correlated interference pulses across the VR chirps (same time of interference occurrence) result in focused interference along the Doppler (speed) axis and a beam according to the virtual aperture towards the direction of interference after beamforming.
- Due to the one-way equivalent beam in the MIMO radar, a higher SLL is expected (~ -13 dB) compared to the two-way equivalent beam pattern in traditional phased array radars. In the background of interference, higher interference power causes much higher sidelobes, which are often comparable in power with the echo signal (Figure A4.4 (b)). This reduces the radar's dynamic range for precise target detection.



(a) (b)

Figure A4.4: Semi-synchronous interference plots: (a) range-Doppler, (b) range-azimuth.

Synchronous and semi-synchronous interference spread across a limited number of frequency (range) bins. Therefore, the range-Doppler and range-azimuth for a single and I/Q channel receiver show a similar appearance of interference.

III. Periodic Interference

The range-Doppler and range-azimuth maps for the slow chirp periodic interference, case 3b from Table A4.1, have been shown in Figure A4.5.

Similar to synchronous and semi-synchronous interference, periodic interference also has coherent interference pulses across the slow-time samples within the CPI and the VR's transmit elements. Consequently, interference appear across a specific Doppler bin, and beamforming results in a beam representing interference direction according to the full MIMO array. However, as discussed in Appendix 3, periodic interference spreads along the range axis, unlike synchronous and semi-synchronous interference. The mean interference power will depend on the amount of interference spread, as defined in (3-29) and (3-30).

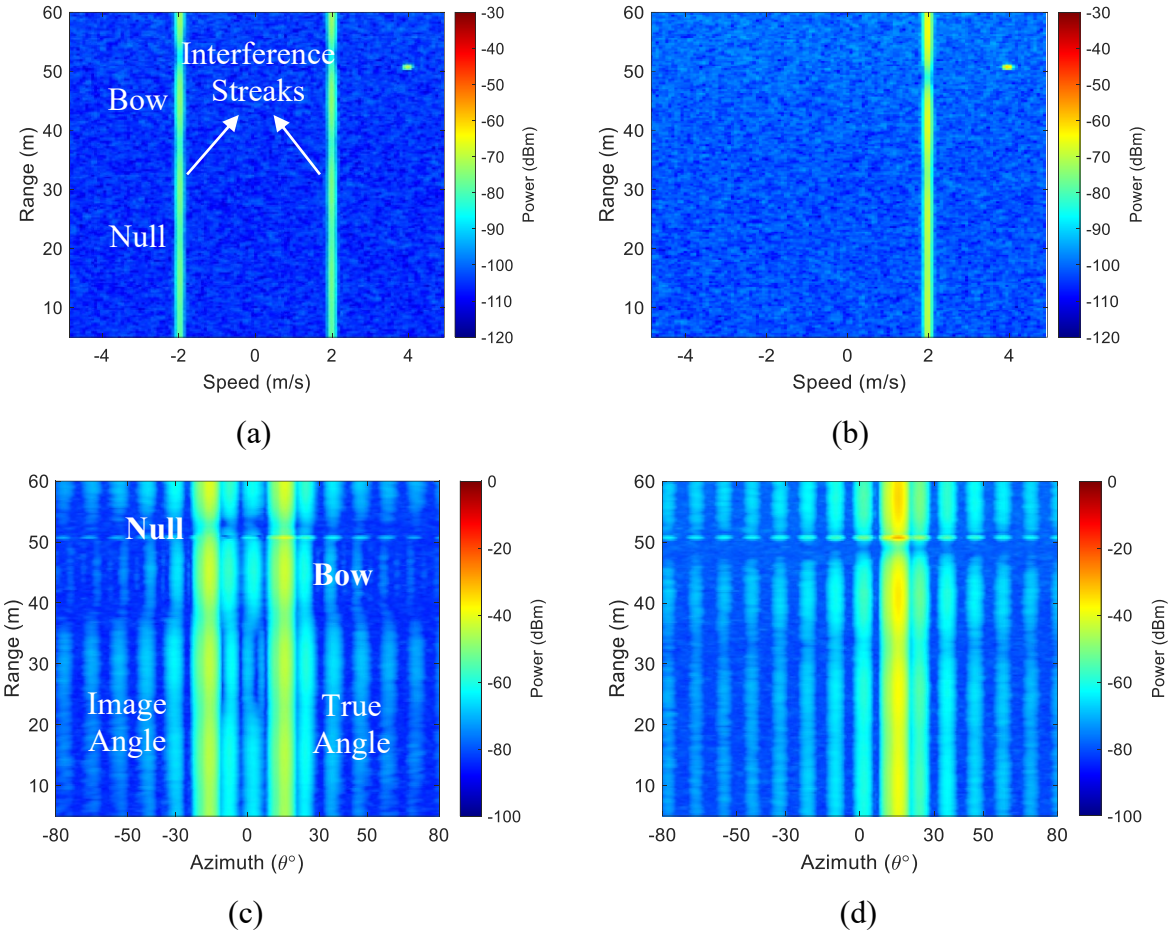


Figure A4.5: Radar plots of periodic interference: (a) range-Doppler of the single-channel receiver, (b) range-Doppler of the I/Q channels receiver, (c) range-azimuth of the single-channel receiver, (d) range-azimuth of the I/Q channels receiver.

The following behaviour has been observed:

- As expected in a single channel receiver, two distinctive lines appears at the positive and negative Doppler frequencies due to image frequency foldback (Figure A4.5 (a)). After beamforming, two AoA are observed, one towards the actual direction (θ_{AoA}) and one towards $-\theta_{AoA}$. Therefore, a broader region of the VR's FoV is masked by interference which often makes interference mitigation challenging and discussed in Chapter 6.
- Due to the absence of image frequency foldback in the I/Q channels receiver, only one specific Doppler frequency and actual AoA of interference have been observed, as demonstrated in Figure A4.5 (b) and (d).

The appearance of periodic interference has been validated in Appendix 5.

Due to a one-way interference propagation compared to the two-way echo signal propagation, the Doppler bin of the collocated target and source of interference are separated along the Doppler axis. This feature has been used in DBS beamforming to reduce the impact of interference in the VR and has been discussed in Chapter 8.

IV. Semi Periodic Interference

The range-Doppler and range-azimuth maps of semi-periodic interference have been presented in Figure A4.6.

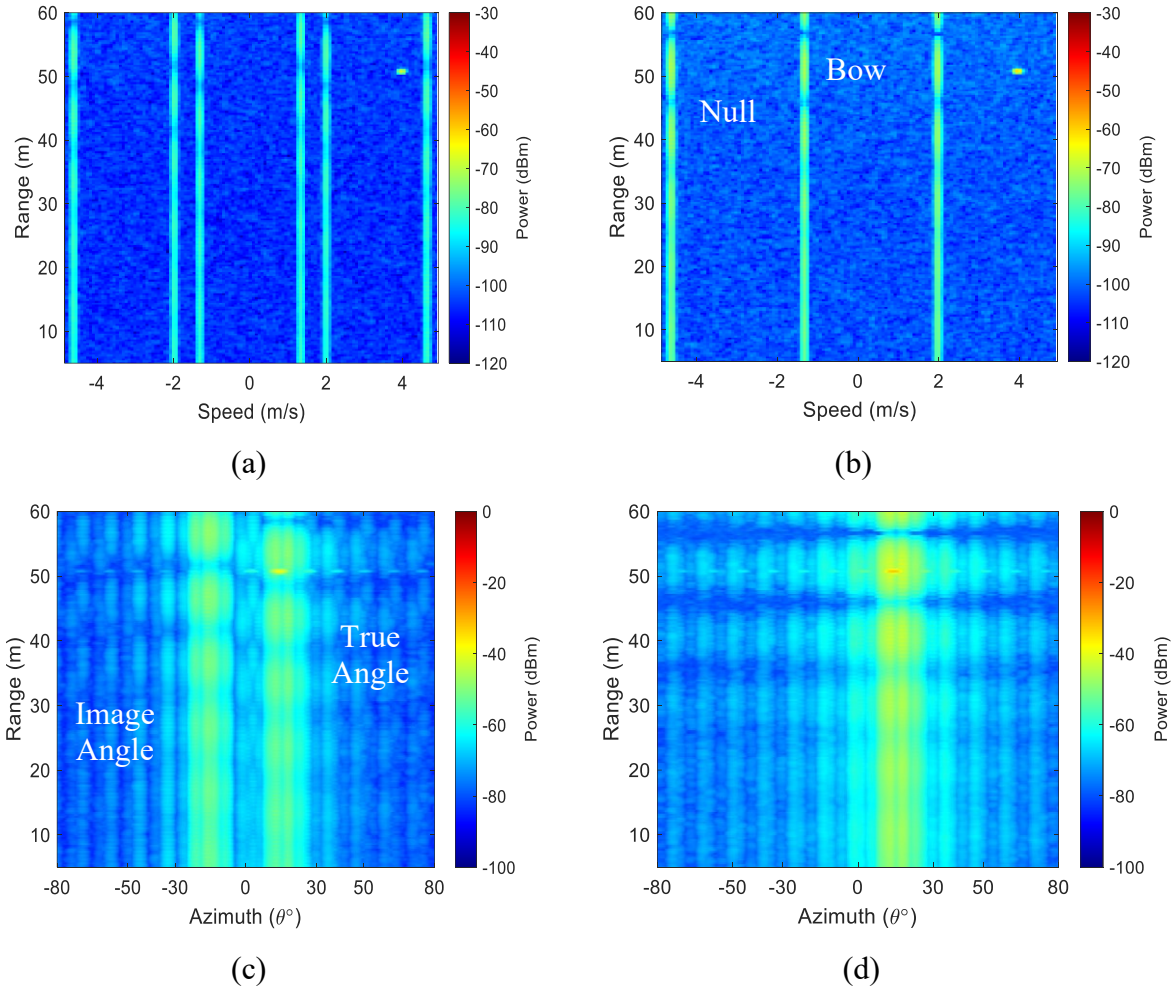


Figure A4.6: Radar plots for semi-periodic interference: (a) range-Doppler for single channel receiver, (b) range-Doppler for I/Q channels receiver, (c) range-azimuth for single channel receiver, (d) range-azimuth for I/Q channels receiver.

For semi-periodic interference, the interference chirp sequence repeats after every '*m*' VR chirps (m = 3 for the example case in Table A4.1). Therefore, three distinct interference streaks are visible in Figure A4.6 (b). The number of interference streaks along the Doppler bins increases with increase in the aperiodic interference repetitions. Due to interference aperiodicity across the virtual aperture, a beam is formed according to the receive aperture $\left(N_{Rx}=16\right)$ with $\sim 7.5^{o}$ angular resolution after beamforming.

Moreover, at most, one interference pulse appears per the VR chirp for this specific case. This results in the scalloping pattern with bows and nulls. For a single channel receiver, the Doppler bins due to the image channel are additionally visible in the range-Doppler map and image angle at -10^{o} in the range-azimuth map.

V. Aperiodic Interference

Aperiodic and hence asynchronous interference is the most common group of interference. The radar plots have been demonstrated in Figure A4.7. Due to interference aperiodicity across the VR chirps within the CPI, hence transmit elements,

- Interference spreads uniformly across all the range and Doppler bins. Their integration results in diagonal ridges, as seen in Figure A4.7.
- After beamforming, a beam is formed according to the receive aperture $\left(N_{Rx}=16\right)$ with a broader resolution.

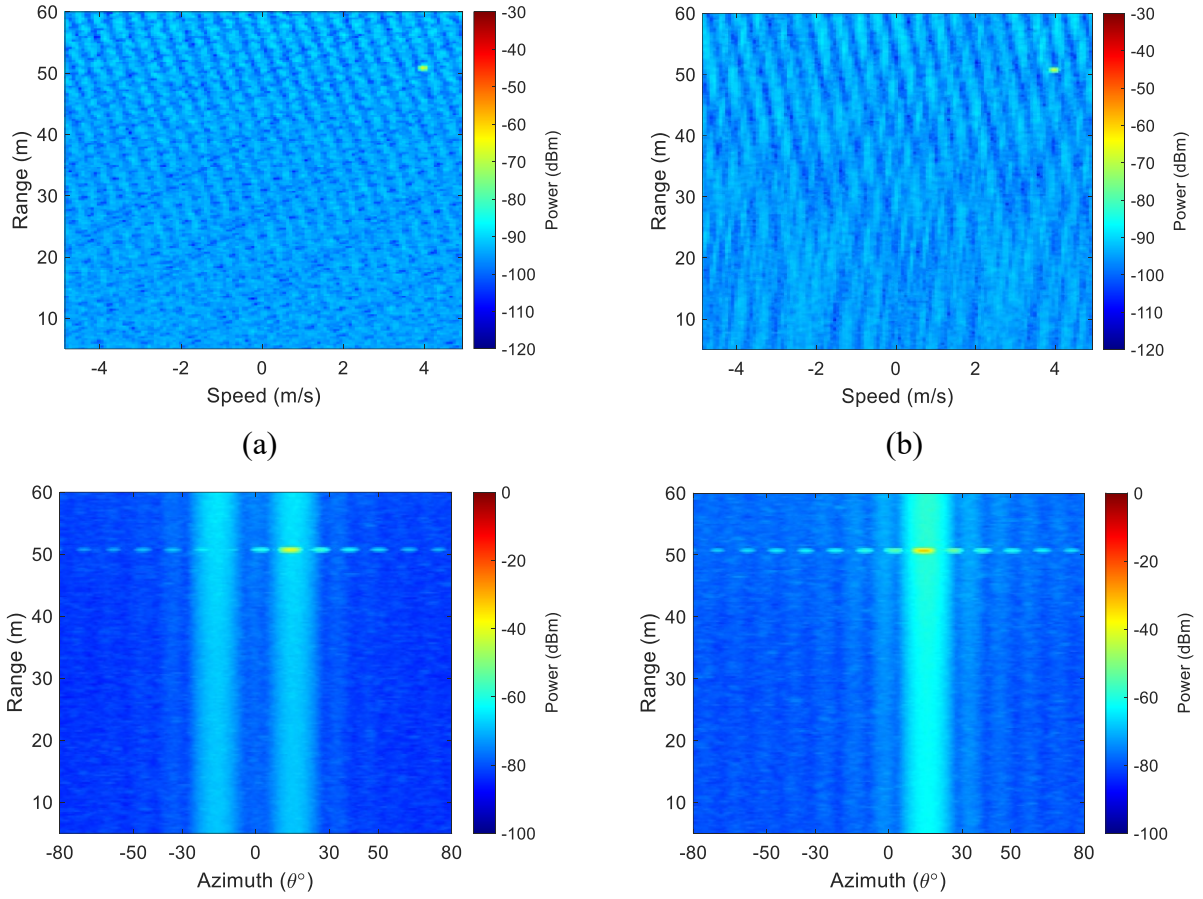


Figure A4.7: Radar plots of aperiodic interference: (a) range-Doppler for fast chirp sequence, (b) range-Doppler for slow chirp sequence, (c) range-azimuth for single channel receiver, (b) range-azimuth for I/Q channels receiver.

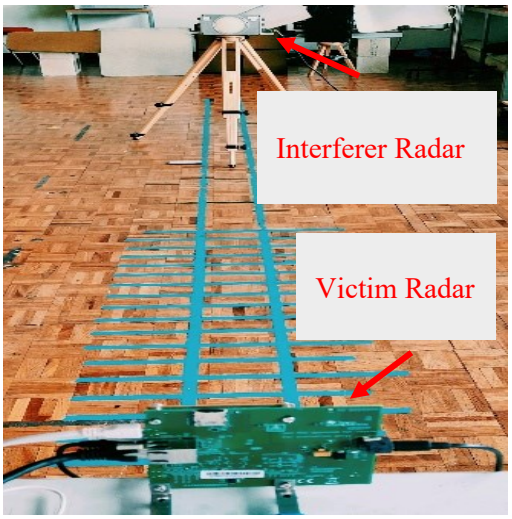
The range-Doppler maps have been shown for a single channel receiver with fast chirp and slow chirp aperiodic interference example from Table A4.1. The appearance of interference in a single channel and I/Q channels receiver after the Doppler processing is comparable, as interference uniformly spreads along the Doppler axis for both receiver configurations. The range-azimuth maps have been shown for fast chirp interference sequence in a single channel and I/Q channels receiver. The image angle of interference is visible in a single-channel receiver at -10^{o}.

The interference pattern is uniform for the fast chirp interference sequence with random peaks and nulls after FFT across the fast-time. Therefore, diagonal ridges after slow-time FFT

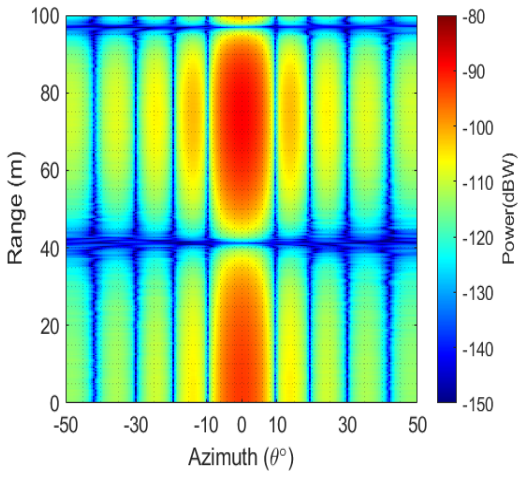
are finer compared to the slow chirp sequence case. Diagonal ridge's density increases when number of interference pulses within each VR chirp increases. Furthermore, due to a uniform spread of aperiodic interference, mean interference power is lower compared to the periodic and semi-periodic interference examples.

Appendix 5. Periodic Interference Validation

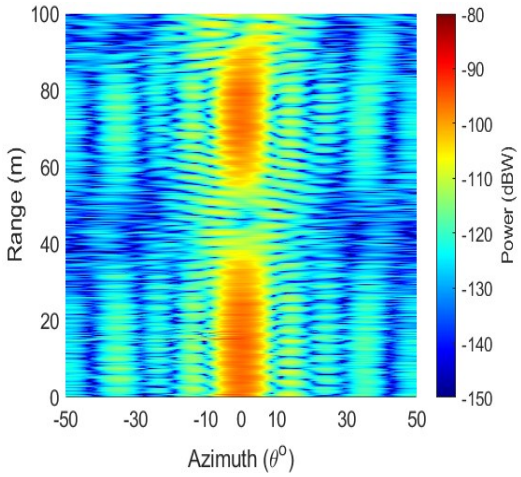
An example test setup to validate the appearance and resolution of periodic interference has been shown in Figure A5.1 (a). A CW signal at 76.2 GHz has been used as the source of interference, positioned at 8 m from the VR. TI AWR1243 radar chipset has been used as the VR with $N_{Tx} = 3$ and $N_{Rx} = 4$. The VR waveform parameters and the radar mode of operation have been stated in section 3.7. The modelled and measured range-azimuth plots have been shown in Figure A5.1 (b) and (c), respectively.



(a)



(b)



(c)

Figure A5.1: Periodic interference example: a) measurement setup, (b) range-azimuth: model, c) range-azimuth: measured.

A close correspondence between the results has been observed with bows and nulls due to a single interference pulse across each VR chirp (Appendix 2). The spatial resolution of periodic interference is similar to the echo signal resolution of ~ 10.4º in this case (12 virtual elements) after the Hann window.

Appendix 6. Interference Analysis in Single and I/Q Channel Receiver

Two main types of receivers are used in SoA automotive radar chipsets.

1. Single channel receiver that uses a single mixer with a real (in-phase only) baseband signal and ADC chain, as used in [39], [40], [91], and
2. Dual channel receiver with a complex baseband architecture composed of in-phase and quadrature (I/Q) channels, as used in [371]. The received signal is down-converted with a phase-shifted LO signal for the quadrature channel.

In both receiver configurations, the echo signal detection can be effectively done [195]. However, the receiver structure has an essential effect on interference appearance and power and has been discussed in this section.

The receiver configurations have been demonstrated in Figure A6.1.

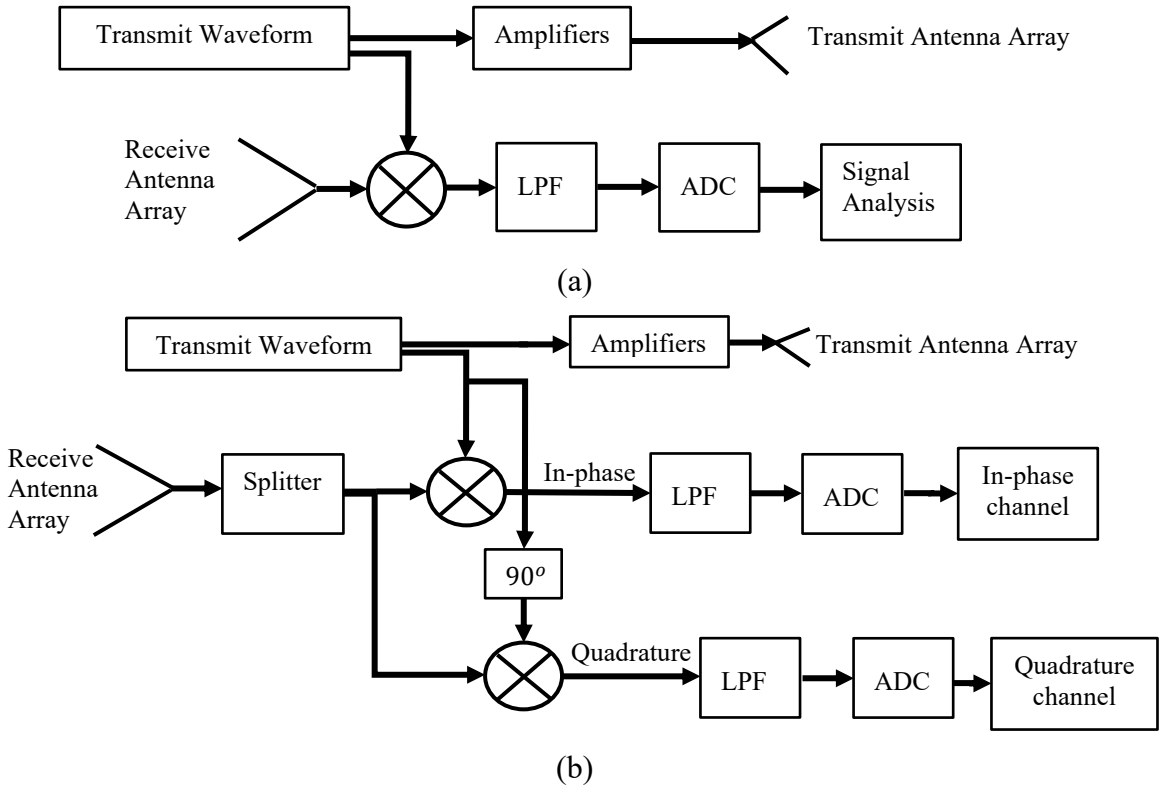


Figure A6.1: Receiver configurations in automotive radar chipsets: (a) single-channel receiver, (b) dual (in phase - quadrature) channels receiver.

For illustration purposes, the concept of positive and negative frequency has been used here. The positive frequency corresponds to the upper sideband, whereas the negative frequency corresponds to the lower sideband after the mixer stage. However, it is to be noted that all the signals are a real function of time with positive frequency. Negative frequencies are merely mathematical abstractions.

The received signal, composed of echoes from targets and interference, has been illustrated in Figure A6.2 (a) and (b) for a real channel and dual (I/Q) channels receiver, respectively. In a real only channel receiver, half of the frequency spectrum is usable, and the remaining half is its image, which is not processed. In contrast, the 'negative' frequency spectrum is folded towards the positive spectrum with dual channels receiver [372].

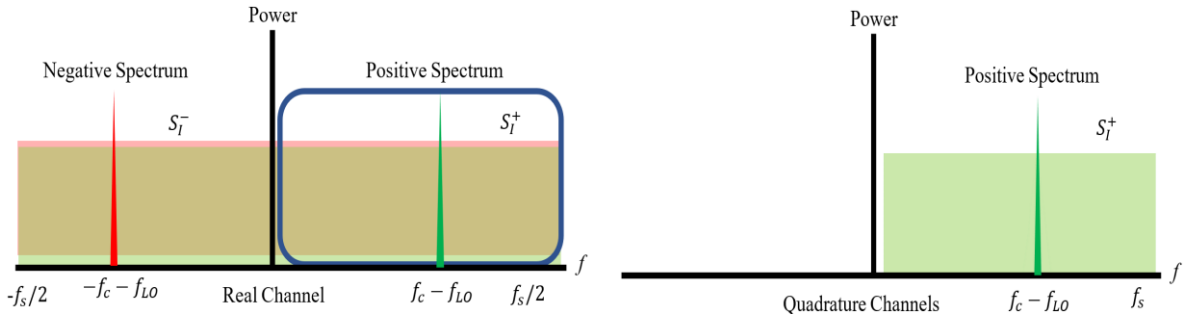


Figure A6.2: The echo signal and interference in SoA automotive radar chipsets: (a) real-channel receiver, (b) dual (I/Q) channels receiver.

After down-conversion, the received echo is a constant frequency signal, whereas interference is a chirp-like modulated signal. Therefore, the baseband representations of the echo signal $s_T\left(t-\tau_D\right)$ and interference $s_I\left(t-\tau_{Di}\right)$ can be expressed as:

$$s_T\left(t-\tau_D\right) \propto \cos\left(x+\theta\right) = \frac{1}{2}\left(e^{-j(x+\theta)} + e^{j(x+\theta)}\right) \tag{A6-1}$$

$$s_I\left(t-\tau_{\text{int}}\right) \propto \cos\left(a\left(t-\tau_{\text{int}}\right)^2 + b + \phi\right) = \frac{1}{2}\left(e^{-j\left(a\left(t-\tau_{\text{int}}\right)^2+b+\phi\right)} + e^{j\left(a\left(t-\tau_{\text{int}}\right)^2+b+\phi\right)}\right) \tag{A6-2}$$

As $e^{j\left(at^2+b\right)} = e^{j\left(a(-t)^2+b\right)}$, interference is an even function and each exponential term spreads along both sides of the frequency spectrum. The positive and negative frequency components of interference $S_{Int}^{+}(f)$ and $S_{Int}^{-}(f)$, respectively cannot be separated in a real-channel receiver. Therefore, the usable frequency band (positive part of the spectrum) will have contributions from both $S_{Int}^{+}(f)$ and $S_{Int}^{-}(f)$, shown in Figure A6.2 (a). Additionally, as the interference in the positive and negative frequency bands are from the same interfering source, they are correlated. Therefore, a distinct effect has been observed after signal processing due to the positive and image interference spectrums. This has been discussed in Appendix 4.

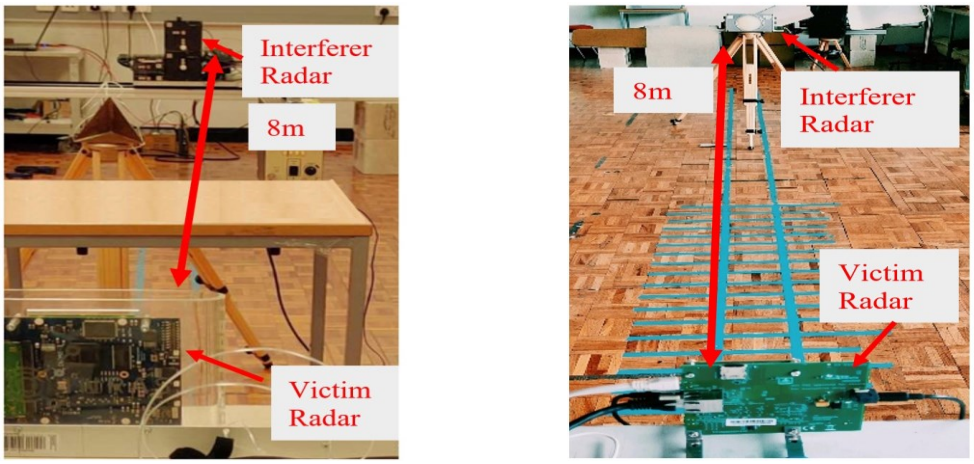
With I/Q channels, the image frequency is folded to the 'positive' spectrum. This avoids the image band contribution of interference, as shown in Figure A6.2(b).

The effect of receiver type on the appearance of interference in the frequency and spatial domains has been shown in sections 3.4 and 3.5, respectively.

Appendix 7. The Validation of Interference Statistics

The analytical study of interference statistics has been discussed in Chapter 4. This section has experimentally validated the results for the aperiodic and periodic interference cases using SoA automotive radar chipsets. Radar measurements have been performed in a controlled laboratory environment.

An FMCW INRAS AN77-06 [40] has been used as the VR for the aperiodic interference case. Aperiodic FMCW interference has been generated by a prototype FMCW radar developed in collaboration with ELVA-1 [373]. To evaluate the periodic interference statistics, a TI AWR1243EVM [374] has been used as the VR in the presence of CW interference. CW signal has been used as periodic interference as it appears across all the VR chirps. In comparison, depending upon the waveform parameters, FMCW periodic interference does not necessarily appear across all the victim chirps (section 5.2.1.II). IRs have been positioned on the boresight of the VR with an 8 m separation from the VR. The measurement setups for the two scenarios have been illustrated in Figure A7.1 (a) and (b) for the aperiodic and periodic examples, respectively. The radar parameters are given in Table A7.1.



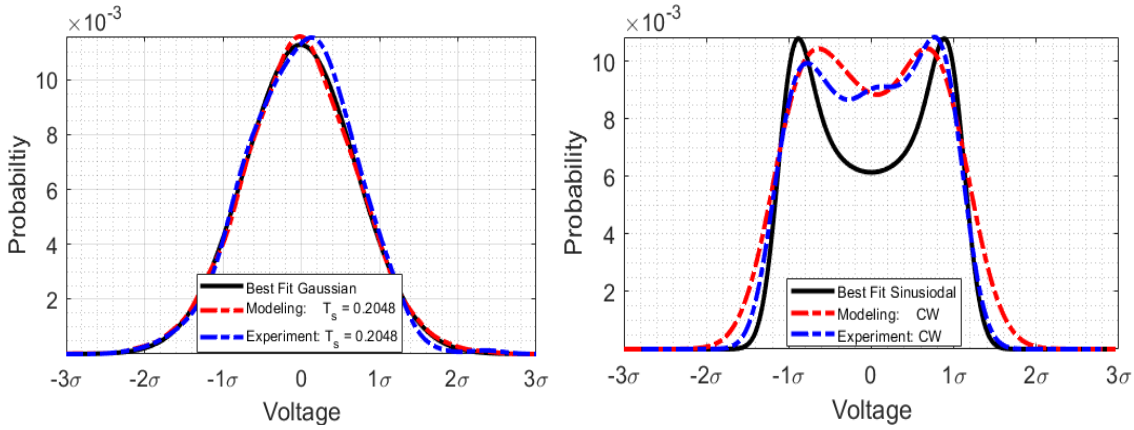
(a) (b)

Figure A7.1: Measurement setup for the radar detector performance analysis: (a) aperiodic interference, (b) periodic interference.

Table A7.1. Radar configuration parameters for the validation of interference statistics.

Parameters	**Value**		
Victim Radar		Interferer Radar	
Signal Type	---	Aperiodic	Periodic
Carrier frequency	76 GHz	76 GHz	76.7 GHz
Bandwidth	1 GHz	5 GHz	CW
Sweep Time	204.8 µs (INRAS) and 20 µs (TI)	1 ms	-
F_{LPF}	3.5 MHz		
P_{FA}	10^{-4}		
No. of Monte Carlo Trails	10^6		

The modelled and measured PDF at the detector's input for a) aperiodic interference example with $T_s = 0.2048, BW_s = 5$, and b) periodic interference example have been given in Figure A7.2 (a) and (b), respectively, along with best fit Gaussian and sinusoidal distributions for comparison. A good agreement between the modelled and measured result has been observed.

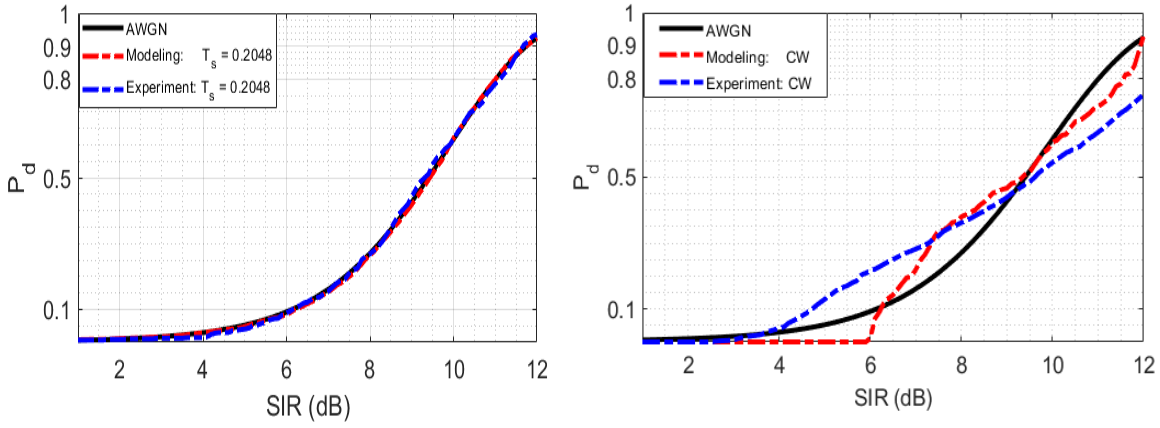


(a) (b)

Figure A7.2: Validation of aperiodic and periodic interference statistics: (a) probability density function - aperiodic, (b) probability density function - periodic.

The detection curves for the two mentioned cases have been presented in Figure A7.3 (a) and (b), respectively, showing the probability of detection as a function of SIR. The results for

aperiodic interference demonstrate a close similarity to the detection characteristics of the AWGN. As discussed in section 4.4.4, a deviation has been observed for periodic interference. For better comparison and illustration with the Gaussian noise detection curve, the detection curves for periodic interference in Figure A7.3 (b) have been scaled by $10\log\left(N_{CPI}\right)$.



(a) (b)

Figure A7.3: Validation of interference detection curves: (a) probability of detection vs. SIR – aperiodic, (b) probability of detection vs. SIR – periodic.

The NRMSE and SIR required to achieve a $P_d = 0.9$ have been used as performance metrics between modelled and measured results. The estimated values in Table A7.2 shows a reasonably close agreement between the two results. For aperiodic interference, the NRMSE value is within the non-critical region identified in section 4.3 (NRMSE ≤ 0.3). In contrast, periodic interference has the NRMSE value in critical region (NRMSE > 0.3).

Table A7.2. SIR required for $P_d = 0.9$ $\left(P_{FA} = 10^{-4}\right)$ – Periodic and aperiodic interference.

Parameters		NRMSE	SIR (dB)
AWGN		---	11.7
Model	Aperiodic Interference	0.17	11.7
	Periodic Interference	0.43	12
Measurement	Aperiodic Interference	0.23	11.7
	Periodic Interference	0.49	14

Appendix 8. Effect of Randomisation on the Echo Signal

Randomisation decorrelates interference pulses across the VR chirps. However, artefacts appear in the processed signal for specific randomisation values, discussed in this section using start frequency randomisation as an example. Due to a unique randomisation value for each VR chirp, a corresponding phase discontinuity is introduced in the Doppler processing.

With start frequency randomisation, the transmit signal from the VR can be expressed as:

$$S_{Tx} = \exp\left(j2\pi \left(\left(F_{cv} + \Delta F_j \right) t + 0.5 K_v t^2 \right) \right) \tag{A8-1}$$

The received echo signal therefore becomes:

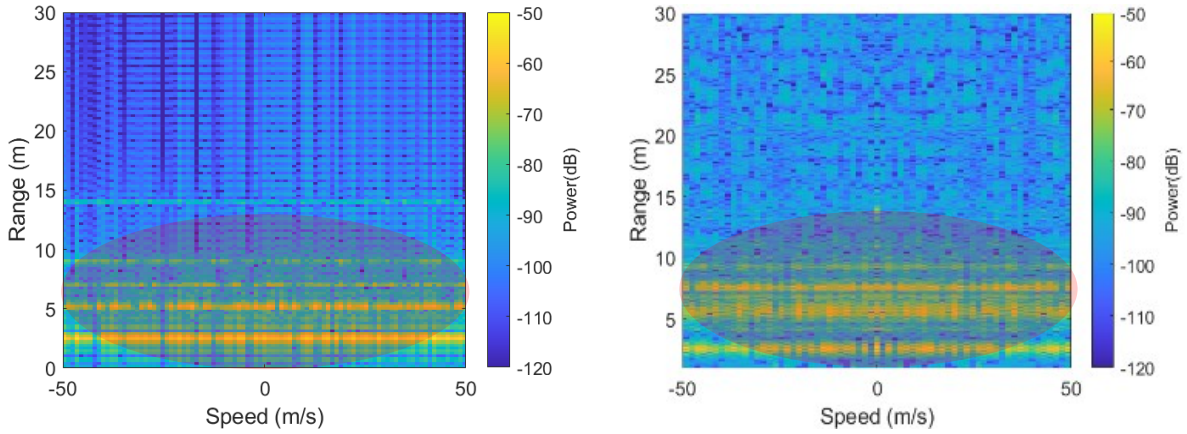
$$S_{Rx_t} = \exp\left(j2\pi \left(\left(F_{cv} + \Delta F_j \right) \left(t - \tau_D \right) + 0.5 K_v \left(t - \tau_D \right)^2 \right) \right) \tag{A8-2}$$

After solving, the down-converted signal can be expressed as:

$$S_{IF}\left(t\right) = \exp\left(j2\pi \left(F_{cv}\tau_D - 0.5 K_v {\tau_D}^2 + K_v t \tau_D + \Delta F_j \tau_D \right) \right) \tag{A8-3}$$

The additional term that appears in the down-converted signal due to start frequency randomisation is $\Delta F_j \tau_v$, where ΔF_j is the start frequency randomisation value for each radar chirp. Consequently, the range-Doppler coupling has been observed in the received echo signal after the FFT across the slow-time if $\Delta F_j \tau_v \gg 0$.

The modelled and measured results after applying start frequency randomisation in the range 1 – 50 MHz have been shown in Figure A8.1 (a) and (b), respectively. In the designed test setup, the TI AWR1243 radar chipset with T_{sv} = 20 µs, B_{sv} = 1 GHz has been used with static targets at 0 Doppler.



(a) (b)

Figure A8.1: Range-Doppler coupling in the received echo due to start frequency randomisation: (a) model, (b) measured.

Due to additional phase term from randomisation, the range-Doppler coupling spreads the Doppler across multiple bins. This indicates a requirement for phase correction to get reliable results.

In order to avoid the range-Doppler coupling, a phase compensation with $-\Delta F_j \tau_v$ has been applied in the discussed results in section 5.5. With a low value of frequency randomisation, typically in the kHz range, $\Delta F_j \tau_v \approx 0$. Therefore, the range-Doppler coupling effect is below the thermal noise floor and hence not dominant.

Appendix 9. The Effect of Randomisation Parameters

Different ranges of idle time and start frequency values can be used in the VR to randomise interference across the chirps. The effect of these randomisation ranges has been analysed in terms of coefficient P and $\overline{NRMSE}$ values. The methodology to generate these has been discussed in section 5.5.3. The results for different ranges have been demonstrated in Figure A9.1 where the P value is shown along the left axis and the $\overline{NRMSE}$ value in linear units along the right axis. The idle time and start frequency randomisation ranges are listed below.

- Lower idle time range: 1 – 10 ns
- Upper idle time range: 1 – 10 µs
- Lower start frequency range: 1 – 50 kHz
- Upper start frequency range: 1 – 50 MHz

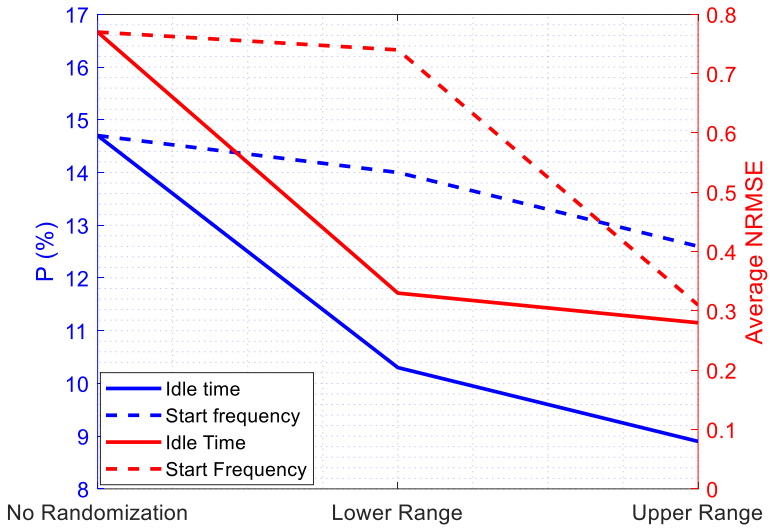


Figure A9.1: Effect of randomisation value on different randomisation techniques.

After idle time randomisation, both P and $\overline{NRMSE}$ values reduce when the idle time value increases from the lower range to the upper range. For start frequency randomisation, the lower range of randomisation values does not show a dominant effect in the P and $\overline{NRMSE}$

values. However, by increasing the randomisation value to the upper range, a slight reduction has been observed in P and a significant reduction in the $\overline{NRMSE}$ value.

Therefore, idle-time randomisation is less dependent on the range of values over which the VR chirps are randomised. Depending upon the hardware capabilities, a suitable range can be selected without compromising the radar performance.

Appendix 10. Interference Appearance in Spatial Domain

Measurements have been performed in an anechoic chamber to validate the appearance of different types of interference in the spatial domain. The INRAS Radarbook [40] in TDM-MIMO mode with $N_{Tx} = 4$ and $N_{Rx} = 8$ has been used as the VR. In this particular chipset, a virtual array of 29 elements is formed. TI AWR1243 radar has been used in a continuous stream mode to generate the CW interference. A 10 dBsm CR has been the reference target in the measurement. The target, victim, and interferer radars have been elevated 0.5 m above the RF absorbers to ensure a clear 1st Fresnel zone. The test setup is shown in Figure A10.1, whereas Table A10.1 shows the radar parameters and respective distances.

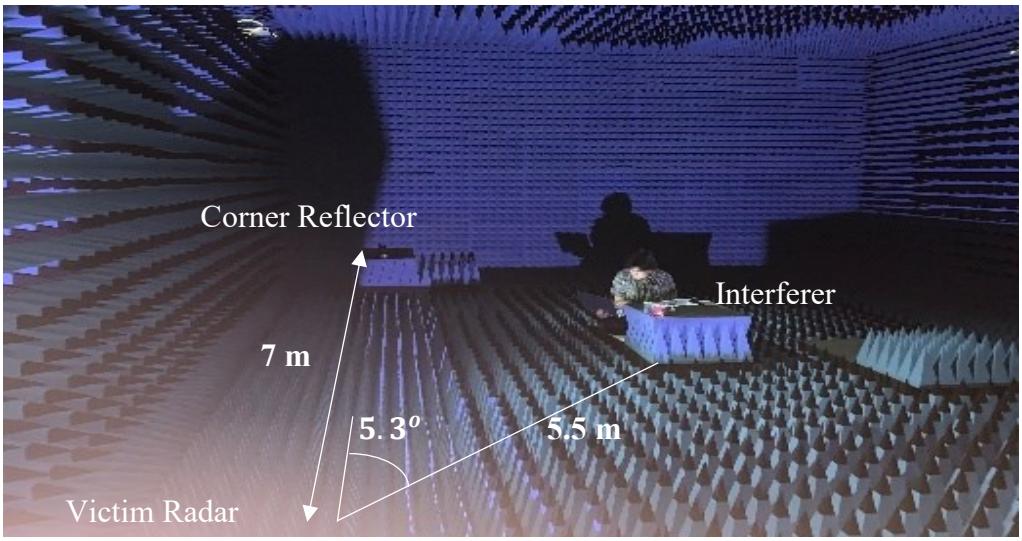


Figure A10.1: Measurement setup in an anechoic chamber for periodic and aperiodic interference analysis in the spatial domain.

Table A10.1: Radar parameters for periodic and aperiodic interference analysis and validation in the spatial domain.

	Victim Radar	**Periodic Interference**	**Aperiodic Interference**
Sweep Time (μs)	204.8	--	800
Sweep Bandwidth (MHz)	500	∞	400
Start Frequency (GHz)	76.5	76.65	76.49

The modelled and measured range-azimuth plots for a periodic CW interference (quasi-coherent case) have been demonstrated in Figure A10.2 (a) and (b), respectively. The modelled and measured range-azimuth plots for an aperiodic FMCW interference (non-coherent case) have been presented in Figure A10.2 (c) and (d), respectively.

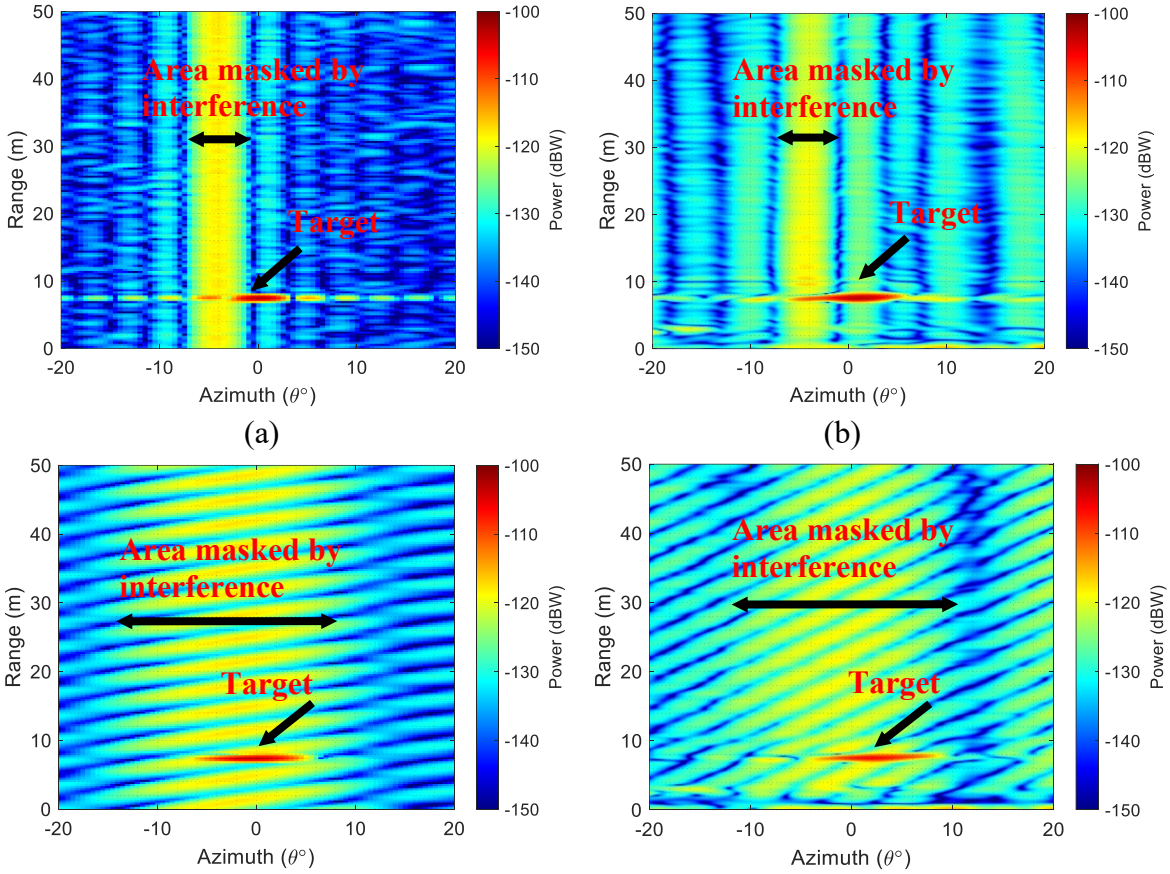


Figure A10.2: Periodic and aperiodic interference in the range-azimuth domain: (a) periodic CW interference – modelled, (b) periodic CW interference – measured, (c) aperiodic FMCW interference – modelled, (d) aperiodic FMCW interference – measured.

A close correspondence between the modelled and measured response has been observed. The angular resolution for periodic interference (Figure A10.2 (a) and (b)) is $\sim 4^{o}$ and follows the virtual aperture of 29 elements. In contrast, the angular resolution of aperiodic interference (Figure A10.2 (c) and (d)) is $\sim 14.5^{o}$ according to the physical receive aperture of the VR. Due to a mismatch in the propagation path length of the radar's transmit and receive channels [191], interference artefacts along the azimuth axis appear in Figure A10.2 (b) and (d).

Appendix 11. COSMOS Dataset Collection and Methodology

For the validation of the developed radar model, the 'COSMOS dataset' has been collected at the test proving ground of HORIBA MIRA [375]. The raw and processed sensor data is available at [346], [351]. The data was collected using time-stamped information from radar, lidar, and stereo camera. Time stamping allows the frame-to-frame synchronisation of the collected data during the post-processing stage. Global positioning system (GPS)/ inertial measurement unit (IMU) system was used to obtain precise ground truth and vehicle kinematics in various road scenario. Furthermore, additional road infrastructure was also incorporated to depict a realistic urban setting.

Ego vehicle with dimensions 4.6*1.9*1.7 m^3, given as length, width, and height, is shown in Figure A11.1.

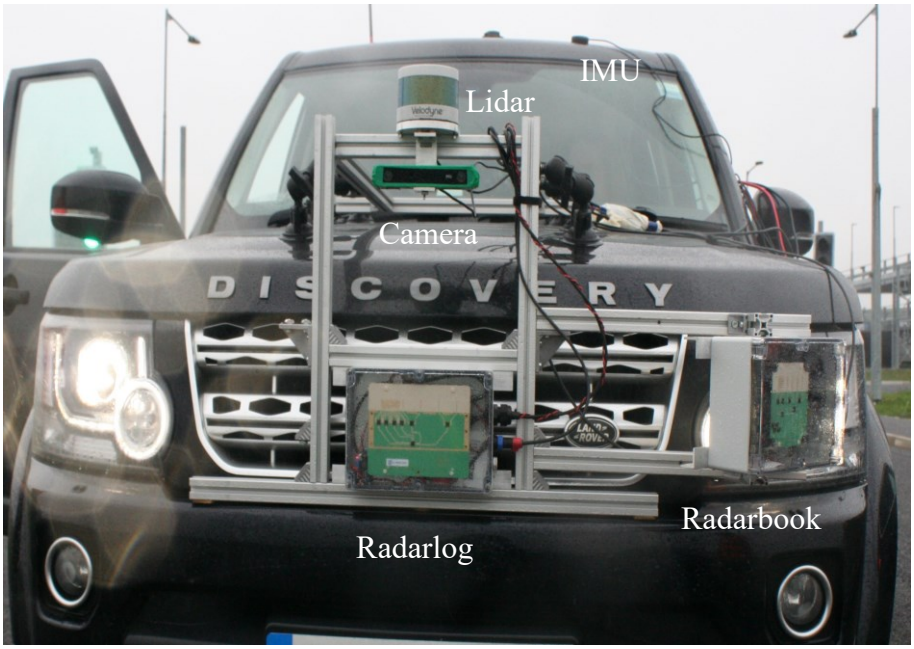


Figure A11.1: Test vehicle with measurement sensor suite for 'COSMOS' dataset collection.

The measurement sensor suite consists of 77 GHz SoA automotive radars installed on two test vehicles. The INRAS Radarlog [91] and Radarbook [40] were installed as forward-looking and corner-looking radars on ego vehicle, respectively. Both radars operated in TDM-

MIMO mode. TI AWR1243 [374] and NXP Dolphin [39] radar chipsets were installed as forward-looking and corner-looking radars on the target vehicle, respectively. These radars were set to transmit signal from a single transmit (Tx) element and interfere with the ego-radars (radars on host vehicle).

The radar configuration parameters are given in Table A11.1. The parameters have been selected to achieve optimal range/ azimuth resolutions whilst ensuring negligible data transfer loss while transferring data from the radar to the device operating it.

Table A11.1: Radar parameters for the 'COSMOS dataset.'

Parameter	**INRAS Radarlog**	**INRAS Radarbook**	**TI AWR1243**	**NXP Dolphin**
Sweep Time (µs)	204.8	51.2	250	102.4
Bandwidth (MHz)	1000	1000	950	1000
Start Frequency (GHz)	76	76	76.05	76.1
Pulse repetition interval (µs)	230	100	266	150
Antenna Configuration	4*16	4*8	1*4	1*4
One-way antennae gain at boresight (dBi)	14.4	14.4	10	17

The full dataset collected during the trials was over 2 TB. Depending upon the scenario and radar frame duration, the size of raw data captured from the INRAS Radarlog varies from 1 GB to 7 GB and from 1 GB to 4 GB for the INRAS Radarbook. Therefore, due to large files size, only the most suitable representative of the defined use cases have been included in the repository. Moreover, the full post-processed radar imagery has only been shown for a few example cases. Additional data may be available on request. The measurement scenarios and data structure of various sensors used during the data collection campaign are available at: https://edata.bham.ac.uk/800/3/COSMOS_Data%20Repository%20Report_UoB_RevC.pdf

A11.1. Adaptive Cruise Control (ACC) Scenario

In these set of measurements, vehicle with host/ victim radar and target vehicle with interfering radar were moving in a straight road in opposite directions, as illustrated in Figure A11.2.

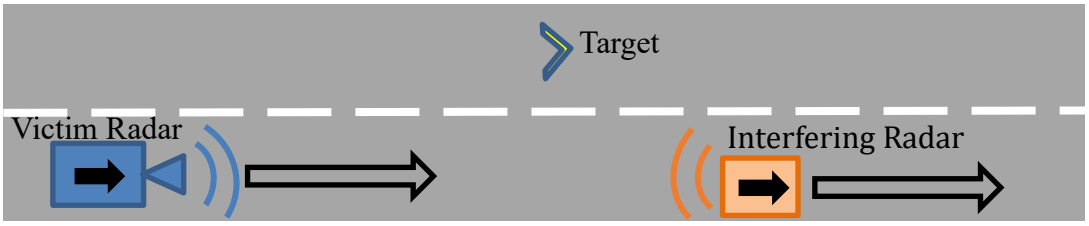


Figure A11.2: Adaptive cruise control scenario for the collection of COSMOS dataset.

A11.2. Cross Traffic Alert (CTA) Scenario

In this scenario, the victim radar stops at the junction and wait for the vehicle with interfering radar to cross. Victim radar will primarily receive interference from the side looking and side-lobe of forward-looking interfering radars. The test setup is illustrated in Figure A11.3

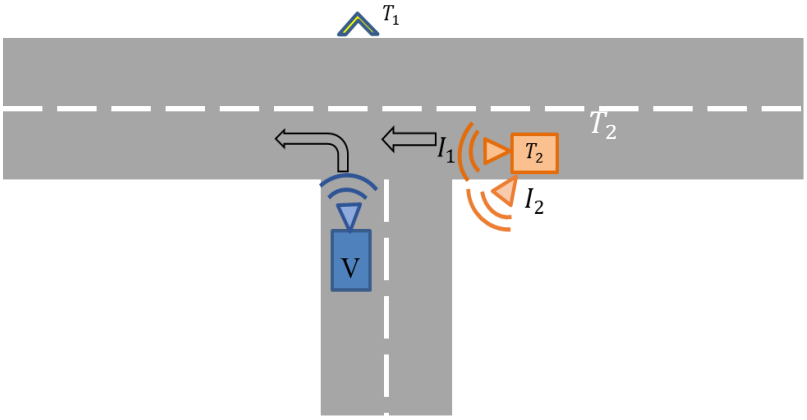


Figure A11.3: Cross traffic alert scenario for the collection of COSMOS dataset.

Appendix 12. Holistic Radar Simulator

It is expected that all the cars in the future will be equipped with radars. This will inevitably lead to the problem of co-existence in real traffic scenarios, where radars directly or indirectly act as sources of interference. Moreover, in an urban environment, as indicated in Figure A12.1, multipath reflections from infrastructure such as guard rails and buildings are also received by the radar. These reflections often result in false (ghost) targets appearing after signal processing [74]. To evaluate and optimise radar performance in diverse scenarios with various traffic, roadside, and interference density conditions, understanding how these factors interact is essential. The only way to do this is to develop a holistic simulation model of radar-to-environment interactions.

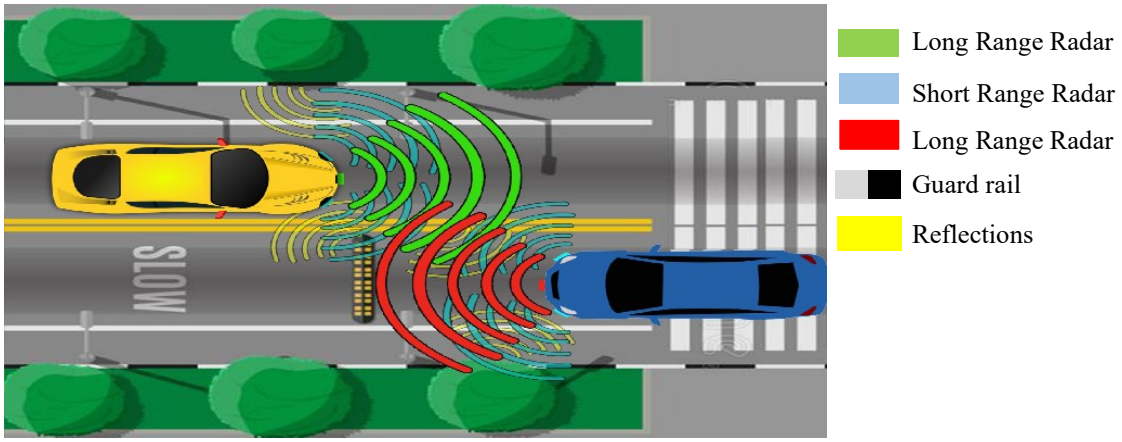


Figure A12.1: Interaction between sensors and road actors in an automotive scenario.

This section has focused on the following:

- Describing the novel fully customisable simulator to model, analyse, and evaluate the performance of millimetre wave (mmWave) automotive radars.
- Analysing various aspects of scene modelling based on the waveform, software, and hardware specifications of SoA automotive sensors.

- Modelling and investigating response from the environment, including extended targets, the effect of reflective roadside infrastructure, clutter, propagation channels, and transmissions from nearby sensors – radar interference.
- Validating the developed model with the real-time radar data recorded by a multi-sensory suite [346].

Compared to similar tools [41], [42], the developed simulator analyses the effect of various hardware and software specifications on the radar's performance. Furthermore, a comparative analysis of various incorporated interference suppression techniques has been presented in terms of the SINR improvement, target detectability, and possible ambiguity in target parameter estimation. The simulator efficiently delivers simulation data to implement advanced signal processing algorithms. Due to the integration of various types of targets, interferers, road types, hardware-specific functionality, and post-processed results in various domains, the tool can optimise SoA sensors.

A12.1. Overview of Holistic Simulator

The modular level description of the developed simulator and signal processing stages have been discussed in this sub-section and summarised in Figure A12.2. The major sections include:

1. Radar modelling where the host (victim) radar and interfering radars are configured.
2. Environment modelling, where road definitions, including road actors, the infrastructure around the road, and multipath propagation between them, are modelled.
3. Wave propagation using free space, 2-ray, or other area mean propagation models.
4. Interference detection and mitigation.
5. Analysing performance metrics to estimate the impact of various configurations/ scenarios on the radar's performance.

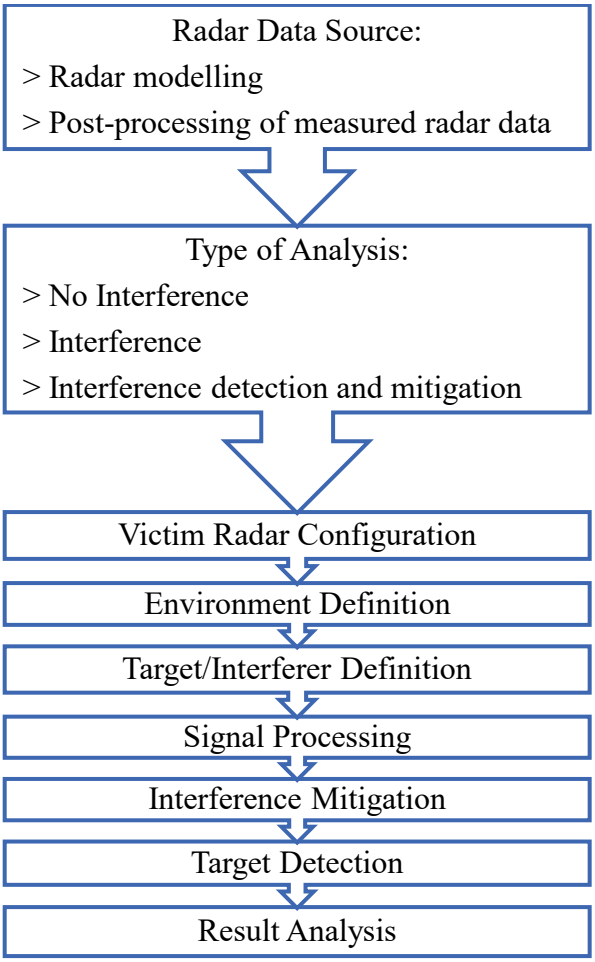


Figure A12.2: Modular description of the developed simulator.

A12.1.1 Block Level Representation

The block-level representation of automotive radar and environment interactions with the considered modelling and signal processing approach has been shown in

Figure A12.3.

A typical radar signal processing chain is composed of the following:

- Analogue signal processing, where down conversion, filtering, and analogue to digital conversion are performed, and
- Digital signal processing, where the 3D-FFT is performed to estimate the range, Doppler, and azimuth information of targets [345]. Resolution enhancement using advanced signal

processing, as will be discussed later, is optionally used for enhanced detection. In the presence of interference from other radars, it is detected and mitigated.

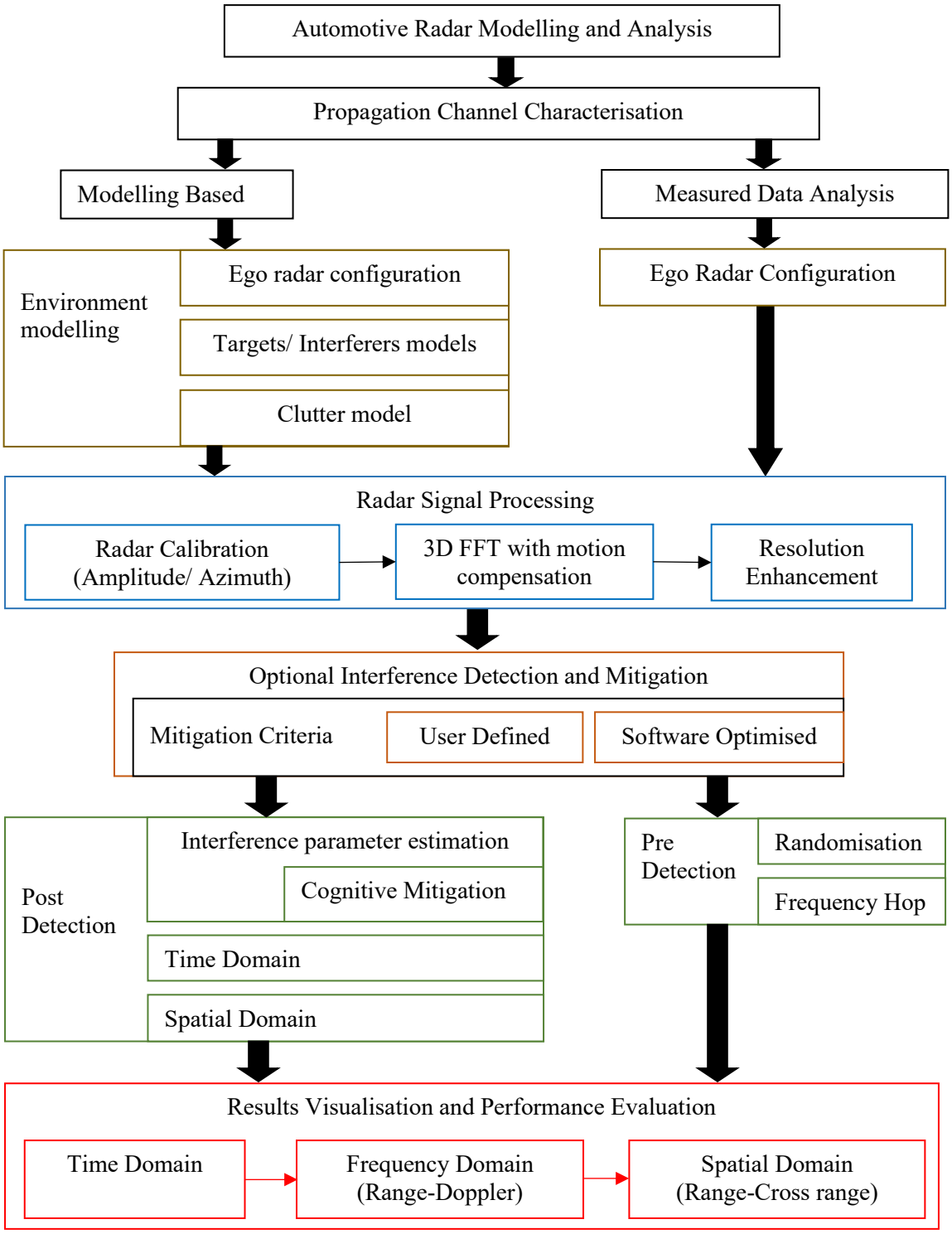


Figure A12.3: Block-level representation of the holistic radar simulator.

In the modelling-based approach, the following steps have been adopted:

- Environment, ego radar, and interfering radars are defined.
- The simulation results are presented in various domains.
- Appropriate mitigation technique is applied, with comparative performance analysis of various techniques.

In the experimental data analysis case,

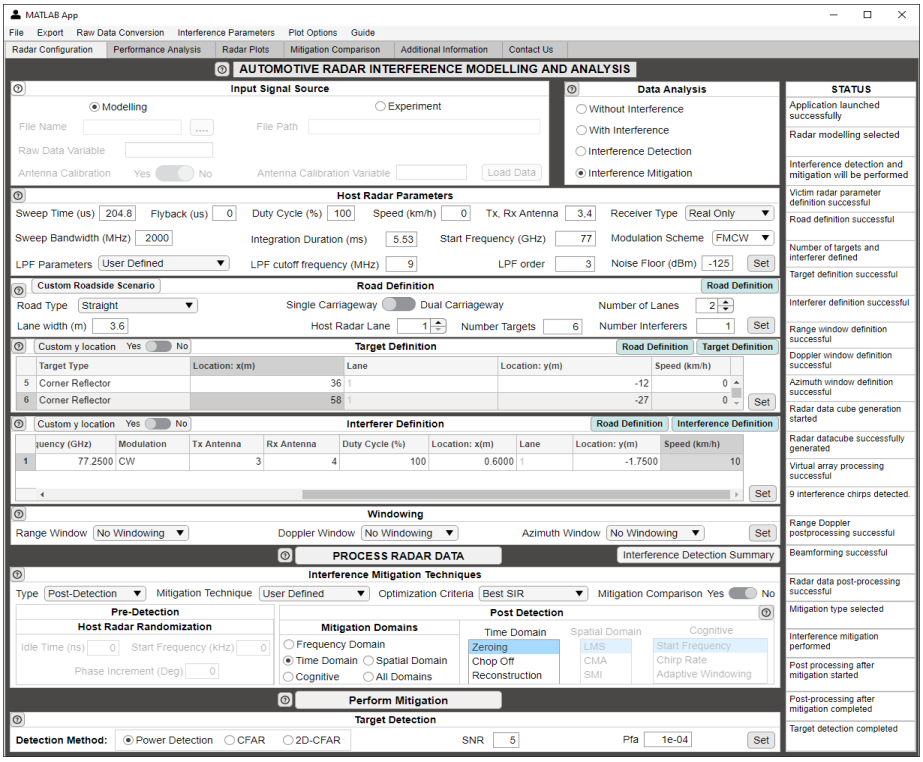
- The measured raw data is imported into the simulator.
- Signal processing is performed, and data is presented in various domains.
- Mitigation technique is applied, and performance is analysed.
- The modelled and measured results can later be compared.

The inputs and outputs of the simulator have been mentioned in Table A12.1.

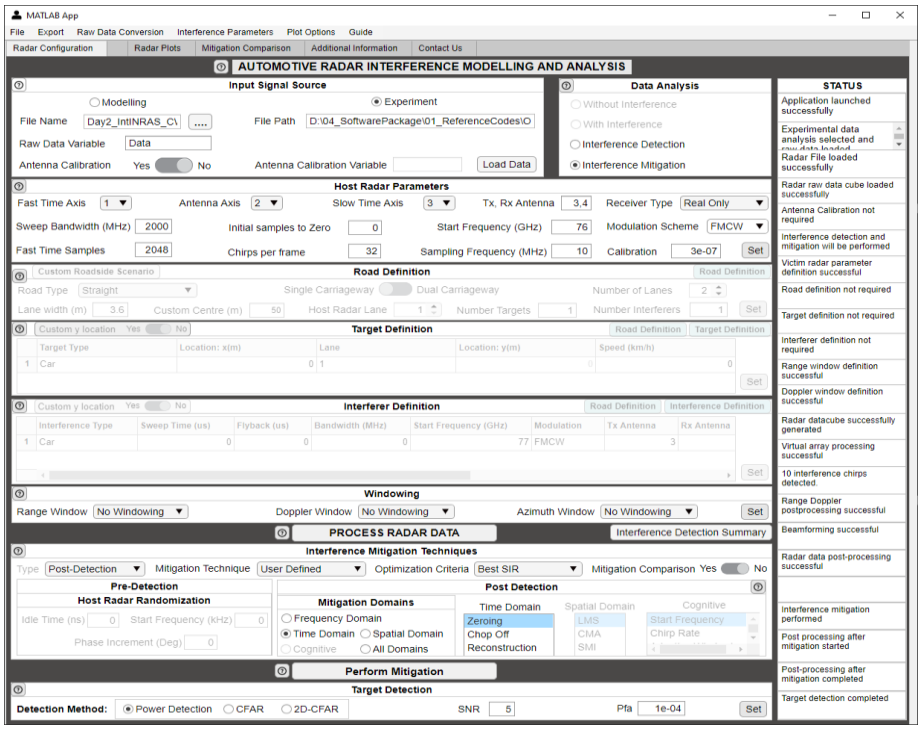
Table A12.1: Input and outputs of the holistic simulator.

Inputs		Outputs	
Scene Definition	Clutter	Scene Mapping	Range profiles
	Point-like targets		Range-Doppler map
	Extended targets		Range-azimuth map
Radar/ Waveform Definition	Ego Radar	Interference Analysis	Time domain
			Frequency domain
	Interfering Radar		Spectrogram, STFT
			Range-Doppler
			Range-azimuth
Antenna configuration	MIMO	Signal Processing	Interference suppression
	SIMO		MIMO beamforming
	Phased Array		MIMO-DBS beamforming
Operational mode	Monostatic	Interference Mitigation	Zeroing
	Bistatic		Reconstruction
			Clipping
			Frequency hopping
			Randomisation
			LCMV beamformer

The simulators' radar and environment configuration interface has been demonstrated in Figure A12.4.



(a)



(b)

Figure A12.4: Radar configuration interface of the simulator: (a) scene modelling, (b) measured data analysis.

A12.1.2. Features of Simulator

The main features of the simulator include the following:

- User-friendly interface with:
    1. Customisable parameters,
    2. Elements patterns of SoA automotive radar chipsets pre-loaded. Custom patterns can additionally be imported.
    3. Aspect-dependent RCS of targets pre-loaded. RCS data of new targets can be imported.
    4. Data and figures can be saved for further analysis.
- The processed results are available for data analysis and implementation of new algorithms. An example has been presented in Figure A12.5.
- Multiple targets and interferers can be modelled at once.
- Capability to add roadside infrastructure such as guard rails.
- Interference mitigation in different domains and their comparative analysis.
- Quantitative and qualitative comparison of mitigation techniques.
- Modular open architecture for higher-level integration.

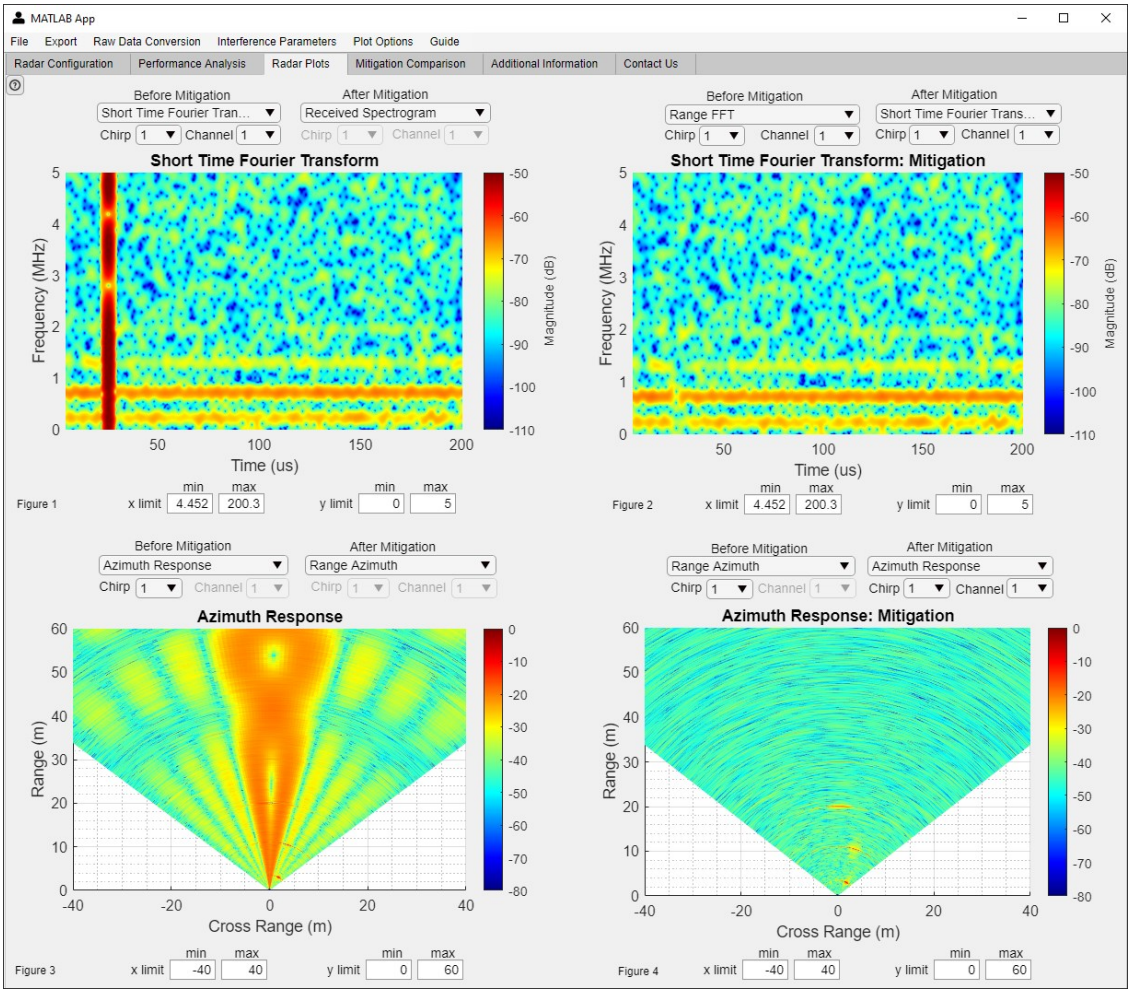


Figure A12.5: An example of post-processed results obtained from the radar simulator. The plots on top show results after a short time Fourier transform (STFT), and the plots on the bottom show azimuth response after beamforming. The plots on the left are before interference mitigation, and those on the right are after interference mitigation (interference zeroing in this case).

A12.2. Sensor Dataset

To validate the functional capabilities of the simulator, the 'COSMOS dataset' has been used. The data collection methodology and sensor parameters have been mentioned in Appendix 11. In this section, the results at the INRAS Radarlog (ego radar) have been discussed for a scenario where both cars move toward each other. Nevertheless, the considered approaches are universally applicable. The waveform parameters for Radarlog provide the

unambiguous range of 153 m, the unambiguous velocity of ± 0.98 ms^{-1} when operating in TDM-MIMO mode, and range and velocity resolutions of 0.15 m and ± 0.015 ms^{-1}, respectively, and has real-channel receiver.

A12.3. Environment Modelling – Propagation Channel Characterisation

The first step to developing a realistic radar model is identifying the propagation channel between the radar and targets. This is especially crucial at mmWave, where surface roughness becomes comparable with the signal's wavelength. Therefore, the reflecting ground surface can either be smooth with a two-ray propagation path or rough with diffuse scattering, where free space propagation can be expected.

To determine the fit of the area mean propagation model to the measured data, the echo signal propagation loss has been estimated. The return power was measured from a trihedral CR (RCS σ = 17.7 dBsm) at ranges (R) from 15 m - 52 m from the radar (Radarlog) installed on a moving vehicle [346]. The free space $\left(P_{FS}\right)$ and two-ray propagation $\left(P_{2-Ray}\right)$ curves have been estimated using:

$$P_{FS} = \frac{P_t G_t G_r \lambda^2 \sigma}{(4\pi)^3 R^4 L} \tag{A12-1}$$

$$P_{2-Ray} = P_{FS} \cdot 16 \sin^4\left(\frac{2\pi H_r H_t}{\lambda R}\right) \tag{A12-2}$$

where, H_r = 0.85 m and H_t = 1 m are the heights of the ego radar and the target, respectively, G_t = G_r = 14 dBi is the gain of transmit and receive antenna, respectively. L represents miscellaneous losses that include loss due to misalignment of CR in the direction of radar, mismatch of radar and CR heights, and CR not being exactly at the boresight of radar. The crossover distance $\left(4\pi H_t H_r/\lambda\right)$ is 2326 m, which is well beyond the unambiguous range of ego radar. The road surface is made of tarmac.

The received signal is high pass filtered with a cut-off range of 2 m to suppress the leakage signal from the transmitter to the receiver. An FFT across the fast-time is applied on the received signal, followed by non-coherent integration across the 128 slow-time samples. The return power is normalised by receiver noise floor: $kTBF$ = -123 dBm in this case, where k is the Boltzmann constant, T = 290 K is room temperature, F = 25 is the noise factor, and $B = 1/T_{sv}$. The measured range profiles and propagation curves are shown in Figure A12.6.

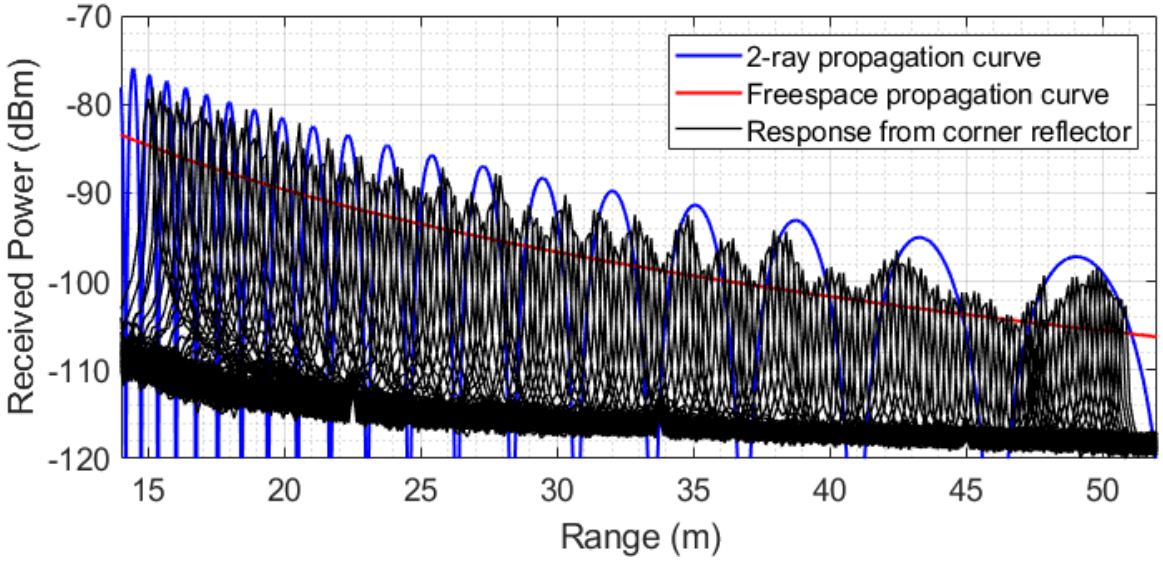


Figure A12.6: Range response from the corner reflector and propagation model curves. The blue line indicates the theoretical 2-ray propagation curve, the red line represents the free-space propagation curve, and the black lines show the response from the corner reflector at various distances.

At closer distances between ego radar and CR, the received power fits well with the free-space propagation model. However, amplitude decays are more significant at longer distances. This indicates a multipath propagation from the road surface that acts as a planar reflector. The superposition of direct and ground-reflected signals at the ego radar's receiver results in these amplitude fluctuations with well-defined peaks and nulls in the measured response. Therefore, a two-ray propagation model would be a good fit for tarmac. In contrast, for rough surfaces, for instance, grass, gravel, monotonic free space propagation behaviour would be a better fit.

It is to be noted that the power difference between the measured received power and theoretical propagation curves is due to the miscellaneous losses discussed earlier.

A12.3.1. Road Definition and Topology

Four common types of roadside scenarios, such as a straight lane, junction, roundabout, and exit lane/ slip road, have been incorporated into the simulator. The road definition segment of the simulator and schematics of these road types obtained from the simulator have been presented in Figure A12.7 (a) - (e), respectively. It is to be noted that MATLAB's driving scenario has been used to define various road layouts [376], [377].

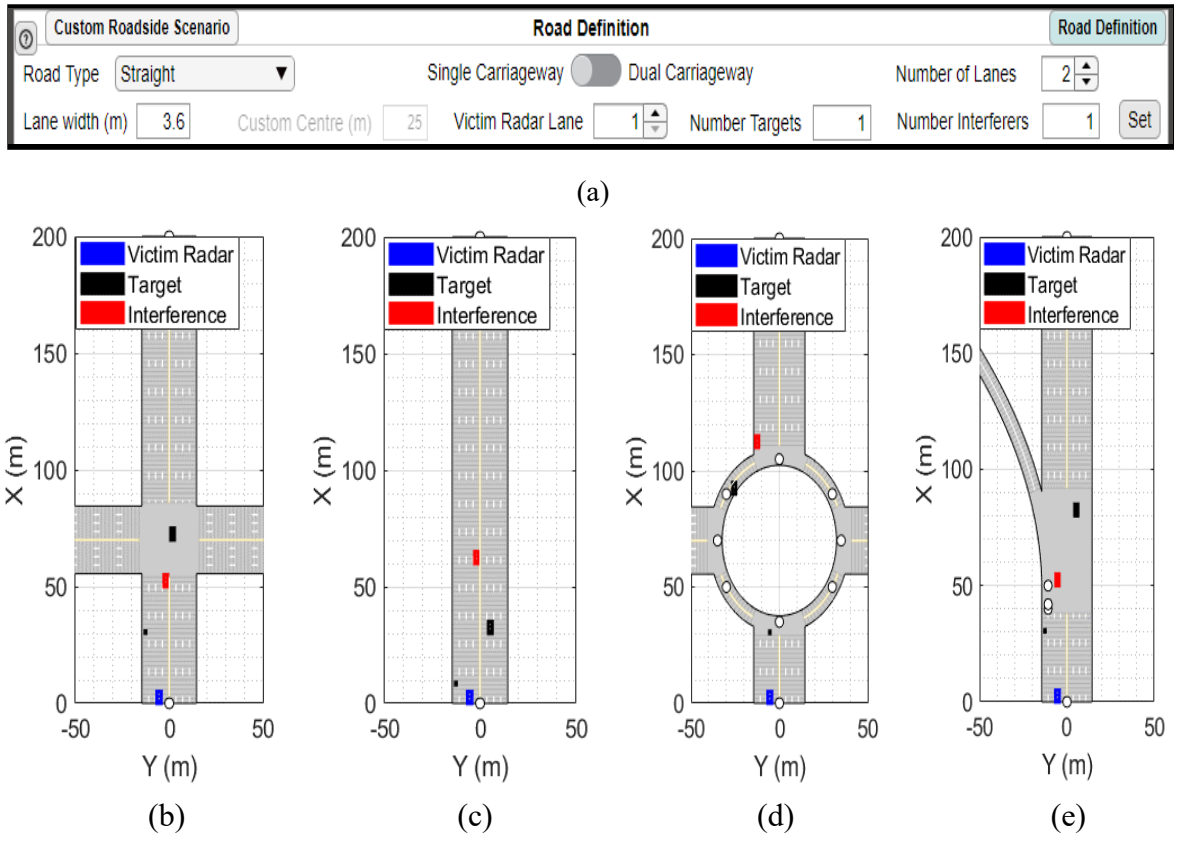


Figure A12.7: Road schematics from the simulator: (a) road definition tool, (b) straight lane, (c) junction, (d) roundabout, (e) exit lane.

The MATLAB driving scenario designer [378] can also be integrated to create arbitrary traffic scenarios.

A12.3.2. Target and Clutter Modelling

For higher levels of automation, modern radars should not only detect and resolve targets but also perceive the whole scene. This includes clutter that needs to be resolved and accurately imaged. Moreover, if necessary, the clutter should be filtered out to decompose the scene into static clutter and the tracks of moving targets. The response from the environment has been modelled for:

- Extended targets,
- Clutter that has been considered as a stationary process, distributed across several range bins. The clutter primarily includes the following:
  1. Reflections from the road at a closer distance from the radar,
  2. Reflections from grass and infrastructure around the road, and
  3. The appearance of false (ghost) targets due to multipath from the reflective surfaces around the road,
- Interference, as discussed in [144].

I. Target Distribution

The vehicle has been modelled as an extended target with a set of scattering points made of a perfect electric conductor (PEC), each with an aspect-dependent RCS. This results in a simplified target representation with a fast yet accurate response [379] compared to the models based on the ray tracing approaches [364].

The integrated RCS (σi) from each side of the vehicle has been obtained from [369] and shown in Figure A12.8. From the front of an average sedan car, $\sigma i = 6 – 8$ dBsm.

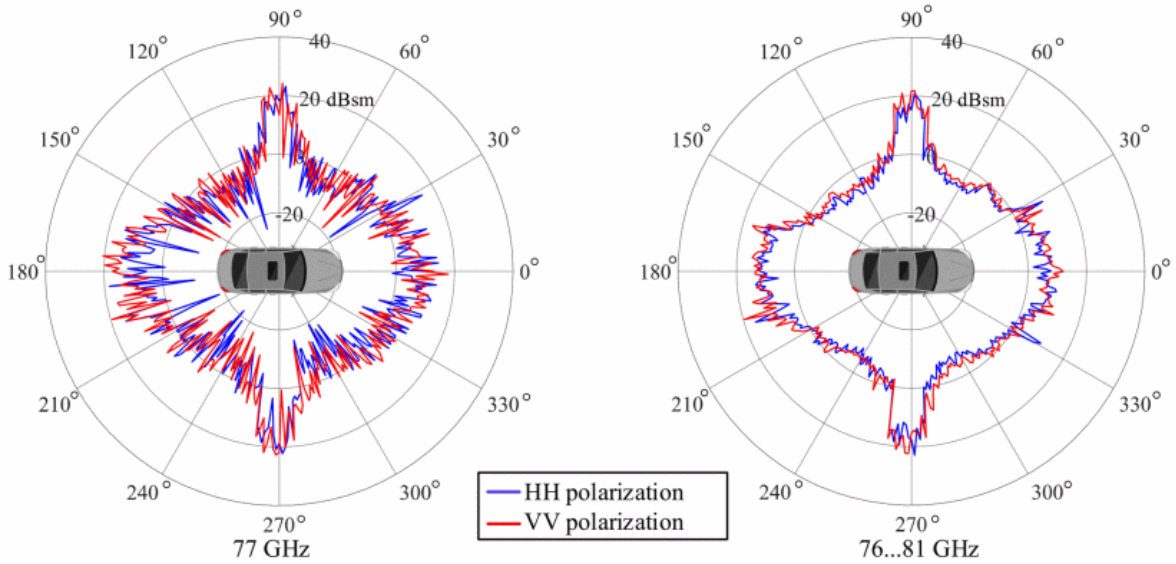


Figure A12.8: Integrated RCS from sedan vehicle as a function of aspect angles.

For the target vehicle – Range Rover –, due to its larger size, σi from the front of the vehicle is expected to be 10 – 12 dBsm. The RCS of each scattering point has then been estimated based on the total scattering points. For reasonable computational processing with reliable results, one scattering point has been set for each resolution cell of the radar, which is defined in the azimuth as $R\theta_B$ where R is the range to the scattering point and θ_B = 1.9° is azimuth beamwidth of the ego radar. For instance, with the resolution cell size of 0.3 m at R = 9.4 m, 4 reflection points have been observed per 'm' of the target vehicle. Considering reflection from the front of the vehicle that is ~ 1.9 m wide, each of the 7 reflection points expected from the front has been assigned 1.4 dBsm RCS. The measured and modelled range-Doppler and range cross-range profiles of the extended target for two different positions of the target vehicle are given in Figure A12.9 and Figure A12.10, respectively. In the test scene, the vehicle with radar (Radarlog) was static, with the target vehicle driving towards it.

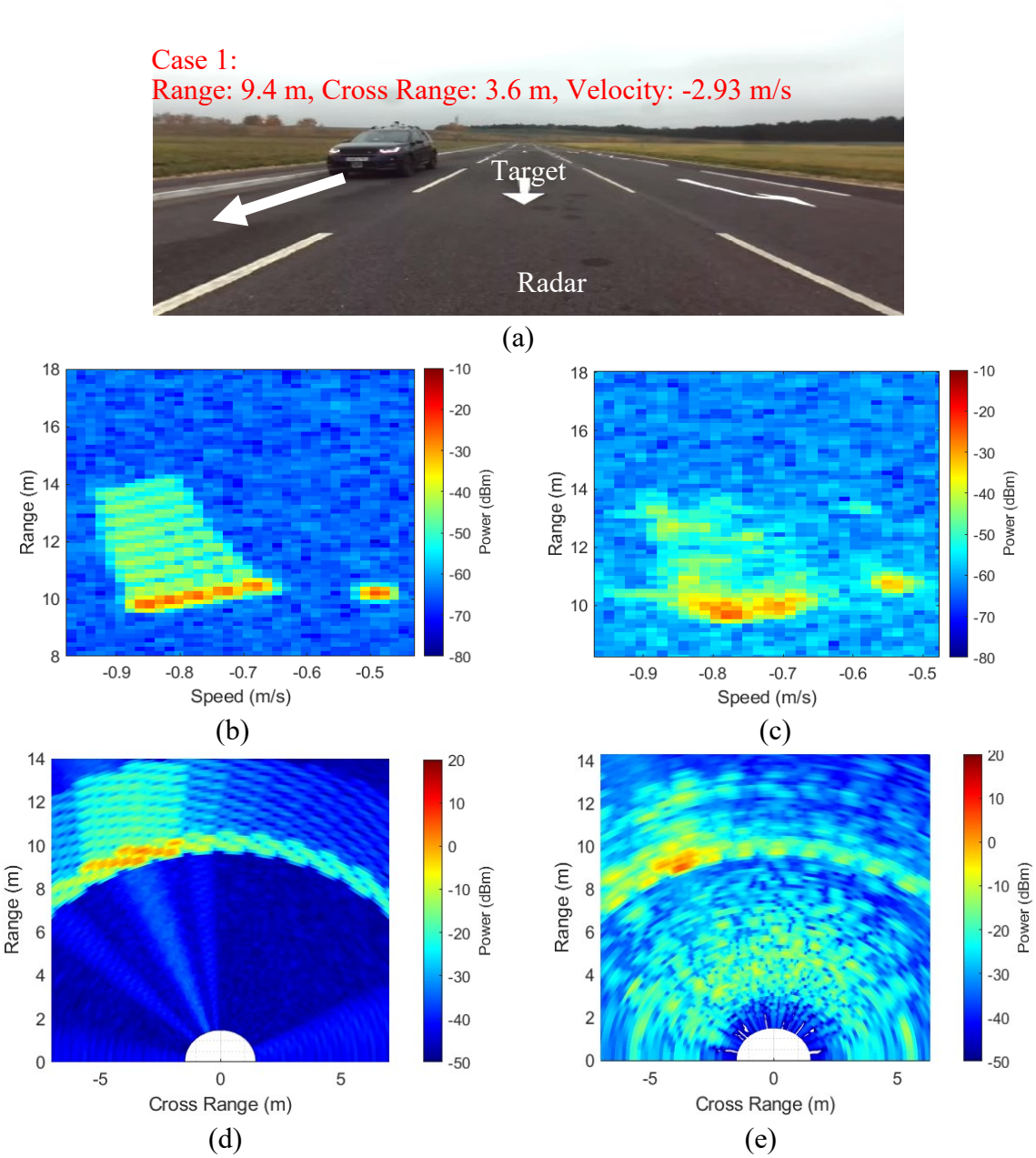


Figure A12.9: Modelled and measured results of the extended target at 9.4 m from the vehicle with ego radar. (a) Test setup, (b) modelled range-Doppler, (c) measured range-Doppler, (d) modelled range cross-range, (e) measured range cross-range.

As the target approaches closer to the ego radar, more target area is illuminated by the radar antenna beam. This results in a larger number of scattering points from the target. Due to a difference in the relative Doppler and radial velocities of these scattering points (different aspect angles), they spread along the range and Doppler bins. Consequently, the returns from the target are distributed across a larger extent of azimuth angles. In Figure A12.10, the target

vehicle is much closer to observing radar (1.8 m). Therefore, the extent of the target along the range and Doppler spread is greater than the case in Figure A12.9.

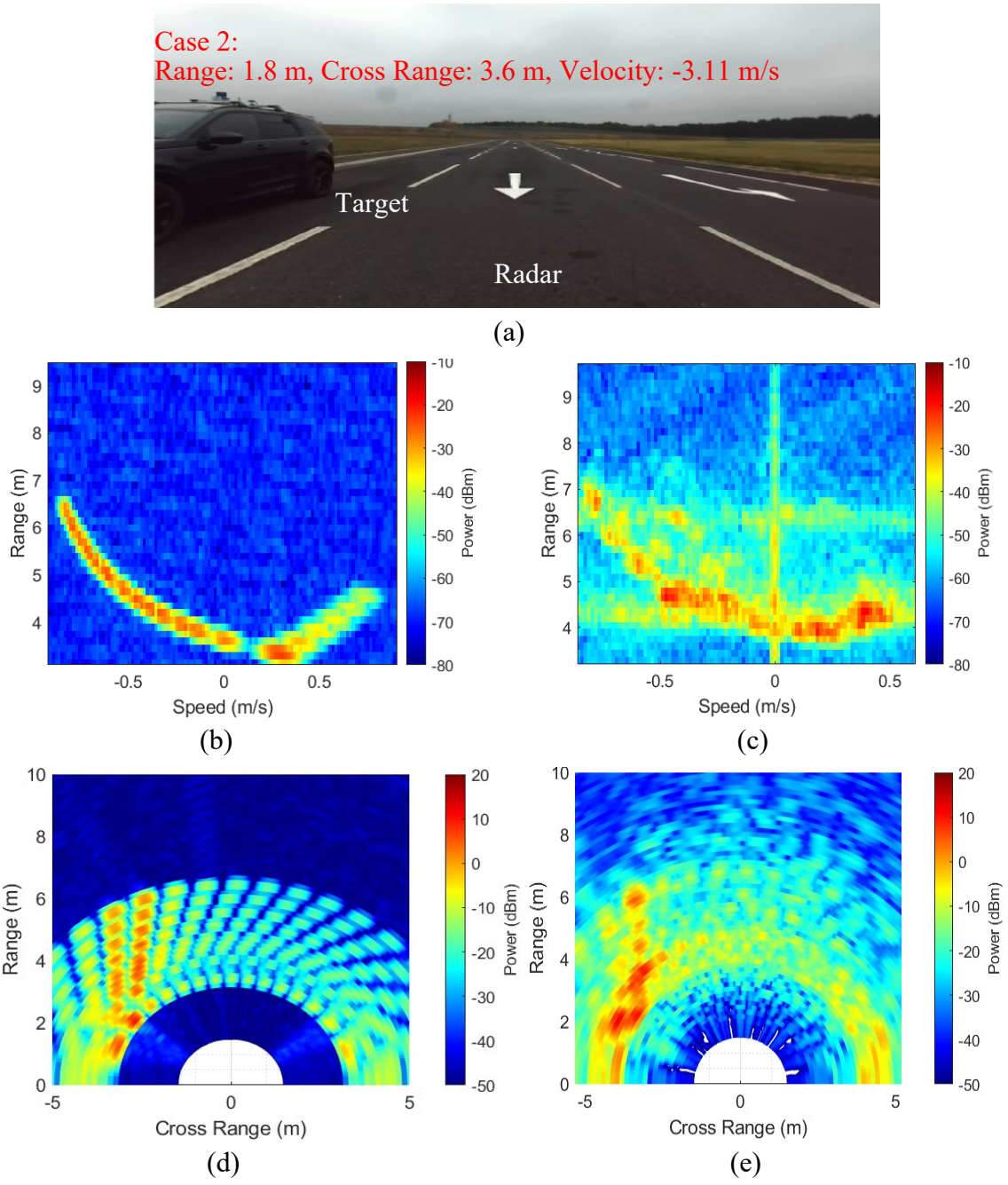


Figure A12.10: Modelled and measured results of the extended target at 1.1 m from the vehicle with ego radar. (a) Test setup, (b) modelled range-Doppler, (c) measured range-Doppler, (d) modelled range cross-range, (e) measured range cross-range.

It is to be noted that in the measured data, the clutter has not been removed. Nevertheless, it can be removed using a moving target indicator (MTI) filter.

II. Clutter Distribution

With a progression toward image-like radars, the clutter needs to be modelled for applications such as vehicle trajectory estimation and path planning.

The surface sensitivity to the EM waves is essential for its imagery. However, with higher frequencies, the increased surface roughness makes their imagery at relatively lower grazing angles and longer ranges possible [380]. The boundary between smooth and rough surfaces has been estimated from the Rayleigh roughness criterion [381], given as:

$$R_r = \frac{2\pi}{\lambda}\sigma_h \sin\left(\theta_g\right) \tag{A12-3}$$

where, σ_h is the RMS surface height, and θ_g is the radar grazing angle. When $R_r < \pi/16$, the surface can be classified as electromagnetically smooth and ego radar receives negligible backscatter from these surfaces, making their imagery relatively difficult. With increased diffused scattering, backscatter is received to a greater extent, and the surface can be imaged.

The clutter includes reflections from the road, grass, roadside infrastructure, and multipath from the infrastructure/ road actors. On a chirp-to-chirp basis (slow-time), the background clutter is correlated and appears as a static target at the 'zero' Doppler. Terrain and road infrastructure are surface distributed, and their reflectivity depends upon the grazing angle and surface roughness, and given as:

$$\sigma = \sigma^o A \tag{A12-4}$$

where, σ^o is the normalised RCS of a particular terrain, and A is the clutter area.

Each region of the surface has been represented by a number of secondary radiators with scattering points separated by $\lambda/2$. This gives $A = (\lambda/2)^2$. Furthermore, each scattering point has RCS according to the area occupied by the secondary radiator. The return from each cell is the sum of individual returns within the cell according to a specific propagation model.

The test scene presented in Figure A12.11 (a) has been used to model clutter.

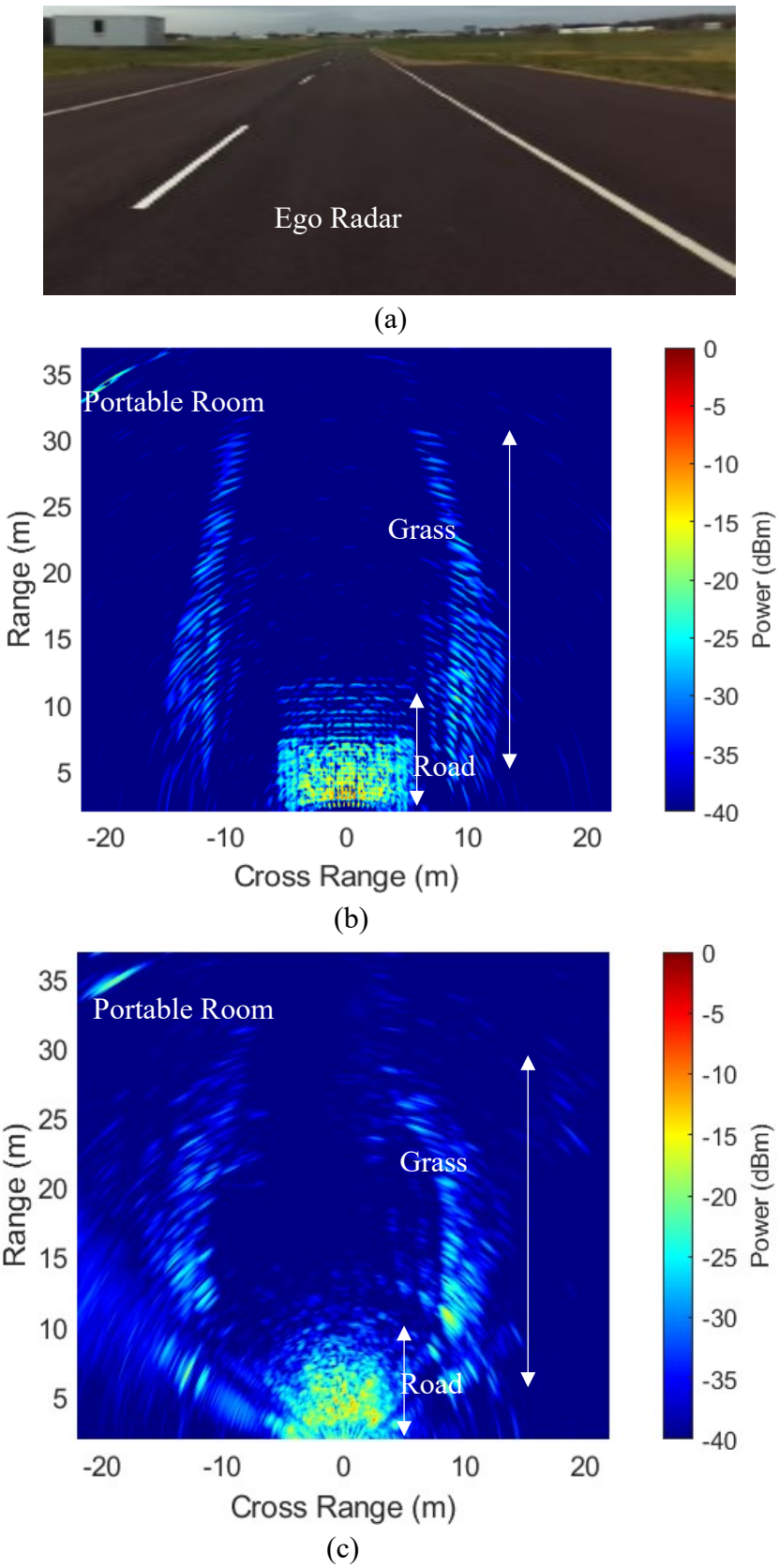


Figure A12.11: Clutter response: (a) test Scene, (b) model, (c) measurement.

Two significant reflecting regions, each with different reflectivity, have been identified: 1) road made of tarmac and 2) roadside grass. In the developed model, σ^o = -40 dB for road surface [382], and by comparing the difference of mean values of grass and road distributions given in [383], σ^o = -22.8 dB for grass. The modelled and measured results have been shown in Figure A12.11 (b) and (c), respectively. Due to a higher reflectivity and roughness of grass, it has been resolved at longer ranges than the reflections from the road that are only visible closer to the radar.

A12.3.3. Multipath propagation from Reflective Infrastructure

In a dense urban scenario, along with the LoS returns from the target, non-line of sight (NLoS) returns due to EM waves reflecting from the nearby reflectors (buildings, guard rails) are also received. These constitute multipaths and create false targets in processed radar data.

For a single bounce, configuration A occurs when the signal travels from the radar to targets, then to the reflecting surface, and back to the radar. In contrast, configuration B occurs when the signal travels from the radar to the reflecting surface, then to the target, and back to the radar. The false targets corresponding to single and double bounce multipaths are more significant and demonstrated in Figure A12.12.

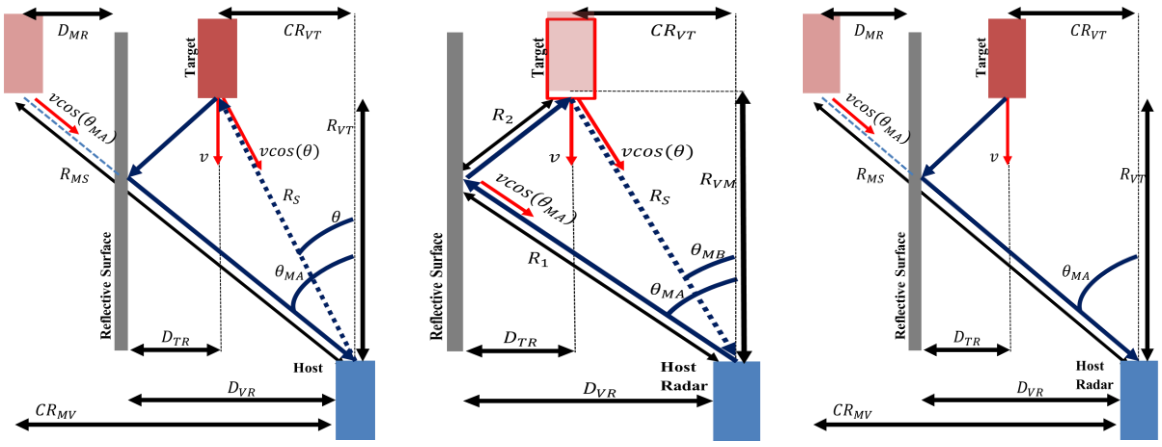


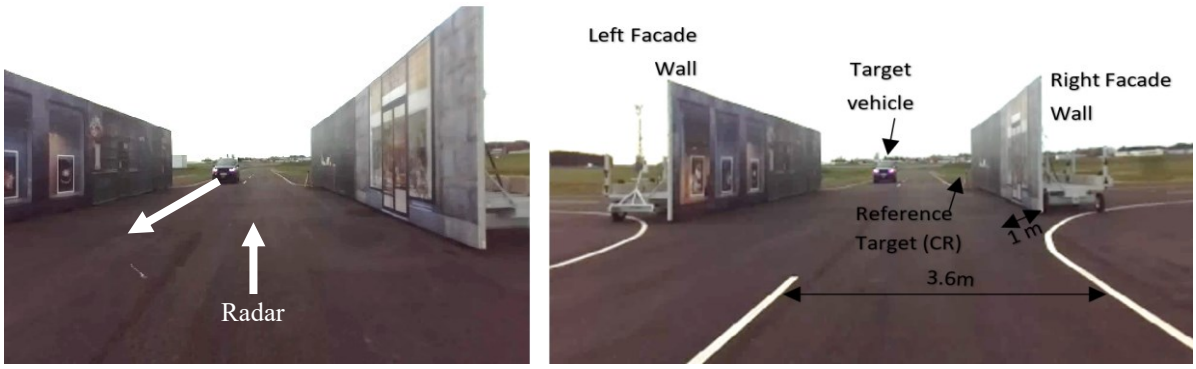
Figure A12.12: Appearance of false targets due to multipath: (a) single bounce – configuration A, (b) single bounce – configuration B, (b) double bounce.

The methodology to estimate the range, velocity, and azimuth of the false targets due to multipath has been given in Table A12.2. Depending upon the position of reflecting surfaces around the road, these values have been used in the model to generate additional false targets.

Table A12.2: One-way range, velocity, and the azimuth of false targets from multipath.

Parameter	Single Bounce: Configuration A	Single Bounce: Configuration B	Double Bounce
R_S	$\sqrt{R_{VT}{}^2 + (D_{VR} - D_{TR})^2}$		
R_{MS}	$\sqrt{R_{VT}{}^2 + (D_{VR} + D_{TR})^2}$		
Azimuth	$\cos^{-1}\left(R_{VT} / R_{MS}\right)$	$\sin^{-1}\left(D_{VR} - D_{TR} / R_{MS}\right)$	$\cos^{-1}\left(R_{VT} / R_{MS}\right)$
Range	$\left(R_s + R_{MS}\right)/2$		$\sqrt{R_{VT}{}^2 + \left(D_{VR} + D_{TR}\right)^2}$
Velocity	$\frac{1}{2} v\cos(\theta) + \frac{1}{2} v\cos(\theta_{MA})$		$v\cos\left(\theta_{MA}\right)$

To depict a reflective urban scenario, 15 m brick wall facades have been positioned in a linear arrangement along each side of the road with a lane width of 3.6 m. The test setup has been shown in Figure A12.13 (a), with the full extent of facades in Figure A12.13 (b).



(a) (b)

Figure A12.13: Test setup for a reflective scenario: (a) scene corresponding to modelled results, (b) the full extent of facades.

The modelled and measured results showing the appearance of false targets have been shown in Figure A12.14. The vehicle with ego radar (2.3 m/s) and the target vehicle (2.4 m/s)

have been driving in adjacent lanes in the opposite direction. A CR has been positioned 0.5 m before the right facade wall and 2.3 m (cross-range) from the radar.

False targets appear on opposite sides of the facades that are the mirrored version of the true target with respect to facades. As shown in Table A12.2, the true target (vehicle) has the shortest range compared to the multipath arising from the target. Due to different AoA and radial speeds of the multipath, the true and false targets have been resolved in the Doppler and azimuth domains. Moreover, due to a different aspect angle (hence radial velocity) of each reflection point from the facade walls, the full extent of the walls is visible in the processed radar imagery in Figure A12.14.

Although the MIMO array provides enhanced angular resolution compared to the traditional phased arrays with the same number of physical elements, the beamformed response have comparatively higher sidelobes due to one-way effective sidelobe level. Moreover, cross-range resolution depends upon the azimuth resolution and degrades as a function of range to the target. This reduces the target's resolvability, especially at a longer range from the radar. DBS beamforming has been used in the developed model to enhance target resolution by utilising the Doppler frequency difference from the targets at different azimuth angles [20]. Figure A12.14 (c) shows the modelled and measured results after applying MIMO-DBS beamforming for resolution enhancement. A significant reduction in the MIMO sidelobes has been observed after MIMO-DBS beamforming, and the full extent of walls is visible and well-resolved. It is to be noted that the amount of resolution enhancement after DBS beamforming depends upon the ego vehicle velocity, which in the discussed case was 2.3 m/s. However, higher velocity is expected in a roadside scenario, further enhancing resolution.

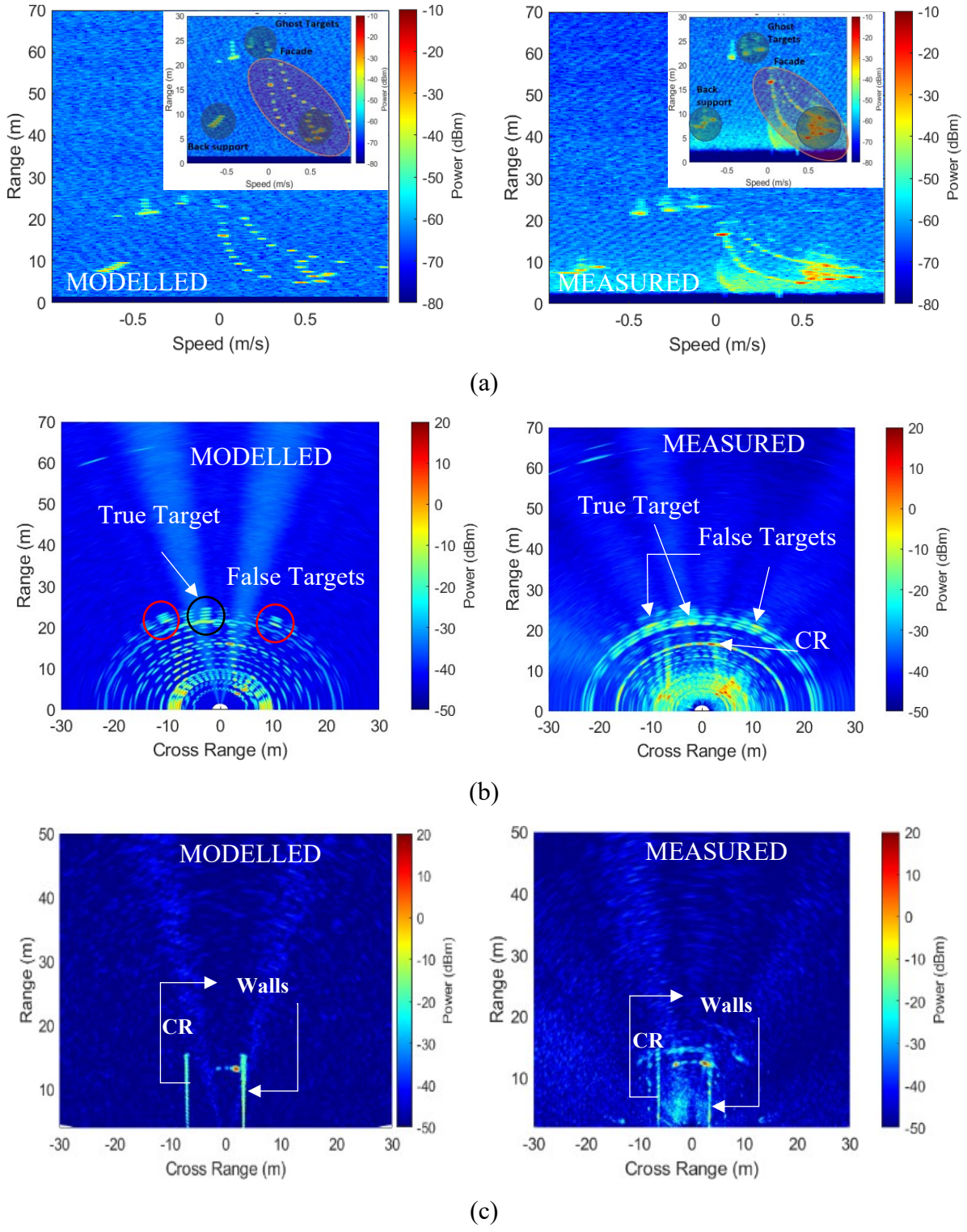


Figure A12.14: Modelled and measured results showing the appearance of false targets: (a) range-Doppler, (b) range cross-range: MIMO beamforming, (c) range cross-range: MIMO-DBS beamforming.

A12.4. Radar Architecture and Modelling

A typical radar processing consists of the following:

1. Analogue signal processing performed at AFE, where down conversion, filtering, and analogue to digital conversion occur,
2. Calibration for amplitude and azimuth/ elevation alignment, and
3. DSP, which can be described as the 3D-FFT and advanced signal processing on the radar data cube.

Each part has been discussed in this section.

A12.4.1. Analogue Signal Processing

The AFE of radar has been modelled according to

- Hardware configuration with specific Tx and Rx array setup (TDM-MIMO, SIMO),
- Antenna and channel gains,
- Waveform parameters, including the modulation scheme,
- Low pass filtering and
- Analogue to digital conversion

The analysis of AFE has been presented in detail in Chapter 7. A summary is included in this section.

I. Antenna Configuration

The aspect-angle dependent antenna gains of all the sensors mentioned in Appendix 11 have been used to estimate the transmitted/ received signal power as a function of the spatial location of targets. The element pattern of each sensor has been generated according to the manufacturer's specification sheet and given in Figure A12.15.

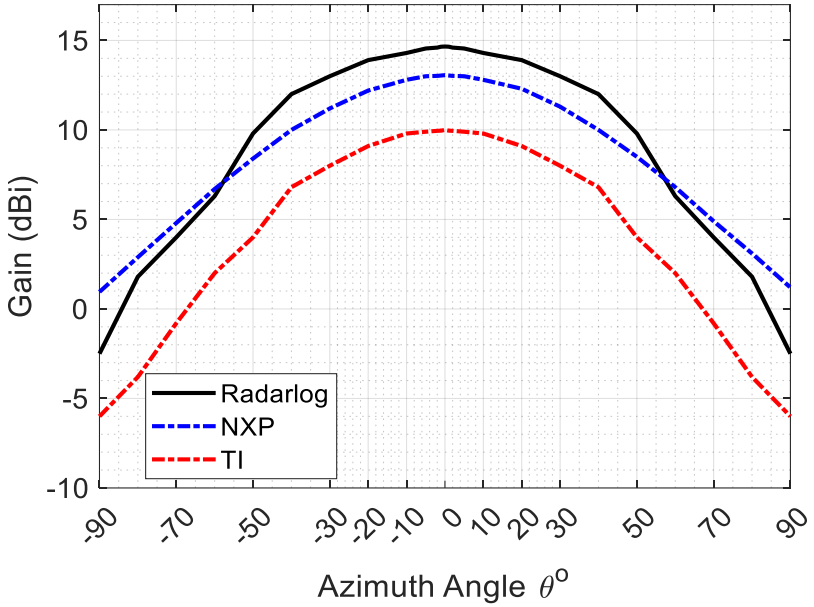


Figure A12.15: Element patterns of the radars used during measurements.

The element pattern of Radarlog is similar to Radarbook.

II. Signal Propagation

In the discussed scenario, the identified propagation model is a two-ray model. Therefore, the received power from a target located at (θ,φ) where θ and φ are the azimuth and elevation angles of the target with respect to the ego radar, respectively, is given as:

$$P_R(\theta,\varphi)=\frac{P_t G_t(\theta,\varphi) G_r(\theta,\varphi)\lambda^2\sigma\cdot 16\sin^4\left(\frac{2\pi H_t H_r}{\lambda R}\right)}{(4\pi)^3 R^4 L} \tag{A12-5}$$

where $G_t(\theta,\varphi)$ and $G_r(\theta,\varphi)$ are the transmit and receive antenna gains as a function of the target's spatial position. For TDM-MIMO, each Tx element transmits the signal at a specific time slot that, after propagation and scattering, is received by individual Rx elements of the radar. Therefore, the azimuth and elevation pattern of each Tx and Rx patch element as a function of angles within the radars' FoV have been modelled and used to define $G_t(\theta,\varphi)$ and $G_r(\theta,\varphi)$ for each reflection point.

III. Link Budget Analysis

While modelling each stage of the AFE, along with the signal processing aspect, each stage's respective gains/ losses have also been incorporated for the correct power budget estimation of the processed signal. The equivalent power contribution of AFE is $P_{AFE} = G_{LNA} + G_{VGA} + L_{Mixer} + P_{FS} + G_{ADC}$ where, G_{LNA} = 42 dB and G_{VGA} = 20 dB are the gains of LNA and VGA, respectively, L_{Mixer} = 20log(0.5) represents the loss due to double sideband to single sideband conversion at the mixer, P_{FS} represents the full-scale ADC input power after which the signal is clopped. For 2 $V_{p\text{-}p}$ amplitude across a 50 ohm resistor for the ego radar, P_{FS} is 10 dBm, $G_{ADC} = 6.02N_{ADC} + 1.74$ represents ADC gain [285], and N_{ADC} = 16 ADC bits for the ego radar. With these parameters, P_{AFE} = 164 dBm.

IV. Low Pass Filtering

The LPF is incorporated in the processing chain of all automotive sensors to remove higher frequencies and limit the unambiguous detection range. The LPF specifications, such as filter type and filter order (section 3.3), are required for accurate radar modelling, especially in a coexistence automotive scenario, where interference is also received by the ego radar. However, these parameters are generally omitted in the manufacturer's radar specifications. Therefore, various types of LPF with finite and infinite impulse responses have initially been modelled. The modelled and measured interference duration for each filter type/ order was then used as a performance metric. After comparison, a 7^{th} order infinite impulse response LPF was selected. It provided the best agreement with the measured interference duration from TI radar (16 μs), according to parameters in Table A11.1. Furthermore, as the frequency of the down-converted signal in automotive radars is much lower than the transmit frequency, for instance, from 60 kHz – 10 MHz for the ego radar parameters in Table A11.1, a finite impulse response

decimation filter has additionally been used after the LPF to reduce the ADC sampling requirements.

The processed results after the LPF are shown in Figure A12.16 for each Tx node. The received signal is a sum of the echo signal from the target vehicle at 10 m and interference from the TI radar.

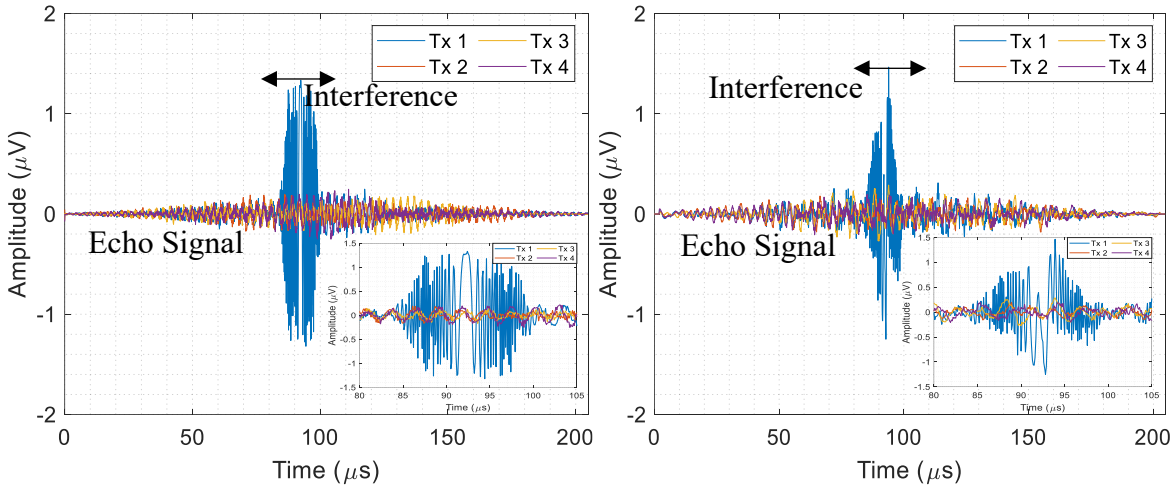


Figure A12.16: Received signal after filtering in the presence of interference from TI radar: (a) model, (b) measurement.

The radar data cube was then generated with fast-time samples, slow-time samples, and MIMO virtual array channels along the first, second, and third dimensions, respectively.

A12.4.2. Radar Calibration

For offline processing, the raw data from sensors is obtained after the ADC stage at the chipset. Therefore, additional calibrations are required for the following:

- Amplitude scaling to compare the results with theoretical power estimates based on the path loss model,
- Azimuth alignment to mitigate the effects of the sensor's hardware impairments.

These calibrations have been discussed in the subsequent sub-sections.

I. Amplitude Scaling

Amplitude scaling has been performed by normalising the raw ADC data with estimated P_{AFE}, discussed in section 12.4.1.III.

II. Azimuth Calibration

In an ideal scenario, transmission line length and signal propagation delay across each transmit and receive path is the same, considering no deliberate delay is added, such as to resolve targets along elevation. This results in an equal phase difference of the echo signal across the adjacent propagation paths, given as:

$$\Delta\psi = kd\sin(\varphi) \tag{A12-6}$$

where, φ is the AoA.

However, in an actual scenario, the transmission line lengths of various propagation channels of the radar are not similar. This results in additional phase shifts across the channels. Therefore,

$$\Delta\psi_i = kd\sin(\varphi) + \phi_i \tag{A12-7}$$

where, ϕ_i is the additional phase due to different transmission lengths and is different between each pair of transmission paths. For example, $\Delta\psi_1$ between pairs Tx1Rx1 and Tx1Rx2 will differ from $\Delta\psi_2$ between Tx1Rx2 and Tx1Rx3. To compensate this phase difference, azimuth calibration has been performed across the MIMO channels by $\exp(-j\phi_i)$, where ϕ_i = 1:*N*, and *N* is the number of MIMO channels. This aligns the azimuth beam toward the correct AoA. A similar approach has been used for the alignment of the elevation angle.

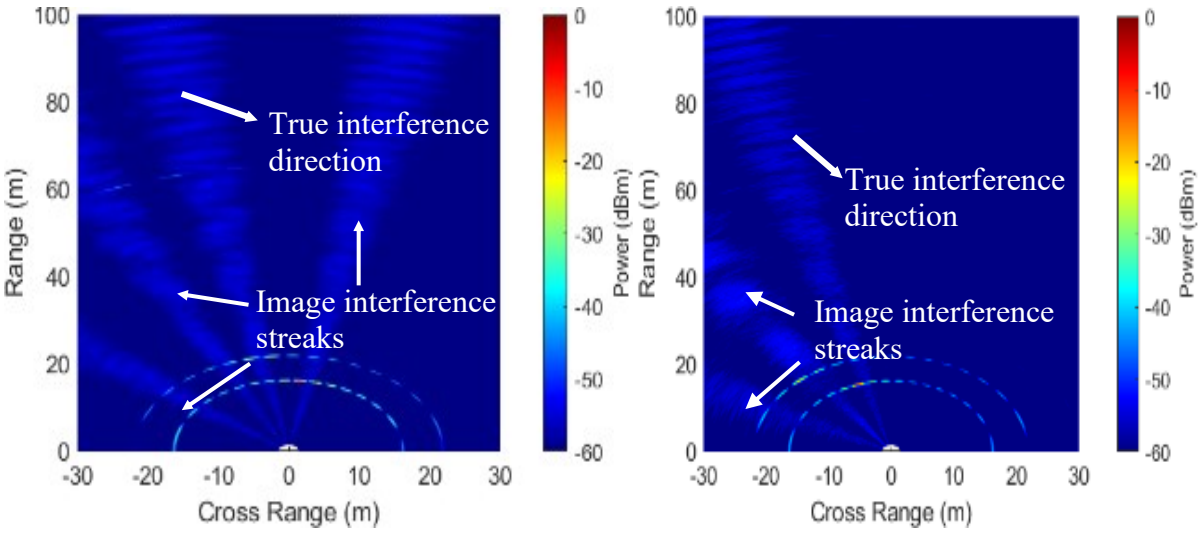
In the presence of interference, for a single (real) channel receiver used in the ego radar, interference contributions from positive (I^+) and negative (I^-) frequency components cannot be separated and appear across the whole frequency spectrum (Appendix 6). Therefore, the

azimuth beam for interference appears along two AoA – one towards its actual direction and one towards the image direction [144]. After azimuth calibration, the calibration factors corresponding to I^+ (actual direction) and I^- (image) can be defined as follows:

$$\begin{aligned} I^{+} &\propto \exp\left(j\left(kd\sin\varphi+\phi_i\right)-j\phi_i\right) = \exp\left(j\left(kd\sin\varphi\right)\right) \\ I^{-} &\propto \exp\left(-j\left(kd\sin\varphi+\phi_i\right)-j\phi_i\right) = \exp\left(j\left(kd\sin\varphi-2\phi_i\right)\right) \end{aligned} \tag{A12-8}$$

As observed, the actual direction of the interferer has been calibrated correctly. However, the direction corresponding to image frequency has not been calibrated; instead, it shifted to $2\phi_i$ [191]. As each MIMO channel is calibrated with a unique phase shift, the image angle smears along the azimuth.

Different azimuth calibration vectors should be applied for different radar chipsets due to different propagation paths between the channels. Consequently, interference streaks due to the image channel will have a unique appearance. The modelled results for two radar sensors have been shown in Figure A12.17.



(a) (b)

Figure A12.17: Azimuth calibration effect on interference: (a) Radarlog (64 MIMO channels), (b) Radarbook (32 MIMO channels).

The position of image channel interference streaks depends upon the specific calibration vector used for azimuth alignment, which is unique for each radar chipset. Moreover, different numbers and the appearance of interference streaks have been observed depending on the total MIMO channels. With an increase in the number of MIMO channels, due to increased ϕ_i variations, the smearing due to image interference angle is expected to increase.

A12.4.3. Digital Signal Processing

Various stages of DSP incorporated in the simulator are illustrated in Figure A12.18.

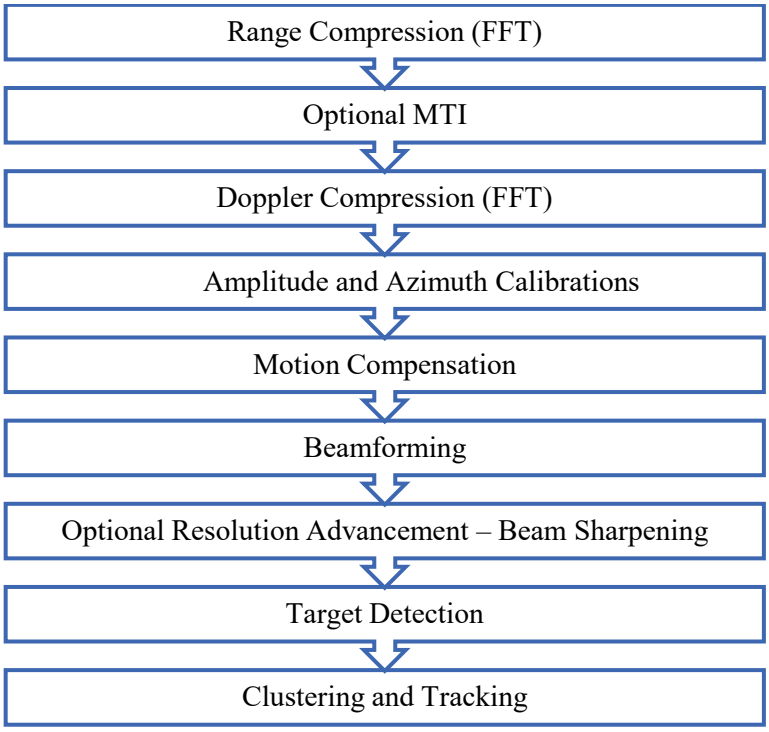


Figure A12.18: Stages of digital signal processing incorporated in the simulator.

DSP in the model is based on the 3D-FFT to estimate the range, relative speed, and azimuth direction of the targets, respectively. In the model, additional HPF with a cut-off range of 2 m has also been applied before FFT to remove transmitter feedback to the receiver and suppress stronger returns from targets at shorter ranges that might saturate the receiver amplifiers. The Blackman Harris window has been applied across fast-time, and the Hann window across the slow-time and antenna elements.

For MIMO radar, motion (phase) compensation has also been applied across the virtual elements to compensate for the velocity-induced phase shift across transmit elements. For N_{Tx} transmit elements, the time delay due to their position is given as follows:

$$\tau_{Tx-Delay} = (0 : N_{Tx} - 1) \cdot T_{sv} \tag{A12-9}$$

The corresponding phase shift vector due to radar velocity can then be defined as:

$$\theta = \frac{4\pi v \tau_{Tx-Delay}}{\lambda} \tag{A12-10}$$

Therefore, the phase-compensated signal is represented as:

$$S_{comp} = S_{uncomp} \cdot \exp(-j\theta) \tag{A12-11}$$

Additional processing stages for target detection and tracking have been mentioned in Figure A12.18 that can be incorporated into the simulator for vehicle path planning.

A12.5. Interference Detection and Mitigation

Interference detection and mitigation are discussed in detail in Chapter 5 - Chapter 8. Various discussed techniques have been incorporated into the simulator, as demonstrated in Figure A12.19.

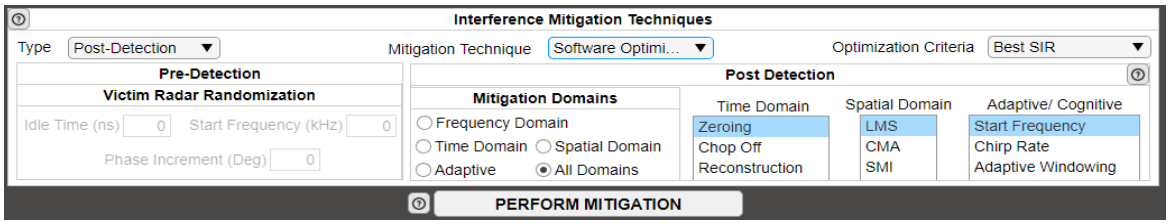


Figure A12.19: Interference detection and mitigation interface.

Various pre-detection and post-detection mitigation techniques have been implemented.

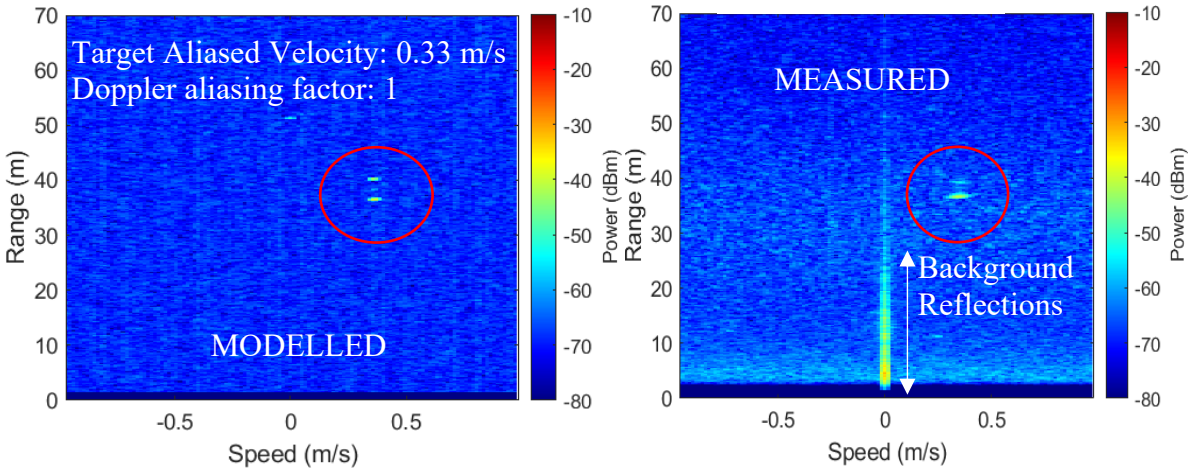
A12.6. Validation and Data Analysis

The measurement setup shown in Figure A12.20 has been used to validate the developed models. The position and velocity of the target vehicle for each scene have also been shown.

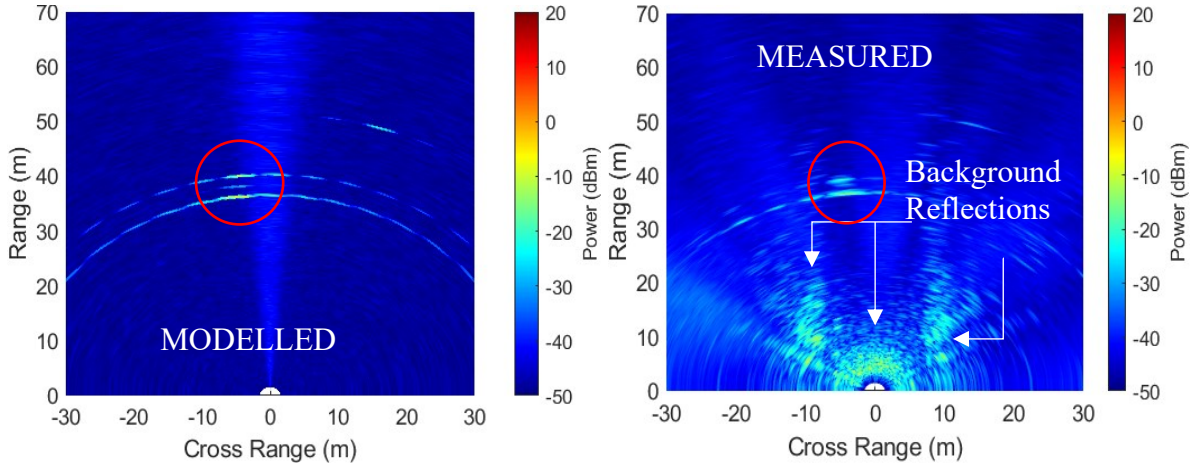
The corresponding modelled and measured results for three corresponding Radarlog frames have been presented in Figure A12.21 - Figure A12.23 (a) and (b) as the range-Doppler and range cross-range maps after beamforming, respectively.



Figure A12.20: Snapshots of measured scenarios with different positions of the target vehicle.



(a)



(b)

Figure A12.21: Modelled and measured results corresponding to case 1 from Figure A12.20. (a) Range-Doppler, (b) range cross-range.

In this setup, the ego vehicle equipped with Radarlog is static, and the target vehicle with sensors and parameters in Appendix 11 has been driving towards it. Vehicle velocity has been measured using a high-precision IMU. Backscatter from clutter has not been included to highlight only target returns in the model. Though, it can be modelled according to the approach discussed in section A12.3.2.II. The Blackman Harris window has been applied across the fast-time, and the Hann window across the slow-time and antenna elements.

The target's velocity is defined as $v = -\lambda f_D / 2\cos\theta$, where f_D is the Doppler frequency and θ is the AoA of reflection point from the target. According to the defined parameters, Radarlog's MIMO frame interval is 1 ms, which limits unambiguous velocity $\left(v_{\max}\right)$ to ± 0.98 m/s. Target velocity '*v'* greater than this is aliased and appears within the interval $-v_{\max}$ to $v_{\max}$ with value v'. These velocities are related by:

$$v = v' \pm 2nv_{\max} \tag{A12-12}$$

where, *n* is the Doppler aliasing factor (integer). The scattering points spread along the range and the Doppler bins due to different radial velocities and azimuth separation.

Due to a larger distance between the radar and target in Figure A12.21, there is a relatively small target extent across the range and Doppler. However, as the target vehicle approaches closer to the ego radar, more region is illuminated by the radar antenna beam. Moreover, more scattering points from the target are resolved due to increased cross-range resolution, and the target appears as a true 'extended' target. Due to a difference in the relative Doppler and radial velocities (different azimuth), the scattering points from the target spread along the range and Doppler bins, and the returns from the target are distributed across a larger extent of azimuth angles, as demonstrated in Figure A12.22.

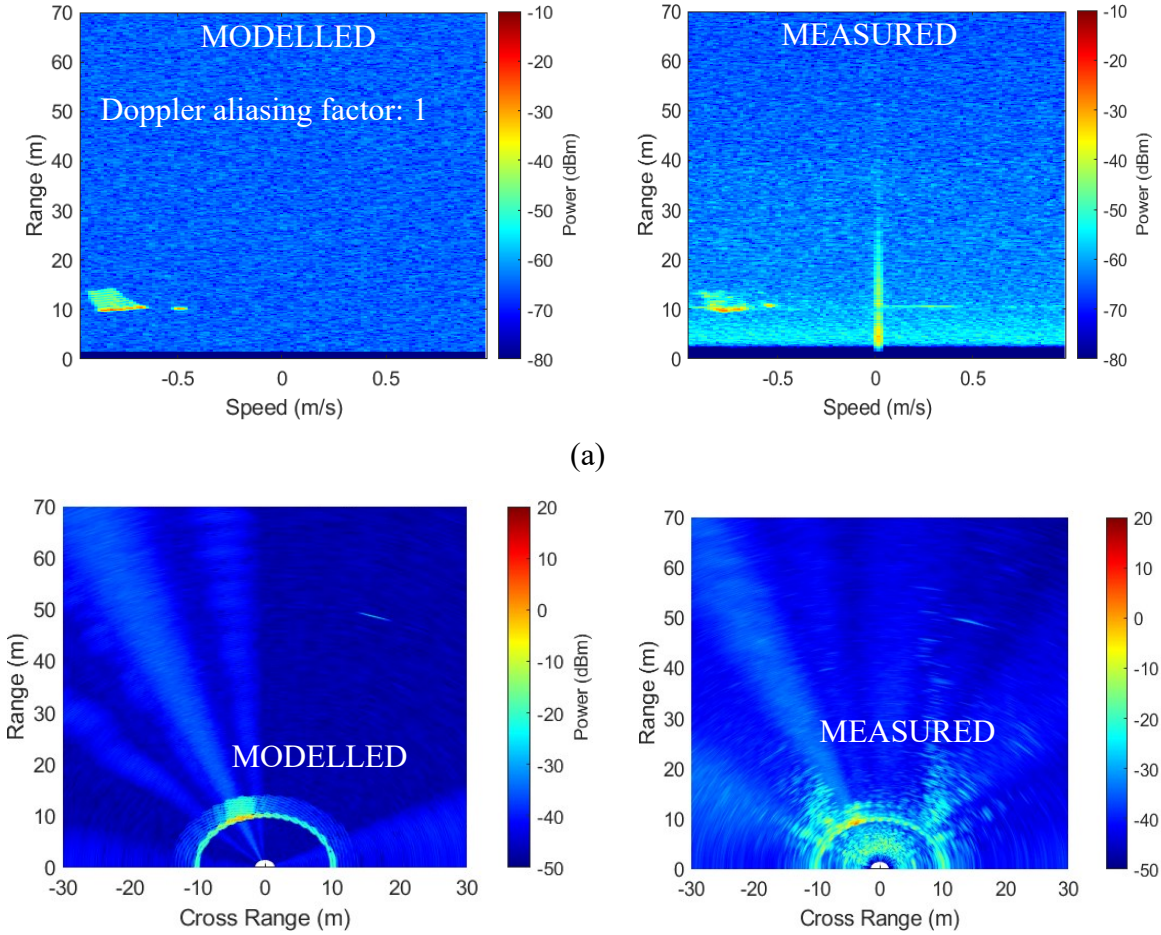


Figure A12.22: Modelled and measured results corresponding to case 2 from Figure A12.20. (a) Range-Doppler, (b) range cross-range.

The extent of the target along the range (N_R) and Doppler (N_D) bins has been estimated as follows:

$$N_R = \frac{R_s}{\Delta R} \tag{A12-12}$$

$$N_D = \frac{v\cos(\theta)}{\Delta v} \tag{A12-13}$$

where, R_s is the range spread, ΔR is the range resolution, v is the relative speed, and Δv is the velocity resolution. With the target's position indicated in Figure A12.22 (9.4 m), the range of

azimuth angles from the front of the vehicle are $15.7^o - 25.8^o$. The extent of the target along the range and velocity has been given in Table A12.3.

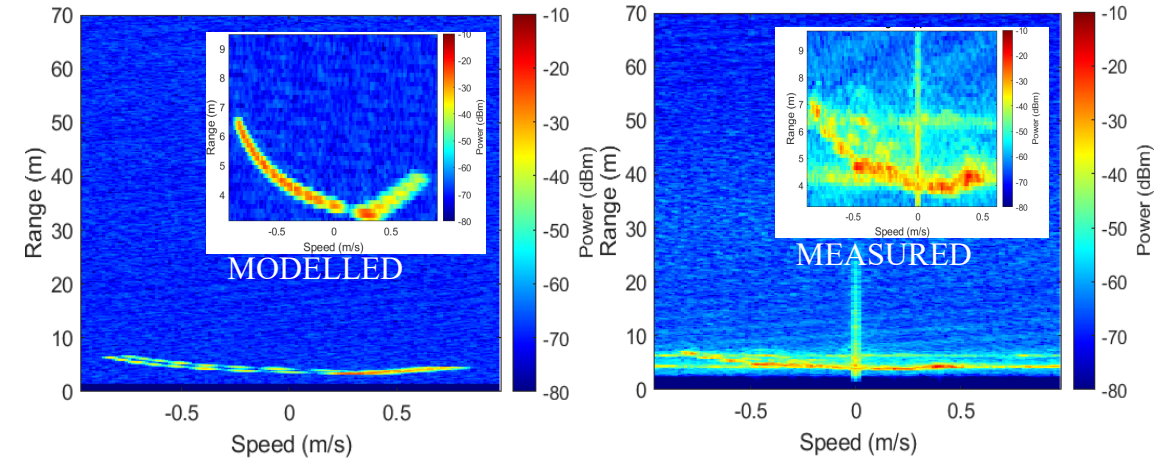
Table A12.3: Target distribution for case 2 from Figure A12.20.

Target Velocity	- 2.93 m/s	Aliased Velocity	- 0.78 m/s
Number of Range Bins			
(Range Spread/ Range Resolution)		Front: 12 (1.9/0.15)	Side: 26 (4/0.15)
Number of Doppler/ velocity bins			
Velocity Spread: $v\cos\theta/\Delta v$		12 (2.82-2.63)/0.015	

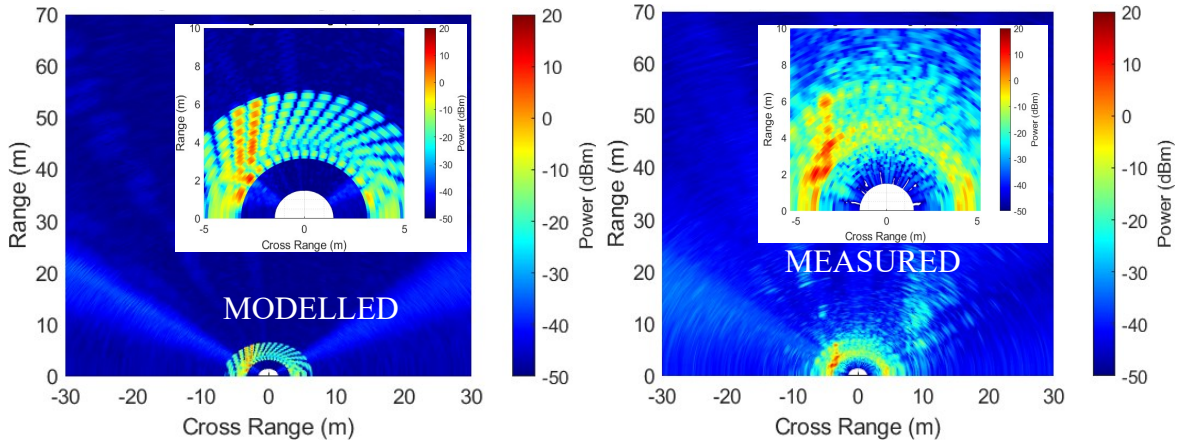
In Case 3 from Figure A12.20, the target vehicle is much closer to the host radar (1.8 m). Consequently, the extent of the target along the range and velocity axes is greater, as shown in Figure A12.23. In this case, major scattering points are from the front and side of the target vehicle, and the target distribution parameters have been given in Table A12.4.

Table A12.4: Target distribution for case 3 from Figure A12.20.

Target Velocity	-3.105483 m/s	Doppler aliasing factor	1
Front radial velocity spread: $v\cos\theta$		-1.63 to -1.317 m/s	
Side radial velocity spread: $v\cos\theta$		-2.75 to -1.63 m/s	
Number of Range bins			
Front: 7		Side: 29	
Number of Doppler/ velocity bins			
Front: 20		Side: 75	



(a)



(b)

Figure A12.23: Modelled and measured results corresponding to case 3 from Figure A12.20. (a) Range-Doppler, (b) range cross-range. Inserts show the zoomed region with the target.

The modelled and measured results show a close approximation demonstrating the suitability of the developed simulator for automotive scenarios.

Appendix 13. Digital Beamforming in MIMO Radar

Instead of using an FFT across the array channels of the radar, digital beamforming can traditionally be performed using the following steps.

1. Defining the radar's FoV from $\vartheta = -90^o$ to 90^o for an ideal array.
2. Computing a steering vector (SV) for each angle ϑ using $SV_n = \exp\left(jkd(n-1)\sin\vartheta\right)$.
3. Applying the SV to the received signal using: $S_{Rx} \cdot SV^*$. When this phase shift is applied to each array element, it allows the signal across each channel to add coherently towards ϑ.
4. Adding all received signals to form a beam towards ϑ.
5. Repeating the process for all values of ϑ, and the maximum value at the end gives the angle of arrival (AoA) of the received signal with the maximum response.

The process has been summarised in Figure A13.1.

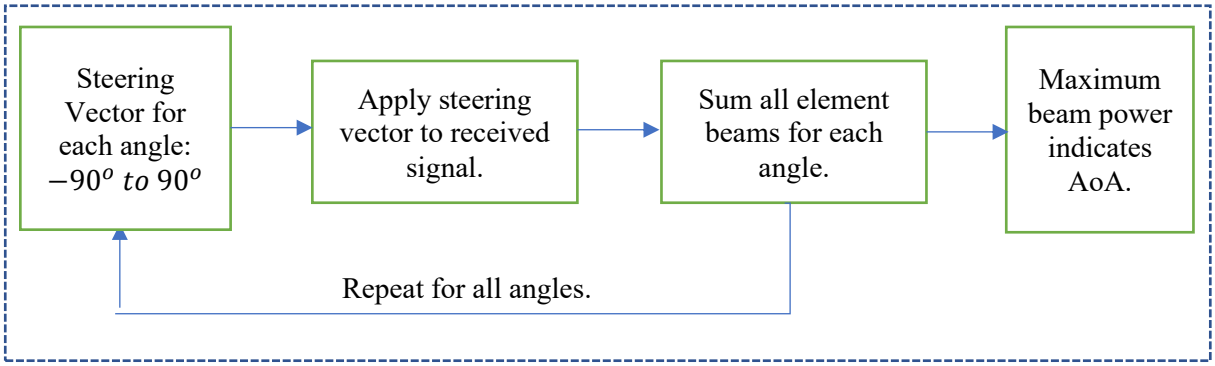


Figure A13.1. Block diagram of the digital beamformer.

Appendix 14. Spatial Mitigation in Congested Scenario - Validation

Spatial suppression of interference has been performed in an outdoor scenario to validate the developed model. Multiple targets and interferers have been positioned in the FoV of the VR with a single channel receiver. The measurement setup and radar parameters are given in Figure A14.1 and Table A14.1, respectively.

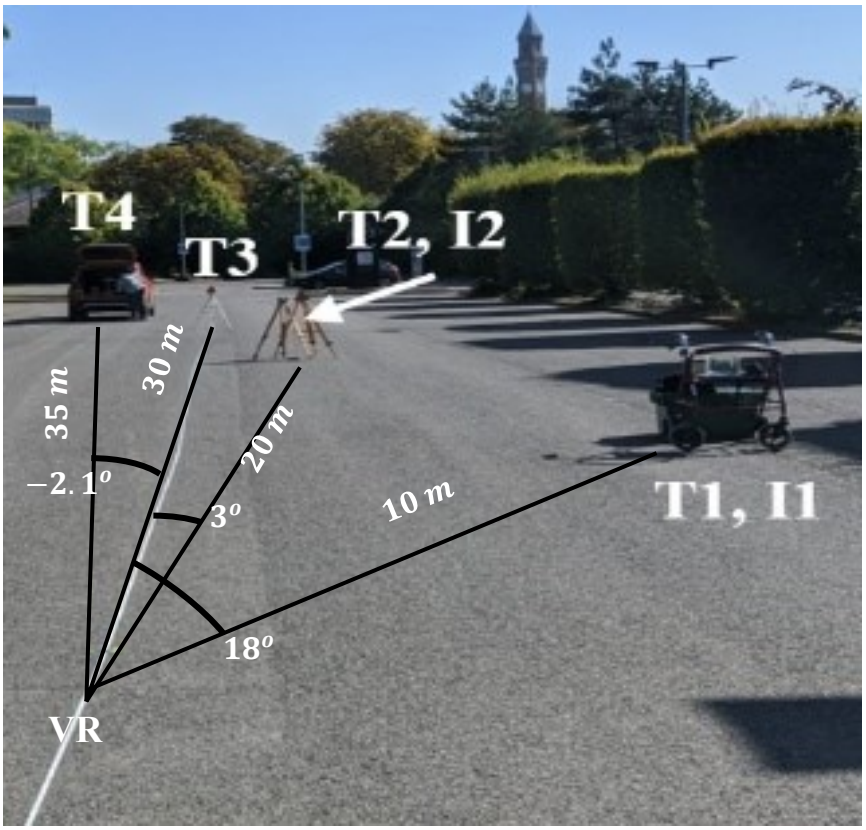


Figure A14.1: Outdoor measurement scenario with multiple targets and interferers.

NXP TEF810X was used as the VR, INRAS Radarbook and Gunn Diode were used to generate FMCW and CW interference, respectively. T1 and T2 have collocated interference represented as I1 and I2, respectively.

It is to be noted that due to a single channel receiver, each interferer appears at two angles after beamforming (Appendix 4 and Appendix 6). Therefore, two nulls are required in the spatial domain to suppress interference completely.

Table A14.1: Targets/ interferer positions and radars parameters for multiple targets and interferers scenario.

Radar parameters	
VR: NXP TEF810X	$T_{sv} = 204.8\ \mu s,\ B_{sv} = 2$ GHz
IR: I1, INRAS Radarbook	$T_{\text{sint}} = 102.4\ \mu s,\ B_{\text{sint}} = 2$ GHz
IR: I2, Gunn Diode	CW
Target/ interferer positions	
T1 (Corner reflector), I1	10 m, 18^o
T2 (Corner reflector), I2	20 m, 3^o
T3 (Corner reflector)	30 m, 0^o
T4 (Car)	35 m, -2.1^o

Figure A14.2 demonstrates the modelled and measured array response after spatial suppression. Spatial nulls have been directed at the interferers' positions at $\pm 3^o$ and $\pm 18^o$. However, as discussed in section 6.6, placing a null closer to the target results in much higher sidelobes, which are visible at $\pm 10^o$. Moreover, return power from collocated targets has been significantly reduced along with the power from targets at 0^o and -2.1^o.

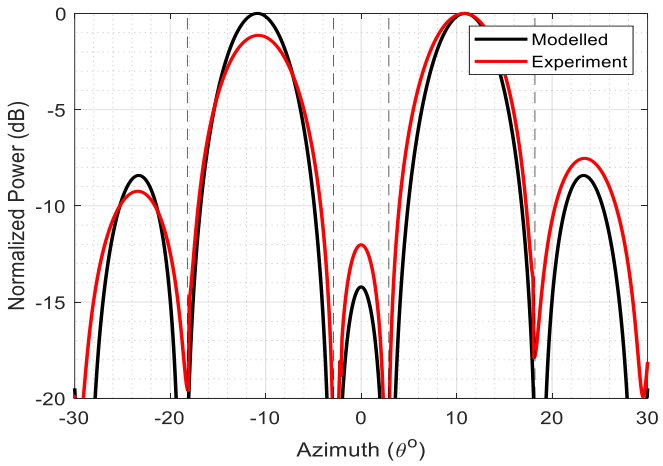


Figure A14.2: Modelled and measured array response after spatial mitigation.

It can therefore be observed that spatial mitigation effectiveness degrades in the presence of multiple interferers in the FoV of the VR, thus, deteriorating the radar performance.

Appendix 15. Limitations of Spatial Domain Mitigation

Adaptive beamforming suppresses interference to enhance the SINR for precise echo signal detection. However, typical adaptive beamformers suffer from considerable performance deterioration under mismatches [384], such as mismatch in the physical array propagation paths (discussed in Appendix 12, section A12.4.2.II) and AoA estimation errors. Moreover, as discussed in Chapter 6, mitigation of interference in the spatial domain depends upon the VR configuration, and often suppressing the interference is accompanied by detrimental effects on the performance of the VR.

Due to a broader interference resolution (according to the real aperture in MIMO radar), a broader null is placed in the direction of interference which:

1. Might suppress the energy from a nearby target and mask it.
2. Result in higher side lobes to conserve the total power.
3. Lead to a larger blind region in the radar's FoV.

The limitations of spatial domain mitigation, specifically for automotive scenarios, have been discussed below.

- Limited degrees of freedom

Spatial mitigation depends upon the number of nulls placed in the beamformed array pattern [385], [386]. In a linear array of M sources uniformly spaced at $\lambda/2$, $M-1$ nulls can be placed. However, nulling each direction would be difficult in a congested automotive environment with multiple interferers due to the limited size array in the SoA automotive radars.

- Convergence factor and computational complexity

Depending upon the spatial mitigation technique, adaptive beamforming to direct nulls towards the interferer direction has a significant computational complexity due to the following:

1. Converging the error between the desired signal and the beamformed signal after each iteration to a minimum value for iterative techniques (NLMS, LMS) or,
2. Computing spatial correlation coefficients (MVDR, LCMV)

Both of these might require either increased convergence time or computational duration.

However, with fast-moving vehicles, the interference vary rapidly with time, needing a fast response time in calculating the adaptive weights. Moreover, if lesser interference samples are available for training [216] or a large number of iterations are required to converge the error below a specified threshold, the weights might not converge during the convergence duration. This leads to incorrect nulls, which might suppress a potential target or generate false targets.

- Dynamic automotive scenario

In practice, there is often a relative motion between the interference and the VR. Since the AoA of each interfering signal is varies with time, the ADBF need to compute the appropriate adaptive weights at each time instant that create the main lobe towards the target's AoA and nulls towards the respective interferer's AoA. However, new interference sources from potentially different directions might appear during the time when the beamformer is processing a specific radar frame to estimate the correlation coefficients and adaptive weights. Therefore, the antenna pattern nulls estimated at the end of each radar frame might not consider these new interference signals, leading to the SINR degradation.

Additionally, the incident direction of the interference signal at the VR constantly changes. Due to the fast-moving interference sources or the VR motion, the AoA of interference may appear across multiple resolution cells. Moreover, the adaptive beamformer weights cannot be computed and updated in real-time according to the radar's surroundings. Consequently, interference might appear out of the adaptive nulls, which deteriorates the adaptive beamformer's performance.

A methodology based on null broadening has been proposed to keep interference within the nulls [387]. Some research has been carried out on null broadening techniques, including virtual interference sources, derivative constraints, and projection transformations [388]. This is, however, outside the scope of the presented work.

- Multiple targets and interferers

In case of multiple targets and interferer – considering that DoF is sufficient to place the required number of nulls – any target that is also a source of interference will have a null directed towards it. This will suppress the echo energy from the target. As the interference signal follows a real aperture, it will be notched out by a broader null compared to the null towards the target which will be narrower due to the virtual MIMO array. However, a significant amount of energy will still be suppressed from the target direction, making it undetectable in some instances.